



The  
University  
Of  
Sheffield.

Department  
Of  
Mechanical  
Engineering

EngD Resilient Decarbonised Fuel  
Energy Systems  
EngD Thesis

**Shock Tube Design and Fabrication for the  
Development of a Kinetic Model for  
Supercritical CO<sub>2</sub> Production**

[James M. **HARMAN-THOMAS**]

[30<sup>th</sup> June 2023]

**[Professor Mohamed Pourkashanian, Dr. Kevin J. Hughes]**

Thesis submitted to the Department of Mechanical Engineering,  
University of Sheffield in fulfilment of the requirements for the  
degree of EngD.

## **Abstract**

Direct-fired supercritical carbon dioxide (sCO<sub>2</sub>) power cycles offer emissions-free electricity production from the combustion of fossil fuels. Chemical kinetic mechanisms are validated for combustion at lower pressures and much lower CO<sub>2</sub> concentrations. The work critically investigates the ability of existing chemical kinetic mechanisms to simulate combustion under these conditions. This is done by investigating ignition delay time (IDT) data recorded using the shock tube experimental technique.

The first key chapter of this Thesis details the development of a new High-Pressure Kinetic Shock Tube (HPST) at the University of Sheffield's (UoS) Translational Energy Research Centre (TERC). The HPST will be utilised for the research of high-pressure chemical kinetics. The project was delivered in the summer of 2022, with commissioning taking until the end of the year. The HPST will be used in a variety of research projects at the TERC from the combustion of supercritical CO<sub>2</sub>, ammonia, and synthetic aviation fuels.

Chapter 3 details the development of a new chemical kinetic mechanism for modelling combustion in CO<sub>2</sub>. The University of Sheffield sCO<sub>2</sub> mechanism (UoS sCO<sub>2</sub>) was developed based on IDT datasets of methane, hydrogen, and syngas. The UoS sCO<sub>2</sub> Mechanism was developed and shown through a detailed qualitative analysis to be on average a better fit to the datasets measured for each of the three fuels.

Chapters 4 and 5 focus on the validation of the UoS sCO<sub>2</sub> 2.0, the second iteration of the mechanism in collaboration with King Abdullah University of Science and Technology (KAUST). Eight IDT datasets for both hydrogen and syngas and ten for methane and methane hydrogen blends were recorded using the KAUST High-Pressure Shock Tube between 20 and 40 bar. This data and subsequent modelling analysis are essential to the detailed understanding of the fundamentals of combustion in CO<sub>2</sub>.

# **Nomenclature and Units**

## **Abbreviations**

ADM	Archer-Daniels-Midlands
Ar	Argon
ASU	Air Separation Unit
BE-4	Blue Engine-4
BRF	Birefringent Filter
CCSU	Carbon Capture, Storage and Utilisation
CFD	Computational Fluid Dynamics
CO	Carbon Monoxide
CO <sub>2</sub>	Carbon Dioxide
CO <sub>2</sub> e	Carbon Dioxide Equivalents
CPOC	Cryogenic Pressurised Oxy-Combustion
CRV	Constrained Reaction Volume
DDA	Double Diaphragm Arrangement
DeSNO <sub>x</sub>	De-sulphur and Nitrogen Oxidation Removal Process
DFST	Diaphragmless Shock Tube
DME	Dimethyl Ether
EOR	Enhanced Oil Recovery
EoS	Equation of State
FHG	Fourth Harmonic Generator
FT	Fischer-Tropsch
GHG	Greenhouse Gas
GTC	Gas Turbine Cycle
GTI	Gas Technology Institute
H <sub>2</sub>	Hydrogen
H <sub>2</sub> O	Water
HPST	High-Pressure Shock Tube
IDT	Ignition Delay Time
ISW	Incident Shock Wave
KAUST	King Abdullah University of Science and Technology
IPCC	Intergovernmental Panel on Climate Change
MFC	Mass Flow Controller
MLO	Mauna Loa Observatory
N <sub>2</sub>	Nitrogen
NH <sub>3</sub>	Ammonia
NIR	Near Infra-Red
NO <sub>x</sub>	Nitrogen Oxides
O <sub>3</sub>	Ozone
ODS	Ozone-Depleting Substances
P&ID	Piping and Instrumentation Diagram
PM	Particulate Matter
PMT	Photomultiplier Tube
PZT	Piezo-Electric Pressure Transducer
RCM	Rapid Compression Machine
RDFES	Resilient Decarbonised Fuel Energy Systems
ROP	Rate of Production

RPA	Reaction Pathway Analysis
RSW	Reflected Shock Wave
SAF	Synthetic Aviation Fuels
sCO <sub>2</sub>	Supercritical Carbon Dioxide
SHG	Second Harmonic Generator
SOFC	Solid Oxide Fuel Cell
SO <sub>x</sub>	Sulphur Oxides
STEP	Supercritical Transformational Electric Power
SWRI	Southwestern Research Institute
TBHP	<i>tert</i> -Butyl Hydroperoxide
TERC	Translational Energy Research Centre
TRL	Technology Readiness Level
UN	United Nations
UK	United Kingdom
UoS	University of Sheffield
U.S.	United States of America
WiSTL	University of Wisconsin Shock Tube Laboratory

## Greek Symbols

$\delta$	Thickness of the Boundary Layer
$\phi$	Equivalence Ratio
$\theta$	Fuel Ratio
$\Delta\tau$	Observation Time
$\chi$	Length
$\gamma$	Specific Heat Ratio
$v$	Particle Velocity
$u$	Shock Velocity
$a$	Local Speed of Sound of a Gas

## Latin Symbols

$a$	Local Speed of Sound of Gas
$E$	Average Absolute Error
$M$	Mach number
$N$	Number of Datapoints
$p$	Pressure
$t$	Time
$T$	Temperature
$u$	Shock Velocity
$X$	Mole Fraction
$X_{exp,l}$	Experimental Datapoint
$X_{sim,l}$	Simulated Datapoint

## Units

atm	Atmosphere
bar	Bar
K	Kelvin
km	Kilometres

L	Litres
m	Metres
MHz	Megahertz
ms	Milliseconds
MW	Megawatt
MWe	Megawatt Equivalent
MWt	Megawatts Thermal
nm	Nanometre
ppm	Parts Per Million
μm	Micrometres

# Contents Page

## Preface

Abstract	I
Nomenclature and Units	II
Contents Page	V
List of Figures	XI
List of Tables	XVII
Acknowledgements	XIX
Declaration	XX

## Thesis

<b>1. Introduction</b> .....	<b>1</b>
<b>1.1. Motivation</b> .....	<b>1</b>
<b>1.2. Direct Fired sCO<sub>2</sub> Power Cycles</b> .....	<b>4</b>
1.2.1. The Allam-Fetvedt Cycle .....	5
1.2.2. Supercritical Transformational Electric Power (STEP) .....	9
<b>1.3. Other High-Pressure Combustion Systems</b> .....	<b>11</b>
1.3.1. Spaceship Engines.....	11
1.3.2. Scramjet/Ramjet Engines.....	12
1.3.3. Aviation Engines.....	12
<b>1.4. Knowledge Gaps Addressed in this Thesis</b> .....	<b>14</b>
<b>1.5. Thesis Overview</b> .....	<b>17</b>
<b>1.6. Conclusion</b> .....	<b>18</b>
<b>2. Fabrication of the University of Sheffield High-Pressure Shock Tube</b> .....	<b>19</b>
<b>2.1. Introduction</b> .....	<b>19</b>
<b>2.2. Types of Shock Tube</b> .....	<b>19</b>

2.2.1.	Incident and Reflected Shock Tubes .....	20
2.2.2.	Single Pulse Shock Tube .....	20
2.2.3.	Double Diaphragm Shock Tube .....	21
2.2.4.	Combustion-Driven Shock Tube .....	21
2.2.5.	Diaphragmless Shock Tube .....	21
2.2.6.	Convergent and Divergent Shock Tubes .....	22
2.2.7.	Inclined Shock Tube .....	22
<b>2.3.</b>	<b>Shock Tube Operation .....</b>	<b>22</b>
2.3.1.	Increasing Shock Tube Test Times .....	24
2.3.2.	Rapid Compression Machines .....	25
<b>2.4.</b>	<b>Non-Ideal Shock Tube Effects .....</b>	<b>26</b>
2.4.1.	Bifurcation .....	26
2.4.2.	Other Non-Ideal Effects .....	28
<b>2.5.</b>	<b>Shock Tube Concept .....</b>	<b>29</b>
2.5.1.	Initial Concept – Temperature and Pressure Range .....	31
2.5.2.	Driver and Driven Section Length .....	32
2.5.3.	Shock Tube Internal Diameter .....	35
2.5.4.	Relationship Between Mach Number, Temperature, and Pressure .....	36
2.5.5.	Maximum Pressure and Safety Factors .....	37
2.5.6.	Maximum Operating Temperature and Heating Jacket .....	37
<b>2.6.</b>	<b>Final Shock Tube Design .....</b>	<b>38</b>
2.6.1.	Shock Tube Material and Sections .....	39
2.6.2.	Driver Section .....	40
2.6.3.	Driven Section .....	40
2.6.4.	Diaphragm Access .....	41
2.6.5.	Mixing Tank .....	42
2.6.6.	Mixing Manifold .....	43
2.6.7.	Windows and Endwall Section .....	46
2.6.8.	Pressure Transducer Arrangement .....	48
2.6.9.	Vacuum System .....	52
2.6.10.	Double Diaphragm Chamber .....	52
2.6.11.	Expansion Vessel .....	53
<b>2.7.</b>	<b>Shock Tube Installation and Assembly .....</b>	<b>54</b>
2.7.1.	Optical Table .....	54
2.7.2.	Floor Plan and Site Preparation .....	55
2.7.3.	Summary of Installation .....	59

<b>2.8.</b>	<b>Shock Tube Calibration and Testing .....</b>	<b>60</b>
<b>2.9.</b>	<b>Diagnostic Equipment – Pressure and Chemiluminescence.....</b>	<b>63</b>
2.9.1.	High-Pressure Dynamic Pressure Transducer .....	63
2.9.2.	Photomultiplier for Ignition Delay Time Measurements .....	64
<b>2.10.</b>	<b>M-Squared Continuous Wave Absorption Diagnostic .....</b>	<b>65</b>
2.10.1.	Continuous Wave Laser Absorption Diagnostics of OH .....	66
2.10.2.	Tender Process and Initial Requirements .....	67
2.10.3.	M-Squared SolSTIS 4000 PSX XF System .....	69
2.10.4.	ECD-A/ECD-Q-A Wavelength Extension Modules (225-230 nm) .....	70
2.10.5.	EMM-532-SFG-A Wavelength Extension Module (306-310 nm) .....	71
2.10.6.	Dial-a-Wavelength Control.....	71
2.10.7.	OH Absorption.....	72
<b>2.11.</b>	<b>Summary and Outlook .....</b>	<b>75</b>
<b>3.</b>	<b><i>Development of the UoS sCO<sub>2</sub> Mechanism.....</i></b>	<b>77</b>
<b>3.1.</b>	<b>Introduction .....</b>	<b>77</b>
<b>3.2.</b>	<b>Oxyfuel Combustion.....</b>	<b>77</b>
3.2.1.	Laminar Flame Speed.....	78
3.2.2.	Ignition Delay Time .....	79
<b>3.3.</b>	<b>Modelling Procedure.....</b>	<b>81</b>
3.3.1.	Determination of Ignition Delay Time .....	81
3.3.2.	Sensitivity Analysis.....	83
3.3.3.	Reaction Pathway Analysis .....	84
3.3.4.	Quantitative Analysis .....	85
3.3.5.	Third Body Efficiencies of CO <sub>2</sub> .....	85
<b>3.4.</b>	<b>Dataset Selection .....</b>	<b>86</b>
3.4.1.	Methane Datasets.....	87
3.4.2.	Hydrogen Datasets.....	89
3.4.3.	Syngas Datasets .....	89
<b>3.5.</b>	<b>Mechanism Selection .....</b>	<b>90</b>
<b>3.6.</b>	<b>Analysis of Methane Datasets .....</b>	<b>91</b>
3.6.1.	High-Pressure Datasets.....	93
3.6.2.	Low-Pressure Datasets .....	99
3.6.3.	Effect of CO <sub>2</sub> Dilution on Mechanism Performance .....	102

<b>3.7. Hydrogen Analysis .....</b>	<b>105</b>
<b>3.8. Syngas Analysis.....</b>	<b>108</b>
3.8.1. High-Pressure Datasets.....	110
3.8.2. Low-Pressure Datasets .....	111
3.8.3. Effect of CO <sub>2</sub> Dilution .....	113
3.8.4. Effect of H <sub>2</sub> :CO Ratio.....	114
<b>3.9. Creation of the UoS sCO<sub>2</sub> 1.0 Mechanism.....</b>	<b>118</b>
3.9.1. H <sub>2</sub> O <sub>2</sub> + H ⇌ HO <sub>2</sub> + H .....	122
3.9.2. CO + O <sub>2</sub> ⇌ CO <sub>2</sub> + O .....	122
3.9.3. CO + HO <sub>2</sub> ⇌ CO <sub>2</sub> + OH .....	123
3.9.4. CH <sub>3</sub> + O <sub>2</sub> ⇌ Products .....	123
3.9.5. CH <sub>3</sub> + HO <sub>2</sub> ⇌ Products.....	123
3.9.6. CH <sub>3</sub> + H <sub>2</sub> O <sub>2</sub> ⇌ CH <sub>4</sub> + HO <sub>2</sub> .....	124
3.9.7. CH <sub>4</sub> + H ⇌ CH <sub>3</sub> + H <sub>2</sub> .....	124
3.9.8. H + O <sub>2</sub> ⇌ Products.....	125
3.9.9. OH + H <sub>2</sub> ⇌ H + H <sub>2</sub> O.....	125
3.9.10. H <sub>2</sub> + O <sub>2</sub> ⇌ HO <sub>2</sub> + H .....	126
3.9.11. OH + OH (+M) ⇌ H <sub>2</sub> O <sub>2</sub> (+M) .....	126
3.9.12. HO <sub>2</sub> + H ⇌ OH + OH.....	127
3.9.13. HO <sub>2</sub> + O ⇌ OH + O <sub>2</sub> .....	128
3.9.14. H <sub>2</sub> O <sub>2</sub> + OH ⇌ HO <sub>2</sub> + H <sub>2</sub> O .....	128
3.9.15. CO + OH ⇌ CO <sub>2</sub> + H .....	128
3.9.16. OH + HO <sub>2</sub> ⇌ H <sub>2</sub> O + O .....	129
3.9.17. HCO (+M) ⇌ H + CO (+M).....	129
3.9.18. CH <sub>3</sub> + OH ⇌ CH <sub>2</sub> * + H <sub>2</sub> O .....	130
3.9.19. CH <sub>2</sub> * + CO <sub>2</sub> ⇌ CH <sub>2</sub> O + CO.....	130
3.9.20. CH <sub>3</sub> + CH <sub>3</sub> ⇌ C <sub>2</sub> H <sub>6</sub> + H .....	130
3.9.21. CH <sub>2</sub> O + O <sub>2</sub> ⇌ HCO + HO <sub>2</sub> .....	131
<b>3.10. Results of the Quantitative Analysis .....</b>	<b>131</b>
<b>3.11. UoS sCO<sub>2</sub> Mechanism at the Conditions of the Allam-Fetvedt Cycle .....</b>	<b>133</b>
3.11.1. Reaction Pathway Analysis.....	134
3.11.2. CH <sub>3</sub> O <sub>2</sub> Reaction Pathway.....	136
3.11.3. Ethane Reaction Pathway .....	139
3.11.4. CH <sub>2</sub> O Formation .....	141
<b>3.12. Summary and Outlook .....</b>	<b>143</b>

<b>4.</b>	<b><i>Autoignition study Hydrogen and Syngas in CO<sub>2</sub></i></b>	<b>145</b>
<b>4.1.</b>	<b>KAUST High-Pressure Shock Tube</b>	<b>145</b>
4.1.1.	Identification of Time Zero	146
4.1.2.	Determination of Ignition Delay Time	147
<b>4.2.</b>	<b>Modelling Procedure</b>	<b>150</b>
4.2.1.	Bimodal Splitting in the Simulated Time History	150
<b>4.3.</b>	<b>Hydrogen IDT Datasets</b>	<b>157</b>
4.3.1.	Effect of CO <sub>2</sub> Dilution at 20 bar	158
4.3.2.	Effect of Equivalence Ratio at 20 bar	163
4.3.3.	Effect of Equivalence Ratio at 40 bar	166
4.3.4.	Validation of the UoS sCO <sub>2</sub> 2.0 Mechanism for H <sub>2</sub> Combustion	168
<b>4.4.</b>	<b>Syngas IDT Datasets</b>	<b>169</b>
4.4.1.	Effect of the H <sub>2</sub> :CO Ratio at $\theta=0.5$ and $\theta=1.0$	170
4.4.2.	Effect of Equivalence Ratio with CO in Excess ( $\theta=0.25$ )	178
4.4.3.	Effect of Equivalence Ratio for H <sub>2</sub> :CO at $\theta=1.0$	181
4.4.4.	Comparison to Existing Dataset from Barak et al. [199]	184
<b>4.5.</b>	<b>Summary and Outlook</b>	<b>188</b>
<b>5.</b>	<b><i>Autoignition Study of Methane/Hydrogen Blends and Methane in CO<sub>2</sub></i></b>	<b>191</b>
<b>5.1.</b>	<b>Experimental Details and Dataset Selection</b>	<b>191</b>
<b>5.2.</b>	<b>Discussion of Methane/Hydrogen Blends</b>	<b>193</b>
5.2.1.	Methane/Hydrogen Blends in CO <sub>2</sub>	194
5.2.2.	Effect of CO <sub>2</sub> Dilution	202
<b>5.3.</b>	<b>Analysis of Methane Mixtures</b>	<b>211</b>
5.3.1.	Stoichiometric Methane Combustion Between 20 and 100 bar	212
5.3.2.	Effect of Equivalence Ratio at 20 and 40 bar	215
<b>5.4.</b>	<b>Conclusion</b>	<b>220</b>
<b>6.</b>	<b><i>Conclusions and Future Work</i></b>	<b>221</b>
<b>6.1.</b>	<b>Conclusion</b>	<b>221</b>
<b>6.2.</b>	<b>Future Work</b>	<b>224</b>
6.2.1.	Direct-Fired sCO <sub>2</sub> Cycles	224
6.2.2.	Shock Tube Sidewall and Endwall Comparison	227
6.2.3.	Ammonia Combustion	228

6.2.4. Synthetic Aviation Fuels.....	229
<b>7. References .....</b>	<b>231</b>
<b>A. Raw IDT Data.....</b>	<b>251</b>
A.1. Hydrogen IDT Data.....	251
A.2. Syngas IDT Data .....	254
A.3. Methane and Methane/Hydrogen IDT Data .....	257
<b>B. UoS sCO<sub>2</sub> 1.0 Modelled IDT Data.....</b>	<b>262</b>
<b>C. Publication Output.....</b>	<b>274</b>
C.1. Poster Presentations .....	274
C.2. Conference Presentations.....	275
C.3. Conference Papers .....	275
C.4. Journal Papers.....	276
C.5. Online/Magazine Articles .....	277
C.6. Previously Published Work .....	278
C.7. Published Mechanisms .....	279

# List of Figures

<b>FIGURE 1.1.</b> ATMOSPHERIC CO <sub>2</sub> CONCENTRATION IN PPM AS A FUNCTION OF TIME FROM 803,719 BCE TO 2018. THESE DATA WERE TAKEN FROM OUR WORLD IN DATA [4].	1
<b>FIGURE 1.2.</b> OVERALL SCHEMATIC OF THE ALLAM-FETVEDT CYCLE ADAPTED FROM NETPOWER [36].	7
<b>FIGURE 1.3.</b> SCHEMATIC REPRESENTATIONS OF THE STAGES IN CONVERTING SYNGAS INTO LONG-CHAIN HYDROCARBONS ADAPTED FROM [83].	13
<b>FIGURE 2.1.</b> SCHEMATIC OF TYPICAL SHOCK TUBE OPERATION: A) SHOCK TUBE BEFORE DIAPHRAGM RUPTURE, B) DIAPHRAGM RUPTURE AND CREATION OF THE INCIDENT SHOCK, C) FORMATION OF THE REFLECTED SHOCK FOLLOWING THE INCIDENT SHOCK HITTING THE ENDWALL.	23
<b>FIGURE 2.2.</b> SCHEMATIC OF TIME AS A FUNCTION OF DISTANCE FROM THE SHOCK TUBE DIAPHRAGM [105].	24
<b>FIGURE 2.3.</b> SCHEMATIC OF TIME AS A FUNCTION OF DISTANCE FROM THE SHOCK TUBE DIAPHRAGM FOR A TAILORED SHOCK TUBE [105].	25
<b>FIGURE 2.4.</b> SCHEMATIC DIAGRAM OF BOUNDARY LAYER GROWTH DURING INCIDENT SHOCK WAVE PROPAGATION [101].	27
<b>FIGURE 2.5.</b> SHOCK TUBE P&ID BY WSP.	30
<b>FIGURE 2.6.</b> WISTL SIMULATED X-T DIAGRAM OF POST-SHOCK CONDITIONS NEAR THE MAXIMUM TEMPERATURE (1960 K) AND PRESSURE (85 BAR) WITH A HELIUM-DRIVER GAS AND NITROGEN-DRIVEN GAS [136].	31
<b>FIGURE 2.7.</b> A PLOT OF MAXIMUM OBSERVATION TIME AGAINST THE SHOCK TUBE DRIVEN SECTION LENGTH FOR AN N <sub>2</sub> (SOLID LINE), AR (DASHED LINE), AND CO <sub>2</sub> (DOTTED LINE) BATH GAS.	33
<b>FIGURE 2.8.</b> A PLOT OF REQUIRED DRIVER SECTION LENGTH AS A FUNCTION OF DRIVEN SECTION LENGTH TO GIVE THE DESIRED OBSERVATION TIME FOR AN N <sub>2</sub> (SOLID LINE), AR (DASHED LINE), AND CO <sub>2</sub> (DOTTED LINE) BATH GAS.	34
<b>FIGURE 2.9.</b> SHOCK TUBE DRIVEN SECTION AND MANIFOLD.	41
<b>FIGURE 2.10.</b> UoS MIXING TANK.	43
<b>FIGURE 2.11.</b> INITIAL SCHEMATIC OF THE UoS HPST DRIVER AND DRIVEN SECTION GAS MIXING MANIFOLDS. PROVIDED BY HEBLAC TECHNOLOGIE.	44
<b>FIGURE 2.12.</b> FINALISED MANIFOLD SCHEMATIC INCLUDING, VACUUM, VENTING, AND MIXING TANK. PROVIDED BY HEBLAC TECHNOLOGIE.	45
<b>FIGURE 2.13.</b> CROSS-SECTION OF THE SIDEWALL MEASUREMENTS FROM THE DRIVEN SECTION WALL, 1-2 CM FROM THE ENDWALL.	47
<b>FIGURE 2.14.</b> UoS SHOCK TUBE ENDWALL SECTION AND WINDOW PORTS.	48
<b>FIGURE 2.15.</b> PRESSURE TRANSDUCER ARRANGEMENT OVER THE LAST 2 METRES OF THE SHOCK TUBE, WHERE P1-P5 DETECT PRESSURE CHANGES AND SP1 AND SP2 GIVE HIGH PRESSURE AND HIGH ACCURACY, DYNAMIC PRESSURE MEASUREMENTS.	49
<b>FIGURE 2.16.</b> UoS HPST MEASURING SYSTEM LOCATION (HEBLAC TECHNOLOGIE).	50
<b>FIGURE 2.17.</b> PCB PRESSURE TRANSDUCER AND PLUG FABRICATION. PROVIDED BY HEBLAC TECHNOLOGIE.	51
<b>FIGURE 2.18.</b> UoS HPST DYNAMIC PRESSURE MEASURING SYSTEM. PROVIDED BY HEBLAC TECHNOLOGIE.	52
<b>FIGURE 2.19.</b> OUTSIDE OF THE UoS HPST DOUBLE DIAPHRAGM CHAMBER (HEBLAC TECHNOLOGIE).	53
<b>FIGURE 2.20.</b> EXPANSION VESSEL MOUNTED TO THE UNDERSIDE OF THE SUPPORT BEAM.	54
<b>FIGURE 2.21.</b> OPTICAL TABLE IN PLACE BEFORE SHOCK TUBE INSTALLATION.	55

<b>FIGURE 2.22.</b> FLOOR PLAN OF THE SHOCK TUBE PREPARED FOR THE INSTILLATION .....	57
<b>FIGURE 2.23.</b> SHOCK TUBE INSTILLATION SCHEMATIC PROVIDED BY HEBLAC TECHNOLOGIE.....	58
<b>FIGURE 2.24.</b> SCHEMATIC OF SHOCK TUBE SUPPORT STRUCTURE AND STANDS PROVIDED BY HEBLAC TECHNOLOGIE. ....	59
<b>FIGURE 2.25.</b> TECHNICAL DRAWING OF THE SHOCK TUBE TEST DIAPHRAGMS PROVIDED BY HEBLAC TECHNOLOGIE GMBH. ....	60
<b>FIGURE 2.26.</b> TRANX RECORDED PRESSURE TRACES FOR THE SHOCK TUBE TEST RUN DURING COMMISSIONING. ....	61
<b>FIGURE 2.27.</b> PLOT OF INCIDENT SHOCK WAVE VELOCITY AS A FUNCTION OF DISTANCE FROM THE SHOCK TUBE ENDWALL. ....	62
<b>FIGURE 2.28.</b> SCREENSHOT OF GASEQ POSTSHOCK CONDITIONS FOR SHOCK TUBE TEST RUN. ....	63
<b>FIGURE 2.29.</b> THE FOOTPRINT OF THE M-SQUARED LASER SYSTEM. PROVIDED BY M-SQUARED. ....	66
<b>FIGURE 2.30.</b> SIMULATED OH SPECTRAL PROFILE FROM 303-316 NM FROM GIRARD ET AL. [166]. ....	72
<b>FIGURE 2.31.</b> SET UP OF OH LASER ABSORPTION DIAGNOSTIC AT 308.61 NM FOR Q <sub>1</sub> (5) FROM [167]. ....	73
<b>FIGURE 2.32.</b> OH ABSORBANCE TIME HISTORIES FROM Q <sub>1</sub> (5) AND R <sub>1</sub> (5) PEAKS DURING SHOCK TUBE OXIDATION EXPERIMENTS IN A 1000 PPM H <sub>2</sub> /1000 PPM O <sub>2</sub> / AR MIXTURE [167] . ....	75
<b>FIGURE 2.33.</b> SIMULATED A <sup>2</sup> Σ <sup>+</sup> -X <sup>2</sup> Π (0,0) TRANSITIONS AT 1000 K (LEFT) AND 2000 K (RIGHT) [167]. ....	75
<b>FIGURE 3.1.</b> OH SENSITIVITY COEFFICIENT AS A FUNCTION OF TIME FOR DATASET M25 AT 1100 K FOR A) ARAMCOMECH 2.0 AND B) USC II [85]. ....	94
<b>FIGURE 3.2.</b> SEQUENTIAL CHANGES TO USC II; A) M22 AND B) M25; [USC II + CH <sub>3</sub> O <sub>2</sub> ]: ADDITION OF CH <sub>3</sub> O <sub>2</sub> CHEMISTRY FROM ARAMCOMECH 2.0, [USC II-ALTERED R6 + CH <sub>3</sub> O <sub>2</sub> ] CHANGE REACTION 3.6 TO ARAMCOMECH 2.0 RATE COEFFICIENT, [USC II-ALTERED R5 AND R6 + CH <sub>3</sub> O <sub>2</sub> ]: CHANGE REACTION 3.5 TO THE ARAMCOMECH 2.0 RATE COEFFICIENT. ....	98
<b>FIGURE 3.3.</b> IDT PLOTS OF M2 AND M4 FROM HARGIS AND PETERSEN [122]. ....	99
<b>FIGURE 3.4.</b> RELATIVE SENSITIVITY OF M2 DATASET AT 1609 K FOR ARAMCOMECH 2.0 AND GRI 3.0 [122]. ....	100
<b>FIGURE 3.5.</b> COMPARISON OF NET REACTION RATES OF REACTION 3.7 AND REACTION 3.8 AT 1609 K AT THE CONDITIONS OF DATASET M2.....	102
<b>FIGURE 3.6.</b> COMPARISON OF M1-M3 DATASETS FROM HARGIS AND PETERSEN [122]. ....	103
<b>FIGURE 3.7.</b> COMPARISON OF M5 AND M11 DATASETS FROM KOROGLU ET AL. [153]. ....	104
<b>FIGURE 3.8.</b> COMPARISON OF M13 AND M14 DATASETS FROM PRYOR ET AL. [195]. ....	104
<b>FIGURE 3.9.</b> COMPARISON OF THE SENSITIVITY ANALYSIS OF H3 FOR ARAMCOMECH 2.0 (BLUE) AND USC II (ORANGE) AT 1274 K. .....	106
<b>FIGURE 3.10.</b> H1 AND H2 DATASETS MODELLED BY ARAMCOMECH 2.0, USC II, AND [USC II-ALTERED R7]: USC II WITH THE UPDATED REACTION 3.9 RATE COEFFICIENT [241]. ....	108
<b>FIGURE 3.11.</b> S16 DATASET SENSITIVITY ANALYSIS OF ARAMCOMECH 2.0 (GREEN) AND GRI 3.0 (ORANGE) 1280 K.....	110
<b>FIGURE 3.12.</b> COMPARISON OF MECHANISM PERFORMANCE FOR THE S16 DATASET WITH AN ALTERED RATE COEFFICIENT OF REACTION 3.12 FROM BAULCH ET AL. [243], DENOTED BY AN ASTERISK (*). ....	111
<b>FIGURE 3.13.</b> MECHANISM COMPARISON OF THE S2 DATASET BETWEEN THE FOUR MECHANISMS.....	112
<b>FIGURE 3.14.</b> NORMALISED SENSITIVITY ANALYSIS OF S2 DATA FOR ARAMCOMECH 2.0 AT 1025 K (GREEN) AND 1145 K (ORANGE). .....	113
<b>FIGURE 3.15.</b> COMPARISON OF S4 AND S5 IDT DATASETS FROM BARAK ET AL. [198]. ....	114
<b>FIGURE 3.16.</b> COMPARISON OF S18, S19 AND S20 IDT DATASETS FROM KARIMI ET AL. [200]. ....	115
<b>FIGURE 3.17.</b> COMPARISON OF DATASETS FROM BARAK ET AL. [192] S14-S17. ....	116

<b>FIGURE 3.18.</b> COMPARISON OF S10-S13 DATASETS FROM BARAK ET AL. [199].	117
<b>FIGURE 3.19.</b> MODELLING LOOP PERFORMED FOR THE CREATION OF THE UoS sCO <sub>2</sub> MECHANISM.	119
<b>FIGURE 3.20.</b> UoS sCO <sub>2</sub> 1.0 SENSITIVITY ANALYSIS OF S15 AT 1086 K AND 1203 K.	127
<b>FIGURE 3.21.</b> REACTION PATHWAY ANALYSIS OF STOICHIOMETRIC METHANE COMBUSTION IN 96% CO <sub>2</sub> AT 300 ATM AND 1100 K.	134
<b>FIGURE 3.22.</b> CH <sub>3</sub> RATE OF PRODUCTION ANALYSIS AT 300 ATM AND 1100 K.	136
<b>FIGURE 3.23.</b> COMPARISON OF COMPETING CH <sub>3</sub> +O <sub>2</sub> REACTION PATHWAYS AT 30 ATM AND 300 ATM.	138
<b>FIGURE 3.24.</b> RATE OF PRODUCTION ANALYSIS OF A) CH <sub>3</sub> O <sub>2</sub> H AND B) CH <sub>3</sub> O <sub>2</sub> AT 300 BAR.	139
<b>FIGURE 3.25.</b> EXPANDED REACTION PATHWAY ANALYSIS OF STOICHIOMETRIC METHANE COMBUSTION IN 96% CO <sub>2</sub> AT 300 ATM AND 1100 K.	140
<b>FIGURE 3.26.</b> MOLE FRACTION OF STABLE COMBUSTION INTERMEDIATE SPECIES.	141
<b>FIGURE 3.27.</b> RATE OF PRODUCTION ANALYSIS OF CH <sub>2</sub> O.	142
<b>FIGURE 4.1.</b> SIDEWALL PRESSURE HISTORY FOR AN 85% CO <sub>2</sub> DILUTED H <sub>2</sub> MIXTURE.	147
<b>FIGURE 4.2.</b> REPRESENTATIVE PROFILES FOR IDT MEASUREMENT OF H <sub>2</sub> EARLY IGNITION AT 40 BAR FROM H <sub>2</sub> DATASET 8.	148
<b>FIGURE 4.3.</b> COMPARISON OF IDTs (H <sub>2</sub> MIXTURE 6) WITH LITERATURE DATA [85].	149
<b>FIGURE 4.4.</b> MOLE FRACTION OF OH, H <sub>2</sub> AND CO FOR (A) H <sub>2</sub> :CO:O <sub>2</sub> :N <sub>2</sub> :CO <sub>2</sub> = 2:8:10:40:40 AT 20 BAR AND 1188 K AND (B) H <sub>2</sub> :CO:O <sub>2</sub> :N <sub>2</sub> :CO <sub>2</sub> = 2.85:2.85:14.3:40:40 AT 20 BAR AND 1169 K MODELLED BY UoS sCO <sub>2</sub> 2.0.	151
<b>FIGURE 4.5.</b> A PLOT OF AVERAGE IDT FOR DATASET 3 H <sub>2</sub> :CO:O <sub>2</sub> :N <sub>2</sub> :CO <sub>2</sub> = 2:8:10:40:40 AT 20 BAR AND THE H <sub>2</sub> AND CO IDTs WHICH ARE THE LOW AND HIGH BOUNDS, RESPECTIVELY.	152
<b>FIGURE 4.6.</b> EXPERIMENTAL PRESSURE TRACE (LEFT-HAND AXIS) AND OH* SIDEWALL AND ENDWALL OH* EMISSIONS TRACES (RIGHT-HAND AXIS) FOR SYNGAS DATASET 3 AT 1191.1 K.	153
<b>FIGURE 4.7.</b> MOLE FRACTION OF OH, H <sub>2</sub> AND CO FOR (A) H <sub>2</sub> :CO:O <sub>2</sub> :CO <sub>2</sub> = 5:5:5:85 AT 40 BAR AND 1175 K AND (B) H <sub>2</sub> :CO:O <sub>2</sub> :N <sub>2</sub> = 5:5:5:85 AT 40 BAR AND 1175 K MODELLED BY UoS sCO <sub>2</sub> 2.0.	155
<b>FIGURE 4.8.</b> CONSTANT PRESSURE AND TEMPERATURE AND CONSTANT UV SIMULATIONS SHOWING H <sub>2</sub> AND CO CONSUMPTION OF SYNGAS DATASET 8 (85% CO <sub>2</sub> ).	157
<b>FIGURE 4.9.</b> COMPARISON OF IDTs OF DATASETS 1, 2 AND 3 WITH ARAMCOMECH 2.0 AND UoS sCO <sub>2</sub> 2.0.	159
<b>FIGURE 4.10.</b> NORMALIZED OH SENSITIVITY ANALYSIS OF DATASET 3 FOR UoS sCO <sub>2</sub> 2.0 AT 1050 K AND 1200 K.	161
<b>FIGURE 4.11.</b> NORMALIZED OH SENSITIVITY ANALYSIS OF DATASETS 1, 2 AND 3 FOR UoS sCO <sub>2</sub> 2.0 AT 1150 K.	162
<b>FIGURE 4.12.</b> MAXIMUM SPECIES CONCENTRATIONS AT THE POINT OF IGNITION FOR KEY INTERMEDIATES RELATIVE TO DATASET 2 WITH 85% CO <sub>2</sub> DILUTION.	163
<b>FIGURE 4.13.</b> COMPARISON OF IDTs OF DATASETS 1, 4 AND 5 WITH ARAMCOMECH 2.0 AND UoS sCO <sub>2</sub> 2.0.	164
<b>FIGURE 4.14.</b> NORMALIZED OH SENSITIVITY ANALYSIS OF DATASETS, 1, 4 AND 5 FOR UoS sCO <sub>2</sub> 2.0 AT 1200 K AND 20 BAR.	165
<b>FIGURE 4.15.</b> COMPARISON OF IDTs OF DATASETS 6, 7 AND 8 WITH ARAMCOMECH 2.0 AND UoS sCO <sub>2</sub> 2.0.	167
<b>FIGURE 4.16.</b> NORMALIZED OH SENSITIVITY ANALYSIS OF DATASETS 6 AND 8 FOR UoS sCO <sub>2</sub> 2.0 AT 1250 K AND 40 BAR.	168
<b>FIGURE 4.17.</b> COMPARISON OF IDTs OF DATASETS 1, 2 AND 3 WITH ARAMCOMECH 2.0 AND UoS sCO <sub>2</sub> 2.0.	171
<b>FIGURE 4.18.</b> COMPARISON OF IDTs OF DATASETS 5, 6, AND 7 WITH ARAMCOMECH 2.0 AND UoS sCO <sub>2</sub> 2.0.	172
<b>FIGURE 4.19.</b> NORMALIZED OH SENSITIVITY ANALYSIS OF DATASETS 1, 2 AND 3 FOR UoS sCO <sub>2</sub> 2.0 AT 1200 K.	173

<b>FIGURE 4.20.</b> RATE OF PRODUCTION ANALYSIS OF HO <sub>2</sub> FOR DATASET 3 AT 1187.5 K AROUND THE POINT OF IGNITION AND FOR THE FOUR KEY REACTIONS. ....	174
<b>FIGURE 4.21.</b> NORMALIZED OH SENSITIVITY ANALYSIS OF DATASET 2 FOR UoS sCO <sub>2</sub> 2.0 AT 1100 K AND 1250 K. ....	175
<b>FIGURE 4.22.</b> RATE OF PRODUCTION ANALYSIS OF H <sub>2</sub> O <sub>2</sub> FOR DATASET 2 AT 1100 K AROUND THE POINT OF IGNITION AND FOR THE FOUR KEY REACTIONS. ....	175
<b>FIGURE 4.23.</b> NORMALIZED OH SENSITIVITY ANALYSIS OF DATASET 5 FOR UoS sCO <sub>2</sub> 2.0 AND ARAMCOMECH 2.0 AT 1100 K. ...	178
<b>FIGURE 4.24.</b> NORMALIZED OH SENSITIVITY ANALYSIS OF DATASETS 3 AND 7 FOR UoS sCO <sub>2</sub> 2.0 AT 1200 K. ....	179
<b>FIGURE 4.25.</b> MOLE FRACTION OF OH, H <sub>2</sub> AND CO FOR DATASETS 3 ( $\phi=0.5$ ) AND 7 ( $\phi=1.0$ ) AT 20 BAR AND 1200 K. ....	180
<b>FIGURE 4.26.</b> COMPARISON OF DATASETS 1, 4, AND 5 WITH ARAMCOMECH 2.0 AND UoS sCO <sub>2</sub> 2.0. ....	181
<b>FIGURE 4.27.</b> NORMALIZED OH SENSITIVITY ANALYSIS OF DATASETS 1, 4 AND 5 FOR UoS sCO <sub>2</sub> 2.0 AT 1175 K. ....	182
<b>FIGURE 4.28.</b> RATE OF PRODUCTION OF OH COMPARISON FOR (A) DATASET 4 ( $\phi=0.25$ ) AND (B) DATASET 5 ( $\phi=1.0$ ) AND MOLE FRACTION OF OH AT 1175 K. ....	183
<b>FIGURE 4.29.</b> RATE OF LOSS OF H RADICAL COMPARISON FOR (A) DATASET 4 ( $\phi=0.25$ ) AND (B) DATASET 5 ( $\phi=1.0$ ) AND THE INCREASE IN THE TEMPERATURE AT 1175 K. ....	184
<b>FIGURE 4.30.</b> COMPARISON OF SIDEWALL AND ENDWALL MEASUREMENTS OF DATASET 8 WITH BARAK ET AL. [199] WITH ARAMCOMECH 2.0 AND UoS sCO <sub>2</sub> 2.0. ....	185
<b>FIGURE 4.31.</b> NORMALIZED OH SENSITIVITY ANALYSIS OF DATASET 8 FOR UoS sCO <sub>2</sub> 2.0 AND ARAMCOMECH 2.0 AT 1200 K AT 40 BAR. ....	187
<b>FIGURE 4.32.</b> NORMALIZED OH SENSITIVITY ANALYSIS OF DATASET 8 FOR UoS sCO <sub>2</sub> 2.0 AT 1175 K AND 1300 K AT 40 BAR. ...	188
<b>FIGURE 5.1.</b> REPRESENTATIVE PRESSURE (SIDEWALL) AND EMISSION (SIDEWALL, ENDWALL) PROFILES FOR TIME ZERO AND IGNITION DETERMINATION FROM MIXTURE 1 AT 20.9 BAR AND 1336 K. ....	192
<b>FIGURE 5.2.</b> COMPARISON OF IDTs OF MIXTURE 4 (CH <sub>4</sub> :O <sub>2</sub> :CO <sub>2</sub> =5:10:85), MIXTURE 1 (CH <sub>4</sub> :H <sub>2</sub> :O <sub>2</sub> :CO <sub>2</sub> =3.4:3.4:8.2:85) A MIXTURE FROM HARMAN-THOMAS ET AL. [88] (H <sub>2</sub> :O <sub>2</sub> :CO <sub>2</sub> =10:5:85) AT 20 BAR WITH NUIGMECH1.1 AND UoS sCO <sub>2</sub> 2.0 SIMULATIONS. ....	194
<b>FIGURE 5.3.</b> COMPARISON OF IDTs OF MIXTURE 4 (CH <sub>4</sub> :O <sub>2</sub> :CO <sub>2</sub> =5:10:85), MIXTURE 1 (CH <sub>4</sub> :H <sub>2</sub> :O <sub>2</sub> :CO <sub>2</sub> =3.4:3.4:8.2:85) A MIXTURE FROM HARMAN-THOMAS ET AL. [88] (H <sub>2</sub> :O <sub>2</sub> :CO <sub>2</sub> =10:5:85) AT 40 BAR WITH NUIGMECH1.1 AND UoS sCO <sub>2</sub> 2.0 SIMULATIONS. ....	195
<b>FIGURE 5.4.</b> NORMALISED OH SENSITIVITY ANALYSES OF MIXTURE 1 (CH <sub>4</sub> :H <sub>2</sub> :O <sub>2</sub> :CO <sub>2</sub> =3.4:3.4:8.2:85) AND A MIXTURE FROM HARMAN-THOMAS ET AL. [88] (H <sub>2</sub> :O <sub>2</sub> :CO <sub>2</sub> =10:5:85) WITH UoS sCO <sub>2</sub> 2.0 SIMULATIONS AT 1265 K AND 20 BAR. ....	196
<b>FIGURE 5.5.</b> MOLE FRACTIONS OF KEY INTERMEDIATE SPECIES OF MIXTURE 1 (CH <sub>4</sub> :H <sub>2</sub> :O <sub>2</sub> :CO <sub>2</sub> =3.4:3.4:8.2:85) AND A MIXTURE FROM HARMAN-THOMAS ET AL. [88] (H <sub>2</sub> :O <sub>2</sub> :CO <sub>2</sub> =10:5:85) WITH UoS sCO <sub>2</sub> 2.0 SIMULATIONS AT 1265 K AND 20 BAR. ....	198
<b>FIGURE 5.6.</b> ROP OF H IN MIXTURE 1 (CH <sub>4</sub> :H <sub>2</sub> :O <sub>2</sub> :CO <sub>2</sub> =3.4:3.4:8.2:85) AND A MIXTURE FROM HARMAN-THOMAS ET AL. [88] (H <sub>2</sub> :O <sub>2</sub> :CO <sub>2</sub> =10:5:85) WITH UoS sCO <sub>2</sub> 2.0 SIMULATIONS AT 1265 K AND 20 BAR. ....	198
<b>FIGURE 5.7.</b> NORMALISED OH SENSITIVITY ANALYSES OF MIXTURE 1 (CH <sub>4</sub> :H <sub>2</sub> :O <sub>2</sub> :CO <sub>2</sub> =3.4:3.4:8.2:85) AND MIXTURE 4 (CH <sub>4</sub> :O <sub>2</sub> :CO <sub>2</sub> =5:10:85) WITH UoS sCO <sub>2</sub> 2.0 SIMULATIONS AT 1425 K AND 20 BAR. ....	200
<b>FIGURE 5.8.</b> ETHANE ROP OF MIXTURE 4 (CH <sub>4</sub> :O <sub>2</sub> :CO <sub>2</sub> =5:10:85), MIXTURE 1 (CH <sub>4</sub> :H <sub>2</sub> :O <sub>2</sub> :CO <sub>2</sub> =3.4:3.4:8.2:85) WITH UoS sCO <sub>2</sub> 2.0 SIMULATIONS AT 1425 K AND 20 BAR. ....	200

<b>FIGURE 5.9.</b> ROP ANALYSES OF KEY INTERMEDIATE SPECIES OF MIXTURE 1 (CH <sub>4</sub> :H <sub>2</sub> :O <sub>2</sub> :CO <sub>2</sub> =3.4:3.4:8.2:85) AND MIXTURE 4 (CH <sub>4</sub> :O <sub>2</sub> :CO <sub>2</sub> =5:10:85), WITH UoS sCO <sub>2</sub> 2.0 SIMULATIONS AT 1425 K AND 20 BAR. ....	201
<b>FIGURE 5.10.</b> COMPARISON OF IDTs OF MIXTURE 1 (CH <sub>4</sub> :H <sub>2</sub> :O <sub>2</sub> :CO <sub>2</sub> =3.4:3.4:8.2:85) AND MIXTURE 2 (CH <sub>4</sub> :H <sub>2</sub> :O <sub>2</sub> :N <sub>2</sub> =3.4:3.4:8.2:85) AT 20 BAR AND 40 BAR WITH NUIGMECH1.1 AND UoS sCO <sub>2</sub> 2.0 SIMULATIONS.....	202
<b>FIGURE 5.11.</b> NORMALISED OH SENSITIVITY ANALYSES FOR MIXTURE 1 (CH <sub>4</sub> :H <sub>2</sub> :O <sub>2</sub> :CO <sub>2</sub> =3.4:3.4:8.2:85) AT 20 BAR AND 40 BAR WITH UoS sCO <sub>2</sub> 2.0 SIMULATIONS AT 1325 K.....	203
<b>FIGURE 5.12.</b> NORMALISED OH SENSITIVITY ANALYSES FOR MIXTURE 1 (CH <sub>4</sub> :H <sub>2</sub> :O <sub>2</sub> :CO <sub>2</sub> =3.4:3.4:8.2:85) WITH UoS sCO <sub>2</sub> 2.0 SIMULATIONS AND MIXTURE 2 (CH <sub>4</sub> :H <sub>2</sub> :O <sub>2</sub> :N <sub>2</sub> =3.4:3.4:8.2:85) WITH NUIGMECH1.1 SIMULATIONS AT 40 BAR AND 1265 K. ....	205
<b>FIGURE 5.13.</b> SPECIES MOLE FRACTION OF H <sub>2</sub> , CH <sub>4</sub> , O <sub>2</sub> AND CO FOR MIXTURE 1 (CH <sub>4</sub> :H <sub>2</sub> :O <sub>2</sub> :CO <sub>2</sub> =3.4:3.4:8.2:85) AND MIXTURE 2 (CH <sub>4</sub> :H <sub>2</sub> :O <sub>2</sub> :N <sub>2</sub> =3.4:3.4:8.2:85) AT 20 BAR WITH UoS sCO <sub>2</sub> 2.0 AND NUIGMECH1.1 SIMULATIONS RESPECTIVELY AT 1265 K AND 40 BAR. ....	206
<b>FIGURE 5.14.</b> ROP ANALYSIS OF CO FOR MIXTURE 1 (CH <sub>4</sub> :H <sub>2</sub> :O <sub>2</sub> :CO <sub>2</sub> =3.4:3.4:8.2:85) WITH UoS sCO <sub>2</sub> 2.0 SIMULATIONS AND MIXTURE 2 (CH <sub>4</sub> :H <sub>2</sub> :O <sub>2</sub> :N <sub>2</sub> =3.4:3.4:8.2:85) WITH NUIGMECH1.1 SIMULATIONS AT 40 BAR AND 1265 K. ....	206
<b>FIGURE 5.15.</b> ROP ANALYSIS OF CH <sub>4</sub> FOR MIXTURE 1 (CH <sub>4</sub> :H <sub>2</sub> :O <sub>2</sub> :CO <sub>2</sub> =3.4:3.4:8.2:85) WITH UoS sCO <sub>2</sub> 2.0 SIMULATIONS AND MIXTURE 2 (CH <sub>4</sub> :H <sub>2</sub> :O <sub>2</sub> :N <sub>2</sub> =3.4:3.4:8.2:85) WITH NUIGMECH1.1 SIMULATIONS AT 40 BAR AND 1265 K. ....	208
<b>FIGURE 5.16.</b> ROP ANALYSIS OF H <sub>2</sub> FOR MIXTURE 1 (CH <sub>4</sub> :H <sub>2</sub> :O <sub>2</sub> :CO <sub>2</sub> =3.4:3.4:8.2:85) WITH UoS sCO <sub>2</sub> 2.0 SIMULATIONS AND MIXTURE 2 (CH <sub>4</sub> :H <sub>2</sub> :O <sub>2</sub> :N <sub>2</sub> =3.4:3.4:8.2:85) WITH NUIGMECH1.1 SIMULATIONS AT 40 BAR AND 1265 K. ....	209
<b>FIGURE 5.17.</b> RPA ANALYSIS OF MIXTURE 1 (CH <sub>4</sub> :H <sub>2</sub> :O <sub>2</sub> :CO <sub>2</sub> =3.4:3.4:8.2:85) AND MIXTURE 2 (CH <sub>4</sub> :H <sub>2</sub> :O <sub>2</sub> :N <sub>2</sub> =3.4:3.4:8.2:85) AT 20 BAR WITH UoS sCO <sub>2</sub> 2.0 AND NUIGMECH1.1 SIMULATIONS RESPECTIVELY AT 1290 K AND 20 BAR. ....	211
<b>FIGURE 5.18.</b> COMPARISON OF IDTs OF MIXTURE 4 (CH <sub>4</sub> :O <sub>2</sub> :CO <sub>2</sub> =5:10:85) AT 20 BAR, 30 BAR [302], 40 BAR AND 100 BAR [127] WITH NUIGMECH1.1 AND UoS sCO <sub>2</sub> 2.0 SIMULATIONS.....	213
<b>FIGURE 5.19.</b> SENSITIVITY ANALYSIS OF MIXTURE 4 (CH <sub>4</sub> :O <sub>2</sub> :CO <sub>2</sub> =5:10:85) AT 20 BAR, 30 BAR [302], 40 BAR AND 100 BAR [127] AT 1430 K WITH UoS sCO <sub>2</sub> 2.0 SIMULATIONS. ....	214
<b>FIGURE 5.20.</b> COMPARISON OF CH <sub>4</sub> CONSUMPTION PATHWAYS OF MIXTURE 4 (CH <sub>4</sub> :O <sub>2</sub> :CO <sub>2</sub> =5:10:85) AT 20 BAR, 30 BAR [302], 40 BAR AND 100 BAR [127] WITH UoS sCO <sub>2</sub> 2.0 SIMULATIONS. ....	215
<b>FIGURE 5.21.</b> COMPARISON OF IDTs OF MIXTURE 3 (CH <sub>4</sub> :O <sub>2</sub> :CO <sub>2</sub> =3:12:85), MIXTURE 4 (CH <sub>4</sub> :O <sub>2</sub> :CO <sub>2</sub> =5:10:85) AND MIXTURE 5 (CH <sub>4</sub> :O <sub>2</sub> :CO <sub>2</sub> =7.5:7.5:85) AT 20 BAR WITH NUIGMECH1.1 AND UoS sCO <sub>2</sub> 2.0 SIMULATIONS.....	216
<b>FIGURE 5.22.</b> COMPARISON OF IDTs OF MIXTURE 3 (CH <sub>4</sub> :O <sub>2</sub> :CO <sub>2</sub> =3:12:85), MIXTURE 4 (CH <sub>4</sub> :O <sub>2</sub> :CO <sub>2</sub> =5:10:85) AND MIXTURE 5 (CH <sub>4</sub> :O <sub>2</sub> :CO <sub>2</sub> =7.5:7.5:85) AT 40 BAR WITH NUIGMECH1.1 AND UoS sCO <sub>2</sub> 2.0 SIMULATIONS. ....	217
<b>FIGURE 5.23.</b> SENSITIVITY ANALYSIS OF MIXTURE 3 (CH <sub>4</sub> :O <sub>2</sub> :CO <sub>2</sub> =3:12:85), MIXTURE 4 (CH <sub>4</sub> :O <sub>2</sub> :CO <sub>2</sub> =5:10:85) AND MIXTURE 5 (CH <sub>4</sub> :O <sub>2</sub> :CO <sub>2</sub> =7.5:7.5:85) AT 20 BAR WITH UoS sCO <sub>2</sub> 2.0 SIMULATIONS. ....	219
<b>FIGURE 5.24.</b> SENSITIVITY ANALYSIS OF MIXTURE 3 (CH <sub>4</sub> :O <sub>2</sub> :CO <sub>2</sub> =3:12:85), MIXTURE 4 (CH <sub>4</sub> :O <sub>2</sub> :CO <sub>2</sub> =5:10:85) AND MIXTURE 5 (CH <sub>4</sub> :O <sub>2</sub> :CO <sub>2</sub> =7.5:7.5:85) AT 40 BAR WITH UoS sCO <sub>2</sub> 2.0 SIMULATIONS. ....	219
<b>FIGURE B.1.</b> HARGIS AND PETERSEN (2015) M1-M4 DATASETS [122]. ....	262
<b>FIGURE B.2.</b> KOROGLU ET AL. (2016) M5-M11 DATASETS [122]. ....	263
<b>FIGURE B.3.</b> PRYOR ET AL. (2017A) M12-M15 DATASETS.....	264

<b>FIGURE B.4.</b> PRYOR ET AL. (2017B) M16-M17 DATASETS.....	264
<b>FIGURE B.5.</b> LIU ET AL. (2018) M18-M19 DATASETS [151].....	265
<b>FIGURE B.6.</b> SHAO ET AL. (2019) M20-M25 DATASET.....	266
<b>FIGURE B.7.</b> SHAO ET AL. (2019) M20-M25 DATASET.....	267
<b>FIGURE B.8.</b> KARIMI ET AL. (2019) M26-M28 DATASETS [127]. .....	268
<b>FIGURE B.9.</b> BARAK ET AL. (2020) M29 DATASET [192]. .....	268
<b>FIGURE B.10.</b> BARAK ET AL. (2020) S14-S17 DATASET [192]. .....	269
<b>FIGURE B.11.</b> VASU ET AL. (2011) S1-S3 DATASETS [353].....	270
<b>FIGURE B.12.</b> BARAK ET AL. (2017) S4-S9 DATASETS [198]. .....	271
<b>FIGURE B.13.</b> BARAK ET AL. (2019) S10-S13 DATASETS. ....	272
<b>FIGURE B.14.</b> KARIMI ET AL. (2020) S18-S20 DATASET [200]. .....	273

## List of Tables

<b>TABLE 1.1.</b> PRODUCTION RATE OF SALEABLE BY-PRODUCTS FROM THE NET POWER PILOT PLANT [44].	8
<b>TABLE 2.1.</b> DESCRIPTION OF THE FIVE REGIONS WITHIN A REFLECTED SHOCK TUBE.	23
<b>TABLE 2.2.</b> FINALISED KEY DESIGN SPECIFICATIONS.	38
<b>TABLE 2.3.</b> REQUIREMENTS FOR THE UOS HPST LASER ABSORPTION DIAGNOSTIC SYSTEM, E: ESSENTIAL AND D: DESIRABLE.	67
<b>TABLE 2.4.</b> PROPERTIES OF THE EQUINOX 532 NM LASER.	70
<b>TABLE 2.5.</b> PROPERTIES OF THE SOLSTIS 4000 PSX XF Tl:SAPPHIRE LASER.	70
<b>TABLE 3.1.</b> TEMPERATURE, PRESSURE RANGES, RELEASE DATE, FUEL TYPE AND AUTHORS FOR THE PUBLISHED IDT DATA SOURCE.	80
<b>TABLE 3.2.</b> METHANE DATASETS ANALYSED.	88
<b>TABLE 3.3.</b> HYDROGEN DATASETS ANALYSED.	89
<b>TABLE 3.4.</b> SYNGAS DATASETS ANALYSED.	90
<b>TABLE 3.5.</b> QUANTITATIVE ANALYSIS OF METHANE DATASETS.	92
<b>TABLE 3.6.</b> REACTIONS OF CH <sub>3</sub> O <sub>2</sub> ADDED TO USC II.	95
<b>TABLE 3.7.</b> RATE COEFFICIENTS OF REACTION 3.7 AND REACTION 3.8 WERE USED IN ARAMCO MECH 2.0 AND GRI 3.0 (PC=PERSONAL COMMUNICATION).	101
<b>TABLE 3.8.</b> QUANTITATIVE ANALYSIS OF HYDROGEN DATASETS.	105
<b>TABLE 3.9.</b> QUANTITATIVE ANALYSIS OF SYNGAS DATASETS.	109
<b>TABLE 3.10.</b> CHANGES MADE TO RATE COEFFICIENTS IN THE USC II MECHANISM TO CREATE UoS SCO <sub>2</sub> 1.0.	120
<b>TABLE 3.11.</b> COMPARISON OF THE DEVELOPED UoS SCO <sub>2</sub> MECHANISM TO THE EXISTING FOUR MECHANISMS STUDIED.	131
<b>TABLE 4.1.</b> HYDROGEN IDT MIXTURES STUDIED IN THIS WORK AND RESULTS OF QUANTITATIVE ANALYSIS.	158
<b>TABLE 4.2.</b> IDT MIXTURES STUDIED IN THIS WORK AND QUANTITATIVE ANALYSIS.	170
<b>TABLE 5.1.</b> CH <sub>4</sub> AND CH <sub>4</sub> /H <sub>2</sub> MIXTURES OF IDT DATASETS RECORDED IN THIS WORK.	193
<b>TABLE 5.2.</b> CH <sub>4</sub> MIXTURES OF IDT DATASETS FROM EXISTING LITERATURE.	193
<b>TABLE A.1.</b> IDT DATA FOR HYDROGEN MIXTURE 1 (* DENOTES SIDEWALL MEASUREMENT).	251
<b>TABLE A.2.</b> IDT DATA FOR HYDROGEN MIXTURE 2.	251
<b>TABLE A.3.</b> IDT DATA FOR HYDROGEN MIXTURE 3.	252
<b>TABLE A.4.</b> IDT DATA FOR HYDROGEN MIXTURE 4.	252
<b>TABLE A.5.</b> IDT DATA FOR HYDROGEN MIXTURE 5.	252
<b>TABLE A.6.</b> IDT DATA FOR HYDROGEN MIXTURE 6.	253
<b>TABLE A.7.</b> IDT DATA FOR HYDROGEN MIXTURE 7.	253
<b>TABLE A.8.</b> IDT DATA FOR HYDROGEN MIXTURE 8.	253
<b>TABLE A.9.</b> MIXTURE UNCERTAINTY AND PRESSURE RISE FOR HYDROGEN IDT DATASETS.	254
<b>TABLE A.10.</b> IDT DATA FOR SYNGAS MIXTURE 1.	254
<b>TABLE A.11.</b> IDT DATA FOR SYNGAS MIXTURE 2.	255
<b>TABLE A.12.</b> IDT DATA FOR SYNGAS MIXTURE 3.	255
<b>TABLE A.13.</b> IDT DATA FOR SYNGAS MIXTURE 4.	255

<b>TABLE A.14.</b> IDT DATA FOR SYNGAS MIXTURE 5.....	256
<b>TABLE A.15.</b> IDT DATA FOR SYNGAS MIXTURE 6.....	256
<b>TABLE A.16.</b> IDT DATA FOR SYNGAS MIXTURE 7.....	256
<b>TABLE A.17.</b> IDT DATA FOR SYNGAS MIXTURE 8 (* DENOTES SIDEWALL MEASUREMENT).....	257
<b>TABLE A.18.</b> MIXTURE UNCERTAINTY AND PRESSURE RISE FOR SYNGAS IDT DATASETS.....	257
<b>TABLE A.19.</b> IDT DATA FOR MIXTURE 1 AT 20 BAR.....	258
<b>TABLE A.20.</b> IDT DATA FOR MIXTURE 1 AT 40 BAR.....	258
<b>TABLE A.21.</b> IDT DATA FOR MIXTURE 2 FOR 20 BAR.....	258
<b>TABLE A.22.</b> IDT DATA FOR MIXTURE 2 FOR 40 BAR.....	259
<b>TABLE A.23.</b> IDT DATA FOR MIXTURE 3 FOR 20 BAR.....	259
<b>TABLE A.24.</b> IDT DATA FOR MIXTURE 3 FOR 40 BAR.....	259
<b>TABLE A.25.</b> IDT DATA FOR MIXTURE 4 FOR 20 BAR.....	260
<b>TABLE A.26.</b> IDT DATA FOR MIXTURE 4 FOR 40 BAR.....	260
<b>TABLE A.27.</b> IDT DATA FOR MIXTURE 5 FOR 20 BAR.....	261
<b>TABLE A.28.</b> IDT DATA FOR MIXTURE 5 FOR 40 BAR.....	261
<b>TABLE A.29.</b> MIXTURE UNCERTAINTY FOR THE IDT DATASETS INVESTIGATED.....	261

## **Acknowledgements**

I would first like to express my gratitude to my supervisors at the University of Sheffield. To Professor Mohamed Pourkashanian for his guidance on the project and the opportunity to study in a world-leading research facility and lead the development of an experimental rig. To Dr Kevin Hughes for his supervision, support, and guidance for the duration of my project. To Professor Derek Ingham for his supervision and for providing vital feedback on all my publications. I would also like to thank everyone in the Energy 2050 research group.

In addition, I would like to thank the CDT for Resilient Decarbonised Fuel Energy Systems (RDFES). I am extremely grateful to Professor Robin Irons, Professor Richard Marsh, Professor Lin Ma, Dr Claudia Matz, Mrs Gina Goddard-Bell, and Mrs Diane Vincent for their organisation of our 'CDT Schools', modules, and get-togethers. I would also like to thank all the members of the CDT who have been incredibly supportive and made these events memorable and the International Flame Research Foundation (IFRF) for acting as my industrial sponsor for my project.

I also would like to thank everyone at the Translational Energy Research Centre (TERC) for their help in the design, fabrication, and installation of the High-Pressure Shock Tube (HPST), most notably Mr Matthew Jee, Mr David Gains, Mr Andrew Delorenzi, and Dr Abdulaziz Gheit. Furthermore, I would like to thank Heblac Technologie GMBH, Professor Alexander Heufer who fabricated the shock tube from my initial concept and provided valuable insight based on his extensive shock tube experience.

I would like to thank King Abdullah University of Science and Technology (KAUST) Clean Combustion Research Centre (CCRC), Professor Aamir Farooq, and Mr Touqeer Anwar Kashif. The three papers we collaborated on provided essential data to this thesis and visiting the fantastic facilities was a highlight of my EngD.

Finally, I would like to acknowledge the input of my family, my wife Evie Harman-Thomas, and two children Arthur and Bluebell Harman-Thomas, as well as my extended family. Their support has been invaluable, and I would not be completing this EngD without them.

## **Declaration**

I, the author, confirm that the Thesis is my work. I am aware of the University's Guidance on the Use of Unfair Means ([www.sheffield.ac.uk/ssid/unfair-means](http://www.sheffield.ac.uk/ssid/unfair-means)). This work has not previously been presented for an award at this, or any other, University.

## **Conference Papers**

J.M. Harman-Thomas, M. Pourkashanian, K.J. Hughes, The chemical kinetic mechanism for combustion in supercritical carbon dioxide, 4th European sCO<sub>2</sub> Conference for Energy Systems, Online, 2021, pp. 28-37.

## **Journal Articles**

J.M. Harman-Thomas, K.J. Hughes, M. Pourkashanian, The development of a chemical kinetic mechanism for combustion in supercritical carbon dioxide, Energy (2022) 124490. <https://doi.org/10.1016/j.energy.2022.124490>

J.M. Harman-Thomas, T.A. Kashif, K.J. Hughes, M. Pourkashanian and A. Farooq. Experimental and modelling study of hydrogen ignition in CO<sub>2</sub> bath gas, Fuel (2023) 126664. <https://doi.org/10.1016/j.fuel.2022.126664>

*Written as a co-first author with Touqeer Anwar Kashif. I wrote the introduction and performed and wrote all the modelling work whilst Touqeer performed the experimental work and wrote the experimental section.*

J.M. Harman-Thomas, T.A. Kashif, K.J. Hughes, M. Pourkashanian, A. Farooq, Experimental and modelling study of syngas combustion in CO<sub>2</sub> bath gas, Fuel (2023) 127865. <https://doi.org/10.1016/j.fuel.2023.127865>

*Written as a co-first author with Touqeer Anwar Kashif. I wrote the introduction and performed and wrote all the modelling work whilst Touqeer performed the experimental work and wrote the experimental section.*

J.M. Harman-Thomas, Derek B. Ingham, K.J. Hughes, M. Pourkashanian, Role of methylidioxy radical chemistry in high-pressure methane combustion in CO<sub>2</sub>, International Journal of Chemical Kinetics (2023) 1-13. <https://doi.org/10.1002/kin.21672>

### **Journal Articles in Preparation**

J.M. Harman-Thomas, T.A. Kashif, K.J. Hughes, M. Pourkashanian, A. Farooq, Autoignition study of methane and methane/hydrogen blends in CO<sub>2</sub> bath gas.

### **Poster Presentations**

Royal Society of Chemistry (RSC) Faraday Joint Interest Group Conference, Online, 29<sup>th</sup>-31<sup>st</sup> March 2021.

1<sup>st</sup> FERIA Conference, Nottingham, UK, 6<sup>th</sup>-8<sup>th</sup> September 2021.

CDT for Resilient Decarbonised Fuel Energy Systems, Spring School, Cardiff, UK, 25<sup>th</sup>-29<sup>th</sup> April 2022.

The University of Sheffield Mechanical Engineering 2<sup>nd</sup> Year Poster Presentation, Sheffield, UK, 14 June 2022.

IFRF TOTeM – Hydrogen for Decarbonisation, Paris, UK, 13<sup>th</sup> October 2022.

### **Conference Presentations**

The 4<sup>th</sup> European sCO<sub>2</sub> Conference for Energy Systems, Online, 23<sup>rd</sup>-24<sup>th</sup> March 2021.

1<sup>st</sup> FERIA Conference, Nottingham, UK, 6<sup>th</sup>-8<sup>th</sup> September 2021.

CDT for Resilient Decarbonised Fuel Energy Systems Autumn School, Nottingham, UK, 8<sup>th</sup>-10<sup>th</sup> September 2021.

TCCS-12, Trondheim, Norway, 19<sup>th</sup>-21<sup>st</sup> June 2023.

# 1. Introduction

## 1.1. Motivation

Since the industrial revolution sparked the flame for the industrial-scale combustion of hydrocarbon fuels in the 1700s, humanity's demand for power generation has continued to grow. The large demand for the combustion of fossil fuels for power has released vast quantities of carbon dioxide (CO<sub>2</sub>) into the atmosphere. Although the implications of unrestricted CO<sub>2</sub> production, have only truly been understood towards the end of the 20<sup>th</sup> Century, Svante Arrhenius discovered the relationship between increased atmospheric CO<sub>2</sub> levels and global temperature rise as early as 1896 [1]. Despite the increasing competitiveness of renewable energy, fossil fuels continue to be the leading global energy source [2]. Anthropogenic emissions of CO<sub>2</sub> and other greenhouse gases (GHGs) have led to the total atmospheric CO<sub>2</sub> equivalent (CO<sub>2e</sub>) concentration now exceeding 480 parts per million (ppm) [3].

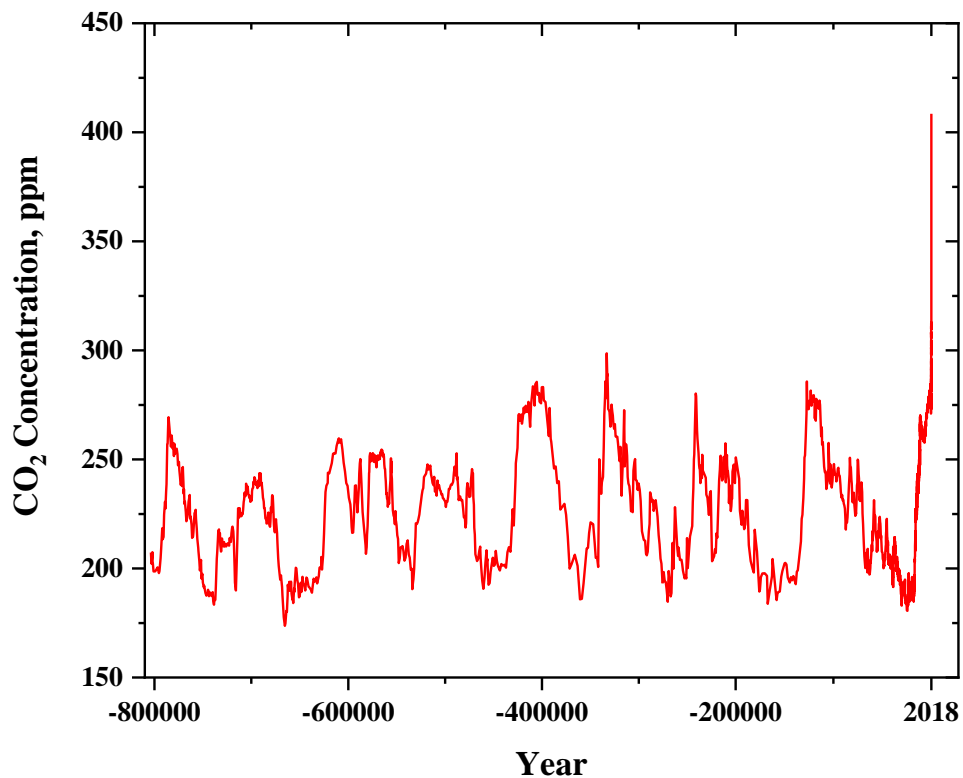


**Figure 1.1.** Atmospheric CO<sub>2</sub> concentration in ppm as a function of time from 803,719 BCE to 2018. These data were taken from Our World in Data [4].

Figure 1.1 taken from Our World in Data [4] shows the historical profile of the atmospheric concentration of CO<sub>2</sub> as a function of time up to 2018, all the way back to 803,719 BCE. Accurate profiles of atmospheric CO<sub>2</sub> concentrations from almost 1 million years ago are determined by analysing Antarctic ice cores. The air trapped within ice cores up to 3200 kilometres (km) in depth is extracted under dry conditions and analysing the sample produced using laser absorption spectroscopy [5]. Figure 1.1 shows natural variations in atmospheric CO<sub>2</sub> concentrations from 200-300 ppm over the last 800,000 years which coincides with ice ages and similar extreme historic events such as ice ages [5]. However, the sharp increase in CO<sub>2</sub> concentrations over 400 ppm since the industrial revolution is not a natural variation and has been induced by anthropogenic activity.

Modern measurements of atmospheric CO<sub>2</sub> concentrations are made at the Mauna Loa Observatory (MLO) in Hawaii and have been since the 1950s. The MLO is located 3400 metres (m) above sea level beyond the atmospheric boundary layer in the lower troposphere, utilising an infrared analyser to make continuous atmospheric measurements of CO<sub>2</sub> [6]. The increasing atmospheric abundance of GHGs has severe climate consequences such as global warming, ocean acidification, sea-level rise, and an increasing regularity of extreme weather events [7-9]. Therefore, legislation and technology are required to reduce anthropogenic CO<sub>2</sub> emissions from all areas of residential and industrial power generation to stabilize, and hopefully reduce, the atmospheric concentrations of GHGs such as CO<sub>2</sub>.

In addition to the environmental effects of rising CO<sub>2</sub> and GHG concentrations, the combustion of fossil fuels in air can lead to harmful pollutants such as sulphur oxides (SO<sub>x</sub>) and nitrogen oxides (NO<sub>x</sub>) from the oxidation of sulphur or nitrogen respectively. Tropospheric NO<sub>x</sub> has been linked to the formation of ground-level particulate matter (PM) and ozone (O<sub>3</sub>) which cause respiratory problems in humans [10, 11]. Sulphur dioxide (SO<sub>2</sub>) is the most toxic and environmentally harmful component of SO<sub>x</sub> and is a major contributor to acid rain [12, 13].

The impact of humanity's actions on the Earth and its atmosphere has prompted a global response to resolve the pressing challenges created by a changing climate. Climate change first became a global scientific and political issue in 1979 [14] with legislation being introduced in the 1980s, such as the Montreal Protocol in 1987 which was implemented to reduce the effect of ozone-depleting substances (ODSs) in the Earth's ozone layer [15]. This was based on the findings of climate scientists such as James Hansen [16]. This was swiftly followed by the formation of the Intergovernmental Panel on Climate Change (IPCC) in 1988 at the First United Nations (UN) General Assembly Resolution on climate change [14]. Based upon the findings of IPCC over the subsequent decade, a global policy was created, culminating in the 170 countries signing the Kyoto Protocol in 1997 to stabilize greenhouse gas concentrations at a concentration below which there would be a dangerous anthropogenic effect on the climate [17]. The Kyoto Protocol was further improved by a series of amendments until it was superseded by the 2015, Paris agreement [18]. The Paris agreement is not legally binding for the countries involved but is an agreement to keep global temperatures below 2 °C above pre-industrial levels and ideally below 1.5 °C [19]. This has led to scepticism surrounding the lack of legality of the Paris Agreement. As countries are not legally bound to fulfil the targets outlined in the Paris Agreement, critics argue it will not be effective in deterring the countries involved from increasing or maintaining their current levels of emissions [20]. These fears appear to be justified by the 2019, 'The Truth Behind the Climate Pledges' report which found 75% of the 184 countries which had signed the Paris agreement had taken insufficient action to curb global temperature rise, with some still increasing their emissions [21].

Despite the increasing competitiveness of renewable energy in terms of price and efficiency [22], future energy scenarios predict that fossil fuels will still be required to meet global energy demands up to the year 2050 and beyond [23].

Coupling all this information leads to the stark conclusion that technological advances are urgently required which allow the continued combustion of fossil fuels in a way that produces no harmful emissions. Current carbon capture technology usually incurs a large overall plant efficiency penalty [24]. High-

pressure power systems offer a potential solution for power generation from the combustion of fossil fuels with a limited impact on the cost to the end consumer. Commercial power generation utilizing direct-fired supercritical CO<sub>2</sub> (sCO<sub>2</sub>) power cycles allows electricity production via natural gas or syngas combustion with 100% inherent carbon capture, at a price competitive with traditional fossil fuel power plants without any carbon capture capabilities [25]. Alternative high-pressure supercritical and ultra-supercritical steam power cycles which operate at high pressures such as Rankine steam, helium Brayton and supercritical steam cycles are stated to have greater efficiency than traditional sub-critical power plants [26]. A comparative study by Dostal et al. [27] of proposed power cycles determined that the sCO<sub>2</sub> power cycle was the strongest performing both technologically and economically if it can be proven on an industrial-scale power plant.

## **1.2. Direct Fired sCO<sub>2</sub> Power Cycles**

Supercritical power cycles were first proposed in 1968 by E.G. Feher [28] who noted that supercritical conditions offer high thermal efficiency, low volume-to-power ratio, and insensitivity to compression efficiency. CO<sub>2</sub> becomes supercritical at a critical pressure and temperature of 73.77 bar and 304 K respectively [29]. In its supercritical state, CO<sub>2</sub> possesses the properties of both gas and liquid. Direct-fired sCO<sub>2</sub> power cycles utilise the greater power density of liquid CO<sub>2</sub> and the high diffusivity of gaseous CO<sub>2</sub> of supercritical CO<sub>2</sub> to provide an efficient working fluid for power generation [30]. The concentration of CO<sub>2</sub> in direct-fired sCO<sub>2</sub> power cycles can be up to 96% [25]. Currently, there are two power cycle projects underway, both based in the U.S.; the Allam-Fetvedt cycle by NetPower and the Supercritical Transformational Electric Power (STEP) project led by the Gas Technology Institute (GTI). Commercial power generation utilizing direct-fired sCO<sub>2</sub> allows for the production of electricity via the combustion of natural gas and coal with inherent 100% carbon capture at prices competitive with current fossil fuel power plants without carbon capture [25]. Due to the combustion of fuel being in pure oxygen and a large dilution of CO<sub>2</sub>, the only products from combustion are water (H<sub>2</sub>O) and CO<sub>2</sub>, with harmful NO<sub>x</sub> and

SO<sub>x</sub> emissions significantly reduced. Both the Allam-Fetvedt cycle and STEP use a Brayton cycle type power plant, which is discussed more in Section 1.2.2.

A direct-fired sCO<sub>2</sub> power cycle differs from an indirect cycle only in heat sources. In a direct cycle, fuel and oxygen are burnt in CO<sub>2</sub> 'directly' to heat the working fluid. In an indirect-fired sCO<sub>2</sub> power cycle, the heat from another reactor is utilised through a heat exchanger to heat a pure stream of CO<sub>2</sub> 'indirectly', which subsequently powers a turbine. Indirect cycles would therefore be implemented as a secondary power generation cycle for any other type of reactor, including solar cycles [31], and are even under consideration for next-generation nuclear reactors [32].

Due to the greater power density of sCO<sub>2</sub> relative to traditional gaseous working fluids such as air or steam and the high pressure of the combustion chamber, direct-fired sCO<sub>2</sub> power cycles require smaller components than traditional steam turbines. A coal-fired NetPower plant that utilizes the Allam-Fetvedt cycle is predicted to have an overall footprint 1/6 the size of a supercritical pulverized coal plant of the same power output [25].

### **1.2.1. The Allam-Fetvedt Cycle**

The Allam-Fetvedt cycle is a thermodynamic cycle for the combustion of natural gas or syngas from coal gasification with almost zero emissions. The pressure and temperature of the Allam-Fetvedt cycle vary across the components from 300 bar and 1423 K at the turbine inlet to 30 bar and 293 K at the compressor inlet [33]. The Allam-Fetvedt cycle has rapidly gained attention over the last decade due to its predicted efficiencies of 53.9% for natural gas-fired plants. All of this whilst inherently capturing 100% of CO<sub>2</sub> emissions. In a comparative review of emerging carbon capture, storage, and utilisation (CCSU) technologies, the Allam-Fetvedt cycle was the only method of coal combustion that could lead to a reduction in the cost of electricity production relative to current coal combustion options without CCSU [34]. This is essential as energy costs have continued to rise globally in recent years due to the rising cost of gas, the unpredictability of renewables, and unanticipated global political events [35].

The Allam-Fetvedt cycle is being developed by an American company, NetPower in collaboration with 8 Rivers Capital. NetPower aims to “provide advanced clean energy to worldwide consumers by generating lower-cost power with zero emissions”. In 2018 NetPowers’ 50 MW natural gas-fired power plant went into operation with plans to have an operational 300 MW demonstration plant by 2022 [36].

One of the major disadvantages of direct-fired  $s\text{CO}_2$  power cycles is the requirement for an on-site air separation unit (ASU) for the production of a high-purity stream of oxygen using cryogenic separation [37]. The ASU component was identified as a technology gap for the cryogenic pressurized oxy-combustion cycle (CPOC) as it could not produce enough oxygen to sustain a 550 MW plant [38]. Whilst the Allam-Fetvedt cycle faces the same difficulty as the energy demands of the ASU, it manages to negate the impact on efficiency by utilizing the heat of compression during separation into the main power cycle. This enhances the overall cycle efficiency by utilizing heat that would have otherwise been lost to the atmosphere. One method to further increase the efficiency of the Allam-Fetvedt cycle is to reduce the energy requirements of the ASU. This can be done by i) using more efficient separation technologies [39], ii) adding oxygen storage capabilities [40] or iii) reducing the purity requirement of the oxygen [41]. Reducing the purity of the oxygen should only be done if it does not significantly reduce the purity of the  $\text{CO}_2$  produced. Lu et al. [42] developed a de-sulphur and nitrogen oxidation removal process ( $\text{DeSNO}_x$ ) process which can be added to the Allam-Fetvedt cycle. A  $\text{DeSNO}_x$  process attached to the Allam-Fetvedt cycle would allow for the combustion of fuels rich in sulphur and nitrogen impurities such as biogas as well as allowing using a lower purity of oxygen, reducing the energy requirements of the ASU whilst maintaining the advantageous low emissions of harmful gases.

Figure 1.2 schematically shows the Allam-Fetvedt cycle for a natural gas plant. The ASU separates the oxygen from the other air constituents such as nitrogen and argon, producing a high-purity stream of oxygen which is fed into the combustion chamber along with natural gas, both in a large dilution of  $\text{CO}_2$ . They react in the combustion chamber to form  $\text{H}_2\text{O}$  and  $\text{CO}_2$ , which power the turbine

and generate electricity. The water is then removed through condensation to leave a high-purity stream of CO<sub>2</sub>, this is important as any water impurities in the CO<sub>2</sub> may cause corrosion due to the formation of carbonic acid in any downstream pipework [43]. Following this, the CO<sub>2</sub> is repressurised back to its pipeline-ready and supercritical state, whilst some of the CO<sub>2</sub> is removed proportionally to the amount produced from combustion, and the rest is recycled into the combustion chamber [25].

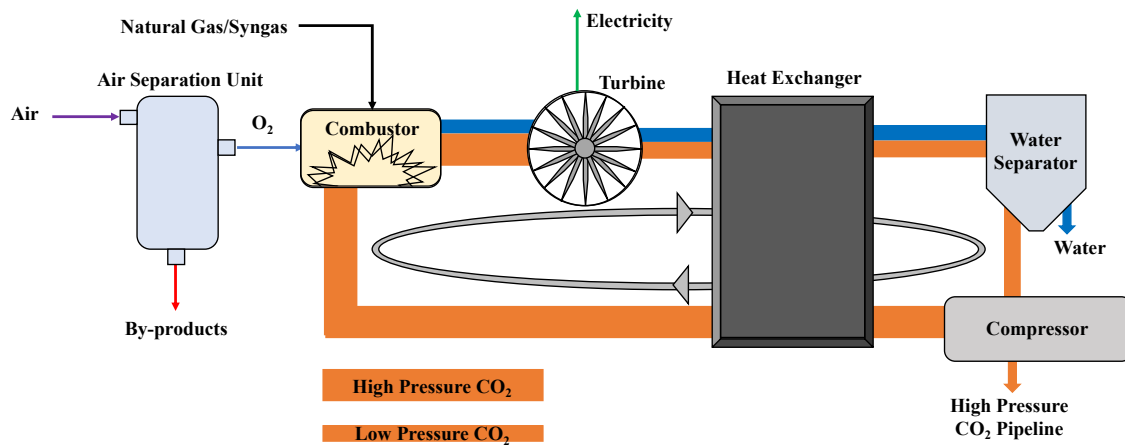


**Figure 1.2.** Overall schematic of the Allam-Fetvedt cycle adapted from NetPower [36].

One final advantage of the Allam-Fetvedt cycle, which can be further used to reduce the final cost of electricity to the end user, is the production of saleable by-products from the ASU. With further separation, high-purity nitrogen and argon could be produced and sold. The Allam-Fetvedt power plant is currently producing CO<sub>2</sub>, Argon (Ar), nitrogen (N<sub>2</sub>), and H<sub>2</sub>O in quantities and purities listed in a 2021 report by Net Power (Table 1.1) for their pilot-scale plant [44]. A 300 MW sCO<sub>2</sub> direct-fired power plant is predicted to generate 1 million gallons of water a day [45]. This is advantageous compared to traditional thermoelectric power plants which consume water as climate change-induced water shortages are driving up the price of electricity [46]. Furthermore, population growth and advancement of developing countries are predicted to lead to 57% of the global population living in water poverty by 2050 [47]. Therefore, producing a high-purity supply of water could become as important as the electricity generated by direct-fired sCO<sub>2</sub> power plants.

**Table 1.1.** Production rate of saleable by-products from the Net Power pilot plant [44].

<b>Gas</b>	<b>Amount (Tonnes/year)</b>	<b>Purity (%)</b>	<b>Potential Uses</b>
CO <sub>2</sub>	865 k	97-99.99	Enhanced oil recovery [48].
Ar	65 k	99.999	Preparation of alloys [49].
N <sub>2</sub>	4.6 MM	98.6-99.99	Inert atmospheres.
H <sub>2</sub> O	1.07 MM	99.99	Agriculture.

Developments on the Allam-Fetvedt cycle include the Allam-Z cycle by Zhu et al. [50] argue that removing the compressors from the Allam-Fetvedt cycle and replacing them with high-pressure pumps to raise the pressure of the recycled gas stream increases the net efficiency of the plant from 45.09% to 48.05%. However, the calculation uses conditions that appear to favour the Allam-Z cycle. For example, the calculation is performed at two inlet temperatures, 700°C and 900°C, whereas the Allam cycle is said to be optimal with an inlet temperature of 1150°C [33]. The value reported for the net efficiency of the Allam Cycle of 45.09% is significantly lower than the 53.9% reported by Rodríguez Hervás and Petrakopoulou [51]. Lastly, the Allam-Z cycle results in a decrease in power output. When constructing demonstration plants with greater energy output, this loss in power output may become more significant than the increase in net efficiency gain. Furthermore, a thermodynamic optimization study of the Allam-Fetvedt cycle has been performed by Scaccabarozzia et al. [52] that demonstrates how to further efficiencies of the Allam-Fetvedt cycle can be achieved by altering the cycle conditions. A detailed and accurate exergoeconomic analysis is required to compare the two plants to decide which is optimal. Further work on simulating the Allam-Fetvedt cycle can lead to further changes to the cycle, such as the combustion chamber, inlet temperature, and pressure ratio [53]. Furthermore, the Allam-Fetvedt cycle has been proposed for coupling with different chemical systems. Xin et al. [54] proposed a methanol and electricity generation system, which utilised an Allam-Fetvedt oxy-combustion cycle following methanol synthesis. This removes the requirement for CO<sub>2</sub> separation following the water-gas shift reaction as it is removed following the oxy-combustion cycle after the syngas by-product reacts.

The potential of a future powered by the Allam-Fetvedt cycle became increasingly possible in 2021 with the announcement of three power plants going into development, with two, 280 MW plants in the USA and one 300 MW plant in the United Kingdom (UK). Firstly, 8 Rivers Capital announced through its Zero Degrees development plan announced a 280 MW plant in Chicago, Illinois with partner company Archer-Daniels-Midlands (ADM) where the captured carbon dioxide will be transported and stored safely underground [55]. The plant is set to begin operations in 2025 and will use an existing CO<sub>2</sub> well currently used to store CO<sub>2</sub> emissions from a nearby ethanol production facility. The second U.S.-based facility will be in Colorado and is working with Southern Ute Indian Tribe Growth Fund. Both of the plants are expected to cost over \$500 Million each [56]. The UK-based plant was announced in the summer of 2021 through NetPowers UK subsidiary Zero Degrees Whitetail Development Ltd with Sembcorp Energy UK in Teesside, County Durham [57]. The port location allows for convenient pipeline access to long-term storage of captured CO<sub>2</sub> in depleted North Sea gas fields and is slated for completion in 2025. The UK, based Teesside power plant is predicted to create over 2,000 jobs during construction and 200 during operation [58]. Furthermore, 8 Rivers Capital, the parent company of NetPower, received a \$100 million investment from SK Group, a South Korean conglomerate, to create a joint venture focusing on the decarbonisation of key Asian markets through projects including the Allam-Fetvedt cycle [59].

### **1.2.2. Supercritical Transformational Electric Power (STEP)**

An alternative sCO<sub>2</sub> power plant currently being designed is the 10 MWe STEP on the Southwestern Research Institute (SWRI) San Antonio campus in Texas. The pilot plant information will be used to assess the performance and operability of a sCO<sub>2</sub> power cycle before scaling up and commercializing the technology, with the pilot plant commissioned in 2022 [60]. The STEP Demo project is led by GTI and it received an \$84 million grant from the U.S. Department of Energy and is open to finding partners across the globe to complement the intermittency of renewable energy production [61]. The 10 MWe pilot plant will demonstrate the technology readiness level (TRL) of sCO<sub>2</sub> direct-fired power cycles by taking it

from TRL 3 to 7 and allowing subsequent commercialization [60]. The details of the design of the STEP facility layout and component design from the turbine to valves and recuperators are detailed in Lariviere et al. [62] and Zhu [63]. Currently, the STEP power cycle isn't as established as the Allam-Fetvedt cycle, and as the pilot plant has only recently been commissioned and at present, there are no plans for future projects.

### **1.2.3. Outlook of Supercritical Combustion**

The true carbon neutrality of the Allam-Fetvedt and STEP power cycles is dependent on the fate of the CO<sub>2</sub> produced. The high-pressure pipeline-ready sCO<sub>2</sub> has particular use in enhanced oil recovery (EOR). EOR is a process where high-pressure sCO<sub>2</sub> is pumped into partially depleted oil fields to extract any remaining oil [64]. sCO<sub>2</sub> is a suitable displacing agent for EOR due to its low miscibility with a variety of crude oils whilst reducing the cost of permanent sequestration [65]. EOR would supply direct-fired sCO<sub>2</sub> power plants with a further income source through the recovery of saleable hydrocarbons from partially depleted oil fields, ideally coupled with the safe long-term storage of CO<sub>2</sub> [66]. However, since captured CO<sub>2</sub> is being used to recover more hydrocarbons, the manner of their combustion is important to the overall carbon neutrality of direct-fired sCO<sub>2</sub> power cycles. If the combustion of the hydrocarbons recovered is without CCSU and is essential to the profitability of the direct-fired sCO<sub>2</sub> power plant, then any CO<sub>2</sub> produced must be incorporated into the carbon life cycle of direct-fired sCO<sub>2</sub> power cycles.

Furthermore, there is the potential to explore biomass-derived syngas to fuel direct-fired sCO<sub>2</sub> power plants. Whilst this may create different impurity issues to coal, as well as differing in mineral content due to 100% inherent emissions coupled with the CO<sub>2</sub> absorption of the growing biomass this has the potential to become a carbon-negative electricity source [67].

A major challenge currently faced by the direct-fired sCO<sub>2</sub> power cycles is the lack of a fundamental understanding of the chemical kinetic mechanism for relevant conditions. The conditions are a high pressure of 300 atm and a CO<sub>2</sub> dilution of up to 96% [25]. A better understanding of the chemical kinetic

mechanism would allow combustion properties to be more accurately modelled and lead to an improvement in the overall efficiency of the plant design. For example, impurities within the cycle will alter the thermodynamic properties of the working fluid which will impact the cycle efficiency [68]. Furthermore, impurities within the gas flow may cause erosion of the turbine blades and pipeline, especially in the case of syngas from coal gasification [69]. The current design of the combustion chamber for direct-fired sCO<sub>2</sub> power plants is being held back by this lack of knowledge of combustion at extreme conditions [70]. A detailed chemical kinetic mechanism optimized for data recorded at high pressures and large CO<sub>2</sub> dilutions would lead to more accurate modelling of combustion at conditions relevant to direct-fired sCO<sub>2</sub> combustion.

### **1.3. Other High-Pressure Combustion Systems**

In addition to the power cycles outlined in this chapter, many other high-pressure combustion systems are outlined in this section. All these applications involve combustion in air and are often applied to the aviation industry. Again, as high-pressure data is more difficult to obtain, there is little experimental data to validate chemical kinetic mechanisms at these conditions, so the development of a high-pressure chemical kinetic mechanism for these conditions is a necessity to further improve the design of combustion systems.

#### **1.3.1. Spaceship Engines**

The extremely high-pressure combustion of liquid hydrocarbons has become a leading candidate to power the formation of space colonies due to their ease of manufacture, handling, and potential power output. SpaceX has produced the Raptor engine which burns liquid methane at a pressure of over 300 atm using a full-flow staged combustion cycle [71]. The exact formulation of the engine is kept as a trade secret and information is scarce. SpaceX CEO Elon Musk has stated the company's intentions to utilise the Raptor engine in the colonisation of Mars [72]. The high-power density of liquid methane and the lower cost relative to traditional rocket fuels reduce the size and costs compared to existing spacecraft. This has led rival company Blue Origin to switch to methane fuel for their new

Blue Engine-4 (BE-4) [73]. The colonisation of Mars is becoming increasingly likely, and it appears that high-pressure combustion chambers are the ideal method to make it a reality. The UAE recently announced its Mars 2117 Vision which aims to build a habitable settlement on Mars in the next 100 years, where one of the key challenges is creating transport that retains enough fuel for the return journey. By using methane as the primary fuel, this problem can be resolved for Mars habitation by utilising the Sabatier reaction to produce methane from Mars' predominantly CO<sub>2</sub> atmosphere [74].

### **1.3.2. Scramjet/Ramjet Engines**

A further application for high-pressure combustion is scramjet and ramjet combustion in supersonic aircraft. The ramjet engine is subsonic and typically operates between Mach 2 and 4.5, whereas the scramjet engine's operating speed is Mach 4 and above and is incapable of operating at subsonic speeds [75]. The concept of the ramjet engine was first proposed over 100 years ago, the engine removes the need for internal moving parts by achieving air compression through forward motion [76]. In a conventional ramjet engine, the air is captured and decelerated to a low subsonic velocity before the addition into the combustor [77]. However, the ramjet or scramjet engine cannot operate at the low pressures of takeoff because the dynamic pressure is inadequate for the engine to operate efficiently [76]. This application of high-pressure combustion is further potential research for a chemical kinetic mechanism for the high-pressure combustion of larger hydrocarbons.

### **1.3.3. Aviation Engines**

The typical operating pressure of a passenger aircraft engine is around 30 atmospheres (atm) with the jet fuel being injected into the combustion chamber at high pressures [78]. Traditionally aviation fuels have been petroleum-based liquid fuels produced from the fractional distillation of crude oil. Longer hydrocarbon kerosene-based fuels are particularly suited to the aviation industry due to their large energy density per unit volume and ease of handling and distribution across a global network [79, 80]. Aviation fuels consist of a mixture of

thousands of linear, branched, and cyclo-alkanes, the exact composition of which can alter the physical and chemical performance of the fuel. Current research is focussing on replacing crude oil-based jet fuels with synthetic jet fuels produced from the Fischer-Tropsch (FT) reaction of syngas and water [81]. This is a particularly pressing area of research as the aviation industry is one of the most challenging industries to decarbonise due to the requirement for a very energy-dense fuel and no method of capturing carbon emissions. In the UK's Sustainable Aviation 'Decarbonisation Road Map' [82] published in 2020, it was identified that synthetic jet fuels could reduce aviation emissions by 32% by 2050. Figure 1.3 shows a flow diagram of how synthesis gas (syngas) is converted into higher hydrocarbon liquid fuels.

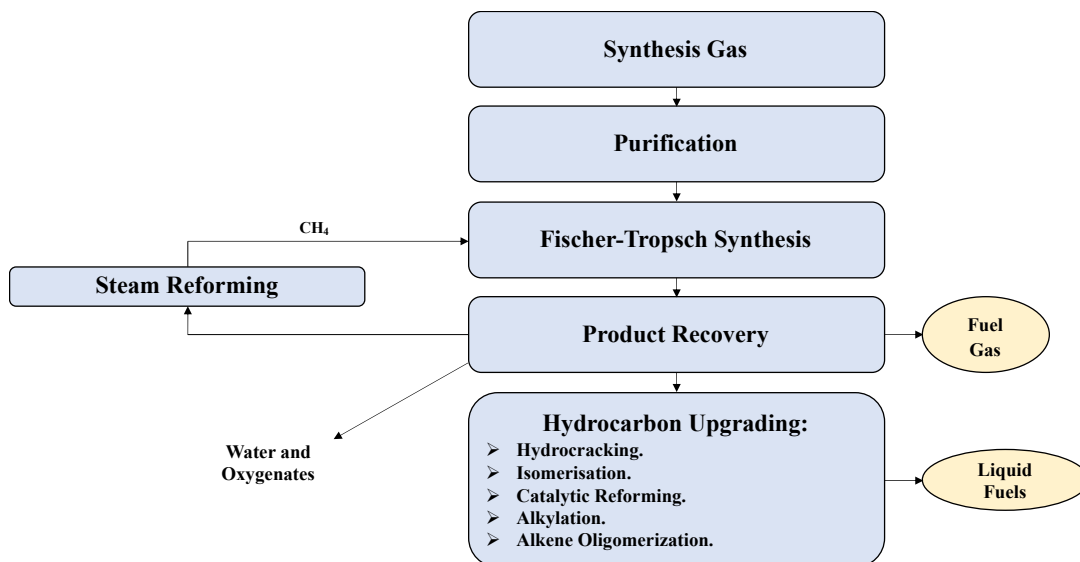


**Figure 1.3.** Schematic representations of the stages in converting syngas into long-chain hydrocarbons adapted from [83].

The University of Sheffield has begun a project in collaboration with Strata Technology to develop synthetic aviation fuels (SAFs) using its flagship FT rig reactor, to produce 1-1.5 litres per hour [84]. The shock tube developed as part of this project could potentially be applied to study the high-pressure combustion of the key components of SAFs produced as part of this project. Not only would an accurate determination of the ignition delay time of the SAF be a useful property for its useful application, but the data and fuel can also be used to improve and expand the high-pressure combustion mechanism to larger hydrocarbon species.

## 1.4. Knowledge Gaps Addressed in this Thesis

At the conditions of the combustion chamber of direct-fired supercritical power cycles such as the Allam-Fetvedt cycle discussed in Section 1.2.1, the chemical kinetic mechanism for combustion is poorly understood. Most chemical kinetic mechanisms have been developed at low pressures (0-20 bar) and low concentrations of CO<sub>2</sub> (0-5%) produced from the reaction. Very few rate coefficients that are utilised in chemical kinetic mechanisms have been deduced considering CO<sub>2</sub> as the main bath gas. More recently, ignition delay time (IDT) data have been published with CO<sub>2</sub> as a bath gas, thus allowing the production of a well-validated chemical kinetic mechanism specifically designed for sCO<sub>2</sub> combustion. This key knowledge gap is addressed in the three research chapters, which focus on three smaller knowledge gaps culminating in the production and validation of a well-validated mechanism for sCO<sub>2</sub> combustion.

Firstly, a high-pressure shock tube (HPST) has been developed at the University of Sheffield for the study of high-temperature and high-pressure chemical kinetics. The University of Sheffield (UoS) HPST can produce post-shock temperatures and pressures of 2000 K and 100 bar respectively. The shock tube is equipped with a state-of-the-art laser absorption diagnostic capable of monitoring OH, NO, and HO<sub>2</sub> concentrations at approximately 308 nm, 225 nm, and 227 nm respectively. Conceptualization, fabrication, and commissioning of the shock tube have taken the full course of this thesis due to the complexity of the two tender processes and the high specifications of the design. However, the HPST will be a vital asset to the University of Sheffield's future research and can be utilised in the future to address numerous knowledge gaps, such as:

- Determination of IDT measurements for key fuels for sCO<sub>2</sub> combustion between 0 and 100 bar, and at a range of bath gas compositions in large dilutions of CO<sub>2</sub>.
- Determination of OH and HO<sub>2</sub> species time histories of methane and hydrogen combustion, for the experimental determination of rate coefficients of key reactions identified in this thesis.

- Study of the chemical kinetics of ammonia combustion behind reflected shock waves using IDT and nitrous oxide (NO) species time history measurements.
- Study of the chemical kinetics of the combustion of potential aviation fuels and their components (this would require a heating jacket for the shock tube driven section and mixing tank).
- Studying the combustion of synthetic jet fuels created using the FT reactor at the Translational Energy Research Centre (TERC).
- Study of the high-pressure combustion of methane in air for proposed spaceship engines such as Raptor-X.

Whilst this list is not exhaustive and the direction of research is always susceptible to change based on new developments, this list highlights some of the important potential applications of the shock tube. Whilst the time constraints of this EngD have limited the potential to address all the intended knowledge gaps using the HPST, its development offers a crucial experimental tool for future research at the TERC, University of Sheffield.

The second major research knowledge gap addressed was the development of a chemical kinetic mechanism specifically designed to simulate high-pressure combustion in CO<sub>2</sub>. The University of Sheffield supercritical CO<sub>2</sub> mechanism (UoS sCO<sub>2</sub> 1.0 Mech) was created based on 52 IDT datasets of methane, hydrogen, and syngas combustion from shock tubes across the world. By assimilating and using such a vast number of datasets, a new chemical kinetic mechanism was created which was determined on average to better model all 52 datasets. This created a base chemical kinetic mechanism, which can be utilised for the simulation of combustion in direct-fired sCO<sub>2</sub> cycles and further improved and refined through the publication of new experimental data and the more accurate determination of the rate coefficients of reactions in a CO<sub>2</sub> bath gas.

The third major research knowledge gap addressed was the lack of IDT data available for hydrogen (H<sub>2</sub>) and syngas combustion in CO<sub>2</sub> between 20 and 40 bar. Before this work, only three IDT datasets for H<sub>2</sub> combustion had been published by Shao et al. [85] at approximately 40, 110, and 270 bar. The eight

datasets in Section 4.3 allow comparison between the bath gas composition and equivalence ratio at both 20 and 40 bar. H<sub>2</sub> combustion is the most basic chemical kinetic mechanism and is the foundation for the combustion of larger fuels. Therefore, developing a much better understanding of H<sub>2</sub> combustion is essential before moving on to syngas and methane combustion. Further to this, the syngas combustion datasets in Section 4.4 extends this to CO combustion. A fundamental understanding of CO combustion is essential for modelling combustion in CO<sub>2</sub>, as CO is formed during the reaction from the large concentration of the CO<sub>2</sub> bath gas. Therefore, understanding the combustion of syngas is not only essential in itself but also for the combustion of any larger hydrocarbon and natural gas mixtures.

Lastly, Chapter 5 further validates the UoS sCO<sub>2</sub> 2.0 mechanism and generates 10 IDT datasets for methane/hydrogen and methane blends in CO<sub>2</sub>. Methane/hydrogen blends haven't been studied using a shock tube for over a decade and these data are modelled by older mechanisms. This chapter compares the stoichiometric combustion of an equal blend of methane and hydrogen blend in 85% CO<sub>2</sub> and 85% N<sub>2</sub>. The literature review of the existing IDT data in Section 3.4.1 identified a lack of data investigating the effect of equivalence ratio on combustion above 20 bar. Six new datasets are produced between  $\phi=0.5$  to  $\phi=2.0$ . The effects of these changes on the datasets are discussed and analysed in detail.

This thesis contributes to science and engineering both in the short term and the long term. In the short term, the key research in Chapters 3, 4, and 5 have generated three research publications. The experimental data and chemical kinetic models and publically available alongside their respective studies allowing researchers to utilize and progress the ability of the current chemical kinetic mechanism to simulate direct-fired sCO<sub>2</sub> combustion. Furthermore, the development of the UoS HPST will contribute substantially to the field of combustion in the long term. The shock tube has been constructed with adaptability in mind and the potential to procure additional components such as a heating jacket, additional laser diagnostics, and additional segments of the driven or driver section to increase the overall length of the shock tube.

## 1.5. Thesis Overview

This thesis is split into the shock tube design and three research chapters followed by a conclusion and a series of appendices detailing training, publications, and opportunities outside of the main thesis body.

Chapter 2 details the conceptualisation and fabrication of the UoS HPST. The initial design was created in 2019 following an extensive literature review that was subsequently refined by working with the consultancy company WSP in 2020/2021 before initiating the tender process. Two tenders were required for the shock tube, the HPST itself, and the laser absorption diagnostic equipment, with some smaller equipment being procured separately out of the tender. The UoS HPST was fabricated and installed in 2022 by Heblac Technologie and commissioned in late 2022.

Chapter 3 details the creation of the UoS sCO<sub>2</sub> mechanism, which was published at the 4<sup>th</sup> European sCO<sub>2</sub> Conference for Energy Systems [86] and a subsequent special edition publication in Energy [87]. The UoS sCO<sub>2</sub> mechanism was created based on a series of IDT datasets for methane, hydrogen, and syngas combustion and the analysis of four existing chemical kinetic mechanisms. The mechanism was based on the USC II mechanism with alterations made to the rate coefficients based on sensitivity and quantitative analysis to create a universal mechanism that is on average a better fit to the IDT datasets across a range of pressures, equivalence ratios and CO<sub>2</sub> dilutions.

Chapter 4 details work undertaken in collaboration with the King Abdullah University of Science and Technology (KAUST) in Saudi Arabia. The IDT data was collected using their high-pressure shock tube for hydrogen and syngas combustion across a range of CO<sub>2</sub> dilutions and pressures. The IDT datasets were compared to simulations of AramcoMech 2.0 and UoS sCO<sub>2</sub> 2.0 Mech and were used to investigate the combustion under these conditions through sensitivity and rate of production analysis. The two different fuels were split into two separate publications in Fuel [88, 89].

Chapter 5 details a further collaboration with KAUST on the autoignition of methane and methane/hydrogen blends. Methane/hydrogen was selected as it is a promising fuel blend for multiple applications and as a good test for UoS sCO<sub>2</sub> 2.0. Whilst both fuels have been used to create the mechanism, it is interesting to see how well the mechanism models the interactions between them.

## **1.6. Conclusion**

Direct-fired sCO<sub>2</sub> power cycles have the potential to bridge the gap between a hydrocarbon-centred energy industries to one focused on renewables in a manner that releases no harmful CO<sub>2</sub> emissions to the atmosphere. The combustion chambers of these cycles operate at pressures and CO<sub>2</sub> concentrations of up to 300 bar and 96% respectively, utilising natural gas or syngas as a fuel. The chemical kinetic mechanism of combustion under these conditions is poorly understood, with most chemical kinetic mechanisms being validated for much lower pressures and CO<sub>2</sub> dilutions. The work detailed in this thesis seeks to produce a chemical kinetic mechanism that is validated for combustion under these conditions. This will allow the combustion of these cycles to be more accurately simulated, generating information that can be used to further refine and optimise their design, increasing overall plant efficiency.

## **2. Fabrication of the University of Sheffield High-Pressure Shock Tube**

### **2.1. Introduction**

The shock tube is an experimental technique that has been used to study high-pressure and high-temperature chemical kinetics of gases and aerosols under almost adiabatic conditions. The first recorded use of the shock tube was in 1899 by French scientist Paul Vielle, who noted the creation of a shock wave when a diaphragm was ruptured between two tubes that propagated from the high-pressure to the low-pressure tube section [90]. Propagation of the shock wave down the tube compresses and heats the test gas creating an almost instantaneous pressure and temperature rise, initiating a reaction that can be monitored using various diagnostic techniques. The earliest recorded use of shock tubes for the study of chemical kinetics was in 1948 to research methane and ethane combustion [91].

Conceptually, a shock tube is very simple. It consists of a high-pressure driver section and a low-pressure driven section of the tube, separated by a burstable diaphragm. The driver section contains high-pressure driver gas. A driver gas is typically an inert gas with low molecular weight and a fast speed of sound, usually, helium is preferred. The driven section contains the test gas being studied in the experiment. For combustion chemistry, this is fuel and oxygen diluted in a bath gas, typically argon or nitrogen. The diaphragm is a thin sheet of metal or plastic that separates the gases between the two sections. In each experiment, the diaphragm is ruptured to form the shock wave and must be removed and replaced.

### **2.2. Types of Shock Tube**

Whilst the basic shock tube follows the same principle of creating a shock wave through the rupture of a diaphragm, there are variations between shock tubes. Whilst most shock tubes are usually round to provide the greatest strength and

avoid creating weak spots in the corner sections, some shock tubes have square-driven sections that minimize boundary layer effects [92].

### **2.2.1. Incident and Reflected Shock Tubes**

The main distinction between shock tubes is whether the test location is studying the incident or reflected shock wave. These terms refer to if the ignition is observed behind the incident or the reflected shock wave. By monitoring the ignition behind the incident shock lower temperatures and pressures can be achieved as the test gas is only compressed by the shock wave once [93]. The reflected shock tube is discussed in more detail in Section 2.3, but put simply, the test section reaches greater temperatures due to the second compression of the reflected shock wave in addition to the incident wave. These two types of shock tubes differ by observation position. Incident shock tubes make measurements approximately halfway down the driven section to prevent interference and perturbation from the adiabatic conditions by the reflected shockwave. Reflected shock tubes have the observation position as close to the endwall as possible to provide a longer test time before the reflected shockwave collides with the contact surface. It is possible to have two observation positions in a shock tube which allows flexibility between the two different operational modes.

### **2.2.2. Single Pulse Shock Tube**

The 'single pulse shock tube' is a type of reflected shock tube that differs from the conventional one due to the presence of a large dump tank, usually next to the diaphragm or towards the end of the driven side of the shock tube [94-96]. Following the reaction on the millisecond scale, expansion waves created in the shock tube rapidly cool the test gas and thus it retains its high-temperature composition [97]. This is important for reactions in which a range of products are formed, or the products are unknown as it allows for intrusive measurements such as gas chromatography to be used.

### **2.2.3. Double Diaphragm Shock Tube**

A 'double diaphragm shock tube' differs from a traditional shock tube by using two diaphragms, separated by a small space in between them. The double diaphragm arrangement (DDA) gives more control over the postshock conditions than a traditional shock tube [98]. In a DDA the space between the diaphragms is filled to a given pressure (typically half the pressure of the driver section) whilst the driver section is filled. The diaphragm rupture is caused by suddenly venting the mid-section between the diaphragms into an expansion vessel which creates a large pressure difference [99]. This then causes the first diaphragm by the driver section to burst, creating an initial shock wave that bursts the second diaphragm. This means for each experiment, the driver and driven section are filled to an exact desired pressure, thus increasing the repeatability between experimental runs. However, this can be problematic as the chances of non-ideal diaphragm rupture increase as two diaphragms are now being used.

### **2.2.4. Combustion-Driven Shock Tube**

Another variation of a traditional shock tube is the 'combustion driven shock tube' which produces shocks of higher Mach number for similar pressure differences between the driver and driven section. This is achieved by using a mixture of hydrogen and oxygen diluted in the helium as a driver gas which is typically ignited using a laser [100]. The combustion of the fuel within the driver section raises the pressure and temperature of the driver section gas and thus increases the pressure ratio across the diaphragm and thus the maximum Mach number achievable. By using a mixture of hydrogen and oxygen, the sound speed can increase in a combustion-driven shock tube by over 70% [101].

### **2.2.5. Diaphragmless Shock Tube**

One unconventional type of shock tube is the diaphragmless shock tube (DFST) [102]. The DFST uses valves to initiate a shock wave in place of the traditional diaphragm. This is beneficial as it reduces the time taken between experimental runs due to changing the diaphragm and this can increase reproducibility.

Furthermore, removing the requirement to open the shock tube between experiments to change the diaphragm reduces the risk of impurities entering the shock tube and reduces the time taken for an experimental run [103].

### **2.2.6. Convergent and Divergent Shock Tubes**

A shock tube can also be convergent or divergent where there is a change in diameter between the driver and driven section. A convergent shock tube such as the high-pressure shock tube utilised by Stanford University [85] has a driven section with a diameter of 5.08 cm which is smaller than the driver section. This increases the Mach number of a shock for a given pressure ratio compared to a constant area shock tube [101]. Conversely, a divergent shock tube used by Texas A & M University [104] has a driven section of greater diameter than the driver section. This reduces the volume of helium required for the driver section.

### **2.2.7. Inclined Shock Tube**

A final and interesting variation of the shock tube is an 'inclined shock tube' as described by Koppenberger [92]. This shock tube is positioned on an I-Beam which can be lifted on one side to tilt the shock tube to a maximum angle of 65°.

## **2.3. Shock Tube Operation**

In a shock tube, the high-pressure driver section (4) and low-pressure driver section (1) are separated by a diaphragm as shown in Figure 2.1. As the pressure inside the driver section increases as it is filled, the pressure ratio across the diaphragm increases. As shown in Figure 2.1 b) eventually the pressure difference becomes so great that the diaphragm ruptures, this creates a shock wave that propagates down the shock tube towards the endwall of the driven section. The incident shock wave heats and compresses the test gas as it goes, creating a distinct region 2. Regions 2 and 4 are separated by the contact surface, the contact surface also moves towards the driven section where the driver gas and driven gas are mixing. Once the incident shock wave hits the driven section endwall, it is reflected and becomes a reflected shock wave Figure 2.1 c). The reflected shock wave moves back towards the driver section and further heats

and compresses the test gas, creating a distinct region 5 of higher pressure and temperature. The regions are described in Table 2.1.

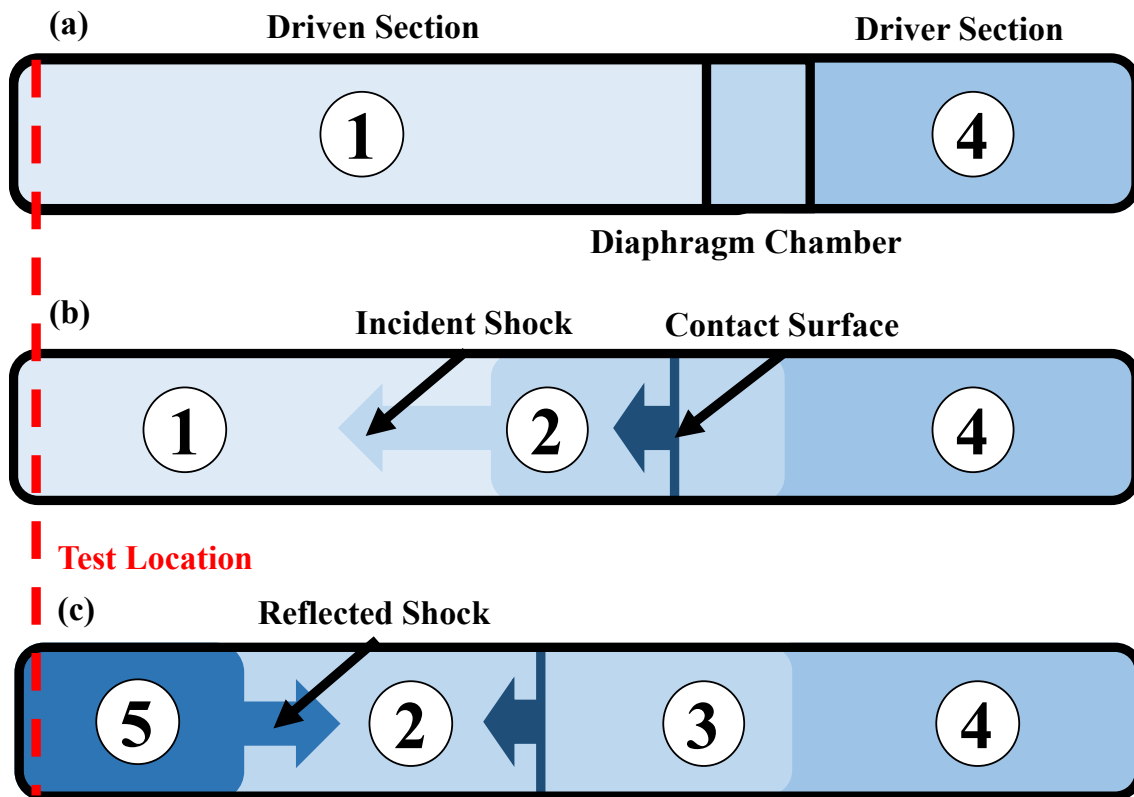


**Figure 2.1.** Schematic of typical shock tube operation: a) shock tube before diaphragm rupture, b) diaphragm rupture and creation of the incident shock, c) formation of the reflected shock following the incident shock hitting the endwall.

**Table 2.1.** Description of the five regions within a reflected shock tube.

Region	Description
1	Initial conditions of the undisturbed low-pressure test-gas.
2	The region of test-gas between the incident shock wave and the contact surface.
3	Region of the driver-gas between the contact surface and the undisturbed driver-gas.
4	Initial conditions of the undisturbed high-pressure driver-gas.
5	The test gas region between the reflected shock wave and the end wall.

The driver gas in region 3 has been affected by rarefaction waves propagating from the diaphragm to the high-pressure driver section endwall. The region and the approximate direction of the rarefaction waves are shown in Figure 2.2. Figure

2.2 also shows the formation of the 5 different shock tube regions and the propagation of the incident and reflected shock waves as a function of shock tube position ( $x$ -axis), where 0 denotes the location of the diaphragm. The maximum possible observation time is the length of time in which region 5 exists at constant pressure and temperature. The collision of the reflected shock wave and contact surface creates waves that perturb the ideal conditions of region 5.

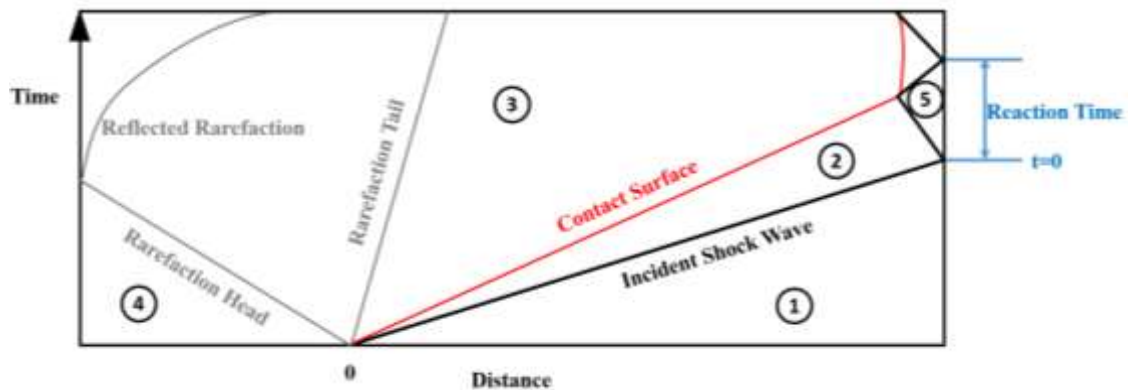


**Figure 2.2.** Schematic of time as a function of distance from the shock tube diaphragm [105].

### 2.3.1. Increasing Shock Tube Test Times

As shown in Figure 2.2, the maximum test time possible in a shock tube is determined by the collision of the reflected shock wave and the contact surface. This is dependent on multiple factors, including the driver and driven gases used as well as the Mach number and the dimensions of the shock tube. Therefore, the maximum available test time will be limited by the actual dimensions of the shock tube. This method allows shock tubes of a fixed dimension to achieve longer test times.

One method is driver gas tailoring (or contact surface tailoring) which reduces matches the acoustic sound speed of the driver and driven gas, meaning no waves are created from the collision of the reflected shock wave and the contact surface, allowing for a longer observation time [106-108]. This is shown in Figure 2.3, where the observation time is longer, meaning combustion on a slower timescale can be studied, i.e., lower temperatures and less reactive fuels.

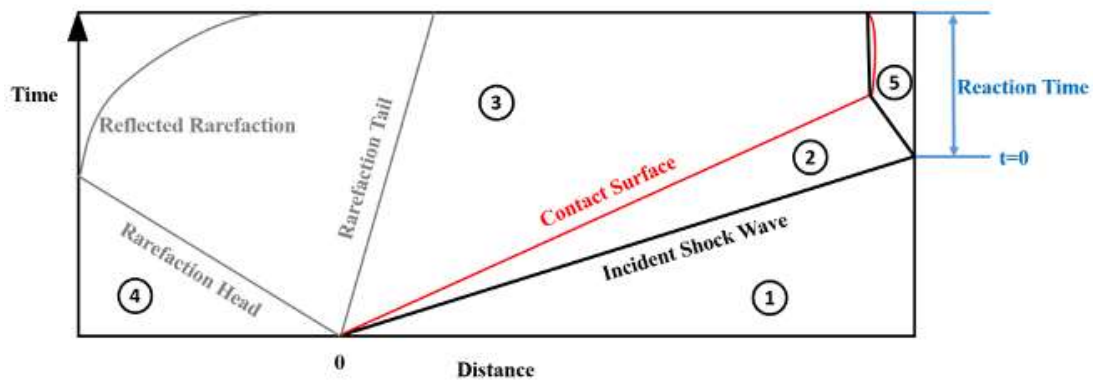


**Figure 2.3.** Schematic of time as a function of distance from the shock tube diaphragm for a tailored shock tube [105].

When designed and implemented correctly, a tailored pressure decrease caused by the reflected shock-contact surface interaction can reduce or remove the non-ideal pressure rise and increase the pressure and temperature stability of the test gas [109]. Tailored conditions have been implemented for the study of slower, low-temperature combustion kinetics in both conventional [110, 111] and convergent shock tubes [108].

Another technique to achieve longer test times within a shock tube is the staged filling of the driver gas [112]. This technique works by partially filling the driver section with a low-speed-of-sound gas before adding the usual driver gas at the diaphragm, thus pushing the low-speed-of-sound gas towards the driver section endwall. This method of pre-filling, when used in conjunction with driver gas tailoring, means that the rarefaction waves take longer to reach the test section, and thus the available test time increases.

### 2.3.2. Rapid Compression Machines

The main rival to the shock tube experimental technique for the study of high-pressure combustion is the rapid compression machine (RCM). RCMs are advantageous as they allow for the determination of IDTs in the order of 15-40 ms [113], much longer than is achievable using shock tubes without using tailored conditions. On the other hand, the heat loss and fluid mechanics of the RCM can cause variations between different RCMs monitoring the same experimental conditions [113]. In an RCM, a piston is used to compress the test gas mixture, a combination of fuel, oxygen, and diluent, like that of a shock tube. A detailed

description and schematic of an RCM can be found in Wang et al. [114]. Usually, researchers utilise both shock tubes and RCMs to monitor IDTs across different timescales and thus increase the temperature range of IDT datasets. RCMs and shock tube experiments have been coupled for the study of the chemical kinetics of *n*-butylbenzene [115], ethanol [116], and diethyl ether [117].

## **2.4. Non-Ideal Shock Tube Effects**

The behaviour of supercritical fluids in a shock tube can be approximated fairly well using a perfect gas equation of state (EoS) when far enough away from the critical point of the gas [118]. This can be used to simplify modelling at sCO<sub>2</sub> conditions as well-validated shock wave equations can be used. A supercritical fluid forms when a gas exceeds its critical temperature and pressure, for CO<sub>2</sub> these are 304.25 K and 73.87 bar, respectively [119]. Using a CO<sub>2</sub> bath gas in place of the traditional argon and nitrogen, more commonly utilised in shock tube experiments can have physical effects on shock tube experiments, such as increasing bifurcation.

### **2.4.1. Bifurcation**

Bifurcation is a non-ideal shock tube effect identified early on in the development of shock tubes [120]. Bifurcation is a physical effect in shock tubes caused by the interaction of the shock wave with the boundary layer. The boundary layer in a shock tube is a thin layer of the driver gas and the test gas that forms along the internal wall of the shock tube due to the viscosity of the gas flow creating a velocity gradient from the centre of the shock tube to the walls [101]. This effect is shown in Figure 2.4 where  $\delta$  is the thickness of the boundary layer which is at a maximum at the diaphragm and a minimum is the rarefaction head and the incident shock front.

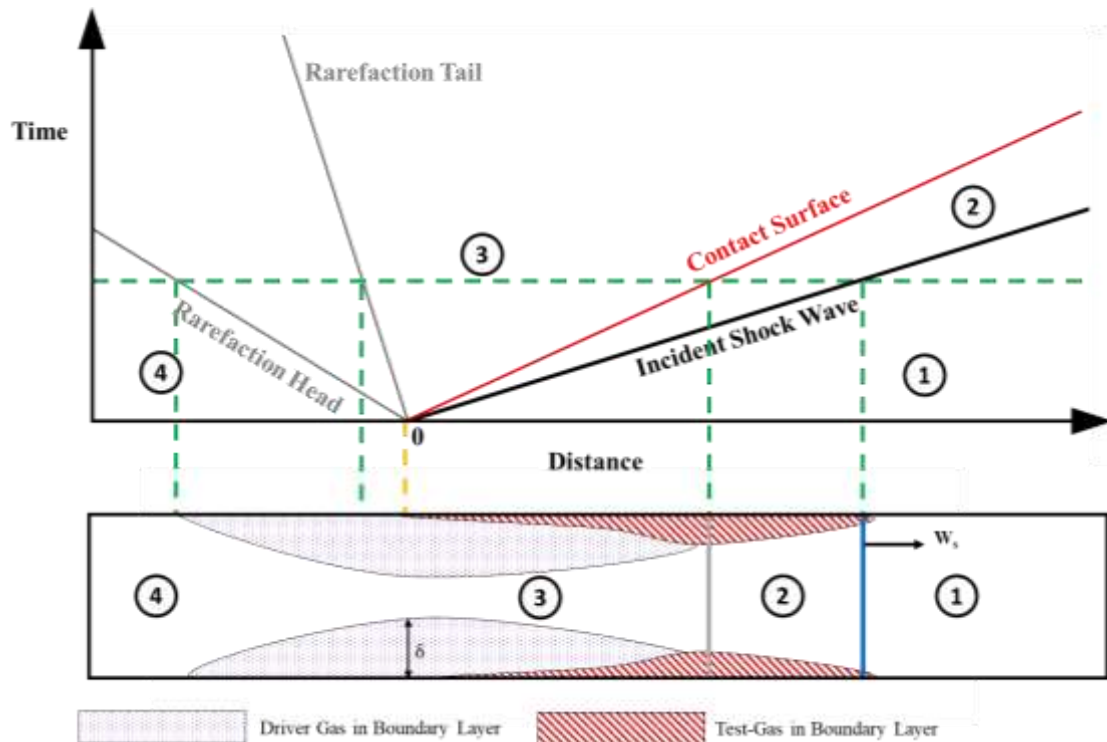


**Figure 2.4.** Schematic diagram of boundary layer growth during incident shock wave propagation [101].

The effect of bifurcation is the creation of two different oblique shock waves inside the test gas region of the shock tube as the reflected shock wave passes through the boundary layer, leading to temperature and pressure fluctuations [85, 121]. These fluctuations make the definition of IDT from the pressure trace more difficult and can induce a larger error in the measurement.

The extent of bifurcation is dependent on the boundary layer thickness, which is in turn, dependent on multiple factors. The main influence prevalent in this work is the test gas composition. Increasing the concentration of polyatomic gas (such as  $\text{CO}_2$ ) in the test gas mixture increases the effect of bifurcation which has been found in mixtures of large dilutions of  $\text{CO}_2$  [122, 123] and other triatomic gases [124]. When studying the absorption cross-section of methane Koroglu et al. [125] observed less severe bifurcation effects in a 30% dilution of  $\text{CO}_2$  compared to when studying a 98% dilution. It is argued that if the measured and predicted pressure profiles are in good agreement, then the effects of bifurcation can be ignored [126]. Normally shock tubes use a monoatomic bath gas to reduce bifurcation and avoid the influence of bifurcation entirely, however, a dilution of  $\text{CO}_2$  is required to study the combustion of direct-fired  $\text{sCO}_2$  combustion. Hargis

and Petersen [123] found it increasingly difficult to make accurate IDT measurements with increased CO<sub>2</sub> concentration during their study of methane combustion in CO<sub>2</sub>. However, this study was at 1.73 atm, Shao et al. [85] found in their 2019 shock tube study at pressures of 286 atm with a CO<sub>2</sub> dilution of 85% and found that bifurcation did not influence the quality of results, only the maximum observable reaction time. The authors argued that the bifurcation effect was lesser due to the greater experimental pressures reducing the size of the boundary layer.

Furthermore, the boundary layers' interaction with the reflected shock can cause a pressure rise in the test gas section ( $dP_5^*/dt \neq 0$ ) which perturbs the temperature and pressure. This effect can be mitigated by using a 'driver insert'. A cone-shaped driver section insert is attached to the endwall of the driver section, causing some rarefaction waves to reflect towards the driven section early [109]. The reflected rarefaction waves cause a slight pressure decrease in the test gas section and when designed correctly, this pressure decrease can cancel out the non-ideal pressure rise and increase the stability of the test gas region [109].

One method used to reduce the influence of bifurcation effects on experimental data is to use endwall measurements as opposed to sidewall. Measurements taken from the endwall can be taken from the centre of the shock tube rather than the side where the effects of the boundary layer are more prominent [127].

#### **2.4.2. Other Non-Ideal Effects**

One non-ideal effect is the remote ignition phenomenon which occurs particularly when studying reactions with long IDTs. During the long delay, ignition occurs away from the endwall, this creates new shock waves which propagate into the test gas region. Remote ignition can be reduced or removed entirely by using a constrained reaction volume (CRV) approach [128]. CRV involves staged filling of the driven section to compress the reactive component of the test gas against the endwall, preventing ignition from occurring from elsewhere within the tube.

Shock attenuation occurs as the shock wave propagates down the shock tube causing it to decelerate from its initial velocity. Attenuation occurs due to the formation of a boundary layer [129, 130] along the walls of the shock tube as well as a non-ideal diaphragm rupture [131]. The extent of attenuation can be reduced by using a larger diameter shock tube meaning the boundary layer has a smaller effect on the shock wave [132].

Another non-ideal shock tube effect is the presence of a small pressure rise and fall after ignition, known as the contact surface bump [108]. A contact surface bump occurs when a shock wave interacts with the non-ideal interface of the mixing zone between the driven and driver gas. This effect can be explained by shock impedance [133] and reduced by the addition of a light buffer gas to the driven section [108].

The final non-ideal effect which can occur in a shock tube is caused by the buildup of impurities over time. Organic products of combustion may condense onto the shock tube walls and interfere with subsequent experiments if the shock tube isn't properly maintained. The presence, and therefore the effects of impurities can be minimized by regular cleaning, lower operating temperatures, and introducing the test gas into the driven section as close to the measurement location as possible [134]. Mulvihill and Petersen [135] investigated the influence of cleaning techniques on the IDT for hydrogen combustion. The authors found that cleaning the shock tube had a negligible effect on the IDT but cleaning the mixing tank with *tert*-butyl hydroperoxide (TBHP) did increase the IDT. This indicates that radical impurities from the mixing tank were causing the reaction to occur faster than it should have done, indicating the formation of impurities in the mixing tank has a greater effect than in the shock tube.

## **2.5. Shock Tube Concept**

The design and fabrication of the UoS HPST have formed a key part of this EngD project. The initial shock tube concept was designed by researching existing shock tubes and tying this into the research aims of the UoS and the TERC whilst working to strict budgetary and space constraints. Section 2.5 details the

conceptualisation of the key parts shock tube before the other shock tube components are introduced in Section 2.6. Figure 2.5 is a piping and instrumentation diagram (P&ID) created by WSP during their consultancy work on the project.

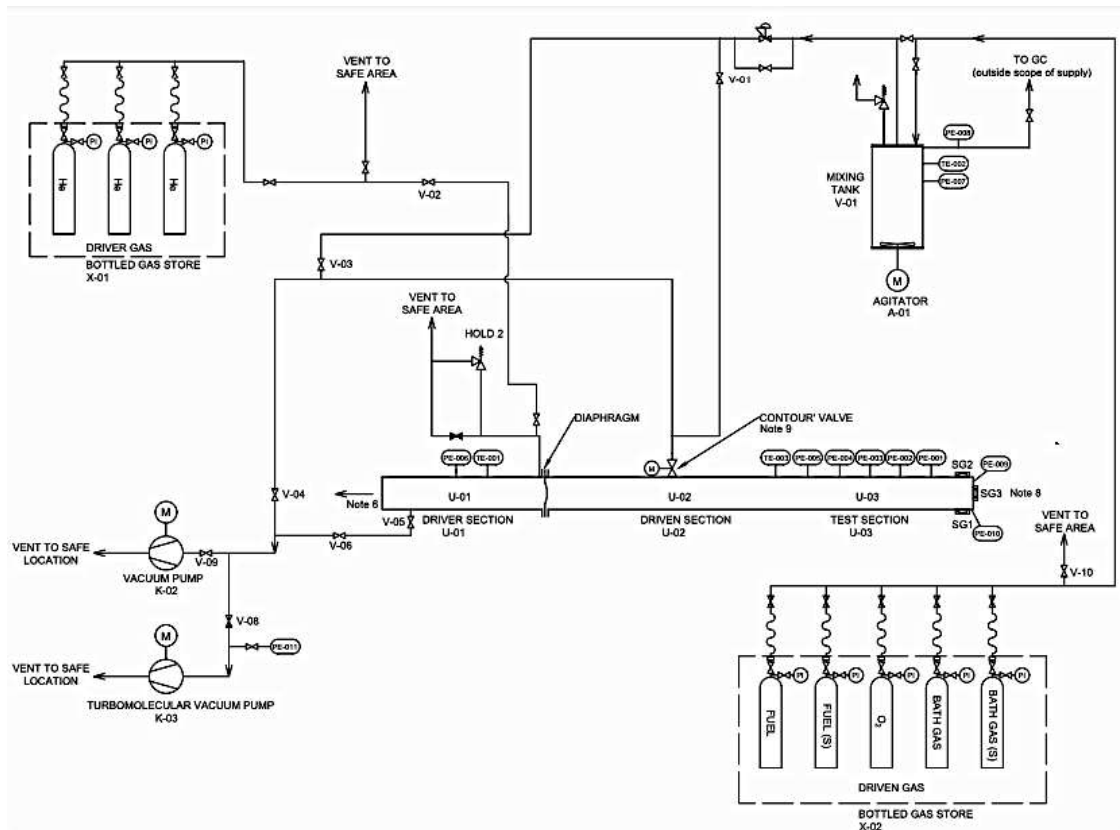
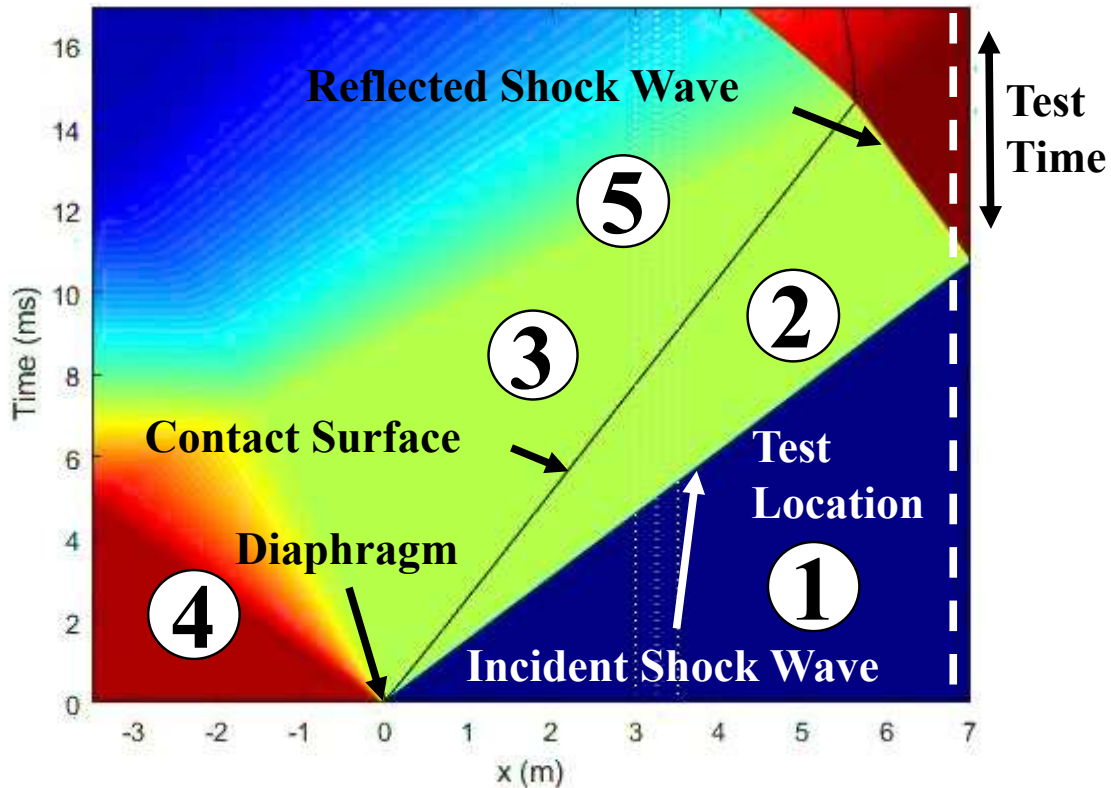


Figure 2.5. Shock tube P&ID by WSP.

Figure 2.6. was created using the freely available University of Wisconsin Shock Tube Laboratory (WiSTL) x-t calculator [136]. This simulates to post-shock conditions of a shock tube experiment, either in traditional operation or using CRV. This condition was performed close to the conceptual maximum operating conditions of the UoS HPST of 85 bar postshock pressure and 1960 K post-shock temperature. The simulation was performed using a helium-driver gas and a nitrogen-driven gas for simplicity. The initial pressure of the driven section was set as 0.1 bar and the driver section pressure was ~100 bar, both at 300 K. This created a Mach number of 3.6 in the simulation. Whilst this is simulated, and there will be differences in a real shock tube, where non-ideal effects come into effect, it does suggest 2 ms of stable postshock pressure for chemical kinetic measurements, before the interference of the rarefaction wave. This confirms the

conceptual configuration will allow sufficient time to measure IDTs and species time histories.



**Figure 2.6.** WiSTL simulated x-t diagram of post-shock conditions near the maximum temperature (1960 K) and pressure (85 bar) with a helium-driver gas and nitrogen-driven gas [136].

### 2.5.1. Initial Concept – Temperature and Pressure Range

The key factors discussed in this section were the initial decisions on which the rest of the shock tube was built around, this includes maximum temperature, maximum pressure, driven and driver section lengths, diameter, and range of Mach number. The Mach number ( $M$ ) is defined using Equation 2.1 as a ratio of the shock velocity ( $u_1$ ) to the local speed of sound of a gas ( $a_1$ ) [101].

**Equation 2.1.** 
$$M_1 = \frac{u_1}{a_1}$$

Therefore, the larger the Mach number, the larger the shock wave velocity, this leads to a shorter observation time as the shock wave and contact surface interaction occurs faster. The shock tube was limited to a maximum length of 11

m and a total budget of £540,000 for both the shock tube and laser diagnostic equipment.

The first decision to be made is the temperature and pressure range the shock tube will operate in, which determines the Mach number range required. The initial concept was to have a maximum post-shock temperature and pressure of 2500 K and 150 bar. However, during the design process, the decision was made to reduce these to 2000 K and 100 bar. The temperature was decreased to improve the selection of pressure transducers available for the shock tube. Many popular transducers used in similar shock tubes only operate at flashpoint temperatures around 2000 K, so reducing the maximum temperature slightly would reduce the specification and thus the cost and competitiveness of the equipment required. Furthermore, as most experiments in the shock tube would be done around 1000-1500 K, the reduction in maximum temperature will not have a large effect on the desired usage of the shock tube. The pressure reduction was made due to reducing the overall safety factor and is discussed more in Section 2.5.5.

### 2.5.2. Driver and Driven Section Length

After deciding on the maximum pressure and temperature, the next consideration is the length of the shock-driven section. The driven section length is determined based on the observation time required and the cost and length restrictions. A longer driven section will give a longer observation time, but this will take up more space and be more costly. The ideal observation time can be calculated using Equation 2.2 [101] which relates maximum observation time ( $\Delta\tau$ ) to driven section length ( $\chi_1$ ). Where  $M_1$  is the Mach number of the incident shock,  $a_1$  is the speed of sound in the driven gas and  $\gamma_1$  is the specific heat ratio of the driven gas.

**Equation 2.2.** 
$$\Delta\tau = \frac{\chi_1}{M_1 a_1} \left( \frac{\gamma_1 - 1}{2\gamma_1} \right)$$

This equation was used to determine the maximum observation time of  $M=2-5$  for the three primary bath gases which will be used by the shock tube nitrogen, argon, and CO<sub>2</sub> in Figure 2.7.

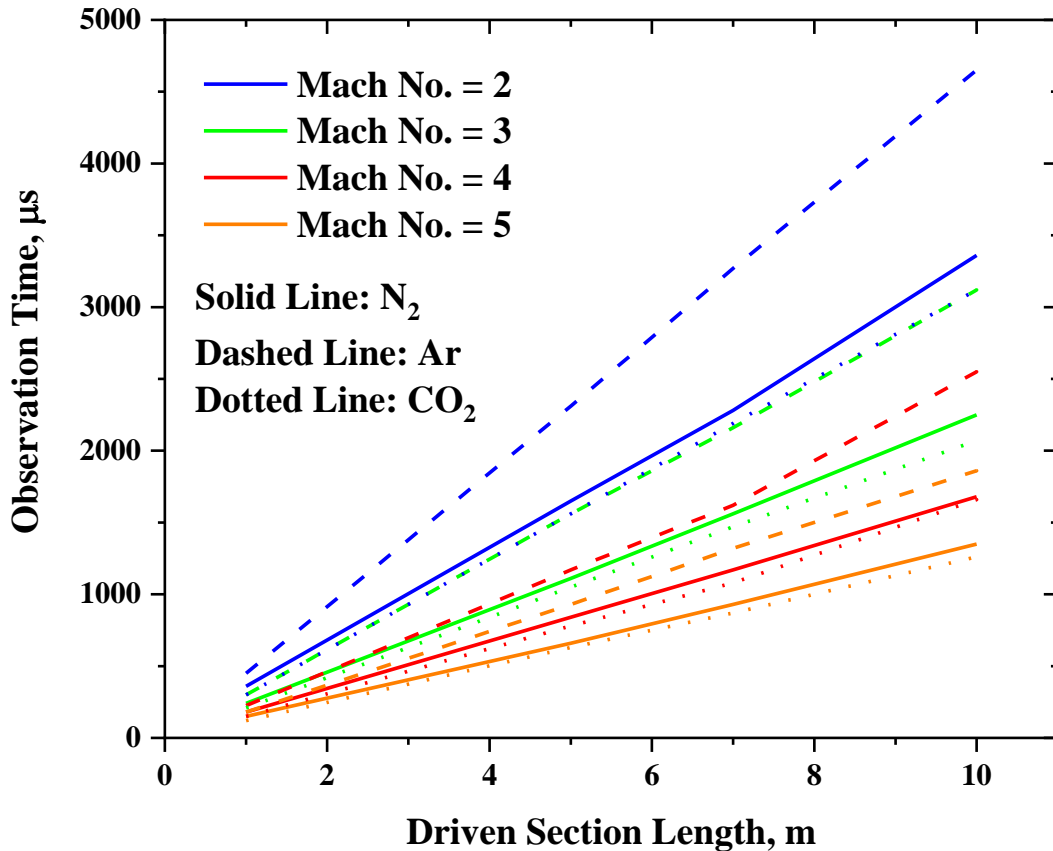


**Figure 2.7.** A plot of maximum observation time against the shock tube driven section length for an N<sub>2</sub> (solid line), Ar (dashed line), and CO<sub>2</sub> (dotted line) bath gas.

As seen in Figure 2.7, the smallest observation time occurs when using CO<sub>2</sub> as a bath gas. To give an observation time of 2 milliseconds (ms) would require a driven section of 7 m in length at  $M=2$ . Allowing for non-ideal effects and making the reasonable assumption that most experiments will be done at  $M=3-4$ , a length of 7 m was decided upon. A driven section length of 9 m was considered but required a driver section length that would take the shock tube over the 11 m space constraints and significantly increase the total cost of the project.

The next decision is the length of the driver section. The minimum driver section length can be estimated using Equation 2.3 as a function of the time taken for the rarefaction wave to reach the test gas region which is calculated using Equation 2.4 [101]. These calculations depend on the driver gas-specific heat ratio ( $\gamma_4$ ) and speed of sound ( $a_4$ ). The driver section length determined from Equation 2.3 is the minimum length of the driver section required to ensure that the collision of

the contact surface and reflected shock ends the experiment, not the arrival of the rarefaction waves.

**Equation 2.3.** 
$$\tau_c = \frac{2\chi_4}{a_4} \left\{ 1 - \frac{\gamma_4 - 1}{\gamma_4 + 1} \frac{a_1}{a_4} \left( \frac{M_1^2 - 1}{M_1^2} \right) \right\}^{-\left( \frac{\gamma_4 + 1}{2(\gamma_4 - 1)} \right)}$$

**Equation 2.4.** 
$$\tau_c = \Delta\tau + \frac{\chi_1}{M_1 a_1}$$

The results from Equation 2.3 are plotted in Figure 2.8 for the same three bath gases. All calculations were performed assuming a driver gas of pure helium, which will be used in all conditions except for driver gas tailoring which will use a He:Ar blend. However, as argon has a slower speed of sound in the gas, the observation time will be longer in these cases.

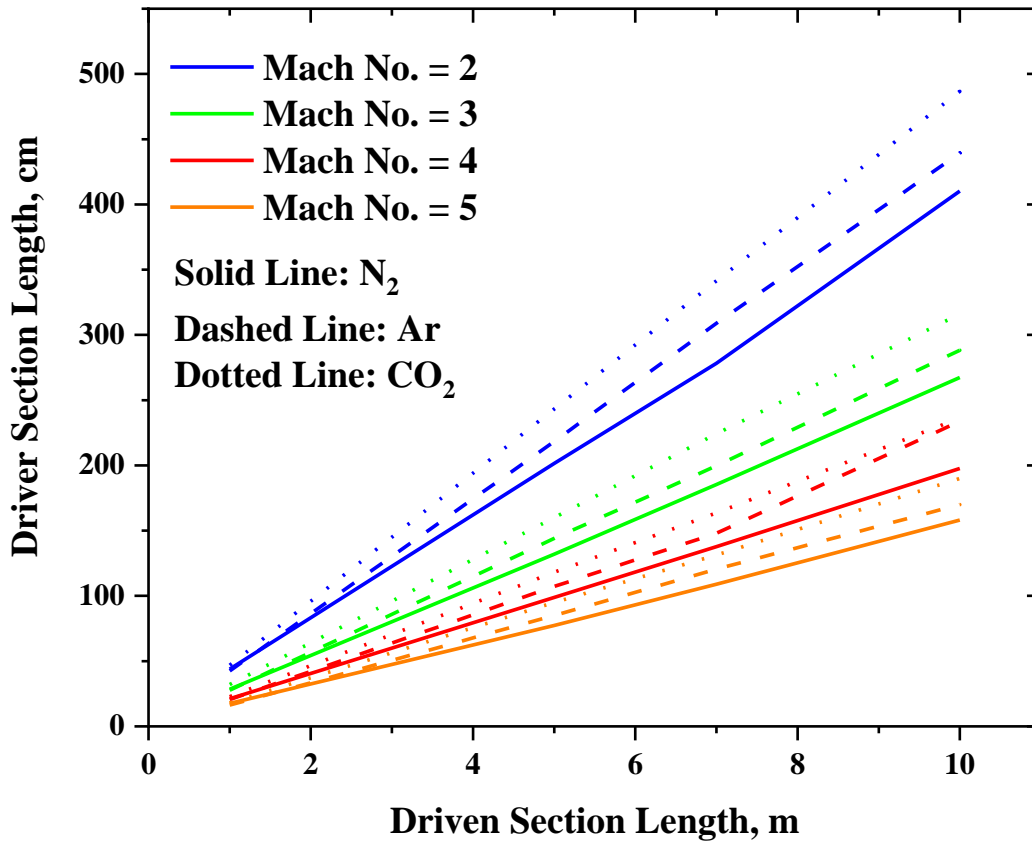


**Figure 2.8.** A plot of required driver section length as a function of driven section length to give the desired observation time for an N<sub>2</sub> (solid line), Ar (dashed line), and CO<sub>2</sub> (dotted line) bath gas.

Using these plots of the required driver section length as a function of the driven section length, the minimum required length of the driver section can be

determined as around 3.5 m, which gives the required observation time for a shock of  $M=2$ . There are some correction factors included in these calculations from Gaydon and Hurlle [101] to better fit with the experimental observations, the required length should be conservatively decided. A driven and driver section length of 7 m and 3.5 m, respectively gives a total shock tube length of 10.5 m. This gives a tube 0.5 m under the 11 m constraint. This leaves room for the optical equipment and the support frame to allow the shock tube sections to move apart from each other to allow the diaphragm to be replaced.

### 2.5.3. Shock Tube Internal Diameter

The next key design decision was the diameter of the shock tube. It was decided to keep the shock tube diameter constant as opposed to convergent or divergent as it was suitable for the desired pressures and temperatures. The play-off in diaphragm size is between the stronger effects of the boundary layer in a smaller diameter shock tube and the longer evacuation time and the gas requirement to fill the larger diameter shock tube [101]. Davidson and Hanson [137] quantify the boundary layer effect by looking at the relative change of temperature ( $T^* = \Delta T_5 / T_5$  *Initial*) in the test gas region which decreases with increasing shock tube diameter. The authors determined a 15 cm diameter shock tube will vary by less than 15 K for a 1500 K shock over 1 ms. Conversely, for a shock tube with a diameter of 10 cm, this change can occur in  $20\text{-}30 \times 10^{-12}$  s. Based on this, and knowledge of existing kinetic shock tubes from Stanford University [138-141] and KAUST [99], a diameter of 15.24 cm was initially decided upon. However, this was reduced to a 10.16 cm diameter based on discussions with other shock tube research groups. It was recommended by Professor Ronald Hanson of Stanford University to have a length-to-diameter ratio of over 50 to ensure the complete formation of the shock waves well before the driven section endwall. This effect was more important than possible variations in the temperature. Furthermore, upon consultation with potential suppliers, reducing the diameter led to a significant reduction in the overall cost of the shock tube, by reducing the size of the shock tube walls. Therefore, the decision was made to reduce the overall shock tube diameter and if bifurcation was an issue, a bath gas blend of  $\text{CO}_2$  and Ar could

be used to reduce the effects. Furthermore, a smaller volume shock tube is more cost-effective in the long term as it reduces the shock tube volume and therefore the amount of gas required for each experimental run.

The decision was made to have a constant area shock tube as opposed to a divergent [142] or convergent tube [85]. This was for the simplicity of the design, ultimately reducing the costs by not having to increase the wall thickness of one section and simplifying the diaphragm chamber separating the two sections.

#### 2.5.4. Relationship Between Mach Number, Temperature, and Pressure

The following equations are all taken from Gaydon and Hurlle [101] which describe the relationship between Mach number, temperature, and pressure. These equations can be used to approximate the driver and driven side pressures required to get the desired postshock conditions. Firstly, Equation 2.5 can be used to determine the Mach number needed to create the desired post-shock temperature ( $T_5$ ) for the conditions being studied. Some shock tubes have a heating jacket or similar heating capabilities which can be used to increase the initial driven section temperature ( $T_1$ ), which will reduce the Mach number required.

**Equation 2.5** 
$$\frac{T_5}{T_1} = \frac{2(\gamma_1-1)M_1^2 + (3-\gamma_1)\{(3\gamma_1-1)M_1^2 - 2(\gamma_1-1)\}}{(\gamma_1+1)^2 M_1^2}$$

Next, Equation 2.6 can be used to calculate the initial driven section required ( $p_1$ ) based on the Mach number calculate in Equation 2.5 and the desired postshock pressure ( $p_5$ ).

**Equation 2.6** 
$$\frac{p_5}{p_1} = \left\{ \frac{2\gamma_1 M_1^2 - (\gamma_1 - 1)}{(\gamma_1 + 1)} \right\} \left\{ \frac{(3\gamma_1 - 1)M_1^2 - 2(\gamma_1 - 1)}{(\gamma_1 - 1)M_1^2 + 2} \right\}$$

Finally, the initial driven section pressure ( $p_1$ ) calculated from Equation 2.6 and the Mach number calculated from Equation 2.5 are input into Equation 2.7 to calculate the required driver side pressure ( $p_4$ ) to create that Mach number.

**Equation 2.7** 
$$\left| \frac{p_4}{p_1} = \frac{2\gamma_1 M_1^2 - (\gamma_1 - 1)}{(\gamma_1 + 1)} \left\{ 1 - \frac{\gamma_4 - 1}{\gamma_1 + 1} \frac{a_1}{a_4} \left( M_1 - \frac{1}{M_1} \right) \right\}^{-\left( \frac{2\gamma_4}{\gamma_4 - 1} \right)} \right|$$

However, it must be noted that Equation 2.5 to Equation 2.7 are ideal and do not account for non-ideal effects such as attenuation and non-ideal diaphragm rupture within the shock tube [131, 143]. Therefore, it can be anticipated that the experimental Mach number will be lower than that calculated using these ideal theory equations. So, a calibration should be performed for the UoS HPST to accurately determine the experimental relationship between Mach number and the ratio of driver section and driven section pressure ( $p_4/p_1$ ). Karimi [143] and Petersen [131] both noticed a discrepancy between the experimental and theoretical  $p_4/p_1$  ratios.

### **2.5.5. Maximum Pressure and Safety Factors**

One key discussion in the shock tube was the appropriate safety factor in determining the wall thickness. Campbell [144] recommends that a shock tube should have a minimum safety factor of 2 in general and 4 at the windows. A greater safety pressure is used for the windows as these are the weakest point of the shock tube. The main risk in the shock tube is the occurrence of detonation. Detonation causes a rapid increase in shock tube pressure beyond the expected maximum working pressure. A safety factor of 5 was decided upon in conversation with suppliers, as the shock tube will be in an open lab, so could pose a potentially larger safety risk. A final design pressure of 500 bar was decided to mitigate the possible risk caused by unexpected detonation.

### **2.5.6. Maximum Operating Temperature and Heating Jacket**

One final important consideration for a shock tube is the maximum static operating temperature. Whilst a shock tube is built to withstand the large postshock temperature up to 2000 K, these conditions are very short-lived and dissipate on the millisecond time scale, meaning the overall effect on the components is small. If a shock tube is going to be pre-heated using a heating jacket the maximum static temperature of the external tube should be considered. As this temperature persists for a long time, the components of the shock tube, from O-rings to pressure transducers must be able to withstand this temperature [145]. Pressure transducers have a maximum flash temperature and a maximum

operating temperature, which again has an impact on their price, so must be considered.

To reduce costs for the UoS HPST, a heating jacket was omitted from the specification as the initial aim would be gaseous fuels, making the heating jacket obsolete for the early research performed using the shock tube. The decision was made to discuss with the shock tube supplier to ensure enough room is left around the shock tube to retrofit a heating jacket when required. Therefore, a maximum operating temperature still needed to be decided upon for the shock tube. 125 °C was chosen as this allowed the maximum possible operating temperature whilst still being able to use more standard equipment.

## 2.6. Final Shock Tube Design

The shock tube contains numerous components, all of which must be sourced separately and thus their specifications must be determined. This section details the purpose and requirements of each of the components for the operation of the UoS HPST. This section details the individual components of the shock tube as manufactured by Heblac Technologie GMBH, based on the initial concept. The key design specifications for the overall shock tube are listed in Table 2.2.

**Table 2.2.** Finalised key design specifications.

Property	Design Specification
Shock tube maximum pressure:	500 bar
Filling pressure driver section:	20 – 160 bar ( $p_4$ )
Filling pressure driven section:	0-5 bar ( $p_1$ )
Initial shock tube temperature:	20 – 125 °C
Normal test pressure:	10 – 50 bar ( $p_5$ )
Normal test temperature:	600 – 1500 K

Although the maximum test pressure of 50 bar incorporates a conservative safety factor of 10 below the 500-bar design pressure. This is a conservative safety factor to incorporate the potential risk of premature detonation. However, with appropriate consideration of the risk, and appropriate chemical kinetic modelling

to determine the maximum possible pressure following detonation, greater post-shock pressures can be achieved.

Table 2.2 states two different maximum temperatures, for the test and initial heating. The reason the test temperature greatly exceeds the preheating temperature is that these temperatures are only maintained on the order of milliseconds, in a small area of the shock tube. Ideal calculations show that a 10000 °C temperature rise inside the shock tube would only lead to a 2 °C temperature rise in the steel [146]. This also highlights that the maximum postshock temperature restrictions are not imposed by the steel but by the diagnostic components, namely, the pressure transducers. In practice, the maximum postshock temperature,  $T_5$ , has no real limitation because it is so short-lived, and heat transfer through the thick steel walls is limited.

### **2.6.1. Shock Tube Material and Sections**

The shock tube is made of three modular sections of smaller tubes connected by weldless flanges. This is advantageous for multiple reasons. Firstly, the weldless connections allow for greater flexibility of the tube itself, sections can be removed and moved, i.e., for experiments where such a long-driven section is not required, a section of the tube could be removed to decrease the total length. Secondly, easier separation of the components makes it easier to clean the inside of the tube sections when required. The driver section is constructed of one 3.5 m section of tube and the driven section two 3.5 m sections of tube, known as the driven section, and measuring section. The internal diameter for all tube sections is 10.16 cm making the total internal volume of the shock tube 89 L.

The shock tube is constructed of stainless steel 316 due to its strength, machinability, and relative inexpensiveness [147]. One of the reasons for the reduction in diameter discussed was the ability to use SS316. If the diameter was the original 15.24 cm this would have made the required wall thickness too large for SS316, meaning more expensive steel would have been required. This is seen in the HPST at RWTH Aachen University which used high-strength stainless steel for their 14 cm diameter shock tube to operate at a maximum working pressure of 1000 bar [148]. The shock tube flange material is EN 10028 –

P265GH steel, commonly utilised in a pressure vessel in the oil and gas industry and the screw material is 42CrMo4 steel.

### **2.6.2. Driver Section**

The components required for the shock tube driver section are relatively simple compared to the driven section. The only connection required for the driver section is one port which allows for the filling and pumping down of the tube. The pressure of the section is monitored by a manometer located on the manifold. The driver section is mounted on rollable support frames which allow for the section to be pulled away from the diaphragm chamber and the diaphragms to be changed.

### **2.6.3. Driven Section**

The driven section is more complex in its component requirements, so some aspects are split into different sections. The driven section requires an inlet from the mixing tank and vacuum valve, a series of 5 pressure transducers along the last 1-3 m of the section, a thermocouple for pre-shock temperature measurements, optical access ports, and a high-pressure dynamic pressure transducer.

Like the driver section, the ideal inlet position is as close to the diaphragm as possible as this allows for the driven section to be operated in a CRV. The access valve for the vacuum pump is often the same as the inlet. In more modern shock tubes, this operation is performed using a contour valve. Contour valves are piston-operated valves that have a contoured surface that matches the internal circumference of the tube. A depiction of a contour valve in action can be found in Karimi [143]. This prevents any effects of surface imperfection caused by the inlet valve from having an impact on the formation of the shock wave. Furthermore, having a contour valve increases the area of the valve when open compared to a traditional inlet valve, meaning that vacuum times are decreased for the driven section. It was decided that a regular inlet valve would be used as opposed to a contour valve to reduce the final shock tube cost, as this was proving to be a large expense on the project due to the complexity of the design.

By placing the inlet valve as close to the diaphragm as possible, the effect of the surface imperfection caused by the valve on the shock wave is minimised as it is at the very start of the shock wave formation. Furthermore, the impact on vacuuming times still allows for 5-6 experimental runs a day which was the aim outlined in the initial concept. The completed driven section of the shock tube is shown in Figure 2.9 along with the low-pressure manifold.



**Figure 2.9.** Shock tube driven section and manifold.

#### **2.6.4. Diaphragm Access**

The UoS HPST has a double diaphragm chamber, which means it can be operated as a single or double diaphragm arrangement. As each experiment ruptures the diaphragm, it needs to be replaced, meaning that quick access is needed to remove and replace the diaphragms between experiments. This can be done in two ways. Firstly the driver section frame can be rollable to move it left/right away from the driver section. The second, simpler option is to have movable mounts for the tube itself to allow it to slide away from the driven section along the frame.

### 2.6.5. Mixing Tank

In a shock tube, test gases are prepared in a mixing tank before the experiment. The mixing is done by the partial pressures of the mixing tank, so the fuel(s), oxygen, and bath gases are added sequentially. Mass flow controllers (MFCs) can't be used in shock tubes as they cannot be trusted to be accurate to the high pressures used in the driven section of the shock tube. Furthermore, using a mixing tank means the test gas mixture for multiple experiments can be prepared at once if the tank is big enough. There is a play-off in mixing tank volume and pressure to get the desired amount of gas for a day's worth of experimental runs. For the UoS HPST, the volume of mixing tank required was decided to allow 5 experimental runs at a driven section pressure of 1 bar. This means the test gas mixture could be prepared first thing in the morning and provide a day's worth of test gas. The mixing tank should maintain a low surface roughness to reduce the risk of autoignition in the tube, resulting in a significant pressure increase and loss of the test gas mixture. The UoS HPST mixing tank fabricated by ASAB GmbH is constructed of stainless steel with an internal volume of 200 Litres (L) and rated to a maximum pressure of 60 bar, incorporating a generous safety factor of 10, in case of explosion and detonation within the mixing vessel, so will only be filled to a pressure of 6 bar. Some mixing tanks have magnetic stirrer capabilities to increase the speed of mixing and heating jackets if liquid fuels are being used [145, 149]. These were omitted from the UoS HPST as the mixing tank is large enough to provide a full day's worth of mixing and there is a second inlet port that can be used to aid mixing via addition through two separate ports. The heating jacket was omitted as the intention is to initially study gaseous fuels, so condensation in the mixing tank is not an immediate issue. As discussed with Heblac Technologie, the mixing vessel will leave enough room around the vessel to leave the option open for future heating as well as the vessel being rated to 125 °C.



**Figure 2.10.** UoS mixing tank.

### **2.6.6. Mixing Manifold**

The UoS HPST needed to be supplied by gases from outside of TERC for safety concerns keeping the gas cylinders inside of the building. All the gas lines run around the perimeter of TERC, and the gases can be accessed for all the relevant experiments. The gases for the shock tube run over 2.2 m tall bridges over the driver and the driven section of the tubes. The gases needed for the shock tube were decided upon at an early stage of the shock tube in 2020 as they needed to be in place for the building handover.

The driver section gases decided upon were helium and argon, set at a pressure of 158 bar at the manifold output. The high-pressure mixing manifold is built to a design pressure and temperature of 170 bar and 40 °C, respectively.

The driven section gases were more complicated and had to be decided upon more carefully, especially at such an early stage of the project. The fuels chosen were methane at 15 bar and hydrogen at 20 bar, along with oxygen as a necessity at 5 bar. The initial concept included carbon monoxide (CO) allowing the study of syngas mixtures. However, this was removed due to safety considerations of

having CO pipelines across the perimeter of the building and potential leakage from the mixing tank. The three bath gases selected were nitrogen (15 bar) for the study of combustion in air, argon (158 bar) to reduce the effect of bifurcation and give the longest test times, and CO<sub>2</sub> (69 bar) to study sCO<sub>2</sub> combustion. Other gases included at the driven section outlet are Mixed ACP gas (1 bar) and compressed air (13 bar). These are currently not in use by the shock tube but are available for use in other experiments in the same vicinity as the shock tube. An initial schematic of the gas mixing manifold is shown in Figure 2.11 which includes lines to the vacuum pump, mixing tank, and pressure relief valves. As connections are made at the manifold, there is future flexibility to substitute the fuel lines using cylinders located in the building, allowing the study of different fuels, such as synthetic jet fuel or ammonia. The low-pressure section of the manifold was constructed from stainless steel and has a maximum design pressure of 60 bar and 125 °C respectively. The design pressure is lower than some of the gas inlets means there is a need to regulate the pressure of the gas flows below the design pressure. The maximum temperature is greater as this allows for flexibility to study liquid fuels in the future through the heating of the supply lines to prevent condensation.

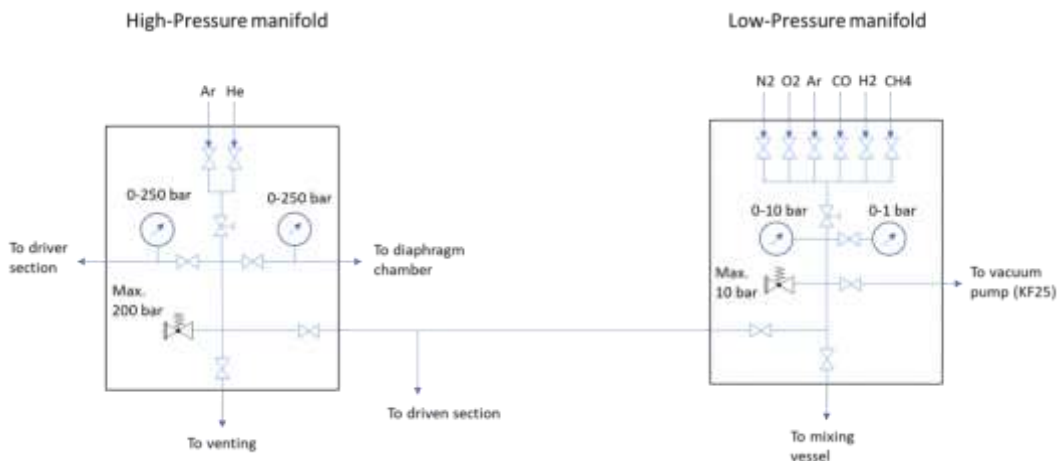


**Figure 2.11.** Initial schematic of the UoS HPST driver and driven section gas mixing manifolds. Provided by Heblac Technologie.

Figure 2.12 shows the finalised manifold schematic including all the valves, the venting and vacuum system, and the mixing vessel. The manifold uses a non-return valve and plug valves for all gas connections. A pressure reducer (DK-Lok

KPR1FRF412A20000) is also used on the line connecting the driven section gases to the low-pressure manifold to prevent over-pressurisation of the manifold by reducing the driven gas pressures from their original pressures down to less than 10 bar. The inlet and outlet pressures are monitored using a high-pressure manometer (0-250 bar, DK-Lok PGI-50-10-4N) and a low-pressure manometer (0-10 bar, DK-Lok PGI-50-250-4N). The driver and driven section pressures are measured using the three manometers/pressure transducers shown in Figure 2.12. There is one pressure transducer (Keller LEO2, 300 bar) on the high-pressure manifold for monitoring the diaphragm chamber pressure and the driven section pressure. The low-pressure section has two pressure transducers on the manifold for monitoring the mixing vessel and driven section pressures. These are a low-pressure manometer (Keller 30 PAA-3SXHTT/ 1 bar) and a slightly higher-pressure manometer (Keller 30 PAA-3SXHTT/ 10 bar). The lower pressure transducer is for more accurately monitoring the filling of fuel into the mixing tank and can be closed off using valve P8 so it doesn't rupture at high-pressures.

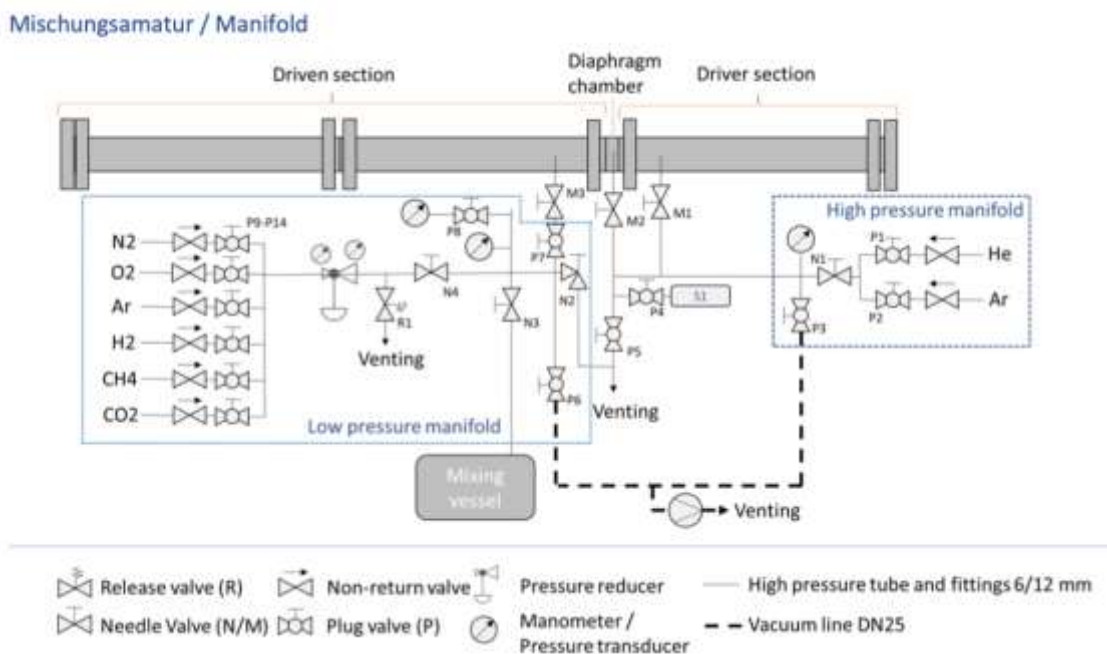


**Figure 2.12.** Finalised manifold schematic including, vacuum, venting, and mixing tank. Provided by Heblac Technologie.

### 2.6.7. Windows and Endwall Section

An important decision when designing a shock tube is determining the position within the shock tube at which in the shock tube the test gas is probed by the detection methods. This decision ultimately affects the available test time within a shock tube. The two competing factors to consider are i) the measurement should be made as close to the endwall as possible to delay collision between the reflected shock wave and the contact surface and have the largest possible test time [101] and ii) the measurement should be made at a distance from the endwall sufficient such that heat transfer effects are minimized [142]. Figure 2.13 shows a schematic of the cross-section at the end of the shock tube driven section. There are two window ports located on the side of the shock tube parallel to the floor to allow a laser absorption diagnostic to enter and pass through the shock tube to a detector.

There is also a dynamic pressure transducer port for the dynamic pressure measurements of the post-shock pressure. The transducers must have a very rapid sensitivity to create an accurate pressure trace. There is one window for a photomultiplier tube (PMT) detector for chemiluminescence. The orientation of these two windows is unimportant and as the pressure transducer and window ports are interchangeable, can easily be swapped to provide the best placement for the PMT.

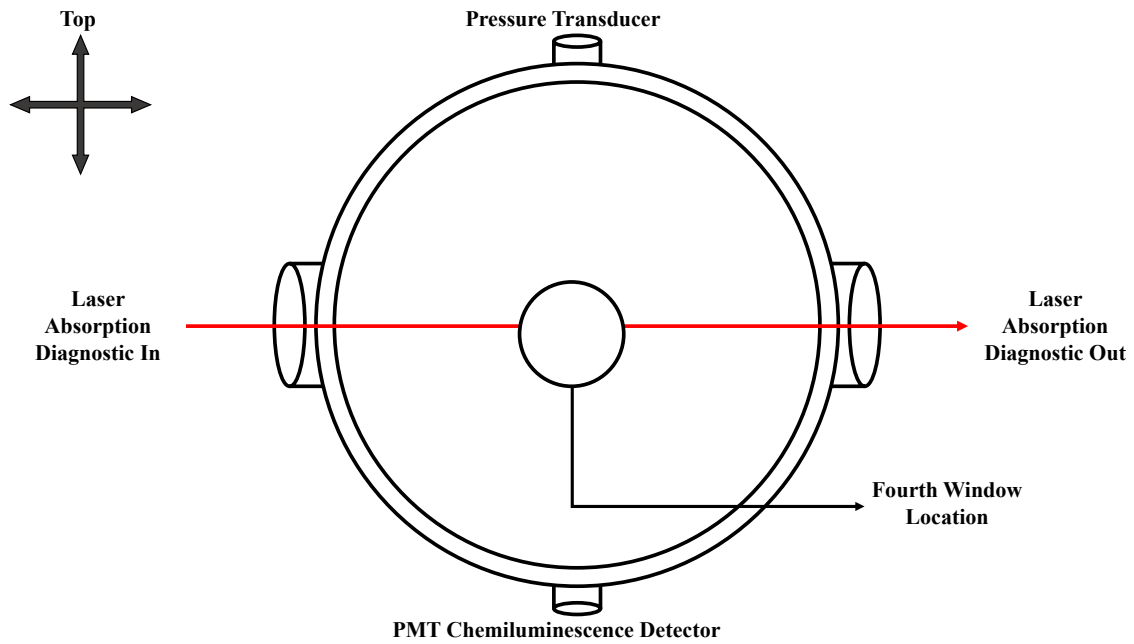


**Figure 2.13.** Cross-section of the sidewall measurements from the driven section wall, 1-2 cm from the endwall.

The UoS shock tube windows are made of quartz glass which is transmissible to wavelengths down to 200 nm. The windows are approximately 10 mm thick with optical access of approximately 4 mm. Figure 2.14 shows the shock tube endwall section, with the pressure transducer in the top port and two window ports parallel to the floor. Furthermore, new sapphire windows have been developed which are only 3.1 mm thick due to the increased strength of the material.

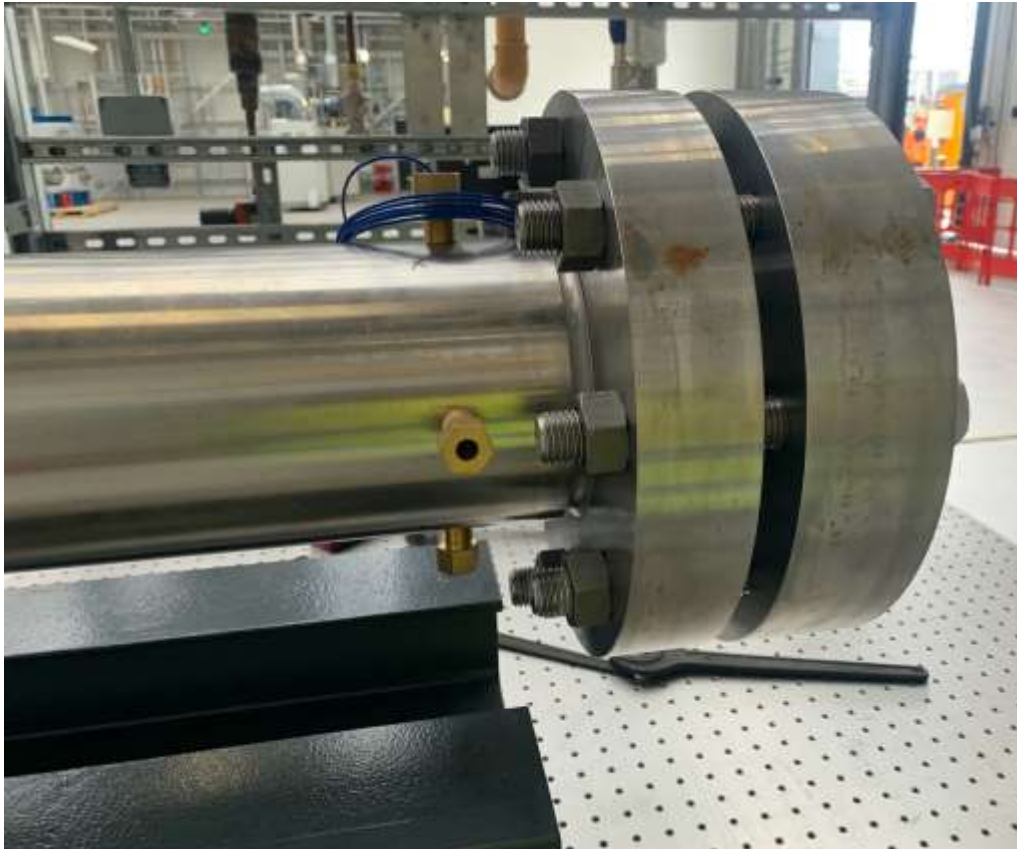


**Figure 2.14.** UoS shock tube endwall section and window ports.

### **2.6.8. Pressure Transducer Arrangement**

A series of five, fast-response dynamic pressure transducers along the top of the shock tube are used to accurately record the velocity of the shock wave, and from this determine the Mach number. Figure 2.15 shows an initial concept for the pressure transducer arrangement along the last 3 m of the tube, which was changed slightly in the later design stages as the actual separation is not key, but the bigger the distance that they cover, the more accurate the final measurement of shock velocity. The pressure transducers are connected to a data-acquisition card which records the time taken for the shock wave to pass between each subsequent transducer.

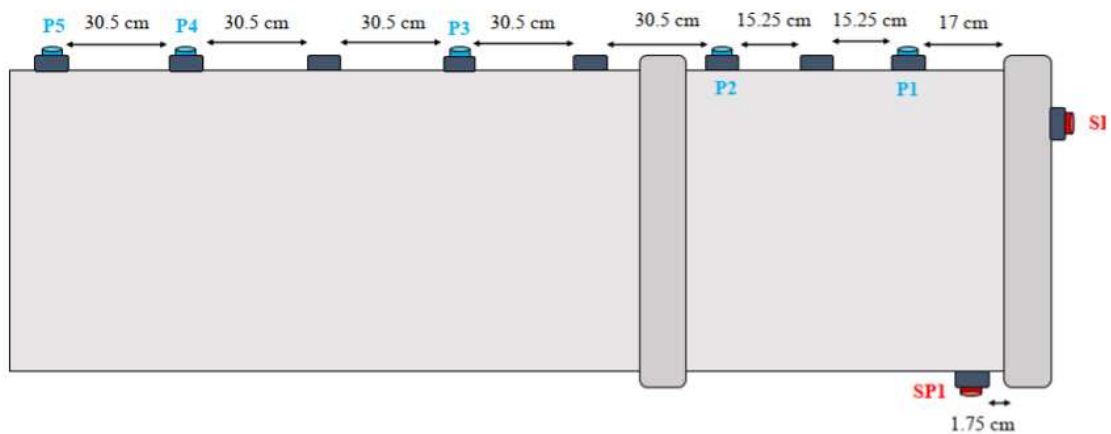


**Figure 2.15.** Pressure transducer arrangement over the last 2 metres of the shock tube, where P1-P5 detect pressure changes and SP1 and SP2 give high pressure and high accuracy, dynamic pressure measurements.

Vivanco [142] noted an average attenuation of 1-1.5% in the shock wave propagation. By recording the time between the shock wave triggering each pressure transducer and knowing the distance between them, the shock velocity can be determined. For a series of five pressure transducers, that gives 4 velocity measurements, which should show a linear decrease as attenuation slows the shock wave down. A linear plot of shock velocity against length (distance between the pressure transducers) can be extrapolated to calculate the actual Mach no. at the endwall. This shock wave velocity is used to calculate the Mach number and subsequently the postshock temperature. The bigger the distance between the transducers the more accurate the shock velocity reading [142], however, they need to be far enough away from the diaphragm that the shock wave has already fully formed.

The error in the shock velocity at the endwall can be calculated using linear regression analysis taken from Herbon [150]. Alternatively, the error from the linear fit could be used.

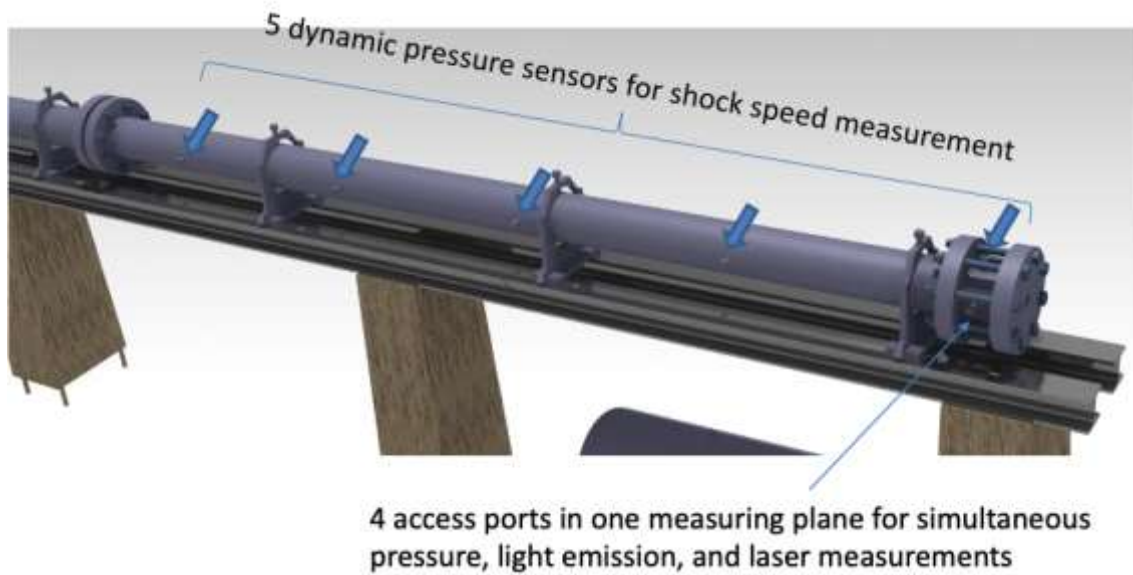


**Figure 2.16.** UoS HPST measuring system location (Heblac Technologie).

The UoS HPST uses five pressure transducers (PCB, 113B22) mounted in a stainless-steel plug shown in Figure 2.16. These plugs are then screwed into the shock tube to ensure they don't move. The first transducers are located 1 cm from the endwall and spaced along the last 288 cm of the driven section. The cables of the pressure transducers are used to connect to a measuring card (Elsys TPCE-LE-1014-85, IEPE Power Supply) in the shock tube PC. Figure 2.17 and Figure 2.18 show the PCB plug fabrication and the overall pressure transducer arrangement over the last 3.5 m of the driven section respectively. The final pressure transducers and the window location is 1 cm from the end of the shock tube as shown in Figure 2.18. The five pressure transducers span, equally distanced across the 3.5 m measuring section. This provides four shock velocity measurements over a large distance, making the extrapolation to the shock velocity at the endwall incredibly accurate and thus the calculated postshock conditions.

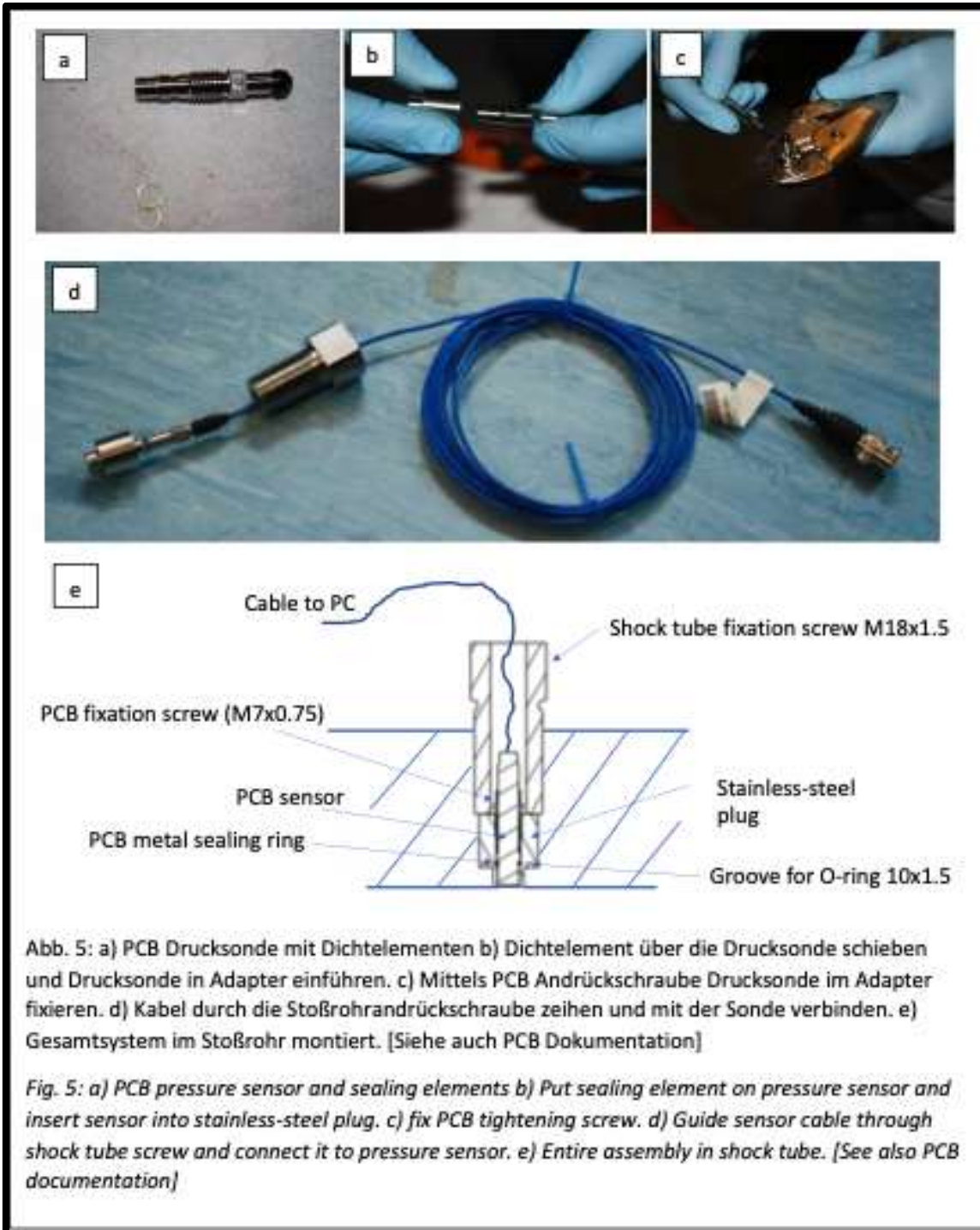
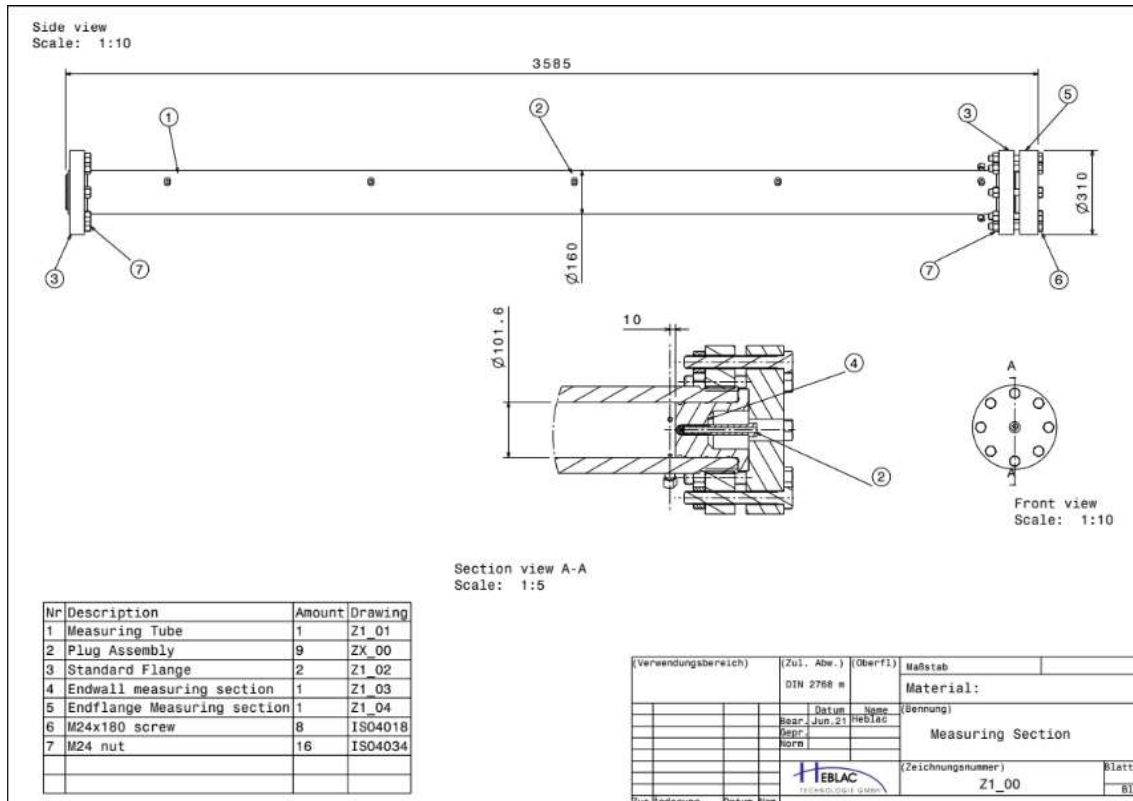


Figure 2.17. PCB pressure transducer and plug fabrication. Provided by Heblac Technologie.



**Figure 2.18.** UoS HPST dynamic pressure measuring system. Provided by Heblac Technologie.

## 2.6.9. Vacuum System

As shown in Figure 2.11, there is only one vacuum pump used in the manifold and shock tube section. This shock tube is connected to the complete manifold, the driver section, the driven section, and the mixing tank. By utilising an efficient manifold and using one vacuum pump for the complete system, the overall cost of the shock tube is reduced. The UoS HPST system uses a HiScroll Vacuum pump (PD100171AT), a dry and oil-free pump system that produces minimal vibrations.

## 2.6.10. Double Diaphragm Chamber

The UoS HPST will operate using a double diaphragm chamber as described in Section 2.2.3. This has two diaphragms housed in a chamber as shown in Figure 2.19. The middle section between the two diaphragms is filled with any gas before the experiment starts, the driver and driven section are then filled to the desired pressure. Once the desired pressures are achieved, the middle chamber

between the diaphragm chamber is evacuated to create a sudden pressure difference, rupturing the first diaphragm. This then creates a large pressure difference between the driver and driven section rupturing the second diaphragm and creating the shock wave.

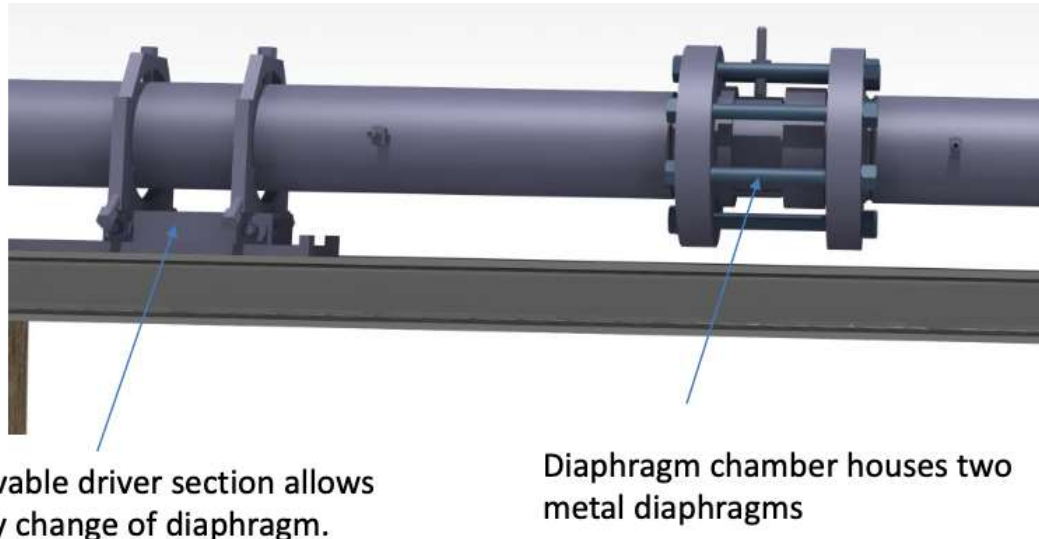


**Figure 2.19.** Outside of the UoS HPST double diaphragm chamber (Heblac Technologie).

The diaphragms utilised are high-purity aluminium. Whilst aluminium alloys may offer beneficial properties, there can be a lot of variation in elemental composition between batches and suppliers. This alters the properties and therefore the achievable postshock temperatures and pressures achieved. To allow consistency either when changing suppliers, using the purest aluminium available is the best option.

### 2.6.11. Expansion Vessel

Due to the double diaphragm arrangement, a method is required to quickly vent the diaphragm chamber to create an extreme pressure difference that does not connect to the venting pipework. If this was connected to the full venting pipework, the shock tube would continue to be pulled down during the experiment after the diaphragms had burst. Therefore, an expansion vessel is used as shown in Figure 2.12. This is a 2 L stainless steel vessel shown in Figure 2.20 that can withstand 200-bar pressure.



**Figure 2.20.** Expansion vessel mounted to the underside of the support beam.

## **2.7. Shock Tube Installation and Assembly**

The UoS HPST was fabricated by Heblac Technologie, the initial contract was awarded in September 2021 and the final installation took place in August 2022. Before the installation, the laser diagnostic table was supplied and installed, and an approximate floor plan was devised.

### **2.7.1. Optical Table**

Figure 2.21 shows the optical table (T1230D) supplied by Thorlabs. This optical table was 3 x 1.2 m which allowed enough space for the laser system and the appropriate detectors, as well as providing enough room for a full laser cover to be created and supported. The table also had a breadboard of 310 mm thickness. The optical table was supported by four independent legs PTL802 which are 600 mm tall, giving the laser table a total height of approximately 910 mm. The legs are also equipped with a passive isolation upgrade kit (PWA076) which reduces the vibrations experienced by the laser system during the diaphragm rupture.



**Figure 2.21.** Optical table in place before shock tube installation.

### **2.7.2. Floor Plan and Site Preparation**

Figure 2.22 shows the proposed floor plan for the shock tube to assist with the initial installation. One of the key concerns when designing the floor plan is adhering to space restrictions. The shock tube was assigned a 12.5 m long area, which needed to account for the shock tube and frame, and the optical table. This space is constrained by walkways on either side which are required to access the emergency exit, so must be maintained. To make this possible, the decision was made to place the optical table underneath the first bridge as shown in Figure 2.21 and Figure 2.22. This required some of the lower rungs on the bridge to have to be removed and moved to an extension to the frame which was placed parallel

to the length of the optical table. This allowed for the laser table and access plugs to be more easily accessed, as well as increased the distance between the electrical lines and hydrogen.

The total length of the shock tube frame is approximately 11 m as shown in Figure 2.23. The driven section is also designed to support a 50 cm overhang off the edge of the frame. This allows the optical table to sit underneath the frame, making it easier to set up laser absorption diagnostics. The shock tube has been moved 80 cm from the bridge termination points to allow for sufficient room to access the manifolds and diaphragms section, which will be located under the second bridge.

One of the key considerations was how to connect the existing gas pipeline infrastructure to the shock tube manifold. Following the installation of the shock tube, the gas lines need to be connected to the shock tube as quickly as possible to allow testing and commissioning. Before delivery, the termination points of the six driven section gases (methane, hydrogen, oxygen, carbon dioxide, nitrogen, and argon) were on the first bridge over the optical table. As the gases need to span almost 6 m down the shock tube to reach the manifold, the decision was made with Heblac Technologie to add six gas lines along the shock tube to the design which went to the edge of the driven section side of the frame. This simplified the gas connections as the distance between the connection points were reduced to 1-2 m. The driver section gases (helium and argon) terminated on the third bridge above the driver section. The shock tube termination points are approximately halfway down the driver section tube. Furthermore, the third bridge had become full due to equipment required for other experimental rigs. Therefore, the decision was made to reduce the gas pipelines back to the top of the bridge over the shock tube and drop them down to make the connection as the manifold.

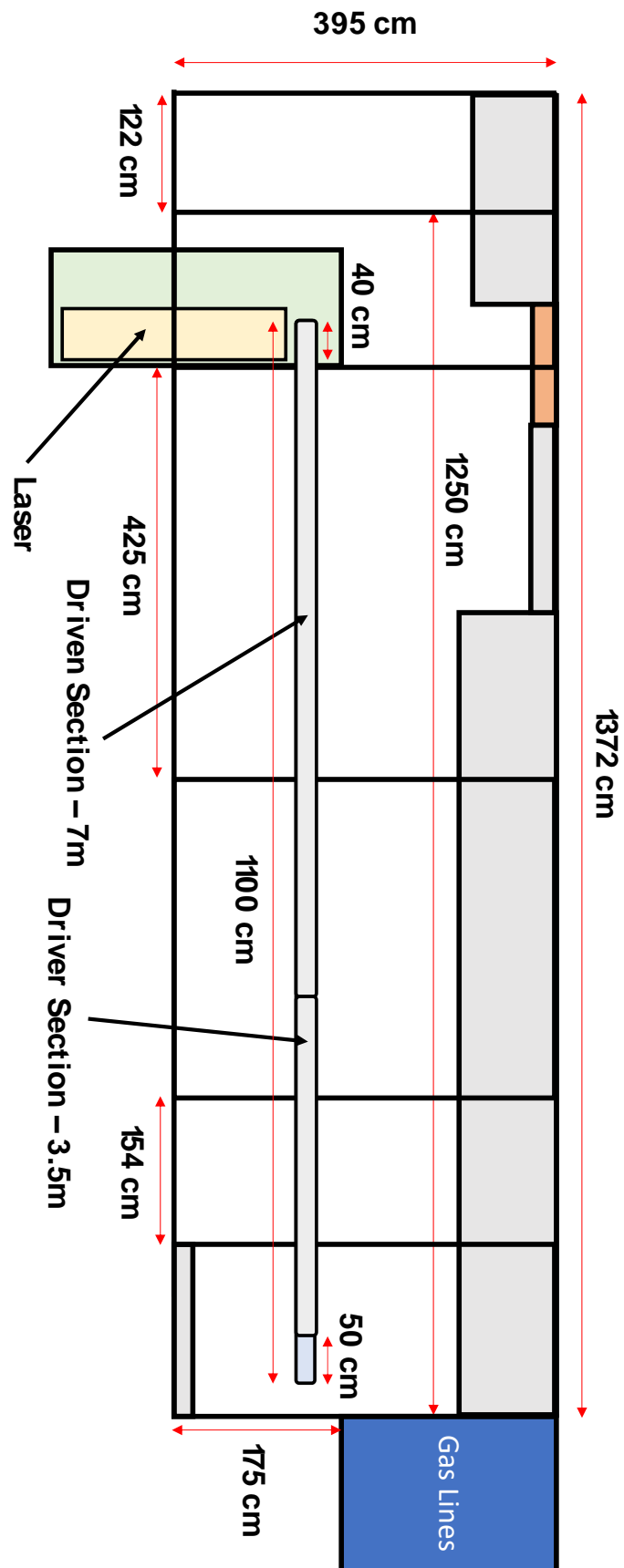


Figure 2.22. Floor plan of the shock tube prepared for the instillation.

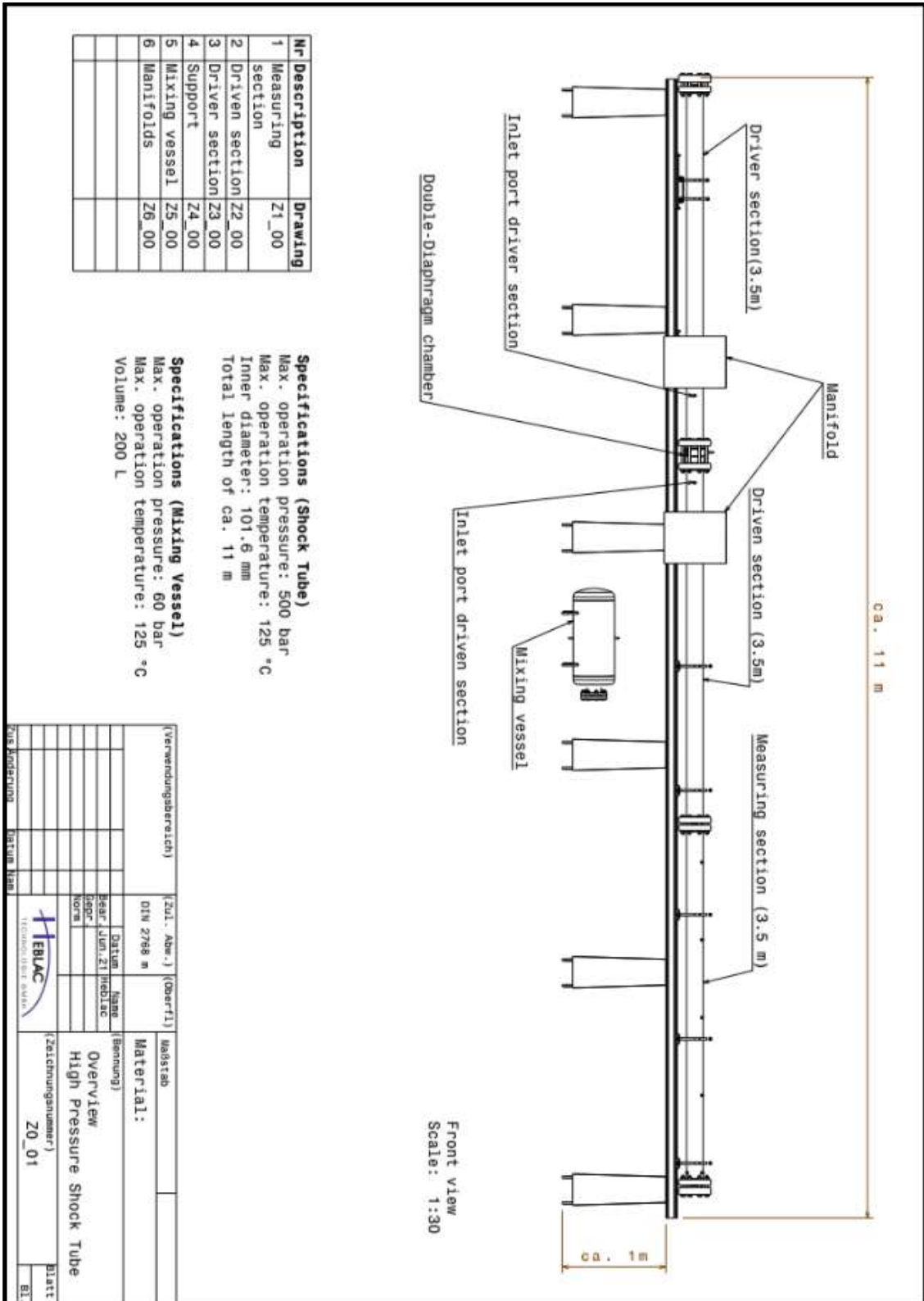
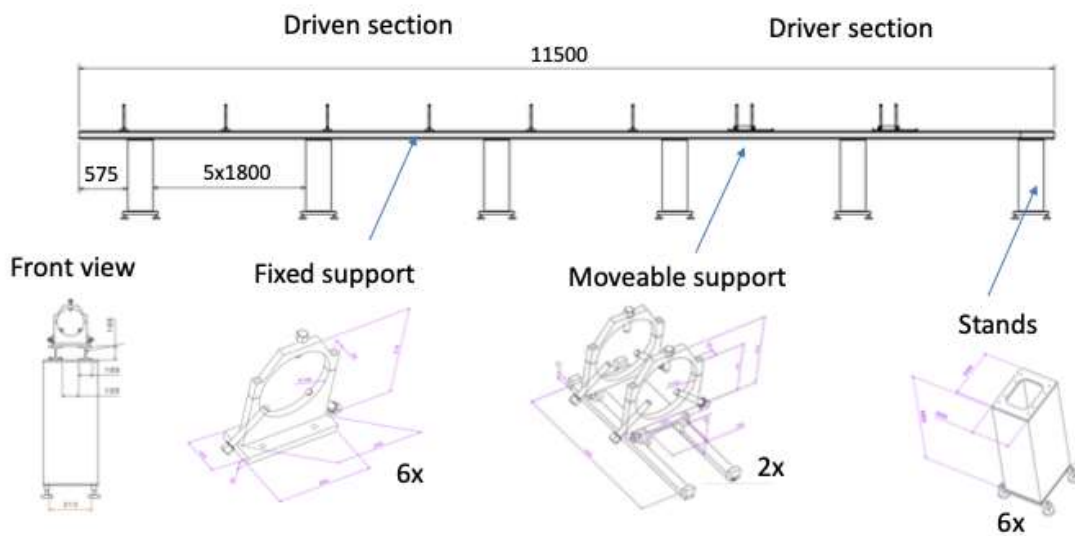


Figure 2.23. Shock tube instillation schematic provided by Heblac Technologie.

### 2.7.3. Summary of Installation

The shock tube was delivered in August 2022 and the installation began immediately. The first step was to set-up the six-shock tube stands and the frame as shown in Figure 2.24. The 575 mm overhang on the driven section side was placed fully over the laser table and the stand was placed just 60 mm from the table to reduce the effects of the vibration of the shock tube on the laser diagnostics. The stand's weight is approximately 200 kg and it is hollow on the inside. This allows for further filling with sand or concrete if the effect of vibrations is so large that it has an impact on the alignment of the laser diagnostics. Following this, the 10 H-beams were mounted on top of the stands. The alignment of the beams and the supports was performed using the four-foot screws once the beams had been placed. The mixing tank was also placed between the middle stands once they were set in place as access was easier to move before the beams were in place as the beams restricted the forklift access.



**Figure 2.24.** Schematic of shock tube support structure and stands provided by Heblac Technologie.

Once the beams were in place and correctly aligned, the six fixed supports and two moveable supports were attached to the beam. Following this, the three beams were placed on the supports. The beams were then connected via the diaphragm section with two diaphragms placed on either side of the chamber.

Subsequently, the three maximator valves to the driver, driven, and diaphragm chamber sections were attached and connected to the manifold via flexible piping.

## 2.8. Shock Tube Calibration and Testing

During the commissioning of the shock tube, a test run was performed to demonstrate how the post-shock properties are calculated and are discussed within this section. The shock was performed using two aluminium diaphragms (99.9%) which were 2 mm thick and scored to a depth of 1 mm as shown in Figure 2.25. The test was run with a driver section pressure of approximately 18 bar using helium and air as a driven gas at a pressure of 0.25 bar. Once the desired pressures were achieved, the diaphragm mid-section was vented to create the sudden pressure difference and initiate the shock wave.

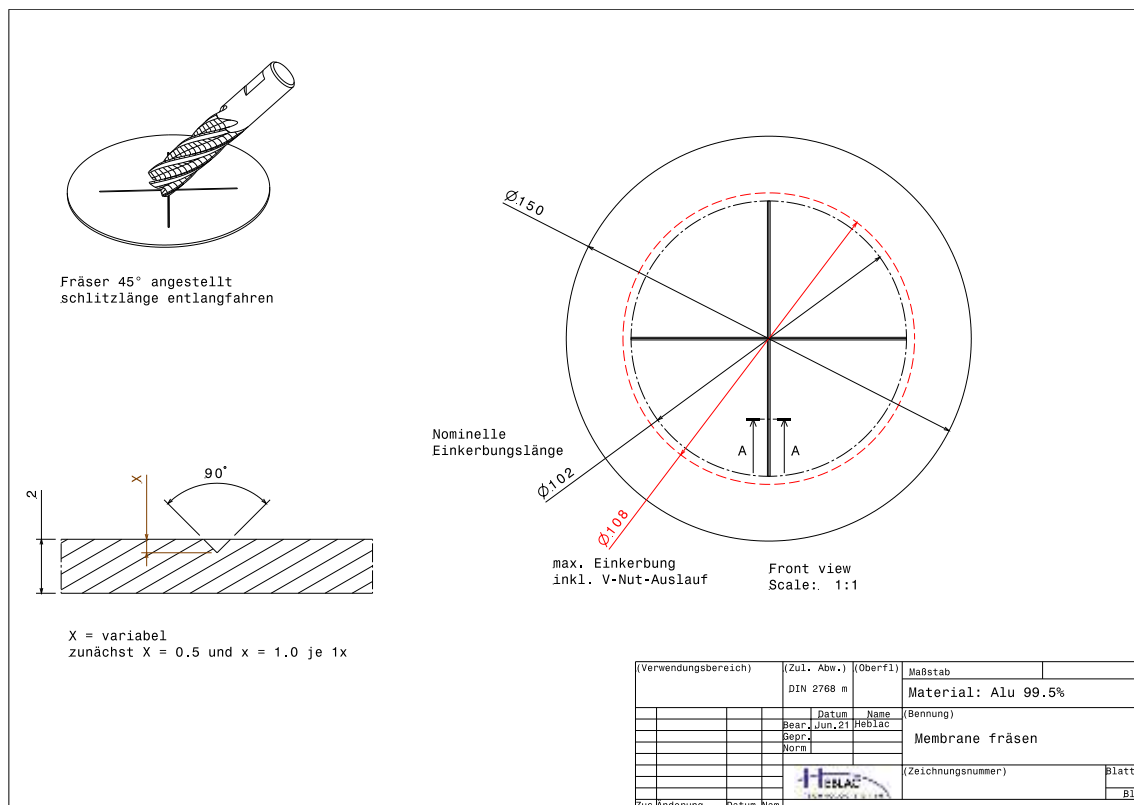


**Figure 2.25.** Technical drawing of the shock tube test diaphragms provided by Heblac Technologie GMBH.

TranX software is used to record the pressure traces from the five different transducers. The software is set up to be continuously running once triggered

and only the transducers closest to the endwall can activate the data recording when a strong enough signal has been detected. This means the arrival of the incident shockwave at the endwall is approximately time zero as shown in Figure 2.26. The software is set to record data 8 ms before and 16 ms after triggering. This ensures that all important behaviour is captured, without taking up too much storage. Figure 2.26 shows that each of the five transducers gets subsequently activated by the passage of the incident shock wave as shown by the sudden pressure increase.

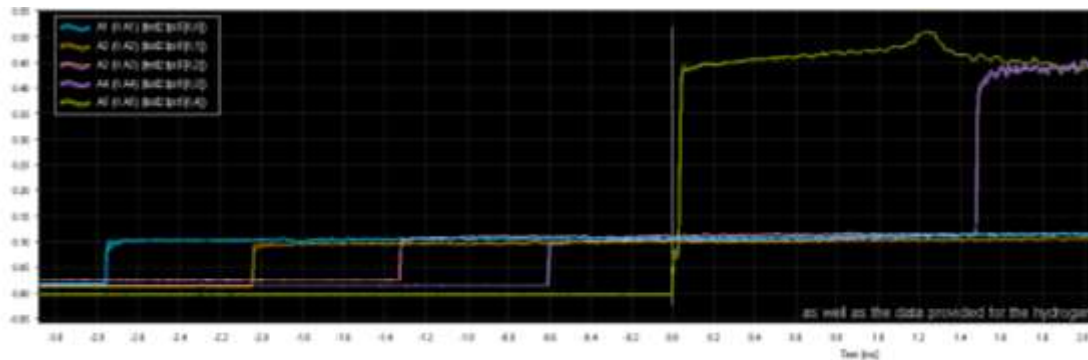


**Figure 2.26.** TranX recorded pressure traces for the shock tube test run during commissioning.

Figure 2.26 shows that each of the five transducers gets subsequently activated by the passage of the incident shock wave as shown by the sudden pressure increase. The time taken for the incident shock to reach each of the transducers is extracted from this plot. By dividing the distance between the transducers by the time taken for the incident shock wave to travel that distance, we can calculate the shock velocity at four different positions. As the velocity of a shock wave in a shock tube is always decreasing due to attenuation, the velocity calculated can be considered an average across the distance and therefore the velocity at the mid-point between two transducers assuming a linear decrease in velocity. By plotting the four-velocity points as a function of distance from the endwall, one can plot Figure 2.27 and use a linear fit to extrapolate the shock velocity to the endwall (the intercept).

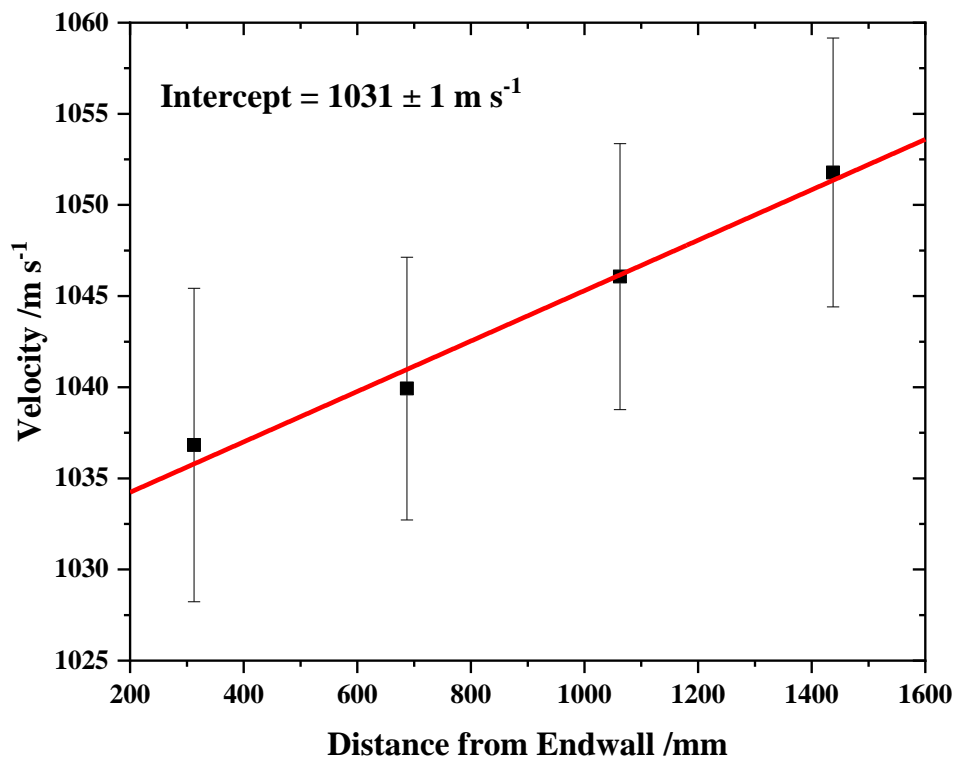


**Figure 2.27.** Plot of incident shock wave velocity as a function of distance from the shock tube endwall.

Once the shock velocity has been calculated, Gaseq software installed on the local shock tube PC is used to calculate the post-shock conditions based on ideal thermodynamic relations. The results of this are shown in Figure 2.28. For the test run a postshock pressure of 13.13 atm and temperature of 1286.6 K were achieved. This shows how the postshock temperature and pressure are calculated during a shockwave experiment. The overall error in postshock conditions for shock tube work is normally assigned to the IDT, rather than the temperature or pressure, usually, experimental errors are in the range of 10-20% [88]. Despite the error in the postshock temperature being ~1%, it is the propagation of this error that leads to a significantly larger error value [85].

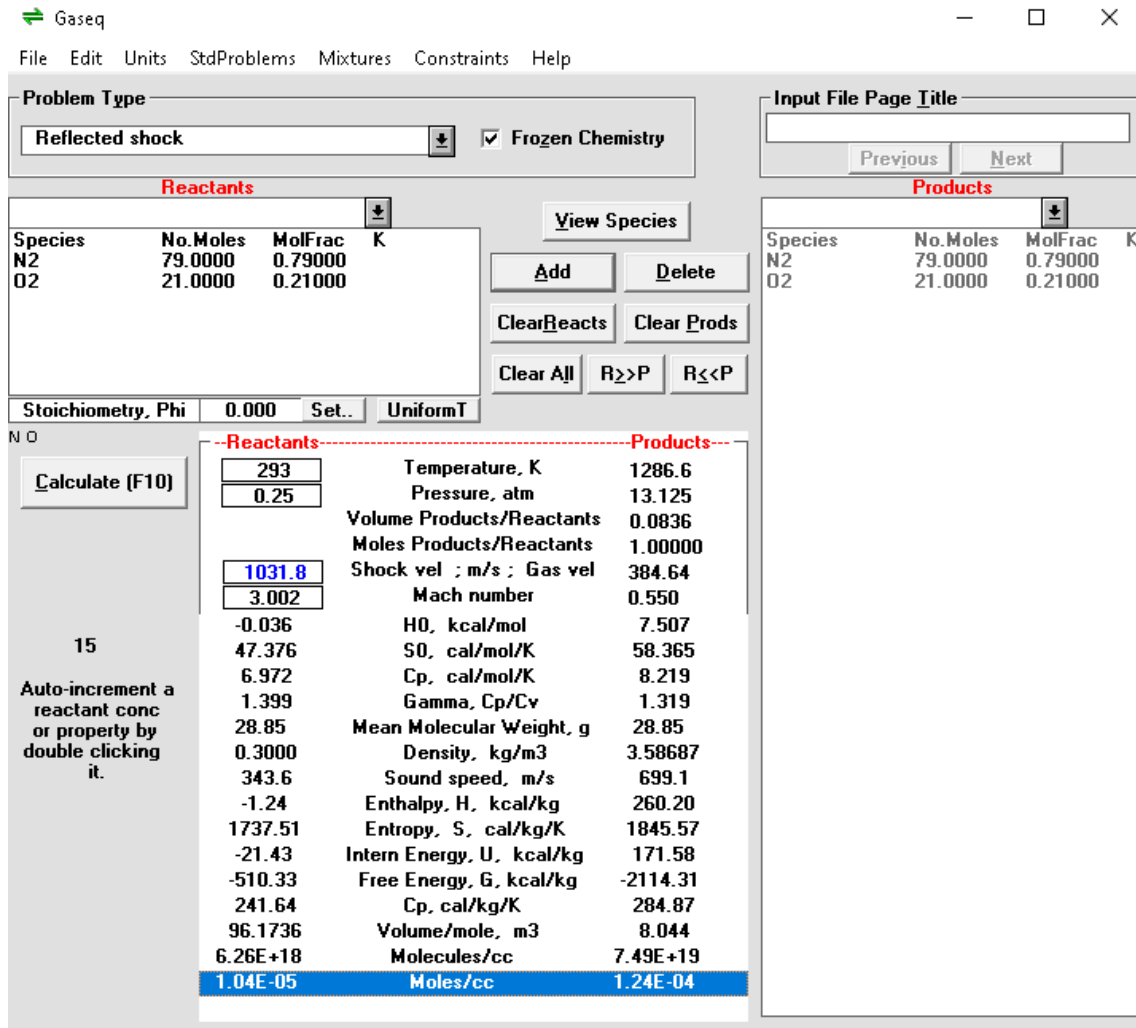


Figure 2.28. Screenshot of Gaseq postshock conditions for shock tube test run.

## 2.9. Diagnostic Equipment – Pressure and Chemiluminescence

Various diagnostic equipment can be utilised for the successful operation of a shock tube. The UoS HPST will operate a high-pressure dynamic transducer to measure the high-pressure created behind the reflected shock at the test measurement location. A PMT is used for chemiluminescence measurements and a continuous wave laser absorption diagnostic, initially to target OH and HO<sub>2</sub>.

### 2.9.1. High-Pressure Dynamic Pressure Transducer

A high-pressure dynamic pressure transducer is used to record the pressure trace behind the reflected shock wave at the test measurement location. Typically, high-pressure transducers are located at the sidewall or on the actual

endwall. These can be significantly affected by the bifurcation effect as discussed in Section 2.4.1. The UoS HPST has a sidewall transducer which also provides a shock velocity measurement.

### 2.9.2. Photomultiplier for Ignition Delay Time Measurements

The UoS HPST photomultiplier is located at the sidewall test location and can record the chemiluminescence of different species, most notably and usefully, OH\* and CH\* at 310 and 430 nm respectively. The chemiluminescence trace of OH\* or CH\* is used to determine the ignition delay time.

The IDT is one of the most important combustion properties and is commonly used to test the validity of a chemical kinetic mechanism. In a shock tube experiment, the IDT is defined as the time interval between the arrival of the reflected shock at the test section and the onset of ignition [85]. The arrival of the reflected shock is determined by extrapolating the maximum gradient pressure profile at the test location down to the time. The onset of ignition is defined by extrapolating the maximum gradient of the OH\* chemiluminescence profile down to the baseline. The difference between the two is defined by the ignition delay time. In shock tube experiments, the bifurcation effect at the sidewall causes a staggered rise in IDT at a sidewall pressure transducer. In these circumstances, it is best to determine the arrival of the reflected shock wave using Equation 2.8 [126, 151].

**Equation 2.8.** 
$$\Delta t_{AO}(\mu s) = 4.6M_1^{0.66}\gamma_2^{-7.1}\bar{M}^{0.57}$$

Where  $\gamma_2$  is the specific heat ratio in region 2 of the shock is tube and  $\bar{M}$  is the average molecular weight of the driven gas.

Chemiluminescence is the spontaneous emissions of a photon from an excited species. Unlike fluorescence spectroscopy, chemiluminescence detection requires no excitation laser. Following a reaction, one of the products in a high-energy state relaxes back down to its ground state, emitting a photon of light. Using an optical access point that transmits light in the appropriate wavelength range, the emitted photon can be detected using a PMT. The chemiluminescence of OH\* has been utilised to determine IDTs over 300 atm [85]. The  $A^2\Sigma^+ - X^2\Pi$

(0,0) band is monitored around 306 nm [127, 152]. Furthermore, a PMT can also be used to monitor the methylidyne radical (CH)  $A^2\Delta \rightarrow X^2\Pi$  transition [153, 154] transition at 431 nm.

Chemiluminescence measurements can be taken at the sidewall (at the test gas location) or in the centre shock tube endwall. Existing experimental work utilising both techniques on a shock tube has found a discrepancy between the two test locations when used to determine IDT [127]. It is recommended to use endwall chemiluminescence measurements to determine IDT under non-dilute conditions ( $[Fuel] > 2\%$ ) [122, 127]. Due to rapid pressure change following ignition and the resultant gas dynamic interactions, sidewall measurements may lead to artificially shorter IDTs [155].

The UoS HPST is currently equipped with one Hamamatsu H10723-110 photosensor module and a corresponding power supply (C10709). The PMT can be used flexibly between the sidewall and endwall with the option to add a second PMT in future through the same power supply for simultaneous measurements. The PMT also has a fibre adaptor (E5576) and C-mount ring (A9865) which can both have the option to be mounted to the sensor.

## **2.10. M-Squared Continuous Wave Absorption Diagnostic**

Laser diagnostics can be used to study a wide range of species, from the ultraviolet to the infrared region. Typically carbon-based species such as  $CH_4$  [156],  $C_2H_4$  [157] and  $CO_2$  [158] absorb in the infrared region and radical species absorb the ultraviolet region such as OH [159],  $HO_2$  [138], CH [153, 154] and  $CH_3$  [160-162]. The decision was made to purchase a laser absorption diagnostic in the UV region, specifically to focus on OH and  $HO_2$ .

A separate tender process to the shock tube was required for the acquisition of a continuous wave laser diagnostic. This tender received two bids and was eventually one by M-Squared who provided a Ti:Sapphire laser absorption diagnostic system capable of studying OH (308 nm), NO (225 nm) and  $HO_2$  (227 nm). The tender process was eventually won by an ultra-narrow linewidth laser system provided by M-Squared.

Figure 2.29 shows the footprint of the UoS M-Squared laser absorption diagnostic, with the measurements shown given in millimetres. As shown in the top-down view, the total length of the system is 236.2 cm, and the width is 52.11 cm.

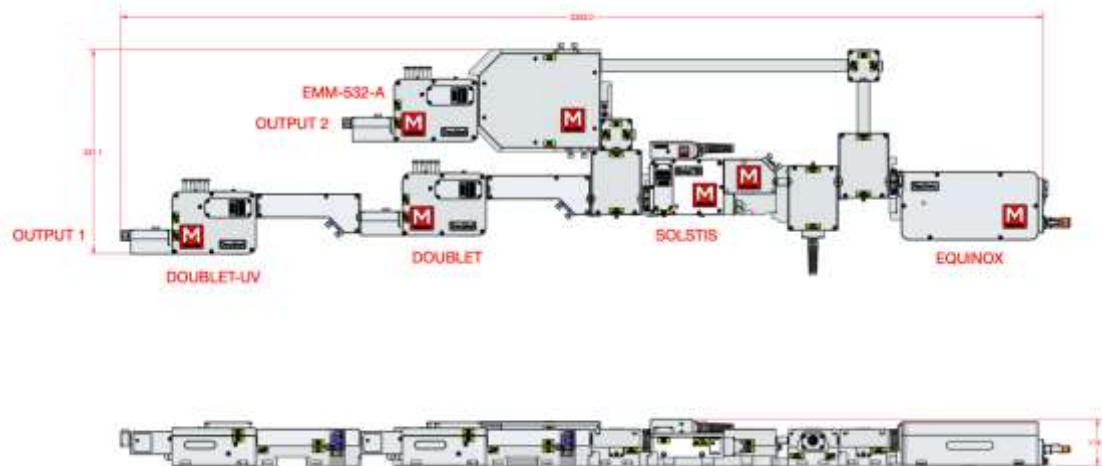


**Figure 2.29.** The footprint of the M-Squared laser system. Provided by M-Squared.

### 2.10.1. Continuous Wave Laser Absorption Diagnostics of OH

OH is essential to the combustion process of any fuel, especially given as an IDT is determined using the gradient of OH production in most shock tube studies. Furthermore, as the first species to study, the OH absorption spectrum is well-validated at pressures up to 60 atm [159]. Until recently, the  $R_1(5)$  transition of the  $A^2\Sigma^+-X^2\Pi(0,0)$  rovibronic band at approximately 306.7 nm [141, 163, 164] was used to study OH concentrations. However, due to recent advancements in laser absorption diagnostics, the  $Q_1(5)$  transition of the  $A^2\Sigma^+-X^2\Pi(0,0)$  band with an absorption peak near 308.6 nm can be used. Utilising this peak is advantageous as it has a greater line strength than  $R_1$  and the individual transitions aren't as densely spaced [165-167].

Multi-pass absorption spectrometry has also been utilized for the detection of OH radicals at 308 nm. By allowing the laser light to pass through the sample numerous times, the amount of light absorbed increases and allows smaller concentrations of OH to be detected [168]. To do this, windows with high reflectivity are required to reflect the light through the shock tube before its eventual passage to the detector.

## 2.10.2. Tender Process and Initial Requirements

The tender for the shock tube laser absorption diagnostic technical specification was developed as part of the EngD project and important laser characteristics were decided upon for the bidding companies to meet and for which they would be evaluated. The technical specification was split into essential requirements and desired features. These requirements were outlined as follows in Table 2.3.

**Table 2.3.** Requirements for the UoS HPST laser absorption diagnostic system, E: Essential and D: Desirable.

Laser Requirements	
E1	The variable final energy output of the laser is $\geq 1$ mW.
E2	Final laser power stability $\leq 5$ %
E3	Continuous wave or pulse rate $\geq 10$ MHz
E4	Required wavelength ranges of 225-230nm and 305-310nm,
E5	Software to control laser, to enable automatic wavelength scanning along with autotuning of any laser tuning components.
D1	Reach wavelengths; 216nm, 240nm, 670nm.
D2	Slip-on covers or alternate methods to conceal the full-beam path.
D3	Two appropriate detectors and software to monitor the required wavelengths and power output.
D4	An accurate method of monitoring the laser beam wavelength.

**E1:** A variable energy laser output of 1 mW or more was selected as this output power has previously been used to study OH and is therefore powerful enough to study OH in shock tube experiments [138, 141].

**E2:** A final power stability of less than 5% was essential to prevent large fluctuations in the final laser output which would ultimately affect the OH concentration profiles produced by the laser. This property is often quantified over a given period and as the shock tube experiments take place over milliseconds, fluctuations over this time will not affect individual experiments.

**E3:** Due to the relatively short milliseconds timescale of the individual shock tube experiment, a high repetition rate of a pulsed laser, or continuous wave laser is required. As a continuous wave laser produces a constant light source there is no time interval between measurements and a continuous concentration profile can

be produced. A pulsed laser with a repetition rate of 10 MHz measures every 0.1  $\mu\text{s}$ , which would be sufficient to measure the ignition delay time typically on the order of hundreds of microseconds.

**E4:** Two wavelength ranges of 225-230 nm and 305-310 nm were essential for the study of  $\text{HO}_2$  and OH respectively. There was no requirement to generate both wavelength ranges through the same attachment or in parallel, just the capability to produce both.

**E5:** The laser absorption diagnostic was expected to be user-friendly and easy to use, this meant automated scanning of wavelength ranges and automatic tuning, with only the requirement for small manual adjustments.

**D1:** Extra wavelengths of 216 nm, 240-250 nm and 670 nm were included to study  $\text{CH}_3$  [169],  $\text{CH}_3\text{O}_2$  [170] and  $\text{N}_2\text{O}$  [171] respectively. As well as this, many more species may fall under the increased wavelength range and increase the future flexibility of the diagnostic.

**D2:** The laser diagnostic beam path was under strict consideration for the shock tube as it would be placed out in the open due to a rearrangement of the layout at TERC. To ensure the safety of the shock tube user and those using other equipment, the full beam path of the high-powered laser must be covered. This was listed as desirable as it was unlikely that the laser company provide could also provide this, and it may prove cheaper to retrofit something at a later stage in-house.

**D3:** Two appropriate detectors were specified to record the laser output power before and after the shock tube, allowing the difference to be calculated and thus the species concentration. Again, these would likely be supplied by 3<sup>rd</sup> party by a laser supplier, so were only added as desirable.

**D4:** An accurate method of monitoring the wavelength which prevents the stray of the laser wavelength once set removes the need for constant recalibration.

The further added benefit of the continuous wave laser is the ultra-narrow linewidth, which is difficult to match using a pulsed system. By having a very narrow linewidth, the laser system can focus on very thin peaks, which is more

important for the narrow peaks of OH radicals. This means that the whole of the laser output sits on the absorption peak, rather than just some of the output laser, thus leading to a greater degree of absorption and therefore a larger difference between the incident and transmitted intensity.

### **2.10.3. M-Squared SolsTiS 4000 PSX XF System**

The M-Squared SolsTiS 4000 PSX XF uses narrow linewidth titanium: sapphire laser which can be tuned between 700 and 1000 nm with a linewidth of less than 100 kHz over 100  $\mu$ s. The full laser system has four additional attachments: the ECD-A, ECD-Q-A, CMM-532-A-SFG and DL3. These attachments can provide a final output of wavelength from 306-310 nm and 225-230 nm.

The initial pump laser utilised is a 15W single-frequency, continuous-wave, 532 nm Equinox laser. This is used to power the SolsTiS 4000 PSX XF, a next-generation solid-state Ti:Sapphire laser, transitioning away from the more cumbersome dye-based laser systems. This seed laser produces wavelengths in the near infra-red (NIR) range from 700-1000 nm with the peak power output of the SolsTiS 4000 peaking at >4W at a wavelength of ~780nm.

The properties of the Equinox 532 nm seed laser and the SolsTiS 4000 PSX XF laser as shown in Table 2.4 and Table 2.5, respectively.

**Table 2.4.** Properties of the Equinox 532 nm laser.

Property	Specification
Average Power	15 W
Wavelength	532 nm
Linewidth	<1 MHz
Beam Diameter	2.3 mm +/- 10%
Beam Divergence	<0.45 mrad, far-field, full angle
Spatial Mode	TEM <sub>Infinity</sub> [M2 < 1.1]
Asymmetry	<10%
Astigmatism	<0.2%
Power Stability	+/- 0.5%
Polarisation	>100:1
Temperature Variation	+/- 2 °C

**Table 2.5.** Properties of the SolsTiS 4000 PSX XF Ti:Sapphire laser.

Property	Specification
Power	>4.0 W
Tuning Range	725-875 nm
Linewidth	<100 kHz
Scan Range	>25 GHz at ~780 nm
Amplitude Noise	<0.075% RMS
Spatial Mode	TEM <sub>Infinity</sub> [M2 < 1.1]
Beam Radius	<0.4 mm, 1/e <sup>2</sup> intensity [nominal, at output port]
Beam Divergence	<1.5 mrad, far field, half-angle
Operating Temperature Range	16-30 °C

#### 2.10.4. ECD-A/ECD-Q-A Wavelength Extension Modules (225-230 nm)

The ECD-A attachment operates at a cavity operating at  $910 \pm 20$  nm to double the laser output power to 455 nm using second harmonic generation (SHG) from the NIR beam with a power greater than 500 mW. The ECD-Q-A produces an output wavelength of 225-230 nm and is required to study HO<sub>2</sub> (227 nm) and NO (225 nm), with a linewidth of less than 400 kHz over 100  $\mu$ s. The ECD-A module

is automatically stabilized to the SolSTiS seed laser through a Hansch-Couillard locking scheme [172].

The ECD-Q-A has typical power stability of 0.6% RMS, well within the 5% specified in the original tender. The ECD-Q-A module uses the fourth harmonic generation (FHG) to convert the deep blue/UV output from the ECD-A into deep UV wavelengths. The M-Squared laser can achieve the essential wavelengths and could have reached the desirable wavelength ranges at an additional cost, but this option was not considered at this point.

#### **2.10.5. EMM-532-SFG-A Wavelength Extension Module (306-310 nm)**

The EMM-532-SFG-A module uses SFG to mix the NIR output from the SolSTiS seed laser with the 532 nm output from the Equinox pump laser. This all-solid-state solution is fully automated, and all the non-linear crystals utilised are designed to be mechanically translated and phase-matched to remove the requirement for manual adjustments. The EMM-532-SFG-A module produces a final output of 306-310 nm to study OH time histories using methods at wavelengths listed in Section 2.10.1. This output location is separate from that of 225-230 nm from the ECD extensions and the two wavelengths cannot be run simultaneously.

#### **2.10.6. Dial-a-Wavelength Control**

The M-Squared continuous-wave laser absorption diagnostic benefits from a DL3 ("dial-a-wavelength") software. Once the laser is aligned the wavelength can be 'locked' in place, which through continuous feedback of a wavemeter, reduces the wavelength drift over long periods. This can be done to a coarse resolution (0.5 nm) using position-indexing of the birefringent filter (BRF) or to a fine resolution ( $\leq 0.0001$  nm) using a readout wavemeter. The wavemeter used in the UoS M-Squared laser is a High-Finesse WS6-600 wavemeter which is integrated into the system. In this instance, the wavemeter continuously monitors the output of the laser beam and makes corrections accordingly to prevent deviations in the wavelength.

### 2.10.7. OH Absorption

The first species to be studied in the UoS shock tube will be OH. The spectral lineshape of OH was determined by Girard et al. [166] at 1800 K as shown in Figure 2.30. This is achieved by using the EMM-532-SFG-A module described In Section 2.10.5. The Q<sub>1</sub>(5) transition is much stronger and more densely spaced than the R<sub>1</sub>(5) transition making it the optimum wavelength to study at 308.61 nm.

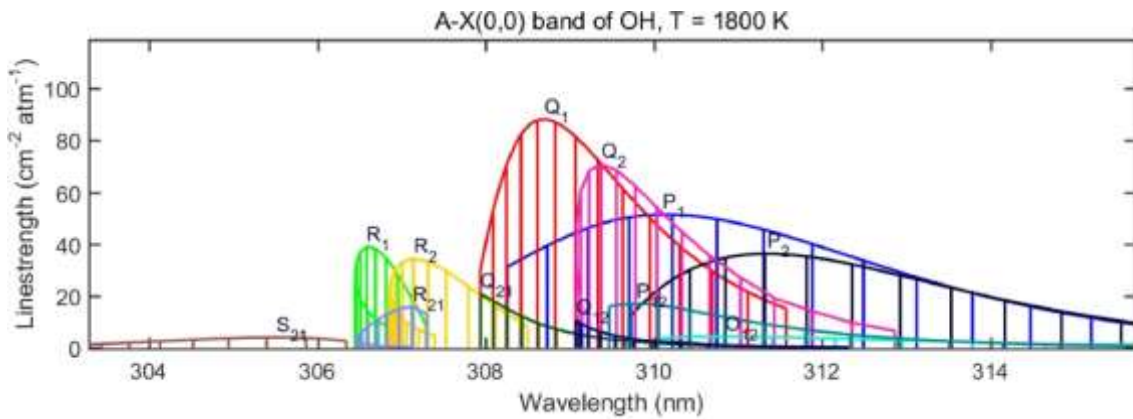


**Figure 2.30.** Simulated OH spectral profile from 303-316 nm from Girard et al. [166].

A similar laser system has been used by Wang and Hanson [167]. Laser absorption determines the mole fraction ( $\chi$ ) of OH to be determined from the logarithmic attenuation of the laser intensity ( $-\ln(I/I_0)$ ). This is also known as the Beer-Lambert law shown in Equation 2.9.

**Equation 2.9**       $\alpha = \chi kPL$

This study focused on an isolated transition so can be interpreted in a simple manner using Equation 2.10.

**Equation 2.10**       $k = S(T)\varphi(v, T, P)$

The temperature dependence of the line strength  $S$  relative to the reference temperature ( $T_0$ ) is given by Equation 2.11.

**Equation 2.11.**       $\frac{S(T)}{S(T_0)} = \frac{Q(T_0)}{Q(T)} \exp \left[ -\frac{hcE''}{k} \left( \frac{1}{T} - \frac{1}{T_0} \right) \right] \left[ 1 - \exp \left( -\frac{hcv_0}{kT} \right) \right]^{-1}$

Where  $Q$  - OH partition function.,  $E''$  - Lower state energy,  $\nu_0$  - Line centre frequency of the OH absorption transition,  $h$  - Planck's constant,  $c$  - Speed of light and  $k$  - Boltzmann Constant. Equation 2.11 is accurate between 1000 and 4000 K within  $\pm 0.3\%$  error:

**Equation 2.12.**  $Q(T) = 11.367 + 1.194 \times 10^{-1}(T/K) + 1.364 \times 10^{-5}(T/K)^2 + 1.600 \times 10^{-9}(T/K)^3$

The  $Q_1(5)$  transition of the  $A^2\Sigma^+ - X^2\Pi$  (0,0) band  $E''$  and  $\nu_0$  has been determined to a high degree of accuracy by Goldman and Gills [173].  $Q(T)$  has also been tabulated by Goldman and Gillis [173] and later correct in Goldman [174] to account for anharmonic oscillator effects ( $E'' = 544.809 \text{ cm}^{-1}$ ,  $\nu_0 = 32403.405 \text{ cm}^{-1}$ ). Furthermore, to make accurate quantitative measurements of OH concentration a detailed understanding of the spectral line shape  $\phi$  is required.

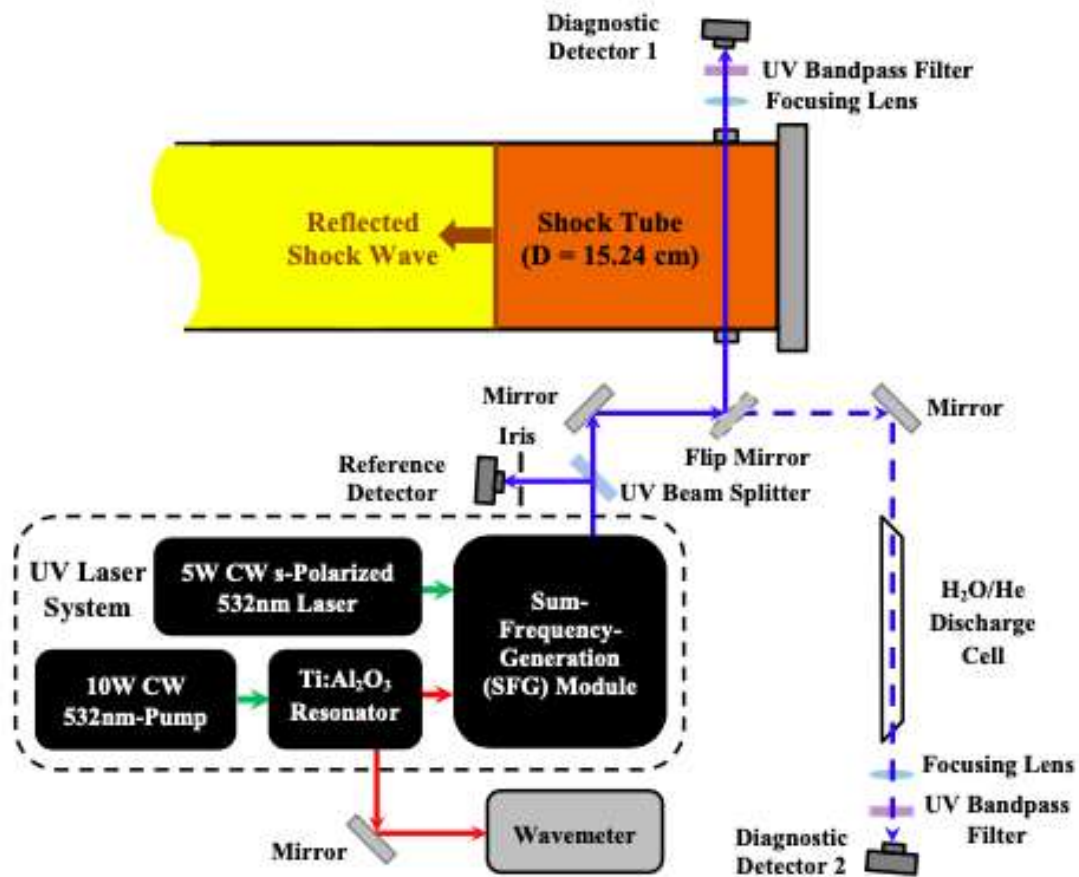
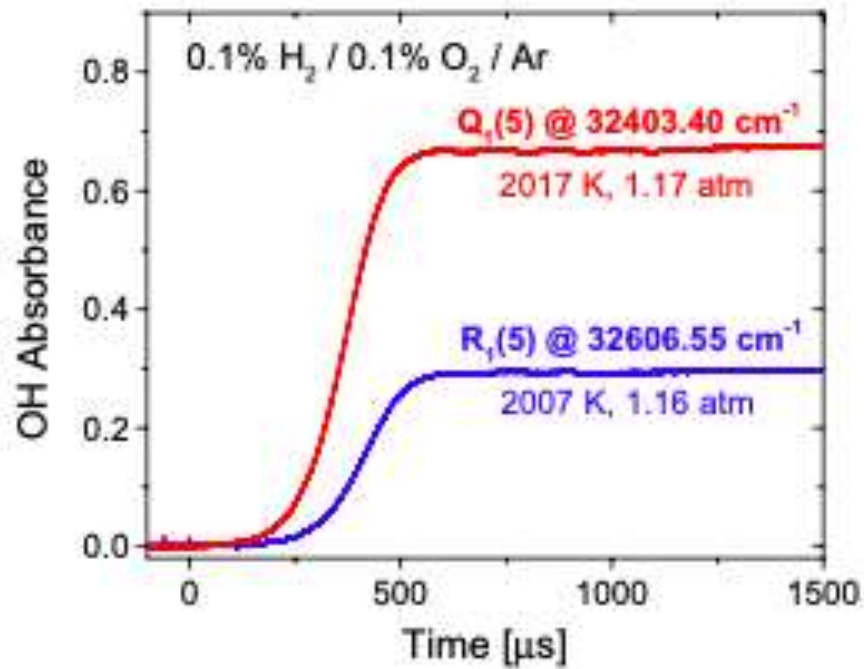


Figure 2.31. Set up of OH laser absorption diagnostic at 308.61 nm for  $Q_1(5)$  from [167].

The laser beam was recorded before and after the beam to determine its incident and transmitted beam power [167]. These detectors were Thorlabs PDA36A Si switchable-gain detectors (20 dB gain setting,  $f_{-3dB}=1$  MHz. The wavelength of the Ti:Sapphire was monitored in real-time with a Burleigh WA-1000 wavemeter with a spectral resolution of  $0.01 \text{ cm}^{-1}$ . The numerical value of the  $k_{OH}$   $Q_1(5)$  line centre has been characterised by Equation 2.13 where  $T_r=T/1000$  K and  $P_r=P/1$  atm.

**Equation 2.13.**  $k_{OH}(cm^{-1}atm^{-1}) = \exp(8.662 - 1.852T_r - 0.4328P_r + 0.1786T_r^2 + 0.1994T_rP_r + 0.0081T_r^2 - 0.0040T_r^3 - 0.0259T_r^2P_r - 0.0028T_rP_r^2 + 0.0002P_r^3)$

For each shock tube measurement in Wang et al. [175] of  $Q_1(5)$  peak (308.60696 nm), a second measurement was repeated at near identical shock tube conditions at a slightly different wavelength (308.5944 nm, OH offline) and a differential absorbance was used to determine  $X_{OH}$ . Since the M-Squared system is ultra-narrow linewidth (<400 kHz), this gives a laser width of approximately 0.1 nm meaning that based on the  $Q_1(5)$  transition shown in Figure 2.33 between 1000 K and 2000 K, the temperature range utilised by the shock tube. Furthermore, by incorporating the 'Dial-a-wavelength' software the laser system shouldn't stray once calibrated to the appropriate wavelength. In addition to this pressure, broadening means that these transitions broaden in terms of wavelength at higher pressures induced by collisions between molecules. With broader wavelength ranges at higher pressures, it will be easier to detect the transitions but may require more work to make sure we are on the most intense part of the transition such that the maximum possible signal is being detected.



**Figure 2.32.** OH absorbance time histories from Q1(5) and R1(5) peaks during shock tube oxidation experiments in a 1000 ppm H<sub>2</sub>/1000 ppm O<sub>2</sub>/ Ar mixture [167].

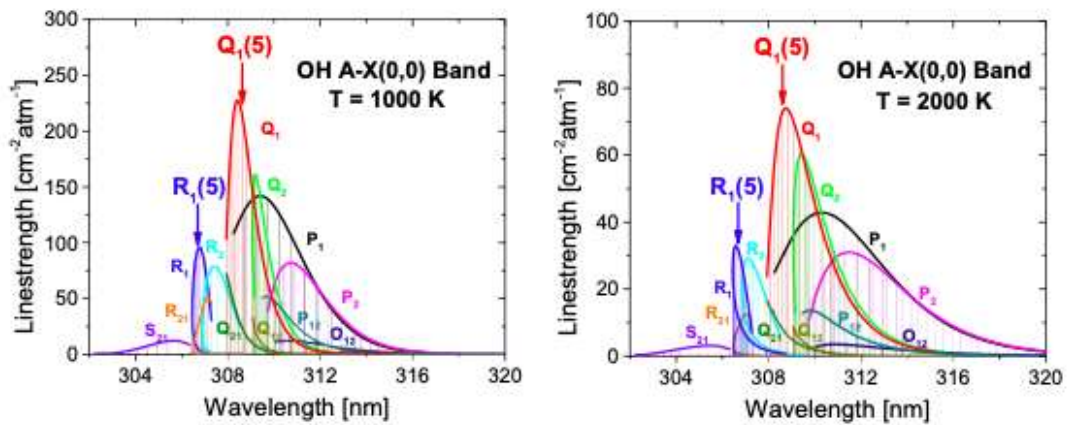


**Figure 2.33.** Simulated A<sup>2</sup>Σ<sup>+</sup>-X<sup>2</sup>Π (0,0) transitions at 1000 K (left) and 2000 K (right) [167].

## 2.11. Summary and Outlook

The University of Sheffield high-pressure shock tube has been designed and fabricated as part of this EngD project. The aims of the shock tube were first determined in terms of desired pressure, diagnostic capabilities and fuels and the restrictions imposed by the location were determined. This information was coupled with well-established shock tube theory to create the initial shock tube concept. This was refined further refined in terms of safety by consultants WSP, to ensure the correct procedure was followed for the high-pressure vessel. Two

separate tenders were created, one for the shock tube itself and the other for a laser diagnostic for the study of OH absorption. The specifications of these tenders were all determined and written in-house. The laser diagnostic tender was awarded to M-Squared, who provided a continuous wave laser diagnostic capable of studying OH, HO<sub>2</sub> and NO. The shock tube was delivered and installed in autumn 2022 after the shock tube. The shock tube tender was unsuccessful, but the project was finally given to Heblac Technologie GMBH, who have experience in shock tubes from their affiliation with Aachen University [148].

The fabrication of the shock tube and the delivery was completed in 2022 whilst the laser diagnostic system is currently still in production. The design is intended to study high-pressure chemical kinetics of the combustion of the Allam-Fetvedt cycle but has been built with the flexibility to adapt for future research. This means the UoS HPST is an incredibly versatile tool for future research and can be utilised for many different areas of combustion, such as ammonia, syngas, and synthetic aviation fuel.

## **3. Development of the UoS sCO<sub>2</sub> Mechanism**

### **3.1. Introduction**

This chapter details the creation of the UoS sCO<sub>2</sub>, a chemical kinetic mechanism specialised for combustion in CO<sub>2</sub>. The work from this chapter focuses on methane, hydrogen and syngas combustion and was originally published at the 4<sup>th</sup> European sCO<sub>2</sub> Conference for Energy Systems in 2021 [86]. The original publication looked at 22 datasets for IDT data in various dilutions and equivalence ratios above 29 atm. The paper was then upgraded to a virtual special edition of Energy and was expanded to include 30 more datasets at pressures below 30 atm [87]. The UoS sCO<sub>2</sub> mechanism better modelled the IDT of 30 of the 52 datasets investigated compared to four existing chemical kinetic mechanisms validated for low pressures and low CO<sub>2</sub> dilutions. Furthermore, the UoS sCO<sub>2</sub> 1.0 mechanism on average best models the IDT data studied across the three different fuels, with the most significant improvement being for syngas combustion.

### **3.2. Oxyfuel Combustion**

Oxyfuel combustion is the combustion of a fuel in pure O<sub>2</sub>, or an O<sub>2</sub>/CO<sub>2</sub> blend, as opposed to the traditional combustion in air. Oxyfuel combustion mitigates Air-NO<sub>x</sub> production with the flue gas being recycled through the combustion chamber to regulate the flame temperature [176]. The chemical kinetic mechanism for combustion at the extreme pressures and large CO<sub>2</sub> dilutions of sCO<sub>2</sub> power cycles of 300 atm and 96% respectively is poorly understood. Existing chemical kinetic mechanisms tend to be validated at low pressures and low CO<sub>2</sub> dilutions, so are not guaranteed to maintain their performance when extrapolated beyond those conditions. Most combustion data are obtained at low pressures and low dilutions of CO<sub>2</sub>, and as any of these two variables is increased, the scarcity of data increases [177]. In addition, various types of data have been published for combustion in CO<sub>2</sub>, including laminar flame speed and ignition delay time for different fuels.

### 3.2.1. Laminar Flame Speed

The laminar flame speed is defined as the speed at which a flame propagates through unburnt reactants under homogeneous, adiabatic conditions [178]. The laminar flame speed is a parameter describing important combustion properties such as reactivity, diffusivity and exothermicity of the fuel/air mixture [179]. The effect of a CO<sub>2</sub> dilution was first measured by Persis et al. [180] who found that the high heat capacity of CO<sub>2</sub> reduces the adiabatic temperature of combustion and subsequently NO<sub>x</sub> emissions. Furthermore, Watanabe et al. [181] found oxy-flames were shorter than air flames and burnt with greater intensity than predicted by laminar flame speed models. Hu et al. [179] studied the laminar flame speed of methane combustion in CO<sub>2</sub> in an oxidant mixture of up to 69% CO<sub>2</sub> and found a good agreement with the GRI 3.0 mechanism [182]. The authors also noted a significant decrease in the laminar flame speed under a CO<sub>2</sub> bath gas relative to a nitrogen bath gas of the same stoichiometric ratio and oxygen and fuel mole fraction. Furthermore, a similar experimental technique has been utilised to study the laminar flame speed of propane combustion in CO<sub>2</sub> and found a similar decrease in the flame speed due to the thermal properties of CO<sub>2</sub> [183].

Hu et al. [184] investigated the performance of IDT, laminar flame speed and concentration-time histories. Whilst the authors concluded the USC II [185] mechanism performed the best on average across these three properties, GRI 3.0 did have the best performance for the laminar flame speed. Furthermore, Natarajan et al. [186] and Shang et al. [187] have investigated the effect of CO<sub>2</sub> dilution on a synthesis gas (syngas) and oxygen blend. Natarajan et al. [186] found that the GRI 3.0 mechanism struggled to model experimental data for fuels with an H<sub>2</sub> concentration of 10% or more compared to the H<sub>2</sub>/CO Mech by Davis et al. [188], which performed well in all of the experimental datasets. Similarly, Shang et al. [187] found that H<sub>2</sub>/CO Mech and Li-Mech [189] both displayed satisfactory agreement with the experimental data out of the four mechanisms studied. However, it should be noted that GRI 3.0 was not included among the mechanisms. Strakey [190] found that when simpler models which ignored turbulence-chemistry interactions were used to predict flame chemistry, the

predicted CO emission was poorly predicted at low oxygen concentrations. Mazas et al. [191] looked at the laminar flame speed of methane combustion in water and CO<sub>2</sub>-diluted mixtures. The authors found it was at smaller CO<sub>2</sub> dilutions ( $X_{CO_2} < 0.3$ ) where GRI 3.0 struggled to accurately model the experimental data. This suggests it may not necessarily be the extremes of CO<sub>2</sub> dilutions that are the most difficult to accurately simulate.

### **3.2.2. Ignition Delay Time**

The IDT is commonly studied in shock tube and RCM experiments using various detection methods such as laser Schlieren [192], OH\* chemiluminescence as discussed in Section 2.9.2 [127], CH\* chemiluminescence [193] or from the pressure trace. Following an extensive literature review as part of the first stage of this project, the development of a new chemical kinetic mechanism for combustion in CO<sub>2</sub>, all available shock tube IDT data were amassed in Table 3.1 for various fuels and fuel combinations.

**Table 3.1.** Temperature, pressure ranges, release date, fuel type and authors for the published IDT data source.

<b>Author</b>	<b>Temperature Range /K</b>	<b>Pressure Range /atm</b>	<b>Year</b>
<b>Methane</b>			
Hargis and Petersen [122]	1420-1841	1.4-18.1	2015
Koroglu et al. [153]	1610-2114	0.5-4.4	2016
Pryor et al. [194]	1724-2038	0.6-1.1	2017
Pryor et al. [195]	1334-1920	0.8-31.0	2017
Liu et al. [151]	1503-1785	0.7-2.0	2018
Shao et al. [85]	1045-1578	27.1-285.5	2019
Karimi et al. [127]	1139-1433	92.9-209.1	2019
Barak et al. [192]	1283-1327	74.8-81.4	2020
Laich et al. [71]	1045-1356	14.1-17.5	2020
Kinney et al. [196]	-	-	2022
<b>Natural Gas</b>			
Kinney et al. [196]	-	-	2022
<b>Syngas</b>			
Vasu et al. [197]	974-1160	1.1-2.6	2011
Barak et al. [198]	1006-1162	1.6-1.8	2017
Barak et al. [199]	1113-1270	34.6-45.5	2019
Barak et al. [192]	1064-1338	72.4-100.4	2020
Karimi et al. [200]	1161-1365	80.8-210.1	2020
<b>Hydrogen</b>			
Shao et al. [85]	1083-1291	37.1-311.0	2019
<b>Ethane</b>			
Liu et al. [201]	1064-1550	0.73-11.0	2019
<b>DME</b>			
Djordjevic et al. [202]	713.7-1316.4	14.1-51.6	2019
Shi et al. [203]	670-795	9.87	2015
<b>DME/Ethane</b>			
Liu et al. [204]	1126-1449	0.8-10	2020
<b>DME/Propane</b>			
Yang et al. [205]	1157-1376	2.0-11.1	2022
<b>Ethylene</b>			
Xiong et al. [206]	1074-1832	2	2020
<b>Propane</b>			
Xia et al. [207]	1206-1587	0.9-11.9	2020
<b>Pyridine</b>			
Luo et al. [208]	1202-1498	2.2-10.6	2020
<b>Iso-Octane</b>			
Di et al. [209]	626-1365	19.5-21.0	2014

This project will focus on modelling IDT data for methane, hydrogen, and syngas combustion then this will be expanded to contain other fuels. The reason these fuels are being studied preferentially is two-fold. Firstly, there are more data available for these fuels which will mean a better-validated model and secondly, the Allam-Fetvedt cycle uses natural gas, which is primarily methane, or synthesis gas produced from coal gasification.

The dataset published by Laich et al. [71] was performed at high fuel loadings ( $X_{CH_4}=0.1667$ ) and studied the preignition event, which means the data cannot be used for mechanism validation in the present work.

Furthermore, the effect of impurities on the IDT of natural gas combustion has been investigated by Rahman et al. [210] at the University of Central Florida. The authors found that the addition of  $N_2O$  to the mixture reduced the IDT, whilst  $H_2S$  impurities increased the rate of carbon monoxide formation. A similar study was performed by Biswas et al. [211] on the effect of  $H_2S$  impurities on syngas combustion at 100 atm, finding even a small concentration of  $H_2S$  of 0.5% significantly reduced the IDT.

### **3.3. Modelling Procedure**

All of the simulations performed in this work were modelled using Chemkin Pro R3 2019 [212] using a zero-dimensional closed homogeneous batch reactor with a 'constrain volume and solve energy equation' problem type which resembles the adiabatic postshock conditions within a shock tube. Chemkin uses a Twopnt, Reaction Designs numerical solver which applies a system of algebraic equations conditioned by integration of the time-dependent version over several steps or until convergence in a steady-state solution. Chemical kinetic mechanisms utilise thermodynamic data for all of the species involved published by Professor Burcat which is essential to the numerical solver [213].

#### **3.3.1. Determination of Ignition Delay Time**

The IDT is an important combustion property that must also be modelled to allow comparisons between the chemical kinetic mechanisms and experimental data.

The IDT can be modelled in two ways using Chemkin. Time-zero is defined as the start of the model run as this is when the initial high-pressure and temperature conditions are achieved. The onset of ignition can be defined as the maximum gradient of either the temperature rise caused by combustion or the increasing OH concentration. The maximum gradient is extrapolated down to the time baseline to give the IDT. Within the closed homogeneous batch reactor model used, the IDT calculated from the temperature can be calculated and selected as an output. The IDT calculated from the OH concentration can be calculated from the differentiation of the OH species concentration output. The peak of the curve of the first differential gives the time of the maximum gradient of the initial concentration curve. This technique is computationally more difficult and requires more time but it more accurately reflects the experimental determination of the IDT. The discrepancy between the two was briefly investigated before beginning the modelling work. It was noted that for the methane and hydrogen datasets, there was a good agreement with an average difference of approximately 5%. Compared to the experimental error of 18-25% [127] this is negligible and means that the quicker temperature method can be used when in the process of updating mechanisms as a good approximation of the IDT. However, in the syngas datasets, the difference between the two methods of IDT determination differed by over 100%. This was likely to be due to a second temperature and OH peak which was much larger and led to an artificially longer IDT determined by Chemkin when using the temperature method. When inspecting the graph visually, the first peak is taken as the IDT which is in much better agreement with the experimental data and conditions where this phenomenon occurs. This discrepancy between the two ways to detect IDT is discussed more in Section 4.2.1.

Based on this observation, when modelling a new IDT dataset, the IDT was determined theoretically using both techniques and compared. If the average error between the two results was less than 5%, then the faster temperature method was used when making mechanism improvements to reduce the time taken to test an alteration. For the final mechanism, however, the OH method is

used for the modelled IDT data within any published medium as this is a more accurate representation of the experimental method of IDT determination.

### **3.3.2. Sensitivity Analysis**

Sensitivity analyses are a vital tool for improving the chemical kinetic mechanisms to better model the experimental data. A sensitivity analysis is performed at a given temperature and identifies which reaction rate coefficients the experimental value is most sensitive to i.e., by changing which rate coefficients will lead to the largest change in the value being studied. By comparing the sensitivity analysis of two mechanisms under the same conditions, the difference, either in the reactions present or their relative sensitivity is indicative of any discrepancies which occur between the mechanisms. This identifies reactions that may be using older rate coefficients that may need to be reevaluated and updated. For sCO<sub>2</sub> combustion, most of the rate coefficients used in these mechanisms haven't been determined under such high pressures and large dilutions of CO<sub>2</sub>, therefore their extrapolation to these conditions may induce some mechanism errors.

The sensitivity analyses were performed for IDT data on Chemkin using OH species sensitivity at the IDT for a given temperature within a dataset. The temperatures were selected at points of a large discrepancy between either the mechanism and the experimental data point or the different mechanisms being studied. The top ten most sensitive reactions were determined and plotted as a bar chart.

The OH sensitivity coefficient is determined is the first-order sensitivity coefficient of the OH species fraction for the reaction rate coefficient. This exploits a computationally efficient sensitivity method based on the differential equations describing the sensitivity coefficients as linear to model the problem. The sensitivity plots show the reactions as reversible and, in the direction, they are inputted into the Chemkin mechanism file. Therefore, some reactions in the sensitivity plots are proceeding in the reverse direction, as indicated by the reversible symbol. Chemkin automatically calculates the rate of a reverse

reaction. This is done using the equilibrium constant (Equation 3.1) which is in turn calculated from Equation 3.2.

**Equation 3.1.** 
$$K = \left(\frac{k_f}{k_r}\right)$$

**Equation 3.2.** 
$$\Delta G^\circ = -RT \ln K$$

This must be considered when interpreting the figures and discussion. The OH sensitivity coefficient ( $\delta_{OH}$ ) is calculated using Equation 3.3 by studying the effect of increasing and decreasing the rate coefficient on the OH concentration. A positive sensitivity coefficient shows that increasing the rate coefficient increases the OH concentration and thus reduces the ignition delay time. Whereas a negative sensitivity coefficient indicates that any increase in the rate coefficient would increase the IDT.

**Equation 3.3.** 
$$\delta_{OH} = \frac{\log([OH])}{\log(k_{+/-})}$$

### 3.3.3. Reaction Pathway Analysis

One way of comparing different chemical kinetic mechanisms is through a reaction pathway analysis (RPA). These are commonly performed on Chemkin Pro R3 2019 [212] and compare the reaction pathway that the reactants take to get to the final product. This is a useful tool to identify if mechanisms favour different intermediates and the influence of the conditions on the reaction pathway. The RPA determines the extent that each reaction contributes to the production and loss of key species in the overall combustion reaction. For a 0-D system, the molar production of a species is calculated using Equation 3.4 and the rate of production of a species is calculated by Equation 3.5. This allows comparison between the rate coefficients of different mechanisms as it shows which species, and therefore reactions, are dominant under different conditions.

**Equation 3.4.** 
$$P_k = \dot{\omega}_k + \sum_{M=1}^M \frac{A_m}{V} \dot{S}_{k,m} = \sum_{i=1}^I U_{ki} q_i + \sum_{m=1}^M \frac{A_m}{V} + \sum_{i=1}^I v_{ki}^s q_i^s$$

**Equation 3.5.** 
$$c_{ki} = v_{ki} q_i$$

### 3.3.4. Quantitative Analysis

The mechanisms were quantitatively evaluated as part of the creation of the UoS sCO<sub>2</sub> mechanism using Equation 3.6 [201] to calculate the average absolute error ( $E$ , %). The quantitative analysis was vital to the creation of this mechanism as it allowed some non-subjective comparison between how the different chemical kinetic mechanisms modelled the IDT data. This gave a clear indication of what conditions mechanisms performed well and identified the temperatures where sensitivity analyses should be performed.

**Equation 3.6.** 
$$E = \frac{1}{N} \sum_{i=1}^N \left| \frac{X_{sim,i} - X_{exp,i}}{X_{exp,i}} \right| \times 100$$

In Equation 3.6,  $N$  represents the number of data points in the experimental set,  $X_{sim,i}$  and  $X_{exp,i}$  are the modelled and experimental results for the  $i$ th IDT datapoint respectively. The  $E$  value of a mechanism gives a quantitative indication of performance. The smaller the  $E$  value, the smaller the difference between the experimental and measured data points and the better the mechanism is performing.

One complication is the large error in the experimental IDT values of approximately 20%, meaning that multiple mechanisms may fit within the error, which is not reflected in the quantitative analysis. However, over many data points across many datasets and different fuels, the average,  $E$  is a strong indication of how well a mechanism can model experimental IDT data.

### 3.3.5. Third Body Efficiencies of CO<sub>2</sub>

In a third body reaction, two species collide to form a new species with high energy, this new species then collides with an inert third body (M) to remove excess energy and stabilise the species ( $A + B \rightleftharpoons AB^* + M \rightleftharpoons AB + M$ ). These reactions are pressure dependent and depend on the efficiency of the third body species to remove the excess energy.

The reaction is pressure dependant in the low-pressure regime where the reaction rate increases linearly with the increasing pressure. This is due to the

number of collisions with M being the limiting factor in the reaction. At the high-pressure regime, M is no longer the limiting factor in the reaction rate and thus any further increase in pressure does not affect the reaction rate. The region in-between this low and high-pressure regime is known as the fall-off region where the chemical kinetics becomes more difficult to predict in Chemkin.

In Chemkin there are two ways to input third-body reactions into the chemical kinetic mechanism. They can be input with Troe parameters which give the low-pressure rate coefficient and parameters which are used to calculate the fall-off region and high-pressure limit. The other method is to input the rate coefficient as a PLOG. This inputs the temperature-dependent rate coefficient at a series of different pressures from low to high-pressure. This method works well if the pressure range being studied is within the input pressure range. This is not always the case for high-pressure combustion of this work and if the high-pressure limit isn't being inputted correctly the reaction rate may be being over-predicted.

One further complication is that the chemical kinetics of third-body reactions are not often studied in  $\text{CO}_2$ . Often the third body efficiencies are given for  $\text{CO}_2$  but are based on estimates and no solid experimental data. Therefore, as  $\text{CO}_2$  is a more efficient third body and these reactions are going to be more important at high-pressures, this lack of understanding may induce significant errors in these rate coefficients.

### **3.4. Dataset Selection**

The original publication for the 4<sup>th</sup> European s $\text{CO}_2$  Conference for Energy Systems [86] focused on 22 datasets for methane, hydrogen and syngas combustion all above 29 atm. Methane, hydrogen and syngas were selected due to there being the three most important fuels to fundamental combustion chemistry under these conditions. Methane is the primary component of natural gas and the simplest hydrocarbon fuel. Hydrogen is the most simple fuel to model and is a key component of syngas, and syngas from coal gasification has been proposed as a potential fuel for the Allam-Fetvedt cycle [34]. For the upgraded

journal publication, this was expanded to all the available, published shock tube ignition delay time datasets below 29 atm for the three fuels, expanding to 52 datasets as this increased the validity of the mechanism over a greater range of conditions.

#### **3.4.1. Methane Datasets**

At the time this work was undertaken 29 methane datasets were available for modelling from 8 different publications. The average pressure ranged from 0.6 atm to 266.3 atm and the equivalence ratio ( $\phi$ ) varied from 0.5 to 2.0, at various CO<sub>2</sub> dilutions. The datasets studied are from Hargis and Petersen [122], Koroglu et al. [153], Pryor et al. [194, 195], Liu et al. [151], Shao et al. [85], Karimi et al. [127], and Barak et al. [192]. Table 3.2 shows the 29 datasets as well as the average pressure (atm), equivalence ratio and CO<sub>2</sub> mole fraction (%).

**Table 3.2.** Methane datasets analysed.

Dataset	Reference	Average Pressure /atm	Equivalence Ratio ( $\Phi$ )	CO <sub>2</sub> Dilution (%)
M1	[122]	1.7	2.00	50.00
M2	[122]	2.5	2.00	50.00
M3	[122]	2.1	2.00	75.00
M4	[122]	12.7	2.00	75.00
M5	[153]	0.8	1.00	30.00
M6	[153]	3.8	1.00	30.00
M7	[153]	0.8	2.00	30.00
M8	[153]	3.9	2.00	30.00
M9	[153]	0.7	0.50	30.00
M10	[153]	3.6	0.50	30.00
M11	[153]	0.6	1.00	60.00
M12	[195]	0.9	1.00	60.00
M13	[195]	7.2	1.00	60.00
M14	[195]	8.9	1.00	85.00
M15	[195]	29.6	1.00	85.00
M16	[194]	0.6	1.00	89.50
M17	[194]	1.0	1.00	85.00
M18	[151]	1.9	2.00	75.00
M19	[151]	0.9	2.00	75.00
M20	[85]	32.2	1.00	77.50
M21	[85]	106.3	1.00	77.50
M22	[85]	260.0	1.00	77.50
M23	[85]	31.4	1.27	86.17
M24	[85]	74.7	1.27	86.17
M25	[85]	266.3	1.27	86.17
M26	[127]	99.0	1.00	85.00
M27	[127]	97.0	0.50	80.00
M28	[127]	201.8	1.00	85.00
M29	[192]	79.9	1.00	36.50

The wide range of conditions provides a large range of conditions and gives a good overview of methane combustion.

### 3.4.2. Hydrogen Datasets

The only published IDT data for hydrogen combustion in CO<sub>2</sub> is by Shao et al. [85]. The authors report an IDT value for hydrogen combustion diluted in 85% CO<sub>2</sub> at two different equivalence ratios over a large pressure range as shown in Table 3.3.

**Table 3.3.** Hydrogen datasets analysed.

Dataset	Reference	Average Pressure /atm	Equivalence Ratio ( $\Phi$ )	CO <sub>2</sub> Dilution (%)
H1	[85]	109.6	1.00	85.00
H2	[85]	270.6	1.00	85.00
H3	[85]	38.4	0.25	85.00

There are fewer hydrogen datasets available to model making it difficult to assume the mechanism would work perfectly across all conditions for hydrogen combustion in CO<sub>2</sub>. However, there is a wide range of pressures from 38.4 to 270.6 atm and equivalence ratios.

### 3.4.3. Syngas Datasets

There are 20 oxy-syngas combustion datasets published by Vasu et al. [197], Karimi et al. [200] and Barak et al. [192, 198, 199] investigated shown in Table 3.4. This collection of datasets covers a large range of CO<sub>2</sub> dilutions and equivalence ratios, at average pressures ranging from 1.2 to 208 atm. Furthermore, there is also a variation in syngas combustion between the ratio of the hydrogen and carbon monoxide mole fraction in the mixture not displayed in the table.

**Table 3.4.** Syngas datasets analysed.

Dataset	Reference	Average Pressure /atm	Equivalence Ratio ( $\Phi$ )	CO <sub>2</sub> Dilution (%)
S1	[197]	1.2	1.00	24.44
S2	[197]	1.7	1.00	24.44
S3	[197]	2.3	1.00	24.44
S4	[198]	1.7	0.50	60.00
S5	[198]	1.7	0.50	80.00
S6	[198]	1.7	0.33	75.00
S7	[198]	1.7	1.00	85.00
S8	[198]	1.7	0.50	80.00
S9	[198]	1.7	0.50	80.00
S10	[199]	41.5	1.00	85.00
S11	[199]	38.6	1.00	85.00
S12	[199]	38.5	1.00	85.00
S13	[199]	38.4	1.00	85.00
S14	[192]	78.9	1.02	91.80
S15	[192]	91.7	0.41	64.50
S16	[192]	89.6	0.41	92.20
S17	[192]	89.7	1.09	63.90
S18	[200]	101.0	1.00	95.50
S19	[200]	84.2	2.00	92.50
S20	[200]	208.0	1.00	95.50

Furthermore, there is also a variation in syngas combustion between the ratio of hydrogen and carbon monoxide mole fraction in the mixture not displayed in the table.

### 3.5. Mechanism Selection

As this work will focus on methane, hydrogen, and syngas, the four mechanisms used in this study were selected based on their suitability for modelling the combustion of lower hydrocarbons. GRI 3.0 [182] contains 53 species and 325 reactions and is validated against IDTs for methane and ethane below 100 atm. USC II [185] was released in 2007 and contains 111 species and 784 reactions and applies to the combustion of H<sub>2</sub>/CO/C1-C4 compounds. AramcoMech 2.0

[214-219] contains the greatest amount of chemistry of the selected mechanisms with 493 species and 2716 reactions and was developed for the combustion of the C1-C4 hydrocarbons and hydrogen. The DTU mechanism [220, 221] contains 102 species and 894 reactions and was developed by the Technical University of Denmark for the high-pressure combustion of hydrogen and C1/C2 hydrocarbons. Other mechanisms which are used by other research groups which are discussed include FFCM-1 [222], Oxymech [201] and Oxymech 2.0 [207]. These were omitted from this work due to the time constraints of modelling so many datasets and the four selected mechanisms provide a sufficient range of rate coefficients used for detailed comparison.

### **3.6. Analysis of Methane Datasets**

Table 3.5 compares the ability of the four mechanisms used to model the 29 datasets using Equation 3.6, where the lowest score shows the best-performing mechanism with the lowest average absolute error. The penultimate row shows the average, average absolute error for each of the four mechanisms to give a quantitative overview of methane combustion. The final row shows the number of best fits that each mechanism has to the 29 datasets. This provides a contrasting overview compared to the average  $E$  (%). This analysis is divided into three sections, high-pressure datasets, low-pressure datasets, and the effect of CO<sub>2</sub> dilution.

**Table 3.5.** Quantitative analysis of methane datasets.

<b>Dataset</b>	<b>AramcoMech 2.0</b>	<b>DTU</b>	<b>GRI 3.0</b>	<b>USC II</b>
<b>M1</b>	44.36	19.26	13.58	14.38
<b>M2</b>	15.24	11.94	31.56	23.69
<b>M3</b>	29.61	12.09	16.70	9.18
<b>M4</b>	14.98	18.96	50.41	34.78
<b>M5</b>	15.06	9.47	3.72	14.43
<b>M6</b>	24.99	17.43	14.06	15.45
<b>M7</b>	25.82	25.38	11.82	24.63
<b>M8</b>	40.19	36.81	13.90	19.26
<b>M9</b>	13.48	6.22	7.15	8.53
<b>M10</b>	32.19	19.47	11.85	15.70
<b>M11</b>	11.18	10.25	5.91	33.81
<b>M12</b>	30.55	23.92	12.20	32.21
<b>M13</b>	30.15	23.93	17.58	16.30
<b>M14</b>	22.95	17.72	15.95	5.08
<b>M15</b>	35.49	31.41	34.69	12.29
<b>M16</b>	33.98	19.42	44.66	114.56
<b>M17</b>	18.25	14.29	9.86	13.06
<b>M18</b>	51.28	32.16	12.14	14.74
<b>M19</b>	71.05	56.08	27.56	38.59
<b>M20</b>	60.57	47.22	23.76	39.03
<b>M21</b>	14.10	16.17	43.14	21.65
<b>M22</b>	13.18	10.03	206.77	327.95
<b>M23</b>	94.45	98.79	31.86	59.85
<b>M24</b>	20.70	24.80	56.44	10.62
<b>M25</b>	11.20	30.75	31.87	131.88
<b>M26</b>	24.68	26.62	54.20	21.84
<b>M27</b>	14.25	13.08	56.72	7.87
<b>M28</b>	7.06	6.50	32.74	45.40
<b>M29</b>	16.92	12.63	54.38	9.62
<b>Average E (%)</b>	<b>28.89</b>	<b>23.89</b>	<b>32.66</b>	<b>39.19</b>
<b>No. Best Fit</b>	<b>3</b>	<b>5</b>	<b>13</b>	<b>8</b>

### 3.6.1. High-Pressure Datasets

Table 3.5 shows the DTU has the lowest average  $E$  value of 23.89%, closely followed by AramcoMech 2.0 with 28.89%. In contrast, GRI 3.0 has the greatest number of best fits with 13 out of the 29 and USC II with 8. It can be inferred that GRI 3.0, and USC II are performing very well across most of the datasets but are performing extremely poorly in a small number of datasets, leading to a large average  $E$  value. Therefore, the performance of AramcoMech 2.0 and USC II was compared across the 29 datasets to identify under what conditions USC II performs poorly, whereas AramcoMech 2.0 performs well. Three datasets were identified, M22, M25, and M28. In all three of these conditions, GRI 3.0 and USC II have much larger  $E$  values compared to their AramcoMech 2.0 and DTU counterparts. This is consistent with Zhang et al. [223] which compared different methane mechanisms for IDT data from shock tubes and RCMs and found AramcoMech 2.0 and DTU performed the best, with AramcoMech 2.0 being the only mechanism capable of simulating the RCM data.

M22, M25, and M28 were the three highest-pressure datasets investigated, all recorded at an average pressure above 200 atm. This suggests a flaw in the GRI 3.0 and USC II mechanisms that leads to a significant overprediction in IDT above 200 atm, leading to a significantly larger average  $E$  value.

The three high-pressure conditions were investigated using sensitivity analysis to determine what was causing the discrepancy between the four mechanisms. Figure 3.1 shows the OH sensitivity coefficient as a function of time for the M25 datasets for both AramcoMech 2.0 and USC II at 1100 K. The most obvious difference is the time taken for the maximum sensitivity peaks, which is close to the ignition delay time indicating a large difference in the chemistry controlling the combustion.

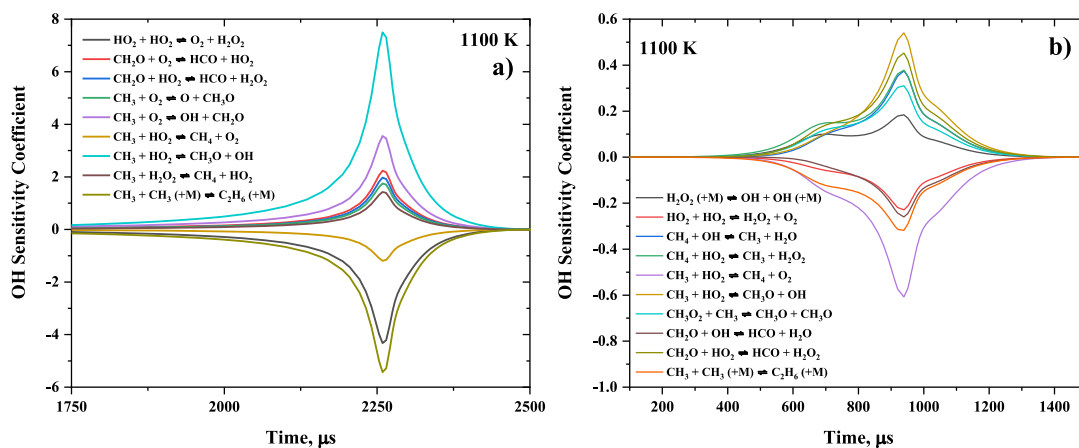


**Figure 3.1.** OH Sensitivity coefficient as a function of time for dataset M25 at 1100 K for a) AramcoMech 2.0 and b) USC II [85].

It was also noted that the sensitivity analysis for AramcoMech 2.0 contained the species  $\text{CH}_3\text{O}_2$  and  $\text{CH}_3\text{O}_2\text{H}$  which was absent from USC II. Further examination of the USC II mechanism reveals it simply does not contain this species or any of its respective chemistry and neither does GRI 3.0. The absence of  $\text{CH}_3\text{O}_2$  formation and subsequent chemistry as an explanation for the overestimation of IDT is supported by the original publication of the M25 dataset [85]. Shao et al. [85] noted that the FFCM-1, a mechanism that also does not contain  $\text{CH}_3\text{O}_2$ , deviated from AramcoMech 2.0 at the highest-pressure conditions.

To investigate the hypothesis that  $\text{CH}_3\text{O}_2$  is an essential component of a high-pressure chemical kinetic mechanism for combustion in  $\text{CO}_2$  was first discussed by Karimi et al. [127]. The kinetic, thermodynamic, and transport data for  $\text{CH}_3\text{O}_2$  and  $\text{CH}_3\text{O}_2\text{H}$  was added to USC II and the IDT was recalculated. All the chemical kinetic data were added from AramcoMech 2.0 and are reported in Table 3.6.

**Table 3.6.** Reactions of  $CH_3O_2$  added to USC II.

Reaction	A (cm <sup>3</sup> mol s)	n	E <sub>a</sub> (cal/mol)	Reference
$CH_3O_2 + CH_3 \rightleftharpoons CH_3O + CH_3O$	$5.08 \times 10^{12}$	0.00	-1411	[224]
$CH_4 + CH_3O_2 \rightleftharpoons CH_3 + CH_3O_2H$	$9.60 \times 10^{-01}$	3.77	17810	[214-219]
$CH_2O + CH_3O_2 \rightleftharpoons HCO + CH_3O_2H$	$1.99 \times 10^{12}$	0.00	11660	[225]
$CH_3 + O_2 (+M) \rightleftharpoons CH_3O_2 (+M)$	$7.81 \times 10^9$	0.90	0	[226]
$CH_3O_2 + O \rightleftharpoons CH_3O + O_2$	$3.60 \times 10^{13}$	0.00	0	[227]
$CH_3O_2 + H \rightleftharpoons CH_3O + OH$	$9.60 \times 10^{13}$	0.00	0	[227]
$CH_3O_2 + OH \rightleftharpoons CH_3OH + O_2$	$6.00 \times 10^{13}$	0.00	0	[227]
$CH_3O_2 + HO_2 \rightleftharpoons CH_3O_2H + O_2$	$2.47 \times 10^{11}$	0.00	-1570	[227]
$CH_3O_2 + H_2O_2 \rightleftharpoons CH_3O_2H + HO_2$	$2.41 \times 10^{12}$	0.00	9936	[225]
$CH_3O_2 + CH_3O_2 \rightleftharpoons CH_2O + CH_3OH + O_2$	$3.11 \times 10^{14}$	-1.61	-1051	[227]
$CH_3O_2 + CH_3O_2 \rightleftharpoons O_2 + CH_3O + CH_3O$	$1.40 \times 10^{16}$	-1.61	1860	[227]
$H_2 + CH_3O_2 \rightleftharpoons CH_2OH + CH_3O_2H$	$1.50 \times 10^{14}$	0.00	26030	[225]
$CH_3OH + CH_3O_2 \rightleftharpoons CH_2OH + CH_3O_2H$	$1.81 \times 10^{12}$	0.00	13710	[228]
$CH_3O_2H \rightleftharpoons CH_3O + OH$	$6.31 \times 10^{14}$	0.00	42300	[227]

$CH_3O_2$  is formed through Reaction 3.1 ( $CH_3 + O_2 (+M) = CH_3O_2 (+M)$ ) the third body reaction of  $CH_3$  and  $O_2$ . This reaction was most recently studied in 2005 by Fernandes et al. [226], using a higher pressure flow reactor up to 1000 bar at 700 K. Although the authors do not report an error in their rate coefficient, they are in good agreement with existing experimental work [229-231]. Therefore, the rate coefficient can be considered well-understood at 700 K. However, extrapolated to over 1000 K may be problematic, especially as the authors did not report an error in the rate coefficient. Furthermore, there is no individual third-body efficiency for this reaction given to each potential species.  $CO_2$  as a good

absorber of heat and energy will likely have a greater third-body efficiency for this reaction than N<sub>2</sub>, in which this experiment was conducted.



Two reactions appear in the sensitivity in the three high-pressure conditions which involve CH<sub>3</sub>O<sub>2</sub>, Reaction 3.2 ( $\text{CH}_4 + \text{CH}_3\text{O}_2 \rightleftharpoons \text{CH}_3 + \text{CH}_3\text{O}_2\text{H}$ ) and Reaction 3.3 ( $\text{CH}_3\text{O}_2 + \text{CH}_3 \rightleftharpoons \text{CH}_3\text{O} + \text{CH}_3\text{O}$ ).



The rate coefficient of Reaction 3.2 ( $\text{CH}_4 + \text{CH}_3\text{O}_2 \rightleftharpoons \text{CH}_3 + \text{CH}_3\text{O}_2\text{H}$ ) used in AramcoMech 2.0 is from an unknown and unpublished source, making it difficult to validate the rate coefficient used. The only published value of the rate coefficient of Reaction 3.2 ( $\text{CH}_4 + \text{CH}_3\text{O}_2 \rightleftharpoons \text{CH}_3 + \text{CH}_3\text{O}_2\text{H}$ ) comes from a review of chemical kinetic data of methane and related compounds by Tsang and Hampson [225]. The authors note there is no direct measurement and thus base their value on Reaction 3.4 ( $\text{HO}_2 + \text{CH}_4 \rightleftharpoons \text{CH}_3 + \text{H}_2\text{O}_2$ ), a reaction that they argue should have a similar rate coefficient. Due to it being an estimated rate coefficient, there is a large amount of uncertainty in the rate coefficient used for Reaction 3.2 ( $\text{CH}_4 + \text{CH}_3\text{O}_2 \rightleftharpoons \text{CH}_3 + \text{CH}_3\text{O}_2\text{H}$ ).



The rate coefficient used for Reaction 3.3 ( $\text{CH}_3\text{O}_2 + \text{CH}_3 = \text{CH}_3\text{O} + \text{CH}_3\text{O}$ ) in AramcoMech 2.0 was theoretically calculated by Keiffer et al. [224] at 0.169 bar from 298-530 K in an oxygen bath gas. The reaction has been measured twice experimentally by Pilling and Smith [231] and Parkes [232] in argon and nitrogen and bath gases respectively, both at 298 K. Due to the importance of Reaction 3.3 ( $\text{CH}_3\text{O}_2 + \text{CH}_3 = \text{CH}_3\text{O} + \text{CH}_3\text{O}$ ) in the high-pressure combustion of methane, it is important to revisit this reaction at conditions more relevant to direct-fired sCO<sub>2</sub> combustion.

Other reactions that were relevant to the CH<sub>3</sub>O<sub>2</sub> chemistry used in AramcoMech 2.0 use rate coefficients from Lightfoot et al. [227] between 600K and 719 K at atmospheric pressure. Previous research into CH<sub>3</sub>O<sub>2</sub> kinetics has focused on atmospheric and low-temperature combustion chemistry [233]. This often means the rate coefficients have been determined at much lower pressures and temperatures than that of a direct-fired sCO<sub>2</sub> combustion chamber and a much lower mole fraction of CO<sub>2</sub>. The chemistry of CH<sub>3</sub>O<sub>2</sub> is discussed more in Section 3.11 using the UoS sCO<sub>2</sub> 1.0 mechanism developed from this work.

In addition to the importance of CH<sub>3</sub>O<sub>2</sub> chemistry for modelling high-pressure combustion in CO<sub>2</sub>, the sensitivity comparison of AramcoMech 2.0 and USC II in the M22 and M25 conditions identified two other important reactions. Firstly, Reaction 3.5 ( $H_2O_2 (+M) \rightleftharpoons OH + OH (+M)$ ) only appeared in the sensitivity analysis for AramcoMech 2.0 shown in Figure 3.1 and is absent from the sensitivity analysis of USC II. from Troe et al. [234] which was calculated with a CO<sub>2</sub> bath gas. The USC II mechanism uses an older rate coefficient from Baulch et al. [235] whereas AramcoMech 2.0 uses a newer theoretical rate coefficient from Troe et al. [234] which was calculated with a CO<sub>2</sub> bath gas.



The second discrepancy noted was the AramcoMech 2.0 mechanism was considerably more sensitive to Reaction 3.6 ( $CH_3 + HO_2 \rightleftharpoons CH_4 + O_2$ ) than USC II. For this reaction, the USC II rate coefficient is taken from Reid et al. [236] which is reported to be private communication and therefore difficult to discuss and evaluate. The theoretically calculated AramcoMech 2.0 rate coefficient from Jasper et al. [237] is in agreement with Srinivasan et al. [238] which incorporated experimental data.



The effect of the addition of the CH<sub>3</sub>O<sub>2</sub> reactions from AramcoMech 2.0 listed in Table 3.6 and making sequential changes of Reaction 3.5 ( $H_2O_2 (+M) \rightleftharpoons OH + OH (+M)$ ) and Reaction 3.6 ( $CH_3 + HO_2 \rightleftharpoons CH_4 + O_2$ ) are shown in Figure 3.2.

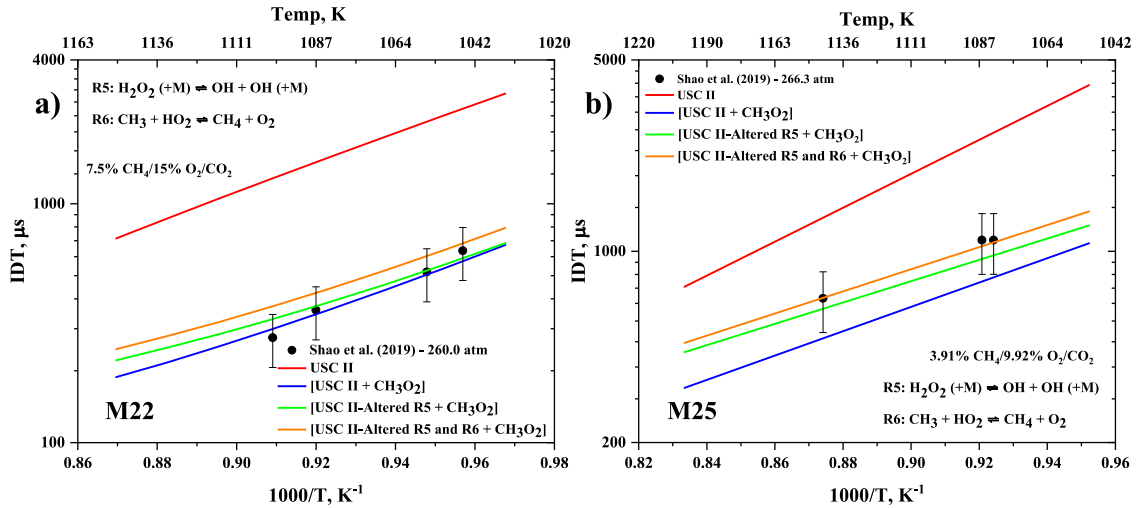


**Figure 3.2.** Sequential changes to USC II; a) M22 and b) M25; [USC II + CH<sub>3</sub>O<sub>2</sub>]: addition of CH<sub>3</sub>O<sub>2</sub> chemistry from AramcoMech 2.0, [USC II-Altered R6 + CH<sub>3</sub>O<sub>2</sub>]: change Reaction 3.6 to AramcoMech 2.0 rate coefficient, [USC II-Altered R5 and R6 + CH<sub>3</sub>O<sub>2</sub>]: change Reaction 3.5 to the AramcoMech 2.0 rate coefficient.

Figure 3.2 highlights the importance of the chemistry of CH<sub>3</sub>O<sub>2</sub> in high-pressure combustion. The addition of the following reactions shown in Table 3.6 and the respective thermodynamic and transport data to the USC II mechanism immediately led to a significant improvement in the mechanism's ability to model the experimental data. This observation is significant in the pursuit of understanding the chemical kinetic mechanism of direct-fired sCO<sub>2</sub> combustion. However, despite the importance of the reactions shown in Table 3.6, these rate coefficients are often from sources concerned with atmospheric and low-temperature combustion and therefore are difficult to extrapolate to the combustion conditions of direct-fired sCO<sub>2</sub> cycles. Furthermore, for some of the rate coefficients, even for these conditions there are large uncertainty factors that could have a huge impact on the modelled IDTs. For example, Tsang and Hampson [225] report an uncertainty factor of 10 in the A factor for the rate coefficient of Reaction 3.2 ( $CH_4 + CH_3O_2 \rightleftharpoons CH_3 + CH_3O_2H$ ) due to it being an estimate based on another reaction with no experimental data. Therefore, to create an accurate comprehensive kinetic mechanism of high-pressure combustion, the rate coefficients of the key reactions in the chemistry of CH<sub>3</sub>O<sub>2</sub> must be determined at larger pressures and temperatures.

### 3.6.2. Low-Pressure Datasets

The low-pressure datasets for this study are defined as any dataset recorded at an average pressure below 10 bar. This includes M1-M14 and M16-19. Across these low-pressure conditions, GRI 3.0 has the lowest average  $E$  value of 17.81%, in contrast to it having the third-largest average  $E$  value for all the methane datasets. GRI 3.0 also has the largest number of best fits to these 18 low-pressure datasets with 11. All the GRI 3.0 simulated IDTs tend to be in good agreement except for M2 and M4 which underpredict the IDT significantly. In contrast, AramcoMech 2.0 and DTU which perform better overall for methane IDT as shown in Table 3.5, tend to overestimate the IDTs. The IDT data plots of M2 and M4 are shown in Figure 3.3.

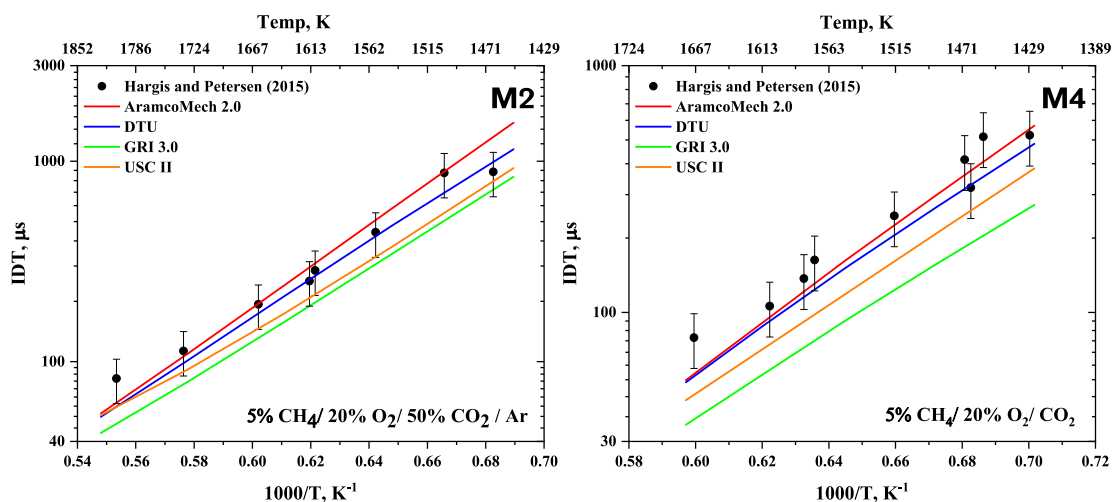
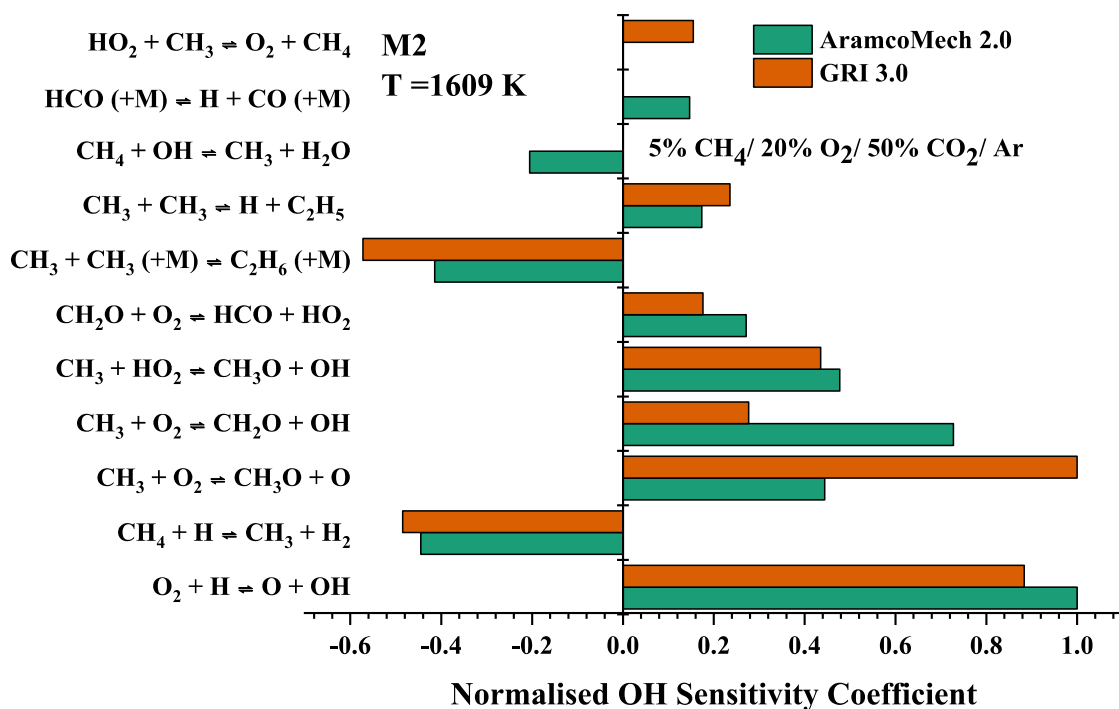


Figure 3.3. IDT plots of M2 and M4 from Hargis and Petersen [122].

Figure 3.4 shows a relative, comparative sensitivity analysis of the M2 dataset for AramcoMech 2.0 and GRI 3.0 at 1609 K. The first obvious discrepancy is the relative importance of competing Reaction 3.7 ( $CH_3 + O_2 \rightleftharpoons CH_3O + O$ ) and Reaction 3.8 ( $CH_3 + O_2 \rightleftharpoons CH_2O + OH$ ), reactions which also compete with Reaction 3.1 ( $CH_3 + O_2 (+M) \rightleftharpoons CH_3O_2 (+M)$ ). Most of the other important reactions show a similar relative sensitivity. Reaction 3.7 ( $CH_3 + O_2 \rightleftharpoons CH_3O + O$ ) is a chain branching reaction whereas Reaction 3.8 ( $CH_3 + O_2 \rightleftharpoons CH_2O + OH$ ) is a propagation reaction with the total number of radicals conserved. Therefore, it may be expected that if the rate coefficient of Reaction 3.7 ( $CH_3 + O_2 \rightleftharpoons CH_3O$

+ O) was larger, and this was the favoured reaction path, then the IDT would be shorter.



**Figure 3.4.** Relative sensitivity of M2 dataset at 1609 K for AramcoMech 2.0 and GRI 3.0 [122].

The different rate coefficients used in the two mechanisms and their source publications are reported in Table 3.7. Where pc denotes a private communication from S. Klippenstein, which is currently unpublished.

**Table 3.7.** Rate coefficients of Reaction 3.7 and Reaction 3.8 were used in AramcoMech 2.0 and GRI 3.0 (*pc*=personal communication).

Reaction	AramcoMech 2.0				GRI 3.0			
	A (cm <sup>3</sup> mol s)	<i>n</i>	<i>Ea</i> (cal/mol)	Ref.	A (cm <sup>3</sup> mol s)	<i>n</i>	<i>Ea</i> (cal/mol)	Ref.
Reaction 3.7	7.55 x 10 <sup>12</sup>	0	28320	[239]	3.56 x 10 <sup>13</sup>	0	30480	[240]
Reaction 3.8	2.641	3.283	8105	<i>pc</i>	2.310 x 10 <sup>12</sup>	0	20315	[240]

The hypothesis is that the chain branching ratio between Reaction 3.7 ( $CH_3 + O_2 \rightleftharpoons CH_3O + O$ ) and Reaction 3.8 ( $CH_3 + O_2 \rightleftharpoons CH_2O + OH$ ) favouring Reaction 3.7 causing the faster IDT in dataset M2 is supported by Figure 3.5. Figure 3.5 shows the net reaction rate plotted against the reaction time for both reactions for the two mechanisms. In AramcoMech 2.0, the net reaction rate of Reaction 3.8 ( $CH_3 + O_2 \rightleftharpoons CH_2O + OH$ ) is approximately five times larger than Reaction 3.7 ( $CH_3 + O_2 \rightleftharpoons CH_3O + O$ ) and, leading to a large difference in the products of this reaction between mechanisms. On the other hand, the net reaction rate for the two reactions for GRI 3.0 is approximately the same, meaning more of the chain branching occurs, which possibly accelerates the IDT. However, in most of the datasets, it is GRI 3.0 that better models the IDT, therefore there is the potential to balance these two reactions to create a mechanism that better fits all the datasets.

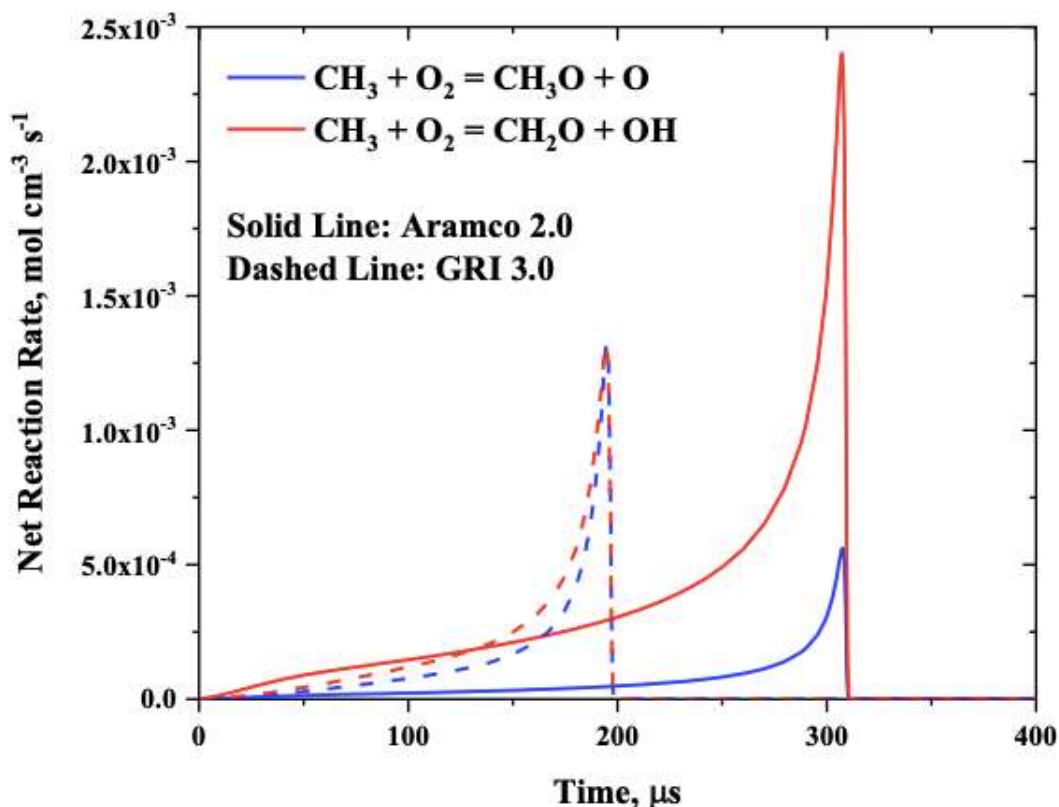


**Figure 3.5.** Comparison of net reaction rates of Reaction 3.7 and Reaction 3.8 at 1609 K at the conditions of dataset M2.

The ratio of chain branching between Reaction 3.7 ( $CH_3 + O_2 \rightleftharpoons CH_3O + O$ ) and Reaction 3.8 ( $CH_3 + O_2 \rightleftharpoons CH_2O + OH$ ) may become more important at higher pressures because, as discussed in Section 3.6.1, Reaction 3.1 ( $CH_3 + O_2 (+M) \rightleftharpoons CH_3O_2 (+M)$ ) will also become competitive. The chain branching ratio between these reactions is most likely when of the decisive factors for direct-fired sCO<sub>2</sub> combustion.

### 3.6.3. Effect of CO<sub>2</sub> Dilution on Mechanism Performance

Three of the IDT publications have datasets that compare the effect of increasing CO<sub>2</sub> dilution. For this study, datasets that were not in CO<sub>2</sub> were omitted from the study so are not discussed here, but more information is available in the original publication. The first study is from Hargis and Petersen [122] where datasets M1-M3 compare increasing the CO<sub>2</sub> mole fraction is increased from 25% to 75%. Figure 3.6 shows the IDT plots of M1 to M3 at approximately 2 atm where the CO<sub>2</sub> mole fraction is 25%, 50% and 75% for M1, M2 and M3, respectively.

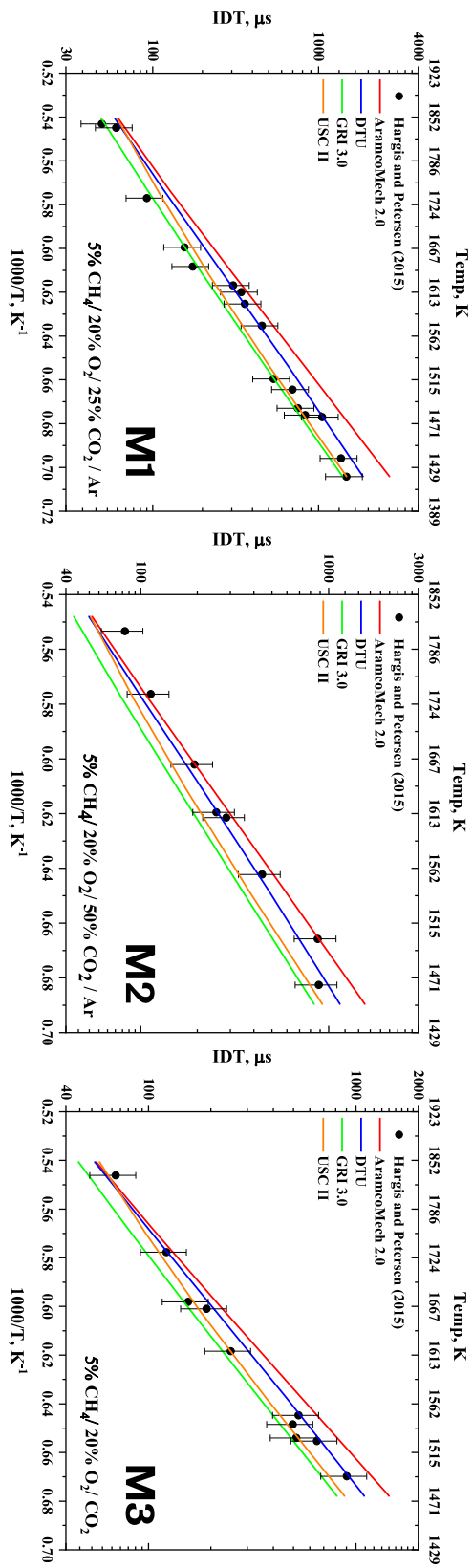
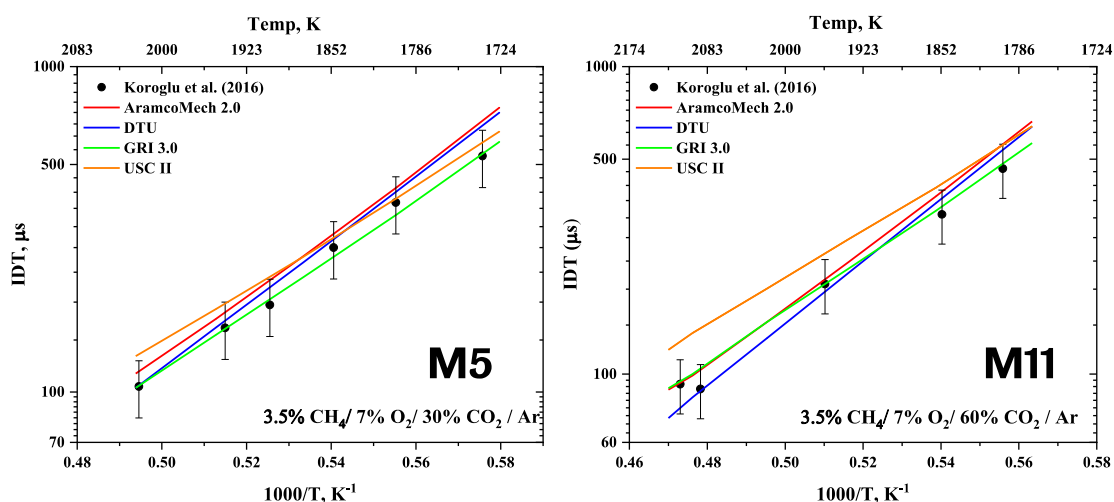


Figure 3.6. Comparison of M1-M3 datasets from Hargis and Petersen [122].

Koroglu et al. [153] compared the effect of increasing CO<sub>2</sub> dilution from 30% to 60% at approximately 0.7 atm in datasets in M5 and M11 as shown in Figure 3.7.



**Figure 3.7.** Comparison of M5 and M11 datasets from Koroglu et al. [153].

The last study comparing CO<sub>2</sub> dilution at the same pressure is from Pryor et al. [195]. Datasets M13 and M14 are recorded at approximately 8 atm and are shown in Figure 3.8.

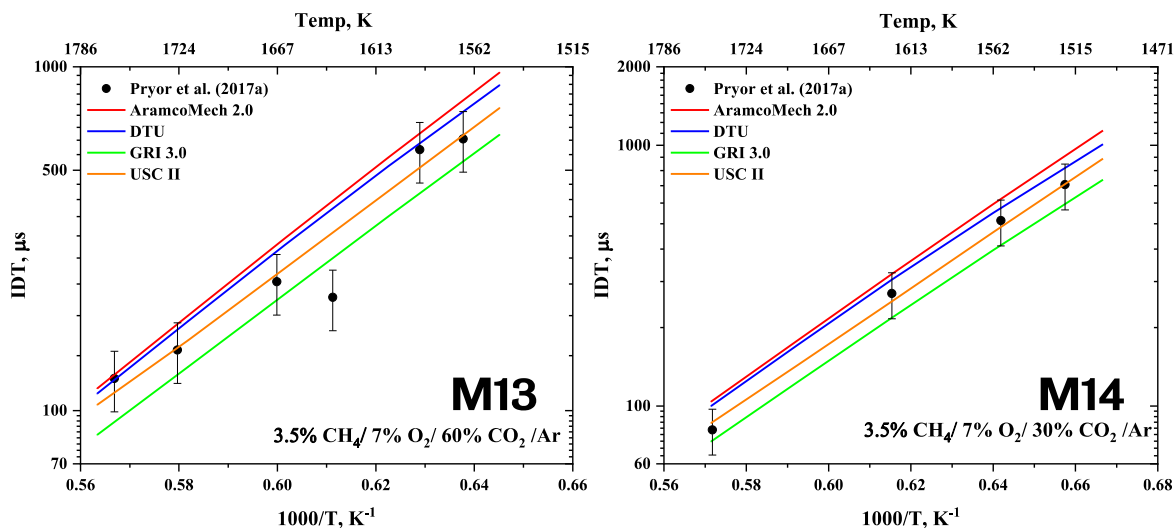


**Figure 3.8.** Comparison of M13 and M14 datasets from Pryor et al. [195].

Coupling these three datasets indicates that increasing the CO<sub>2</sub> dilution across this range has very little effect on the mechanism's ability to model the IDT. As the CO<sub>2</sub> mole fraction increases, the discrepancy between the mechanisms and the data is largely unchanged at all three of the conditions studied. Whilst the IDT

values do change due to the physical effect of CO<sub>2</sub> being a better absorber of heat than other bath gases such as argon and nitrogen due to its larger heat capacity, reducing the overall temperature. This suggests that the priority for creating a mechanism to better model direct-fired sCO<sub>2</sub> combustion should prioritize high-pressure data over CO<sub>2</sub> dilution. However, a comparison of IDT data above 30 atm would be useful to see if CO<sub>2</sub> dilution is still unimportant in mechanism performance at higher pressures.

### 3.7. Hydrogen Analysis

Analysis of the three datasets from Shao et al. [85] is shown in Table 3.8. AramcoMech 2.0 has the lowest average *E* value at 37.80%, with an *E* value of less than 20% for the H1 and H2 datasets, which is within the error of the shock tube IDT datapoints. The increase in average *E* (%) is due to poor performance in the H3, where all four mechanisms perform poorly. The trend of performing worse in the H3 datasets is shared by all four mechanisms and interesting is the lowest pressure dataset, where the mechanism is validated and predicted to perform better. However, in the H3 dataset, there is also a reduced equivalence ratio from  $\phi=1.0$  to  $\phi=0.25$ , which could have caused the shift in performance.

**Table 3.8.** Quantitative analysis of hydrogen datasets.

Dataset	AramcoMech 2.0	DTU	GRI 3.0	USC II
H1	18.74	35.42	71.72	44.51
H2	9.19	20.27	69.29	72.33
H3	85.46	111.48	123.09	75.48
<b>Average <i>E</i> (%)</b>	<b>37.80</b>	<b>55.72</b>	<b>88.03</b>	<b>64.11</b>
<b>No. Best Fit</b>	<b>2</b>	<b>0</b>	<b>0</b>	<b>1</b>

A sensitivity analysis of H3 was used to investigate AramcoMech 2.0 and USC II in the H3 dataset at 1274 as shown in Figure 3.9. The sensitivity analysis reveals in addition to a large sensitivity to the previously discussed Reaction 3.5 ( $H_2O_2 (+M) \rightleftharpoons OH + OH (+M)$ ) in Section 3.6.1. There is a large sensitivity to Reaction 3.9 ( $H_2O_2 + H \rightleftharpoons H_2 + HO_2$ ) for both USC II and AramcoMech 2.0. The rate coefficient used in AramcoMech 2.0 for R7 [241] is significantly faster at the

temperatures concerned compared to the value used in USC II [225], which is a possible explanation for the overprediction of the IDT in the H1 and H2 datasets by USC II.

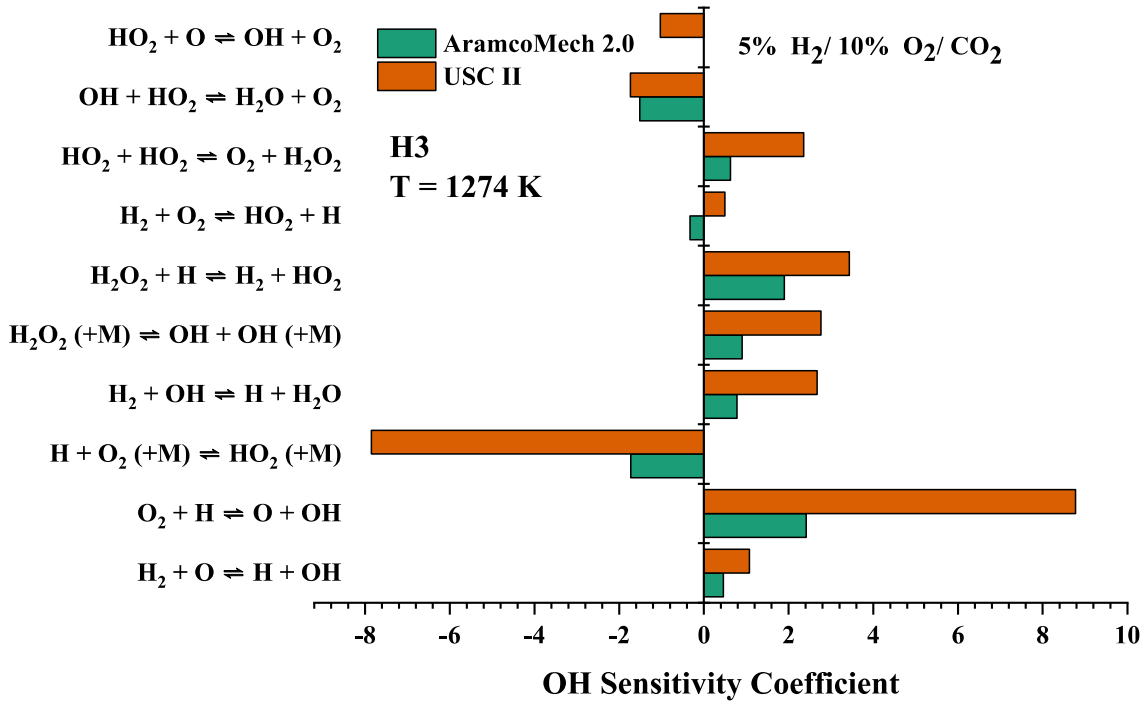


**Figure 3.9.** Comparison of the sensitivity analysis of H3 for AramcoMech 2.0 (blue) and USC II (orange) at 1274 K.

As AramcoMech 2.0 can already model the H1 and H2 datasets, the challenge is to create a mechanism that better models H3, without affecting these datasets. One large discrepancy between the two mechanisms' relative sensitivity coefficient to the two reactions of H and O<sub>2</sub>, Reaction 3.10 (O<sub>2</sub> + H ⇌ O + OH) and Reaction 3.11 (H + O<sub>2</sub> (+M) ⇌ HO<sub>2</sub> (+M)). The older rate coefficient for Reaction 3.10 (O<sub>2</sub> + H ⇌ O + OH) used by USC II from Masten et al. [242] is approximately 50 times larger than the rate coefficient reported by Hong et al. [140] used in AramcoMech 2.0. Conversely, the difference in the rate coefficient used in AramcoMech 2.0 and USC II only differs by 10% for Reaction 3.11 (H + O<sub>2</sub> (+M) ⇌ HO<sub>2</sub> (+M)). The ratio between Reaction 3.10 (O<sub>2</sub> + H ⇌ O + OH) and Reaction 3.11 (H + O<sub>2</sub> (+M) ⇌ HO<sub>2</sub> (+M)) is therefore important and influential on the combustion chemistry as one has a positive sensitivity coefficient and reduces the IDT and the other has a negative sensitivity coefficient and increases

the IDT. This is because Reaction 3.10 ( $O_2 + H \rightleftharpoons O + OH$ ) is a chain-branching reaction that doubles the number of radicals available to react, increasing the reaction rate. On the other hand, Reaction 3.11 ( $H + O_2 (+M) \rightleftharpoons HO_2 (+M)$ ) is a proxy-termination reaction as the  $HO_2$  radical is much less reactive than the H radical, slowing the reaction down. The ratio at which H and  $O_2$  proceed down these two competing pathways and thus extremely important in determining the IDT and other flame properties for hydrogen combustion.



The sensitivity analysis for H1 and H2 datasets showed a similar discrepancy between Reaction 3.10 ( $O_2 + H \rightleftharpoons O + OH$ ) and Reaction 3.11 ( $H + O_2 (+M) \rightleftharpoons HO_2 (+M)$ ) between AramcoMech 2.0 and USC II.

The mixed performance between AramcoMech 2.0 and USC II appears to be caused by the large difference in rate coefficients for Reaction 3.10 ( $O_2 + H \rightleftharpoons O + OH$ ) and Reaction 3.11 ( $H + O_2 (+M) \rightleftharpoons HO_2 (+M)$ ). The effect of altering the rate coefficient of Reaction 3.9 ( $H_2O_2 + H \rightleftharpoons H_2 + HO_2$ ) in USC II to the much faster and newer rate coefficient from Ellingson et al. [241] to create [USC II-Altered R7] as shown in Figure 3.10. Furthermore, for the H3 condition, this change causes the  $E$  value to fall from 85% and 75% for AramcoMech 2.0 and USC II respectively to 30 for [USC II-Altered R7].

More datasets of hydrogen combustion over a greater range of pressures and equivalence ratios confirm any mechanistic changes made. Following this work, it was made a priority for further investigation in Chapter 4.

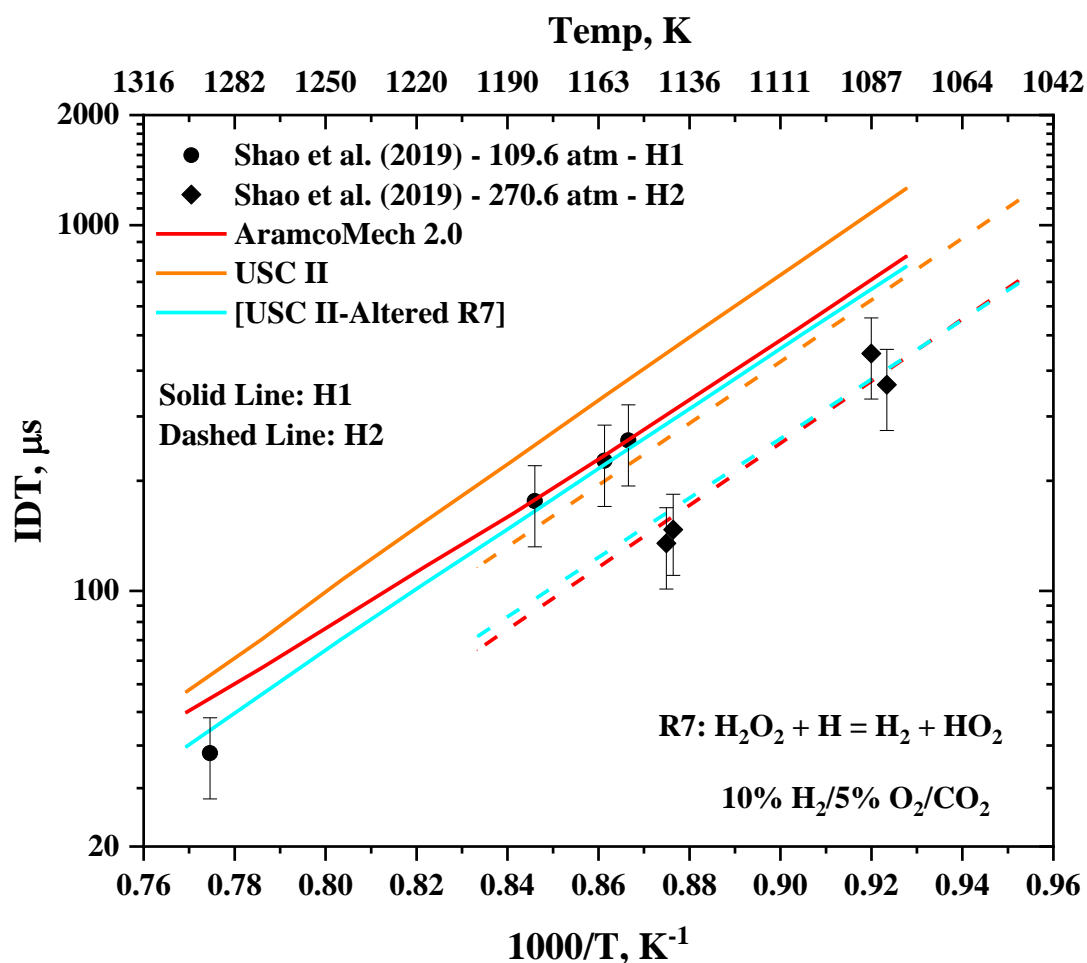


**Figure 3.10.** H1 and H2 datasets modelled by AramcoMech 2.0, USC II, and [USC II-Altered R7]: USC II with the updated Reaction 3.9 rate coefficient [241].

### 3.8. Syngas Analysis

Table 3.9 shows that the average  $E$  (%) value across the 20 IDT datasets for syngas combustion, USC II had the lowest value in addition to having the greatest number of best fits to the datasets. However, despite having the greatest number of best fits 50% of the datasets, USC II still only fits three datasets within a 25% error and the average  $E$  value is much larger than the other two fuels studied. Interestingly, the mechanisms generally performed worse at the lowest pressure conditions, generally due to a large overestimation in the IDT and the difficulty in replicating the curved IDT profile at low temperatures.

**Table 3.9.** Quantitative analysis of syngas datasets.

<b>Dataset</b>	<b>AramcoMech 2.0</b>	<b>DTU</b>	<b>GRI 3.0</b>	<b>USC II</b>
<b>S1</b>	82.43	104.76	43.15	17.37
<b>S2</b>	596.64	615.50	169.56	131.45
<b>S3</b>	451.26	498.30	64.18	45.72
<b>S4</b>	786.89	855.04	191.59	70.34
<b>S5</b>	1058.09	1067.39	233.86	81.54
<b>S6</b>	1194.31	1122.91	243.97	43.57
<b>S7</b>	578.21	552.32	147.77	38.61
<b>S8</b>	972.45	1030.92	430.73	121.73
<b>S9</b>	410.50	490.88	115.41	37.33
<b>S10</b>	185.79	238.56	127.08	179.79
<b>S11</b>	259.59	341.14	156.84	256.95
<b>S12</b>	191.64	277.53	49.77	128.86
<b>S13</b>	174.54	287.50	22.94	85.36
<b>S14</b>	43.34	58.13	37.93	40.22
<b>S15</b>	65.84	94.40	31.29	101.28
<b>S16</b>	117.67	180.82	39.81	115.51
<b>S17</b>	128.43	155.49	84.85	194.53
<b>S18</b>	31.18	57.83	52.42	45.40
<b>S19</b>	6.85	16.64	19.73	23.73
<b>S20</b>	10.83	5.09	11.18	4.53
<b>Average <i>E</i></b>	<b>367.32</b>	<b>402.56</b>	<b>113.70</b>	<b>88.19</b>
<b>No. Best Fit</b>	<b>1</b>	<b>1</b>	<b>8</b>	<b>10</b>

The results from Table 3.9 clearly show that GRI 3.0 and USC II are by far the best-performing mechanisms, mostly due to AramcoMech 2.0 and DTU's poor performance in low-pressure datasets. Interestingly it is S20, one of the three highest-pressure datasets from Karimi et al. [200] that is the only dataset where all mechanisms fit the data within 20%. This result is unexpected as these mechanisms are all validated for low-pressure combustion, so one would expect this is where they would perform best, and they would deviate at higher pressures.

### 3.8.1. High-Pressure Datasets

Figure 3.11 shows the sensitivity analysis of the S16 dataset of AramcoMech 2.0 and GRI 3.0 at 1280 K. The large discrepancy can potentially be explained by the large discrepancy between Reaction 3.9 ( $H_2O_2 + H \rightleftharpoons H_2 + HO_2$ ) and Reaction 3.12 ( $CO + HO_2 \rightleftharpoons CO_2 + OH$ ).



The rate coefficient of Reaction 3.12 ( $CO + HO_2 \rightleftharpoons CO_2 + OH$ ) used in GRI 3.0 [243] is significantly faster than that in AramcoMech 2.0 [244] leading to six orders of magnitude difference in the rate at 1200 K. Thus, explaining the much greater temperature sensitivity of Reaction 3.12 ( $CO + HO_2 \rightleftharpoons CO_2 + OH$ ) in GRI 3.0 compared to AramcoMech 2.0, DTU, and USC II which use the same rate coefficient. This also explains the much larger  $E$  (%) observed in AramcoMech 2.0, often due to an overprediction in IDT, due to the much slower Reaction 3.12 ( $CO + HO_2 \rightleftharpoons CO_2 + OH$ ).

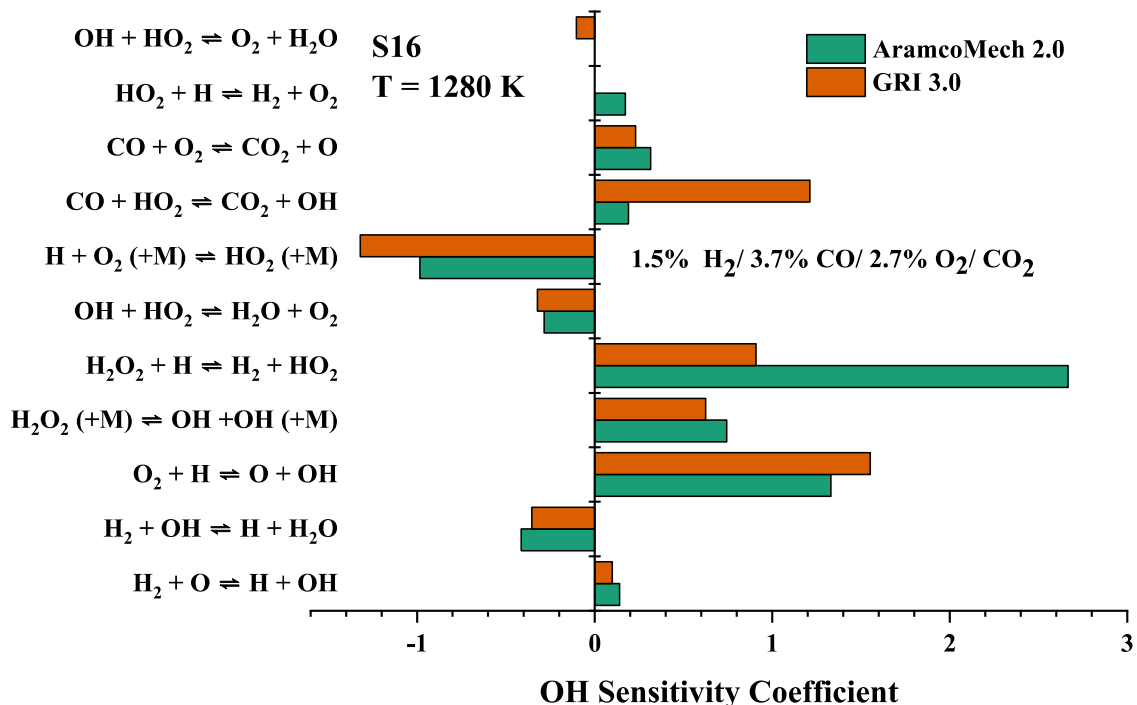


**Figure 3.11.** S16 dataset sensitivity analysis of AramcoMech 2.0 (green) and GRI 3.0 (orange) 1280 K.

Changing the rate coefficient of Reaction 3.12 ( $\text{CO} + \text{HO}_2 \rightleftharpoons \text{CO}_2 + \text{OH}$ ) for AramcoMech 2.0, DTU and USC II to the much faster rate coefficient led to a significant improvement for all three mechanisms in the high-pressure datasets, above 40 atm, and some improvement at lower pressures.

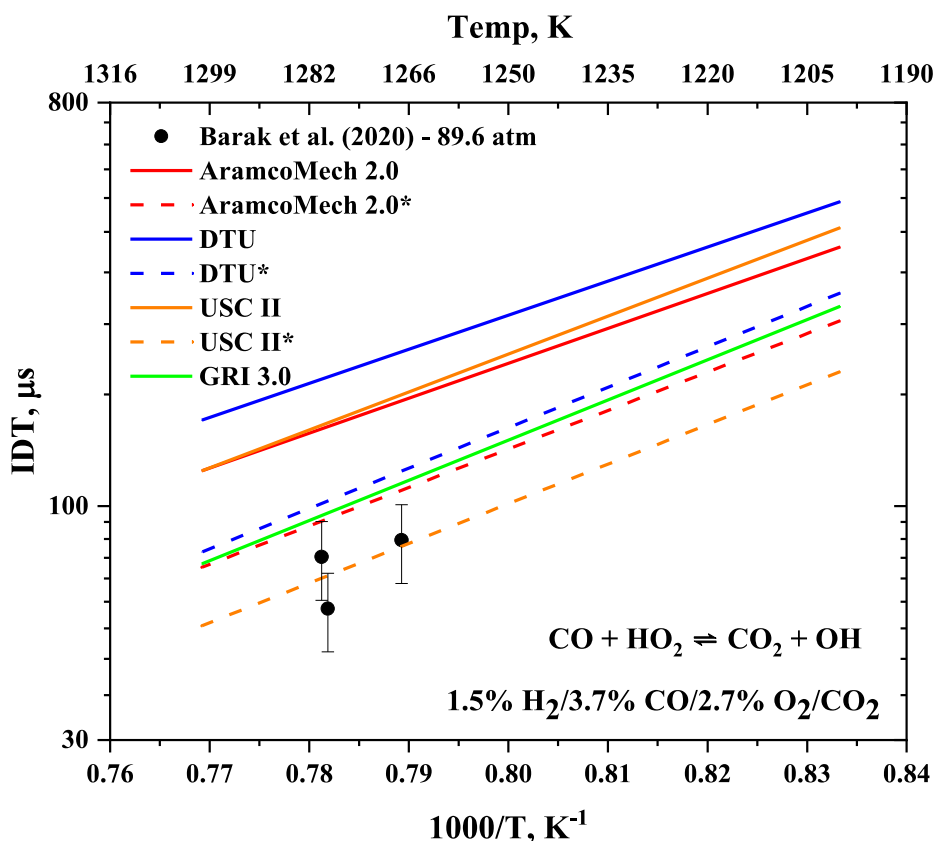


**Figure 3.12.** Comparison of mechanism performance for the S16 dataset with an altered rate coefficient of Reaction 3.12 from Baulch et al. [243], denoted by an asterisk (\*).

### 3.8.2. Low-Pressure Datasets

At lower pressures (S1-S10), the IDT plots show a curved profile as opposed to the linear relationship at higher pressures. As shown in Figure 3.13 for the S2 dataset at 1.7 atm, the mechanisms all predict a curved relationship, which leads to a large overestimation in IDT in the lowest temperature conditions. Whilst all the mechanisms show a curvature, the S2 dataset could be fitted with a linear plot.

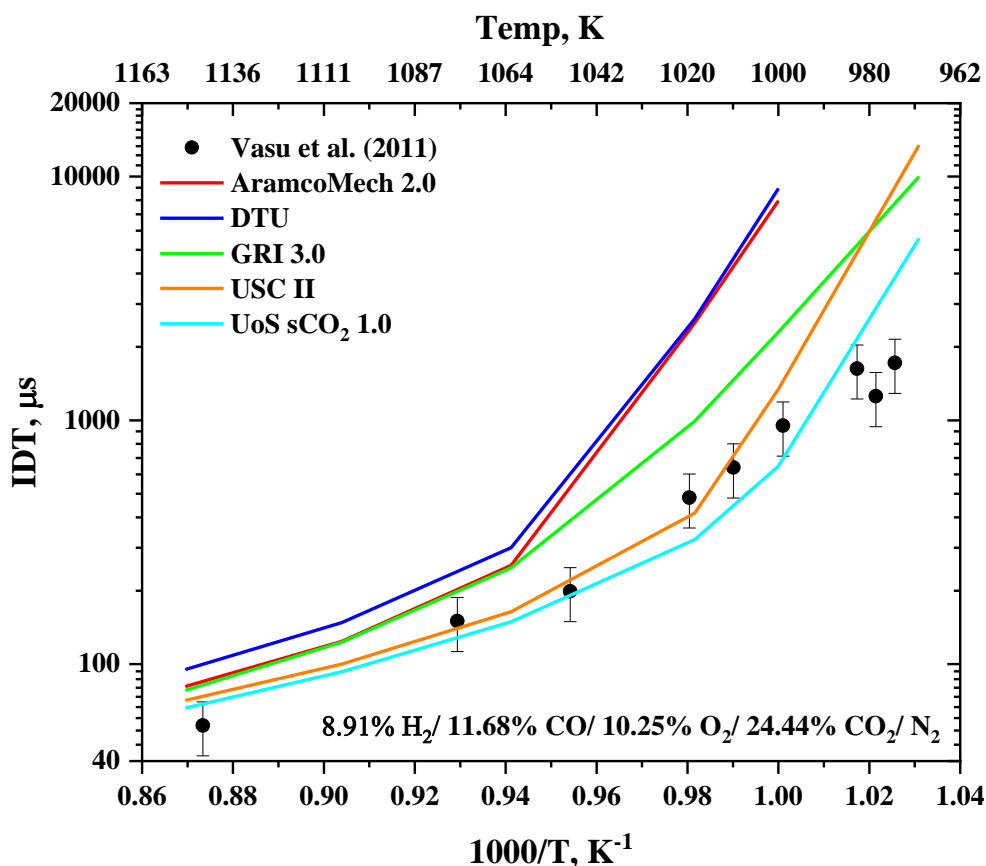


**Figure 3.13.** Mechanism comparison of the S2 dataset between the four mechanisms.

Figure 3.14 shows a normalised sensitivity analysis for the S2 dataset that highlights the importance of the branching ratio of H and O<sub>2</sub> between Reaction 3.10 ( $O_2 + H \rightleftharpoons O + OH$ ) and Reaction 3.11 ( $H + O_2 (+M) \rightleftharpoons HO_2 (+M)$ ). As seen in Figure 3.14, the relative OH sensitivity coefficient for Reaction 3.11 ( $H + O_2 (+M) \rightleftharpoons HO_2 (+M)$ ) is less than half that of Reaction 3.10 ( $O_2 + H \rightleftharpoons O + OH$ ), indicating the rate of the chain branching is far exceeding that of recombination to HO<sub>2</sub>. At 1025 K, the relative OH sensitivity coefficients are approximately similar, explaining the sudden and dramatic increase in IDT as the rate of radical reduction has slowed and the same is observed in the USC II sensitivity analysis which better models the experimental data. Therefore, it is again the importance of the chain branching ratio between Reaction 3.10 ( $O_2 + H \rightleftharpoons O + OH$ ) and Reaction 3.11 ( $H + O_2 (+M) \rightleftharpoons HO_2 (+M)$ ) in determining the curvature in the IDT at lower temperatures.

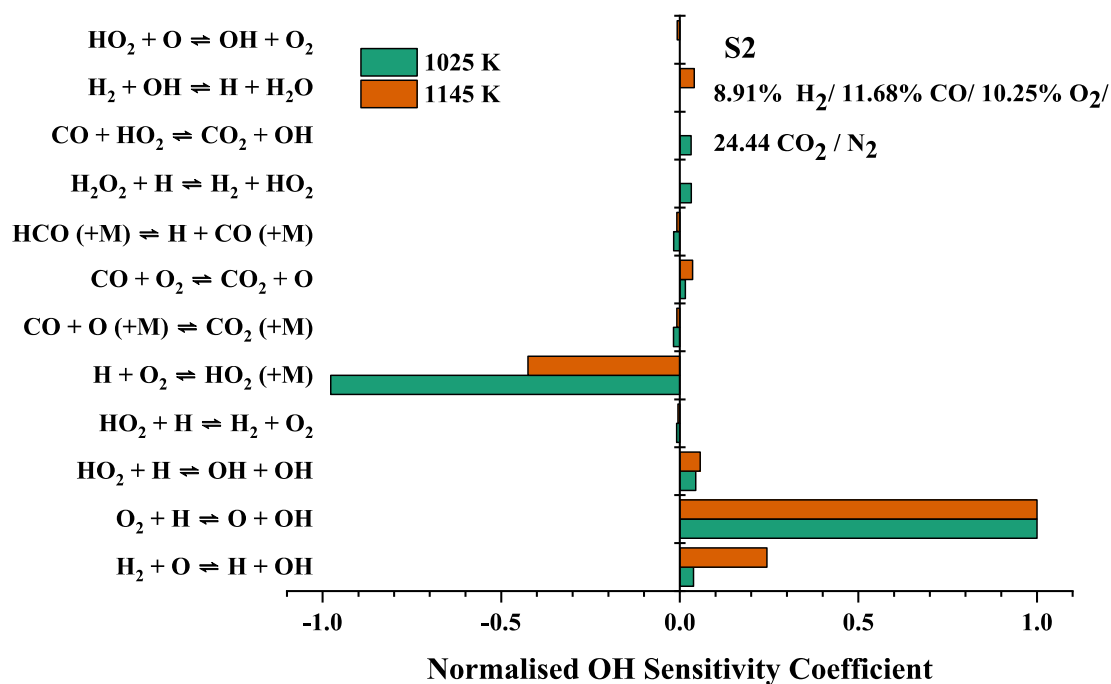


**Figure 3.14.** Normalised sensitivity analysis of S2 data for AramcoMech 2.0 at 1025 K (green) and 1145 K (orange).

### 3.8.3. Effect of CO<sub>2</sub> Dilution

The only datasets which compare the effect of CO<sub>2</sub> dilution are S4 and S5, where the CO<sub>2</sub> mole fraction is raised from 60 to 80%, respectively. The IDT data plot for the two datasets is shown in Figure 3.15. There is very little difference between the increasing CO<sub>2</sub> mole fraction in the mechanism's ability to model the IDT. Under these conditions, the performance of every mechanism, except for USC II, is incredibly poor and has an average *E* value above 100%. Therefore, it is difficult to extract any useful information from this analysis. Further study is required at conditions where agreement between the simulated and experimental data points is required to accurately understand the effect of increasing the CO<sub>2</sub> dilution.

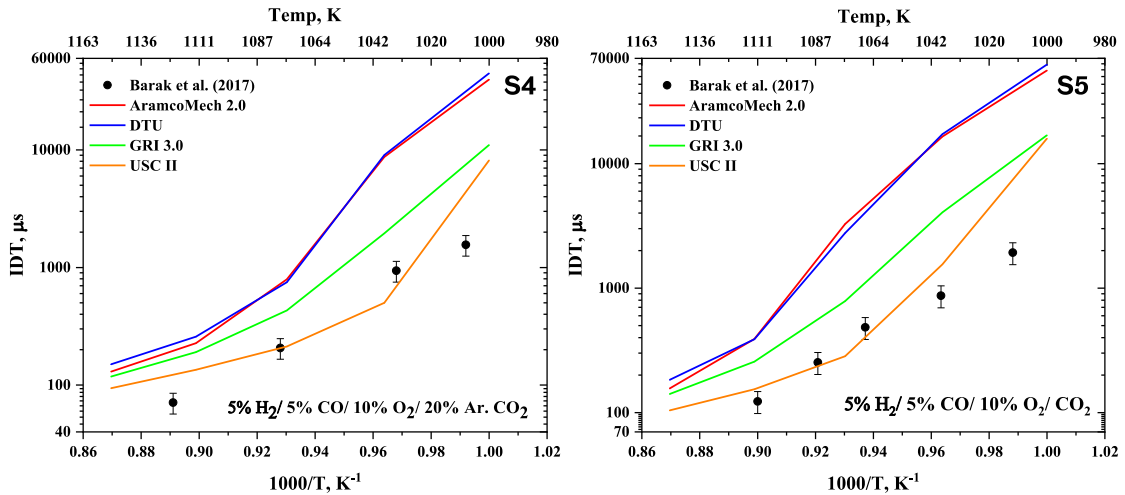


Figure 3.15. Comparison of S4 and S5 IDT datasets from Barak et al. [198].

### 3.8.4. Effect of H<sub>2</sub>:CO Ratio

Due to the poor performance of all mechanisms modelling the syngas IDT datasets, it is difficult to make firm conclusions, as for most datasets the IDT is significantly overpredicted. The only datasets that were reasonably well simulated by all four datasets were S18-S20 from Karimi et al. [200]. Interestingly S18 and S19 were recorded at similar pressures to S14-S17 from Barak et al. [192] but all the mechanisms simulate the experimental data much more accurately. Figure 3.16 shows the S18-S20 datasets where there is a good agreement between all four of the mechanisms, as well as with the experimental data.

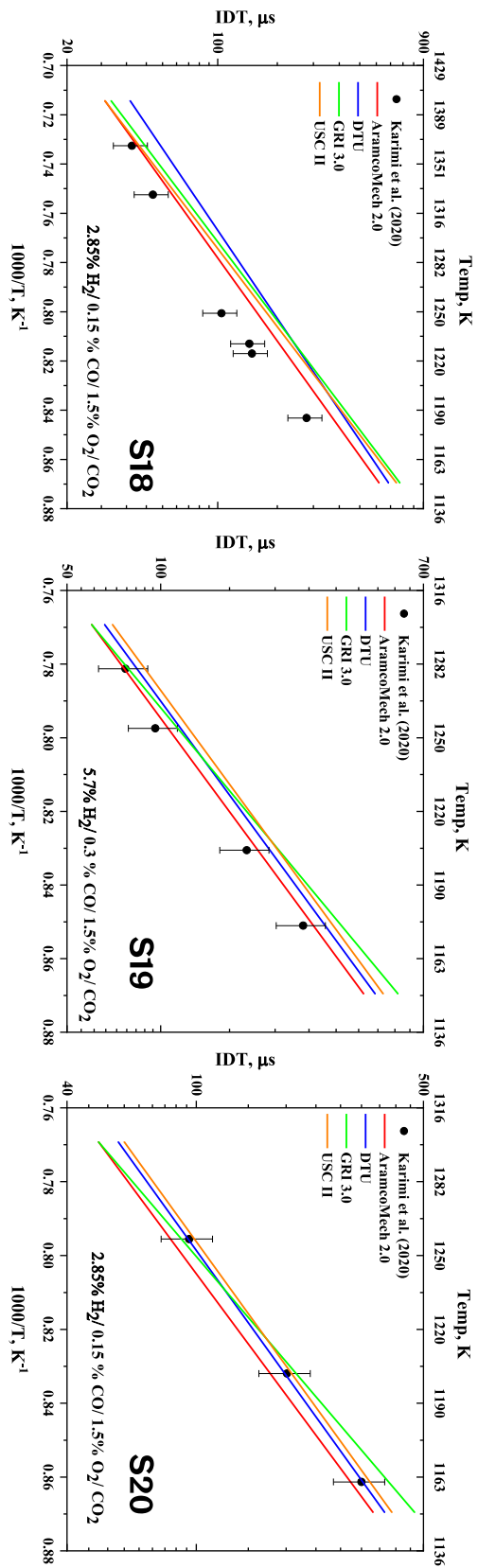


Figure 3.16. Comparison of S18, S19 and S20 IDT datasets from Karimi et al. [200].

However, Figure 3.17 shows the datasets S14-S17 recorded at a similar pressure of approximately 80 bar. The better agreement observed in S18-S20 is possibly due to the larger H<sub>2</sub>:CO ratio because as seen in Section 3.7, all four mechanisms have a good agreement for hydrogen IDT data. The addition of CO complicating the kinetics may be the explanation for the poor performance of all mechanisms when modelling syngas combustion.

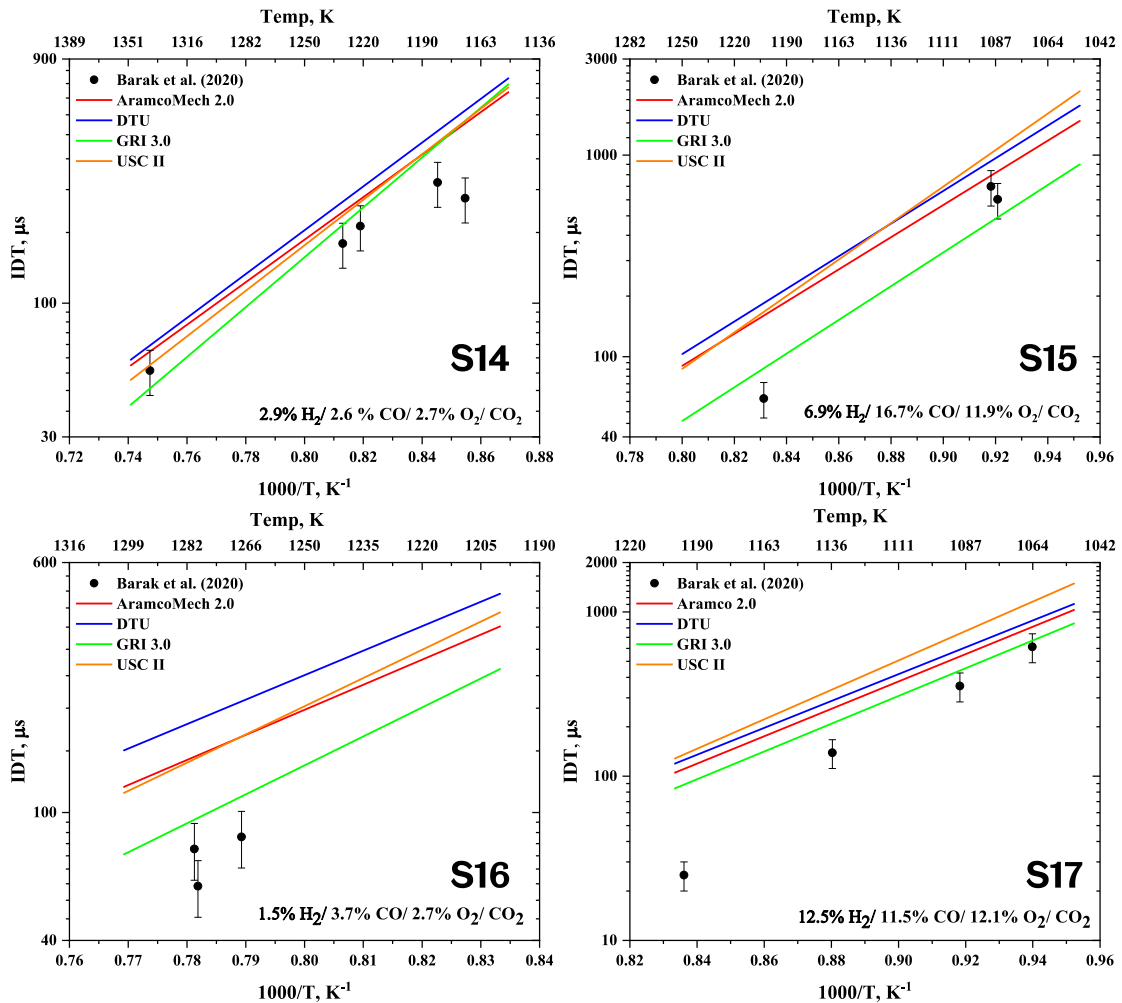
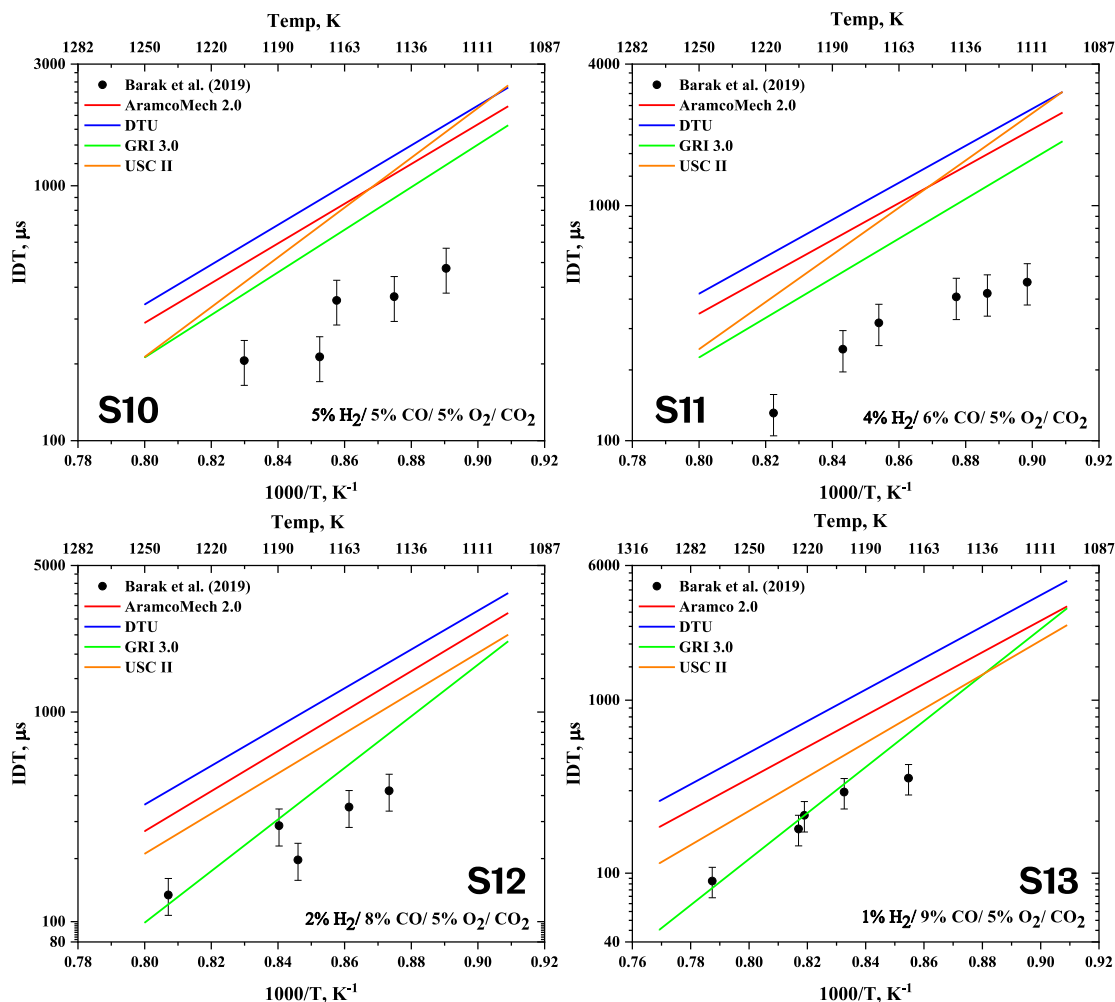


Figure 3.17. Comparison of datasets from Barak et al. [192] S14-S17.

In contrast, datasets S10-S13 from Barak et al. [199] were recorded at various H<sub>2</sub>:CO ratios. In S12 and S13, where the ratio is decreased, CO is the primary fuel component shown in Figure 3.18. The GRI 3.0 mechanism becomes a better fit for the experimental data and deviates from its previously good agreement with the other four mechanisms in S10 and S11. In addition, this behaviour is seen in Figure 3.17. In S14 and S17 where the mole fraction of H<sub>2</sub> and CO is similar, the

agreement between all four mechanisms is good. In the S15 and S16 datasets, where the mole fraction of CO is approximately 2.5 larger than that of H<sub>2</sub>, GRI 3.0 provides a much faster IDT than the other three mechanisms.



**Figure 3.18.** Comparison of S10-S13 datasets from Barak et al.[199].

The effect of altering the H<sub>2</sub>:CO ratio on the mechanism's ability to model the IDT is more pronounced when the ratio is close to 1, and the mole fractions are similar. Under these conditions, all mechanisms appear to struggle to simulate the IDT data but are in good agreement with each other above 10 atm. All mechanisms are much better at modelling IDT data with a large H<sub>2</sub>:CO ratio and a small mole fraction of CO. GRI 3.0's better performance with an H<sub>2</sub>:CO ratio much less than 1 is due to the much faster rate coefficient for Reaction 3.12 ( $\text{CO} + \text{HO}_2 \rightleftharpoons \text{CO}_2 + \text{OH}$ ) as discussed in Section 3.8.1.

### 3.9. Creation of the UoS sCO<sub>2</sub> 1.0 Mechanism

The challenge of mechanism creation is to assimilate all the information observed from Section 3.6 to Section 3.8 to create one mechanism that best models all the datasets. Any mechanistic changes made can have a knock-on effect in other conditions if the IDT is also sensitive to the reaction under those conditions. Therefore, after each significant change, or series of changes, each of the datasets must be re-run to check there are no adverse effects on other reactions.

For the creation of the UoS sCO<sub>2</sub> 1.0 mechanism, the USC II mechanism was chosen as a base. This was done for several reasons. Firstly, USC II was the best performing in the syngas datasets with the lowest average  $E$  value and the greatest number of best fits. As the syngas datasets for each mechanism had a much greater average  $E$  value than for the other two fuels, it seemed sensible to choose the mechanism which gave the best starting point. Secondly, as discussed in Section 3.6.1, the simple addition of CH<sub>3</sub>O<sub>2</sub> chemistry to USC II led to a significant reduction in the average  $E$  value by reducing the IDT in high-pressure conditions. Thirdly, as discussed in Section 3.7, altering the rate coefficient of Reaction 3.9 ( $CH_3 + O_2 \rightleftharpoons CH_3O + O$ ) led to an improvement in the H1 and H2 datasets. Making these small changes vastly improves the average  $E$  value of USC II across the three fuels and gives a very good starting point for mechanism creation. Figure 3.19 shows the modelling loop used to create the UoS sCO<sub>2</sub> 1.0 mechanism.

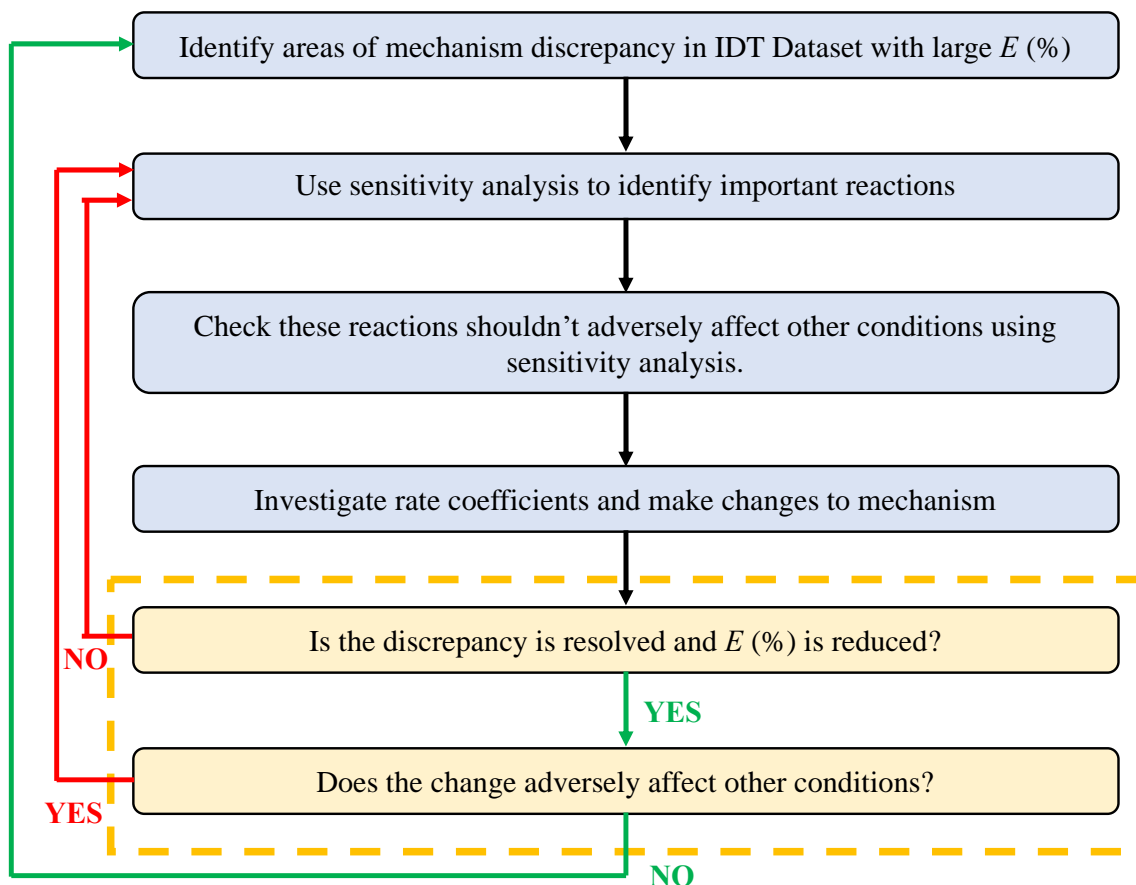


**Figure 3.19.** Modelling loop performed for the creation of the UoS sCO<sub>2</sub> mechanism.

The first change is the addition of the rate coefficients listed in Table 3.6. The subsequent changes made to other reactions are listed in Table 3.10. The source of each rate coefficient is listed along with the old and new values, and the magnitude of the change from the source if it was made.

**Table 3.10.** Changes made to rate coefficients in the USC II mechanism to create UoS sCO<sub>2</sub> 1.0.

Reaction	Mechanism	A (cm <sup>3</sup> mol <sup>-1</sup> s)	n	Ea (cal/mol)	Reference
H <sub>2</sub> O <sub>2</sub> + H ⇌ HO <sub>2</sub> + H <sub>2</sub>	USC II	6.1 x 10 <sup>6</sup>	2	5200	[225]*0.5
	New	1.85x 10 <sup>10</sup>	1	6000	[241]*1.2
CO + O <sub>2</sub> ⇌ CO <sub>2</sub> + O	USC II	1.1 x 10 <sup>12</sup>	0	47700	[225]
	New	2.5 x 10 <sup>12</sup>	0	47800	[245]
CO + HO <sub>2</sub> ⇌ CO <sub>2</sub> + OH	USC II	1.6 x 10 <sup>5</sup>	2.18	17940	[246]
	New	4 x 10 <sup>5</sup>	2.18	17942	[246]*2.5
CH <sub>3</sub> + O <sub>2</sub> ⇌ O + CH <sub>3</sub> O	USC II	3.1 x 10 <sup>13</sup>	0	28800	[240]
	New	1.0 x 10 <sup>13</sup>	0	28320	[239]*1.3
CH <sub>3</sub> + O <sub>2</sub> ⇌ OH + CH <sub>2</sub> O	USC II	3.6 x 10 <sup>10</sup>	0	8940	[240]
	New	1.7 x 10 <sup>11</sup>	0	9842	[239]*0.9
CH <sub>3</sub> + HO <sub>2</sub> ⇌ CH <sub>4</sub> + O <sub>2</sub>	USC II	1.0 x 10 <sup>12</sup>	0	0	[236]
	New	1.2 x 10 <sup>5</sup>	2.23	-3022	[237]
CH <sub>3</sub> + HO <sub>2</sub> ⇌ CH <sub>3</sub> O + OH	USC II	1.3 x 10 <sup>13</sup>	0	0	[225]
	New	1.10 x 10 <sup>12</sup>	0.269	-687.5	[237]
CH <sub>3</sub> + H <sub>2</sub> O <sub>2</sub> ⇌ CH <sub>4</sub> + HO <sub>2</sub>	USC II	2.5 x 10 <sup>4</sup>	2.47	5180	[247]
	New (R)	4.7 x 10 <sup>4</sup>	2.5	21000	[248]
CH <sub>4</sub> + H ⇌ CH <sub>3</sub> + H <sub>2</sub>	USC II	6.6 x 10 <sup>8</sup>	1.62	10840	[249]
	New	6.1 x 10 <sup>5</sup>	2.5	9587	[248]
H + O <sub>2</sub> ⇌ O + OH	USC II	2.644 x 10 <sup>16</sup>	- 0.671	17041	[250]
	New	3.0 x 10 <sup>16</sup>	- 0.671	17041	[250]*1.1 3
OH + H <sub>2</sub> ⇌ H + H <sub>2</sub> O	USC II	1.734 x 10 <sup>8</sup>	1.51	3430	[251]
	New	4.0 x 10 <sup>8</sup>	1.51	3430	[251]*2.3 1
H + O <sub>2</sub> (+M) ⇌ HO <sub>2</sub> (+M)	USC II	5.116 x 10 <sup>12</sup>	0.44	0	[252]*1.1
	New	3.00 x 10 <sup>12</sup>	0.44	0	[252]*0.6 4
H <sub>2</sub> + O <sub>2</sub> ⇌ HO <sub>2</sub> + H	USC II	5.916 x 10 <sup>5</sup>	2.433	53502	[253]*0.8
	New	4.5 x 10 <sup>5</sup>	2.433	53502	[253]*0.6 1
	USC II	1.11 x 10 <sup>14</sup>	-0.37	0	[254]

OH + OH (+M) $\rightleftharpoons$ H <sub>2</sub> O <sub>2</sub> (+M)	New	9.5 x 10 <sup>13</sup>	-0.37	0	[254]*0.8 6
HO <sub>2</sub> + H $\rightleftharpoons$ OH + OH	USC II	7.485 x 10 <sup>13</sup>	0	295	[255]
	New	4.5 x 10 <sup>13</sup>	0	295	[255]*0.6
HO <sub>2</sub> + O $\rightleftharpoons$ OH + O <sub>2</sub>	USC II	4 x 10 <sup>13</sup>	0	0	[245]*2
	New	2 x 10 <sup>13</sup>	0	0	[245]
H <sub>2</sub> O <sub>2</sub> + OH $\rightleftharpoons$ HO <sub>2</sub> + H <sub>2</sub> O (DUP)	USC II	2 x 10 <sup>12</sup>	0	427	[256]
	New	1 x 10 <sup>12</sup>	0	427	[256]*0.5
H <sub>2</sub> O <sub>2</sub> + OH $\rightleftharpoons$ HO <sub>2</sub> + H <sub>2</sub> O (DUP)	USC II	2.67 x 10 <sup>41</sup>	-7	37600	[256]
	New	1.5 x 10 <sup>41</sup>	-7	37600	[256]*0.5 6
CO + OH $\rightleftharpoons$ CO <sub>2</sub> + H (DUP)	USC II	7.04 x 10 <sup>4</sup>	2.053	-355.67	[257]
	New	9 x 10 <sup>4</sup>	2.053	-355.67	[257]*1.2 8
CO + OH $\rightleftharpoons$ CO <sub>2</sub> + H (DUP)	USC II	5.757 x 10 <sup>12</sup>	- 0.664	331.83	[257]
	New	7.5 x 10 <sup>12</sup>	- 0.664	331.83	[257]*1.3 0
OH + HO <sub>2</sub> $\rightleftharpoons$ H <sub>2</sub> O + O <sub>2</sub> (DUP)	USC II	1.41 x 10 <sup>18</sup>	-1.76	60	[185]
	New	2.8 x 10 <sup>18</sup>	-1.76	60	[185]*2
OH + HO <sub>2</sub> $\rightleftharpoons$ H <sub>2</sub> O + O <sub>2</sub> (DUP)	USC II	1.12 x 10 <sup>85</sup>	-22.3	26900	[185]
	New	2.24 x 10 <sup>85</sup>	-22.3	26900	[185]*2
OH + HO <sub>2</sub> $\rightleftharpoons$ H <sub>2</sub> O + O <sub>2</sub> (DUP)	USC II	5.37 x 10 <sup>70</sup>	- 16.72	32900	[185]
	New	1.2 x 10 <sup>71</sup>	- 16.72	32900	[185]*2.2 3
OH + HO <sub>2</sub> $\rightleftharpoons$ H <sub>2</sub> O + O <sub>2</sub> (DUP)	USC II	2.51 x 10 <sup>12</sup>	2	40000	[185]
	New	5 x 10 <sup>12</sup>	2	40000	[185]*2
OH + HO <sub>2</sub> $\rightleftharpoons$ H <sub>2</sub> O + O <sub>2</sub> (DUP)	USC II	1.00 x 10 <sup>136</sup>	-40	34800	[185]
	New	2 x 10 <sup>136</sup>	-40	34800	[185]*2
HCO (+M) $\rightleftharpoons$ CO + H (+M)	USC II	1.87 x 10 <sup>17</sup>	-1	17000	[258]*2
	New	4 x 10 <sup>17</sup>	-1	17000	[258]*2.1
CH <sub>3</sub> + OH $\rightleftharpoons$ CH <sub>2</sub> * + H <sub>2</sub> O	USC II	2.501 x 10 <sup>13</sup>	0	0	[259-264]
	New	1.75 x 10 <sup>13</sup>	0	0	[259- 264]*0.7
CH <sub>2</sub> * + CO <sub>2</sub> $\rightleftharpoons$ CH <sub>2</sub> O + CO	USC II	1.4 x 10 <sup>13</sup>	0	0	[265]

	New	$7.0 \times 10^{12}$	0	0	[265]*0.5
$\text{CH}_3 + \text{CH}_3 \rightleftharpoons \text{C}_2\text{H}_6 + \text{H}$	USC II	$4.99 \times 10^{12}$	0.1	10600	[266]
	New	$7.5 \times 10^{12}$	0.1	10600	[266]*1.5
$\text{CH}_2\text{O} + \text{O}_2 \rightleftharpoons \text{HCO} + \text{HO}_2$	USC II	$1.00 \times 10^{14}$	0	40000	[267]
	New	$1.50 \times 10^{14}$	0	40000	[267]*1.5

This section details all the rate coefficient changes made to the reactions listed in Table 3.10.

### 3.9.1. $\text{H}_2\text{O}_2 + \text{H} \rightleftharpoons \text{HO}_2 + \text{H}$

Reaction 3.9 ( $\text{H}_2\text{O}_2 + \text{H} \rightleftharpoons \text{H}_2 + \text{HO}_2$ ) was discussed in more detail in Section 3.7. The older rate coefficient used in USC II taken from Tsang and Hampson [225] was reported with an uncertainty factor of 5 at temperatures less than 1000 K. The method of determination was also unreported. This rate coefficient was changed to the much faster, and more recent rate coefficient from AramcoMech 2.0 reported by Ellingson et al. in 2007 [241] which was determined from ab-initio calculations. Speeding up Reaction 3.9 ( $\text{H}_2\text{O}_2 + \text{H} \rightleftharpoons \text{H}_2 + \text{HO}_2$ ) was essential to improving the ability of USC II to model the H1 and H2 datasets as discussed in Section 3.7. The alteration of this rate coefficient also maintained a better simulation of USC II for the H3 dataset.

### 3.9.2. $\text{CO} + \text{O}_2 \rightleftharpoons \text{CO}_2 + \text{O}$

Reaction 3.13 ( $\text{CO} + \text{O}_2 \rightleftharpoons \text{CO}_2 + \text{O}$ ) is important in syngas combustion, especially in conditions where the mole fraction of CO exceeds that of  $\text{H}_2$ . The rate coefficient used in USC II was reported by Tsang and Hampson in 1986 [225]. This source took the rate coefficient from Baluch et al. (1976) [243]. Whilst the authors report an uncertainty factor of 2, the decision was made in the UoS sCO<sub>2</sub> to increase the rate coefficient by 2.27x to create a much better fit to the syngas data, where a large reduction in the IDT was required. This was in line with another rate coefficient used in GRI 3.0 by Warnatz [245] which was reported using shock tube measurements of syngas combustion.

**Reaction 3.13.**  $\text{CO} + \text{O}_2 \rightleftharpoons \text{CO}_2 + \text{O}$

### 3.9.3. $\text{CO} + \text{HO}_2 \rightleftharpoons \text{CO}_2 + \text{OH}$

Reaction 3.12 ( $\text{CO} + \text{HO}_2 \rightleftharpoons \text{CO}_2 + \text{OH}$ ) was discussed in more detail in Section 3.8 as one of the key reactions identified by the sensitivity analysis. It was observed that changing the rate coefficient in USC II to that of GRI 3.0 led to a large reduction in IDT. However, across all the datasets, this effect of increase became an issue, especially at low pressures, where the IDT reduced too much. Therefore, the rate coefficient was increased only slightly to provide a balance that better simulated all the syngas conditions. Furthermore, the temperature dependence in the USC II rate coefficient from You et al. [244] helped simulate the datasets.

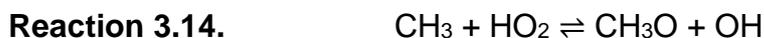
### 3.9.4. $\text{CH}_3 + \text{O}_2 \rightleftharpoons \text{Products}$

There are three possible pathways for this reaction, discussed in more detail in Section 3.6. They are Reaction 3.1 ( $\text{CH}_3 + \text{O}_2 (+M) \rightleftharpoons \text{CH}_3\text{O}_2 (+M)$ ), Reaction 3.7 ( $\text{CH}_3 + \text{O}_2 \rightleftharpoons \text{CH}_3\text{O} + \text{O}$ ) and Reaction 3.8 ( $\text{CH}_3 + \text{O}_2 \rightleftharpoons \text{CH}_2\text{O} + \text{OH}$ ). The rate coefficient for Reaction 3.1 was added directly to USC II as the  $\text{CH}_3\text{O}_2$  species wasn't present in USC II. The rate coefficient was from Fernandes et al. [226] as used in AramcoMech 2.0. For Reaction 3.7 ( $\text{CH}_3 + \text{O}_2 \rightleftharpoons \text{CH}_3\text{O} + \text{O}$ ) and Reaction 3.8 ( $\text{CH}_3 + \text{O}_2 \rightleftharpoons \text{CH}_2\text{O} + \text{OH}$ ) in USC II, both rate coefficients originate from Yu et al. (1995) [240] were updated to those from Srinivasan et al. [239] published in 2005. From this, the rate coefficient of Reaction 3.7 ( $\text{CH}_3 + \text{O}_2 \rightleftharpoons \text{CH}_3\text{O} + \text{O}$ ) was increased slightly to increase the chain branching pathway and reduce IDT. The rate coefficient of Reaction 3.8 ( $\text{CH}_3 + \text{O}_2 \rightleftharpoons \text{CH}_2\text{O} + \text{OH}$ ) was decreased slightly to compensate for this increase.

### 3.9.5. $\text{CH}_3 + \text{HO}_2 \rightleftharpoons \text{Products}$

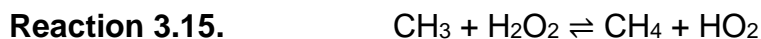
There are two key reaction pathways for  $\text{CH}_3$  and  $\text{HO}_2$ . Reaction 3.6 ( $\text{CH}_3 + \text{HO}_2 \rightleftharpoons \text{CH}_4 + \text{O}_2$ ) was introduced in Section 3.6.1 for its importance in high-pressure combustion. Reaction 3.14 ( $\text{CH}_3 + \text{HO}_2 \rightleftharpoons \text{CH}_3\text{O} + \text{OH}$ ) is an alternative reaction pathway. Both of these rate coefficients were updated to those from a more recent 2009 publication by Jasper et al. [237]. The addition of the temperature

dependence of these rate coefficients led to an improvement across the IDT dataset.



### 3.9.6. $\text{CH}_3 + \text{H}_2\text{O}_2 \rightleftharpoons \text{CH}_4 + \text{HO}_2$

The rate coefficient for Reaction 3.15 ( $\text{CH}_3 + \text{H}_2\text{O}_2 \rightleftharpoons \text{CH}_4 + \text{HO}_2$ ) was updated from the older rate coefficient from Baldwin et al. (1988) [247] to the reverse reaction from Baulch et al. [248]. Reaction 3.15 ( $\text{CH}_3 + \text{H}_2\text{O}_2 \rightleftharpoons \text{CH}_4 + \text{HO}_2$ ) was identified as important low-pressure methane combustion through sensitivity analysis. The rate coefficient was updated to that of a more recent publication from Baulch et al. [248]. Baulch et al. (2005) is a comparative review of lots of reaction data, including Baldwin et al. [247]. This rate coefficient from Baldwin et al. [247] is the only experimental rate coefficient considered, which was recorded at 716 K using gas chromatography. Ideally, this rate coefficient should be revisited using more modern experimental techniques over a wider range of pressures and temperatures.



### 3.9.7. $\text{CH}_4 + \text{H} \rightleftharpoons \text{CH}_3 + \text{H}_2$

Sensitivity analysis identified Reaction 3.16 ( $\text{CH}_4 + \text{H} \rightleftharpoons \text{CH}_3 + \text{H}_2$ ) as important at 30 atm and below for methane combustion. The rate coefficient was updated from the 1991 publication from Rabinowitz et al. [249] to a more recent rate coefficient from Baulch et al. [248]. The uncertainty factor in this rate coefficient is reported to be 1.5. Again, as this rate coefficient comes from a comparative review that looks at numerous publications of rate coefficients for this reaction, this is a sensible change to a more accurate rate coefficient which improved the fit to the available IDT data where the reaction was identified as important.



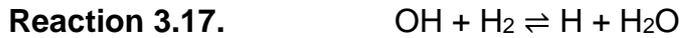
### 3.9.8. $H + O_2 \rightleftharpoons$ Products

The two reactions of H and  $O_2$ , Reaction 3.10 ( $O_2 + H \rightleftharpoons O + OH$ ) and Reaction 3.11 ( $H + O_2 (+M) \rightleftharpoons HO_2 (+M)$ ) were discussed in more detail in Section 3.7. As these two branching pathways have different effects on the IDT, the ratio at which the reactions progress down them is a critical factor in determining IDT, especially in hydrogen and syngas combustion. Whilst the original rate coefficients were maintained for both reactions small changes were made to favour the chain branching Reaction 3.10 ( $O_2 + H \rightleftharpoons O + OH$ ). These two small alterations to Reaction 3.10 ( $O_2 + H \rightleftharpoons O + OH$ ) and Reaction 3.11 ( $H + O_2 (+M) \rightleftharpoons HO_2 (+M)$ ) shown in Table 3.10 slightly reduced the IDT, for the syngas datasets and improves the poor fitting H3 dataset of hydrogen. However, the change was minimal in datasets that were already well fitting. Bates et al. [268] show that Reaction 3.11 ( $H + O_2 (+M) \rightleftharpoons HO_2 (+M)$ ) transitions into the fall-off region around 20 bar and does not reach the high-pressure limit until the pressure is greater than 1000 bar for a water bath gas. This means given the importance of this reaction to all of the conditions studied, being able to accurately model the fall-off region is essential to a chemical kinetic mechanism.

### 3.9.9. $OH + H_2 \rightleftharpoons H + H_2O$

The rate coefficient used for Reaction 3.17 ( $OH + H_2 \rightleftharpoons H + H_2O$ ) was from Michael and Sutherland (1988) [251] and is retained for the UoS  $sCO_2$ . The rate coefficient was enhanced by a factor of 2.31 to improve the mechanisms that fit the syngas datasets. Interestingly, Reaction 3.17 ( $OH + H_2 \rightleftharpoons H + H_2O$ ) had a negative sensitivity coefficient for the S19 and S20 [200] datasets and a positive sensitivity coefficient for the low-pressure datasets from Barak et al. (2017) [198], S4-S9. By increasing the rate coefficient of Reaction 3.17 ( $OH + H_2 \rightleftharpoons H + H_2O$ ), it was possible to reduce the IDT for S4-S9 and increase the IDT for S19 and S20, creating a better fit for all the datasets being investigated. The reaction did not appear in any sensitivity analysis for hydrogen datasets, meaning the change had little on these IDTs. This is reasonable as an alternative rate coefficient

published by Lam et al. [269] using shock tube laser absorption diagnostic much faster but does not incorporate a temperature dependence.



### 3.9.10. $\text{H}_2 + \text{O}_2 \rightleftharpoons \text{HO}_2 + \text{H}$

The rate coefficient of Reaction 3.18 ( $\text{H}_2 + \text{O}_2 \rightleftharpoons \text{HO}_2 + \text{H}$ ) was obtained from Michael et al. [253] published in 2000. In addition, the same rate coefficient is used in AramcoMech 2.0, although the reverse reaction is used. The only mechanism using a more recent rate coefficient was DTU using that of Burke et al. (2012) [270]. Based on better fitting the available datasets, the same rate coefficient from USC II was kept for the UoS sCO<sub>2</sub> mechanism, The rate coefficient was reduced slightly to improve the fit to the available datasets.



### 3.9.11. $\text{OH} + \text{OH} (+\text{M}) \rightleftharpoons \text{H}_2\text{O}_2 (+\text{M})$

The rate coefficient used in USC II was published in 1988 by Zellner et al. [254]. A more recent rate coefficient has been published by Troe et al. (2011) [234] for the dissociation of H<sub>2</sub>O<sub>2</sub>. The decision to keep the original rate coefficient from USC II with a slight reduction in the A factor to improve the fit to the syngas datasets, as Reaction 3.19 ( $\text{OH} + \text{OH} (+\text{M}) \rightleftharpoons \text{H}_2\text{O}_2 (+\text{M})$ ) also appeared in the sensitivity analysis for the hydrogen datasets.



For the UoS sCO<sub>2</sub> 1.0 mechanism sensitivity analysis, all datasets above atmospheric pressure (S14-S20) all featured Reaction 3.19 ( $\text{OH} + \text{OH} (+\text{M}) \rightleftharpoons \text{H}_2\text{O}_2 (+\text{M})$ ) and under some conditions was the second most important reaction as shown in Figure 3.20. The rate coefficient was decreased slightly to improve the simulation in the S18-S20 datasets, where the UoS sCO<sub>2</sub> 1.0 mechanism was beginning to under predict the IDT. As Troe [234] has demonstrated that the dissociation of H<sub>2</sub>O<sub>2</sub> enters the fall-off region at approximately 10 bar at 1150 K

in an Ar bath gas, it is imperative that the selected rate coefficient can accurately simulate the chemical kinetics up to the high-pressure limit at 1000 bar.

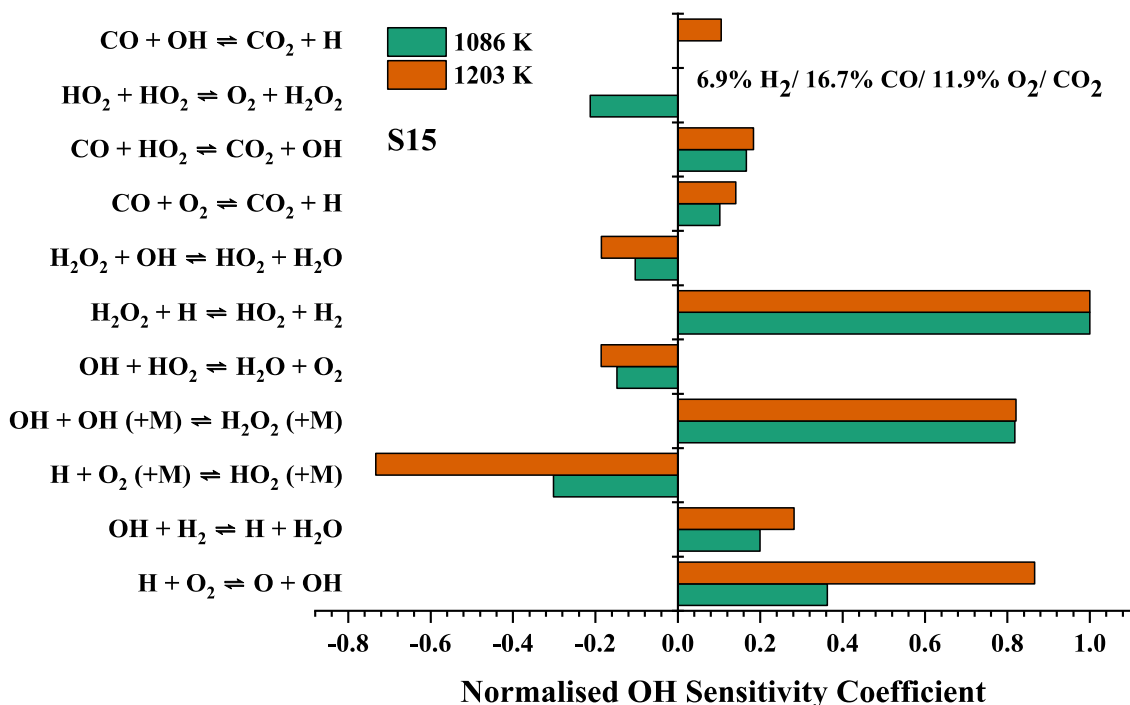


Figure 3.20. UoS sCO<sub>2</sub> 1.0 sensitivity analysis of S15 at 1086 K and 1203 K.

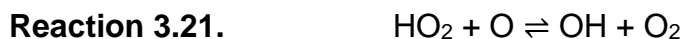
### 3.9.12. HO<sub>2</sub> + H $\rightleftharpoons$ OH + OH

The rate coefficient used by USC II by Mueller et al. [255] is the same as AramcoMech 2.0 and DTU. The rate coefficient was determined using a flow reactor between 0.3 and 15.7 atm, and 950 and 1040 K. GRI 3.0 uses a least-squares fitting based on three datasets [245, 271, 272]. There is also a more recently published rate coefficient available determined using transition state theory [273]. The original rate coefficient from USC II was kept and the A factor was reduced by almost half. This was done to keep the better fit of the USC II mechanism to the H1 and H2 datasets, which this reaction had a higher sensitivity too, whilst making other changes to decrease the IDT of the H3 condition.

**Reaction 3.20.** HO<sub>2</sub> + H  $\rightleftharpoons$  OH + OH

### 3.9.13. $\text{HO}_2 + \text{O} \rightleftharpoons \text{OH} + \text{O}_2$

The rate coefficient used in USC II was published by Gardiner and Burcat [245] and doubled for the creation of USC II. This is in good agreement with the slightly slower rate coefficient used in AramcoMech 2.0 from Baulch et al. [235]. This was reduced by half to the original rate coefficient and more in line with a recent publication from Burke et al. [270] without the temperature dependence and Baulch et al. [248]. The Burke et al. rate coefficient was based on a theoretically calculated rate coefficient from Fernandez-Ramos et al. [274]. Although the pressure is not stated, this work was done concerning atmospheric chemistry and thus relates to atmospheric or sub-atmospheric pressures. Therefore, there may be some difficulties in extrapolating this to the much greater pressures of the Allam-Fetvedt cycle. Whilst there are a lot of rate coefficients for Reaction 3.21 ( $\text{HO}_2 + \text{O} \rightleftharpoons \text{OH} + \text{O}_2$ ) with a relatively good agreement between them, there is still a large degree of uncertainty that can have a large influence on the IDT.



### 3.9.14. $\text{H}_2\text{O}_2 + \text{OH} \rightleftharpoons \text{HO}_2 + \text{H}_2\text{O}$

Reaction 3.22 ( $\text{H}_2\text{O}_2 + \text{OH} \rightleftharpoons \text{HO}_2 + \text{H}_2\text{O}$ ) is duplicated reaction in the USC II mechanism with two separate rate coefficients from Hippler et al. [256]. A more recent rate coefficient has been published by Hong et al. [141] using shock tube laser absorption of  $\text{H}_2\text{O}$  and  $\text{OH}$  in 2010. There is a large discrepancy between these two rate coefficients and for the UoS s $\text{CO}_2$  1.0 mechanism, the older mechanism by Hippler et al. was retained and both rate coefficients were approximately halved.



### 3.9.15. $\text{CO} + \text{OH} \rightleftharpoons \text{CO}_2 + \text{H}$

The rate coefficient here is another duplicate reaction, this time from Joshi et al. [257]. The same rate coefficient is used in AramcoMech 2.0, whereas DTU uses a pressure dependant rate coefficient from Senosiain et al. published in 2005

[275]. The same rate coefficient from USC II was retained with a slight increase of around 1.3x to reduce the IDT of the syngas datasets. This reaction is important to the IDT and was identified in some sensitivity analysis as it consumes OH. However, at the point of IDT, the mole fraction of CO is still large in the combustion of any fuel. It is the post-IDT conversion of CO to CO<sub>2</sub> where this reaction will be more important.



### 3.9.16. $\text{OH} + \text{HO}_2 \rightleftharpoons \text{H}_2\text{O} + \text{O}$

Reaction 3.24 ( $\text{OH} + \text{HO}_2 \rightleftharpoons \text{H}_2\text{O} + \text{O}$ ) has five different rate coefficients in the USC II mechanism [185]. DTU uses a different rate coefficient from Burke et al. [276], which was determined theoretically. Whereas AramcoMech 2.0 uses a rate coefficient published in 2013 by Hong et al. [138] using shock tube diagnostics at 1.7 atm. Both rate coefficients from AramcoMech 2.0 and DTU only use two duplicate reactions. The same rate coefficients for the reaction from USC II were maintained but each of the five rate coefficients was approximately doubled.



### 3.9.17. $\text{HCO} (+\text{M}) \rightleftharpoons \text{H} + \text{CO} (+\text{M})$

The rate coefficient Reaction 3.25 ( $\text{HCO} (+\text{M}) \rightleftharpoons \text{H} + \text{CO} (+\text{M})$ ) used in USC II is taken from Friedrichs et al. [258]. AramcoMech 2.0 uses an alternative rate coefficient from Li et al. [189] in a comparative review. The issue with third-body reactions, particularly in this case with a reaction so influential in CO<sub>2</sub> production, is that CO<sub>2</sub> is very rarely considered as the third body. As the CO<sub>2</sub> mole fraction is so large in direct-fired sCO<sub>2</sub> combustion, it is important to understand how it affects each of these 3<sup>rd</sup> body reactions, especially as it is such an efficient absorber of energy. Reaction 3.25 ( $\text{HCO} (+\text{M}) \rightleftharpoons \text{H} + \text{CO} (+\text{M})$ ) is also one of the key reactions in the formation of CO, it is incredibly important in determining an accurate chemical kinetic mechanism. In UoS sCO<sub>2</sub> 1.0, the rate coefficient for Reaction 3.25 ( $\text{HCO} (+\text{M}) \rightleftharpoons \text{H} + \text{CO} (+\text{M})$ ) was increased by just over double, which improved the fit to IDT data in both methane and hydrogen datasets.



Reactions such as Reaction 3.26 ( $\text{CH}_3 + \text{OH} \rightleftharpoons \text{CH}_2^* + \text{H}_2\text{O}$ ) which involve the excited methylene radical ( $\text{CH}_2^*$ ) only become important at very high temperatures of 1500 K or greater in methane combustion. As these temperatures were not reached with the high-pressure datasets, these reactions were only considered with relevance to low-pressure datasets. The rate coefficient used in the USC II for Reaction 3.26 ( $\text{CH}_3 + \text{OH} \rightleftharpoons \text{CH}_2^* + \text{H}_2\text{O}$ ) was determined from a range of different publications [259-264]. A different rate coefficient from Jasper et al. [277] is used in AramcoMech 2.0. The rate coefficient was reduced slightly but kept as that from USC II as it better modelled the high-temperature, low-pressure data were AramcoMech 2.0 performed poorly.



USC II uses a rate coefficient from Koch et al. [265] published in 1990 for Reaction 3.27 ( $\text{CH}_2^* + \text{CO}_2 \rightleftharpoons \text{CH}_2\text{O} + \text{CO}$ ). This rate coefficient is very important when  $\text{CH}_2^*$  forms, as it is reactive enough to react with the usually inert  $\text{CO}_2$ . A similar rate coefficient is used in DTU by Koch M. (reference unclear from mechanism). The rate coefficient was reduced slightly to improve the fit in high-temperature, low-pressure methane IDTs.



USC II uses a rate coefficient for Reaction 3.28 ( $\text{CH}_3 + \text{CH}_3 \rightleftharpoons \text{C}_2\text{H}_5 + \text{H}$ ) from Stewart [266] published in 1989. DTU uses a rate coefficient around a magnitude of 10 smaller than this from Baulch et al. [248]. In the creation of UoS sCO<sub>2</sub> 1.0, the rate coefficient of Reaction 3.28 was increased by approximately 50%.



The rate coefficient of Reaction 3.29 ( $\text{CH}_2\text{O} + \text{O}_2 \rightleftharpoons \text{HCO} + \text{HO}_2$ ) was used in USC II from Baldwin and Walker [267], published in 1973. The reaction rate coefficient was increased by 50% of the original in the creation of UoS sCO<sub>2</sub> 1.0.



### 3.10. Results of the Quantitative Analysis

Table 3.11 shows the results of the quantitative analysis of the UoS sCO<sub>2</sub> 1.0 mechanism developed against the four existing chemical kinetic mechanisms investigated in the current work. The average *E* (%) value is reported for each of the individual fuels studied as well as an overall average *E* (%) value, which is an average of the average *E* for the three fuels, not for each dataset, although the values worked out to be very similar.

**Table 3.11.** Comparison of the developed UoS sCO<sub>2</sub> mechanism to the existing four mechanisms studied.

<b>Dataset</b>		<b>AramcoMech 2.0</b>	<b>DTU</b>	<b>GRI 3.0</b>	<b>USC II</b>	<b>UoS sCO<sub>2</sub></b>
<b>Hydrogen</b>	<i>Average E</i> (%)	37.8	55.7	88.0	64.1	11.7
	No. Best Fit	1	0	0	0	2
<b>Methane</b>	<i>Average E</i> (%)	28.9	23.9	32.7	39.2	17.5
	No. Best Fit	2	4	5	5	13
<b>Syngas</b>	<i>Average E</i> (%)	367.3	402.6	113.7	88.2	36.2
	No. Best Fit	1	0	2	2	15
<b>Average <i>E</i></b>		<b>144.7</b>	<b>160.7</b>	<b>78.1</b>	<b>63.8</b>	<b>21.79</b>
<b>Total No. Best Fit</b>		<b>4</b>	<b>4</b>	<b>7</b>	<b>7</b>	<b>30</b>

Firstly, the UoS sCO<sub>2</sub> mechanism shows a significant reduction in the average *E* (%) value of 11.7%, given most shock tube IDTs have an error of approximately 20%, this can be a good mechanism performance. In addition, the UoS sCO<sub>2</sub> is the best fit for two of the three datasets, fitting all the datasets with an average *E* (%) of less than 20% in all three datasets. The problem is the lack of experimental

data for hydrogen IDTs in CO<sub>2</sub>. More datasets are required to fill in the gaps between the three average pressures studied and look at different equivalence ratios and CO<sub>2</sub> concentrations.

For the methane IDT data, the UoS sCO<sub>2</sub> has reduced the average  $E$  value to 17.5% from 23.9% of USC II, the next best-performing mechanism DTU. Furthermore, the UoS sCO<sub>2</sub> is the best fitting mechanism to thirteen of the twenty-nine datasets, fitting 22 of the datasets within an average  $E$  of 20%. Unlike the performance of hydrogen fuel, there is a vast number of datasets covering a wide range of pressures and conditions. This provides significant confidence that the UoS sCO<sub>2</sub> mechanism can model the IDT of methane in oxyfuel conditions within an average absolute error of  $17.5 \pm 12.1\%$ . The error was calculated using the standard deviation.

The existing mechanisms used in the study struggled to model the syngas IDT data, with AramcoMech 2.0 and DTU both having an average  $E$  (%) value of more than 350%. As previously discussed, this was predominantly due to an overestimation in the ignition delay time and a lack of capturing the correct curvature of the low-pressure datasets. The UoS sCO<sub>2</sub> average  $E$  (%) value of  $36.2 \pm 24.5\%$  is a significant improvement on the existing mechanisms in addition to being the best fit for 75% of the twenty datasets studied. However, the average  $E$  for UoS sCO<sub>2</sub> for syngas IDT data is still over double that of methane and hydrogen, and therefore there is still some room for improvement in the worse-performing datasets. The challenge is doing so without adversely affecting the better-fitting datasets.

It should be noted that the smallest  $E$  (%) value does not necessarily indicate the best fit due to the large error of 18-25% in the IDT, meaning multiple mechanisms may be within the error. However, across many datasets, the average  $E$  (%) value is a good indication of the best-performing mechanism. Table 3.9 shows the UoS sCO<sub>2</sub> mechanism produces the best average  $E$  (%) for all the fuels studied and is the best fit for over half of the datasets. It is important to note that the rate coefficients selected are not a reflection of the quality of the rate coefficient, as

the majority were not measured in a CO<sub>2</sub> bath gas, the selection was based on creating the best fit to the available experimental data available.

### **3.11. UoS sCO<sub>2</sub> Mechanism at the Conditions of the Allam-Fetvedt Cycle**

The next step was investigating how the UoS sCO<sub>2</sub> mechanism performs at the conditions of the Allam-Fetvedt cycle. Having the ability to accurately understand the combustion chamber of a direct-fired sCO<sub>2</sub> power plant allows for more detailed designs that can be used to further improve efficiencies. For this, Chemkin Pro R3 was used to simulate the conditions using a closed homogeneous batch reactor. This zero-dimensional reactor does not accurately represent the actual flame formation and mixing which would happen in a combustion chamber but does allow investigation into the actual chemical kinetic mechanism under the conditions. Once the mechanism is completed it can be utilised in more accurate computational fluid dynamics (CFD) models. As the exact conditions of the Allam-Fetvedt cycle are not reported, the conditions used are approximate but give a good indicator of important reactions and

The closed homogeneous reactor used a 'constrain volume and solve energy' set up at 300 atm and 1100 K. The first run-through used pure methane as a proxy for natural gas, as it is 97% of the composition. The reactant gases were CH<sub>4</sub> and O<sub>2</sub> with an equivalence ratio of 1, with a 96% dilution of CO<sub>2</sub>. There were several key routes of investigation to the chemical kinetic mechanism. The first was reaction pathway analysis (RPA) under these conditions. The second was looking at the rate of production (ROP) for different, key species in the reactant, to see which reactions are more important for its formation and removal. Thirdly, by looking at the net reaction rate of different competing reactions, to see which are more important under different conditions. One of the key considerations of this chapter is the CH<sub>3</sub>O<sub>2</sub> chemistry, which was identified as an important species for methane combustion at high pressures in Section 3.6.1.

### 3.11.1. Reaction Pathway Analysis

A reaction pathway analysis (RPA) was performed at 1100 K and 300 atm for stoichiometric methane combustion in a 96% CO<sub>2</sub> dilution. The results of the reaction pathway analysis are shown in Figure 3.21 in terms of the carbon flux through the reaction and all the carbon-based species involved are shown.

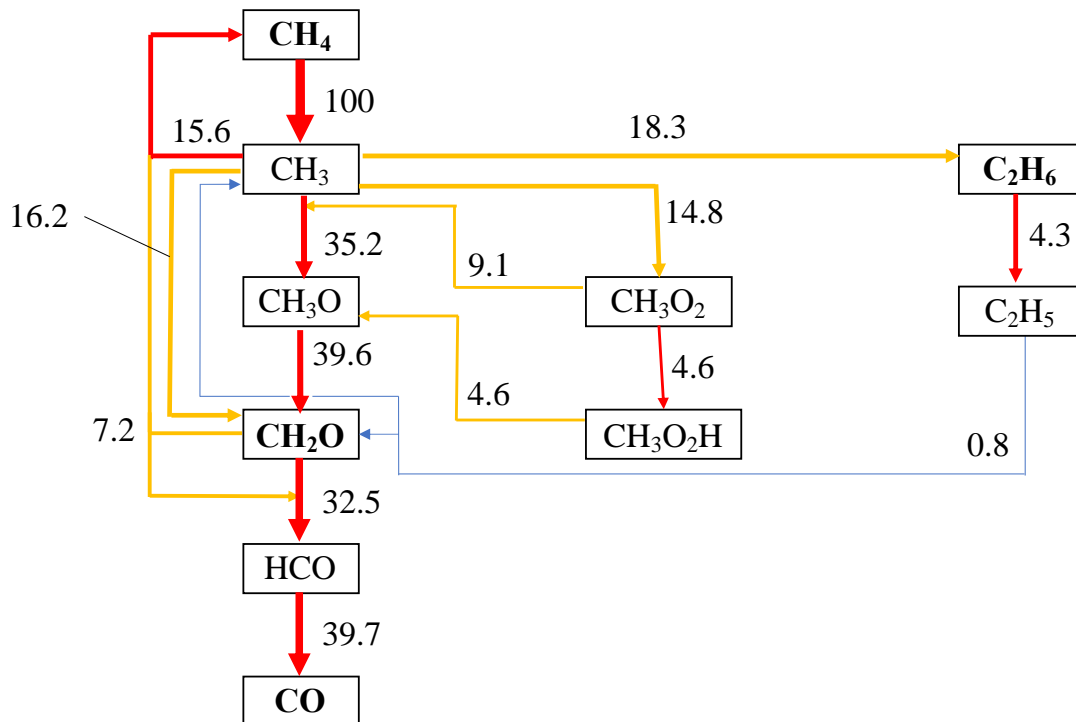


**Figure 3.21.** Reaction pathway analysis of stoichiometric methane combustion in 96% CO<sub>2</sub> at 300 atm and 1100 K.

This reaction pathway shows 10 species, connected by arrows where the colour denotes the type of reaction and the thickness of the arrow, the amount of carbon moving down that pathway. A red arrow presents multiple reaction pathways, an orange arrow signifies there is only one reaction, and a blue arrow shows that the reaction pathway has two products shown in the RPA. The species in bold are non-radical species that form significant ‘carbon sinks’ during the reaction. The other species are radicals or highly reactive and form a steady-state during combustion, this means once a small initial concentration is created, the rate of production becomes equal to the rate of loss, so the concentration remains constant. As shown in Figure 3.21, 100% of methane reacts to form CH<sub>3</sub>. Whilst

there are multiple reactions, 94.6% of CH<sub>4</sub> reacts with OH via Reaction 3.30 to form CH<sub>3</sub>.



15.6% of CH<sub>3</sub> react back to reform CH<sub>4</sub> via Reaction 3.6 (CH<sub>3</sub> + HO<sub>2</sub> ⇌ CH<sub>4</sub> + O<sub>2</sub>) and Reaction 3.31 (CH<sub>3</sub> + CH<sub>2</sub>O ⇌ CH<sub>4</sub> + HCO) in roughly equal amounts. Reaction 3.31 CH<sub>3</sub> + CH<sub>2</sub>O ⇌ CH<sub>4</sub> + HCO also forms HCO as shown in Figure 3.21.



There are four other products of CH<sub>3</sub> from five different CH<sub>3</sub> reactions. Reaction 3.1, Reaction 3.3 (CH<sub>3</sub>O<sub>2</sub> + CH<sub>3</sub> ⇌ CH<sub>3</sub>O + CH<sub>3</sub>O), Reaction 3.8 (CH<sub>3</sub> + O<sub>2</sub> ⇌ CH<sub>2</sub>O + OH), Reaction 3.14 (CH<sub>3</sub> + HO<sub>2</sub> ⇌ CH<sub>3</sub>O + OH) and Reaction 3.32 (CH<sub>3</sub> + CH<sub>3</sub> (+M) ⇌ C<sub>2</sub>H<sub>6</sub> (+M)).

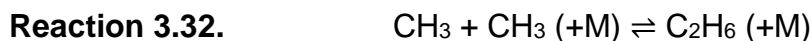


Figure 3.22 shows the ROP analysis of CH<sub>3</sub>. The plot shows that almost of CH<sub>3</sub> is formed via Reaction 3.30 (CH<sub>4</sub> + OH ⇌ CH<sub>3</sub> + H<sub>2</sub>O).

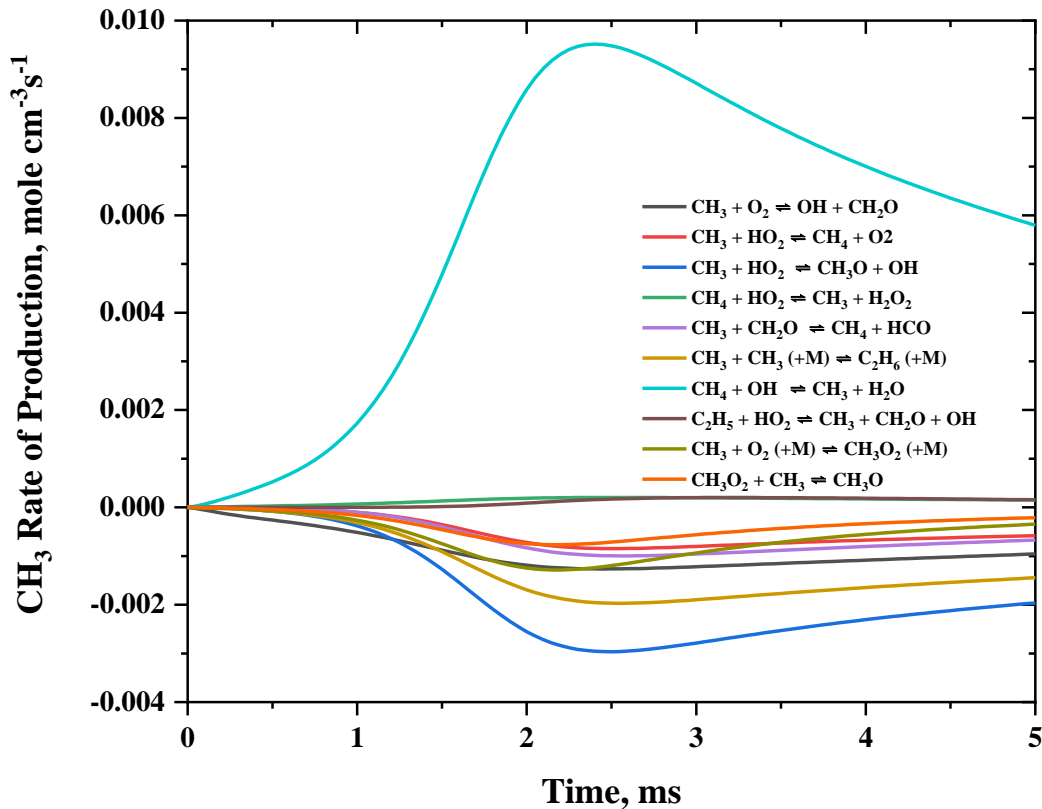


Figure 3.22. CH<sub>3</sub> rate of production analysis at 300 atm and 1100 K.

Whilst the majority of the remaining CH<sub>3</sub> is converted into CH<sub>3</sub>O and CH<sub>2</sub>O, 14.8% and 18.3% of CH<sub>3</sub> goes on to form CH<sub>3</sub>O<sub>2</sub> and C<sub>2</sub>H<sub>6</sub> respectively.

### 3.11.2. CH<sub>3</sub>O<sub>2</sub> Reaction Pathway

All CH<sub>3</sub>O<sub>2</sub> is formed through Reaction 3.1 ( $CH_3 + O_2 (+M) \rightleftharpoons CH_3O_2 (+M)$ ). The work of Fernandes et al. [226] demonstrates that for an N<sub>2</sub> bath gas at 293 K, Reaction 3.1 ( $CH_3 + O_2 (+M) \rightleftharpoons CH_3O_2 (+M)$ ) enters the high-pressure limit at approximately 100-500 bar. Whilst it cannot be assumed this behaviour is translatable to the conditions of direct-fired sCO<sub>2</sub> combustion, it can be approximated that chemistry is close to the fall-off region if not within it. Approximately two-thirds of the CH<sub>3</sub>O<sub>2</sub> formed reacts with CH<sub>3</sub> in Reaction 3.3 to form CH<sub>3</sub>O and the other third reacts primarily via three different reactants to form CH<sub>3</sub>O<sub>2</sub>H and some other by-products. These reactions are Reaction 3.2 ( $CH_4 + CH_3O_2 \rightleftharpoons CH_3 + CH_3O_2H$ ), Reaction 3.33 ( $CH_2O + CH_3O_2 \rightleftharpoons HCO + CH_3O_2H$ ) and Reaction 3.34 ( $CH_3O_2 + HO_2 \rightleftharpoons CH_3O_2H + O_2$ ). The contribution of CH<sub>3</sub> and CH<sub>4</sub> Reaction 3.2 ( $CH_4 + CH_3O_2 \rightleftharpoons CH_3 + CH_3O_2H$ ) is omitted from the RPA in Figure

3.21 for clarity and due to it being a minor reaction pathway relative to Reaction 3.33 ( $CH_2O + CH_3O_2 \rightleftharpoons HCO + CH_3O_2H$ ) and Reaction 3.34 ( $CH_3O_2 + HO_2 \rightleftharpoons CH_3O_2H + O_2$ ).



There is only one reaction of  $CH_3O_2H$  in which it dissociates into  $CH_3O$  and  $OH$  via Reaction 3.35 ( $CH_3O_2H \rightleftharpoons CH_3O + H$ ). The effect of a third body isn't considered in this reaction, however, the dissociation is almost instantaneous so the presence of  $CO_2$  is unlikely to have a large influence on this reaction.



As identified in Section 3.6.1, most of the rate coefficients used in these reactions have large uncertainty values and have been studied concerning atmospheric chemistry, so are studied at sub-atmospheric pressures. The lack of experimental studies of the  $CH_3O_2$  pathway with regards to combustion is due to its unimportance at low pressures where most combustion takes place, and therefore analysis and experimentation take place. Figure 3.23 shows the net reaction rate of three  $CH_3$  and  $O_2$  reaction pathways first 5 ms of the stoichiometric combustion of methane in a 96%  $CO_2$  dilution at 300 atm and 30 atm. The three reactions shown are Reaction 3.1 ( $CH_3 + O_2 (+M) \rightleftharpoons CH_3O_2 (+M)$ ), Reaction 3.7 ( $CH_3 + O_2 \rightleftharpoons CH_3O + O$ ) and Reaction 3.8 ( $CH_3 + O_2 \rightleftharpoons CH_2O + OH$ ). As seen in the figures in both conditions the rate of Reaction 3.7 ( $CH_3 + O_2 \rightleftharpoons CH_3O + O$ ) is negligible. However, Reaction 3.1 ( $CH_3 + O_2 (+M) \rightleftharpoons CH_3O_2 (+M)$ ) shows more interesting behaviour, as it is also negligible at 30 atm, and Reaction 3.8 ( $CH_3 + O_2 \rightleftharpoons CH_2O + OH$ ) is the dominant pathway. At 300 atm, the pressure of the Allam-Fetvedt cycle displays the net reaction rates of Reaction 3.1 ( $CH_3 + O_2 (+M) \rightleftharpoons CH_3O_2 (+M)$ ) and Reaction 3.8 ( $CH_3 + O_2 \rightleftharpoons CH_2O + OH$ ) show a similar net reaction rate, with Reaction 3.1 ( $CH_3 + O_2 (+M) \rightleftharpoons CH_3O_2 (+M)$ ) becoming dominant around the IDT. This highlights the need to revisit the reaction rate coefficients of these  $CH_3O_2$  at high pressures to determine their

accuracy. In addition, species time history measurements would also be useful to confirm the presence of  $\text{CH}_3\text{O}_2$ . Whilst shock tube measurements have not been performed before to the best of the authors' knowledge,  $\text{CH}_3\text{O}_2$  has been detected in a flow detector up to 1000 bar in a 2.2. internal diameter tube and 10 cm optical path length [226]. The authors used UV absorption spectroscopy of  $\text{CH}_3\text{O}_2$  at 240 nm using a high-pressure Xe-Hg lamp source and a PMT for detection. The cross-sectional area of  $\text{CH}_3\text{O}_2$  has also been studied previously [278, 279].  $\text{CH}_3\text{O}_2$  reactions have also been studied by Pilling and Smith in 1985 [231] using laser absorption diagnostic of  $\text{CH}_3\text{O}_2$  at 254 nm and  $\text{CH}_3$  at 216.36 nm. The absorption cross-section of  $\text{CH}_3\text{O}_2$  has more recently been measured by Yan and Krasnoperov [170] at 210 nm and 224 nm using laser absorption spectroscopy, however under these conditions there is a lot of interference from the  $\text{HO}_2$  radical, which may make shock tube spectroscopy of combustion reactions difficult.

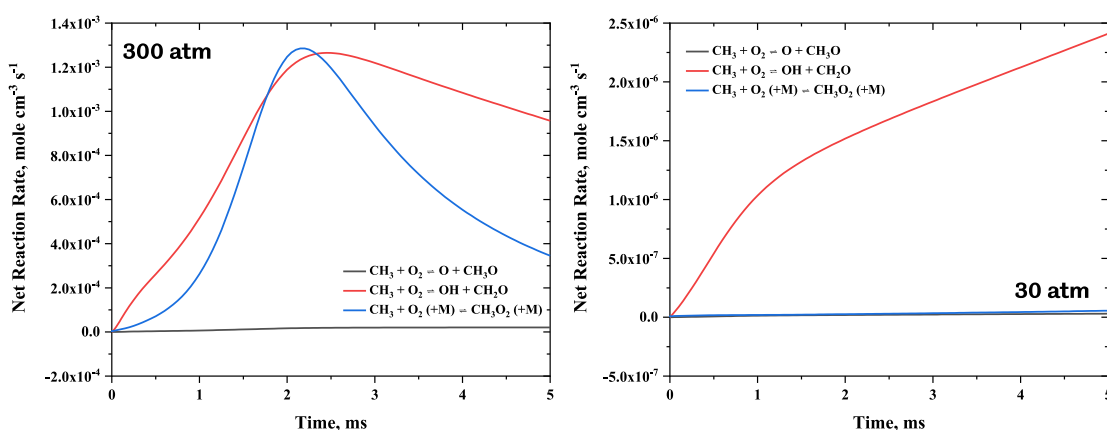


**Figure 3.23.** Comparison of competing  $\text{CH}_3+\text{O}_2$  reaction pathways at 30 atm and 300 atm.

Figure 3.24 shows the ROP analysis of both  $\text{CH}_3\text{O}_2$  and  $\text{CH}_3\text{O}_2\text{H}$  during the reaction at 300 bar. The first point to note is the smaller number of reactions in  $\text{CH}_3\text{O}_2\text{H}$  is due to their being only seven reactions that involve the species. In addition, Reaction 3.2 ( $\text{CH}_4 + \text{CH}_3\text{O}_2 \rightleftharpoons \text{CH}_3 + \text{CH}_3\text{O}_2\text{H}$ ) has one of the smallest peaks at the maximum for  $\text{CH}_3\text{O}_2$  formation, as shown in Figure 3.24 b), it is the most important over the first 0.5 ms of the reaction. This explains why it was identified as a negligible pathway in the RPA but did appear in some of the sensitivity analyses mentioned previously in Section 3.6 as it plays an important role in the early formation of  $\text{CH}_3\text{O}_2$ .

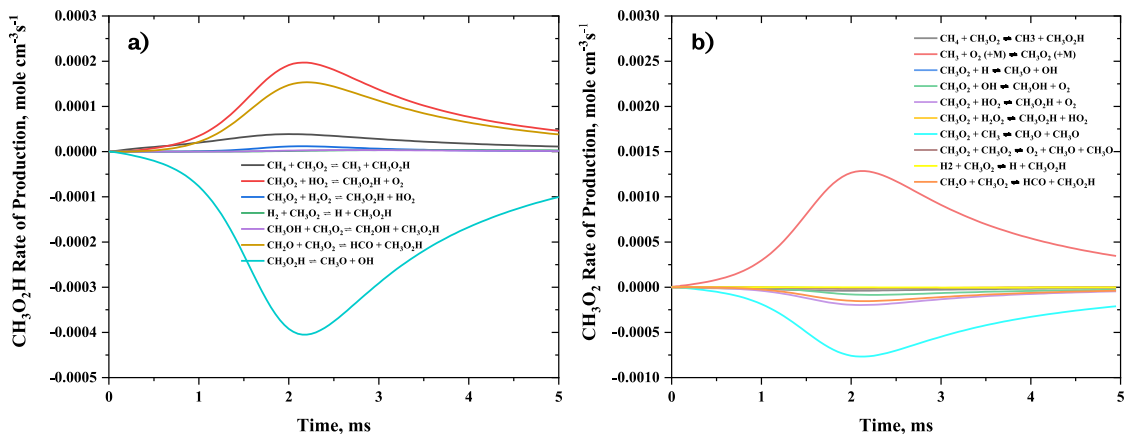


**Figure 3.24.** Rate of production analysis of a)  $\text{CH}_3\text{O}_2\text{H}$  and b)  $\text{CH}_3\text{O}_2$  at 300 bar.

### 3.11.3. Ethane Reaction Pathway

As well as the important  $\text{CH}_3\text{O}_2$  pathway, another important pathway shown in Figure 3.21, is the formation of  $\text{C}_2\text{H}_6$ , which accounts for 18.3% of the carbon flux from  $\text{CH}_3$ . Figure 3.25 shows an expanded pathway of  $\text{C}_2\text{H}_6$  to form  $\text{CO}$ . This reaction pathway is not given a numerical value past  $\text{C}_2\text{H}_4$  in Figure 3.25, as the values become negligible but give an indication of the reaction pathway. With this pathway, two significant species act as carbon sinks with low reaction rates at the point of IDT, this reaction pathway is a slower route to  $\text{CO}$  production. These are  $\text{C}_2\text{H}_6$  and  $\text{C}_2\text{H}_4$ , at the IDT, the rate of loss of  $\text{C}_2\text{H}_6$  is 23.6% of its rate of production, meaning that the species mole fraction is increasing. Similarly, the rate of loss of  $\text{C}_2\text{H}_4$  is 5.3% of its rate of production, meaning the species is accumulating quickly in the reaction.

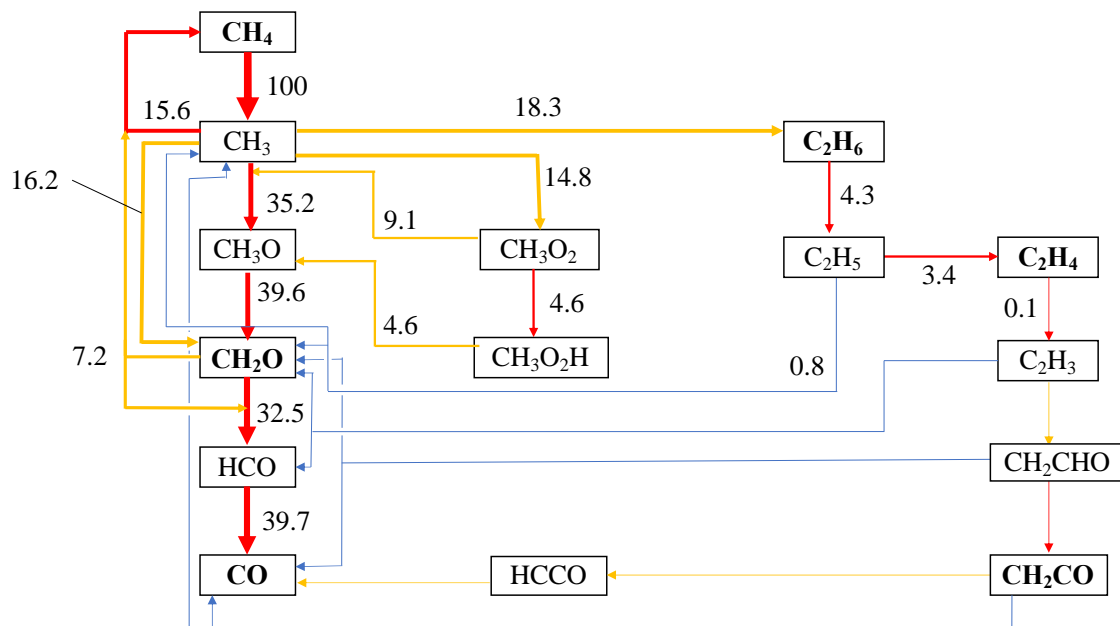


**Figure 3.25.** Expanded reaction pathway analysis of stoichiometric methane combustion in 96% CO<sub>2</sub> at 300 atm and 1100 K.

Figure 3.26 shows the mole fraction of four key stable intermediates of the combustion mechanism. The mole fraction of CO continues to increase throughout the first five ms of the reaction and continues to react to form CO<sub>2</sub> long after the initial onset of ignition. The graph on the right-hand side of Figure 3.26 is zoomed into the three remaining species, CH<sub>2</sub>O, C<sub>2</sub>H<sub>4</sub> and C<sub>2</sub>H<sub>6</sub>. At the IDT, the mole fraction of CH<sub>2</sub>O is over two times larger than that of C<sub>2</sub>H<sub>6</sub> and over eight times larger than that of C<sub>2</sub>H<sub>4</sub>. However, after approximately four and a half ms, the mole fraction of C<sub>2</sub>H<sub>4</sub> becomes the largest of the three species, due to its slow reactivity it continues to act as a carbon sink long into the reaction. Understanding the combustion of C<sub>2</sub>H<sub>4</sub> is therefore essential to understanding the latter stages of direct-fired sCO<sub>2</sub> combustion. This could be achieved by using the shock tube experimental technique by looking at the combustion of C<sub>2</sub>H<sub>4</sub> directly and making IDT and species concentration measurements. Therefore, this reaction pathway is going to be more important at the latter stages of combustion as C<sub>2</sub>H<sub>4</sub> is removed more slowly.

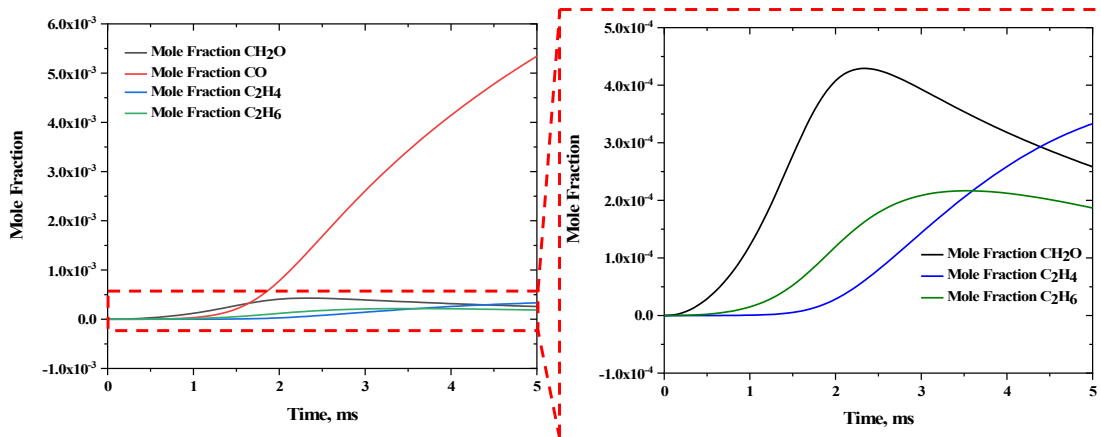


Figure 3.26. Mole fraction of stable combustion intermediate species.

### 3.11.4. CH<sub>2</sub>O Formation

Through the main formation pathway, the only stable intermediate formed is CH<sub>2</sub>O. CH<sub>3</sub>O is formed through three reactions of CH<sub>3</sub>, CH<sub>3</sub>O<sub>2</sub> and CH<sub>3</sub>O<sub>2</sub>H. Through investigating the ROP analysis of CH<sub>3</sub>O, the three key reactions are Reaction 3.3 ( $CH_3O_2 + CH_3 \rightleftharpoons CH_3O + CH_3O$ ), Reaction 3.14 ( $CH_3 + HO_2 \rightleftharpoons CH_3O + OH$ ) and Reaction 3.35 ( $CH_3O_2H \rightleftharpoons CH_3O + H$ ). This again highlights the importance of CH<sub>3</sub>O<sub>2</sub> to high-pressure combustion kinetics as 36.6% of CH<sub>3</sub>O is via Reaction 3.3 ( $CH_3O_2 + CH_3 \rightleftharpoons CH_3O + CH_3O$ ) which involves CH<sub>3</sub>O<sub>2</sub>, and 9.3% from the dissociation of CH<sub>3</sub>O<sub>2</sub> in Reaction 3.35. Combined this means that almost half of the CH<sub>3</sub>O is formed from reactions that involve the CH<sub>3</sub>O<sub>2</sub> pathway.

Almost 100% of CH<sub>3</sub>O reacts to form CH<sub>2</sub>O via Reaction 3.8 ( $CH_3 + O_2 \rightleftharpoons CH_2O + OH$ ) and Reaction 3.36 ( $CH_3O (+M) \rightleftharpoons CH_2O + H (+M)$ ) with each reaction accounting for 16.3% 83.2% of CH<sub>3</sub>O loss respectively. The rate coefficient used in USC II and the UoS sCO<sub>2</sub> mechanism is taken from GRI 3.0 based on both theoretical [280] and experimental work [281]. A more recent rate coefficient has been published in 2001 by Hippler et al. [282] at higher pressures so may be more relevant to the conditions of direct-fired sCO<sub>2</sub> combustion, which was not identified as important during the sensitivity analysis and is worth considering for future mechanism alterations. The other key reaction in the formation of CH<sub>2</sub>O is directly from Reaction 3.8 ( $CH_3 + O_2 \rightleftharpoons CH_2O + OH$ ) which contributes to 24.6% of the ROP of CH<sub>2</sub>O.



Figure 3.27 shows the rate of production analysis of  $\text{CH}_2\text{O}$  at 300 bar and 1100 K. Initially it is Reaction 3.8 ( $\text{CH}_3 + \text{O}_2 \rightleftharpoons \text{CH}_2\text{O} + \text{OH}$ ) is the most important reaction, which is overtaken by Reaction 3.36 ( $\text{CH}_3\text{O} (+\text{M}) \rightleftharpoons \text{CH}_2\text{O} + \text{H} (+\text{M})$ ) after the concentration of  $\text{CH}_3\text{O}$  increases. Interestingly, after the IDT, the rate of production/loss begins to tend to zero for all reactions except for Reaction 3.37 ( $\text{C}_2\text{H}_5 + \text{HO}_2 \rightleftharpoons \text{CH}_3 + \text{CH}_2\text{O} + \text{OH}$ ) which shows a constant increase across the first 5 ms of the reaction. This highlights how the ethane reaction pathway becomes more important at the latter stages of the reaction.

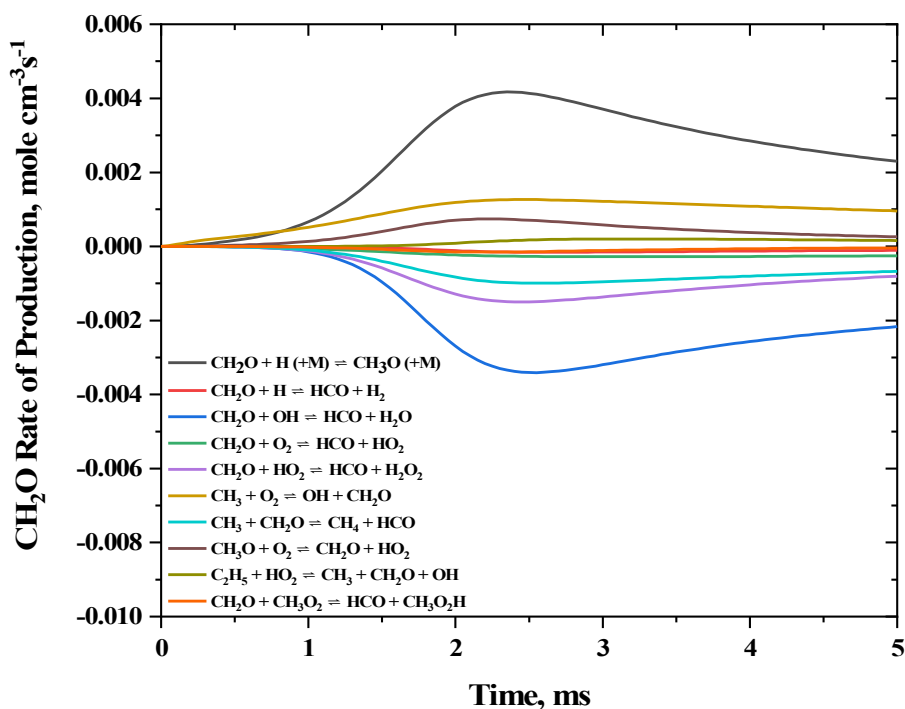
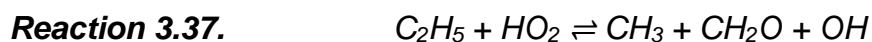


**Figure 3.27.** Rate of production analysis of  $\text{CH}_2\text{O}$ .

$\text{CH}_2\text{O}$  is a key intermediate of combustion [283] and understanding its chemistry has always been vital to understanding the overall chemistry, and this is no different in the conditions of direct-fired  $\text{sCO}_2$  combustion.

### 3.12. Summary and Outlook

The key output of this research chapter was the creation and development of the UoS sCO<sub>2</sub> mechanism for modelling combustion at the conditions of direct-fired sCO<sub>2</sub> combustion. The mechanism was created by collating all available IDT data in any dilution of CO<sub>2</sub>, at various equivalence ratios and sub-atmospheric pressures to over 250 bar. There were three fuels investigated, methane, hydrogen, and syngas due to methane being the primary component of natural gas and syngas from the gasification of coal and biomass being considered an alternative fuel. Furthermore, hydrogen and carbon monoxide are key intermediates of methane combustion and form at the latter stages of the reaction. By using four existing chemical kinetic mechanisms validated for low-pressure and low CO<sub>2</sub> dilutions to 52 datasets, the four mechanisms were compared quantitatively by looking at the percentage difference between the simulated and experimental data. This information, coupled with the sensitivity analysis performed at conditions of interest was used to identify important reactions in determining the IDT. This information was subsequently used to create the UoS sCO<sub>2</sub> Mech by altering the rate coefficients to better model the IDT of the 52 datasets as assessed by a detailed quantitative analysis. The UoS sCO<sub>2</sub> mechanism showed an improvement in all three fuels in terms of the average absolute error and was the best fit of 57.7% of the datasets. The next step was using the UoS sCO<sub>2</sub> Mech to model the chemical kinetic mechanism of combustion at the conditions of direct-fired sCO<sub>2</sub> power cycles. RPA and ROP analyses were used to investigate which reactions were consuming and forming different species, as well as identifying what was the key reaction pathways.

The UoS sCO<sub>2</sub> 1.0 Mechanism is the first chemical kinetic mechanism created based on IDT data from three fuels recorded on more than one shock tube. No sCO<sub>2</sub> mechanism developed has been created using so many datasets at such a variety of pressures, temperatures, and test gas compositions. Therefore, the UoS sCO<sub>2</sub> mechanism is validated over a greater range of conditions through its low average  $E$  (%) as proved in the sensitivity analysis. The UoS sCO<sub>2</sub> 1.0 Mechanism has been made available through Harman-Thomas et al. [87] and

therefore can be subsequently utilised by any researchers for modelling the combustion of methane, hydrogen and syngas in CO<sub>2</sub>.

Whilst the UoS sCO<sub>2</sub> Mech is an improvement over the existing chemical kinetic mechanisms for modelling combustion at high pressures and large dilutions of CO<sub>2</sub>, there is still some room for improvement.

- Firstly, more IDT data of hydrogen and syngas is required to expand the current limited number of datasets to a larger range of conditions, ensuring the accuracy of the model. These datasets would expand the current range and be used to further tune UoS sCO<sub>2</sub> Mech.
- Secondly, more IDT data for methane and methane/hydrogen blends is needed to validate the rate coefficients made. As the mechanism was created to fit all available data, more datasets would prove that these changes are valid, and prove the reliability of the datasets. Utilising different blends such as methane/hydrogen is useful as it would validate the mechanism under completely new conditions.
- Thirdly, IDT data of important intermediate species identified through the RPA, such as CH<sub>2</sub>O, C<sub>2</sub>H<sub>6</sub> and C<sub>2</sub>H<sub>4</sub> would be useful in ensuring that the different aspects of the reaction pathways are being accurately modelled.
- Finally, species concentration over long-time periods beyond IDT, most likely using tailored shock tube conditions would be good to monitor the proposed reactivity of species and different reaction pathways. This data could be used to tune the key rate coefficients more finely for species production and consumption.

## **4. Autoignition study Hydrogen and Syngas in CO<sub>2</sub>**

The experimental work undertaken as part of this EngD project is described within this section and the results are critically discussed. This work was performed in collaboration with the King Abdullah University of Science and Technology (KAUST) using their high-pressure shock tube (HPST) and was subsequently published as two journal articles [88, 89].

### **4.1. KAUST High-Pressure Shock Tube**

As the theory behind shock tubes was discussed in detail in Chapter 2 so only an overview of the KAUST HPST is given here. The KAUST HPST can withstand pressures of up to 300 bar and is fabricated from stainless steel with an electropolished internal surface [218]. The driver section of the tube is 6.6 m long, and the driven section is variable up to 6.6 m in 2.2 m intervals, depending on the desired test time, with both sections having an internal diameter of 10.16 cm [284]. A DDA usually operating with two pre-scored aluminium diaphragms is used for greater control and repeatability between the experimental runs [285].

The incident shock speed is determined using six PCB 113B26 piezo-electric pressure transducers (PZTs) over the last 3.6 m of the driven section [99]. The PZTs trigger five ultrafast (350 MHz) Agilent 53220A frequency counters, which are used to calculate shock velocity as described in Section 2.6.8 [218]. The pressure trace is determined at 1.0 cm from the endwall using a Kistler 603B1 PZT [99].

Before filling, the shock tube is evacuated to less than  $10^{-5}$  Torr using a turbomolecular pump and mixtures are prepared manometrically in a stirred 20L mixing vessel [218]. The chemiluminescence is monitored at the endwall through a sapphire window using Thorlabs PDA36A photo-detectors [99]. A detailed schematic of the endwall arrangement for the KAUST HPST is available in AlRamadan et al. [284]. Research grade gases (99.999%) were used for each of the mixtures to ensure homogeneity.

For the hydrogen (H<sub>2</sub>) IDT data, the measured uncertainties in the determined post-shock pressure and temperature,  $p_5$  and  $T_5$  respectively, were determined to be <1%. The incident shock attenuation rates varied from 0.5 to 1.8 %/m, depending on the composition of the test gas mixture.

#### **4.1.1. Identification of Time Zero**

The complexity of the identification of time-zero is increased significantly when using test gas mixtures with a large dilution of CO<sub>2</sub> due to the large influence of bifurcation [122, 200]. Following the bifurcation, an oblique shock forms and proceeds the normal shock close to the boundary layer, thus altering the effect of the test gas region 5. This effect varies across the shock tube, being more pronounced closer to the shock tube walls and in regions further from the endwall. Previous research into the study of IDTs in CO<sub>2</sub> by Hargis et al. [122] recommends the use of endwall pressure transducers for the determination of time-zero. However, the KAUST HPST does not have the facilities to make endwall pressure measurements, so the IDT was determined using a Kistler transducer 10.48 mm from the endwall. Time zero determination in this study differed by extrapolation of the onset of the reflected shock wave. Instead, time zero is determined using the start of the reflected shock pressure rise based on previous research [122, 200].

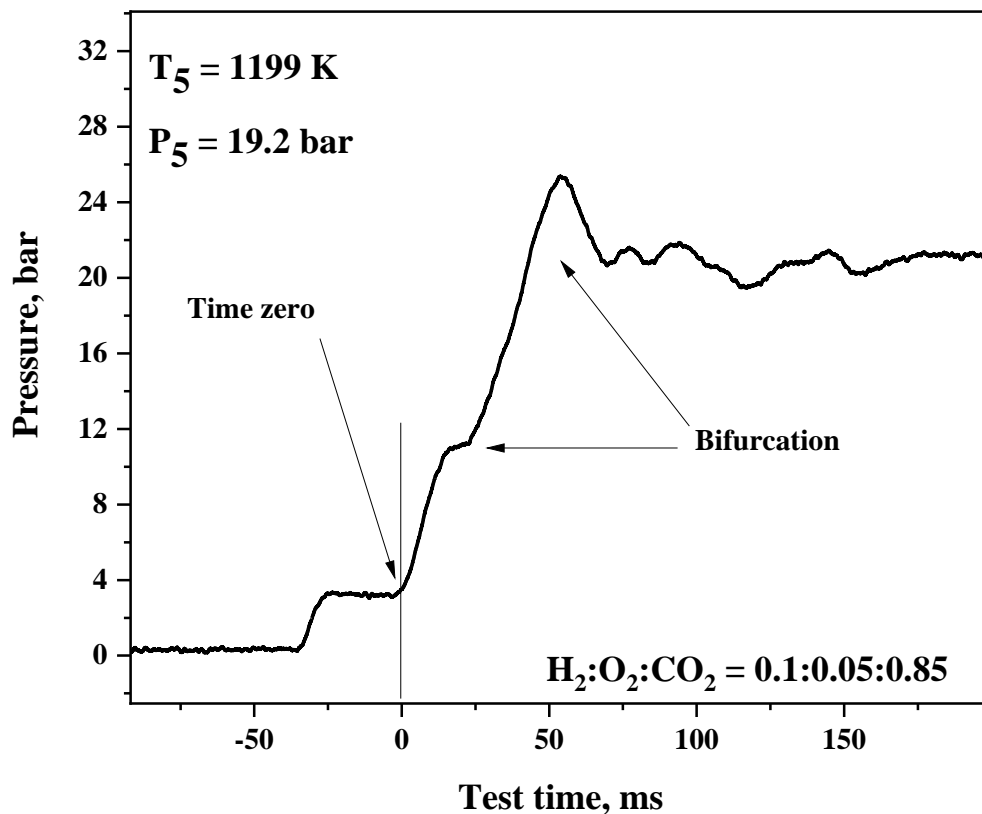


**Figure 4.1.** Sidewall pressure history for an 85% CO<sub>2</sub> diluted H<sub>2</sub> mixture.

Figure 4.1 shows one of the sidewall emissions traces for a hydrogen test gas mixture in an 85% CO<sub>2</sub>-diluted mixture at 20 bar. The extent of the bifurcation is smaller than in Hargis et al. [122], and this is most likely due to the sidewall pressure transducer in the Texas A & M shock tube facility being further from the endwall than in the KAUST HPST at 16 mm. Figure 4.1 shows three different increases in pressure. The first is due to the passage of the incident shock wave (ISW). The second is the time-zero, which as discussed is the passage of the reflected shock wave. Lastly, the third increase is due to the bifurcation splitting the passage of the reflected shock wave (RSW) into two distinct peaks.

#### 4.1.2. Determination of Ignition Delay Time

Ideally, the temperature and pressure field behind the RSW will be homogeneous and will ignite near the endwall, as the test gas here is exposed to the highest temperature for the longest duration. The onset of ignition is determined by the

steepest point in the endwall pressure rise of the OH\* chemiluminescence trail as recorded by a PMT.

In the test gas mixtures with large concentrations of CO<sub>2</sub>, small hot spots can develop as the RSW interacts with the boundary layer [286]. These hot spots disrupt the homogeneity of the test gas mixture and can lead to early ignition away from the endwall and false interpretation of the IDT from both the pressure and emissions traces. In this study, there was a noticeable rise in the OH\* chemiluminescence trail. A similar observation was also made by Karimi et al [200] in their heavily diluted CO<sub>2</sub> mixtures. The authors linked the formation of ignition kernels, which are detected by the sidewall, to the increased effect of bifurcation. Endwall emissions avoid this as it sees the centre of the shock tube and thus responds to the bulk volume of the gas [155]. An example of the early IDT from the sidewall OH\* measurements from the present work is shown in Figure 4.2.

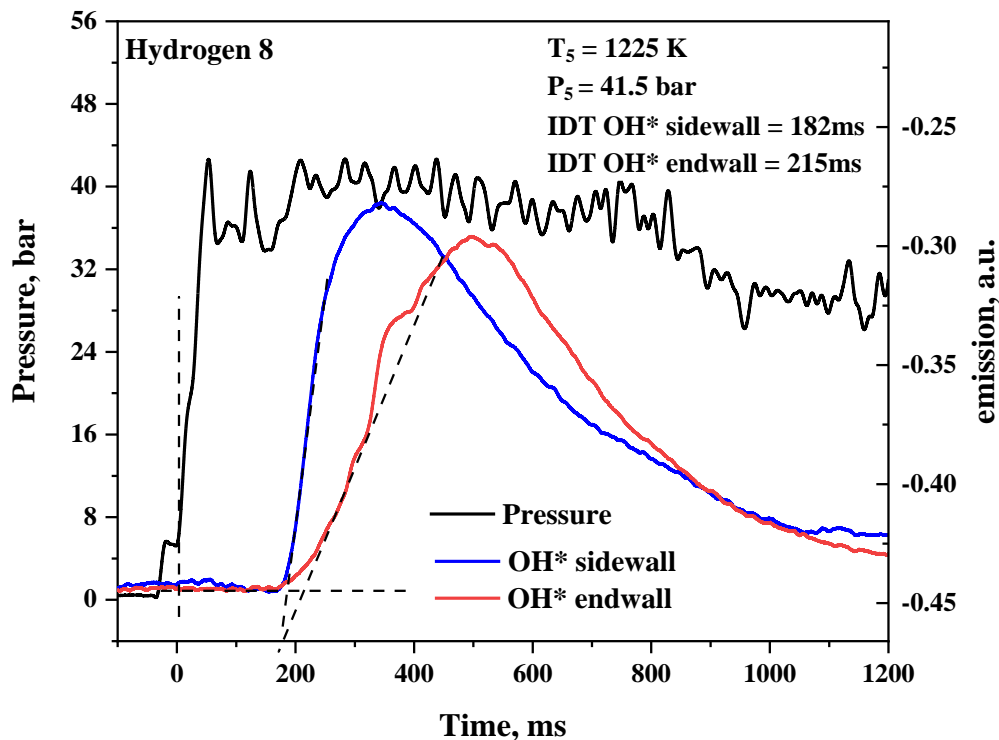


**Figure 4.2.** Representative profiles for IDT measurement of H<sub>2</sub> early ignition at 40 bar from H<sub>2</sub> dataset 8.

A comparison of endwall IDTs for H<sub>2</sub> mixture 6 is shown in Figure 4.3 alongside sidewall IDT data from Shao et al. [85], recorded at the same pressure and test gas composition. The measurements from both facilities agree with experimental error for the lowest temperature datasets, but the discrepancy decreases significantly at the highest temperatures. The disagreement at higher temperatures is partly due to the larger error in the fastest IDTs (< 100 μs), due to the increased uncertainty in the determination of time zero. However, the discrepancy across the dataset can be attributed to the difference in experimental technique. The sidewall emissions used by Shao et al. [85] suffer from premature ignition by the sidewall as discussed, leading to an underprediction of the IDT compared to the present study.

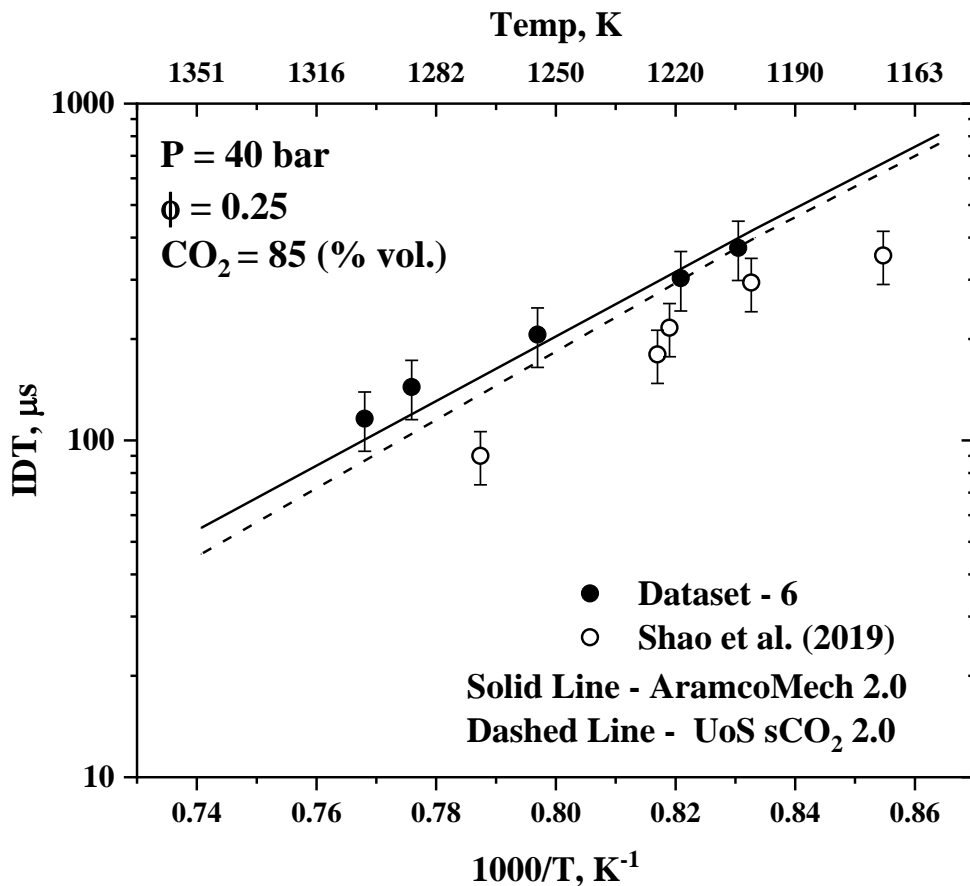


Figure 4.3. Comparison of IDTs (H<sub>2</sub> mixture 6) with literature data [85].

## 4.2. Modelling Procedure

The modelling procedure used in this chapter is similar to that described in Section 3.3, so only a brief overview is given. The most significant change was the identification of the double peak in the simulated OH mole fraction, which determined the simulated IDT difficult. The shock tube IDTs were modelled using Chemkin-Pro (zero-D, batch reactor, constant UV) using two chemical kinetic mechanisms, namely AramcoMech 2.0 and UoS sCO<sub>2</sub> 2.0. UoS sCO<sub>2</sub> 2.0 was based on UoS sCO<sub>2</sub> 1.0 developed and discussed in Section 3. The only change was the change of the third body efficiency of CO<sub>2</sub> in Reaction 4.1 ( $H + O_2 (+M) \rightleftharpoons HO_2 (+M)$ ) from 2.18 to 3.6 as reported in AramcoMech 2.0, as this important reaction led to an underprediction in IDT as the smaller reaction, likely an artefact of trying to match the faster sidewall measurements reported for syngas and hydrogen combustion during the creation of the mechanism. The importance of this reaction is discussed in detail in this chapter.



The mechanisms' performance was investigated using normalised OH sensitivity analysis to identify the important reactions in IDT prediction under the various conditions studied. ROP analysis was also used to study the key reaction pathways for the two different fuels. The performance of the two mechanisms was compared quantitatively using Equation 3.6 and the onset of ignition was determined by using the maximum gradient of the simulated OH time history.

### 4.2.1. Bimodal Splitting in the Simulated Time History

During the modelling work undertaken as part of this chapter, it was noted that the OH time history sometimes contained two steepest points in the gradient. This was normally due to two distinct peaks in the OH time history as shown in Figure 4.4. In Figure 4.4 (a), there is one peak in the OH time history, which contains both the H<sub>2</sub> and CO ignition event. Whereas in Figure 4.4 (b), there are two distinct peaks in the OH time history, each one corresponding to separate ignition of H<sub>2</sub> and CO. The extent of the splitting of the two ignition events is

dependent on the test gas composition, pressure, temperature and most importantly, the H<sub>2</sub>:CO ratio and equivalence ratio.

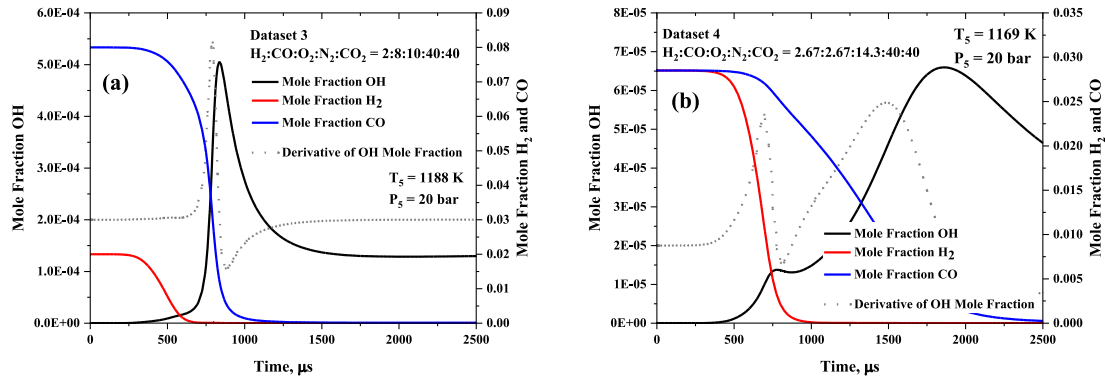


**Figure 4.4.** Mole fraction of OH, H<sub>2</sub> and CO for (a) H<sub>2</sub>:CO:O<sub>2</sub>:N<sub>2</sub>:CO<sub>2</sub> = 2:8:10:40:40 at 20 bar and 1188 K and (b) H<sub>2</sub>:CO:O<sub>2</sub>:N<sub>2</sub>:CO<sub>2</sub> = 2.85:2.85:14.3:40:40 at 20 bar and 1169 K modelled by UoS sCO<sub>2</sub> 2.0.

As shown in Figure 4.4 (a) for mixture 3, the concentration of CO exceeds that of H<sub>2</sub>, and this is likely to contribute to the single peak in the OH mole fraction, as the small peak caused by H<sub>2</sub> ignition is covered by that of CO. This effect can make the determination of IDT from the simulated OH mole fraction difficult, especially if all this behaviour is not being modelled correctly. The first peak in the OH time history should be used to determine the IDT, as this is the peak that will be observed experimentally on the OH\* chemiluminescence trace as in most instances, the ignition of CO does not occur until after 1500  $\mu$ s, well past the observable test time in a non-tailored shock tube. However, the complication arises when there are two ignition events close together ( $\sim$ 100  $\mu$ s), this usually occurs at the highest temperature datapoints, where the error in the experimental IDTs is also larger as the determination of time-zero becomes more difficult.

As shown in Figure 4.4 (a), mixture 3 appears to only have one peak in the OH time history, which consists of two steepest points within this peak, so there are two possible IDTs. Figure 4.5 shows a plot of the IDT against the inverse of the temperature for dataset 3, with the IDT for H<sub>2</sub> ignition and CO ignition, along with the average of the two peaks for both AramcoMech 2.0 and UoS sCO<sub>2</sub> 2.0. At the highest temperature datapoint, the simulated IDT for H<sub>2</sub> and CO ignition vary only by 50  $\mu$ s. Experimentally, the difference between these two separate ignition

events would be indistinguishable from the OH\* chemiluminescence trace. This may explain why at the highest temperatures, the average of the two simulated ignitions agrees best with the experimental data.

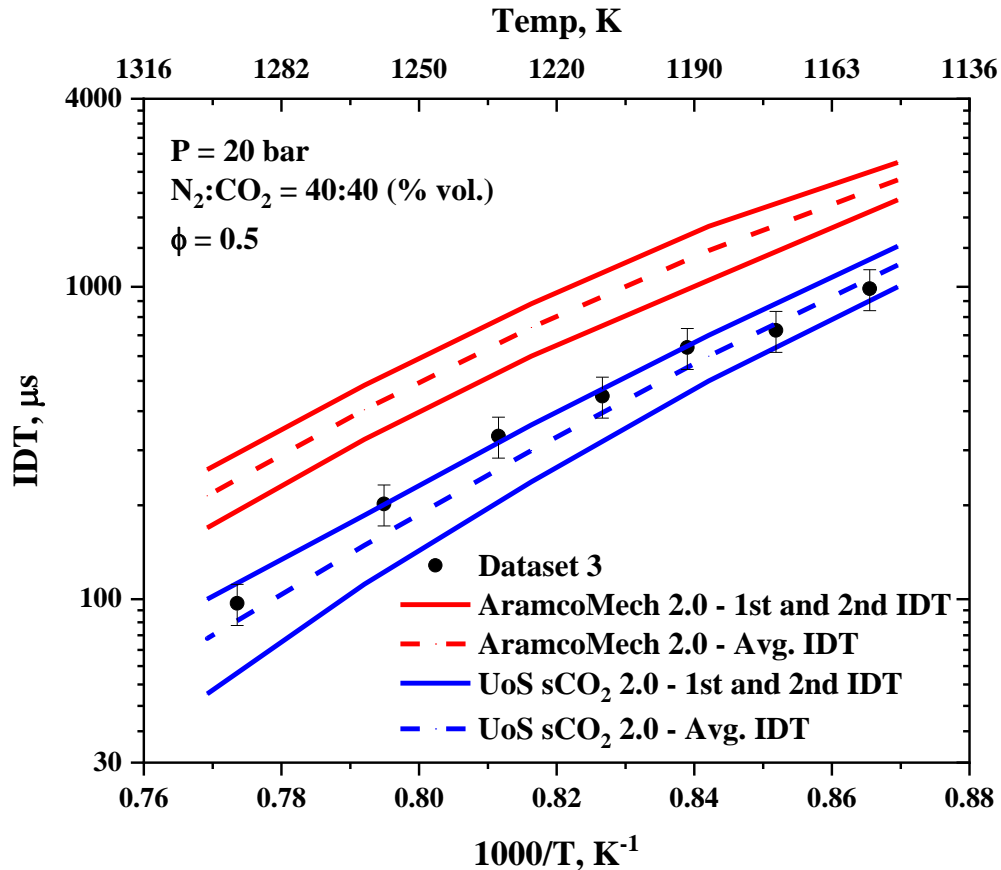


**Figure 4.5.** A plot of average IDT for dataset 3  $\text{H}_2:\text{CO}:\text{O}_2:\text{N}_2:\text{CO}_2 = 2:8:10:40:40$  at 20 bar and the  $\text{H}_2$  and  $\text{CO}$  IDTs which are the low and high bounds, respectively.

Therefore, under conditions where the two ignition events of  $\text{H}_2$  and  $\text{CO}$  are close (within  $\sim 100$  ms), it may be preferable to use an average value. However, in the case of dataset 3, the first ignition of  $\text{H}_2$  is much smaller than that of  $\text{CO}$  and is barely detectable at the lowest temperatures, it would not be detectable experimentally and the larger IDT is used for consistency across the dataset. This highlights the subjectivity of IDT determination of syngas in a  $\text{CO}_2$  bath gas; therefore, care should be taken to determine the simulated IDT as close to what is being observed experimentally, and the method of IDT determination discussed for each dataset.

The OH\* chemiluminescence traces were also investigated to see if this simulated bimodal production of OH is observed experimentally. Figure 4.6

shows the sidewall pressure trace as well as the OH\* sidewall and endwall chemiluminescence traces for one IDT data point for syngas mixture 3 at 1145.1 K. In this case, the endwall chemiluminescence traces display two peaks, indicating that the production of OH is bimodal as seen in the modelling simulations. Karimi et al. [200] also saw a bimodal peak in their OH\* sidewall and endwall chemiluminescence traces, without deviating from constant pressure. Both observations support the simulated bimodal time history of OH of syngas combustion in CO<sub>2</sub> being a real effect.

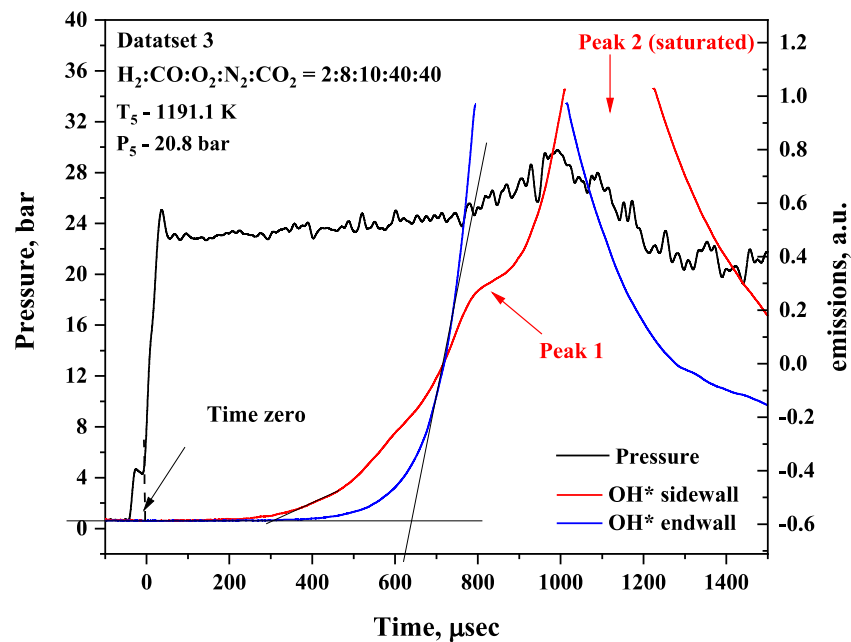


**Figure 4.6.** Experimental pressure trace (left-hand axis) and OH\* sidewall and endwall OH\* emissions traces (right-hand axis) for syngas dataset 3 at 1191.1 K.

Chemkin was used to investigate why this splitting of the OH time history occurred when in a large dilution of CO<sub>2</sub>. Syngas dataset 8 was performed in an 85% dilution of CO<sub>2</sub>, so theoretically should experience this effect to the largest extent and be thus used for this investigation. Figure 4.7 shows the mole fraction of OH, H<sub>2</sub> and CO for (a) mixture 8 and (b) mixture 8 in an 85% dilution of N<sub>2</sub>. Figure 4.7 (a) shows that the ignition of CO is slowed relative to H<sub>2</sub>, whereas in Figure 4.7 (b) the ignition of H<sub>2</sub> and CO are almost simultaneous, suggesting this is a chemical effect of CO<sub>2</sub>. ROP analysis showed that for the two conditions, the majority of CO reacts via Reaction 4.2 ( $CO + OH \rightleftharpoons CO_2 + H$ ). It was noted, however, that the rate of Reaction 4.2 ( $CO + OH \rightleftharpoons CO_2 + H$ ) was significantly

faster in N<sub>2</sub>. It is important to note that for the majority of the figures Reaction 4.2 ( $CO + OH \rightleftharpoons CO_2 + H$ ) is proceeding in the reverse direction to form CO and OH. This is done as it is common notation to display the reactions in the direction they are inputted into the Chemkin mechanism file.



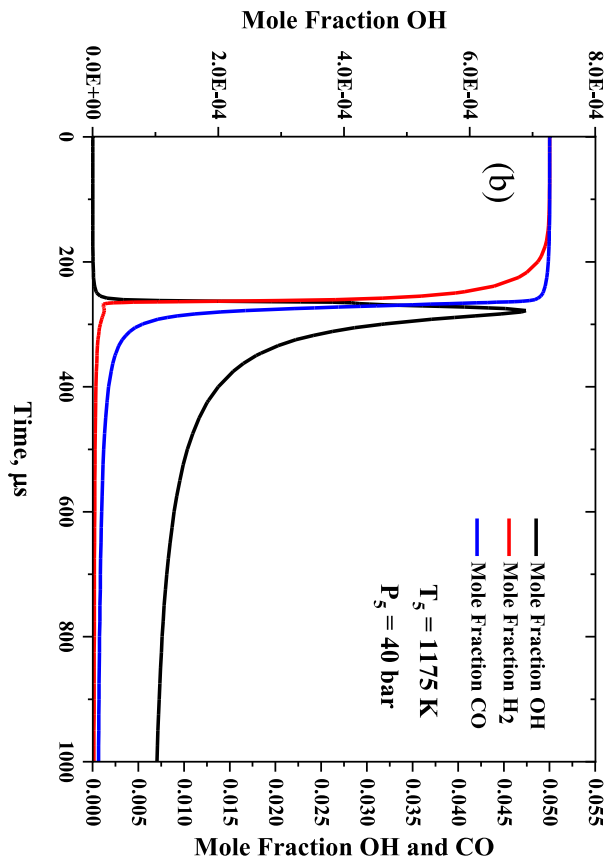
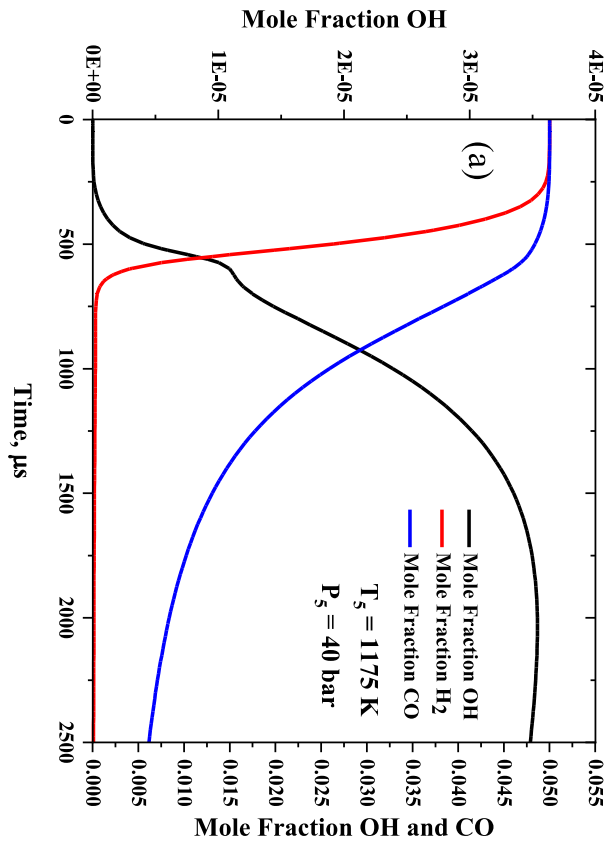


**Figure 4.7.** Mole fraction of OH, H<sub>2</sub> and CO for (a) H<sub>2</sub>:CO:O<sub>2</sub>:CO<sub>2</sub> = 5:5:5:85 at 40 bar and 1175 K and (b) H<sub>2</sub>:CO:O<sub>2</sub>:N<sub>2</sub> = 5:5:5:85 at 40 bar and 1175 K modelled by UoS sCO<sub>2</sub> 2.0.

Looking at the rate of reactions using Chemkin-Pro, it was noted that for Reaction 4.2 ( $CO + OH \rightleftharpoons CO_2 + H$ ), the rate of the forward reaction far exceeded the reverse, and the rate of the reverse is negligible. However, when combusting in a  $CO_2$  bath gas, the rate of the reverse reaction is not negligible, owing to the large initial concentration of  $CO_2$ . Therefore, in  $CO_2$ , the rate of the reverse reaction is so large that it slows down the ignition of CO by slowing down the overall rate of CO consumption. Therefore, under these conditions, and when using test gas compositions, where this effect is large enough, the ignition of the two different fuels splits into two different IDTs, creating a bimodal OH time history. This effect, if not simulated correctly, may lead to the incorrect determination of IDT from simulated OH time histories as the overlap of the two ignitions can significantly alter the determined IDT. Furthermore, the slower consumption of CO relative to  $H_2$  is also because  $CO_2$  bath gas reduces the maximum temperature achieved during combustion. This limits the rate of the temperature-dependant forward reaction, meaning that CO consumption occurs slower compared to  $N_2$  bath gas. This can be shown via constant temperature simulations which indicate that CO consumption is significantly slowed relative to constant UV simulations (see Figure 4.8). These two effects couple to reduce the overall rate of CO consumption via Reaction 4.2 ( $CO + OH \rightleftharpoons CO_2 + H$ ) meaning the two fuels get separated in two separate ignition events, making the determination of IDT more difficult.

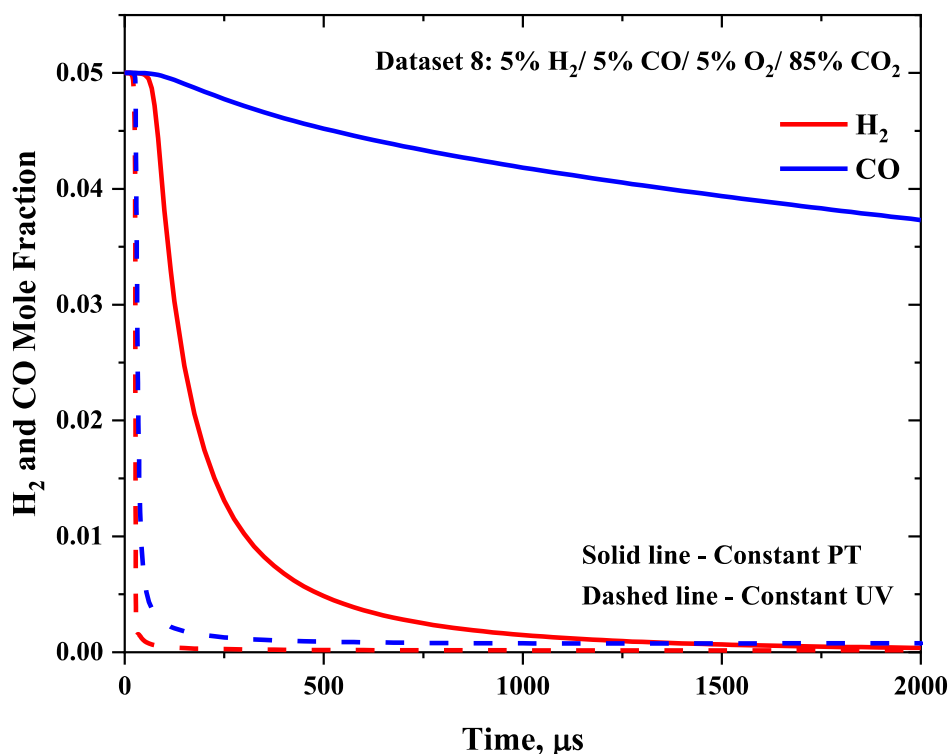


**Figure 4.8.** Constant pressure and temperature and constant UV simulations showing H<sub>2</sub> and CO consumption of syngas dataset 8 (85% CO<sub>2</sub>).

There is also a further complication that CO formation can also be a prominent factor in the ignition of other fuels, as it forms so readily from CO<sub>2</sub> during combustion. Therefore, being able to accurately simulate CO combustion may be one of the most important factors for the combustion of any fuels in CO<sub>2</sub>. Further investigation into the experimental species' time histories of both CO and OH at a range of experimental conditions is essential to demonstrate a chemical kinetic mechanism's ability to model this behaviour.

### 4.3. Hydrogen IDT Datasets

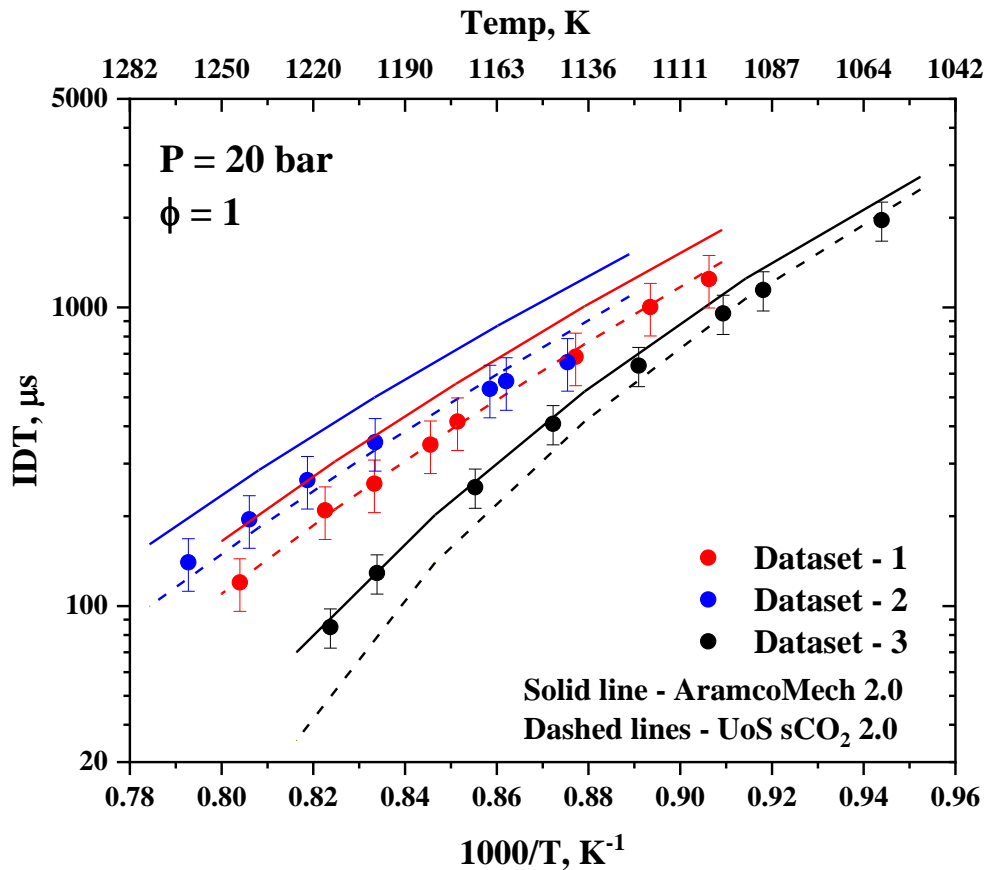
The KAUST HPST was used to record eight IDT datasets for H<sub>2</sub> as shown in Table 4.1. Seven datasets were recorded in some dilution of CO<sub>2</sub> in the test gas mixture and one in a pure N<sub>2</sub> bath gas as a comparison. These datasets were selected to fill the existing gaps in the literature for H<sub>2</sub> IDT in CO<sub>2</sub> as well as compare our results to available literature data.

**Table 4.1.** Hydrogen IDT mixtures studied in this work and results of quantitative analysis.

Mix.	Species Mole Fraction				Mixture Conditions			Average Absolute Error ( <i>E</i> ) (%)	
	H <sub>2</sub>	O <sub>2</sub>	N <sub>2</sub>	CO <sub>2</sub>	T [K]	P [bar]	$\phi$	AramcoMech 2.0	UoS sCO <sub>2</sub> 2.0
<b>1</b>	10	5	35	50	1103- 1243	20.5- 21.7	1.0	40.9	3.1
<b>2</b>	10	5	-	85	1142- 1261	18.5- 19.6	1.0	50.0	11.8
<b>3</b>	10	5	85	-	1059- 1214	19.2- 20.5	1.0	13.6	18.2
<b>4</b>	12	3	35	50	1123- 1238	20.2- 21.0	2.0	11.4	22.4
<b>5</b>	4.3	10.7	35	50	1162- 1255	19.4- 19.9	0.2	59.5	29.0
<b>6</b>	5	10	-	85	1204- 1302	42.0- 43.0	0.25	17.0	14.4
<b>7</b>	7.5	7.5	-	85	1164- 1300	41.4- 42.1	0.5	7.8	18.1
<b>8</b>	10	5	-	85	1123- 1266	40.5- 41.6	1.0	24.4	11.6
<b>Average <i>E</i> (%)</b>								28.1	16.1

#### 4.3.1. Effect of CO<sub>2</sub> Dilution at 20 bar

Datasets 1-3 concern the effect of changing the concentration of CO<sub>2</sub> in the bath gas from 85% N<sub>2</sub> to 85% CO<sub>2</sub> for stoichiometric H<sub>2</sub> combustion. Dataset 1 was composed of 50% CO<sub>2</sub> and 35% N<sub>2</sub>, whereas Datasets 2 and 3 were composed of 85% CO<sub>2</sub> and 85% N<sub>2</sub> respectively. Figure 4.9 shows these three datasets simulated by AramcoMech 2.0 and UoS sCO<sub>2</sub> 2.0.



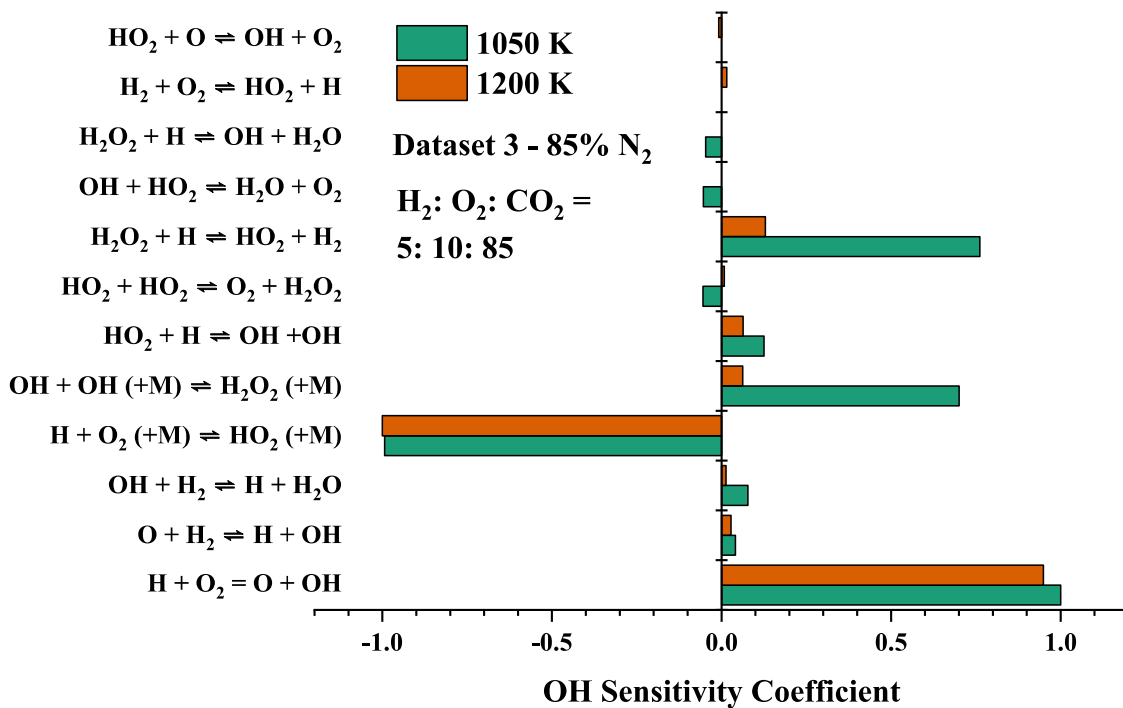
**Figure 4.9.** Comparison of IDTs of datasets 1, 2 and 3 with AramcoMech 2.0 and UoS sCO<sub>2</sub> 2.0.

Figure 4.9 shows that as the concentration of CO<sub>2</sub> is increased, the IDT increases, owing to the decreasing of the mixture reactivity. The reason for this is due to the smaller rate of OH production. Sensitivity analysis reveals that this is due to the ratio of the H + O<sub>2</sub> reaction between the chain propagation Reaction 4.1 ( $H + O_2 (+M) \rightleftharpoons HO_2 (+M)$ ) and chain branching Reaction 4.3 ( $H + O_2 \rightleftharpoons O + OH$ ). As the concentration of CO<sub>2</sub> is increased, Reaction 4.1 ( $H + O_2 (+M) \rightleftharpoons HO_2 (+M)$ ) is favoured, thus slowing down the overall rate of OH production.



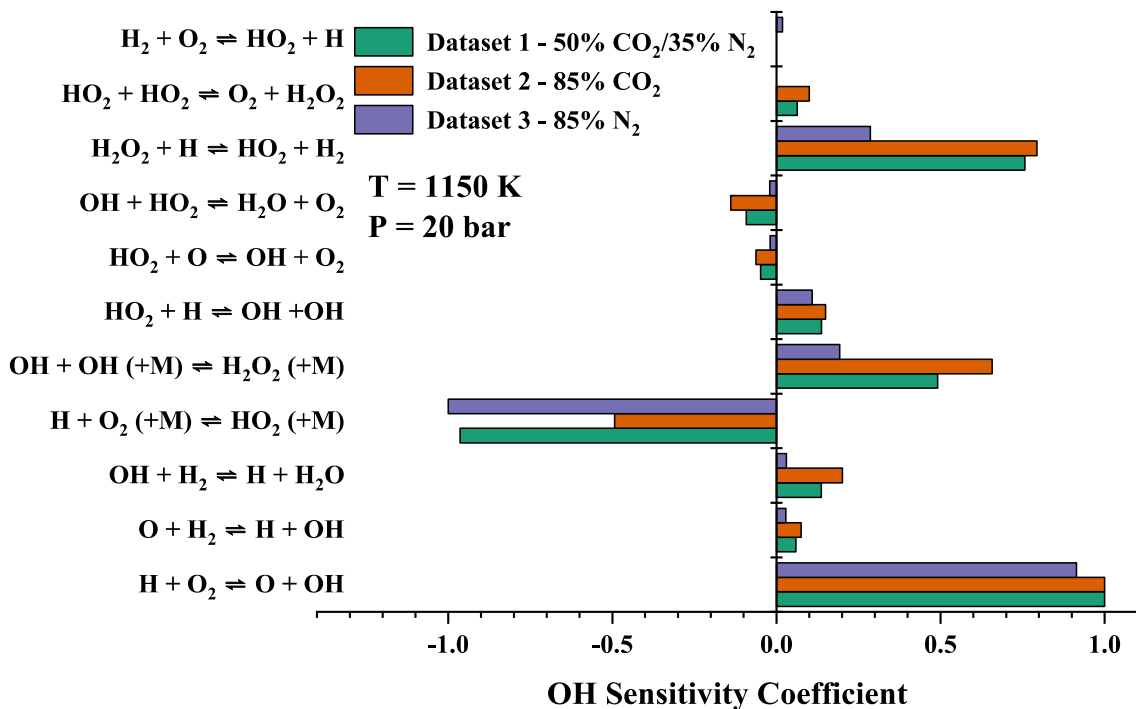
Furthermore, there is the added complication that CO<sub>2</sub> is also competing for H radicals via Reaction 4.2 ( $CO + OH \rightleftharpoons CO_2 + H$ ) to form CO and OH. Karimi et al. [200] noted there was no significant difference between the experimental IDTs for syngas in a CO<sub>2</sub> or Ar bath gas.

One observation from Figure 4.9 is the convergence of the IDTs for all three datasets as the lower temperatures, which isn't modelled particularly well by either of the mechanisms. There are two possible explanations for this. Either the mechanisms are lacking some fundamental chemistry required to model the IDT at low temperatures, or the longer IDTs studied in 85% CO<sub>2</sub> suffer from premature ignition because of bifurcation. UoS sCO<sub>2</sub> 2.0 is shown in Figure 4.9 and the quantitative analysis shown in Table 4.1 is a better fit than AramcoMech 2.0 for datasets 1 and 2 which contain some dilution of CO<sub>2</sub>. On the other hand, AramcoMech 2.0 performs better for dataset 3 in 85% N<sub>2</sub>, whereas UoS sCO<sub>2</sub> 2.0 underpredicts the IDT at higher temperatures, but still agrees within experimental error for the lower temperature datasets. This is to be expected as UoS sCO<sub>2</sub> 2.0 was created specifically for modelling combustion in CO<sub>2</sub>. Figure 4.10 shows a normalised OH sensitivity analysis of dataset 3 at 1050 K and 1200 K. At 1200 K, the two key reactions in the sensitivity analysis are Reaction 4.1 ( $H + O_2 (+M) \rightleftharpoons HO_2 (+M)$ ) and Reaction 4.3 ( $H + O_2 \rightleftharpoons O + OH$ ), which have a positive and negative sensitivity coefficient respectively of approximately one. The steep curve in UoS sCO<sub>2</sub> 2.0's simulation is most likely due to the relatively large temperature coefficient ( $n$ ) in Reaction 4.3 ( $H + O_2 \rightleftharpoons O + OH$ ). Investigation into the mechanism found the even a small change of -0.01 in the temperature coefficient had a large effect on the highest temperature datapoints. However, as UoS sCO<sub>2</sub> 2.0 was developed for modelling CO<sub>2</sub>, this discrepancy when modelling the IDT data in an N<sub>2</sub> bath gas is unsurprising. Furthermore, due to the importance of Reaction 4.1 ( $H + O_2 (+M) \rightleftharpoons HO_2 (+M)$ ) in the high-pressure combustion of H<sub>2</sub> and syngas [200], it should be studied to accurately determine the third body efficiency of CO<sub>2</sub> and CO, which are important for combustion in CO<sub>2</sub> [197, 287].



**Figure 4.10.** Normalized OH sensitivity analysis of dataset 3 for UoS sCO<sub>2</sub> 2.0 at 1050 K and 1200 K.

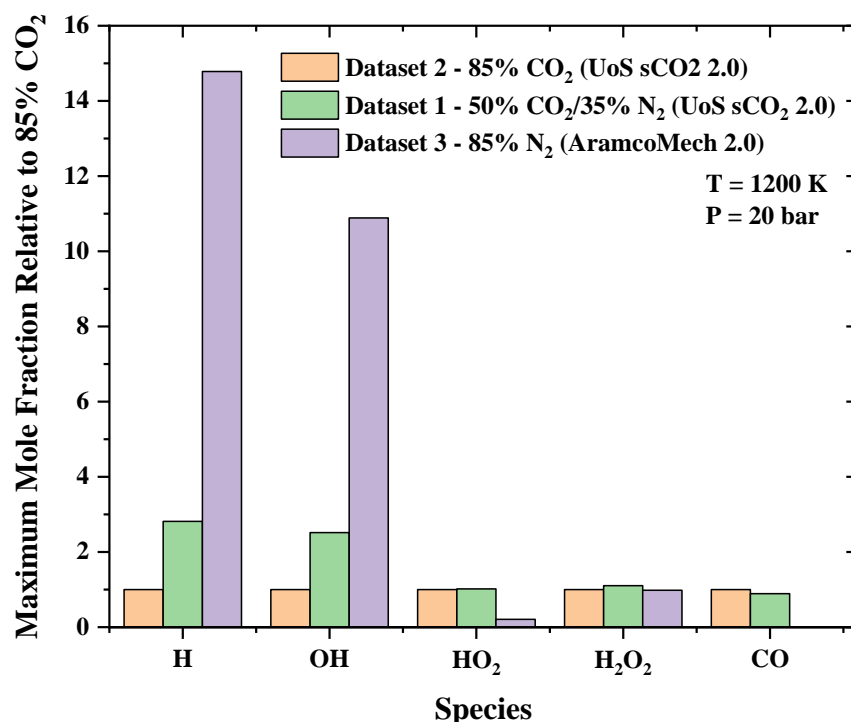
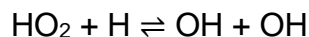
Figure 4.11 shows that the sensitivity analysis of dataset 1 (50% CO<sub>2</sub>) shows greater similarity to that of dataset 2 (85% CO<sub>2</sub>) than dataset 3 (85% N<sub>2</sub>). Furthermore, there is a significant overlap between the experimental IDTs for datasets 1 and 2, despite the 35% difference in bath gas composition as shown in Figure 4.9.



**Figure 4.11.** Normalized OH sensitivity analysis of datasets 1, 2 and 3 for UoS sCO<sub>2</sub> 2.0 at 1150 K.

The key differences in the formation of the radical pool during combustion at the point of ignition were investigated for the three different bath gas compositions (85% CO<sub>2</sub>, 50% CO<sub>2</sub>, 85% N<sub>2</sub>) studied at 20 bar and 1200 K. Figure 4.12 shows the maximum concentration of selected species for the three different conditions. The majority of CO is formed from Reaction 4.2 ( $CO + OH \rightleftharpoons CO_2 + H$ ), but as this also consumes the H radical, its concentration is much smaller in a CO<sub>2</sub> bath gas. Interestingly, this does not translate to an increased OH concentration and dataset 3 (85% N<sub>2</sub>) has a significantly larger OH concentration at the point of ignition. In 85% N<sub>2</sub>, more OH is formed through Reaction 4.3 ( $H + O_2 \rightleftharpoons O + OH$ ) and subsequently Reaction 4.4 ( $H_2 + O \rightleftharpoons H + OH$ ). Since there is greater competition for H radical in CO<sub>2</sub>, this reaction pathway is reduced and therefore less OH is formed. Under both conditions, the majority of OH is formed via Reaction 4.5. Due to the greater concentration of H radicals in N<sub>2</sub>, this reaction is faster and subsequently leads to a faster depletion of HO<sub>2</sub> as supported by Figure 4.12.



**Reaction 4.5.**

**Figure 4.12.** Maximum species concentrations at the point of ignition for key intermediates relative to Dataset 2 with 85% CO<sub>2</sub> dilution.

These trends suggest that IDT data measured to develop a chemical kinetic mechanism for CO<sub>2</sub> combustion do not need to be done in 100% CO<sub>2</sub> bath gas. As the controlling reactions and IDTs are similar for datasets 1 and 2, measuring datasets at only 50% CO<sub>2</sub> produces results that are just as useful as 85% CO<sub>2</sub>. Reduction in the CO<sub>2</sub> concentration helps in lowering non-ideal effects (e.g., bifurcation), as discussed in Section 2, which means that IDTs can be measured with smaller uncertainty and at longer test times. This is not to say that IDT datasets in a pure CO<sub>2</sub> bath gas are not important, but CO<sub>2</sub>/N<sub>2</sub> bath gas blends provide a useful benchmark with reduced uncertainty in IDT measurements.

#### 4.3.2. Effect of Equivalence Ratio at 20 bar

The effect of altering the equivalence ratio was investigated at 20 bar using datasets 1, 4 and 5 and at 40 bar using datasets 6, 7 and 8. Figure 4.13 shows the effect of increasing the equivalence ratio at 20 bar from  $\phi=0.2$  and  $\phi=2.0$  in a bath gas mixture of 50% CO<sub>2</sub> and 35% N<sub>2</sub>. Datasets 1 and 4 overlap over the

entire temperature range studied within the experimental error. Furthermore, there is a significant overlap in the IDT with dataset 5 ( $\phi=0.2$ ) which begins to exhibit longer IDTs at higher temperatures. These findings are consistent with Hu et al. [288], who found that shock tube IDTs for  $H_2$  combustion in argon at 16 bar for  $\phi=0.5$ ,  $\phi=1.0$  and  $\phi=2.0$  at 16 bar showed a similar overlap between datasets.

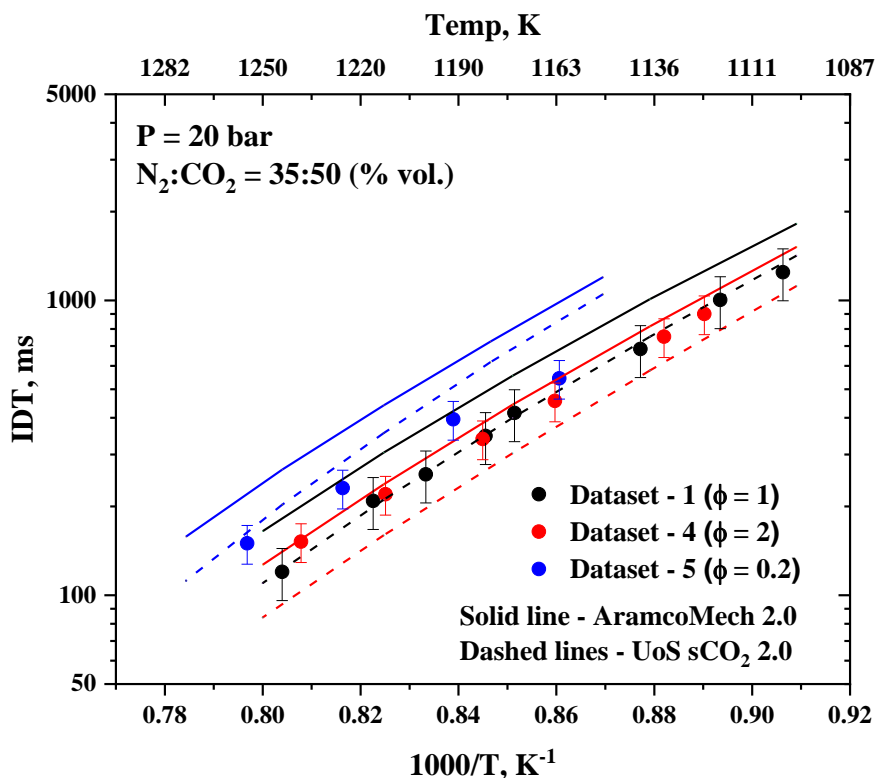


**Figure 4.13.** Comparison of IDTs of datasets 1, 4 and 5 with AramcoMech 2.0 and UoS sCO<sub>2</sub> 2.0.

Figure 4.14 shows the sensitivity analysis of Datasets 1, 4, and 5 at 1200 K for UoS sCO<sub>2</sub> 2.0, which have similar sensitivity coefficients across the reactions featured. The  $E$  (%) value for dataset 5 is the largest for both AramcoMech 2.0 and UoS sCO<sub>2</sub> 2.0, indicating that mechanisms struggle to model IDT at the lowest equivalence ratio. Whilst UoS sCO<sub>2</sub> 2.0 has a better agreement at  $\phi=1.0$  than  $\phi=2.0$ , AramcoMech 2.0 shows an inverse relationship and has a lower  $E$  (%) value at  $\phi=2.0$ . This is likely due to the strong overlap in the IDT of datasets 4 and 5, which is not well predicted by any of the mechanisms.



Figure 4.13 shows that UoS sCO<sub>2</sub> 2.0 overpredicts IDT for dataset 5 ( $\phi = 0.5$ ) and underpredicts the IDT for dataset 4 ( $\phi = 2.0$ ). The sensitivity analysis of Figure 4.14 indicates that Reaction 4.6 ( $H_2 + O_2 \rightleftharpoons HO_2 + H$ ) may be responsible for this, which has the opposite sensitivity coefficient for datasets 4 and 5, in addition to not being featured in the sensitivity analysis of dataset 1.

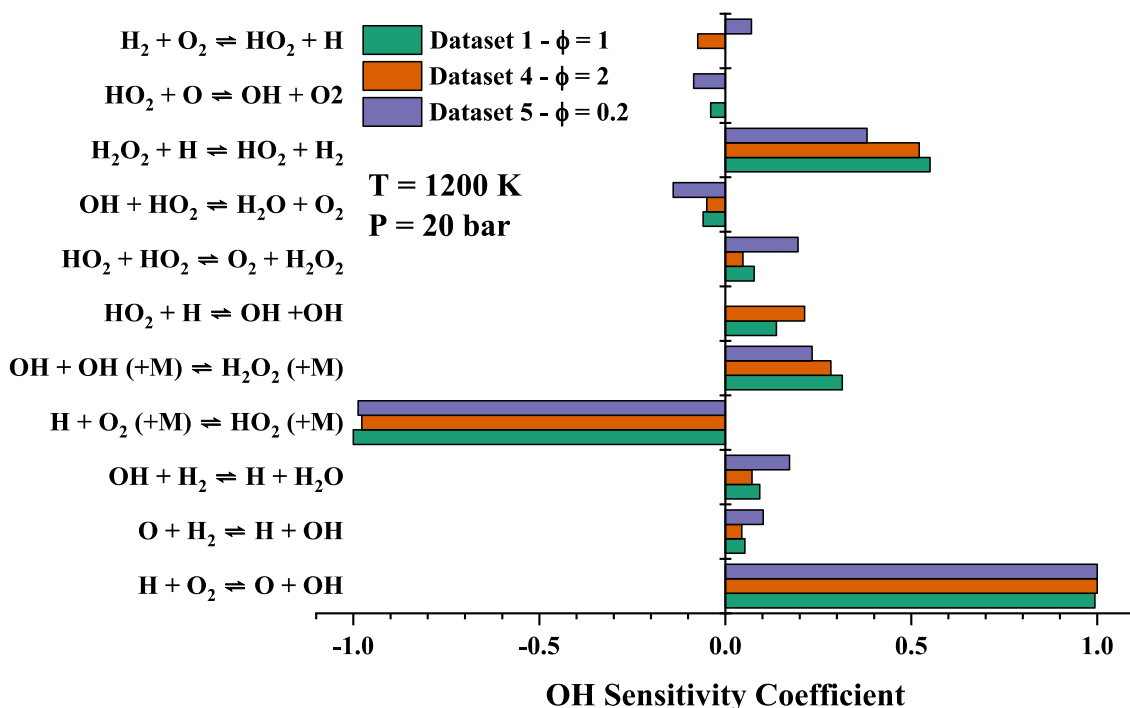


**Figure 4.14.** Normalized OH sensitivity analysis of datasets, 1, 4 and 5 for UoS sCO<sub>2</sub> 2.0 at 1200 K and 20 bar.

While Reaction 4.5 ( $HO_2 + H \rightleftharpoons OH + OH$ ) is the only reaction that has a significantly higher sensitivity coefficient for  $\phi=1.0$  and  $\phi=0.2$ , Reaction 4.7 ( $HO_2 + HO_2 \rightleftharpoons O_2 + H_2O_2$ ), Reaction 4.8 ( $OH + HO_2 \rightleftharpoons H_2O + O_2$ ) and Reaction 4.9 ( $OH + H_2 \rightleftharpoons H + H_2O$ ) have a much larger normalised sensitivity coefficient at  $\phi=0.2$ . Therefore, it may be anticipated that some of these rate coefficients may require further tuning within their respective experimental errors to improve the mechanisms' agreement with the experimental IDTs.



**Reaction 4.9.**  $\text{OH} + \text{H}_2 \rightleftharpoons \text{H} + \text{H}_2\text{O}$

Whilst there have been mechanism changes outlined with could potentially improve the performance and reduce the average  $E$  (%) across these three datasets. It must be noted that the UoS sCO<sub>2</sub> 2.0 mechanism significantly outperforms AramcoMech 2.0 in predicting the effect of changing the equivalence ratio on the IDT.

**4.3.3. Effect of Equivalence Ratio at 40 bar**

Datasets 6, 7, and 8 allow the comparison of changing the equivalence ratio from  $\phi=0.25$  and  $\phi=1.0$ . In this instance in an 85% CO<sub>2</sub> dilution. This was to allow intercomparison between dataset 6 and a similar dataset from Shao et al. [85]. Compared to those IDT datasets of changing equivalence ratio taken at 20 bar in only a 50% bath gas AramcoMech 2.0 becomes increasingly competitive under these conditions. This is surprising as the mechanism was developed for low-pressure combustion in air, so, interestingly, the performance improves as the conditions are extrapolated beyond the mechanism's point of validation. Furthermore, the performance of UoS sCO<sub>2</sub> 2.0 is seen to improve at 40 bar. This is likely due to the three mechanisms for the creation of UoS sCO<sub>2</sub> 1.0 from Shao et al. [85] were recorded at 40 bar and above. This means that the UoS sCO<sub>2</sub> 2.0 mechanism wasn't validated for modelling combustion below 40 bar. Additionally, the 40-bar dataset from Shao et al. [85] was recorded using sidewall measurements, which as discussed in Section 4.1, could have caused a reduced IDT. This shows the importance of the low-pressure H<sub>2</sub> endwall IDT in further developing the performance of UoS sCO<sub>2</sub> 2.0. Figure 4.15 shows the effect of increasing from  $\phi=0.25$  to  $\phi=1.0$  in Datasets 6-8. Whilst these are not directly comparable to the IDT datasets discussed in Section 4.3.2 due to the different bath gas compositions, the trends seen in Figure 4.15 are very similar. Whilst the range of the equivalence ratios studied is smaller at 40 bar, there is predictable a large overlap in each of the three datasets, with dataset 8 ( $\phi=1.0$ ) being slightly faster. AramcoMech 2.0 predicts a negligible dependence on the equivalence

ratio, whilst UoS sCO<sub>2</sub> predicts a small increase in IDT as the equivalence ratio tends to one.

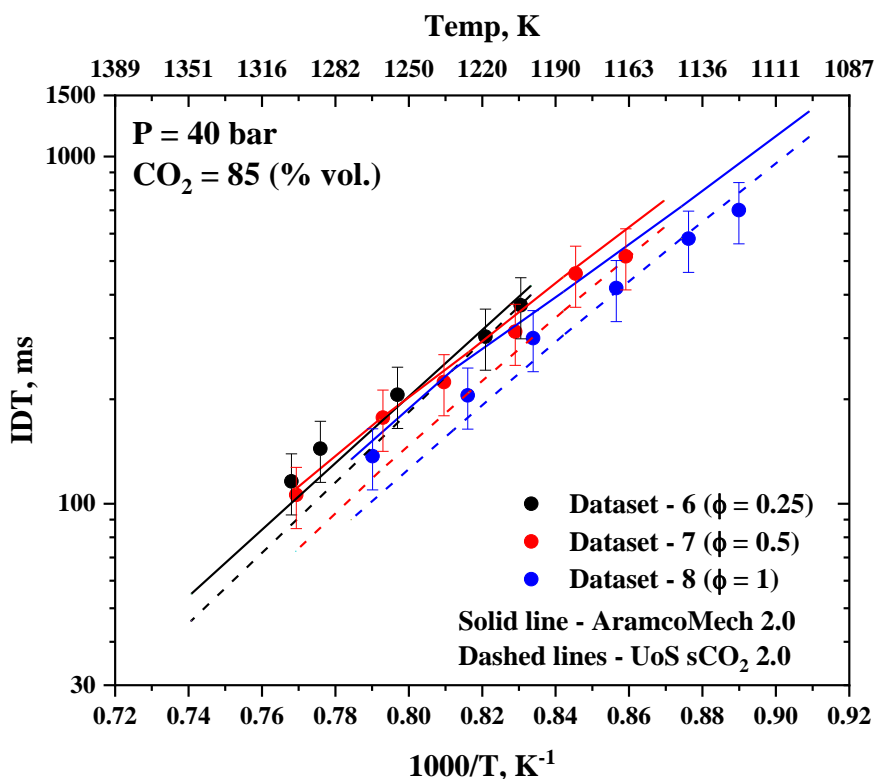


**Figure 4.15.** Comparison of IDTs of datasets 6, 7 and 8 with AramcoMech 2.0 and UoS sCO<sub>2</sub> 2.0.

Figure 4.16 shows a normalised OH sensitivity analysis of datasets 6 ( $\phi=0.25$ ) and 8 ( $\phi=1.0$ ) at 1250 K. This can be used to visualise the effect of increasing the equivalence ratio on the ignition chemistry of H<sub>2</sub> at 40 bar. Figure 4.15 shows that UoS sCO<sub>2</sub> 2.0 begins to underpredict the IDT at high temperatures. This is possibly due to the temperature dependence of Reaction 4.3 ( $H + O_2 \rightleftharpoons O + OH$ ), but also an overprediction of Reaction 4.10 ( $H_2O_2 + H \rightleftharpoons HO_2 + H_2$ ) which has the second largest positive sensitivity coefficient for both datasets as shown in Figure 4.16.



Further experiments at high and low-temperature ends of the current datasets would be helpful. Longer test times can be achieved using driver gas tailoring [112], but achieving shorter test times is more complex due to large uncertainty measurements in shock tube IDT data below 100  $\mu$ s.

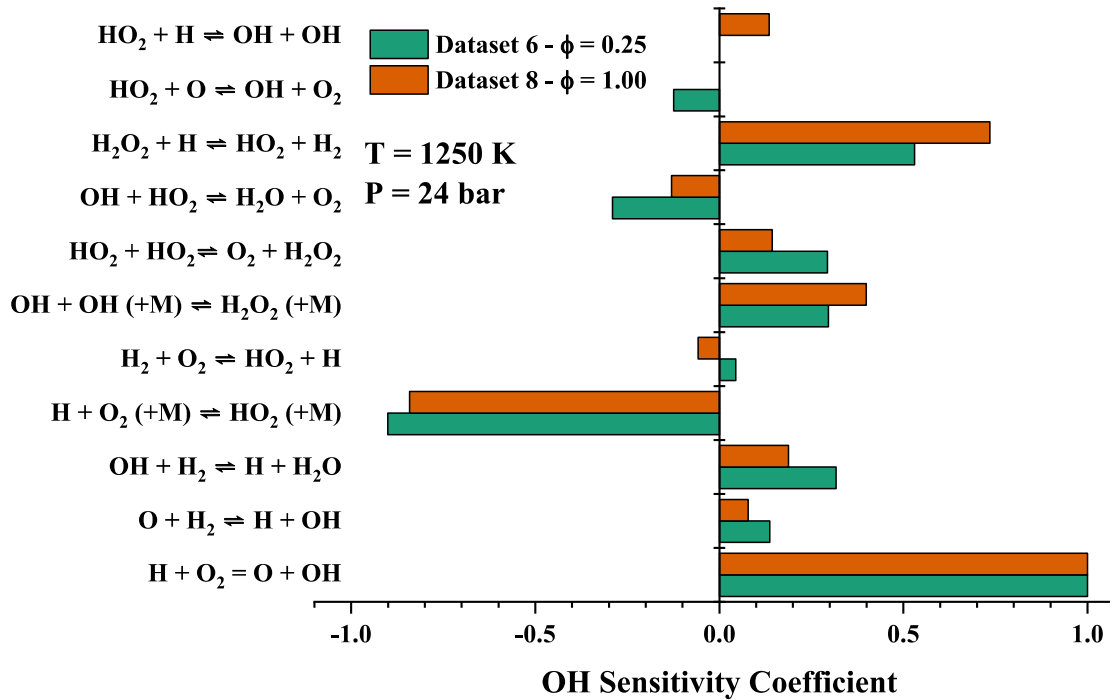


**Figure 4.16.** Normalized OH sensitivity analysis of datasets 6 and 8 for UoS sCO<sub>2</sub> 2.0 at 1250 K and 40 bar.

#### 4.3.4. Validation of the UoS sCO<sub>2</sub> 2.0 Mechanism for H<sub>2</sub> Combustion

A key objective was to validate the performance of UoS sCO<sub>2</sub> 2.0, in simulating H<sub>2</sub> IDTs across a range of experimental conditions. As H<sub>2</sub> is the simplest fuel, this is a good starting point for the further development of UoS sCO<sub>2</sub> and its validation, and it provides useful information for the expansion to more complex fuels. For the eight datasets recorded, the average absolute error ( $E$ , %), was determined to be 16.1% for UoS sCO<sub>2</sub> 2.0, a significant improvement over the 28.1% of AramcoMech 2.0. Additionally, UoS sCO<sub>2</sub> 2.0 fits six of the eight datasets within a 20% error, the maximum experienced in the shock tube during the experiments. The UoS sCO<sub>2</sub> 1.0 mechanism was based on a small amount of H<sub>2</sub> IDT data, with syngas and methane data forming a more pivotal role. The UoS sCO<sub>2</sub> 2.0 mechanism is shown to be able to be the better-performing mechanism for modelling combustion in CO<sub>2</sub>, whilst also identifying areas for future improvement. These areas include the accurate measurement of the rate coefficient of Reaction 4.1 ( $\text{H} + \text{O}_2 (+\text{M}) \rightleftharpoons \text{HO}_2 (+\text{M})$ ) in a CO<sub>2</sub> bath gas, which is identified as one of the most important reactions for each of the datasets studied. Another useful area for future research would be OH time histories for H<sub>2</sub>

combustion in CO<sub>2</sub>, to validate the mechanisms' ability to model the complete combustion process, in addition to the ignition. These measurements can be used to further validate the rate coefficients used in the UoS sCO<sub>2</sub> mechanism.

#### **4.4. Syngas IDT Datasets**

The KAUST HPST was used to record eight IDT for syngas combustion across various test gas compositions shown in Table 4.2. Seven of the datasets were recorded in an 80% bath gas of equal parts N<sub>2</sub> and CO<sub>2</sub>. This was done to reduce the effects of bifurcation on the mixture, which would increase the uncertainty of the IDT whilst still encapsulating the physical and chemical effects of having CO<sub>2</sub> present. The eight datasets were recorded with an 85% CO<sub>2</sub> dilution to allow direct comparison with an existing 40-bar dataset from Barak et al. [199].

**Table 4.2.** IDT mixtures studied in this work and quantitative analysis.

Mix.	Species Mole Fraction					Mixture Conditions				Average Absolute Error ( <i>E</i> ) (%)	
	H <sub>2</sub>	CO	O <sub>2</sub>	CO <sub>2</sub>	N <sub>2</sub>	T [K]	P [bar]	$\phi$	$\theta$	AramcoMech 2.0	UoS sCO <sub>2</sub> 2.0
1	5	5	10	40	40	1135-1257	19.9-22.0	0.5	1.0	77.0	4.2
2	8	2	10	40	40	1102-1231	20.2-21.4	0.5	4.0	70.0	18.0
3	2	8	10	40	40	1155-1293	20.3-21.2	0.5	0.25	106.4	13.1
4	2.85	2.85	14.3	40	40	1142-1279	20.0-21.3	0.25	1.0	72.0	8.0
5	6.67	6.67	6.67	40	40	1127-1202	19.1-20.4	1.0	1.0	71.1	4.5
6	10.67	2.67	6.67	40	40	1139-1226	19.8-20.4	1.0	4.0	68.6	18.3
7	2.67	10.67	6.67	40	40	1135-1267	20.2-20.8	1.0	0.25	113.6	12.8
8	5	5	5	85	-	1145-1302	40.5-43.9	1.0	1.0	30.1	23.4
<b>Average <i>E</i> (%)</b>										76.1	12.9

In Table 4.2, in addition to the equivalence ratio ( $\phi$ ), the ratio of H<sub>2</sub>:CO is also given which is calculated by dividing the mole fraction of H<sub>2</sub> by the mole fraction of CO.

#### 4.4.1. Effect of the H<sub>2</sub>:CO Ratio at $\phi=0.5$ and $\phi=1.0$

The effect of altering the H<sub>2</sub>:CO ratio ( $\theta$ ) at  $\phi=0.5$  and  $\phi=1.0$  as shown in Figure 4.17 and Figure 4.18 (datasets 1-3 and 5-7). The first point to note from Figure 4.17 and Figure 4.18 along with the results of the quantitative analysis from Table 4.2 is that the UoS sCO<sub>2</sub> 2.0 mechanism is a significantly superior fit for each of these six datasets. Table 4.2 shows that at both equivalence ratios, UoS sCO<sub>2</sub> 2.0 shows the best agreement with the experimental data at  $\theta=1.0$ . However, in

each of the six datasets, except for dataset 3, UoS sCO<sub>2</sub> 2.0 fits within a 20% average absolute error ( $E$ , %), any deviation from  $\theta=1.0$  causes an overprediction of the IDT. This is interesting that either H<sub>2</sub> or CO becoming in excess would lead to a similar overprediction in IDT.

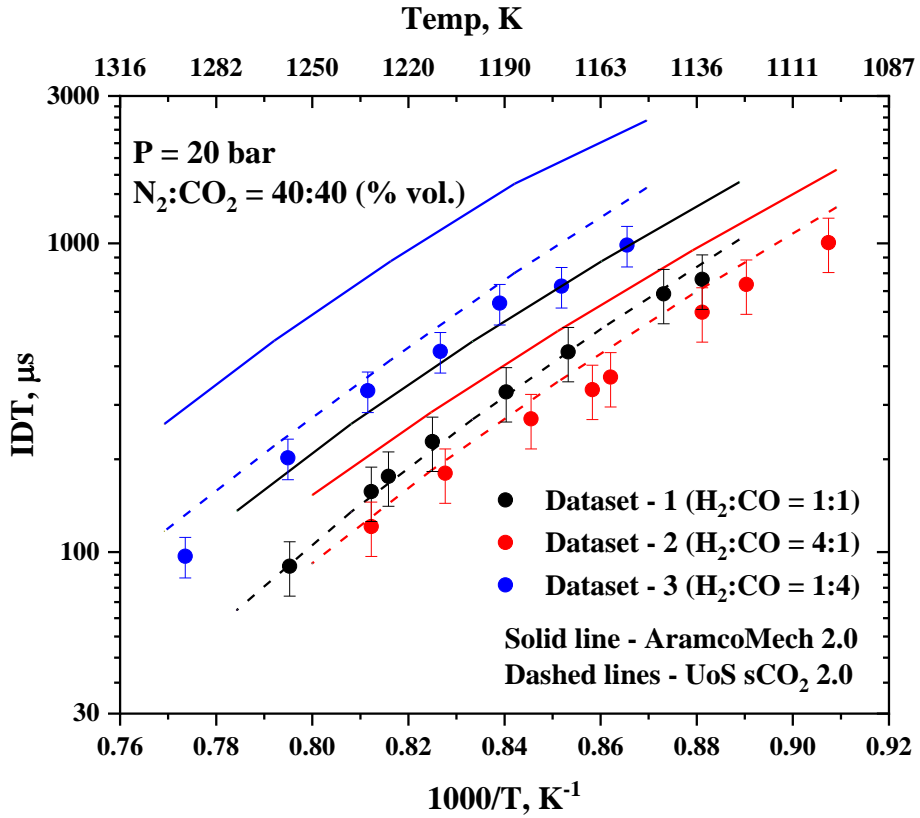
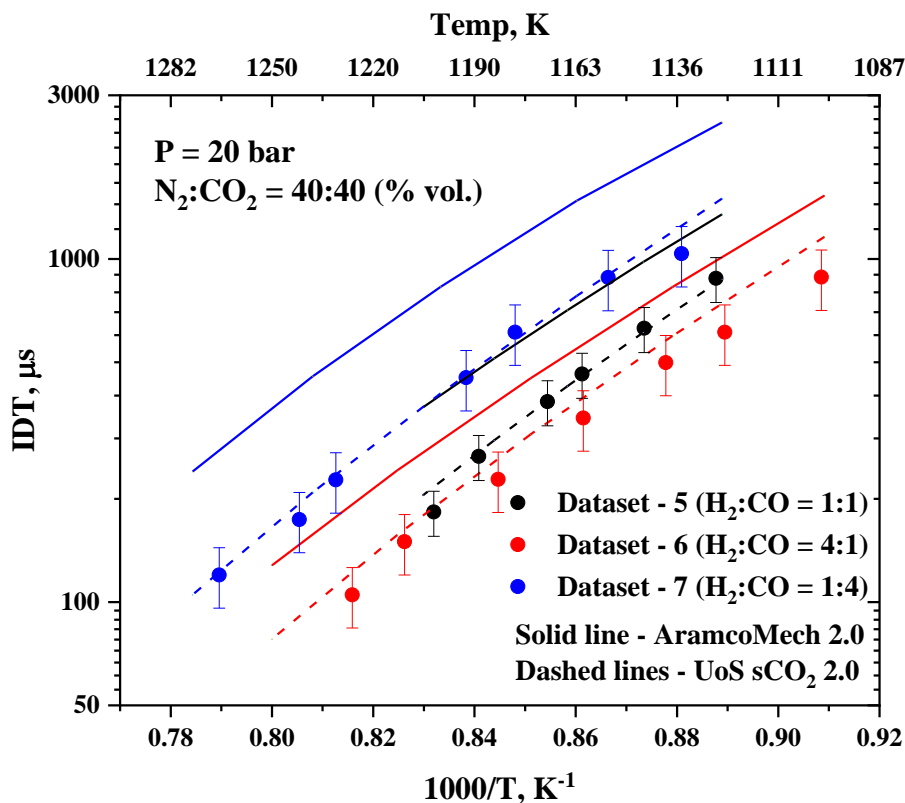


Figure 4.17. Comparison of IDTs of datasets 1, 2 and 3 with AramcoMech 2.0 and UoS sCO<sub>2</sub> 2.0.



**Figure 4.18.** Comparison of IDTs of datasets 5, 6, and 7 with AramcoMech 2.0 and UoS sCO<sub>2</sub> 2.0.

Figure 4.19 shows a sensitivity analysis of datasets 1-3 to compare the effect of changing the ratio of H<sub>2</sub> and CO from  $\theta=0.25$  to  $\theta=4.0$  at  $\phi=0.5$ . Most of the reactions in Figure 4.19 are related to the combustion of H<sub>2</sub>, with CO only featuring in two of the reactions. This can be explained by the discussion of Section 4.2.1 and the two separate ignition events of H<sub>2</sub> and CO in CO<sub>2</sub>. Furthermore, ROP analysis shows CO combustion is much simpler with fewer reactions contributing. As the IDT is therefore usually dominated by the ignition of H<sub>2</sub>, therefore, it makes sense that its chemistry would dominate the sensitivity analysis at the point of the IDT. For dataset 2 ( $\theta=4.0$ ), when hydrogen is in excess, the normalised sensitivity is very similar to ( $\theta=1.0$ ). This highlights the dominance of the H<sub>2</sub> ignition. The sensitivity analysis of Figure 4.19 highlights the difference in the normalised sensitivity coefficient of dataset 3 ( $\theta=0.25$ ), which shows a much greater sensitivity for many of the key reactions of H<sub>2</sub> combustion, likely highlighting differences in the combustion mechanism. One key difference is the decrease in the importance of HO<sub>2</sub> when CO is in excess ( $\theta>1$ ). ROP of

HO<sub>2</sub> (see Figure 4.20) was investigated for dataset 3 to look at why H<sub>2</sub>O<sub>2</sub> becomes less important to the overall combustion mechanism when CO is in excess. ROP revealed that despite being a dominant reaction pathway at the point of H<sub>2</sub> ignition, Reaction 4.7 ( $OH + HO_2 \rightleftharpoons H_2O + O_2$ ) only accounts for a small amount of HO<sub>2</sub> loss when CO is in excess.

Furthermore, the key points of improvement for UoS sCO<sub>2</sub> 2.0 as shown in Figure 4.17 is that it agrees better at higher temperatures but begins to slightly overpredict the IDT as the temperature decreases.

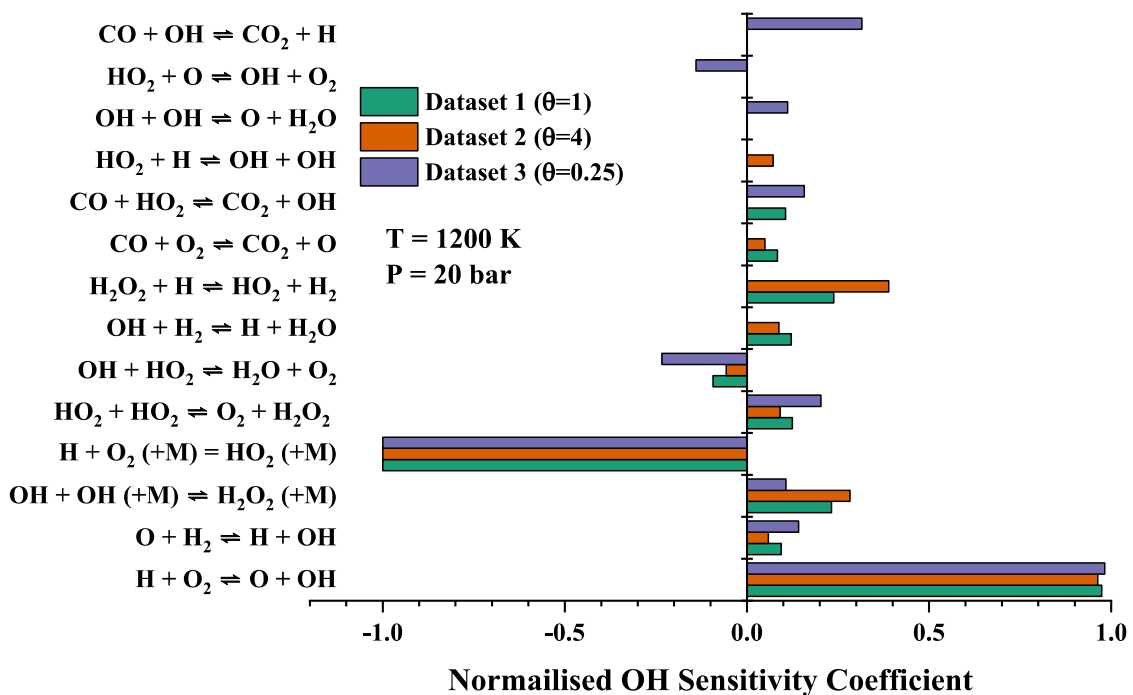
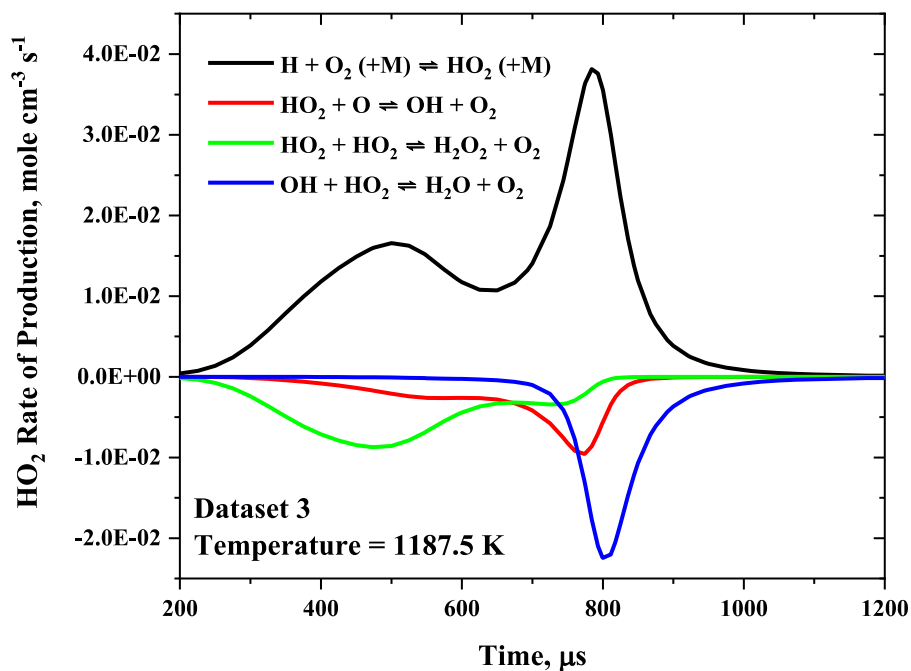
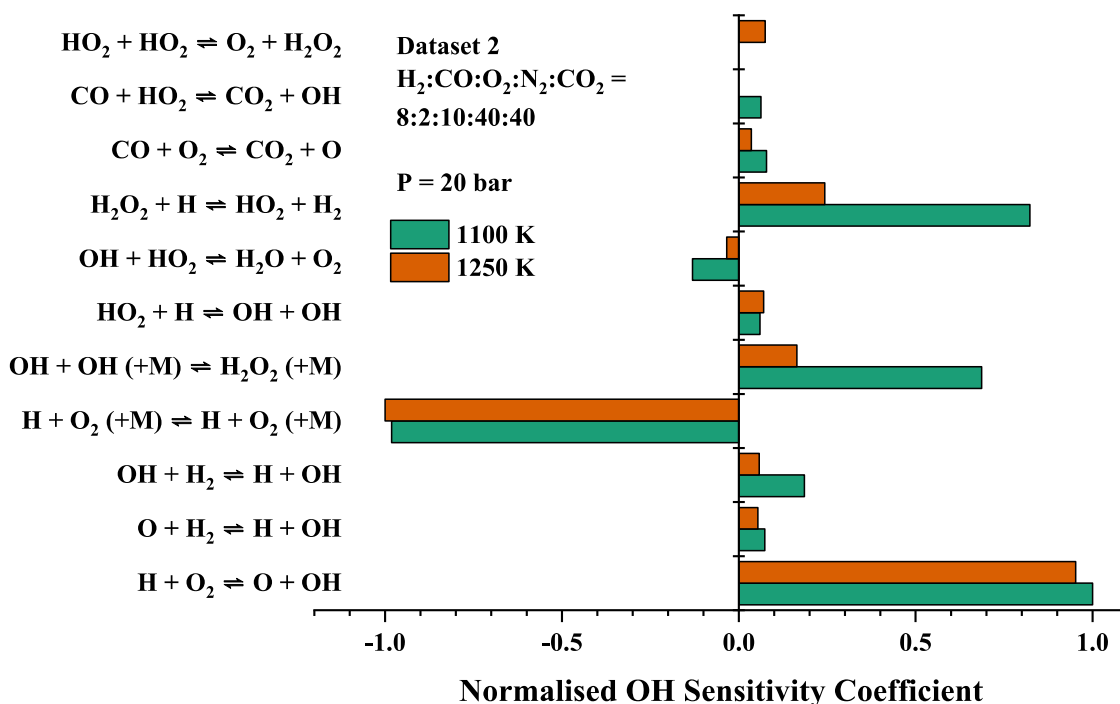


Figure 4.19. Normalized OH sensitivity analysis of datasets 1, 2 and 3 for UoS sCO<sub>2</sub> 2.0 at 1200 K.



**Figure 4.20.** Rate of production analysis of  $\text{HO}_2$  for dataset 3 at 1187.5 K around the point of ignition and for the four key reactions.

Figure 4.21 displays the normalised OH sensitivity analysis of dataset 2 ( $\theta=4.0$ ) at 1100 K and 1250 K, which does display a similar sensitivity for Reaction 4.1 ( $\text{H} + \text{O}_2 (+\text{M}) \rightleftharpoons \text{HO}_2 (+\text{M})$ ) and Reaction 4.3 ( $\text{H} + \text{O}_2 \rightleftharpoons \text{O} + \text{OH}$ ), the two key reactions of H and  $\text{O}_2$ . The largest discrepancies between the two temperatures, are in Reaction 4.10 ( $\text{H}_2\text{O}_2 + \text{H} \rightleftharpoons \text{HO}_2 + \text{H}_2$ ) and Reaction 4.11 ( $\text{OH} + \text{OH} (+\text{M}) \rightleftharpoons \text{H}_2\text{O}_2 (+\text{M})$ ). Both reactions include  $\text{H}_2\text{O}_2$ , indicating its importance as an intermediate species in syngas combustion at 1100 K, and becomes decreasingly important as the temperature increases. ROP analysis shows that the majority of  $\text{H}_2\text{O}_2$  is formed through Reaction 4.12 ( $\text{HO}_2 + \text{HO}_2 \rightleftharpoons \text{H}_2\text{O}_2 + \text{O}_2$ ), the reaction of two molecules of  $\text{HO}_2$ .



**Figure 4.21.** Normalized OH sensitivity analysis of dataset 2 for UoS sCO<sub>2</sub> 2.0 at 1100 K and 1250 K.

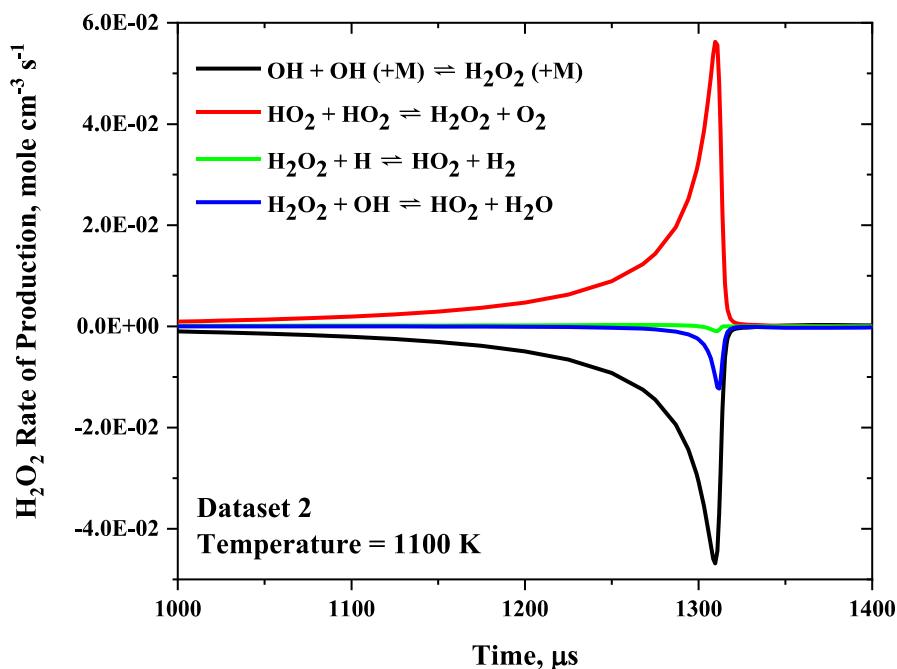


**Figure 4.22.** Rate of production analysis of H<sub>2</sub>O<sub>2</sub> for dataset 2 at 1100 K around the point of ignition and for the four key reactions.

Once formed, the majority of H<sub>2</sub>O<sub>2</sub> undergoes a decomposition via Reaction 4.11 ( $\text{OH} + \text{OH} (+\text{M}) \rightleftharpoons \text{H}_2\text{O}_2 (+\text{M})$ ), which generate two OH radicals. The ROP analysis reveals at 1100 K (see Figure 4.22), that this reaction pathway via

Reaction 4.11 ( $OH + OH (+M) \rightleftharpoons H_2O_2 (+M)$ ) contributes to over 76% of OH production at its maximum. However, at 1250 K, the same pathway only contributes to 36% of the OH production at its peak.



UoS sCO<sub>2</sub> 2.0 utilises a rate coefficient for Reaction 4.11 ( $OH + OH (+M) \rightleftharpoons H_2O_2 (+M)$ ) from Zellner et al. [254] calculated using laser flash-photolysis. This rate coefficient was determined in an N<sub>2</sub> bath gas at temperatures and pressures below 353 K and 1100 mbar, respectively. Therefore, in this instance, this rate coefficient is being extrapolated well beyond its intended use in terms of pressure, temperature, and CO<sub>2</sub> dilution. This may explain why the mechanism struggles to predict the complete temperature profile of some of the IDT datasets. AramcoMech 2.0 uses a more recent, theoretical rate coefficient from Troe et al. [234] which was determined in a CO<sub>2</sub> bath gas. However, overall AramcoMech 2.0 is a worse fit for the datasets recorded. Therefore, it would be useful to experimentally determine Reaction 4.11 ( $OH + OH (+M) \rightleftharpoons H_2O_2 (+M)$ ) in a CO<sub>2</sub> bath gas, at higher pressures more relevant to sCO<sub>2</sub> combustion due to its importance in low-pressure H<sub>2</sub> and syngas combustion.

In Section 3.8, it was noted that AramcoMech 2.0 struggled to model syngas IDTs, especially at lower pressures. The same trend was observed in this work, where an average  $E$  value of 81.6% was recorded, and the best dataset was the highest-pressure dataset. This discrepancy was investigated using a normalised OH sensitivity analysis of dataset 5. This dataset was selected as it had the best agreement with UoS sCO<sub>2</sub> 2.0 when  $\theta=1.0$  and AramcoMech 2.0 performs best when  $\phi=1.0$ . Figure 4.23 shows this sensitivity analysis for dataset 5 of UoS sCO<sub>2</sub> 2.0 and AramcoMech 2.0 at 1175 K. Again, the sensitivity coefficients for the key reactions are similar, whilst there are larger differences between the minor reactions, the substantial overprediction of AramcoMech 2.0 is more likely down to differences in rate coefficients of these more important reactions. Reaction 4.1 ( $H + O_2 (+M) \rightleftharpoons HO_2 (+M)$ ) is the only one with a large negative sensitivity coefficient

for both reactions, which has a rate coefficient which only differs slightly between the two mechanisms [289]. Two reactions with significant positive coefficients are Reaction 4.3 ( $H + O_2 \rightleftharpoons O + OH$ ) and Reaction 4.11 ( $OH + OH (+M) \rightleftharpoons H_2O_2 (+M)$ ). For both reactions, AramcoMech 2.0 has significantly slower rate coefficients, which likely couples to explain the large overprediction in the IDT. The rate coefficients in UoS sCO<sub>2</sub> 2.0 for Reaction 4.3 ( $H + O_2 \rightleftharpoons O + OH$ ) and Reaction 4.11 ( $OH + OH (+M) \rightleftharpoons H_2O_2 (+M)$ ) are from Yu et al. [250] and Zellner et al. [254] respectively are significantly older than their counterparts from AramcoMech 2.0 [140, 234]. The discrepancy between the two mechanisms for the syngas IDT datasets is much larger than was observed for H<sub>2</sub> IDTs in Section 4.3, despite all the important reactions featuring the combustion of H<sub>2</sub>. This can potentially be explained by the mechanisms using different third-body efficiencies of CO in AramcoMech 2.0 [234] and UoS sCO<sub>2</sub> 2.0 [250] for Reaction 4.11 ( $OH + OH (+M) \rightleftharpoons H_2O_2 (+M)$ ) having some effect when the concentration is significant enough. This would also explain why syngas IDT datasets from Karimi et al. [200] show good agreement with AramcoMech 2.0, as a much smaller mole fraction of CO is used compared to H<sub>2</sub>. A larger third body efficiency for Reaction 4.11 ( $OH + OH (+M) \rightleftharpoons H_2O_2 (+M)$ ) would promote H<sub>2</sub>O<sub>2</sub> formation and thus slow down the rate of production of OH radicals. In turn, this would increase the IDT. Furthermore, this is supported by the decline in the performance of AramcoMech 2.0 as the mole fraction of CO increases. Unlike UoS sCO<sub>2</sub> 2.0 which has the lowest  $E$  (%) value when  $\theta=1.0$ , AramcoMech 2.0 performs best at larger concentrations of H<sub>2</sub> and is significantly worse in datasets 3 and 7 when CO is in excess ( $\theta=0.25$ ).

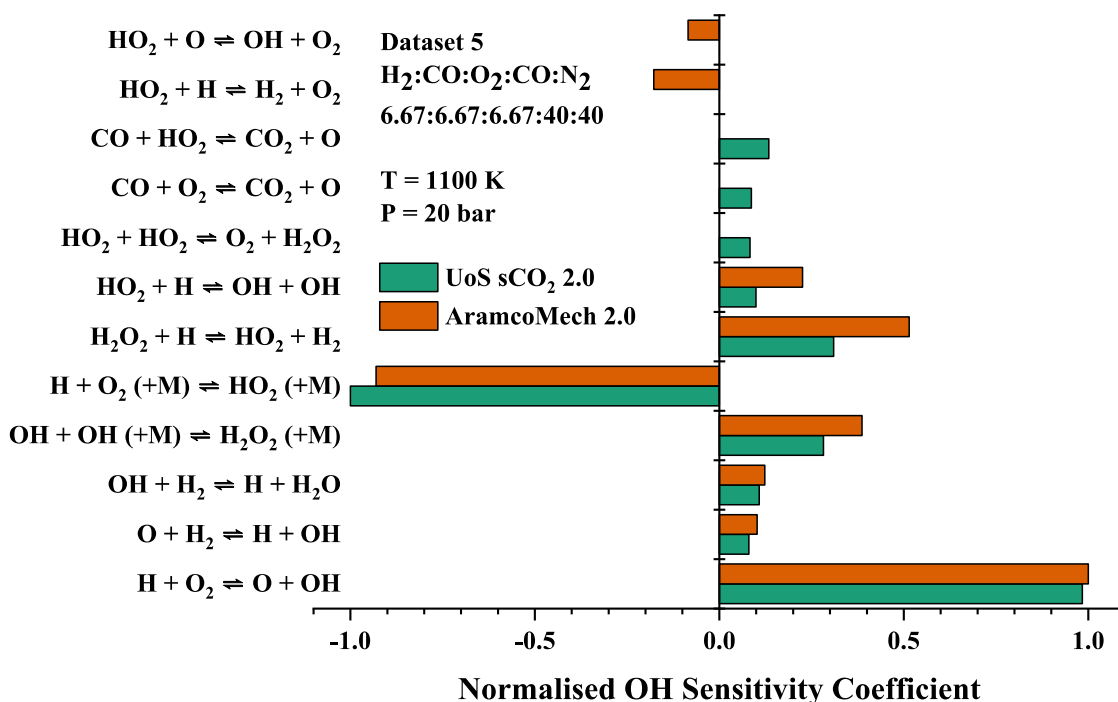


**Figure 4.23.** Normalized OH sensitivity analysis of dataset 5 for UoS sCO<sub>2</sub> 2.0 and AramcoMech 2.0 at 1100 K.

#### 4.4.2. Effect of Equivalence Ratio with CO in Excess ( $\theta=0.25$ )

Interestingly, the CO-rich conditions for datasets 3 and 7 display the biggest discrepancy in the quantitative analysis for the two equivalence ratios as shown in Table 4.2. The simulated IDTs of UoS sCO<sub>2</sub> 2.0 for dataset 7 ( $\phi=1.0$ ) are within the 20% uncertainty of the shock tube measurements, whereas dataset 3 ( $\phi=0.5$ ) had the largest calculated  $E$  (%) of the eight datasets studied. The discrepancy between the simulated and experimental IDTs kept constant across the two temperature profiles. Therefore, the normalised OH sensitivity analysis was performed at a temperature mid-point of 1200 K as shown in Figure 4.24. The normalised OH sensitivity analysis shows that the chemistry between the two datasets at the point of ignition is very similar, indicating it must be a small, and specific, change in chemistry which causes the poor performance of dataset 3.

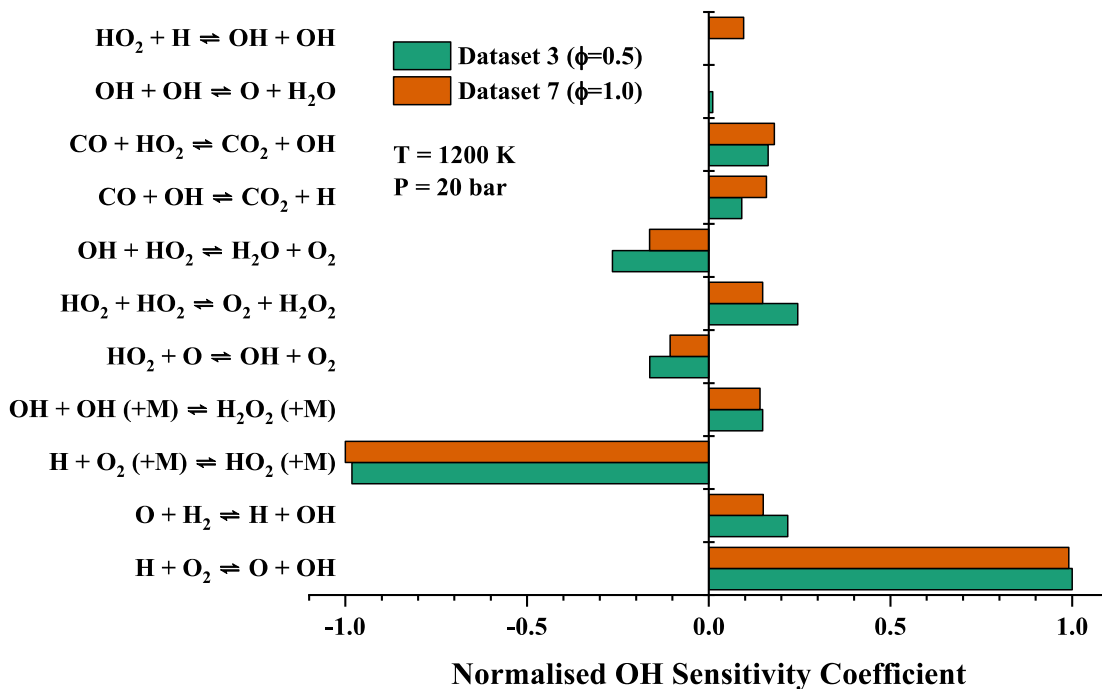


**Figure 4.24.** Normalized OH sensitivity analysis of datasets 3 and 7 for UoS sCO<sub>2</sub> 2.0 at 1200 K.

Figure 4.25 shows the mole fractions of OH, H<sub>2</sub> and CO for datasets 3 and 7 at 1200 K. Clearly in this instance there is only one peak on the OH mole fraction curve. Whilst in some of these datasets two IDTs were observed, the peak in the OH mole fraction caused by H<sub>2</sub> is almost undetectable as it is dwarfed by the much larger CO concentration. Figure 4.25 shows from the H<sub>2</sub> mole fractions are happening between 300 and 450  $\mu\text{s}$  for both datasets. However, for dataset 3, the subsequent ignition of CO occurs a lot later than it does for dataset 7, which is almost instantaneous. The position of this overlap affects the overall shape of the OH mole fraction curve. Therefore, the overprediction in IDT may be due to the overlap of these curves not matching what was seen experimentally.

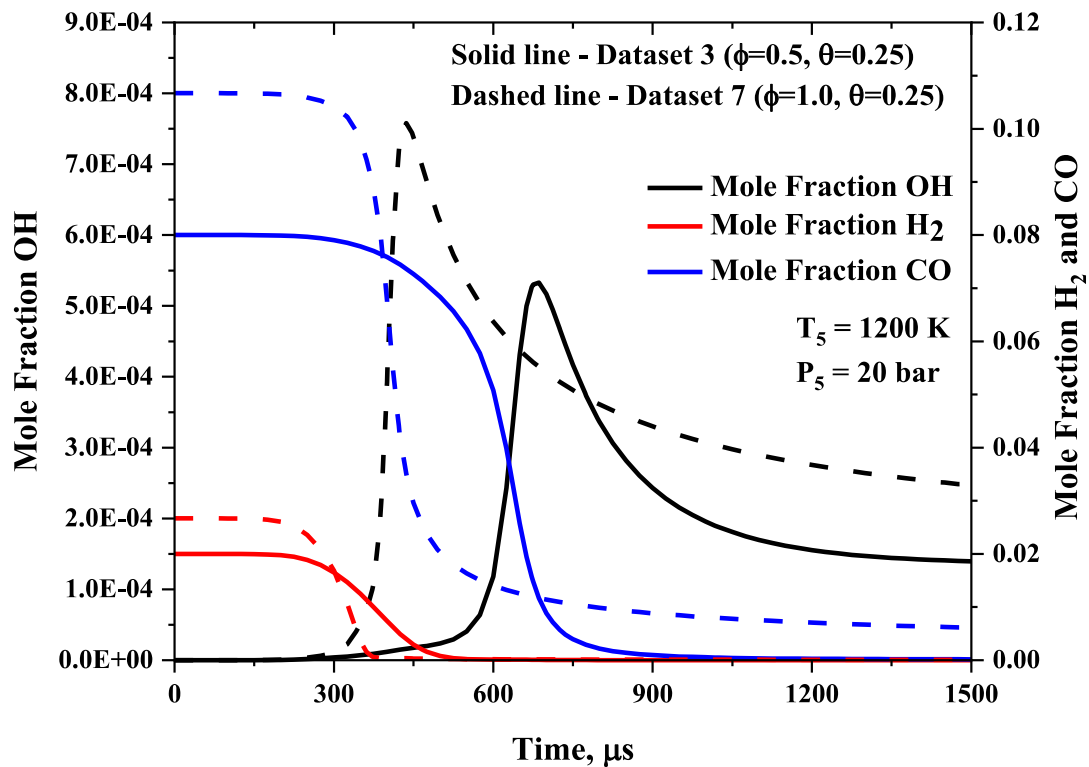


**Figure 4.25.** Mole fraction of OH, H<sub>2</sub> and CO for datasets 3 ( $\phi=0.5$ ) and 7 ( $\phi=1.0$ ) at 20 bar and 1200 K.

The chemistry between the two datasets is so similar as revealed by sensitivity analysis (Figure 4.24). The overestimation likely arises due to the incorrect simulation of CO combustion. If the CO ignition overlaps with the H<sub>2</sub> ignition event too late, the maximum gradient of the OH time history will be late and thus the IDT will increase. This effect can be explained by the smaller equivalence ratio of dataset 3, meaning that less O<sub>2</sub> is available. As there is less O<sub>2</sub> available, it will react preferentially with the more reactive H<sub>2</sub>. This will reduce the concentration of O<sub>2</sub> available to react with CO and thus spread the two ignition events. Therefore, the most likely candidate for the overprediction of dataset 3 is Reaction 4.2 ( $CO + OH \rightleftharpoons CO_2 + H$ ) which is shown in sensitivity analysis to be the key reaction of CO ignition and is revealed by ROP analysis to account for almost all CO consumption in datasets 3 and 7 at 1200 K.

#### 4.4.3. Effect of Equivalence Ratio for H<sub>2</sub>:CO at $\theta=1.0$

Figure 4.26 shows the effect of altering the equivalence ratio at  $\theta=1.0$  for the combustion of syngas from  $\phi=0.25$  to  $\phi=1.0$ . Across the three datasets, UoS sCO<sub>2</sub> 2.0 agrees extremely well with the experimental data, having an  $E$  value of less than 10% for all three of the datasets. Whilst AramcoMech 2.0 has a much larger  $E$ , the result is consistent across the three datasets. This suggests that despite the large effect that changing the equivalence ratio has a significant effect on the IDT as shown in Figure 4.26, this change is modelled by both chemical mechanisms. This indicates that the mechanisms struggle more with modelling the change in the H<sub>2</sub>:CO ratio as shown in Section 4.4.1 rather than the equivalence ratio, especially by UoS sCO<sub>2</sub> 2.0.

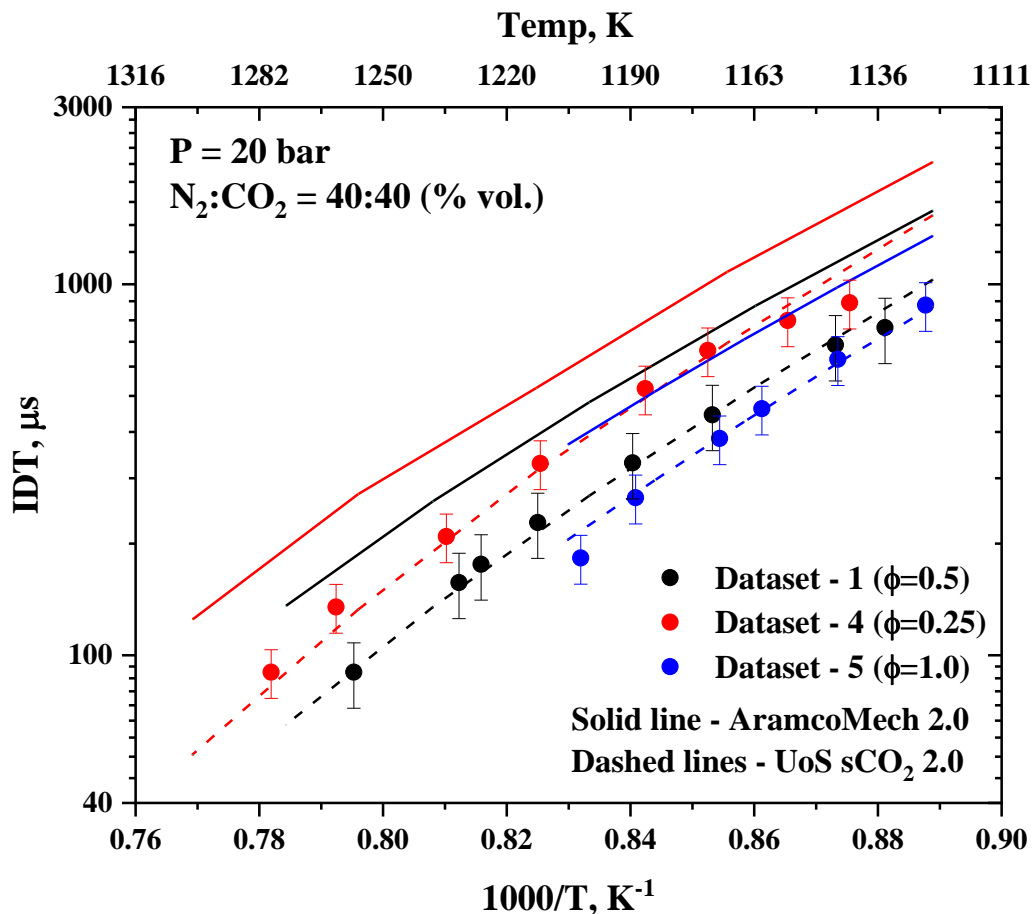
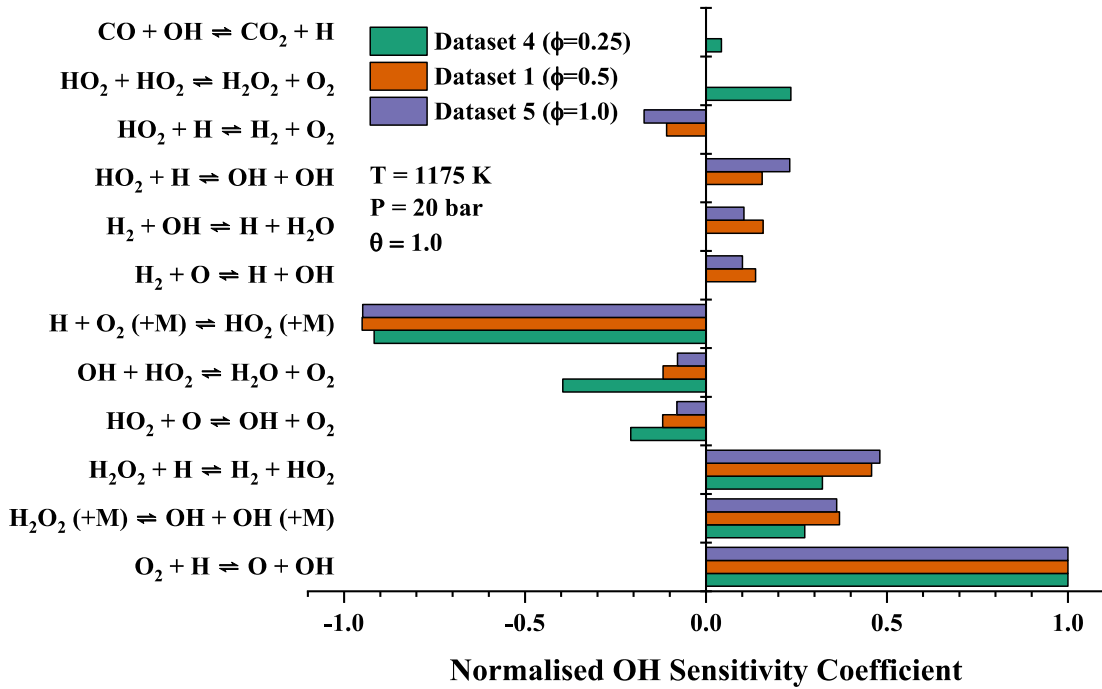


Figure 4.26. Comparison of datasets 1, 4, and 5 with AramcoMech 2.0 and UoS sCO<sub>2</sub> 2.0.

To investigate the change in chemistry due to the change in equivalence ratio, a normalised OH sensitivity analysis was performed for datasets 1, 4 and 5 at 1175

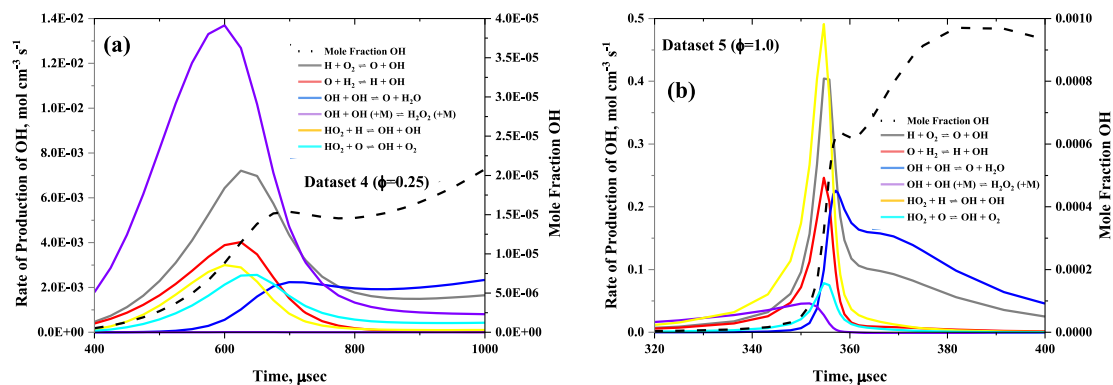
K shown in Figure 4.27. Figure 4.27 shows that at  $\phi=0.25$ , the reactions of  $\text{HO}_2$  are more prominent and have a larger OH sensitivity coefficient. In dataset 4 ( $\phi=0.25$ ), there were distinct dual peaks in the OH mole fraction of  $\text{H}_2$  and CO ignitions events.



**Figure 4.27.** Normalized OH sensitivity analysis of datasets 1, 4 and 5 for UoS sCO<sub>2</sub> 2.0 at 1175 K.

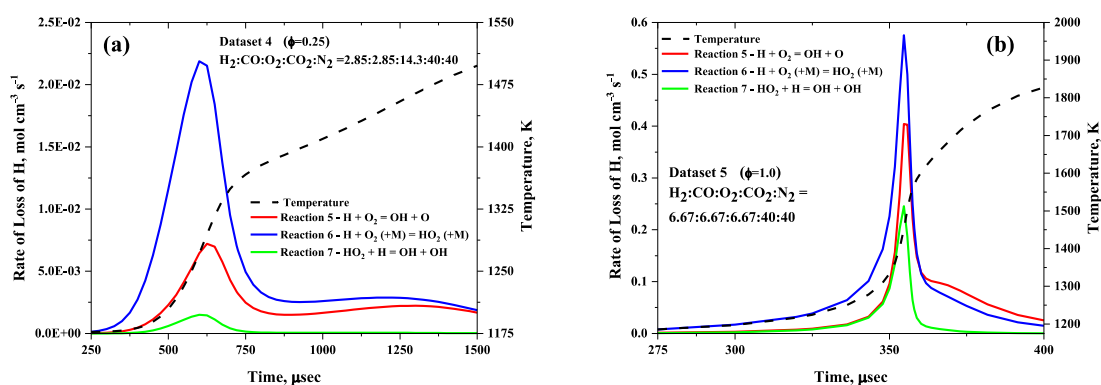
Figure 4.28 shows the mole fraction of OH showing that whilst both datasets have two distinct OH peaks, they are more distinct at the lower equivalence ratio. Figure 4.28 also shows the route of OH production varies between the two different equivalence ratios. Reaction 4.11 ( $\text{OH} + \text{OH} (+\text{M}) \rightleftharpoons \text{H}_2\text{O}_2 (+\text{M})$ ) is responsible for the majority of OH production at  $\phi=0.25$ . However, at  $\phi=1.0$  Reaction 4.11 ( $\text{OH} + \text{OH} (+\text{M}) \rightleftharpoons \text{H}_2\text{O}_2 (+\text{M})$ ) plays a relatively small role in OH production at  $\phi=1.0$ , where Reaction 4.5 ( $\text{HO}_2 + \text{H} \rightleftharpoons \text{OH} + \text{OH}$ ) and Reaction 4.3 ( $\text{H} + \text{O}_2 \rightleftharpoons \text{O} + \text{OH}$ ). This can be explained by the smaller concentration of H radicals in dataset 4 at the point of ignition. As revealed in Figure 4.27, the reactions of Reaction 4.1 ( $\text{H} + \text{O}_2 (+\text{M}) \rightleftharpoons \text{HO}_2 (+\text{M})$ ) and Reaction 4.3 ( $\text{H} + \text{O}_2 \rightleftharpoons \text{O} + \text{OH}$ ) are two of the most important for all three of the datasets. Due to the greater concentrations of  $\text{O}_2$  in dataset 4, any H produced reacts quickly with  $\text{O}_2$ .

This means that there are fewer H atoms available to react via Reaction 4.5 ( $HO_2 + H \rightleftharpoons OH + OH$ ) and thus it wasn't as important in terms of OH production.



**Figure 4.28.** Rate of production of OH comparison for (a) dataset 4 ( $\phi=0.25$ ) and (b) dataset 5 ( $\phi=1.0$ ) and mole fraction of OH at 1175 K.

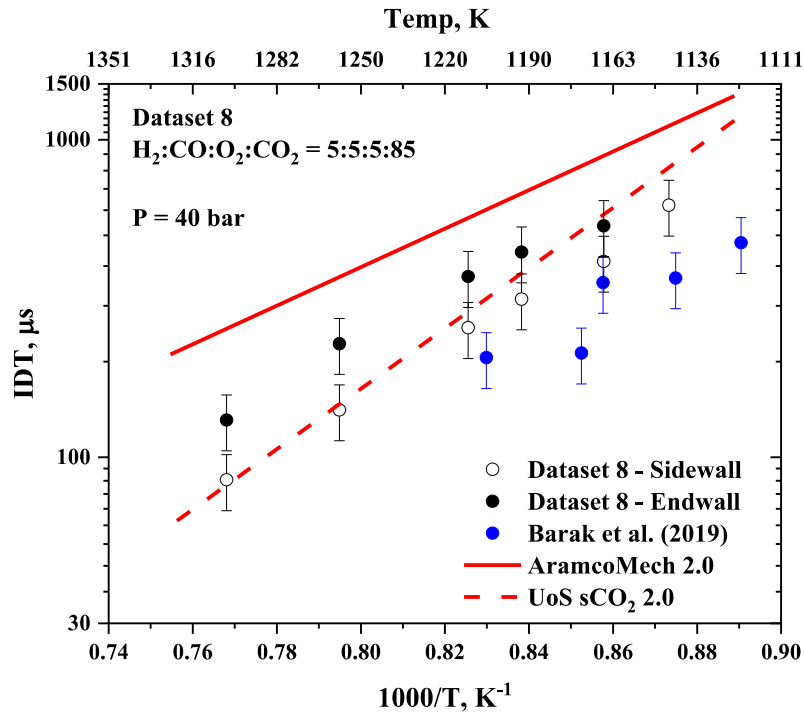
The rate of these three competing reactions for H loss is shown in Reaction 4.1 ( $H + O_2 (+M) \rightleftharpoons HO_2 (+M)$ ), Reaction 4.3 ( $H + O_2 \rightleftharpoons O + OH$ ) and Reaction 4.5 ( $HO_2 + H \rightleftharpoons OH + OH$ ), as well as the temperature increase in the reaction is shown in Figure 4.29. As expected, due to the abundance of  $O_2$  at  $\phi=0.25$ , Reaction 4.5 ( $HO_2 + H \rightleftharpoons OH + OH$ ), is a much smaller pathway. Interestingly, the rate of Reaction 4.1 ( $H + O_2 (+M) \rightleftharpoons HO_2 (+M)$ ) is much faster than Reaction 4.3 ( $H + O_2 \rightleftharpoons O + OH$ ) for dataset 4 ( $\phi=0.25$ ), whereas they are more similar at ( $\phi=1.0$ ). This difference can be explained by the lower temperatures achieved from the combustion in dataset 4. As the temperature increases, the rate of third body Reaction 4.1 ( $H + O_2 (+M) \rightleftharpoons HO_2 (+M)$ ) decreases and the rate of Reaction 4.3 ( $H + O_2 \rightleftharpoons O + OH$ ) increases, meaning the consumption of H down each pathway becomes more similar. This effect is well simulated by UoS sCO<sub>2</sub> 2.0 as the IDT is correctly predicted at the two different equivalence ratios despite the dramatic difference in the production of OH.



**Figure 4.29.** Rate of loss of H radical comparison for (a) dataset 4 ( $\phi=0.25$ ) and (b) dataset 5 ( $\phi=1.0$ ) and the increase in the temperature at 1175 K.

#### 4.4.4. Comparison to Existing Dataset from Barak et al. [199]

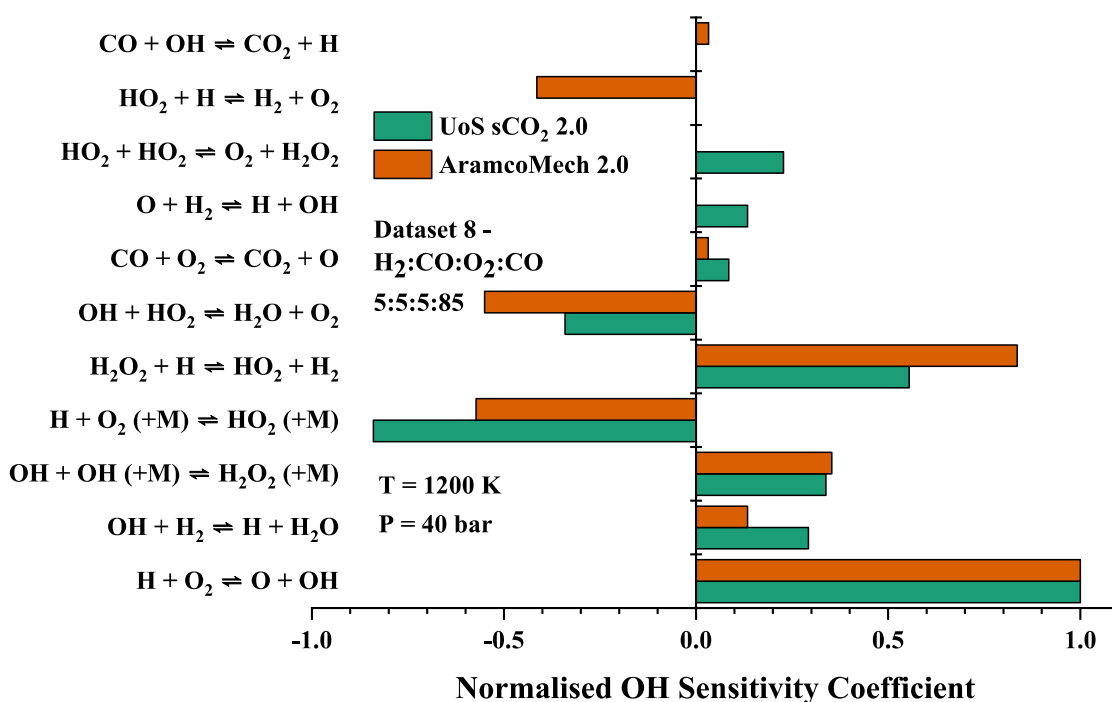
In addition to the seven datasets recorded at 20 bar, a further dataset was recorded at 40 bar in an 85% CO<sub>2</sub>-dilution, which allowed for direct comparison with an existing dataset from Barak et al. [199]. The IDT in this instance was recorded using sidewall and endwall chemiluminescence detection for OH\*. Figure 4.30 shows these datapoints alongside the sidewall measurements from Barak et al. [199]. The existing IDTs are faster than those recorded in the present study, possibly due to the different impact of bifurcation between the two shock tubes or the different techniques for IDT determination. Barak et al. [199] used chemiluminescence detection without a bandpass filter with a detector between 150 and 550 nm, which captured the emissions of more species, notably OH\* and CH\*. The reported endwall measurements are faster than the sidewall measurements, consistent with the H<sub>2</sub> data as discussed in Section 4.3. More interestingly, Figure 4.30 shows that AramcoMech 2.0 showed a significant improvement in simulating the experimental data in dataset 8, compared to any of the other datasets at lower pressure and lower CO<sub>2</sub> dilutions. As AramcoMech 2.0 was created to model low-pressure combustion with a small concentration of CO<sub>2</sub>, it is surprising that the  $E$  (%) value would improve as the test gas composition and pressures move further from the conditions of mechanism validation.



**Figure 4.30.** Comparison of sidewall and endwall measurements of dataset 8 with Barak et al. [199] with AramcoMech 2.0 and UoS sCO<sub>2</sub> 2.0.

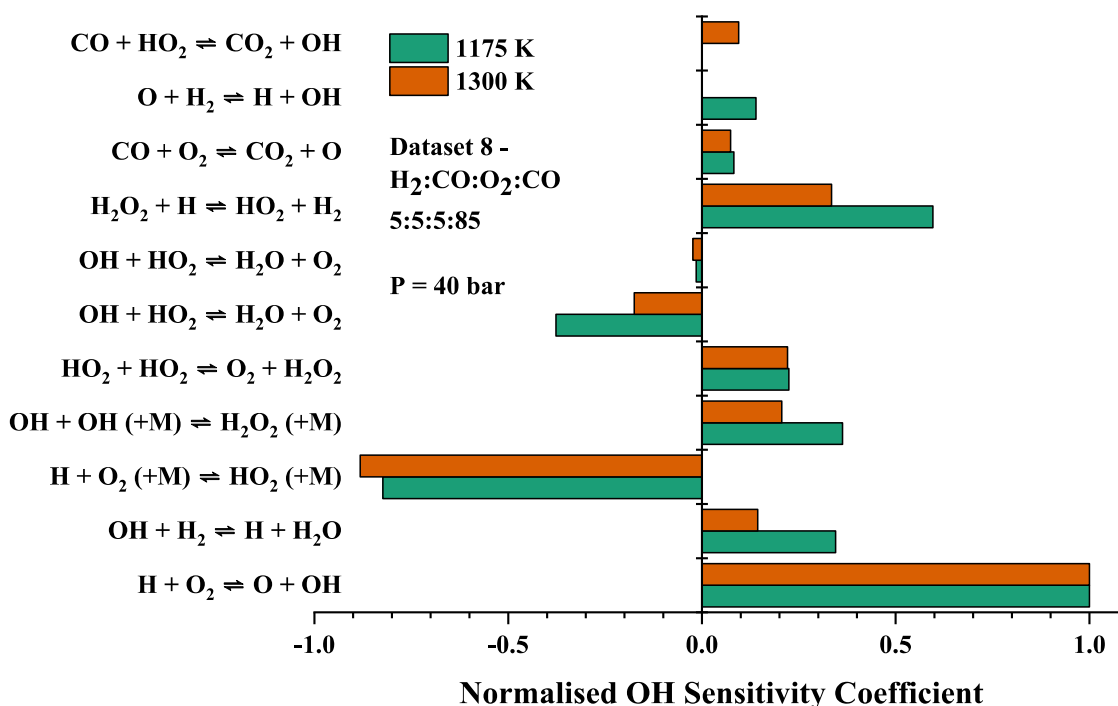
As previously discussed in Section 4.1, endwall measurements are preferential for determining the IDT using shock tubes to prevent the effect of premature ignition on the PMT detector in CO<sub>2</sub> dilutions on sidewall measurements. The underprediction of the IDT from UoS sCO<sub>2</sub> 2.0 is likely an artefact of UoS sCO<sub>2</sub> 1.0 being created to model the faster sidewall datasets available for syngas combustion and thus faster rate coefficients were selected to reduce the average  $E$  (%). This means that UoS sCO<sub>2</sub> 1.0 was trying to model the data from Barak et al. [199] in Figure 4.30, which required a dramatic reduction in IDT and would explain the underprediction of the mechanisms for the longer IDTs of the endwall data. Going forward preference in mechanisms creation should be given to endwall OH\* measurements when in a CO<sub>2</sub> bath gas. This also likely explains why the underprediction for the H<sub>2</sub> dataset wasn't as dramatic, as only one dataset was recorded at this temperature using sidewall measurements. It is also consistent with Section 3.8 which found out in all of the 20 syngas datasets investigated, the best agreement with UoS sCO<sub>2</sub> 1.0 and between the other mechanisms studied was for endwall OH\* IDT measurements from Karimi et al. [200] at the largest pressure investigated.

Figure 4.31 shows the normalised OH sensitivity analysis for UoS sCO<sub>2</sub> 2.0 and AramcoMech 2.0 for dataset 8 at 1200 K. The improved performance of AramcoMech 2.0 under these conditions appears to be explained by the relative OH sensitivity coefficients of Reaction 4.1 ( $H + O_2 (+M) \rightleftharpoons HO_2 (+M)$ ) and Reaction 4.3 ( $H + O_2 \rightleftharpoons O + OH$ ). Whereas previous sensitivity analyses are similar for AramcoMech 2.0 at 20 bar in Figure 4.23, for AramcoMech 2.0 at 40 bar and 85% CO<sub>2</sub> dilution, the OH sensitivity coefficient of Reaction 4.1 ( $H + O_2 (+M) \rightleftharpoons HO_2 (+M)$ ) is almost half that of Reaction 4.3 ( $H + O_2 \rightleftharpoons O + OH$ ). The larger rate of the branching reaction will favour OH production and thus reduce the IDT, making the mechanism more competitive with UoS sCO<sub>2</sub> 2.0. Another key difference highlighted by the sensitivity analysis is the greater sensitivity of AramcoMech 2.0 to Reaction 4.10 ( $H_2O_2 + H \rightleftharpoons HO_2 + H_2$ ). Despite Reaction 4.10 ( $H_2O_2 + H \rightleftharpoons HO_2 + H_2$ ) having a slightly larger rate coefficient in UoS sCO<sub>2</sub> 2.0, the greater sensitivity coefficient may highlight the greater importance of the H<sub>2</sub>O<sub>2</sub> pathway in AramcoMech 2.0. This reaction in practice proceeds in the reverse reaction, forming H<sub>2</sub>O<sub>2</sub> and H from HO<sub>2</sub> and H<sub>2</sub>. As the rate of production analysis shows that almost all H<sub>2</sub>O<sub>2</sub> reacts via dissociation into two molecules of OH, the overall effect of this reaction is to generate three radicals from the consumption of one, relatively unreactive, HO<sub>2</sub> radical and one molecule of H<sub>2</sub>. Interestingly, the sensitivity coefficient for Reaction 4.11 ( $OH + OH (+M) \rightleftharpoons H_2O_2 (+M)$ ) is similar for both mechanisms, despite the different rate coefficients employed in UoS sCO<sub>2</sub> 2.0 [254] and AramcoMech 2.0 [234]. It would be expected that the importance of a third body recombination reaction such as this would increase with pressure, however, the inverse effect is seen for Reaction 4.1 ( $H + O_2 (+M) \rightleftharpoons HO_2 (+M)$ ) in AramcoMech 2.0.



**Figure 4.31.** Normalized OH sensitivity analysis of dataset 8 for UoS sCO<sub>2</sub> 2.0 and AramcoMech 2.0 at 1200 K at 40 bar.

With regards to the UoS sCO<sub>2</sub> 2.0 mechanism, whilst it shows good agreement with the lowest temperature data point, it begins to underpredict the IDT as the temperature increases. Figure 4.32 shows the normalised OH sensitivity analysis of UoS sCO<sub>2</sub> 2.0 at 1175 K and 1300 K. As the temperature increases, the sensitivity of Reaction 4.1 ( $H + O_2 (+M) \rightleftharpoons HO_2 (+M)$ ) and Reaction 4.3 ( $H + O_2 \rightleftharpoons O + OH$ ) relative to other reactions. This appears to be due to the temperature coefficient ( $n$ ) of Reaction 4.3 ( $H + O_2 \rightleftharpoons O + OH$ ). Therefore, the overprediction here compared to that seen in the other seven datasets is likely due to reactions which become more important at 40 bar such as Reaction 4.8 ( $OH + HO_2 \rightleftharpoons H_2O + O_2$ ) and Reaction 4.10 ( $H_2O_2 + H \rightleftharpoons HO_2 + H_2$ ). Furthermore, as the concentration of CO<sub>2</sub> in the bath gas has increased, the underprediction observed could be due to the incorrect third body efficiencies in some of the recombination reactions, such as Reaction 4.1 ( $H + O_2 (+M) \rightleftharpoons HO_2 (+M)$ ) and Reaction 4.11 ( $OH + OH (+M) \rightleftharpoons H_2O_2 (+M)$ ). Often these are estimations, and the source of the third body is usually not included, so accurate experimental determination of the rate coefficients would be good to confirm these.



**Figure 4.32.** Normalized OH sensitivity analysis of dataset 8 for UoS sCO<sub>2</sub> 2.0 at 1175 K and 1300 K at 40 bar.

## 4.5. Summary and Outlook

Chapter 4 of this thesis provides a total of sixteen new IDT datasets for the investigation of the effect of a CO<sub>2</sub> bath gas on the combustion of H<sub>2</sub> and syngas. The experimental data were recorded on the KAUST HPST, a 10.16 cm, 13.2 m shock tube capable of withstanding pressures of up to 300 bar, although the module nature of the shock tube means the length of the driver and driven section can be varied. The experimental data recorded was used to validate the UoS sCO<sub>2</sub> 2.0 chemical kinetic mechanism based on the work of Chapter 3 and make suggestions for further improvements based on sensitivity analysis and investigating the ROP. One of the important effects noted for the combustion of syngas combustion is the effect of Reaction 4.2 ( $\text{CO} + \text{OH} \rightleftharpoons \text{CO}_2 + \text{H}$ ) reforming CO from the reaction of the prominent CO<sub>2</sub> bath gas and the H atom. Due to the large concentration of CO<sub>2</sub> when utilised as a bath gas, this pathway to form CO becomes significant and this slows down the overall rate of CO consumption, delaying the IDT relative to H<sub>2</sub>. This effect in some instances, can create separate ignition events, leading to two different possible IDTs. This not only further

complicates the experimental determination of IDT, which is already complicated by the effects of bifurcation, but it also increases the complexity of determining the IDT from the simulations. The two separate ignition events can cause two peaks in the OH time history or two points of the steepest gradient. In these instances, care must be taken to determine the IDT as close to what is being observed as possible.

The eight datasets for H<sub>2</sub> IDT were recorded at 20 and 40 bar, at a range of test gas compositions. It was found that UoS sCO<sub>2</sub> 2.0 outperformed AramcoMech 2.0 for modelling H<sub>2</sub> datasets in terms of quantitative analysis. UoS sCO<sub>2</sub> 2.0 fits all datasets recorded at  $\phi=1.0$  within an average absolute error of 20%, the largest observed experimental error. The two largest  $E$  (%) values are for datasets 4 and 5, which were recorded at  $\phi=0.2$  and  $\phi=2.0$ , respectively, the most fuel-lean and fuel-rich datasets investigated. This suggests further work is required to improve the performance of UoS sCO<sub>2</sub> 2.0 at the extremes of equivalence ratios. This can be explained by the compositions of the twenty datasets used to create UoS sCO<sub>2</sub> 1.0. Of the twenty datasets, eighteen were recorded between  $\phi=0.41$  and  $\phi=1.1$ , with two datasets on either side of this range. Whilst this does suggest the need for more datasets at the extremes of equivalence ratio, the intended application of direct-fired sCO<sub>2</sub> power cycles should be considered, as this is where it is important for the mechanism to perform best, which would be at fuel-lean conditions, high-pressures and large CO<sub>2</sub> dilutions [25]. Whilst UoS sCO<sub>2</sub> 2.0 is the superior mechanism for modelling the IDT of H<sub>2</sub> combustion, there is still room for improvement.

A further eight datasets were measured for syngas IDT at 20 and 40 bar, at a range of equivalence ratios, rate of H<sub>2</sub> and CO and bath gas compositions. There were more difficulties determining the IDT for syngas combustion due to the observed dual peaks in the OH time history. In most instances, the first peak of H<sub>2</sub> ignition should be used, as this would match what was observed experimentally. However, in some instances at low concentrations of H<sub>2</sub>, this first peak in the OH time history was negligible and thus the more prominent ignition event was used. The UoS sCO<sub>2</sub> 2.0 chemical kinetic mechanism was proven to be superior in simulating the IDT of syngas over AramcoMech 2.0, which vastly

overpredicted the IDT at 20 bar and in a 40% dilution of CO<sub>2</sub>. It was found that changing the equivalence ratio in this instance had little effect on the ability of UoS sCO<sub>2</sub> 2.0 to simulate the experimental data at  $\theta=1.0$ , but the mechanism performance did slightly decline as the H<sub>2</sub>:CO ratio was changed in either direction. More interestingly, the performance of AramcoMech 2.0 significantly improved at dataset 8 where the pressure and CO<sub>2</sub> dilution were increased to 40 bar and 85% respectively. This is likely an artefact of UoS sCO<sub>2</sub> 1.0 being created from sidewall IDT measurements such as Barak et al. [199] which significantly underpredict IDTs relative to endwall measurements, which are much less likely to be effected by premature ignition due to ignition hot spots.

## **5. Autoignition Study of Methane/Hydrogen Blends and Methane in CO<sub>2</sub>**

The combustion of methane and hydrogen blends is being introduced as a lower-carbon fuel mixture for traditional power plants to gradually phase out fossil fuels [290]. Adding hydrogen to methane increases the reactivity, which can lead to issues such as flame stability, meaning additional technological development is required for increasing the hydrogen concentration in the fuel [291]. The autoignition of methane and hydrogen blends has been comprehensively studied using both the shock tube and rapid compressions machine experimental techniques in argon and nitrogen (N<sub>2</sub>) [292-301]. However, all this available data is over 10 years old and has limited comparison to simulations from outdated chemical mechanisms, with no new studies published, therefore new data recorded using more modern experimental techniques and equipment is essential to bolster the database currently available as well as validate existing datasets.

This chapter contains ten new IDT datasets that populate gaps in the existing literature and allows for detailed intercomparison between various conditions. The ignition delay time of a mixture of methane and methane/hydrogen blends in CO<sub>2</sub> and N<sub>2</sub> has been studied over a pressure range of 20-40 bar. The experimental IDTs are compared to simulated IDTs and sensitivity and reaction pathway analysis are used to compare the chemical kinetics of combustion under various conditions. The experimental data from the present work is also compared to hydrogen IDT datasets recorded in a CO<sub>2</sub> bath gas previously reported in Harman-Thomas et al. [88] (Chapter 4) and methane IDT datasets for the same test gas composition from Pryor et al. [302] and Karimi et al. [127].

### **5.1. Experimental Details and Dataset Selection**

This work was also performed in collaboration with KAUST on the HPST which is detailed in Section 4.1 and the modelling techniques are the same as in Section 4.2. Therefore, the explanation is not repeated but Figure 5.1 shows a

representative emissions profile used to determine the IDT. Interestingly the sidewall emissions still show a dual peak in the ignition, this is most likely due to the pressure dropping at this point, so it is difficult to extract any information. The uncertainty in the IDTs is estimated to be  $\pm 15\%$  for an  $N_2$  bath gas and  $\pm 20\%$  for a  $CO_2$  bath gas.

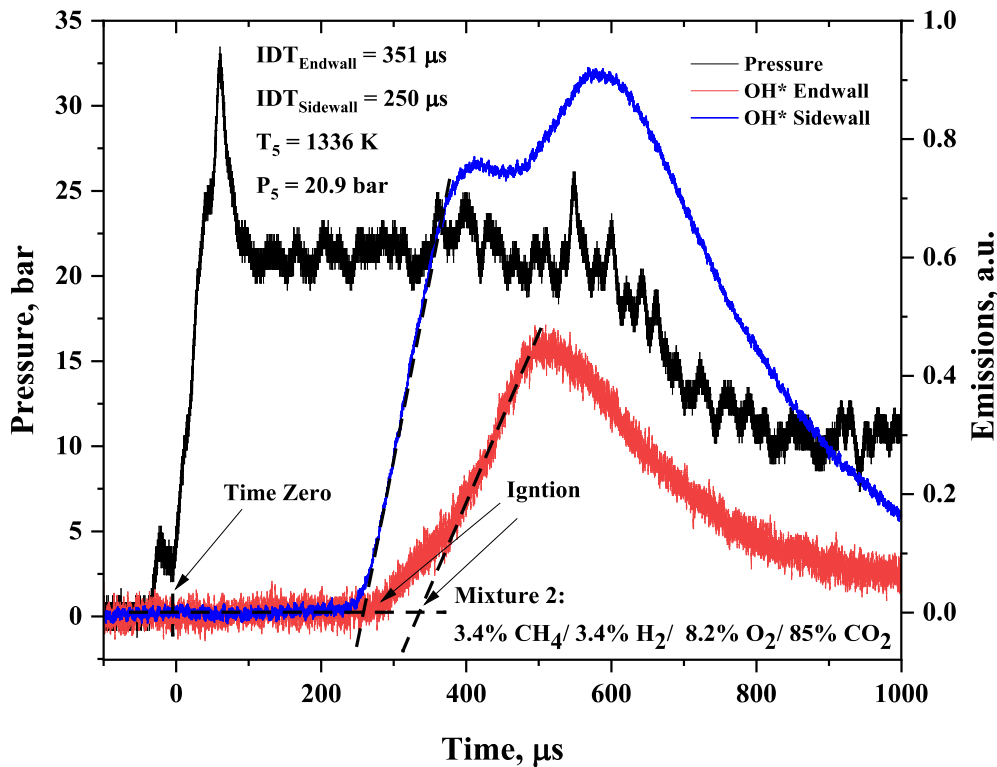


**Figure 5.1.** Representative pressure (sidewall) and emission (sidewall, endwall) profiles for time zero and ignition determination from mixture 1 at 20.9 bar and 1336 K.

Table 5.1 shows the five different mixtures studied at both 20 and 40 bar giving 10 new IDT datasets in total. The first two datasets were selected to study the effect of  $CO_2$  on modelling a methane/hydrogen blend as this mixture hasn't previously been investigated in  $CO_2$  using a shock tube. Comparing this mixture to nitrogen shows how well UoS s $CO_2$  2.0 can encapsulate the behaviour of combustion of the two fuels by validating against a fuel blend that the mechanism wasn't based on. Mixtures 3-5 were selected to investigate the effect of equivalence ratio on methane ignition in  $CO_2$ . Despite a wealth of data being available for methane combustion in  $CO_2$ , little has been done to investigate the effect of an equivalence ratio above 20 bar. Chapter 4 highlights the failure to capture the autoignition chemistry for hydrogen and syngas when the

equivalence ratio deviates in any direction from stoichiometric. These mixtures were selected to investigate if this behaviour was also observed for methane. In this work, NUIGMech1.1 [303-306] is used as a comparison mechanism. NUIGMech1.1 is a new iteration of the Aramco series of mechanisms which contains chemistry up to C7 hydrocarbons. This was avoided in Chapter 4 as the extra and unnecessary chemistry greatly increased the reaction time. However, as this was recommended by reviewers of the syngas paper, it was decided to make that change for this chapter. It was noted however that the base chemistry of H<sub>2</sub>/CH<sub>4</sub> is largely unchanged and thus the difference in IDT between AramcoMech 2.0 and NUIGMech1.1 was found to be small.

**Table 5.1.** CH<sub>4</sub> and CH<sub>4</sub>/H<sub>2</sub> mixtures of IDT datasets recorded in this work.

Mixture	Species Mole Fraction					Mixture Conditions		
	CH <sub>4</sub>	H <sub>2</sub>	O <sub>2</sub>	N <sub>2</sub>	CO <sub>2</sub>	T [K]	P [bar]	$\phi$
1	3.4	3.4	8.2	-	85	1257-1425	20, 40	1.0
2	3.4	3.4	8.2	85	-	1141-1295	20, 40	1.0
3	3	-	12	-	85	1387-1574	20, 40	0.5
4	5	-	10	-	85	1431-1554	20, 40	1.0
5	7.5	-	7.5	-	85	1470-1614	20, 40	2.0

Table 5.2 shows IDT datasets from previously published literature which are used to provide a comparison in the present study.

**Table 5.2.** CH<sub>4</sub> mixtures of IDT datasets from existing literature.

Source	Species Mole Fraction				Mixture Conditions		
	CH <sub>4</sub>	H <sub>2</sub>	O <sub>2</sub>	CO <sub>2</sub>	T [K]	P [bar]	$\phi$
<b>Pryor et al. [302]</b>	5	-	10	85	1334-1515	30	1.0
<b>Karimi et al. [127]</b>	5	-	10	85	1274-1433	100	1.0
<b>Harman-Thomas et al. [88]</b>	-	10	5	85	1142-1261	20	1.0
<b>Harman-Thomas et al. [88]</b>	-	10	5	85	1124-1266	40	1.0

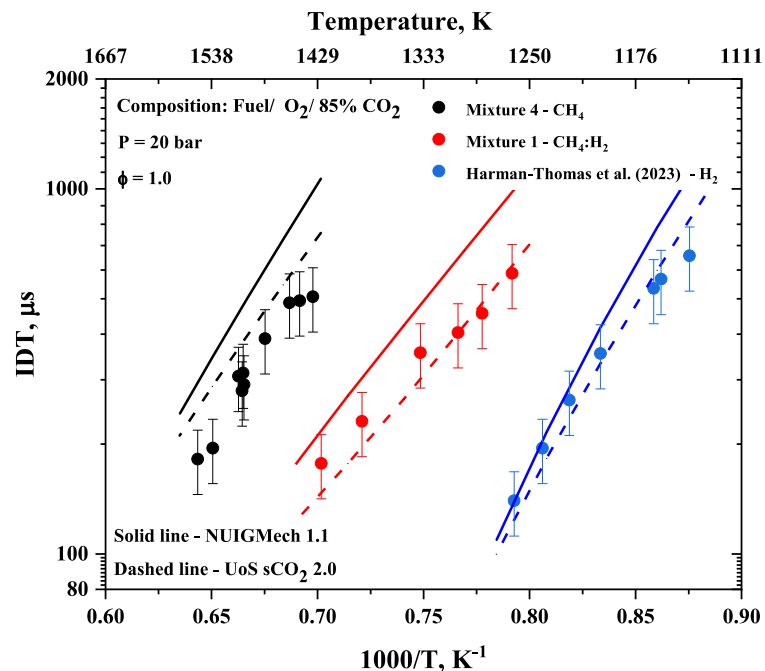
## 5.2. Discussion of Methane/Hydrogen Blends

This work presents the first-ever autoignition study of methane/hydrogen blends in CO<sub>2</sub>. Section 5.2.1 validates the performance of UoS sCO<sub>2</sub> 2.0 chemical kinetic mechanism for modelling a new fuel blend and compares this performance to

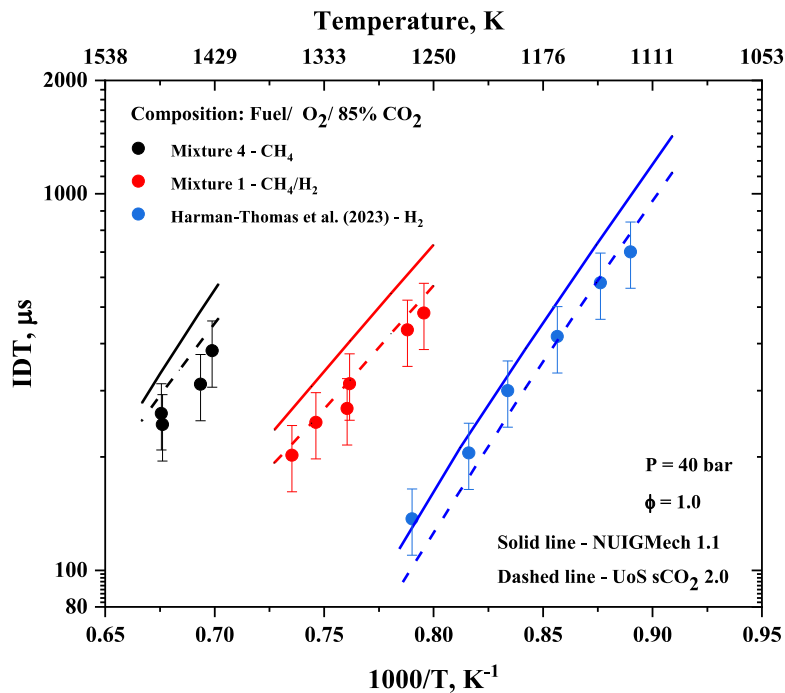
pure methane and pure hydrogen ignition. Section 5.2.2 compares the autoignition properties of stoichiometric methane/hydrogen ignition in CO<sub>2</sub> and N<sub>2</sub>.

### 5.2.1. Methane/Hydrogen Blends in CO<sub>2</sub>

As the autoignition of methane/hydrogen blends has not previously been investigated in a pure CO<sub>2</sub> bath gas. Therefore a 50:50 blend of the two fuels was selected for mixture 1 under stoichiometric conditions as a starting point for investigation. An 85% dilution of CO<sub>2</sub> was selected to allow for comparison with a stoichiometric hydrogen IDT dataset published in Harman-Thomas et al. [88] at the same pressures Figure 5.2 and Figure 5.3 show the IDTs of these two mixtures alongside mixture 4, a pure methane dataset recorded at 20 bar and 40 bar respectively. Despite having not been validated for methane/hydrogen blends, UoS sCO<sub>2</sub> 2.0 shows excellent agreement with the autoignition data for mixture 1 at both 20 and 40 bar, agreeing with every data point within the 20% experimental error. What is more surprising is the poor agreement of UoS sCO<sub>2</sub> 2.0 with the pure methane mixture (mix. 4), where there is a slight over-prediction in IDT across the full temperature range at both pressures.



**Figure 5.2.** Comparison of IDTs of mixture 4 (CH<sub>4</sub>:O<sub>2</sub>:CO<sub>2</sub>=5:10:85), mixture 1 (CH<sub>4</sub>:H<sub>2</sub>:O<sub>2</sub>:CO<sub>2</sub>=3.4:3.4:8.2:85) a mixture from Harman-Thomas et al. [88] (H<sub>2</sub>:O<sub>2</sub>:CO<sub>2</sub>=10:5:85) at 20 bar with NUIGMech1.1 and UoS sCO<sub>2</sub> 2.0 simulations.



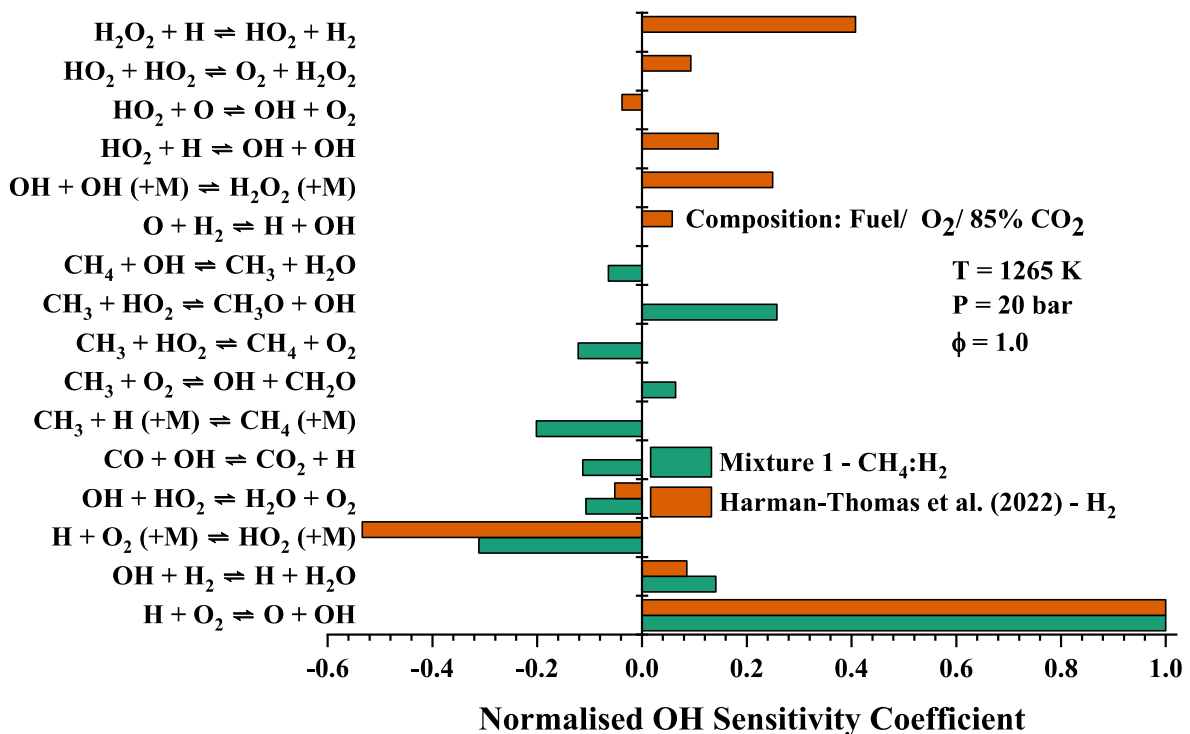
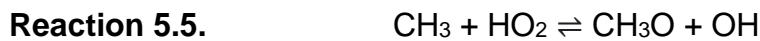
**Figure 5.3.** Comparison of IDTs of mixture 4 ( $\text{CH}_4:\text{O}_2:\text{CO}_2=5:10:85$ ), mixture 1 ( $\text{CH}_4:\text{H}_2:\text{O}_2:\text{CO}_2=3.4:3.4:8.2:85$ ) a mixture from Harman-Thomas et al. [88] ( $\text{H}_2:\text{O}_2:\text{CO}_2=10:5:85$ ) at 40 bar with NUIGMech1.1 and UoS sCO<sub>2</sub> 2.0 simulations.

Figure 5.4 shows the difference in normalised OH sensitivity analysis for mixture 1 and a mixture for Harman-Thomas et al. [88] of stoichiometric hydrogen combustion in 85% CO<sub>2</sub> at 20 bar. As one would expect, due to the lack of carbon in the hydrogen mixture, the key reactions in the sensitivity analysis are very different, with reactions containing CH<sub>4</sub>/CH<sub>3</sub> being more important for mixture 1. One of the most striking differences between the comparable reactions is the almost 2 times greater sensitivity coefficient the pure hydrogen mixture has for Reaction 5.1 ( $\text{H} + \text{O}_2 (+M) \rightleftharpoons \text{HO}_2 (+M)$ ). This reaction pathway consumes one H radical to form HO<sub>2</sub>, a much less reactive radical and therefore slows down the overall reaction rate. The reaction also competes with Reaction 5.2 ( $\text{H} + \text{O}_2 \rightleftharpoons \text{O} + \text{OH}$ ), a chain-branching reaction which promotes further combustion.



The reason for Reaction 5.1 ( $\text{H} + \text{O}_2 (+M) \rightleftharpoons \text{HO}_2 (+M)$ ) being identified as less important in the sensitivity analysis is due to its interaction with the simultaneous

methane ignition. Whilst HO<sub>2</sub> slows the rate of reaction for hydrogen combustion, waiting for its slow self-reaction to form H<sub>2</sub>O<sub>2</sub> (Reaction 5.3 (HO<sub>2</sub> + HO<sub>2</sub> ⇌ H<sub>2</sub>O<sub>2</sub> + O<sub>2</sub>)) or reacting with another H<sub>2</sub> molecule to form H<sub>2</sub>O<sub>2</sub> (Reaction 5.4 (H<sub>2</sub>O<sub>2</sub> + H ⇌ HO<sub>2</sub> + H<sub>2</sub>)). With methane present in the mixture, HO<sub>2</sub> can react with the methyl radical via Reaction 5.5 (CH<sub>3</sub> + HO<sub>2</sub> ⇌ CH<sub>3</sub>O + OH) to simultaneously promote the methane combustion pathway and form an OH radical. This can also be seen by the large positive sensitivity coefficient for Reaction 5.5 (CH<sub>3</sub> + HO<sub>2</sub> ⇌ CH<sub>3</sub>O + OH) in Figure 5.4 for mixture 1, thus explaining why the retarding effect of HO<sub>2</sub> in mixture 1 is not as important.



**Figure 5.4.** Normalised OH sensitivity analyses of mixture 1 (CH<sub>4</sub>:H<sub>2</sub>:O<sub>2</sub>:CO<sub>2</sub>=3.4:3.4:8.2:85) and a mixture from Harman-Thomas et al. [88] (H<sub>2</sub>:O<sub>2</sub>:CO<sub>2</sub>=10:5:85) with UoS sCO<sub>2</sub> 2.0 simulations at 1265 K and 20 bar.

Furthermore, the alternative reaction pathways available for HO<sub>2</sub> in a methane/hydrogen blend reduce the importance of H<sub>2</sub>O<sub>2</sub> formation to the overall

chemistry as shown in Figure 5.4. Figure 5.5 shows the ROP analysis of mixture 1 and the respective hydrogen mixture at 1265 K and 20 bar for key hydrogen combustion intermediates. As deduced from the sensitivity analysis, the mole fraction of  $H_2O_2$  is much smaller for the  $CH_4/H_2$  mixture, the  $HO_2$  species profiles are more difficult to compare due to the longer reaction time of the  $CH_4/H_2$  mixture, however, the maximum mole fraction reached is under half of that of the  $H_2$  mixture, indicating faster consumption. Interestingly, another key difference is the maximum concentrations of the H radical being much greater for the pure  $H_2$  mixture. This greater concentration of H and O is due to a more rapid temperature rise at the shorter ignition time, which favours Reaction 5.6 ( $OH + H_2 \rightleftharpoons H + H_2O$ ) and Reaction 5.7 ( $CO + OH \rightleftharpoons CO_2 + H$ ) whilst hindering Reaction 5.1 ( $H + O_2 (+M) \rightleftharpoons HO_2 (+M)$ ). Furthermore, the ROP analysis of the H radical (see Figure 5.6) for these mixtures shows that Reaction 5.6 ( $OH + H_2 \rightleftharpoons H + H_2O$ ) is the dominant reaction pathway for both mixtures, and this reaction is faster in the pure hydrogen mixture due to the greater concentration of  $H_2$ .



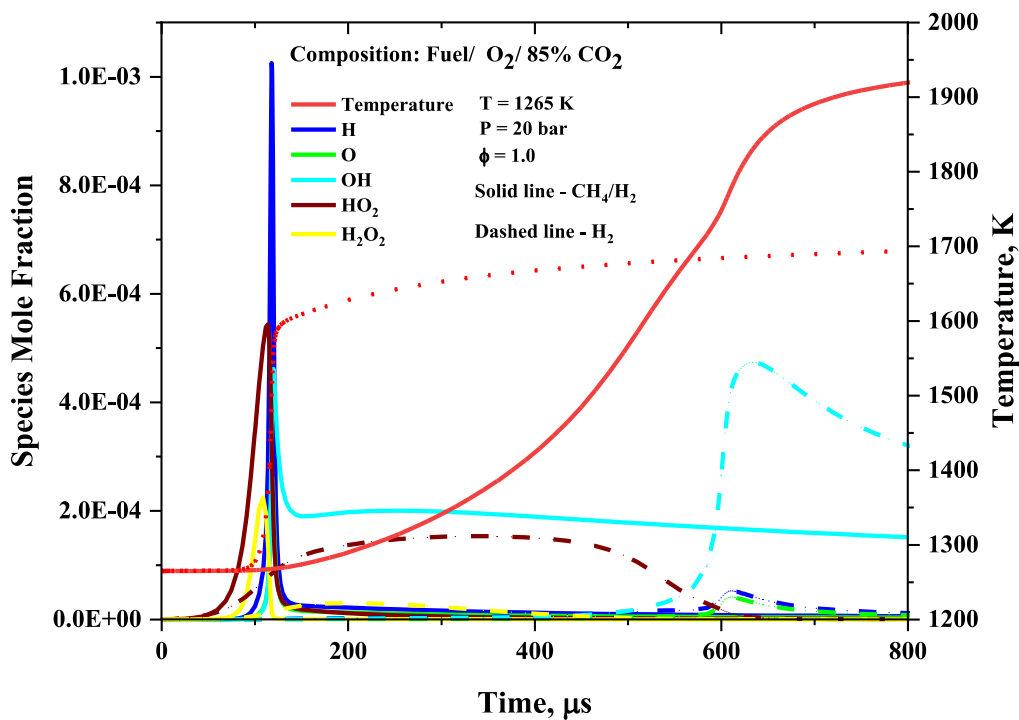


**Figure 5.5.** Mole fractions of key intermediate species of mixture 1 (CH<sub>4</sub>:H<sub>2</sub>:O<sub>2</sub>:CO<sub>2</sub>=3.4:3.4:8.2:85) and a mixture from Harman-Thomas et al. [88] (H<sub>2</sub>:O<sub>2</sub>:CO<sub>2</sub>=10:5:85) with UoS sCO<sub>2</sub> 2.0 simulations at 1265 K and 20 bar.

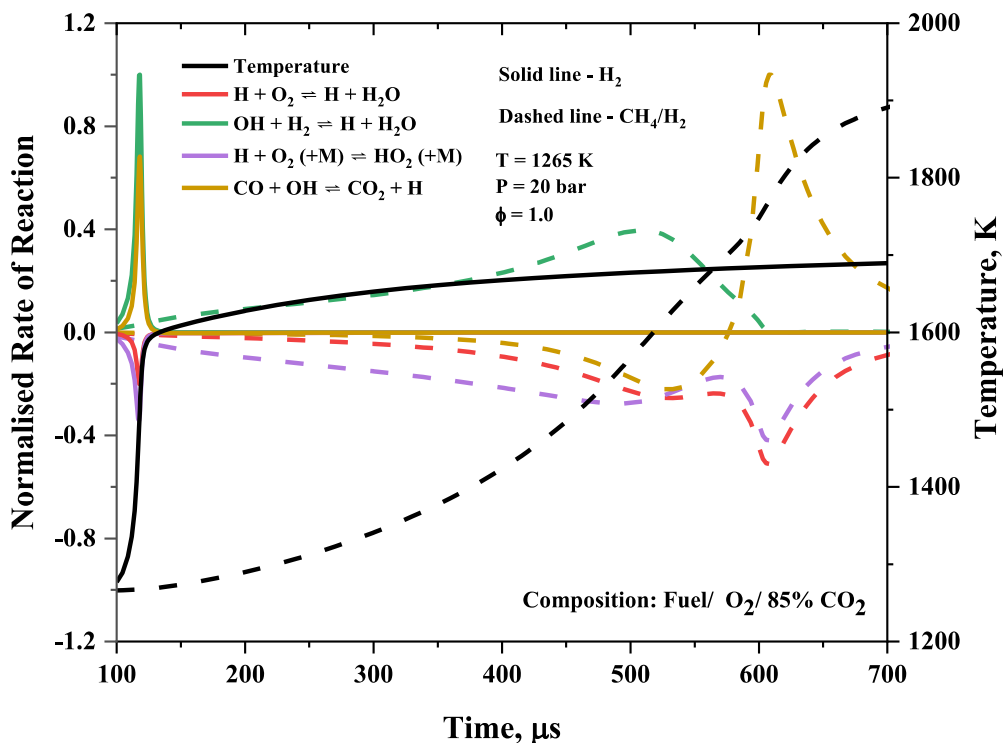


**Figure 5.6.** ROP of H in mixture 1 (CH<sub>4</sub>:H<sub>2</sub>:O<sub>2</sub>:CO<sub>2</sub>=3.4:3.4:8.2:85) and a mixture from Harman-Thomas et al. [88] (H<sub>2</sub>:O<sub>2</sub>:CO<sub>2</sub>=10:5:85) with UoS sCO<sub>2</sub> 2.0 simulations at 1265 K and 20 bar.

Figure 5.7 shows the normalised OH sensitivity analysis of mixture 1 and mixture 4 at 1425 K and 20 bar to study the influence of hydrogen on ignition. The first thing to note is, as this is a normalised sensitivity analysis, all methane-based reactions for mixture 1 appear relatively less sensitive than for mixture 4. This is an artefact of substituting CH<sub>4</sub> in the fuel composition, and therefore these reactions appear less sensitive due to the smaller methane concentration. Figure 5.7 shows ethane formation via the recombination of two methyl radicals is identified as much more important to mixture 4 in the sensitivity analysis. For both mixtures, Reaction 5.8 ( $CH_3 + CH_3 (+M) \rightleftharpoons C_2H_6 (+M)$ ) is the primary consumption pathway of CH<sub>3</sub> for both mixtures due to the third body efficiency of CO<sub>2</sub> making this a fast reaction, which has been seen in previous work on methane combustion in CO<sub>2</sub>, especially at high pressures [122, 127, 151]. Wang et al. [307] show at 700 K in a He bath gas, the high-pressure limit for this reaction is approximately 1 bar. Therefore even for a CO<sub>2</sub> bath gas, it is likely that at 300 bar the reaction is far from the fall-off region. The influence on OH sensitivity analysis comes from the difference in ethane reactivity at the point of ignition. For mixture 1, the hydrogen fuel provides more H radicals meaning Reaction 5.9 ( $C_2H_6 + H \rightleftharpoons C_2H_5 + H_2$ ) is more prominent whereas Reaction 5.10, which consumes OH, is the larger reaction pathway for mixture 4 (see Figure 5.8). This results in Reaction 5.8 ( $CH_3 + CH_3 (+M) \rightleftharpoons C_2H_6 (+M)$ ) having a larger negative OH sensitivity coefficient in Figure 5.7.



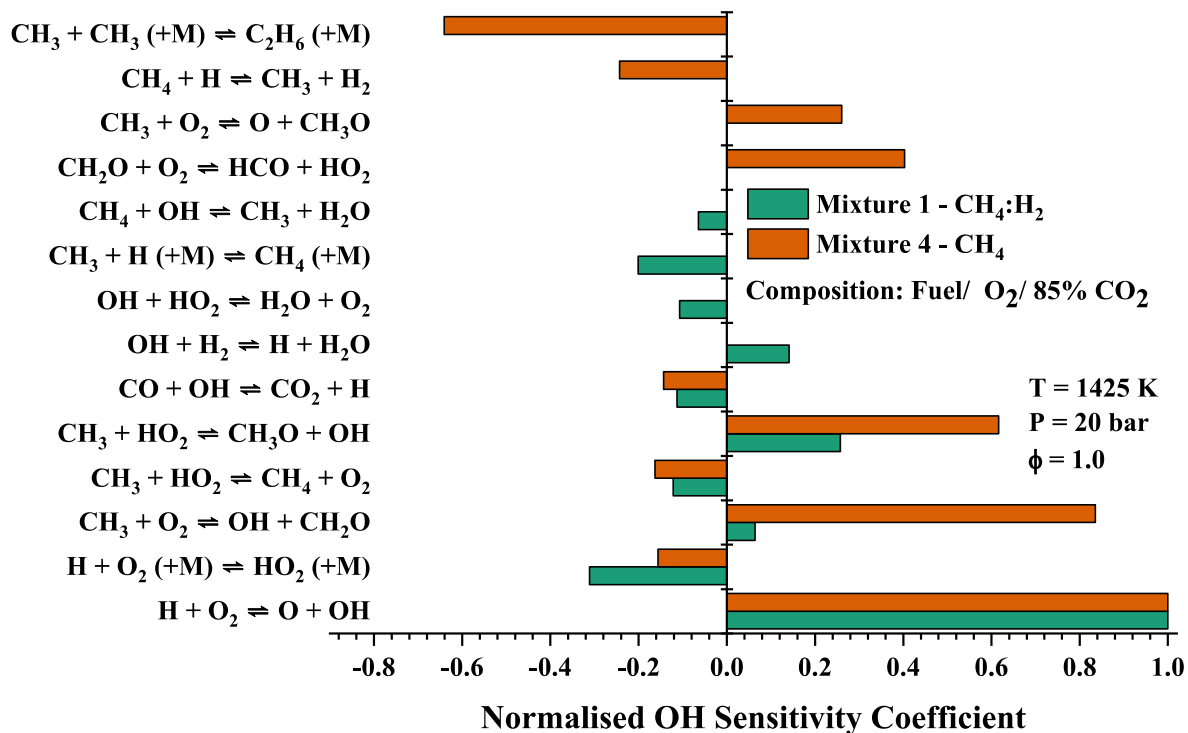


Figure 5.7. Normalised OH sensitivity analyses of mixture 1 (CH<sub>4</sub>:H<sub>2</sub>:O<sub>2</sub>:CO<sub>2</sub>=3.4:3.4:8.2:85) and mixture 4 (CH<sub>4</sub>:O<sub>2</sub>:CO<sub>2</sub>=5:10:85) with UoS sCO<sub>2</sub> 2.0 simulations at 1425 K and 20 bar.

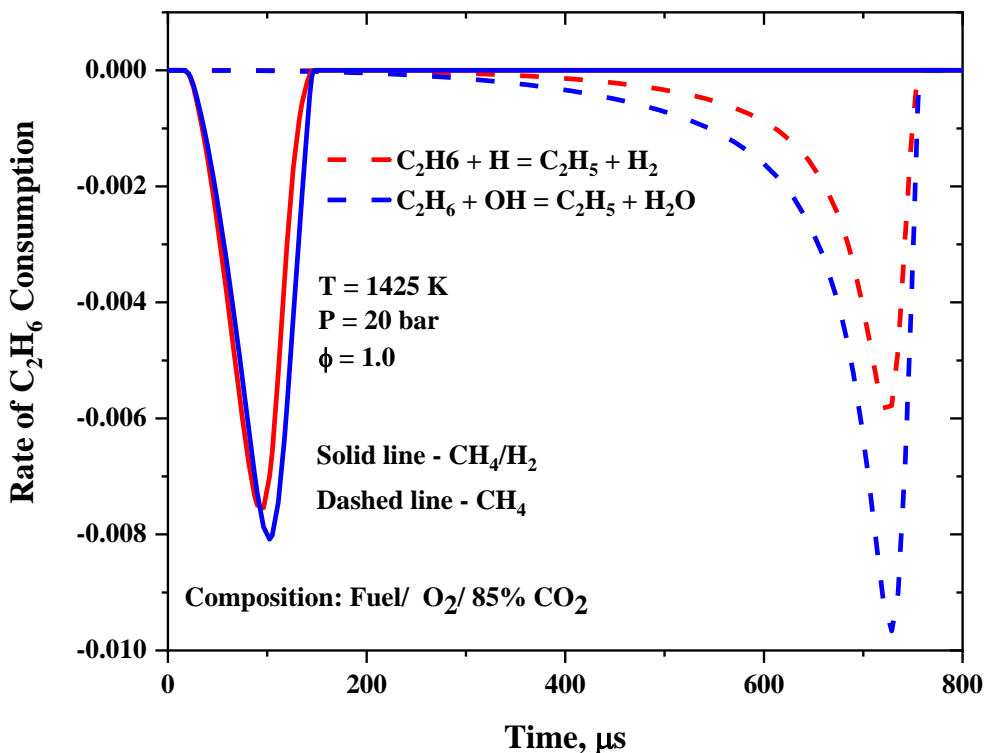
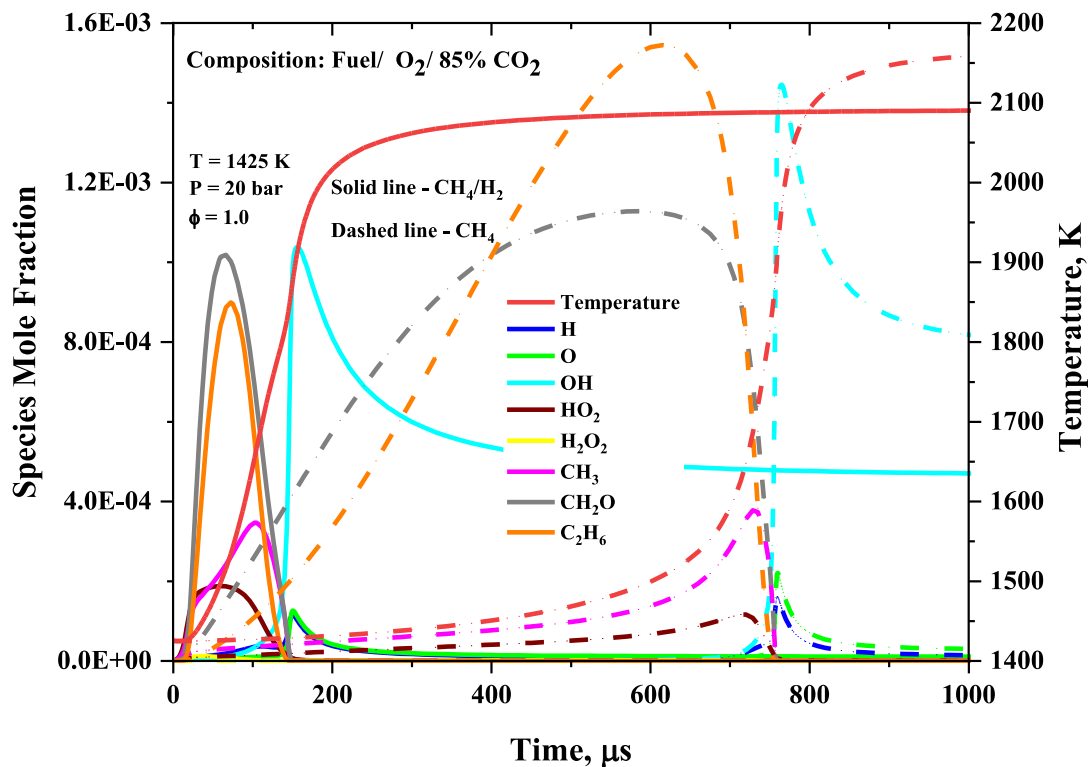


Figure 5.8. Ethane ROP of mixture 4 (CH<sub>4</sub>:O<sub>2</sub>:CO<sub>2</sub>=5:10:85), mixture 1 (CH<sub>4</sub>:H<sub>2</sub>:O<sub>2</sub>:CO<sub>2</sub>=3.4:3.4:8.2:85) with UoS sCO<sub>2</sub> 2.0 simulations at 1425 K and 20 bar.

The ROP of seven key intermediates of methane and hydrogen combustion at 1425 K and 20 bar for mixtures 1 and 4 over the first 1000 μs of the ignition

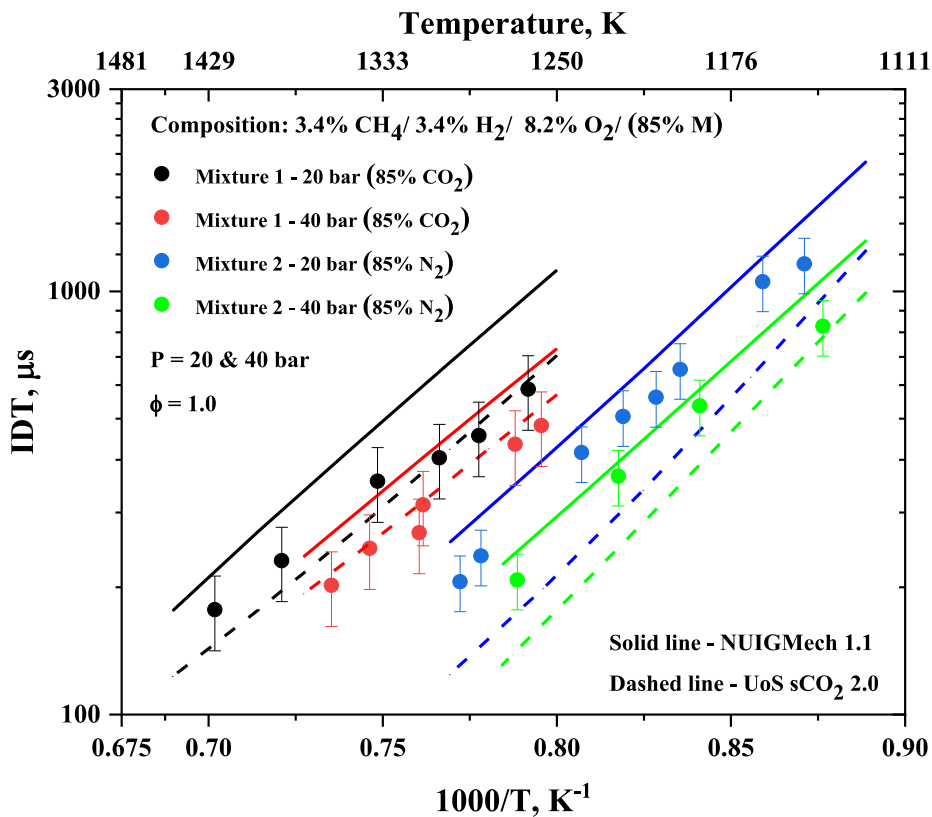
reaction is shown in Figure 5.9. Despite the difference in fuel composition, the maximum species mole fractions of all seven species are similar, unlike what was observed when compared to hydrogen ignition. Figure 5.9 shows that the maximum species mole fraction of  $C_2H_6$  is much greater for mixture 4 than mixture 1, showing the much greater importance of Reaction 5.8 ( $CH_3 + CH_3 (+M) \rightleftharpoons C_2H_6 (+M)$ ) and the  $C_2H_6$  formation pathway for the pure methane fuel. Whilst this is partially due to the lower concentration of methane and thus carbon-based radicals, for other carbon-based species such as  $CH_2O$  and  $CH_3$ , the maximum mole fraction remains similar across the two mixtures. Subsequently, the greater influence of  $C_2H_6$  for mixture 4 is two-fold. Firstly, the quicker increase in temperature over the first part of the reaction seen for the  $CH_4/H_2$  mixture means the recombination reaction to form  $C_2H_6$  is less favourable and therefore will have a slower reaction rate. Secondly, the greater relative mole fraction of  $HO_2$  compared to  $CH_3$  gives promotes an alternate reaction pathway via Reaction 5.5 ( $CH_3 + HO_2 \rightleftharpoons CH_3O + OH$ ). These two factors coupled reduce the importance of the ethane formation pathway for the methane/hydrogen mixture.



**Figure 5.9.** ROP analyses of key intermediate species of mixture 1 ( $CH_4:H_2:O_2:CO_2=3.4:3.4:8.2:85$ ) and mixture 4 ( $CH_4:O_2:CO_2=5:10:85$ ), with UoS sCO<sub>2</sub> 2.0 simulations at 1425 K and 20 bar.

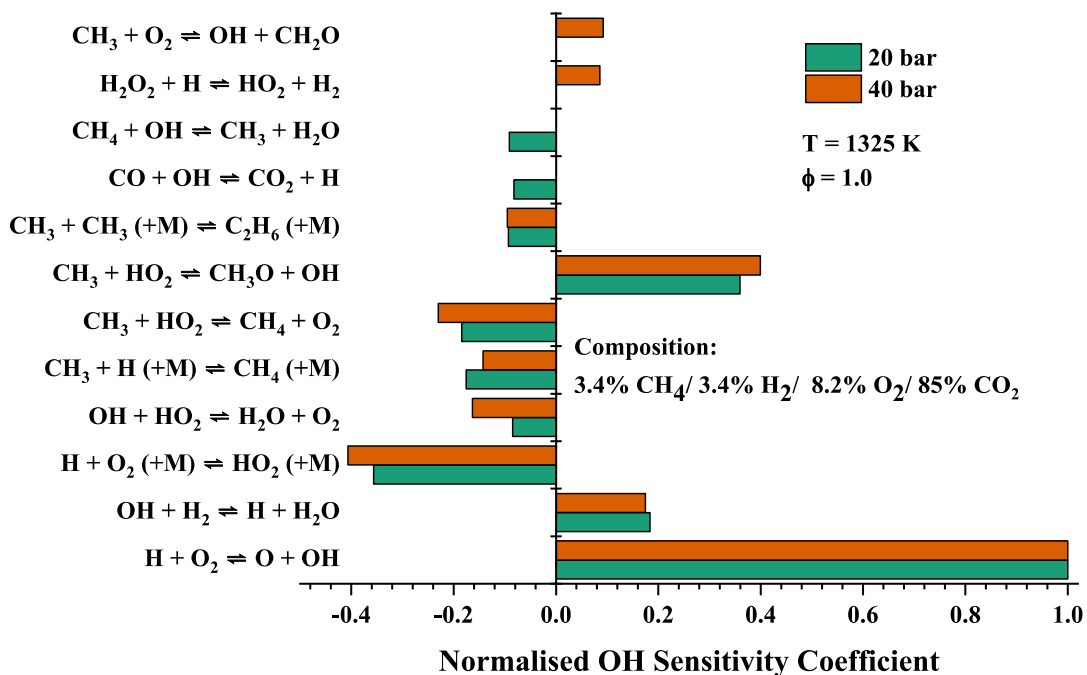
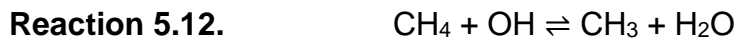
### 5.2.2. Effect of CO<sub>2</sub> Dilution

As discussed in the introduction, the autoignition of methane/hydrogen blends has been well-researched in N<sub>2</sub> and argon using shock tubes and rapid compression machines. However, most of these studies were performed at least a decade ago, with less sophisticated chemical kinetic mechanisms and modelling software. Therefore, mixture 2 was recorded in an 85% N<sub>2</sub> bath gas to investigate the effects of utilising CO<sub>2</sub> as a bath gas. As expected, the IDTs in CO<sub>2</sub> are much slower than in N<sub>2</sub> at a given temperature due to the greater third-body effect of CO<sub>2</sub> to moderate the reaction temperature. Despite the excellent performance of UoS sCO<sub>2</sub> 2.0 for mixture 1, it is unsurprising Figure 5.10 shows that UoS sCO<sub>2</sub> 2.0 displays poor agreement for mixture 2 as it was developed for mixtures with large CO<sub>2</sub> concentrations. What is more surprising, is the poor performance of NUIGMech1.1 under these conditions despite the mechanism being well-versed in the autoignition of H<sub>2</sub> and C1-C7 hydrocarbons in N<sub>2</sub> which slightly over-predicts IDT across the full temperature range.



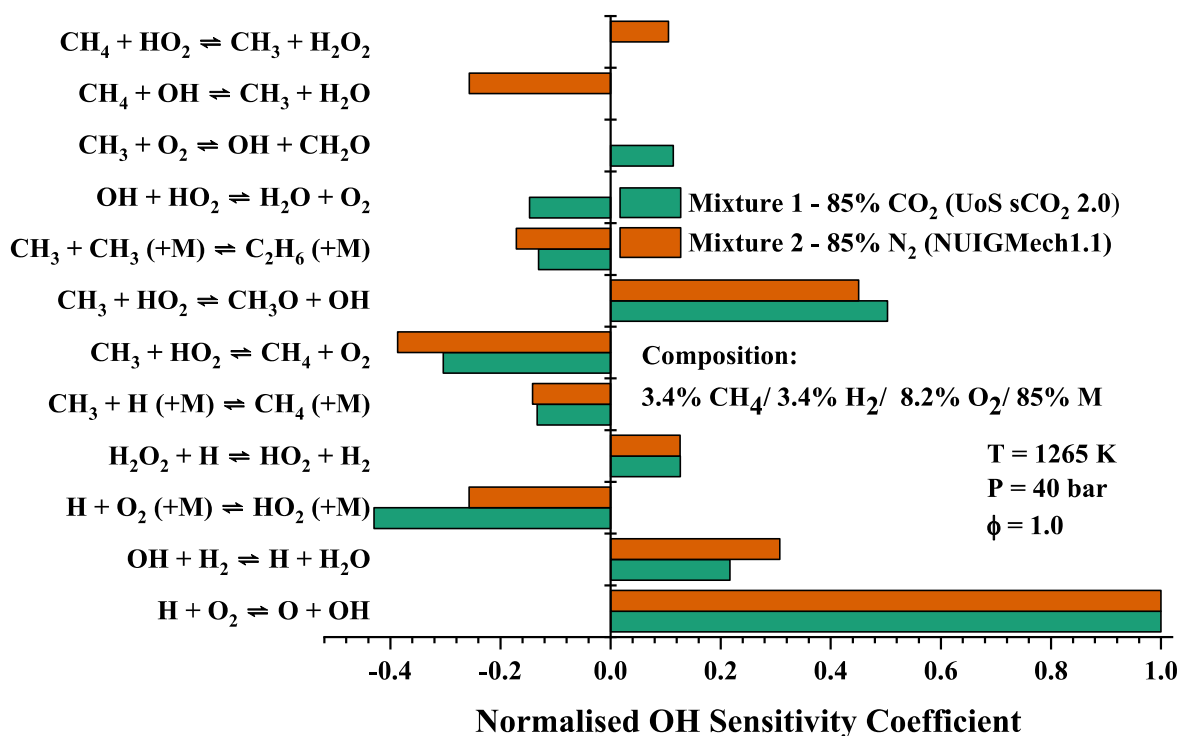
**Figure 5.10.** Comparison of IDTs of mixture 1 (CH<sub>4</sub>:H<sub>2</sub>:O<sub>2</sub>:CO<sub>2</sub>=3.4:3.4:8.2:85) and mixture 2 (CH<sub>4</sub>:H<sub>2</sub>:O<sub>2</sub>:N<sub>2</sub>=3.4:3.4:8.2:85) at 20 bar and 40 bar with NUIGMech1.1 and UoS sCO<sub>2</sub> 2.0 simulations.

The sensitivity analysis shown in Figure 5.11 was performed for UoS sCO<sub>2</sub> 2.0 mechanism for mixture 1 to investigate what effect pressure has on the combustion chemistry CO<sub>2</sub>. As the agreement of the mechanism with the data is good for the complete temperature profile, a mid-point in the temperature was selected to perform the analysis. The analysis shows that despite the chemistry remaining very similar, as the pressure is increased, the third body Reaction 5.11 ( $CH_3 + H (+M) \rightleftharpoons CH_4 (+M)$ ) becomes more important, thus favouring HO<sub>2</sub> and subsequently H<sub>2</sub>O<sub>2</sub> formation via Reaction 5.4 ( $H_2O_2 + H \rightleftharpoons HO_2 + H_2$ ). In contrast, the greater sensitivity of mixture 1 at 20 bar for Reaction 5.11 ( $CH_3 + H (+M) \rightleftharpoons CH_4 (+M)$ ) and Reaction 5.12 ( $CH_4 + OH \rightleftharpoons CH_3 + H_2O$ ), suggests that in the presence of smaller HO<sub>2</sub> concentrations, CH<sub>3</sub> radicals are more likely to reform the methane which slows down the overall rate of combustion. Given the importance of Reaction 3.11 ( $H + O_2 (+M) \rightleftharpoons HO_2 (+M)$ ) under these conditions, it is important to revisit work in CO<sub>2</sub> to determine the high-pressure limit of this reaction [308].



**Figure 5.11.** Normalised OH sensitivity analyses for mixture 1 (CH<sub>4</sub>:H<sub>2</sub>:O<sub>2</sub>:CO<sub>2</sub>=3.4:3.4:8.2:85) at 20 bar and 40 bar with UoS sCO<sub>2</sub> 2.0 simulations at 1325 K.

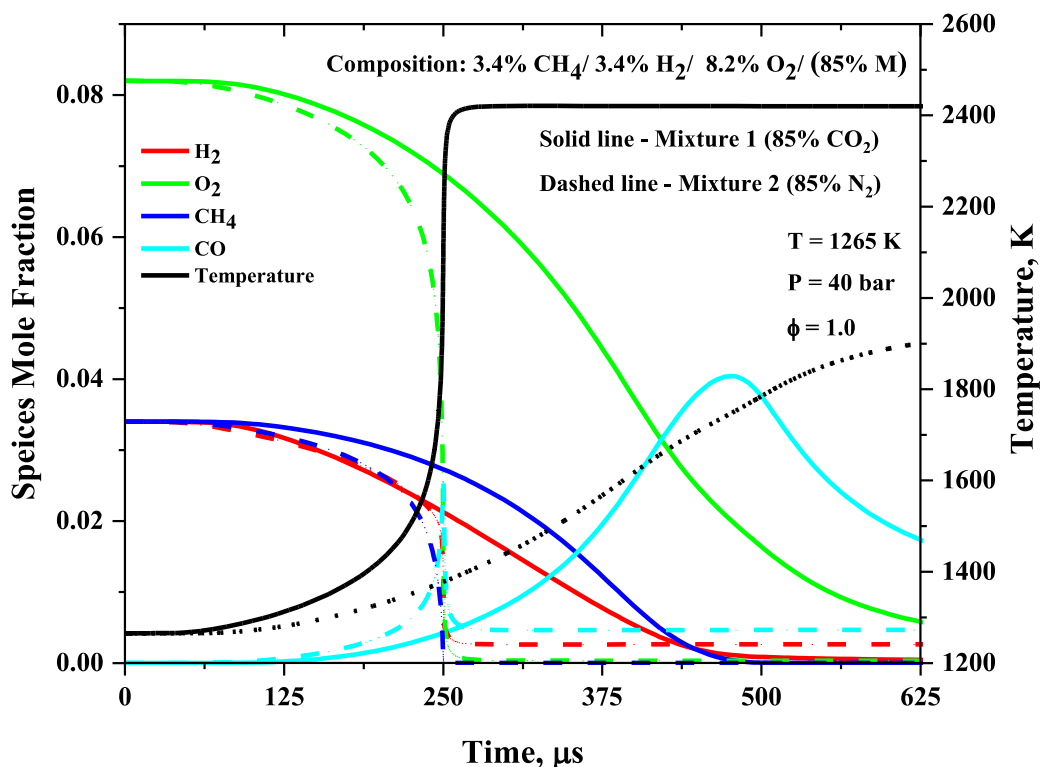
Figure 5.12 shows the normalised OH sensitivity analysis of mixture 1 and mixture 2 at 1265 K and 20 bar. For this analysis, UoS sCO<sub>2</sub> 2.0 was used to simulate mixture 1 and NUIGMech1.1 for mixture 2 due to each mechanism's better performance with its respective mixture meaning it gives a more accurate interpretation of the chemical kinetics. As Figure 5.12 reveals that both mechanisms are sensitive to seven key reactions under their respective conditions, it could be inferred that the bath gas composition has little effect on the ignition chemistry of methane/hydrogen blends. However, as Figure 5.10 shows, UoS sCO<sub>2</sub> 2.0 significantly under predicts the IDT of mixture 2 and NUIGMech1.1 significantly over predicts the IDT of mixture 1. This means that, whilst both mechanisms do a reasonable job modelling IDT of the methane/hydrogen blend in the bath gas for which they were validated, the rate coefficients of these key reactions must be chemically or physically affected by the presence of such large quantities in a manner which causes the mechanisms to fail to model both mixtures 1 and 2. Another key difference in Figure 5.12 is the large sensitivity of mixture 2 to Reaction 5.12 ( $CH_4 + OH \rightleftharpoons CH_3 + H_2O$ ), which did not appear as one of the top 10 most sensitive reactions for UoS sCO<sub>2</sub> 2.0 at 1265 K but did appear as one of the lesser reactions at 1325 K and 20 bar (see Figure 5.11). Although the rate coefficient used for Reaction 5.12 ( $CH_4 + OH \rightleftharpoons CH_3 + H_2O$ ) from Cohen et al. [309] in UoS sCO<sub>2</sub> 2.0 has a larger A factor than its counterpart from NUIGMech1.1, the NUIGMech1.1 rate coefficient has a larger temperature dependence ( $n=1.93$ ). Therefore, as the reaction temperature is greater in N<sub>2</sub>, this reaction will become more important and the sensitivity to the reaction is larger.



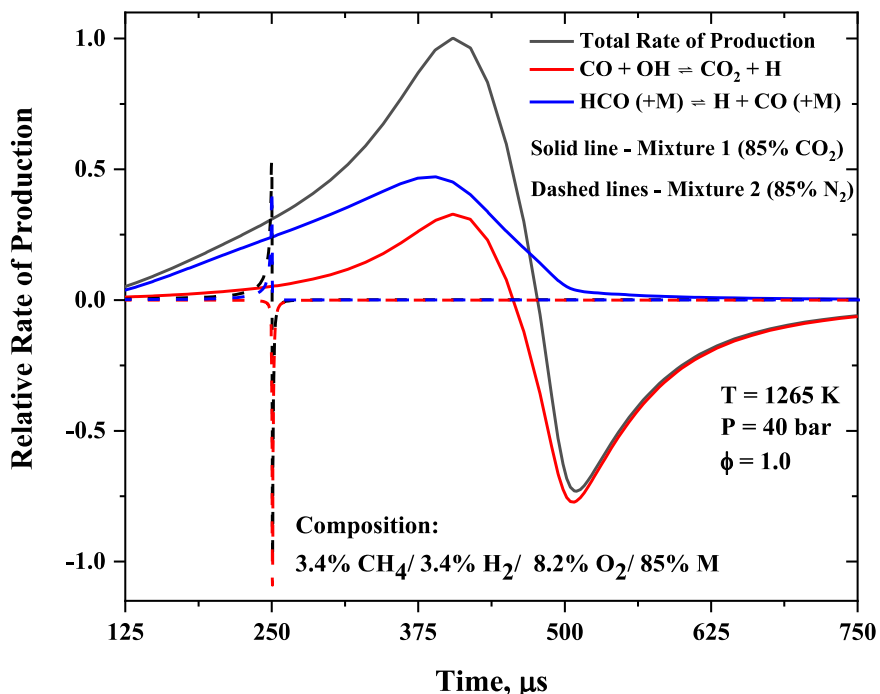
**Figure 5.12.** Normalised OH sensitivity analyses for mixture 1 (CH<sub>4</sub>:H<sub>2</sub>:O<sub>2</sub>:CO<sub>2</sub>=3.4:3.4:8.2:85) with UoS sCO<sub>2</sub> 2.0 simulations and mixture 2 (CH<sub>4</sub>:H<sub>2</sub>:O<sub>2</sub>:N<sub>2</sub>=3.4:3.4:8.2:85) with NUIGMech1.1 simulations at 40 bar and 1265 K.

In Harman-Thomas et al. [310], it was noted that for syngas ignition in CO<sub>2</sub>, the reformation of CO due to the large availability of CO<sub>2</sub> to react via Reaction 5.7 ( $CO + OH \rightleftharpoons CO_2 + H$ ). Figure 5.13 compares the species mole fractions of CH<sub>4</sub>, H<sub>2</sub>, CO and O<sub>2</sub> for mixtures 1 and 2 at 1265 K and 40 bar. As anticipated due to the role of Reaction 5.7 ( $CO + OH \rightleftharpoons CO_2 + H$ ), the maximum concentration of CO is greater for mixture 1, but it also changes the shape of the curve, with the post-ignition consumption being much slower than the almost instantaneous loss of CO observed in mixture 2. For both mixtures, Reaction 5.7 ( $CO + OH \rightleftharpoons CO_2 + H$ ) is responsible for almost all CO loss (Figure 5.14), however, in CO<sub>2</sub> the reverse of this reaction is responsible for some CO production before the ignition event, as well as the expected production through Reaction 5.13 ( $HCO (+M) = H + CO (+M)$ ).





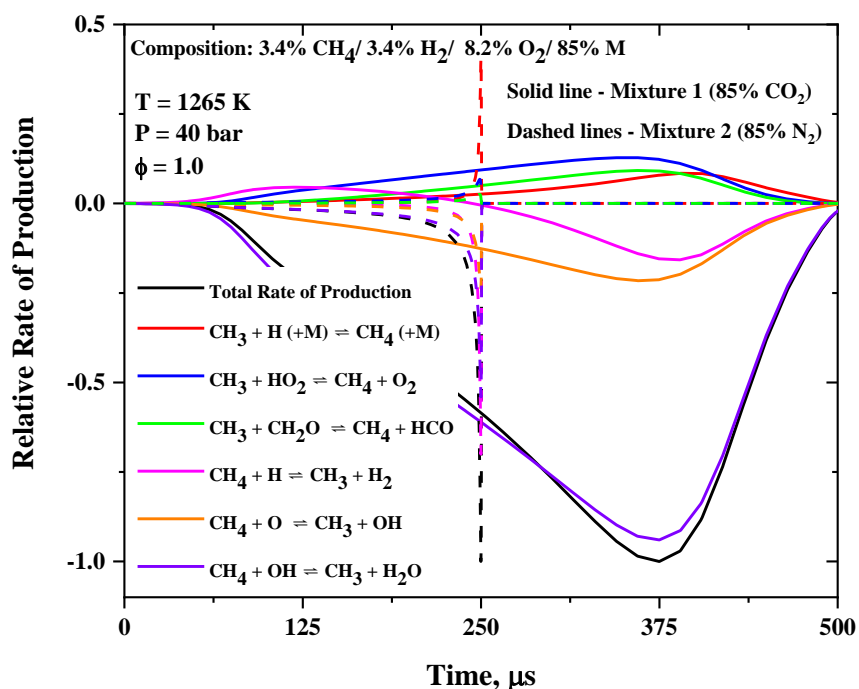
**Figure 5.13.** Species mole fraction of H<sub>2</sub>, CH<sub>4</sub>, O<sub>2</sub> and CO for mixture 1 (CH<sub>4</sub>:H<sub>2</sub>:O<sub>2</sub>:CO<sub>2</sub>=3.4:3.4:8.2:85) and mixture 2 (CH<sub>4</sub>:H<sub>2</sub>:O<sub>2</sub>:N<sub>2</sub>=3.4:3.4:8.2:85) at 20 bar with UoS sCO<sub>2</sub> 2.0 and NUIGMech1.1 simulations respectively at 1265 K and 40 bar.



**Figure 5.14.** ROP analysis of CO for mixture 1 (CH<sub>4</sub>:H<sub>2</sub>:O<sub>2</sub>:CO<sub>2</sub>=3.4:3.4:8.2:85) with UoS sCO<sub>2</sub> 2.0 simulations and mixture 2 (CH<sub>4</sub>:H<sub>2</sub>:O<sub>2</sub>:N<sub>2</sub>=3.4:3.4:8.2:85) with NUIGMech1.1 simulations at 40 bar and 1265 K.

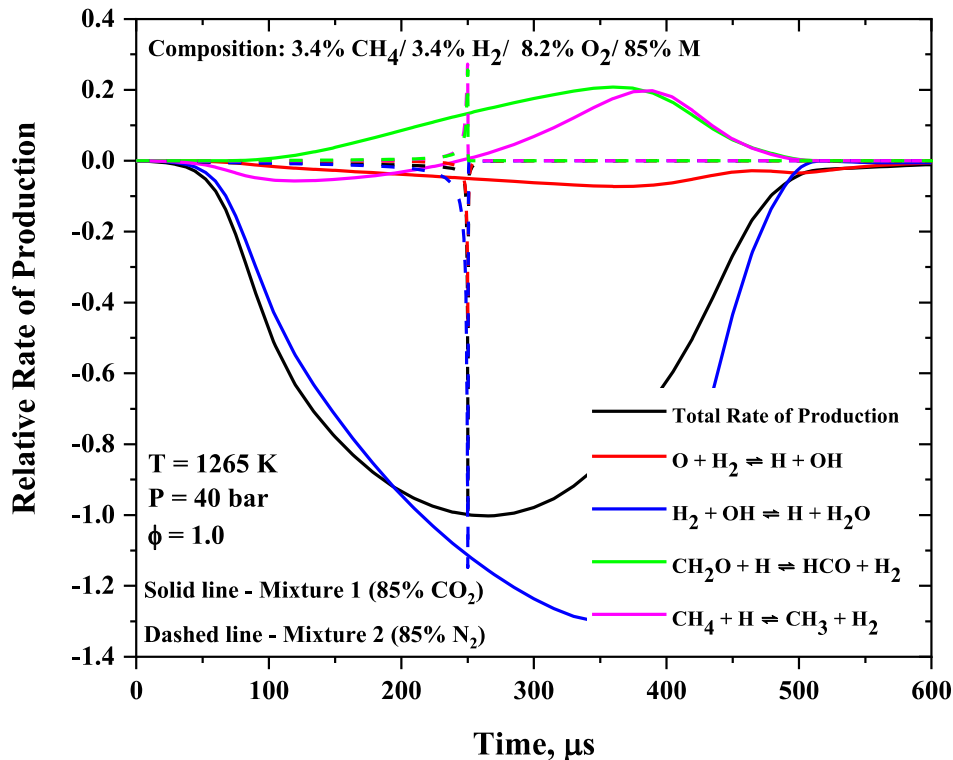
It is the CH<sub>4</sub> chemistry, which is most notably different between the mixtures, thus highlighting the importance that CO<sub>2</sub> has on the chemical kinetics (Figure 5.15). Not only is the ignition event much longer for mixture 1 the reactions responsible for the loss and formation are very different. In mixture 2 Reaction 5.11 ( $CH_3 + H (+M) \rightleftharpoons CH_4 (+M)$ ) is responsible for almost all CH<sub>4</sub> reformation, whereas, for mixture 1, Reaction 5.11 ( $CH_3 + H (+M) \rightleftharpoons CH_4 (+M)$ ) and Reaction 5.14 ( $CH_3 + CH_2O \rightleftharpoons CH_4 + HCO$ ) play a similarly important role. Furthermore, whilst Reaction 5.12 ( $CH_4 + OH \rightleftharpoons CH_3 + H_2O$ ) is responsible for the majority of CH<sub>4</sub> consumption in CO<sub>2</sub>, in mixture 2 Reaction 5.15 ( $CH_4 + H \rightleftharpoons CH_3 + H_2$ ) is equally important. The greater importance of Reaction 5.11 ( $CH_3 + H (+M) \rightleftharpoons CH_4 (+M)$ ) and Reaction 5.15 ( $CH_4 + H \rightleftharpoons CH_3 + H_2$ ) for mixture 2 indicates the greater importance of the hydrogen radical (H) in a nitrogen bath gas. This can be explained by a smaller pool of H radicals in CO<sub>2</sub> due to Reaction 5.11 ( $CH_3 + H (+M) \rightleftharpoons CH_4 (+M)$ ) being more favourable in CO<sub>2</sub> and the reverse of Reaction 5.7 ( $CO + OH \rightleftharpoons CO_2 + H$ ) due to the large concentration of CO<sub>2</sub> making this reaction pathway favourable before the main ignition event (Figure 5.14). Also, the absence of the H radical promotes alternative reaction pathways in CO<sub>2</sub>.





**Figure 5.15.** ROP analysis of CH<sub>4</sub> for mixture 1 (CH<sub>4</sub>:H<sub>2</sub>:O<sub>2</sub>:CO<sub>2</sub>=3.4:3.4:8.2:85) with UoS sCO<sub>2</sub> 2.0 simulations and mixture 2 (CH<sub>4</sub>:H<sub>2</sub>:O<sub>2</sub>:N<sub>2</sub>=3.4:3.4:8.2:85) with NUIGMech1.1 simulations at 40 bar and 1265 K.

Figure 5.13 was plotted to compare how the consumption of H<sub>2</sub> and CH<sub>4</sub> differs when combusted in CO<sub>2</sub>. In nitrogen, the consumption of both fuel species is very similar, with H<sub>2</sub> being consumed slightly slower at the point of ignition which is surprising given its greater reactivity. For mixture 1, Figure 5.13 shows a difference in the consumption rate, with methane being the slower reactant in this whilst the hydrogen mole fraction decreases almost linearly over the reaction. The slower reactivity of CH<sub>4</sub> can be explained through the lower reaction temperature due to the greater efficiency of CO<sub>2</sub> as a third body reducing the reaction temperature, whereas the more linear decrease of H<sub>2</sub> is due to the longer reaction time (Figure 5.16).



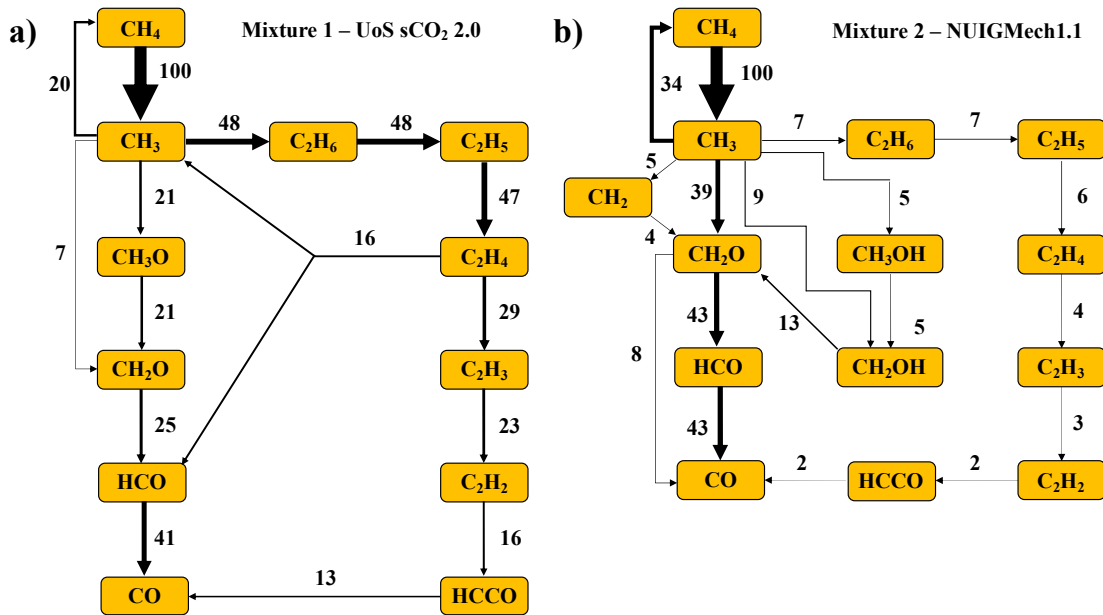
**Figure 5.16.** ROP analysis of H<sub>2</sub> for mixture 1 (CH<sub>4</sub>:H<sub>2</sub>:O<sub>2</sub>:CO<sub>2</sub>=3.4:3.4:8.2:85) with UoS sCO<sub>2</sub> 2.0 simulations and mixture 2 (CH<sub>4</sub>:H<sub>2</sub>:O<sub>2</sub>:N<sub>2</sub>=3.4:3.4:8.2:85) with NUIGMech1.1 simulations at 40 bar and 1265 K.

Figure 5.17 shows the reaction pathway analysis (RPA) for mixtures 1 and 2 using UoS sCO<sub>2</sub> 2.0 and NUIGMech1.1, respectively. The two different mechanisms were used for each bath gas based on simulation being better able to model the IDT dataset, therefore it can be assumed that each mechanism better models the actual chemistry of the respective conditions. The RPA was performed for methane, at the time when consumption is largest, which was found to be similar to that of the overall consumption. There are three key differences between the reaction pathway of the two mixtures i) the main reaction pathway in N<sub>2</sub> bypasses CH<sub>3</sub>O formation to form CH<sub>2</sub>O directly, ii) ethane formation is much more important in CO<sub>2</sub> and iii) CH<sub>3</sub>OH formation is more important in N<sub>2</sub>.

Interestingly, in both conditions, the majority of CH<sub>3</sub>O is formed through Reaction 5.5 ( $CH_3 + HO_2 \rightleftharpoons CH_3O + OH$ ), for which both mechanisms have the same rate coefficient. Therefore, the reason for the lack of CH<sub>3</sub>O formation is a direct result of slower HO<sub>2</sub> formation. UoS sCO<sub>2</sub> 2.0 uses an optimised rate coefficient reduced from the same rate coefficient utilised in NUIGMech1.1. Despite this smaller rate coefficient, the rate of HO<sub>2</sub> formation via Reaction 5.1 ( $H + O_2 (+M)$ )

$\rightleftharpoons HO_2 (+M)$ ), the presence of  $CO_2$  as a more efficient third body promotes this reaction by a factor of 3.8 and the lower reaction temperature reduces the rate of competitor reaction, Reaction 5.2 ( $H + O_2 \rightleftharpoons O + OH$ ). These two factors coupled reduce  $HO_2$  formation and thus in  $N_2$ ,  $CH_3$  reacts predominantly with H and OH radicals which subsequently reduces the importance of  $CH_3O$  formation. The reason for  $C_2H_6$  formation being favoured in  $CO_2$  is again due to the greater third-body efficiency of  $CO_2$  favouring Reaction 5.8 ( $CH_3 + CH_3 (+M) \rightleftharpoons C_2H_6 (+M)$ ). In this case, both the rate coefficient used for Reaction 5.8 ( $CH_3 + CH_3 (+M) \rightleftharpoons C_2H_6 (+M)$ ) in UoS s $CO_2$  2.0 is approximately a factor of 10 larger than NUIGMech1.1. However, NUIGMech1.1 simulations for mixture 1 show that 35% of  $CH_3$  reacts to form  $C_2H_6$ ; thus, the presence of  $CO_2$  as a third body is the largest factor in the prominence of the ethane reaction pathway in  $CO_2$  diluted mixtures. The  $CH_3OH$  reaction pathway is introduced to mixture 2 via Reaction 5.16 ( $CH_3 + OH \rightleftharpoons CH_2OH + H$ ) and Reaction 5.17 ( $CH_3 + OH (+M) \rightleftharpoons CH_3OH (+M)$ ). The reason for Reaction 5.16 ( $CH_3 + OH \rightleftharpoons CH_2OH + H$ ) is most likely to be purely mechanistic, with NUIGMech 1.1 using a more sophisticated and recent pressure dependant rate coefficient from Jasper et al. [277], whereas UoS s $CO_2$  2.0 uses an older and more simplistic rate coefficient created using RRKM theory to model decomposition data during the creation of GRI Mech 3.0 [182]. Reaction 5.17 ( $CH_3 + OH (+M) \rightleftharpoons CH_3OH (+M)$ ) being favoured is more interesting, as typically recombination reactions are preferred in  $CO_2$  due to the third body efficiency discussed. Again, this is somewhat due to the mechanism as NUIGMech1.1 predicts 4%  $CH_3OH$  formation for mixture 1. However, this is strikingly similar to that of mixture 2 despite the different bath gas. The most probable explanation for this is the lack of  $HO_2$  radicals in mixture 2 so all reactions of  $CH_3$  with OH are favoured, meaning Reaction 5.17 ( $CH_3 + OH (+M) \rightleftharpoons CH_3OH (+M)$ ) remains important even though logic dictates recombination reactions are less favourable in  $N_2$ .





**Figure 5.17.** RPA analysis of mixture 1 ( $\text{CH}_4:\text{H}_2:\text{O}_2:\text{CO}_2=3.4:3.4:8.2:85$ ) and mixture 2 ( $\text{CH}_4:\text{H}_2:\text{O}_2:\text{N}_2=3.4:3.4:8.2:85$ ) at 20 bar with UoS sCO<sub>2</sub> 2.0 and NUIGMech1.1 simulations respectively at 1290 K and 20 bar.

The most surprising observation from this dataset was the over-prediction of NUIGMech1.1 when simulating the ignition of a methane/hydrogen blend in CO<sub>2</sub>. NUIGMech1.1 has been developed and validated over a long period to model combustion in the air of H<sub>2</sub> and C1-C7 species and has its roots in historically trusted mechanisms. Although there have been no recently published IDT datasets for methane/hydrogen blends and previous work is limited by the mechanisms available at the time, it was expected stoichiometric combustion of an equal blend of methane and hydrogen should be accurately simulated, even at these higher pressures. Figure 5.10 shows that the disagreement is approximately constant across the studied temperature range and for the two pressures studied. This poor agreement is only slight and needs firmer refinement and investigations using a range of mechanisms designed for combustion in N<sub>2</sub> with more datasets over a wider range of experimental conditions.

### 5.3. Analysis of Methane Mixtures

Despite the influx into the research of ignition properties in CO<sub>2</sub> since the development of supercritical power cycles at the turn of the millennium mainly

focusing on methane ignition, there are still gaps remaining in the literature data and difficult conditions to model as identified in Harman-Thomas et al. [87]. There remains a significant gap in any autoignition data in CO<sub>2</sub> with only three published datasets between 15 and 80 bar, one from Pryor et al. [302] and two from Shao et al. [85], all at approximately 30 bar. Furthermore, in Harman-Thomas et al. [87], the final mechanism UoS sCO<sub>2</sub> 1.0 could fit the data of Pryor et al. [302], however, it was noted that the existing mechanism utilised in the study and the newly developed mechanism largely over-predicted the IDT of the two Shao et al. [85] datasets. These two studies utilised sidewall measurements as opposed to the endwall measurements of the current studies. Previous research [88, 310] shows that sidewall measurements can suffer from premature ignition events in a mixture highly diluted with CO<sub>2</sub>, leading to an under prediction of the IDT. Furthermore, these three existing datasets were studied over a narrow range of equivalence ratios ( $\phi=1.00-1.27$ ). Studying over a range of equivalence ratios is important Harman-Thomas et al. [88] for hydrogen combustion in CO<sub>2</sub>, any deviation from stoichiometric led to an increase in the error of the UoS sCO<sub>2</sub> 2.0 mechanism. As most of the combustion system operates in fuel-lean conditions, it is particularly important to ensure that any decrease in equivalence ratio doesn't affect the performance of a mechanism. Section 5.3.1 looks at the effect of pressure on ignition between 20 and 100 bar whilst Section 5.3.2 investigates the effect of increasing the equivalence ratio from  $\phi=0.5-2.0$  in the combustion chemistry of methane ignition.

### **5.3.1. Stoichiometric Methane Combustion Between 20 and 100 bar**

The objective of these datasets is to analyse the effect of changing the equivalence ratio at 20 and 40 bar, so only a brief commentary is provided here. This initial mixture composition was selected as it allows for direct comparison with one dataset from Pryor et al. [302] at 30 bar and one from Karimi et al. [127] at 100 bar. In contrast with previous research [88, 310], the sidewall data from Pryor et al. is in excellent agreement with the data recorded during this work. The endwall data reported in Figure 5.18 is also in good agreement with the sidewall data recorded in the present study (Table A.25 and Table A.26) with the sidewall

datasets being on average only 10-15% slower than the endwall measurements and thus within the 20% experimental error. The reason for this improved agreement relative to the hydrogen [88], syngas [310], and the methane/hydrogen blend datasets is likely the absence of hydrogen decreasing the reactivity of the mixture and therefore reducing the chance of premature ignition events and reducing the amount of time before the main ignition event. Interestingly, it is as the pressure decreases, the agreement of UoS sCO<sub>2</sub> 2.0 with the experimental data deteriorates, particularly at the highest temperature datasets.

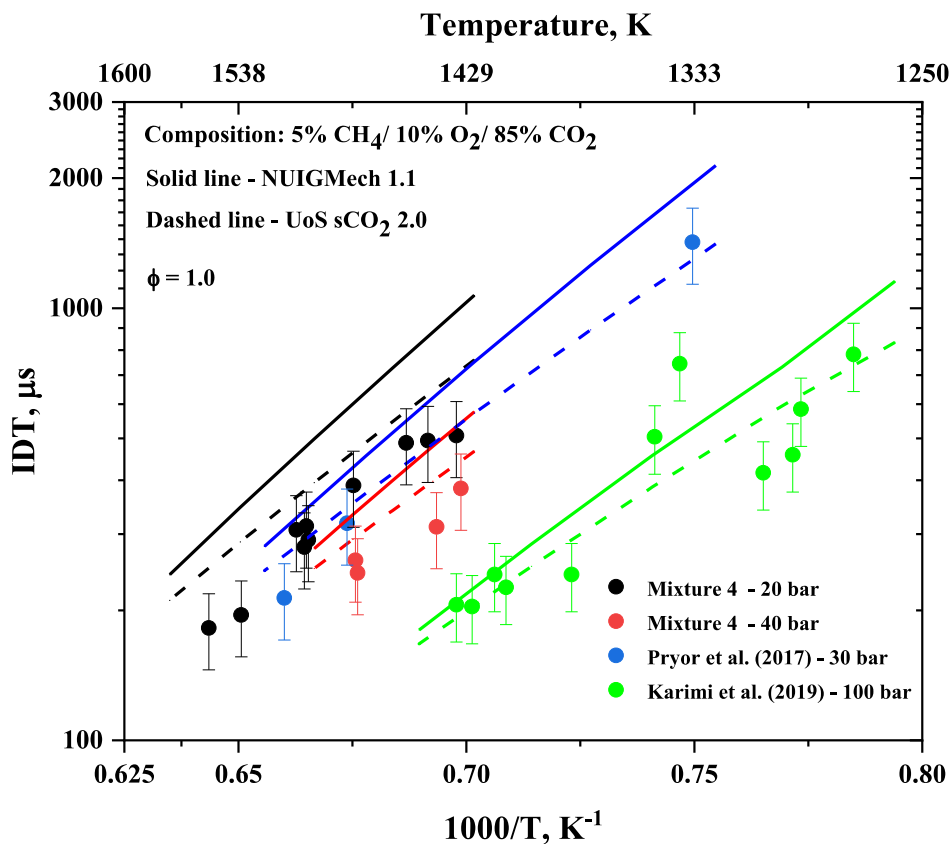


**Figure 5.18.** Comparison of IDTs of mixture 4 (CH<sub>4</sub>:O<sub>2</sub>:CO<sub>2</sub>=5:10:85) at 20 bar, 30 bar [302], 40 bar and 100 bar [127] with NUIGMech1.1 and UoS sCO<sub>2</sub> 2.0 simulations.

Figure 5.19 shows the sensitivity analysis for the four different pressures measured. Unsurprisingly, as the pressure increases in the presence of CO<sub>2</sub>, Reaction 5.1 ( $H + O_2 (+M) \rightleftharpoons HO_2 (+M)$ ) becomes more important. As previously discussed, this increases the sensitivity of all reactions involving HO<sub>2</sub> and H<sub>2</sub>O<sub>2</sub> at the higher-pressure datasets. Conversely, Reaction 5.7 ( $CO + OH \rightleftharpoons CO_2 + H$ )

and Reaction 5.15 ( $CH_4 + H \rightleftharpoons CH_3 + H_2$ ) become more important at lower pressures, two reactions which slow down the overall reaction rate at the point of ignition. It can therefore be deduced that the slower rate of H consumption via Reaction 5.1 ( $H + O_2 (+M) \rightleftharpoons HO_2 (+M)$ ) increases the available radical pool and has a larger effect on these reactions. This could partially explain why the mechanism agreement worsens at lower pressures. However, the sensitivity analysis shows no major discrepancies across the pressure range studied and further mechanism refinement of these key rate coefficients is required based on these new datasets.

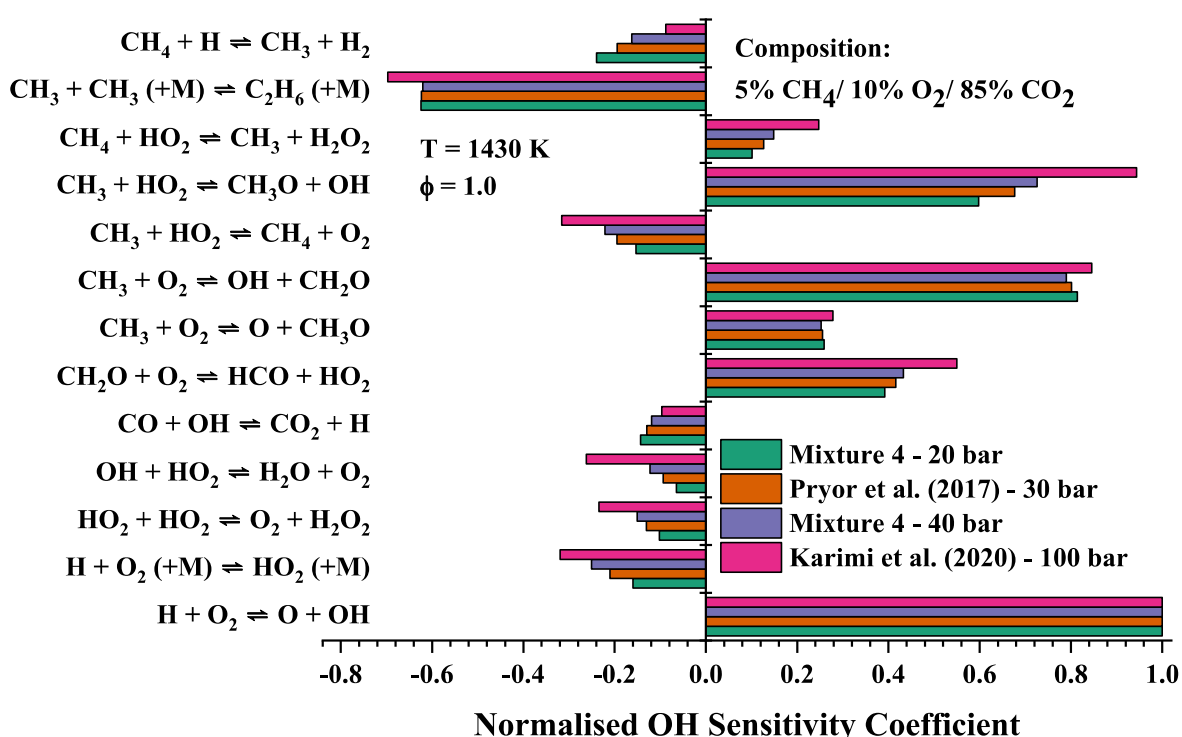


**Figure 5.19.** Sensitivity analysis of mixture 4 ( $CH_4:O_2:CO_2=5:10:85$ ) at 20 bar, 30 bar [302], 40 bar and 100 bar [127] at 1430 K with UoS sCO<sub>2</sub> 2.0 simulations.

A rate of production analysis of methane (Figure 5.20) was performed to compare the key decomposition of the methane fuel at four different pressures. Whilst Reaction 5.12 ( $CH_4 + OH \rightleftharpoons CH_3 + H_2O$ ) remains the predominant reaction pathway under all four conditions, the chemistry of methane reformation changes significantly over the studied pressure range. At 20 and 30 bar,  $CH_4$  is predominantly reformed via Reaction 5.11 ( $CH_3 + H (+M) \rightleftharpoons CH_4 (+M)$ ), consistent with a greater concentration of H radicals. As the pressure increases, Reaction

5.14 ( $\text{CH}_3 + \text{CH}_2\text{O} \rightleftharpoons \text{CH}_4 + \text{HCO}$ ) becomes more important. This is an important propagation reaction for the  $\text{CH}_2\text{O}$  radical to form  $\text{HCO}$ , which dissociates immediately via Reaction 5.13 ( $\text{HCO} (+M) = \text{H} + \text{CO} (+M)$ ). Therefore, at higher pressures, a more favourable  $\text{CH}_4$  formation pathway that also propagates the combustion reaction, coupled with the difference in  $\text{H}$  radical and  $\text{HO}_2$  chemistry are the key changes in chemistry across the 20-100 bar pressure range.

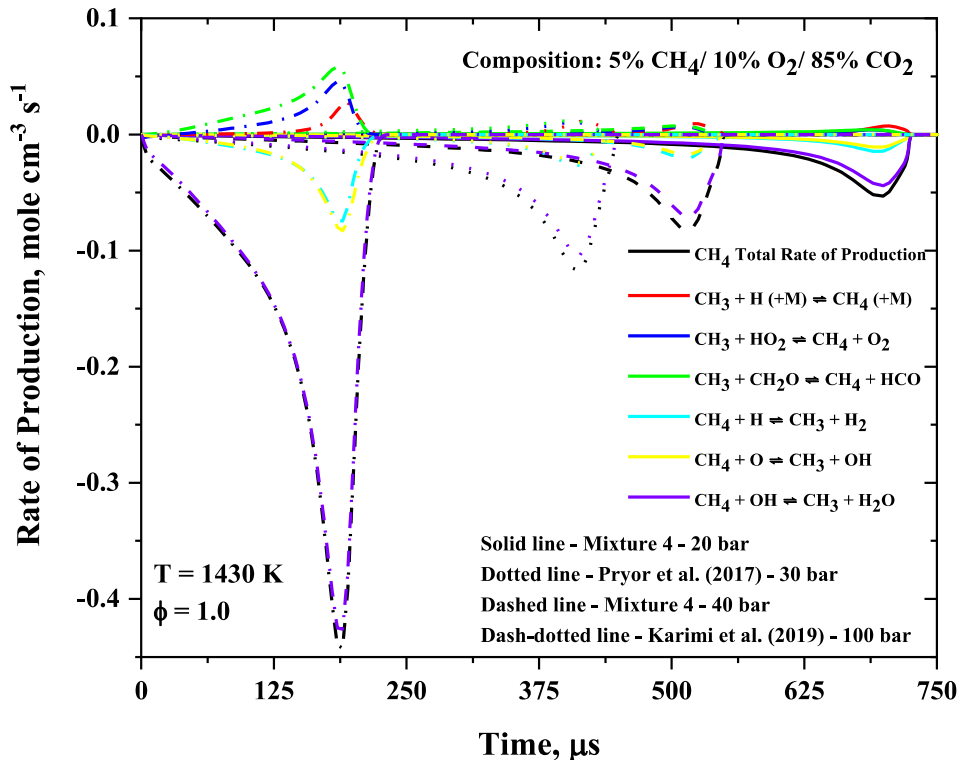


**Figure 5.20.** Comparison of  $\text{CH}_4$  consumption pathways of mixture 4 ( $\text{CH}_4:\text{O}_2:\text{CO}_2=5:10:85$ ) at 20 bar, 30 bar [302], 40 bar and 100 bar [127] with UoS sCO<sub>2</sub> 2.0 simulations.

### 5.3.2. Effect of Equivalence Ratio at 20 and 40 bar

The effect of changing the equivalence ratio from  $\phi=0.5$  to  $\phi=2.0$  at both 20 and 40 bar is shown in Figure 5.21 and Figure 5.22 respectively. In contrast to previous research that showed for hydrogen and syngas UoS sCO<sub>2</sub> 2.0 best simulates IDT at stoichiometric conditions and any deviation from this led to a poorer performance of the mechanism, in the present work, at both 20 bar and 40 bar, the best agreement is at  $\phi=0.5$  and any increase leads to an increasingly significant over-prediction in the simulated IDT. Whilst the simulated IDT profile at  $\phi=0.5$  fits within the experimental error of each of the data points at both 20

bar and 40 bar, at  $\phi=2.0$  there is a significant over-prediction, especially at 20 bar. This identifies a significant shortcoming in the mechanism that needs to be addressed and investigated to simulate IDTs in CO<sub>2</sub> more accurately across a broader range of conditions.

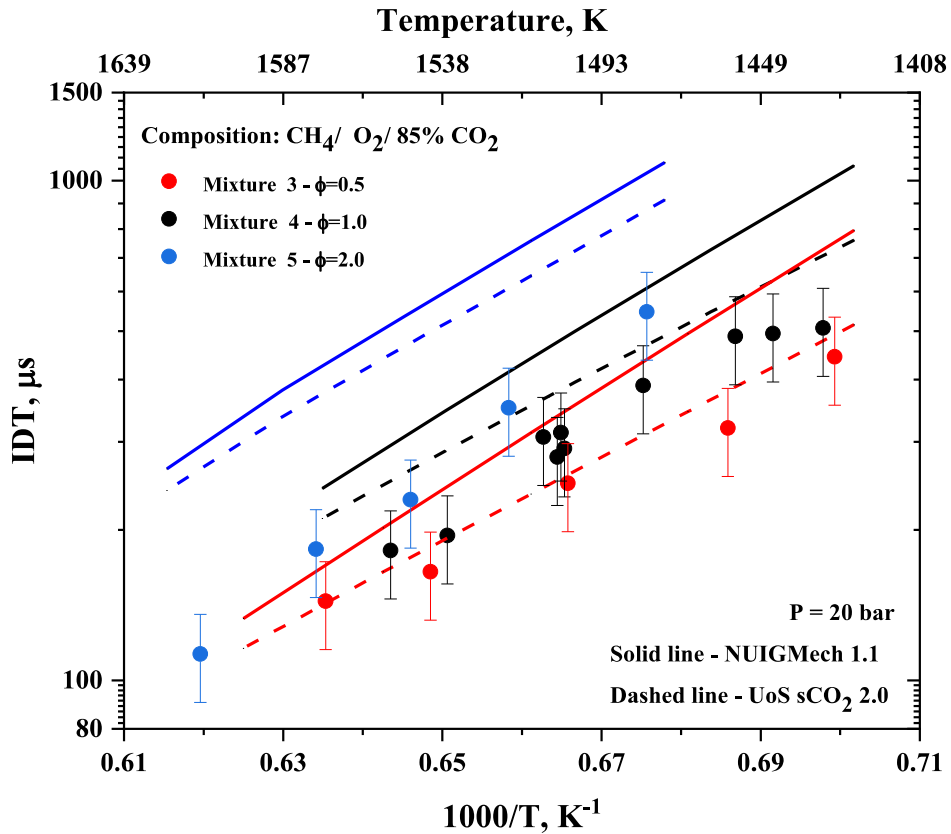


**Figure 5.21.** Comparison of IDTs of mixture 3 (CH<sub>4</sub>:O<sub>2</sub>:CO<sub>2</sub>=3:12:85), mixture 4 (CH<sub>4</sub>:O<sub>2</sub>:CO<sub>2</sub>=5:10:85) and mixture 5 (CH<sub>4</sub>:O<sub>2</sub>:CO<sub>2</sub>=7.5:7.5:85) at 20 bar with NUIGMech1.1 and UoS sCO<sub>2</sub> 2.0 simulations.

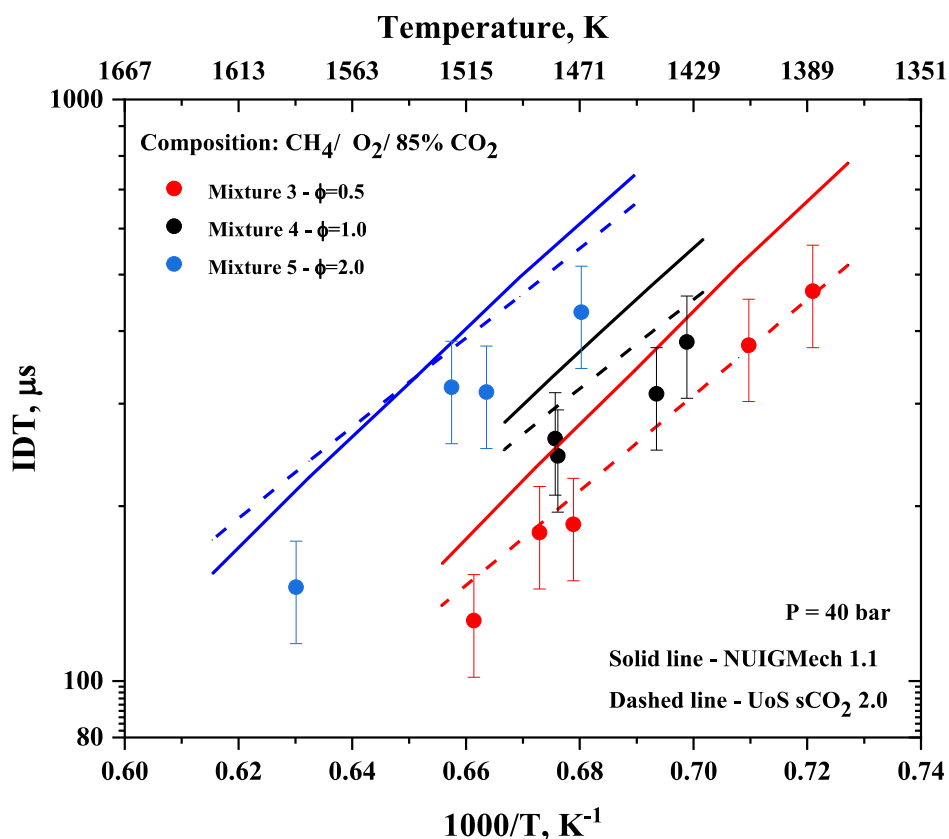


**Figure 5.22.** Comparison of IDTs of mixture 3 ( $\text{CH}_4:\text{O}_2:\text{CO}_2=3:12:85$ ), mixture 4 ( $\text{CH}_4:\text{O}_2:\text{CO}_2=5:10:85$ ) and mixture 5 ( $\text{CH}_4:\text{O}_2:\text{CO}_2=7.5:7.5:85$ ) at 40 bar with NUIGMech1.1 and UoS sCO<sub>2</sub> 2.0 simulations.

Figure 5.23 shows a normalised sensitivity analysis of mixtures 3-5 at 1515 K and 20 bar to compare the effect of the equivalence ratio on the chemical kinetics. The most striking difference is that the sensitivity coefficient of Reaction 5.1 ( $\text{H} + \text{O}_2 (+M) \rightleftharpoons \text{HO}_2 (+M)$ ) from strongly negative for mixture 3 to slightly positive for mixture 5, showing that as the relative fuel concentration increases, indicating that the formation of  $\text{HO}_2$  eventually begins to promote OH formation. Secondly, as the fuel content increases relative to  $\text{O}_2$ , the reactions of  $\text{CH}_3$  radicals via Reaction 5.8 ( $\text{CH}_3 + \text{CH}_3 (+M) \rightleftharpoons \text{C}_2\text{H}_6 (+M)$ ) and Reaction 5.18 ( $\text{CH}_3 + \text{CH}_3 \rightleftharpoons \text{C}_2\text{H}_5 + \text{H}$ ) become increasingly important. Lastly, Figure 5.23 shows that Reaction 5.12 ( $\text{CH}_4 + \text{OH} \rightleftharpoons \text{CH}_3 + \text{H}_2\text{O}$ ) and Reaction 5.15 ( $\text{CH}_4 + \text{H} \rightleftharpoons \text{CH}_3 + \text{H}_2$ ) become increasingly important as the equivalence ratio increases, both of which hurt the OH production and subsequently the rate of the reaction. Similar trends can be observed in Figure 5.24. Furthermore, Figure 5.24 highlights the increasing importance of the rate coefficients of the reactions of  $\text{O}_2$  (Reaction

5.19 ( $CH_3 + O_2 \rightleftharpoons OH + CH_2O$ ), Reaction 5.20 ( $CH_3 + O_2 \rightleftharpoons O + CH_3O$ ), and Reaction 5.21 ( $CH_2O + O_2 \rightleftharpoons HCO + HO_2$ ) as the equivalence ratio increases, meaning its consumption becomes increasingly important. Under fuel-rich conditions, and especially in such large dilutions of  $CO_2$  as shown in Figure 5.23 and Figure 5.24, ethane formation Reaction 5.8 ( $CH_3 + CH_3 (+M) \rightleftharpoons C_2H_6 (+M)$ ) is an essential combustion pathway for methane. Whilst Reaction 5.8 ( $CH_3 + CH_3 (+M) \rightleftharpoons C_2H_6 (+M)$ ) has been studied in particular relevance to supercritical conditions in a  $CO_2$  bath gas by Wang et al. [311], Reaction 5.18 ( $CH_3 + CH_3 \rightleftharpoons C_2H_5 + H$ ) hasn't been studied in over two decades with the rate coefficients of both UoS s $CO_2$  2.0 and NUIGMech1.1 based on the theoretically derived by Stewart et al. [266] was published in 1989, although NUIGMech1.1 does incorporate a pressure dependence. This rate coefficient should be revisited, ideally theoretically and experimentally given its importance to ethane and methane combustion in nitrogen as well as in  $CO_2$ . Furthermore, given the importance of ethane formation to methane combustion in  $CO_2$ , a more thorough investigation into ethane autoignition in  $CO_2$  is required. Ethane IDTs have only been investigated in  $CO_2$  by Liu et al. [201] between 0.8 and 10 bar and even at these low pressures, the authors found that AramcoMech 2.0 generally showed poor agreement with the data and create an optimised OXYMECH mechanism to better simulate the data. Lastly, Figure 5.23 and Figure 5.24 show the interesting behaviour of Reaction 5.1 ( $H + O_2 (+M) \rightleftharpoons HO_2 (+M)$ ) as the equivalence ratio is increased, becoming slightly positive at  $\phi=2.0$ . This is likely due to the importance of the  $O_2$  reaction pathway when it is deficient as  $HO_2$  is required for OH production through reactions such as Reaction 5.5 ( $CH_3 + HO_2 \rightleftharpoons CH_3O + OH$ ) which promote methane combustion.



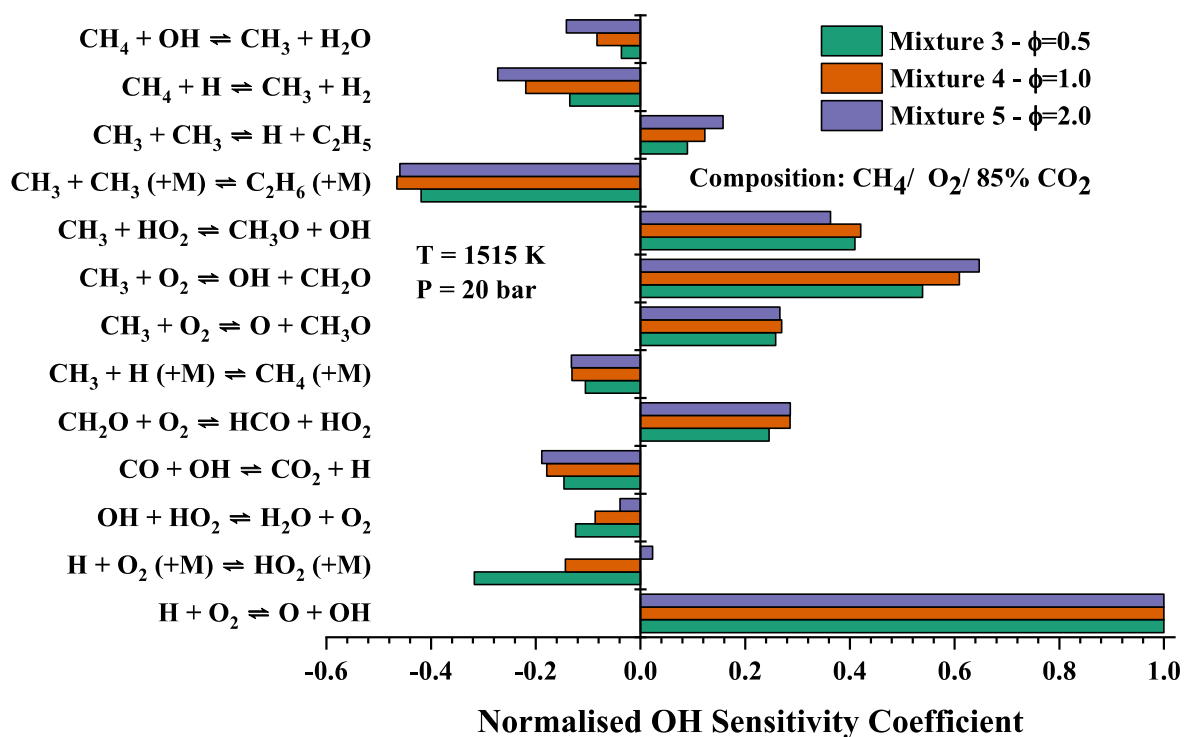


**Figure 5.23.** Sensitivity analysis of mixture 3 (CH<sub>4</sub>:O<sub>2</sub>:CO<sub>2</sub>=3:12:85), mixture 4 (CH<sub>4</sub>:O<sub>2</sub>:CO<sub>2</sub>=5:10:85) and mixture 5 (CH<sub>4</sub>:O<sub>2</sub>:CO<sub>2</sub>=7.5:7.5:85) at 20 bar with UoS sCO<sub>2</sub> 2.0 simulations.

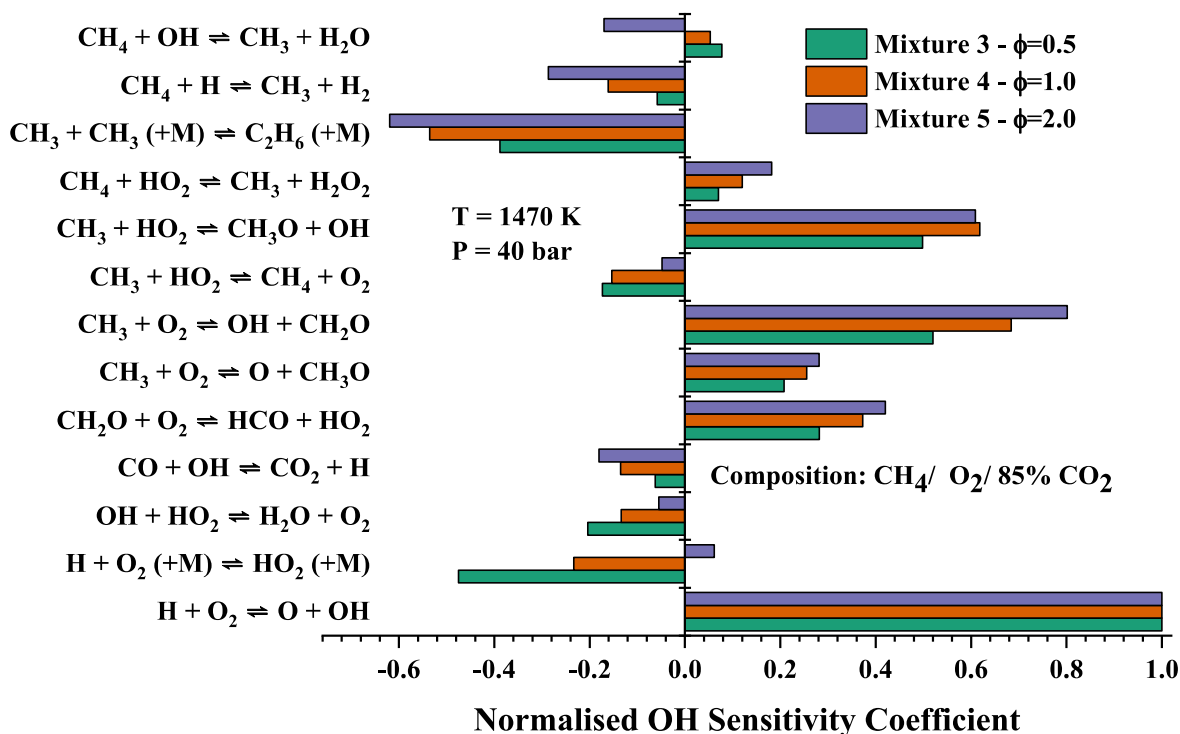


**Figure 5.24.** Sensitivity analysis of mixture 3 (CH<sub>4</sub>:O<sub>2</sub>:CO<sub>2</sub>=3:12:85), mixture 4 (CH<sub>4</sub>:O<sub>2</sub>:CO<sub>2</sub>=5:10:85) and mixture 5 (CH<sub>4</sub>:O<sub>2</sub>:CO<sub>2</sub>=7.5:7.5:85) at 40 bar with UoS sCO<sub>2</sub> 2.0 simulations.

## 5.4. Conclusion

Ten IDT datasets of methane/hydrogen blends and methane autoignition with relevance to combustion in CO<sub>2</sub> between 20 and 40 bar have been presented and discussed. The autoignition properties of methane/hydrogen blends haven't been studied experimentally in over a decade. The presented analysis shows that even well-validated mechanisms, such as NUIGMech1.1, struggle to correctly simulate the observed behaviour. This study presents the first-ever IDT datasets of methane/hydrogen fuel blends in CO<sub>2</sub> alongside a comprehensive discussion on the role of CO<sub>2</sub> on reactivity as well as how the reactivity changes compared to pure hydrogen and methane mixtures. The UoS sCO<sub>2</sub> 2.0 mechanism was demonstrated to be able to correctly simulate the recorded IDTs at both 20 and 40 bar within the experimental error. Furthermore, six IDT datasets were recorded between  $\phi=0.5$  and  $\phi=2.0$  to investigate the effect of the equivalence ratio on the ability of UoS sCO<sub>2</sub> 2.0 to simulate IDT. Whilst agreement at  $\phi=0.5$  and 1.0 was reasonable, at  $\phi=2.0$  began to vastly over-predict the IDT and OH sensitivity analysis identified the large difference in the chemistry under these conditions, with the reaction pathway of CH<sub>3</sub> becoming particularly important. These ten IDT datasets provide a novel assessment of combustion in CO<sub>2</sub> through previously unstudied fuel blends and broader equivalence ratios of methane than those covered in previous works at high pressures, alongside a detailed analysis of the underlying chemical kinetics of the conditions studied. This work is essential to the advancement of UoS sCO<sub>2</sub> 2.0 and other chemical kinetic mechanisms for modelling combustion in CO<sub>2</sub>, as well as identifying the shortcomings of NUIGMech1.1 for modelling methane/hydrogen blends. Further IDT studies of methane/hydrogen blends at different fuel and equivalence ratios across a wider pressure and temperature range of required to accurately address these discrepancies.

## **6. Conclusions and Future Work**

Direct-fired sCO<sub>2</sub> power cycles offer the opportunity to continue burning fossil fuels for energy production without the release of harmful emissions into the atmosphere. With the rising cost of energy and slow progress of renewables in replacing more traditional methods of power generation, there is a need to find a carbon-neutral way to bridge the gap to a sustainable future.

This chapter overviews the key findings from the three research chapters presented in this EngD thesis. Section 6.1 discusses these findings and how the knowledge gaps identified in Section 1.4 were addressed. Section 6.2.1 details the future work for the next stage in the development of a chemical kinetic mechanism for sCO<sub>2</sub> production both experimentally and theoretically. Sections 6.2.3 and 6.2.4 detail the potential future uses for the UoS HPST, namely the study of the combustion of ammonia and synthetic jet fuels.

### **6.1. Conclusion**

The focus of this project was the development of a chemical kinetic mechanism for the combustion of supercritical CO<sub>2</sub> production. The UoS sCO<sub>2</sub> 1.0 mechanism is the only chemical kinetic mechanism specialised for sCO<sub>2</sub> combustion based on over 50 IDT datasets for three different fuels. The datasets used in this work were from a variety of shock tubes across a range of equivalence ratios, pressures, and temperatures. The mechanism's performance significantly outperforms any existing mechanisms based on quantitative analysis, making it the most accurate mechanism available for the simulation of the IDT of methane, hydrogen, and syngas in CO<sub>2</sub>. The mechanism has been subsequently improved to form UoS sCO<sub>2</sub> 2.0 making one small change, and this was subsequently validated for the combustion of hydrogen and syngas IDTs determined experimentally on the KAUST high-pressure shock tube. These fuels were used for validation due to the lack of hydrogen IDT datasets in CO<sub>2</sub> and the need to study syngas over a larger range of equivalence ratios at higher pressures.

The greatest achievement from this EngD was the fabrication of a high-pressure shock tube for the study of combustion kinetics. The UoS HPST can produce postshock pressures and temperatures of up to 100 bar and 2000 K respectively. This project was started in 2019 and reached commissioning at the end of 2022, costing a total of £540,000. The UoS HPST is capable of recording sidewall and endwall IDTs as well as HO<sub>2</sub>, NO and OH time histories three essential combustion species and opening its future application to a vast array of research. The future was also planned into the shock tube, with the opportunity to add an endwall port for endwall IDT determination. Furthermore, ample space was allowed around the tube, mixing tank and pipelines, to allow room for a heating jacket for future heating of the heating shock tube up to 125 °C, allowing for the study of liquid fuels. As discussed in Section 1.4, the shock tube can address many knowledge gaps in its future use in experiments at the University of Sheffield as similar shock tubes have routinely been in operation for over 20 years.

The development of UoS sCO<sub>2</sub> 1.0 as outlined in Chapter 3 has been an essential step forward in the development of a chemical kinetic mechanism for simulation sCO<sub>2</sub> production. The mechanism was based on 52 IDT datasets of methane, hydrogen, and syngas combustion compiled from multiple shock tube research groups across the globe. Based on the quantitative investigation, USC II was identified as the best mechanism for modelling the IDT of the three different fuels. Sensitivity analysis was subsequently used to identify important reactions for the combustion of the different fuels under different conditions. Subsequent iterations of changes were made to USC II to reduce the average absolute error ( $E$ , %) across all the datasets. The rate coefficients were altered within their experimental error to create UoS sCO<sub>2</sub> 1.0, a mechanism which performed significantly better than the existing four mechanisms, validated for low-pressures and small dilutions of CO<sub>2</sub>. The mechanism is a significant step-forward and the only publically available mechanism for modelling sCO<sub>2</sub> production based on three different fuels and using such a significant bank of datasets covering a vast number of conditions.

Chapter 4 details the experimental aspect of this EngD thesis, used to validate the UoS sCO<sub>2</sub> mechanism. One small change was made to UoS sCO<sub>2</sub> 1.0 to the third body efficiency of CO<sub>2</sub> for the recombination reaction of H and O<sub>2</sub> to form HO<sub>2</sub>. This was found to improve the mechanisms' ability to simulate H<sub>2</sub> and syngas IDTs and was thus renamed UoS sCO<sub>2</sub> 2.0. An international collaboration was set-up between UoS and KAUST. Sixteen IDT datasets for hydrogen and syngas were recorded on the KAUST HPST. These were subsequently modelled using two chemical kinetic mechanisms; UoS sCO<sub>2</sub> 2.0, and AramcoMech 2.0. UoS sCO<sub>2</sub> 2.0 was determined to be the superior mechanism through the quantitative analysis and sensitivity analysis was used to determine the important discrepancies between the different mixtures and pressures. The reactions and rate coefficients identified can subsequently be used in the next iteration of the UoS sCO<sub>2</sub> mechanism.

Chapter 5 details 10 new IDT datasets focusing on methane combustion between 20 and 40 bar. The first four datasets study the effect of CO<sub>2</sub> on the chemical kinetics of the combustion of an equal, stoichiometric blend of methane and hydrogen. UoS sCO<sub>2</sub> 2.0 is demonstrated to successfully model both pressures in CO<sub>2</sub> within the experimental error. More interestingly, NUIGMech1.1 which is well-validated for these fuels and conditions overpredicts the IDT in N<sub>2</sub>. Given the importance of gradual hydrogen doping to phase out natural gas combustion in many industries, methane/hydrogen combustion should be studied as a research priority over a wider range of conditions and test gas compositions. These analyses fill an existing gap in the literature as well as provide further validation of UoS sCO<sub>2</sub> 2.0 as a superior mechanism for modelling combustion in CO<sub>2</sub>.

The summation of this EngD thesis:

- The creation of a new HPST for the continued chemical kinetics.
- The creation of the best-performing detailed mechanism for modelling IDTs of methane, hydrogen, and carbon monoxide in a CO<sub>2</sub> bath gas.
- The generation of sixteen new IDT datasets of methane and syngas fuels between 20 and 40 bar.
- Ten IDT datasets of methane and methane/hydrogen blends.

This work is impactful to the wider research community in the long term by providing a new experimental system which will generate data for 20+ years. A novel mechanism which can be used to improve CFD simulations in CO<sub>2</sub> and new IDT datasets and essential chemical kinetic analysis to provide direction for future research and assist new mechanism development.

## **6.2. Future Work**

The current work was divided into two key aspects, and these are combined in future work. Firstly, there are the future uses of the shock tube, which are defined in both the short and long-term, through adjusting and improvements through future funding applications. Secondly, there are the modelling aims for the UoS sCO<sub>2</sub> 2.0, which should be further improved based on this present work and similar work by other groups involved in shock tube research. Furthermore, more shock tube IDT campaigns should be planned to assist the mechanism development.

### **6.2.1. Direct-Fired sCO<sub>2</sub> Cycles**

Chapters 3, 4, and 5 are dedicated to the development of the chemical kinetic mechanism for combustion in sCO<sub>2</sub>. Chapter 3 shows the development of UoS sCO<sub>2</sub> 1.0, from 52 IDT datasets at a range of test gas compositions and pressures for methane, hydrogen, and syngas. This mechanism was further improved into UoS sCO<sub>2</sub> 2.0 which was validated in its ability to simulate hydrogen and syngas IDTs between 20 and 40 bar in Chapter 4. There are therefore multiple ways that this research can be furthered experimentally using the HPST and theoretically through mechanism development.

Firstly Chapter 4 found that there was a large discrepancy between the sidewall and endwall measurements for IDT determination. Since so much of the data used for methane IDT in Chapter 3 has come from shock tubes utilising sidewall measurements, the effect of sidewall versus endwall should be investigated in a CO<sub>2</sub> bath gas. With the addition of an endwall window plug in place of the current blank plug and a second PMT, this will be possible on the UoS HPST.

Secondly, whilst a significant amount of IDT data has been published, presently, there are no species' time history measurements for combustion in CO<sub>2</sub>. The UoS laser absorption diagnostic can monitor two important intermediate combustion species; OH (308 nm) and HO<sub>2</sub> (227 nm). Whilst IDT is an important property of combustion, showing a mechanism's ability to accurately simulate the formation and loss of these key species would demonstrate their capability to monitor the complete combustion process. Similarly, to the IDT work discussed in Chapter 4, it would be logical to do this in terms of increases fuel complexity. This would also allow more detailed tuning of key chemical reactions which may be affected by the presence of the CO<sub>2</sub> bath gas.

Thirdly, one of the key discussions from Chapter 4 is the formation of CO from the CO<sub>2</sub> bath gas in Section 4.2.1. Whilst this is seen in all fuels, it is most notable for syngas combustion, as it slows down the rate of CO consumption and in some instances led to two distinct peaks in the OH species' time history. This effect is down solely to the reverse of Reaction 4.2 ( $CO + OH = CO_2 + H$ ) and therefore its rate coefficient has a huge impact on combustion in CO<sub>2</sub>. Key chemical mechanisms shown in this study used a duplicate rate coefficient from Joshi and Wang [257] using RRKM/master equation analysis. This rate coefficient is based on limited experimental data and is only validated up to 80 bar, well below the 300 bar of the Allam-Fetvedt cycle combustion chamber. Given this reaction's importance to combustion in CO<sub>2</sub>, it is important to revisit this rate coefficient and make an accurate determination based on both theoretical and experimental data at greater pressures. The easiest way to do this experimentally would be to investigate hydrogen combustion in a CO<sub>2</sub> bath gas and look at the rate of CO and OH loss and consumption. Being able to accurately recreate both species' time histories at a range of conditions would allow for an accurate determination of this rate coefficient. CO has been studied experimentally in shock tubes using a quantum cascade laser to access the R(12) transition at 4566.17 cm<sup>-1</sup> by Texas A&M University as detailed in Mulvihill and Petersen [312] and Mathieu et al. [313]. This research can be used to verify recent predictions of this rate coefficient in a supercritical CO<sub>2</sub> environment using the RRKM theory published by Masunov et al. [314].

The fourth area is to make further improvements to UoS sCO<sub>2</sub> 2.0 and create the next iteration of the mechanisms. This can be approached in multiple ways, and thus will likely require several iterations. Firstly, new chemical kinetic data for methane, hydrogen and syngas combustion, such as species time-histories, laminar flame speeds and new IDT data can be used for further refinement of these key fuels using an optimization approach similar to Varga et al. [315] and compare its performance with more recent experimental mechanisms such as Li et al. [316]. Furthermore newer the uncertainty of rate coefficients must be further considered in the next mechanism iteration for the reactions identified as Important In this thesis [317]. By confirming the uncertainty of the rate coefficients, further refinement would be within the uncertainty of every given rate coefficient and thus any changes made would be more accurate optimisation [318]. Secondly, the model can be expanded to model the combustion of larger and more complex hydrocarbon fuels with DME [202, 203], ethane [201], ethylene [206], propane [207] or blends of these fuels [204, 205]. The UoS HPST could also be used to generate new IDT data to support this mechanism expansion.

By combining these methodologies, the UoS sCO<sub>2</sub> 2.0 mechanism will be subsequently improved In terms of accuracy of the chemical kinetics based on more detailed rate coefficients based on reaction rates specific to combustion In CO<sub>2</sub>, to give a more accurate starting point for the rate coefficients. Furthermore optimising within predetermined uncertainty values means that any alterations are done within a more rigidly defined range of error and thus the resultant mechanism will in turn be more accurate. Furthermore, it should be a research priority to reinvestigate third-body reactions In CO<sub>2</sub> and at pressures up to 300 bar. The reactions identified as important in this work (e.g. methyl recombination and H+O<sub>2</sub>) should be investigated using the *ab-initio* method for combustion In these conditions are performed In Jasper [319]. The accurate determination of the chemistry of the fall-off region for important recombination reactions is essential to the development of an accurate chemical kinetic mechanism.

## 6.2.2. Shock Tube Sidewall and Endwall Comparison

Chapter 4 identified a significant difference in the IDT of hydrogen and syngas in a CO<sub>2</sub> bath gas when determined from the sidewall and the endwall. Many IDT measurements have been reported using the sidewall, which could give falsely fast IDT, due to premature ignition at the sidewall. Whilst simultaneous sidewall and endwall measurements have been reported [127, 200], and are only briefly discussed. This cross-facility unreliability of shock tube IDTs has consequences that affect the validity of any mechanisms created using the data. More research is required to understand the difference in the sidewall and endwall measurements. Petersen [155] has performed the only research available which directly compares sidewall and endwall measurements in N<sub>2</sub> and Ar bath gases. Petersen [155] concluded that endwall measurements can lead to artificially longer IDTs when studying fuels under dilute conditions, and sidewall measurements can be artificially shorter highly reactive mixtures with strong ignition events.

Ideally, a large cross-facility study of IDTs should be performed which can directly compare sidewall and endwall IDT measurements, to determine under what conditions sidewall or endwall measurements should be prioritised. The study should alter key variables such as dilution, bath gas composition, fuel, equivalence ratio, pressure, and temperature. Further to this, some shock tube record simultaneous sidewall and endwall emissions [88], meaning most facilities will also have a bank of sidewall and endwall IDT datasets which could further aid this research. RCMs would also allow for the determination of IDTs over longer timescales, and therefore at lower temperatures [320]. This would allow a useful comparison to see if the trend of IDT data at lower temperatures better matches the IDTs from the sidewall or endwall. The conclusions would guide the future of shock tube research and improve the validity of mechanisms created based on IDTs from shock tubes. Furthermore, accurate CFD models of shock tube formation and progression under these conditions would also aid this investigation into the discrepancy between sidewall and endwall measurements.

### 6.2.3. Ammonia Combustion

Ammonia ( $\text{NH}_3$ ) has been proposed as a green, carbon-free fuel for future energy technologies. Whilst  $\text{NH}_3$  can be produced from various sources, including biomass and renewables [321], most  $\text{NH}_3$  is synthesised using the energy-intensive Haber-Bosch Process [322].  $\text{NH}_3$  can act as an efficient carrier of  $\text{H}_2$  in terms of storage cost and energy density [321] and has been especially linked with future transportation fuels [323] as it avoids the challenges of hydrogen distribution [324]. One of the major problems with  $\text{NH}_3$  combustion is  $\text{NO}_x$  emissions which have historically prevented any ammonia technology from being further developed [325]. One method of reducing  $\text{NO}_x$  emissions is to blend with other hydrocarbon fuels, such as methane [326]. In addition, the world's first  $\text{NH}_3$  gas turbine was designed by Hideaki Kobayashi in 2016 [327]. Since the development of  $\text{NO}_x$ -reducing technologies, there has been a resurgence in  $\text{NH}_3$ -powered gas turbines. Valera-Medina [328] proposed a premixed  $\text{NH}_3/\text{H}_2$  (70:30 blend) swirl combustion gas turbine, where the hydrogen increased the chemical reactivity of the unburned ammonia, reducing the total emissions. In 2020, Ezzat and Dincer [329] develop a conceptual gas turbine cycle (GTC) which runs on  $\text{NH}_3$ , using hydrogen as a promoter and an  $\text{NH}_3$ -fed solid oxide fuel cell (SOFC). Like the research of  $\text{NH}_3$ -fuelled GTCs, there was a wealth of shock tube data published between the 1960s and 1990s [330-337] and has similarly undergone a resurgence with new shock tube and RCM data being published. Shu et al. [326] used an RCM to study the IDT of  $\text{NH}_3$  and methane blends over a temperature range of 900-1100 K at 20 and 40 bar. Furthermore, He et al. [338] have looked at the auto-ignition properties of pure  $\text{NH}_3$  and  $\text{NH}_3/\text{H}_2$  mixtures in an RCM at pressures from 20 to 60 bar. More recent shock tube IDT measurements have been made for  $\text{NH}_3$  in nitrogen using the KAUST HPST shock tube at temperatures of 1100-1600 K over similar pressures of 20 and 40 bar at equivalence ratios of  $\phi=0.5$  to  $\phi=2.0$  [339]. Higher temperature measurements of pure ammonia IDTs using the shock tube experimental technique from Mathieu and Petersen [340] at 1.4, 11 and 30 atm found a poor agreement compared to a variety of chemical kinetic mechanisms. The best-

performing mechanism was identified by Dagaut et al. [341], which was subsequently improved with various sub-mechanisms [219, 342-345]. Lastly, RCM measurements have been performed for  $\text{NH}_3/\text{DME}$  and  $\text{NH}_3/\text{diethyl ether}$  (DEE) blends between 20 and 40 bar below 1000 K [346, 347]. This blend has been proposed as a promising fuel for future power generation with DME acting as a combustion promoter. The blending of ammonia with different fuels is essential to increase its reactivity and makes the laminar flame speed more in line with that expected of existing hydrocarbon fuels [348].

The UoS HPST can in future be utilised for the study of  $\text{NH}_3$  combustion in both IDT determination and laser absorption measurements of NO at 225 nm. This data can subsequently be used to validate, improve, and create mechanisms for the combustion of  $\text{NH}_3$  and  $\text{NH}_3$  blends, to improve our understanding of the chemical kinetic mechanism of  $\text{NH}_3$  combustion. Subsequently, accurate measurements of NO species time history can be used to determine blend compositions which reduce the total  $\text{NO}_x$  production.

In terms of IDT data. The UoS HPST can be used to expand the current IDT data from the four RCM and shock tube studies. The priority should be to study the IDT of  $\text{NH}_3/\text{H}_2$  and  $\text{NH}_3/\text{CH}_4$  blends between 20 and 40 bar. As of now, these blends have only been studied in RCM, using the HPST, these can be expanded to larger temperature ranges and test gas compositions. Furthermore, the IDT of ammonia can be investigated at pressures greater than 40 bar, at more equivalence ratios and in an inert bath gas such as argon. Using argon as a bath gas would remove the thermal  $\text{NO}_x$  produced from the  $\text{N}_2$  and allow a more detailed focus on the combustion of  $\text{NH}_3$  itself.

#### **6.2.4. Synthetic Aviation Fuels**

As discussed in Section 1.3.3, TERC is being developed with an FT reactor capable of generating clean SAFs. These capabilities can be complimented using the shock tube in future research. The SAFs created will contain a range of longer-chain hydrocarbons. The shock tube can be used to study the auto-ignition properties of the key larger chain hydrocarbons, or blends. This allows some comparison in reactivity to traditional fossil-fuel-based aviation fuels. Whilst shock

tube studies of aviation fuels are well established [349] there are only a few studies published over the last 5 years which focus on the autoignition properties of SJFs using shock tubes [350], RCMs [351] and flow reactors [352].

Autoignition data of the key chemical components of the SAF would allow for the development of a chemical kinetic mechanism for the combustion of the fuel. This is essential for comparing the fuel to existing jet fuels to determine compatibility with existing engines, and the properties of traditional and synthetic blends. The development of a chemical kinetic mechanism for the UoS SJF and accurate determination of its key combustion properties using the shock tube data is the first key step in validating it as a new potential fuel. Furthermore, an accurate understanding of the combustion chemistry will be required for the optimisation of new aviation engines to be developed for the combustion of pure synthetic jet fuels.

## 7. References

- [1] S. Arrhenius, "On the influence of carbonic acid in the air upon the temperature of the ground," *Phil. Mag*, vol. 41, 1896.
- [2] S. H. Mohr, J. Wang, G. Ellem, J. Ward, and D. Giurco, "Projection of world fossil fuels by country," *Fuel*, vol. 141, pp. 120-135, 2015/02/01/ 2015, doi: <https://doi.org/10.1016/j.fuel.2014.10.030>.
- [3] S. Chu, Y. Cui, and N. Liu, "The path towards sustainable energy," *Nature Materials*, Perspective vol. 16, p. 16, 12/20/online 2016, doi: 10.1038/nmat4834.
- [4] H. Richie and M. Roser. "CO<sub>2</sub> and greenhouse gas emissions." <https://ourworldindata.org/co2-and-other-greenhouse-gas-emissions> (accessed 27th July, 2021).
- [5] B. Bereiter *et al.*, "Revision of the EPICA Dome C CO<sub>2</sub> record from 800 to 600 kyr before present," *Geophysical Research Letters*, vol. 42, no. 2, pp. 542-549, 2015, doi: <https://doi.org/10.1002/2014GL061957>.
- [6] C. D. Keeling *et al.*, "Atmospheric carbon dioxide variations at Mauna Loa Observatory, Hawaii," *Tellus*, vol. 28, no. 6, pp. 538-551, 1976/01/01 1976, doi: 10.3402/tellusa.v28i6.11322.
- [7] J. P. Gattuso *et al.*, "Contrasting futures for ocean and society from different anthropogenic CO<sub>2</sub> emissions scenarios," *Science*, vol. 349, no. 6243, p. aac4722, 2015, doi: 10.1126/science.aac4722.
- [8] Global Greenhouse Gas Reference Network. "Trends in atmospheric carbon dioxide: Monthly average Mauna Loa CO<sub>2</sub>." U.S. Department of Commerce. <https://www.esrl.noaa.gov/gmd/ccgg/trends/mlo.html> (accessed 13th November, 2019).
- [9] P. Stott, "How climate change affects extreme weather events," *Science*, vol. 352, no. 6293, p. 1517, 2016, doi: 10.1126/science.aaf7271.
- [10] T. Boningari and P. G. Smirniotis, "Impact of nitrogen oxides on the environment and human health: Mn-based materials for the NO<sub>x</sub> abatement," *Current Opinion in Chemical Engineering*, vol. 13, pp. 133-141, 2016/08/01/ 2016, doi: <https://doi.org/10.1016/j.coche.2016.09.004>.
- [11] N. Gascoin, Q. Yang, and K. Chetehouna, "Thermal effects of CO<sub>2</sub> on the NO<sub>x</sub> formation behavior in the CH<sub>4</sub> diffusion combustion system," *Applied Thermal Engineering*, vol. 110, pp. 144-149, 2017/01/05/ 2017, doi: <https://doi.org/10.1016/j.applthermaleng.2016.08.133>.
- [12] U. Asghar *et al.*, "Review of the progress in emission control technologies for the abatement of CO<sub>2</sub>, SO<sub>x</sub> and NO<sub>x</sub> from fuel combustion," *Journal of Environmental Chemical Engineering*, p. 106064, 2021/07/16/ 2021, doi: <https://doi.org/10.1016/j.jece.2021.106064>.
- [13] Andri, B. H. Basuki, E. S. Seputro, and E. Kusuma, "Efforts to reduce SO<sub>2</sub> emission in Paiton coal-fired power plant," *IOP Conference Series: Materials Science and Engineering*, vol. 1096, no. 1, p. 012125, 2021/03/01 2021, doi: 10.1088/1757-899x/1096/1/012125.
- [14] J. Gupta, "A history of international climate change policy," *WIREs Climate Change*, <https://doi.org/10.1002/wcc.67> vol. 1, no. 5, pp. 636-653, 2010/09/01 2010, doi: <https://doi.org/10.1002/wcc.67>.
- [15] M. P. Chipperfield, S. S. Dhomse, W. Feng, R. L. McKenzie, G. J. M. Velders, and J. A. Pyle, "Quantifying the ozone and ultraviolet benefits already achieved by the Montreal Protocol," *Nature Communications*, vol. 6, no. 1, p. 7233, 2015/05/26 2015, doi: 10.1038/ncomms8233.
- [16] J. Hansen *et al.*, "Climate impact of increasing atmospheric carbon dioxide," *Science*, vol. 213, no. 4511, pp. 957-966, 1981.
- [17] S. Oberthür and H. E. Ott, *The Kyoto Protocol: international climate policy for the 21st century*. Springer Science & Business Media, 1999.
- [18] G. Iacobuta, N. K. Dubash, P. Upadhyaya, M. Deribe, and N. Höhne, "National climate change mitigation legislation, strategy and targets: a global update," *Climate Policy*, vol. 18, no. 9, pp. 1114-1132, 2018/10/21 2018, doi: 10.1080/14693062.2018.1489772.
- [19] J. Rogelj *et al.*, "Paris Agreement climate proposals need a boost to keep warming well below 2 °C," *Nature*, vol. 534, no. 7609, pp. 631-639, 2016/06/01 2016, doi: 10.1038/nature18307.

- [20] D. Bodansky, "The legal character of the Paris Agreement," *Review of European, Comparative & International Environmental Law*, <https://doi.org/10.1111/reel.12154> vol. 25, no. 2, pp. 142-150, 2016/07/01 2016, doi: <https://doi.org/10.1111/reel.12154>.
- [21] R. Watson, J. McCarthy, P. Canziani, N. Nakicenovic, and L. Hisas, *The truth behind the climate pledges*. FEU-US, 2019.
- [22] T. Kåberger, "Progress of renewable electricity replacing fossil fuels," *Global Energy Interconnection*, vol. 1, no. 1, pp. 48-52, 2018/01/01/ 2018, doi: <https://doi.org/10.14171/j.2096-5117.gei.2018.01.006>.
- [23] Royal Dutch Shell plc. "Could Renewable Energy Completely Replace Fossil Fuels." Royal Dutch Shell plc. <https://www.shell.com/energy-and-innovation/the-energy-future/scenarios/shell-scenario-sky/could-society-reach-the-goals-of-the-paris-agreement/can-renewables-replace-fossil-fuels.html> (accessed 13th November, 2019).
- [24] N. Abas, A. Kalair, and N. Khan, "Review of fossil fuels and future energy technologies," *Futures*, vol. 69, pp. 31-49, 2015/05/01/ 2015, doi: <https://doi.org/10.1016/j.futures.2015.03.003>.
- [25] R. J. Allam *et al.*, "High efficiency and low cost of electricity generation from fossil fuels while eliminating atmospheric emissions, including carbon dioxide," *Ghgt-11*, vol. 37, pp. 1135-1149, 2013, doi: 10.1016/j.egypro.2013.05.211.
- [26] K. Stępczyńska-Drygas, H. Łukowicz, and S. Dykas, "Calculation of an advanced ultra-supercritical power unit with CO<sub>2</sub> capture installation," *Energy Conversion and Management*, vol. 74, pp. 201-208, 2013/10/01/ 2013, doi: <https://doi.org/10.1016/j.enconman.2013.04.045>.
- [27] V. Dostal, P. Hejzlar, and M. J. Driscoll, "The supercritical carbon dioxide power cycle: comparison to other advanced power cycles," *Nuclear Technology*, vol. 154, no. 3, pp. 283-301, 2006/06/01 2006, doi: 10.13182/NT06-A3734.
- [28] E. G. Feher, "The supercritical thermodynamic power cycle," *Energy Conversion*, vol. 8, no. 2, pp. 85-90, 1968/09/01/ 1968, doi: [https://doi.org/10.1016/0013-7480\(68\)90105-8](https://doi.org/10.1016/0013-7480(68)90105-8).
- [29] Y. Kim, "Equation of state for carbon dioxide," *Journal of Mechanical Science and Technology*, journal article vol. 21, no. 5, pp. 799-803, May 01 2007, doi: 10.1007/bf02916358.
- [30] G. L. Weibel and C. K. Ober, "An overview of supercritical CO<sub>2</sub> applications in microelectronics processing," *Microelectronic Engineering*, vol. 65, no. 1, pp. 145-152, 2003/01/01/ 2003, doi: [https://doi.org/10.1016/S0167-9317\(02\)00747-5](https://doi.org/10.1016/S0167-9317(02)00747-5).
- [31] C. K. Ho *et al.*, "High-temperature receiver designs for supercritical CO<sub>2</sub> closed-loop Brayton cycles," in *ASME 2014 8th International Conference on Energy Sustainability collocated with the ASME 2014 12th International Conference on Fuel Cell Science, Engineering and Technology*, 2014, vol. 1, V001T02A003, doi: 10.1115/es2014-6328. [Online]. Available: <https://doi.org/10.1115/ES2014-6328>
- [32] J. Syblik, L. Vesely, S. Entler, J. Stepanek, and V. Dostal, "Analysis of supercritical CO<sub>2</sub> Brayton power cycles in nuclear and fusion energy," *Fusion Engineering and Design*, vol. 146, pp. 1520-1523, 2019/09/01/ 2019, doi: <https://doi.org/10.1016/j.fusengdes.2019.02.119>.
- [33] R. J. Allam, J. E. Fetvedt, B. A. Forrest, and D. A. Freed, "The oxy-fuel, supercritical CO<sub>2</sub> Allam cycle: new cycle developments to produce even lower-cost electricity from fossil fuels without atmospheric emissions," *Proceedings of the Asme Turbo Expo: Turbine Technical Conference and Exposition*, vol. 3b, 2014, Art no. V03bt36a016.
- [34] T. Lockwood, "A comparative review of next-generation carbon capture technologies for coal-fired power plant," *13th International Conference on Greenhouse Gas Control Technologies, GHGT-13*, vol. 114, pp. 2658-2670, 2017, doi: 10.1016/j.egypro.2017.03.1850.
- [35] I. Liadze, C. Macchiarelli, P. Mortimer-Lee, and P. S. Juanino, "The economic costs of the Russia Ukraine conflict," 2022.
- [36] NetPower. "Home." NetPower. <https://www.netpower.com/> (accessed 7th November, 2019).
- [37] R. J. Allam, "Improved oxygen production technologies," *Greenhouse Gas Control Technologies* 9, vol. 1, no. 1, pp. 461-470, 2009, doi: 10.1016/j.egypro.2009.01.062.
- [38] A. McClung, K. Brun, and L. Chordia, "Technical and economic evaluation of supercritical oxy-combustion for power generation," in *Fourth Supercritical CO<sub>2</sub> Power Cycles Symposium, Pittsburgh, PA, Sept*, 2014, pp. 9-10.

- [39] J. Repasky, L. L. Anderson, V. E. Stein, P. Armstrong, and E. P. Foster, "ITM oxygen technology: Scale-up toward clean energy applications," *29th Annual International Pittsburgh Coal Conference 2012, PCC 2012*, vol. 1, pp. 158-174, 01/01 2012.
- [40] C. Mitchell, V. Avagyan, H. Chalmers, and M. Lucquiaud, "An initial assessment of the value of Allam Cycle power plants with liquid oxygen storage in future GB electricity system," *International Journal of Greenhouse Gas Control*, vol. 87, pp. 1-18, 2019/08/01/ 2019, doi: <https://doi.org/10.1016/j.ijggc.2019.04.020>.
- [41] A. Rogalev, E. Grigoriev, V. Kindra, and N. Rogalev, "Thermodynamic optimization and equipment development for a high efficient fossil fuel power plant with zero emissions," *Journal of Cleaner Production*, vol. 236, p. 117592, 2019/11/01/ 2019, doi: <https://doi.org/10.1016/j.jclepro.2019.07.067>.
- [42] X. Lu, S. Martin, M. McGroddy, M. Swanson, J. Stanislawski, and J. D. Laumb, "Testing of a novel post combustion acid removal process for the direct-fired, oxy-combustion Allam cycle power generation system," *Journal of Engineering for Gas Turbines and Power*, vol. 140, no. 8, 2018, doi: 10.1115/1.4038459.
- [43] Y.-S. Choi, S. Nestic, and D. Young, "Effect of impurities on the corrosion behavior of CO<sub>2</sub> transmission pipeline steel in supercritical CO<sub>2</sub>-water environments," *Environmental Science & Technology*, vol. 44, no. 23, pp. 9233-9238, 2010/12/01 2010, doi: 10.1021/es102578c.
- [44] Net Power, "Net power performance data," Net Power, Online, 2021. [Online]. Available: <https://netpower.com/wp-content/uploads/2021/05/2021-NET-Power-Performance-Data-1-pager.pdf>
- [45] K. R. V. Manikantachari, R. K. Rahman, S. M. Martin, C. Velez, and S. S. Vasu, "Influence of equation-of-states on supercritical CO<sub>2</sub> combustion mixtures," *Journal of Energy Resources Technology*, vol. 143, no. 6, 2020, doi: 10.1115/1.4048666.
- [46] E. A. Byers, G. Coxon, J. Freer, and J. W. Hall, "Drought and climate change impacts on cooling water shortages and electricity prices in Great Britain," *Nature Communications*, vol. 11, no. 1, p. 2239, 2020/05/07 2020, doi: 10.1038/s41467-020-16012-2.
- [47] A. Boretti and L. Rosa, "Reassessing the projections of the World Water Development Report," *npj Clean Water*, vol. 2, no. 1, p. 15, 2019/07/31 2019, doi: 10.1038/s41545-019-0039-9.
- [48] M. Mahdaviara *et al.*, "Toward smart schemes for modeling CO<sub>2</sub> solubility in crude oil: Application to carbon dioxide enhanced oil recovery," *Fuel*, vol. 285, p. 119147, 2021/02/01/ 2021, doi: <https://doi.org/10.1016/j.fuel.2020.119147>.
- [49] T. Gan *et al.*, "High carrier mobility tungsten-doped indium oxide films prepared by reactive plasma deposition in pure argon and post annealing," *Materials Science in Semiconductor Processing*, vol. 138, p. 106257, 2022/02/01/ 2022, doi: <https://doi.org/10.1016/j.mssp.2021.106257>.
- [50] Z. L. Zhu, Y. P. Chen, J. F. Wu, S. B. Zhang, and S. X. Zheng, "A modified Allam cycle without compressors realizing efficient power generation with peak load shifting and CO<sub>2</sub> capture," *Energy*, vol. 174, pp. 478-487, May 2019, doi: 10.1016/j.energy.2019.01.165.
- [51] G. Rodríguez Hervás and F. Petrakopoulou, "Exergoeconomic analysis of the Allam cycle," *Energy & Fuels*, vol. 33, no. 8, pp. 7561-7568, 2019/08/15 2019, doi: 10.1021/acs.energyfuels.9b01348.
- [52] R. Scaccabarozzia, M. Gatti, and E. Martelli, "Thermodynamic optimization and part-load analysis of the NET Power Cycle," in *13th International Conference on Greenhouse Gas Control Technologies, Ghgt-13*, vol. 114, T. Dixon, L. Laloui, and S. Twinning Eds., (Energy Procedia, 2017, pp. 551-560.
- [53] E. Dokhaee, A. Saraei, S. Jafari Mehrabadi, and P. Yousefi, "Simulation of the Allam cycle with carbon dioxide working fluid and comparison with Brayton cycle," (in English), *International Journal of Energy and Environmental Engineering*, Article vol. 12, p. 543+, 2021/09//
- // 2021.
- [54] T. Xin, C. Xu, R. Li, Z. Feng, and Y. Yang, "An advanced coal-based zero-emission polygeneration system using water-gas shift reaction and syngas recycle to achieve different methanol and electricity distributions," *Journal of Cleaner Production*, vol. 364, p. 132649, 2022/09/01/ 2022, doi: <https://doi.org/10.1016/j.jclepro.2022.132649>.
- [55] C. Distribution. "8 Rivers Capital ADM announce intention to make Illinois home to game-changing zero-emissions project." PRNewsWire. <https://www.prnewswire.com/news-releases/8-rivers->

- [capital-adm-announce-intention-to-make-illinois-home-to-game-changing-zero-emissions-project-301269296.html?tc=eml\\_cleartime](https://www.bloombergenvironment.com/finance/energy/capital-adm-announce-intention-to-make-illinois-home-to-game-changing-zero-emissions-project-301269296.html?tc=eml_cleartime) (accessed 3rd August, 2021).
- [56] A. Rathi. "U.S. startup plans to build first zero-emission gas power plants." Bloomberg Green. <https://www.bloomberg.com/news/articles/2021-04-15/u-s-startup-plans-to-build-first-zero-emission-gas-power-plants> (accessed 15th April, 2021).
- [57] G. Kelsall. "8 Rivers Capital and Sembcorp Energy UK's first zero emissions power plant." IFRF. <https://ifrf.net/ifrf-blog/8-rivers-capital-and-semcorp-energy-uk-to-develop-uks-first-net-zero-emissions-power-plant/> (accessed 2nd August, 2021).
- [58] Whitetail Energy. "Clean power, clean air, clean jobs, Teesside, UK." Whitetail Energy. <https://whitetail.energy/> (accessed 3rd August, 2021).
- [59] P. N. N. p. b. R. C. LLC). "8 Rivers secures \$100M investment from SK Group and establishes Asian joint venture with SK Group to accelerate global decarbonization." PR Newswire. <https://www.prnewswire.com/news-releases/8-rivers-secures-100m-investment-from-sk-group-and-establishes-asian-joint-venture-with-sk-group-to-accelerate-global-decarbonization-301497243.html> (accessed 15th May, 2022).
- [60] J. Marion, M. Kutin, A. McClung, J. Mortzheim, and R. Ames, "The STEP 10 MWe sCO<sub>2</sub> pilot plant demonstration," presented at the ASME Turbo Expo 2019: Turbomachinery Technical Conference and Exposition, 2019. [Online]. Available: <https://doi.org/10.1115/GT2019-91917>.
- [61] STEP-DEMO. "STEP DEMO: The Project." STEP-DEMO. <https://www.qti.energy/step-demo/step-demo-project/> (accessed 22nd April, 2021).
- [62] B. Lariviere *et al.*, "sCO<sub>2</sub> power cycle development and STEP demo pilot project," 2021.
- [63] Q. Zhu, "Power generation from coal using supercritical CO<sub>2</sub> cycle," International Centre for Sustainable Carbon, Online, 2017.
- [64] L. W. Lake, R. Johns, W. R. Rossen, and G. A. Pope, "Fundamentals of enhanced oil recovery," 2014.
- [65] Z. Dai *et al.*, "CO<sub>2</sub> accounting and risk analysis for CO<sub>2</sub> sequestration at enhanced oil recovery sites," *Environmental Science & Technology*, vol. 50, no. 14, pp. 7546-7554, 2016/07/19 2016, doi: 10.1021/acs.est.6b01744.
- [66] A. Majumdar and J. Deutch, "Research opportunities for CO<sub>2</sub> utilization and negative emissions at the gigatonne scale," *Joule*, vol. 2, no. 5, pp. 805-809, 2018/05/16/ 2018, doi: <https://doi.org/10.1016/j.joule.2018.04.018>.
- [67] M. E. Capron *et al.*, "Restoring pre-industrial CO<sub>2</sub> levels while achieving sustainable development goals," *Energies*, vol. 13, no. 18, 2020, doi: 10.3390/en13184972.
- [68] L. Vesely, K. R. V. Manikantachari, S. Vasu, J. Kapat, V. Dostal, and S. Martin, "Effect of impurities on compressor and cooler in supercritical CO<sub>2</sub> cycles," *Journal of Energy Resources Technology-Transactions of the Asme*, vol. 141, no. 1, Jan 2019, Art no. 012003, doi: 10.1115/1.4040581.
- [69] M. T. White, G. Bianchi, L. Chai, S. A. Tassou, and A. I. Sayma, "Review of supercritical CO<sub>2</sub> technologies and systems for power generation," *Applied Thermal Engineering*, vol. 185, p. 116447, 2021/02/25/ 2021, doi: <https://doi.org/10.1016/j.applthermaleng.2020.116447>.
- [70] Y. Iwai, M. Itoh, Y. Morisawa, S. Suzuki, D. Cusano, and M. Harris, "Development approach to the combustor of gas turbine for oxy-fuel, supercritical CO<sub>2</sub> cycle," 2015 2015, vol. 56802: American Society of Mechanical Engineers, p. V009T36A013.
- [71] A. R. Laich *et al.*, "Effects of high fuel loading and CO<sub>2</sub> dilution on oxy-methane ignition inside a shock tube at high pressure," *Journal of Energy Resources Technology*, vol. 142, no. 10, 2020, doi: 10.1115/1.4047023.
- [72] J. Foust. "Musk offers more technical details on BFR system." SpaceNews. <https://spacenews.com/musk-offers-more-technical-details-on-bfr-system/> (accessed 11th February, 2021).
- [73] J. O'Callaghan. "The wild physics of Elon Musk's methane-guzzling super-rocket." Wired. <https://www.wired.co.uk/article/spacex-raptor-engine-starship> (accessed 11th February, 2021).
- [74] K. P. Brooks, J. Hu, H. Zhu, and R. J. Kee, "Methanation of carbon dioxide by hydrogen reduction using the Sabatier process in microchannel reactors," *Chemical Engineering Science*, vol. 62, no. 4, pp. 1161-1170, 2007/02/01/ 2007, doi: <https://doi.org/10.1016/j.ces.2006.11.020>.

- [75] P. J. Waltrup, M. E. White, F. Zarlingo, and E. S. Gravlin, "History of U.S. Navy ramjet, scramjet, and mixed-cycle propulsion development," *Journal of Propulsion and Power*, vol. 18, no. 1, pp. 14-27, 2002/01/01 2002, doi: 10.2514/2.5928.
- [76] C. Segal, *The scramjet engine: processes and characteristics*. Cambridge University Press, 2009.
- [77] R. J. Weber and J. S. MacKay, "An analysis of ramjet engines using supersonic combustion," 1958.
- [78] A. H. Lefebvre, *Gas turbine combustion*. CRC press, 1998.
- [79] G. Liu, B. Yan, and G. Chen, "Technical review on jet fuel production," *Renewable and Sustainable Energy Reviews*, vol. 25, pp. 59-70, 2013/09/01/ 2013, doi: <https://doi.org/10.1016/j.rser.2013.03.025>.
- [80] J. T. Cabbage, "Fractional distillation," ed: Google Patents, 1967.
- [81] C. Zhang, X. Hui, Y. Lin, and C.-J. Sung, "Recent development in studies of alternative jet fuel combustion: Progress, challenges, and opportunities," *Renewable and Sustainable Energy Reviews*, vol. 54, pp. 120-138, 2016/02/01/ 2016, doi: <https://doi.org/10.1016/j.rser.2015.09.056>.
- [82] Sustainable Aviation, "Decarbonisation road map: A path to Net Zero," Sustainable Aviation, sustainableaviation.co.uk, 2020. [Online]. Available: [https://www.sustainableaviation.co.uk/wp-content/uploads/2020/02/SustainableAviation\\_CarbonReport\\_20200203.pdf](https://www.sustainableaviation.co.uk/wp-content/uploads/2020/02/SustainableAviation_CarbonReport_20200203.pdf)
- [83] R. W. Dörner, D. R. Hardy, F. W. Williams, and H. D. Willauer, "Heterogeneous catalytic CO<sub>2</sub> conversion to value-added hydrocarbons," *Energy & Environmental Science*, 10.1039/C001514H vol. 3, no. 7, pp. 884-890, 2010, doi: 10.1039/C001514H.
- [84] The University of Sheffield Energy Institute. "Strata Technology to deliver the flagship Fischer-Tropsch rig for the Translational Energy Research Centre." <https://terc.ac.uk/strata-technology-to-deliver-the-flagship-fischer-tropsch-rig-for-the-translational-energy-research-centre/> (accessed 10th August, 2020).
- [85] J. K. Shao, R. Choudhary, D. E. Davidson, R. K. Hanson, S. Barak, and S. Vasu, "Ignition delay times of methane and hydrogen highly diluted in carbon dioxide at high pressures up to 300 atm," *Proceedings of the Combustion Institute*, vol. 37, no. 4, pp. 4555-4562, 2019, doi: 10.1016/j.proci.2018.08.002.
- [86] J. M. Harman-Thomas, M. Pourkashanian, and K. J. Hughes, "The chemical kinetic mechanism for combustion in supercritical carbon dioxide," presented at the 4th European sCO<sub>2</sub> Conference for Energy Systems, Online, 2021, 2. [Online]. Available: [https://duepublico2.uni-due.de/receive/duepublico\\_mods\\_00073944](https://duepublico2.uni-due.de/receive/duepublico_mods_00073944).
- [87] J. Harman-Thomas, K. J. Hughes, and M. Pourkashanian, "The development of a chemical kinetic mechanism for combustion in supercritical carbon dioxide," *Energy*, p. 124490, 2022/06/16/ 2022, doi: <https://doi.org/10.1016/j.energy.2022.124490>.
- [88] J. M. Harman-Thomas, T. A. Kashif, K. J. Hughes, M. Pourkashanian, and A. Farooq, "Experimental and modelling study of hydrogen ignition in CO<sub>2</sub> bath gas," *Fuel*, vol. 334, p. 126664, 2023/02/15/ 2023, doi: <https://doi.org/10.1016/j.fuel.2022.126664>.
- [89] J. M. Harman-Thomas, T. A. Kashif, K. J. Hughes, M. Pourkashanian, and A. Farooq, "Experimental and modelling study of syngas combustion in CO<sub>2</sub> bath gas," *Fuel*, vol. 342, p. 127865, 2023/06/15/ 2023, doi: <https://doi.org/10.1016/j.fuel.2023.127865>.
- [90] M. P. Vieille, "On the discontinuities produced by the sudden release of compressed gases," in *Shock Tubes*, I. I. Glass Ed., (Proceedings of the Seventh International Shock Tube Symposium held at University of Toronto, Toronto, Canada 23-25 June 1969: University of Toronto Press, 1970, pp. 6-10.
- [91] W. C. F. Shepherd, "The Ignition of gas mixtures by impulsive pressures," *Symposium on Combustion and Flame, and Explosion Phenomena*, vol. 3, no. 1, pp. 301-316, 1948/01/01/ 1948, doi: [https://doi.org/10.1016/S1062-2896\(49\)80037-7](https://doi.org/10.1016/S1062-2896(49)80037-7).
- [92] P. K. Koppenberger, "Shock tube design," BEng, Mechanical Engineering, Texas A & M Univeristy, 2010.
- [93] A. D. Kiverin and I. S. Yakovenko, "Ignition and detonation onset behind incident shock wave in the shock tube," *Combustion and Flame*, vol. 204, pp. 227-236, 2019/06/01/ 2019, doi: <https://doi.org/10.1016/j.combustflame.2019.03.012>.

- [94] M. E. Fuller, M. Skowron, R. S. Tranter, and C. F. Goldsmith, "A modular, multi-diagnostic, automated shock tube for gas-phase chemistry," *Review of Scientific Instruments*, vol. 90, no. 6, p. 064104, 2019/06/01 2019, doi: 10.1063/1.5095077.
- [95] A. Bar-Nun and A. Lifshitz, "Kinetics of the homogeneous exchange reaction:  $^{14-14}\text{N}_2 + ^{15-15}\text{N}_2 \rightleftharpoons 2^{14-15}\text{N}_2$ . Single-pulse shock-tube studies," *The Journal of Chemical Physics*, vol. 47, no. 8, pp. 2878-2888, 1967/10/15 1967, doi: 10.1063/1.1712311.
- [96] A. Lifshitz, S. H. Bauer, and E. L. Resler Jr, "Studies with a single-pulse shock tube. I. The cis—trans isomerization of butene-2," *The Journal of Chemical Physics*, vol. 38, no. 9, pp. 2056-2063, 1963.
- [97] A. Lifshitz, "The single pulse shock tube: its Odyssey in chemical kinetics," presented at the Shock Waves, Berlin, Heidelberg, 2005//, 2005.
- [98] I. Stotz, G. Lamanna, H. Hettrich, B. Weigand, and J. Steelant, "Design of a double diaphragm shock tube for fluid disintegration studies," *The Review of scientific instruments*, vol. 79, p. 125106, 01/01 2009, doi: 10.1063/1.3058609.
- [99] M. AlAbbad, T. Javed, F. Khaled, J. Badra, and A. Farooq, "Ignition delay time measurements of primary reference fuel blends," *Combustion and Flame*, vol. 178, pp. 205-216, 2017/04/01/ 2017, doi: <https://doi.org/10.1016/j.combustflame.2016.12.027>.
- [100] B. Bobbitt, S. Sahaner, and B. Schmidt, "The combustion driven shock tube: Ae 104c final report," Caltech, 2012. [Online]. Available: [https://shepherd.caltech.edu/T5/Ae104/ae104c\\_CDST.pdf](https://shepherd.caltech.edu/T5/Ae104/ae104c_CDST.pdf)
- [101] A. G. Gaydon and I. R. Hurle, *The shock tube in high-temperature chemical physics*, 1st Edition ed. (London, England). Chapman and Hall Ltd., 1963, p. 307.
- [102] R. S. Tranter and B. R. Giri, "A diaphragmless shock tube for high temperature kinetic studies," *Review of Scientific Instruments*, vol. 79, no. 9, p. 094103, 2008/09/01 2008, doi: 10.1063/1.2976671.
- [103] S. Kugimiya, K. Ichizono, S. Nourgostar, K. N. Sato, S. Kawasaki, and T. Exp.Group, "Development of a new type shock tube without a diaphragm for gas-dynamic laser research," 10/25 2004.
- [104] C. J. E. Aul, "An experimental study into the ignition of methane and ethane blends in a new shock-tube facility," MSc, Mechanical Engineering, Texas A&M University, Texas, 2009.
- [105] T. Malewicki, "Development of a jet a chemical surrogate model using high pressure shock tube speciation data," PhD, Mechanical Engineering, University of Illinois at Chicago, Chicago, Illinois, 2012.
- [106] A. L. Russo and A. Hertzberg, *Modifications of the basic shock tube to improve its performance*. Buffalo, N.Y.: Cornell Aeronautical Laboratory (in English), 1958.
- [107] H. J. Davis and H. D. Curchack, "Shock tube techniques and instrumentation," Harry Diamond Laboratories, Washington, D.C, 1969.
- [108] Z. Hong, D. F. Davidson, and R. K. Hanson, "Contact surface tailoring condition for shock tubes with different driver and driven section diameters," *Shock Waves*, vol. 19, no. 4, pp. 331-336, 2009/08/01 2009, doi: 10.1007/s00193-009-0212-z.
- [109] Z. Hong, G. A. Pang, S. S. Vasu, D. F. Davidson, and R. K. Hanson, "The use of driver inserts to reduce non-ideal pressure variations behind reflected shock waves," *Shock Waves*, vol. 19, no. 2, pp. 113-123, 2009/06/01 2009, doi: 10.1007/s00193-009-0205-y.
- [110] J. M. Kerwin, "Design of a shock tube for jet noise research," 1996.
- [111] A. R. Amadio, M. W. Crofton, and E. L. Petersen, "Test-time extension behind reflected shock waves using CO 2–He and C 3 H 8–He driver mixtures," *Shock Waves*, vol. 16, no. 2, pp. 157-165, 2006.
- [112] M. F. Campbell, T. Parise, A. M. Tulgestke, R. M. Spearrin, D. F. Davidson, and R. K. Hanson, "Strategies for obtaining long constant-pressure test times in shock tubes," *Shock Waves*, vol. 25, no. 6, pp. 651-665, 2015/11/01 2015, doi: 10.1007/s00193-015-0596-x.
- [113] G. Mittal and C.-J. SUNG\*, "A rapid compression machine for chemical kinetics studies at elevated pressures and temperatures," *Combustion Science and Technology*, vol. 179, no. 3, pp. 497-530, 2007.

- [114] X. Wang, H. Wei, J. Pan, Z. Hu, Z. Zheng, and M. Pan, "Analysis of diesel knock for high-altitude heavy-duty engines using optical rapid compression machines," *Energies*, vol. 13, p. 3080, 06/14 2020, doi: 10.3390/en13123080.
- [115] H. Nakamura *et al.*, "An experimental and modeling study of shock tube and rapid compression machine ignition of n-butylbenzene/air mixtures," *Combustion and Flame*, vol. 161, no. 1, pp. 49-64, 2014/01/01/ 2014, doi: <https://doi.org/10.1016/j.combustflame.2013.08.002>.
- [116] C. Lee *et al.*, "On the chemical kinetics of ethanol oxidation: Shock tube, rapid compression machine and detailed modeling study," *Zeitschrift für Physikalische Chemie*, vol. 226, no. 1, pp. 1-28, 2012, doi: doi:10.1524/zpch.2012.0185.
- [117] M. Werler, L. R. Cancino, R. Schiessl, U. Maas, C. Schulz, and M. Fikri, "Ignition delay times of diethyl ether measured in a high-pressure shock tube and a rapid compression machine," *Proceedings of the Combustion Institute*, vol. 35, no. 1, pp. 259-266, 2015/01/01/ 2015, doi: <https://doi.org/10.1016/j.proci.2014.06.143>.
- [118] H. Ksibi and A. Ben Moussa, "Numerical simulation of a one-dimensional shock tube problem at supercritical fluid conditions," *International Journal of Physical Sciences*, vol. 3, no. 12, pp. 314-320, Dec 2008.
- [119] L. F. Cabeza, A. de Gracia, A. I. Fernández, and M. M. Farid, "Supercritical CO<sub>2</sub> as heat transfer fluid: A review," *Applied Thermal Engineering*, vol. 125, pp. 799-810, 2017/10/01/ 2017, doi: <https://doi.org/10.1016/j.applthermaleng.2017.07.049>.
- [120] H. Mark, "The interaction of a reflected shock wave with the boundary layer in a shock tube," in "Technical Memorandum," Cornell University, Ithaca, New York, United States, 1958.
- [121] M. Ihme, Y. Sun, and R. Deiterding, "Detailed simulations of shock-bifurcation and ignition of an argon-diluted hydrogen/oxygen mixture in a shock tube," in *51st AIAA Aerospace Sciences Meeting including the New Horizons Forum and Aerospace Exposition*, (Aerospace Sciences Meetings: American Institute of Aeronautics and Astronautics, 2013.
- [122] J. W. Hargis and E. L. Petersen, "Methane ignition in a shock tube with high levels of CO<sub>2</sub> dilution: consideration of the reflected-shock bifurcation," *Energy & Fuels*, vol. 29, no. 11, pp. 7712-7726, 2015/11/19 2015, doi: 10.1021/acs.energyfuels.5b01760.
- [123] J. W. Hargis and E. L. Petersen, "Shock-tube boundary-layer effects on reflected-shock conditions with and without CO<sub>2</sub>," *AIAA Journal*, vol. 55, no. 3, pp. 902-912, 2017/03/01 2017, doi: 10.2514/1.J055253.
- [124] R. A. Strehlow and A. Cohen, "Comment on reflected shock wave studies," *The Journal of Chemical Physics*, vol. 28, no. 5, pp. 983-985, 1958/05/01 1958, doi: 10.1063/1.1744314.
- [125] B. Koroglu, S. Neupane, O. Pryor, R. E. Peale, and S. S. Vasu, "High temperature infrared absorption cross sections of methane near 3.4  $\mu\text{m}$  in Ar and CO<sub>2</sub> mixtures," *Journal of Quantitative Spectroscopy and Radiative Transfer*, vol. 206, pp. 36-45, 2018/02/01/ 2018, doi: <https://doi.org/10.1016/j.jqsrt.2017.11.003>.
- [126] E. L. Petersen and R. K. Hanson, "Measurement of reflected-shock bifurcation over a wide range of gas composition and pressure," *Shock Waves*, vol. 15, no. 5, pp. 333-340, 2006/09/01 2006, doi: 10.1007/s00193-006-0032-3.
- [127] M. Karimi, B. Ochs, Z. F. Liu, D. Ranjan, and W. T. Sun, "Measurement of methane autoignition delays in carbon dioxide and argon diluents at high pressure conditions," *Combustion and Flame*, vol. 204, pp. 304-319, Jun 2019, doi: 10.1016/j.combustflame.2019.03.020.
- [128] R. K. Hanson, G. A. Pang, S. Chakraborty, W. Ren, S. Wang, and D. F. Davidson, "Constrained reaction volume approach for studying chemical kinetics behind reflected shock waves," *Combustion and Flame*, vol. 160, no. 9, pp. 1550-1558, 2013/09/01/ 2013, doi: <https://doi.org/10.1016/j.combustflame.2013.03.026>.
- [129] H. Mirels, "Shock tube test time limitation due to turbulent wall boundary layer," *AIAA Journal*, vol. 2, no. 1, pp. 84-93, 1964/01/01 1964, doi: 10.2514/3.2218.
- [130] H. Mirels, "Test time in low-pressure shock tubes," *The Physics of Fluids*, vol. 6, no. 9, pp. 1201-1214, 1963/09/01 1963, doi: 10.1063/1.1706887.
- [131] E. L. Petersen, "A shock tube and diagnostics for chemistry measurements at elevated pressures with application for methane ignition," PhD, Department of Mechanical Engineering, Stanford University, Stanford, 1998.

- [132] C. T. Bowman and R. K. Hanson, "Shock tube measurements of rate coefficients of elementary gas reactions," *The Journal of Physical Chemistry*, vol. 83, no. 6, pp. 757-763, 1979/03/01 1979, doi: 10.1021/j100469a023.
- [133] H. Polachek and R. J. Seeger, "On shock-wave phenomena; refraction of shock waves at a gaseous interface," *Physical Review*, vol. 84, no. 5, pp. 922-929, 12/01/ 1951, doi: 10.1103/PhysRev.84.922.
- [134] G. Pang, Anne, "Experimental determination of rate constants for reactions of the hydroxyl radical with alkanes and alcohols.," PhD, Mechanical Engineering, Stanford University, Stanford, United States, 2012.
- [135] C. R. Mulvihill and E. L. Petersen, "Concerning shock-tube ignition delay times: An experimental investigation of impurities in the H<sub>2</sub>/O<sub>2</sub> system and beyond," *Proceedings of the Combustion Institute*, vol. 37, no. 1, pp. 259-266, 2019/01/01/ 2019, doi: <https://doi.org/10.1016/j.proci.2018.05.024>.
- [136] *x-t Diagram Tools*. (2008). The University of Wisconsin, [Online].
- [137] D. F. Davidson and R. K. Hanson, "Interpreting shock tube ignition data," *International Journal of Chemical Kinetics*, vol. 36, no. 9, pp. 510-523, 2004/09/01 2004, doi: 10.1002/kin.20024.
- [138] Z. Hong, K.-Y. Lam, R. Sur, S. Wang, D. F. Davidson, and R. K. Hanson, "On the rate constants of OH+HO<sub>2</sub> and HO<sub>2</sub>+HO<sub>2</sub>: A comprehensive study of H<sub>2</sub>O<sub>2</sub> thermal decomposition using multi-species laser absorption," *Proceedings of the Combustion Institute*, vol. 34, no. 1, pp. 565-571, 2013/01/01/ 2013, doi: <https://doi.org/10.1016/j.proci.2012.06.108>.
- [139] Z. Hong, D. F. Davidson, K.-Y. Lam, and R. K. Hanson, "A shock tube study of the rate constants of HO<sub>2</sub> and CH<sub>3</sub> reactions," *Combustion and Flame*, vol. 159, no. 10, pp. 3007-3013, 2012/10/01/ 2012, doi: <https://doi.org/10.1016/j.combustflame.2012.04.009>.
- [140] Z. Hong, D. F. Davidson, E. A. Barbour, and R. K. Hanson, "A new shock tube study of the H + O<sub>2</sub> → OH + O reaction rate using tunable diode laser absorption of H<sub>2</sub>O near 2.5 μm," *Proceedings of the Combustion Institute*, vol. 33, no. 1, pp. 309-316, 2011/01/01/ 2011, doi: <https://doi.org/10.1016/j.proci.2010.05.101>.
- [141] Z. Hong, R. D. Cook, D. F. Davidson, and R. K. Hanson, "A shock tube study of OH + H<sub>2</sub>O<sub>2</sub> → H<sub>2</sub>O + HO<sub>2</sub> and H<sub>2</sub>O<sub>2</sub> + M → 2OH + M using laser absorption of H<sub>2</sub>O and OH," *The Journal of Physical Chemistry A*, vol. 114, no. 18, pp. 5718-5727, 2010/05/13 2010, doi: 10.1021/jp100204z.
- [142] J. E. Vivanco, "A new shock-tube facility for the study of high-temperature chemical kinetics," MSc, Mechanical Engineering, Texas A&M University, Texas, United States, 2014.
- [143] M. Karimi, "Investigation of high-pressure methane and syngas autoignition delay times," School of Aerospace Engineering, Georgia Institute of Technology, Georgia, PhD, 2019.
- [144] M. F. Campbell, "Studies of biodiesel surrogates using novel shock tube techniques," PhD, Mechanical Engineering, Stanford University, Stanford, 2014.
- [145] R. L. Rebagay, "Heated shock tube design and characterisation for fuel combustion experiments," MSc, Mechanical Engineering, Texas A&M University, Texas, 2017.
- [146] Heblac Technologie GMBH, "Shock tube for investigating the ignition behaviour of hydrocarbons: Operation and risk assessment," ed, 2022.
- [147] W. R. Seeker, "The design, assembly, and testing of a shock tube for study of coal combustion kinetics," MSc, Nuclear Engineering, Kansas State University, Kansas, 1976.
- [148] K. A. Heufer and H. Olivier, "Determination of ignition delay times of different hydrocarbons in a new high pressure shock tube," *Shock Waves*, vol. 20, no. 4, pp. 307-316, 2010/08/01 2010, doi: 10.1007/s00193-010-0262-2.
- [149] J. Lopez, "Combustion of 1,3-butadiene behind reflected shocks," MSc, Mechanical and Aerospace Engineering, University of Central Florida, Texas, 2017.
- [150] J. T. Herbon, "Shock tube measurements of CH<sub>3</sub>+O<sub>2</sub> kinetics and the heat of formation of the OH radical," PhD, Mechanical Engineering, Stanford University, Stanford, 2004.
- [151] Y. Liu, C. Zou, J. Cheng, H. Q. Jia, and C. G. Zheng, "Experimental and numerical study of the effect of CO<sub>2</sub> on the ignition delay times of methane under different pressures and temperatures," *Energy & Fuels*, vol. 32, no. 10, pp. 10999-11009, Oct 2018, doi: 10.1021/acs.energyfuels.8b02443.

- [152] J. K. Shao, R. Choudhary, Y. Z. Peng, D. F. Davidson, and R. K. Hanson, "Shock tube measurement of the  $C_2H_4 + H$  double left right arrow  $C_2H_3 + H_2$  rate constant," *Journal of Physical Chemistry A*, vol. 123, no. 1, pp. 15-20, Jan 2019, doi: 10.1021/acs.jpca.8b09452.
- [153] B. Koroglu, O. M. Pryor, J. Lopez, L. Nash, and S. S. Vasu, "Shock tube ignition delay times and methane time-histories measurements during excess  $CO_2$  diluted oxy-methane combustion," *Combustion and Flame*, vol. 164, pp. 152-163, 2016/02/01/ 2016, doi: <https://doi.org/10.1016/j.combustflame.2015.11.011>.
- [154] A. Vandersickel *et al.*, "The autoignition of practical fuels at HCCI conditions: High-pressure shock tube experiments and phenomenological modeling," *Fuel*, vol. 93, pp. 492-501, 2012/03/01/ 2012, doi: <https://doi.org/10.1016/j.fuel.2011.10.062>.
- [155] E. L. Petersen, "Interpreting endwall and sidewall measurements in shock-tube ignition studies," *Combustion Science and Technology*, vol. 181, no. 9, pp. 1123-1144, 2009/09/04 2009, doi: 10.1080/00102200902973323.
- [156] S. H. Pyun, J. Cho, D. F. Davidson, and R. K. Hanson, "Interference-free mid-IR laser absorption detection of methane," *Measurement Science and Technology*, vol. 22, no. 2, p. 025303, 2011/01/11 2011, doi: 10.1088/0957-0233/22/2/025303.
- [157] W. Ren, D. F. Davidson, and R. K. Hanson, "IR laser absorption diagnostic for  $C_2H_4$  in shock tube kinetics studies," *International Journal of Chemical Kinetics*, <https://doi.org/10.1002/kin.20599> vol. 44, no. 6, pp. 423-432, 2012/06/01 2012, doi: <https://doi.org/10.1002/kin.20599>.
- [158] A. Farooq, D. F. Davidson, R. K. Hanson, L. K. Huynh, and A. Violi, "An experimental and computational study of methyl ester decomposition pathways using shock tubes," *Proceedings of the Combustion Institute*, vol. 32, no. 1, pp. 247-253, 2009/01/01/ 2009, doi: <https://doi.org/10.1016/j.proci.2008.06.084>.
- [159] D. F. Davidson, M. Roehrig, E. L. Petersen, M. D. Di Rosa, and R. K. Hanson, "Measurements of the OH A-X (0,0) 306 nm absorption bandhead at 60 atm and 1735 K," *Journal of Quantitative Spectroscopy and Radiative Transfer*, vol. 55, no. 6, pp. 755-762, 1996/06/01/ 1996, doi: [https://doi.org/10.1016/0022-4073\(96\)00024-6](https://doi.org/10.1016/0022-4073(96)00024-6).
- [160] M. T. Macpherson, M. J. Pilling, and M. J. C. Smith, "Determination of the absorption cross section for methyl at 216.36 nm and the absolute rate constant for methyl radical recombination over the temperature range 296-577 K," *The Journal of Physical Chemistry*, vol. 89, no. 11, pp. 2268-2274, 1985/05/01 1985, doi: 10.1021/j100257a024.
- [161] D. F. Davidson, M. D. Di Rosa, A. Y. Chang, R. K. Hanson, and C. T. Bowman, "A shock tube study of methane decomposition using laser absorption by  $CH_3$ ," *Symposium (International) on Combustion*, vol. 24, no. 1, pp. 589-596, 1992/01/01/ 1992, doi: [https://doi.org/10.1016/S0082-0784\(06\)80072-X](https://doi.org/10.1016/S0082-0784(06)80072-X).
- [162] D. F. Davidson, A. Y. Chang, M. D. Di Rosa, and R. K. Hanson, "A cw laser absorption diagnostic for methyl radicals," *Journal of Quantitative Spectroscopy and Radiative Transfer*, vol. 49, no. 5, pp. 559-571, 1993/05/01/ 1993, doi: [https://doi.org/10.1016/0022-4073\(93\)90067-R](https://doi.org/10.1016/0022-4073(93)90067-R).
- [163] S. Wang, S. Li, D. F. Davidson, and R. K. Hanson, "Shock tube measurement of the high-temperature rate constant for  $OH + CH_3 \rightarrow$  products," *The Journal of Physical Chemistry A*, vol. 119, no. 33, pp. 8799-8805, 2015/08/20 2015, doi: 10.1021/acs.jpca.5b05725.
- [164] L. T. Zaczek, K. Y. Lam, D. F. Davidson, and R. K. Hanson, "A shock tube study of  $CH_3OH+OH \rightarrow$  Products using OH laser absorption," *Proceedings of the Combustion Institute*, vol. 35, no. 1, pp. 377-384, 2015/01/01/ 2015, doi: <https://doi.org/10.1016/j.proci.2014.05.051>.
- [165] R. Choudhary, J. J. Girard, Y. Peng, J. Shao, D. F. Davidson, and R. K. Hanson, "Measurement of the reaction rate of  $H + O_2 + M \rightarrow HO_2 + M$ , for  $M = Ar, N_2, CO_2$ , at high temperature with a sensitive OH absorption diagnostic," *Combustion and Flame*, vol. 203, pp. 265-278, 2019/05/01/ 2019, doi: <https://doi.org/10.1016/j.combustflame.2019.02.017>.
- [166] J. J. Girard, R. Choudhary, and R. K. Hanson, "Collisional-induced broadening and shift parameters of OH with Ar and  $N_2$  near 308.6 nm, measured at  $T = 1300-2000$  K and  $P = 20-100$  atm," *Journal of Quantitative Spectroscopy and Radiative Transfer*, vol. 221, pp. 194-201, 2018/12/01/ 2018, doi: <https://doi.org/10.1016/j.jqsrt.2018.10.007>.
- [167] S. Wang and R. K. Hanson, "High-sensitivity 308.6-nm laser absorption diagnostic optimized for OH measurement in shock tube combustion studies," *Applied Physics B*, vol. 124, no. 3, p. 37, 2018/02/08 2018, doi: 10.1007/s00340-018-6902-4.

- [168] R. Sivaramakrishnan and J. V. Michael, "Shock tube measurements of high temperature rate constants for OH with cycloalkanes and methylcycloalkanes," *Combustion and Flame*, vol. 156, no. 5, pp. 1126-1134, 2009/05/01/ 2009, doi: <https://doi.org/10.1016/j.combustflame.2008.10.010>.
- [169] S. Wang, K. Sun, D. F. Davidson, J. B. Jeffries, and R. K. Hanson, "Cavity-enhanced absorption spectroscopy with a ps-pulsed UV laser for sensitive, high-speed measurements in a shock tube," *Optics Express*, vol. 24, no. 1, pp. 308-318, 2016/01/11 2016, doi: 10.1364/OE.24.000308.
- [170] C. Yan and L. N. Krasnoperov, "Pressure-dependent kinetics of the reaction between CH<sub>3</sub>O<sub>2</sub> and OH: TRIOX formation," *The Journal of Physical Chemistry A*, vol. 123, no. 39, pp. 8349-8357, 2019/10/03 2019, doi: 10.1021/acs.jpca.9b03861.
- [171] R. M. Mihalcea, D. S. Baer, and R. K. Hanson, "Tunable diode-laser absorption measurements of NO<sub>2</sub> near 670 and 395 nm," *Applied Optics*, vol. 35, no. 21, pp. 4059-4064, 1996/07/20 1996, doi: 10.1364/AO.35.004059.
- [172] T. W. Hansch and B. Couillaud, "Laser frequency stabilization by polarization spectroscopy of a reflecting reference cavity," *Optics Communications*, vol. 35, no. 3, pp. 441-444, 1980/12/01/ 1980, doi: [https://doi.org/10.1016/0030-4018\(80\)90069-3](https://doi.org/10.1016/0030-4018(80)90069-3).
- [173] A. Goldman and J. R. Gillis, "Spectral line parameters for the A<sub>2</sub>Σ<sup>-</sup>-X<sub>2</sub>Π(0,0) band of OH for atmospheric and high temperatures," *Journal of Quantitative Spectroscopy and Radiative Transfer*, vol. 25, no. 2, pp. 111-135, 1981/02/01/ 1981, doi: [https://doi.org/10.1016/0022-4073\(81\)90004-2](https://doi.org/10.1016/0022-4073(81)90004-2).
- [174] A. Goldman, "Line parameters for the atmospheric band system of OH," *Applied Optics*, vol. 21, no. 12, pp. 2100-2102, 1982/06/15 1982, doi: 10.1364/AO.21.002100.
- [175] S. Wang, D. F. Davidson, and R. K. Hanson, "Shock tube measurements of OH concentration time-histories in benzene, toluene, ethylbenzene and xylene oxidation," *Proceedings of the Combustion Institute*, vol. 37, no. 1, pp. 163-170, 2019/01/01/ 2019, doi: <https://doi.org/10.1016/j.proci.2018.06.116>.
- [176] R. Stanger *et al.*, "Oxyfuel combustion for CO<sub>2</sub> capture in power plants," *International Journal of Greenhouse Gas Control*, vol. 40, pp. 55-125, 2015/09/01/ 2015, doi: <https://doi.org/10.1016/j.ijggc.2015.06.010>.
- [177] S. Coogan, X. Gao, A. McClung, and W. Sun, "Evaluation of kinetic mechanisms for direct fired supercritical oxy-combustion of natural gas," presented at the Conference: ASME Turbo Expo 2016: Turbo-machinery Technical Conference and Exposition, Seoul, South Korea, 2016. [Online]. Available: <https://doi.org/10.1115/GT2016-56658>.
- [178] A. C. Benim and K. J. Syed, "Chapter 2 - Concepts related to combustion and flow in premix burners," in *Flashback Mechanisms in Lean Premixed Gas Turbine Combustion*, A. C. Benim and K. J. Syed Eds. Boston: Academic Press, 2015, pp. 5-18.
- [179] X. Hu, Q. Yu, J. Liu, and N. Sun, "Investigation of laminar flame speeds of CH<sub>4</sub>/O<sub>2</sub>/CO<sub>2</sub> mixtures at ordinary pressure and kinetic simulation," *Energy*, vol. 70, pp. 626-634, 2014/06/01/ 2014, doi: <https://doi.org/10.1016/j.energy.2014.04.029>.
- [180] S. de Persis, F. Foucher, L. Pillier, V. Osorio, and I. Gökalp, "Effects of O<sub>2</sub> enrichment and CO<sub>2</sub> dilution on laminar methane flames," *Energy*, vol. 55, pp. 1055-1066, 2013/06/15/ 2013, doi: <https://doi.org/10.1016/j.energy.2013.04.041>.
- [181] H. Watanabe, S. J. Shanbhogue, S. Taamallah, N. W. Chakroun, and A. F. Ghoniem, "The structure of swirl-stabilized turbulent premixed CH<sub>4</sub>/air and CH<sub>4</sub>/O<sub>2</sub>/CO<sub>2</sub> flames and mechanisms of intense burning of oxy-flames," *Combustion and Flame*, vol. 174, pp. 111-119, 2016/12/01/ 2016, doi: <https://doi.org/10.1016/j.combustflame.2016.09.015>.
- [182] G. P. Smith *et al.* "GRI Mechanism 3.0." University of California, Berkeley. <http://combustion.berkeley.edu/gri-mech/version30/text30.html> (accessed 16th December, 2019).
- [183] X. Hu and H. Wei, "Experimental investigation of laminar flame speeds of propane in O<sub>2</sub>/CO<sub>2</sub> atmosphere and kinetic simulation," *Fuel*, vol. 268, p. 117347, 2020/05/15/ 2020, doi: <https://doi.org/10.1016/j.fuel.2020.117347>.
- [184] F. Hu, P. F. Li, J. J. Guo, K. Wang, Z. H. Liu, and C. G. Zheng, "Evaluation, development, and validation of a new reduced mechanism for methane oxy-fuel combustion," *International Journal of Greenhouse Gas Control*, vol. 78, pp. 327-340, Nov 2018, doi: 10.1016/j.ijggc.2018.08.018.
- [185] H. Wang *et al.*, "USC Mech Version II. High-Temperature Combustion Reaction Model of H<sub>2</sub>/CO/C<sub>1</sub>-C<sub>4</sub> Compounds," ed, 2007.

- [186] J. Natarajan, T. Lieuwen, and J. Seitzman, "Laminar flame speeds of H<sub>2</sub>/CO mixtures: Effect of CO<sub>2</sub> dilution, preheat temperature, and pressure," *Combustion and Flame*, vol. 151, no. 1, pp. 104-119, 2007/10/01/ 2007, doi: <https://doi.org/10.1016/j.combustflame.2007.05.003>.
- [187] R. Shang, Y. Zhang, M. Zhu, Z. Zhang, D. Zhang, and G. Li, "Laminar flame speed of CO<sub>2</sub> and N<sub>2</sub> diluted H<sub>2</sub>/CO/air flames," *International Journal of Hydrogen Energy*, vol. 41, no. 33, pp. 15056-15067, 2016/09/07/ 2016, doi: <https://doi.org/10.1016/j.ijhydene.2016.05.064>.
- [188] S. G. Davis, A. V. Joshi, H. Wang, and F. Egolfopoulos, "An optimized kinetic model of H<sub>2</sub>/CO combustion," *Proceedings of the combustion Institute*, vol. 30, no. 1, pp. 1283-1292, 2005.
- [189] J. Li, Z. Zhao, A. Kazakov, M. Chaos, F. L. Dryer, and J. J. Scire Jr, "A comprehensive kinetic mechanism for CO, CH<sub>2</sub>O, and CH<sub>3</sub>OH combustion," *International Journal of Chemical Kinetics*, vol. 39, no. 3, pp. 109-136, 2007.
- [190] P. A. Strakey, "Oxy-combustion modeling for direct-fired supercritical CO<sub>2</sub> power cycles," *Journal of Energy Resources Technology*, vol. 141, no. 7, 2019, doi: 10.1115/1.4043124.
- [191] A. N. Mazas, D. A. Lacoste, and T. Schuller, "Experimental and numerical investigation on the laminar flame speed of CH<sub>4</sub>/O<sub>2</sub> mixtures diluted with CO<sub>2</sub> and H<sub>2</sub>O," 2010. [Online]. Available: <https://doi.org/10.1115/GT2010-22512>.
- [192] S. Barak *et al.*, "Ignition delay times of oxy-syngas and oxy-methane in supercritical CO<sub>2</sub> mixtures for direct-fired cycles," *Journal of Engineering for Gas Turbines and Power*, vol. 142, no. 2, 2020, doi: 10.1115/1.4045743.
- [193] O. Pryor, "High temperature shock tube ignition studies of CO<sub>2</sub> diluted mixtures," MSc, Mechanical and Aerospace Engineering, University of Central Florida, Florida, 2016.
- [194] O. Pryor, S. Barak, B. Koroglu, E. Ninnemann, and S. S. Vasu, "Measurements and interpretation of shock tube ignition delay times in highly CO<sub>2</sub> diluted mixtures using multiple diagnostics," *Combustion and Flame*, vol. 180, pp. 63-76, 2017/06/01/ 2017, doi: <https://doi.org/10.1016/j.combustflame.2017.02.020>.
- [195] O. Pryor *et al.*, "Ignition delay times of high pressure oxy-methane combustion with high levels of CO<sub>2</sub> dilution," presented at the Proceedings of ASME Turbo Expo 2017: Turbo-machinery Technical Conference and Exposition, Charlotte, NC, USA, 2017. [Online]. Available: <https://doi.org/10.1115/GT2017-63666>.
- [196] C. Kinney, M. Pierro, A. Laich, J. J. Urso, J. McGaunn, and S. Vasu, "High pressure ignition study of methane and natural gas in highly CO<sub>2</sub> diluted mixtures," in *AIAA SCITECH 2022 Forum*, (AIAA SciTech Forum: American Institute of Aeronautics and Astronautics, 2021).
- [197] S. S. Vasu, D. F. Davidson, and R. K. Hanson, "Shock tube study of syngas ignition in rich CO<sub>2</sub> mixtures and determination of the rate of H+O<sub>2</sub>+ CO<sub>2</sub> → HO<sub>2</sub>+CO<sub>2</sub>," *Energy & Fuels*, vol. 25, no. 3, pp. 990-997, 2011.
- [198] S. Barak, O. Pryor, J. Lopez, E. Ninnemann, S. Vasu, and B. Koroglu, "High-speed imaging and measurements of ignition delay times in oxy-syngas mixtures with high CO<sub>2</sub> dilution in a shock tube," *Journal of Engineering for Gas Turbines and Power*, vol. 139, no. 12, 2017, doi: 10.1115/1.4037458.
- [199] S. Barak, E. Ninnemann, S. Neupane, F. Barnes, J. Kapat, and S. Vasu, "High-pressure oxy-syngas ignition delay times with CO<sub>2</sub> dilution: Shock tube measurements and comparison of the performance of kinetic mechanisms," *Journal of Engineering for Gas Turbines and Power*, vol. 141, no. 2, 2018, doi: 10.1115/1.4040904.
- [200] M. Karimi, B. Ochs, W. Sun, and D. Ranjan, "High pressure ignition delay times of H<sub>2</sub>/CO mixture in carbon dioxide and argon diluent," *Proceedings of the Combustion Institute*, 2020/09/06/ 2020, doi: <https://doi.org/10.1016/j.proci.2020.06.268>.
- [201] Y. Liu, J. Cheng, C. Zou, L. X. Lu, and H. X. Jing, "Ignition delay times of ethane under O<sub>2</sub>/CO<sub>2</sub> atmosphere at different pressures by shock tube and simulation methods," *Combustion and Flame*, vol. 204, pp. 380-390, Jun 2019, doi: 10.1016/j.combustflame.2019.03.031.
- [202] N. Djordjevic, M. Rekus, J. Vinkeloe, and L. Zander, "Shock tube and kinetic study on the effects of CO<sub>2</sub> on dimethyl ether autoignition at high pressures," *Energy & Fuels*, vol. 33, no. 10, pp. 10197-10208, Oct 2019, doi: 10.1021/acs.energyfuels.9b01575.
- [203] Z. Shi, H. Zhang, H. Liu, H. Lu, J. Li, and X. Gao, "Effects of buffer gas composition on autoignition of dimethyl ether," *Energies*, vol. 8, no. 9, 2015, doi: 10.3390/en80910198.

- [204] L. Lu, C. Zou, W. Xia, Q. Lin, and H. Shi, "Experimental and numerical study on the ignition delay times of dimethyl ether/ethane/oxygen/carbon dioxide mixtures," *Fuel*, vol. 280, p. 118675, 2020.
- [205] J. Yang, C. Zou, W. Li, Q. Lin, L. Lu, and W. Xia, "Experimental and numerical study on the ignition delay times of dimethyl ether/propane mixtures in O<sub>2</sub>/CO<sub>2</sub> atmospheres," *Fuel*, vol. 316, p. 123301, 2022/05/15/ 2022, doi: <https://doi.org/10.1016/j.fuel.2022.123301>.
- [206] X. Xiong, Z. Lv, H. Tan, Z. Peng, and Y. Ding, "Shock tube evaluation on C<sub>2</sub>H<sub>4</sub> ignition delay differences among N<sub>2</sub>, Ar, He, CO<sub>2</sub> diluent gases," *Journal of the Energy Institute*, vol. 93, no. 4, pp. 1271-1277, 2020.
- [207] W. Xia *et al.*, "Shock tube and modeling study of ignition delay times of propane under O<sub>2</sub>/CO<sub>2</sub>/Ar atmosphere," *Combustion and Flame*, vol. 220, pp. 34-48, 2020/10/01/ 2020, doi: <https://doi.org/10.1016/j.combustflame.2020.06.024>.
- [208] J. Luo *et al.*, "A shock tube and modeling study on ignition delay times of pyridine under O<sub>2</sub>/CO<sub>2</sub> atmospheres at elevated pressures," *Proceedings of the Combustion Institute*, 2020.
- [209] H. Di *et al.*, "Effects of buffer gas composition on low temperature ignition of iso-octane and n-heptane," *Combustion and Flame*, vol. 161, no. 10, pp. 2531-2538, 2014/10/01/ 2014, doi: <https://doi.org/10.1016/j.combustflame.2014.04.014>.
- [210] R. K. Rahman *et al.*, "Probing the effects of NO<sub>x</sub> and SO<sub>x</sub> impurities on oxy-fuel combustion in supercritical CO<sub>2</sub>: shock tube experiments and chemical kinetic modeling," *Journal of Energy Resources Technology*, vol. 142, no. 12, 2020, doi: 10.1115/1.4047314.
- [211] P. Biswas, J. Shao, R. Choudhary, D. Davidson, and R. Hanson, *Ignition delay time measurements and model improvements of syngas with H<sub>2</sub>S in supercritical CO<sub>2</sub> systems*. 2022.
- [212] CHEMKIN-PRO. (2019).
- [213] A. Burcat. "Prof. Burcat's Thermodynamic Data." Institute of Chemistry, Eötvös University (ELTE) ., <http://garfield.chem.elte.hu/Burcat/burcat.html> (accessed 23rd June, 2023).
- [214] W. K. Metcalfe, S. M. Burke, S. S. Ahmed, and H. J. Curran, "A hierarchical and comparative kinetic modeling study of C1 – C2 hydrocarbon and oxygenated fuels," *International Journal of Chemical Kinetics*, vol. 45, no. 10, pp. 638-675, 2013/10/01 2013, doi: 10.1002/kin.20802.
- [215] Y. Li, C.-W. Zhou, K. P. Somers, K. Zhang, and H. J. Curran, "The oxidation of 2-butene: A high pressure ignition delay, kinetic modeling study and reactivity comparison with isobutene and 1-butene," *Proceedings of the Combustion Institute*, vol. 36, no. 1, pp. 403-411, 2017/01/01/ 2017, doi: <https://doi.org/10.1016/j.proci.2016.05.052>.
- [216] C.-W. Zhou *et al.*, "A comprehensive experimental and modeling study of isobutene oxidation," *Combustion and Flame*, vol. 167, pp. 353-379, 2016/05/01/ 2016, doi: <https://doi.org/10.1016/j.combustflame.2016.01.021>.
- [217] U. Burke, W. K. Metcalfe, S. M. Burke, K. A. Heufer, P. Dagaut, and H. J. Curran, "A detailed chemical kinetic modeling, ignition delay time and jet-stirred reactor study of methanol oxidation," *Combustion and Flame*, vol. 165, pp. 125-136, 2016/03/01/ 2016, doi: <https://doi.org/10.1016/j.combustflame.2015.11.004>.
- [218] S. M. Burke *et al.*, "An experimental and modeling study of propene oxidation. Part 2: Ignition delay time and flame speed measurements," *Combustion and Flame*, vol. 162, no. 2, pp. 296-314, 2015/02/01/ 2015, doi: <https://doi.org/10.1016/j.combustflame.2014.07.032>.
- [219] A. Kéromnès *et al.*, "An experimental and detailed chemical kinetic modeling study of hydrogen and syngas mixture oxidation at elevated pressures," *Combustion and Flame*, vol. 160, no. 6, pp. 995-1011, 2013/06/01/ 2013, doi: <https://doi.org/10.1016/j.combustflame.2013.01.001>.
- [220] H. Hashemi, J. M. Christensen, and P. Glarborg, "High-pressure pyrolysis and oxidation of DME and DME/CH<sub>4</sub>," *Combustion and Flame*, vol. 205, pp. 80-92, 2019/07/01/ 2019, doi: <https://doi.org/10.1016/j.combustflame.2019.03.028>.
- [221] H. Hashemi, J. M. Christensen, S. Gersen, H. Levinsky, S. J. Klippenstein, and P. Glarborg, "High-pressure oxidation of methane," *Combustion and Flame*, vol. 172, pp. 349-364, 2016/10/01/ 2016, doi: <https://doi.org/10.1016/j.combustflame.2016.07.016>.
- [222] G. P. Smith, Y. Tao, and H. Wang. "Foundational Fuel Chemistry Model Version 1.0 (FFCM-1)." FFCM-1. <http://web.stanford.edu/group/haiwanglab/FFCM1/pages/FFCM1.html> (accessed 7th November 2019).

- [223] P. Zhang, I. G. Zsély, V. Samu, T. Nagy, and T. Turányi, "Comparison of methane combustion mechanisms using shock tube and rapid compression machine ignition delay time measurements," *Energy & Fuels*, vol. 35, no. 15, pp. 12329-12351, 2021/08/05 2021, doi: 10.1021/acs.energyfuels.0c04277.
- [224] M. Keiffer, A. J. Miscampbell, and M. J. Pilling, "A global technique for analysing multiple decay curves. Application to the  $\text{CH}_3 + \text{O}_2$  system," *Journal of the Chemical Society, Faraday Transactions 2: Molecular and Chemical Physics*, vol. 84, no. 5, pp. 505-514, 1988.
- [225] W. Tsang and R. F. Hampson, "Chemical kinetic data base for combustion chemistry. Part I. Methane and related compounds," *Journal of Physical and Chemical Reference Data*, vol. 15, no. 3, pp. 1087-1279, 1986/07/01 1986, doi: 10.1063/1.555759.
- [226] R. X. Fernandes, K. Luther, and J. Troe, "Falloff curves for the reaction  $\text{CH}_3 + \text{O}_2 (+\text{M}) \rightarrow \text{CH}_3\text{O}_2 (+\text{M})$  in the pressure range 2–1000 bar and the temperature range 300–700 K," *The Journal of Physical Chemistry A*, vol. 110, no. 13, pp. 4442-4449, 2006/04/01 2006, doi: 10.1021/jp056850o.
- [227] P. D. Lightfoot, P. Roussel, F. Caralp, and R. Lesclaux, "Flash-photolysis study of the  $\text{CH}_3\text{O}_2 + \text{CH}_3\text{O}_2$  and  $\text{CH}_3\text{O}_2 + \text{HO}_2$  reactions between 60 K and 719 K - Unimolecular decomposition of methylhydroperoxide," *Journal of the Chemical Society-Faraday Transactions*, vol. 87, no. 19, pp. 3213-3220, Oct 1991, doi: 10.1039/ft9918703213.
- [228] W. Tsang, "Chemical kinetic data base for combustion chemistry. Part 2. Methanol," *Journal of Physical and Chemical Reference Data*, vol. 16, no. 3, pp. 471-508, 1987/07/01 1987, doi: 10.1063/1.555802.
- [229] E. W. Kaiser, "Pressure dependence of the rate constants for the reactions methyl+ oxygen and methyl+ nitric oxide from 3 to 104 torr," *The Journal of Physical Chemistry*, vol. 97, no. 45, pp. 11681-11688, 1993.
- [230] W. Forst and F. Caralp, "Microcanonical variational theory of radical recombination by inversion of interpolated partition function. Part 2.— $\text{CX}_3 + \text{O}_2$  (X= H, F, Cl)," *Journal of the Chemical Society, Faraday Transactions*, vol. 87, no. 15, pp. 2307-2315, 1991.
- [231] M. J. Pilling and M. J. C. Smith, "A laser flash photolysis study of the reaction  $\text{CH}_3 + \text{O}_2 \rightarrow \text{CH}_3\text{O}_2$  at 298 K," *The Journal of Physical Chemistry*, vol. 89, no. 22, pp. 4713-4720, 1985/10/01 1985, doi: 10.1021/j100268a014.
- [232] D. A. Parkes, "The oxidation of methyl radicals at room temperature," *International Journal of Chemical Kinetics*, vol. 9, no. 3, pp. 451-469, 1977.
- [233] E. Assaf *et al.*, "The reaction between  $\text{CH}_3\text{O}_2$  and OH radicals: Product yields and atmospheric implications," *Environmental Science & Technology*, vol. 51, no. 4, pp. 2170-2177, 2017/02/21 2017, doi: 10.1021/acs.est.6b06265.
- [234] J. Troe, "The thermal dissociation/recombination reaction of hydrogen peroxide  $\text{H}_2\text{O}_2 (+\text{M}) \rightleftharpoons 2\text{OH} (+\text{M})$  III.: Analysis and representation of the temperature and pressure dependence over wide ranges," *Combustion and Flame*, vol. 158, no. 4, pp. 594-601, 2011/04/01/ 2011, doi: <https://doi.org/10.1016/j.combustflame.2010.08.013>.
- [235] D. L. Baulch *et al.*, "Evaluated kinetic data for combustion modelling," *Journal of Physical and Chemical Reference Data*, vol. 21, no. 3, pp. 411-734, 1992/05/01 1992, doi: 10.1063/1.555908.
- [236] I. A. B. Reid, C. Robinson, and D. B. Smith, "Spontaneous ignition of methane: Measurement and chemical model," *Symposium (International) on Combustion*, vol. 20, no. 1, pp. 1833-1843, 1985/01/01/ 1985, doi: [https://doi.org/10.1016/S0082-0784\(85\)80681-0](https://doi.org/10.1016/S0082-0784(85)80681-0).
- [237] A. W. Jasper, S. J. Klippenstein, and L. B. Harding, "Theoretical rate coefficients for the reaction of methyl radical with hydroperoxyl radical and for methylhydroperoxide decomposition," *Proceedings of the Combustion Institute*, vol. 32, no. 1, pp. 279-286, 2009/01/01/ 2009, doi: <https://doi.org/10.1016/j.proci.2008.05.036>.
- [238] N. K. Srinivasan, J. V. Michael, L. B. Harding, and S. J. Klippenstein, "Experimental and theoretical rate constants for  $\text{CH}_4 + \text{O}_2 \rightarrow \text{CH}_3 + \text{HO}_2$ ," *Combustion and Flame*, vol. 149, no. 1, pp. 104-111, 2007/04/01/ 2007, doi: <https://doi.org/10.1016/j.combustflame.2006.12.010>.
- [239] N. K. Srinivasan, M. C. Su, J. W. Sutherland, and J. V. Michael, "Reflected shock tube studies of high-temperature rate constants for  $\text{CH}_3 + \text{O}_2$ ,  $\text{H}_2\text{CO} + \text{O}_2$ , and  $\text{OH} + \text{O}_2$ ," *The Journal of Physical Chemistry A*, vol. 109, no. 35, pp. 7902-7914, 2005/09/01 2005, doi: 10.1021/jp0581330.
- [240] C. L. Yu, C. Wang, and M. Frenklach, "Chemical kinetics of methyl oxidation by molecular oxygen," *The Journal of Physical Chemistry*, vol. 99, no. 39, pp. 14377-14387, 1995.

- [241] B. A. Ellingson, D. P. Theis, O. Tishchenko, J. Zheng, and D. G. Truhlar, "Reactions of hydrogen atom with hydrogen peroxide," *The Journal of Physical Chemistry A*, vol. 111, no. 51, pp. 13554-13566, 2007/12/01 2007, doi: 10.1021/jp077379x.
- [242] D. A. Masten, R. K. Hanson, and C. T. Bowman, "Shock tube study of the reaction  $H + O_2 \rightarrow OH + O$  using OH laser absorption," *The Journal of Physical Chemistry*, vol. 94, no. 18, pp. 7119-7128, 1990/09/01 1990, doi: 10.1021/j100381a033.
- [243] D. L. Baulch, D. D. Drysdale, J. Duxbury, and S. Grant, *Evaluated kinetic data for high temperature reactions, Vol. 3: Homogeneous gas phase reactions of the  $O_2$ - $O_3$  systems, the  $CO$ - $O_2$ - $H_2$  system, and of sulphur-containing species* (no. 3). Butterworths, , 1976.
- [244] X. You, H. Wang, E. Goos, C.-J. Sung, and S. J. Klippenstein, "Reaction kinetics of  $CO + HO_2 \rightarrow$  products: ab initio transition state theory study with master equation modeling," *The Journal of Physical Chemistry A*, vol. 111, no. 19, pp. 4031-4042, 2007.
- [245] J. Warnatz, "Rate coefficients in the C/H/O system," in *Combustion Chemistry*, W. C. Gardiner Ed. New York, NY: Springer New York, 1984, pp. 197-360.
- [246] X. You, H. Wang, E. Goos, C.-J. Sung, and S. J. Klippenstein, "Reaction kinetics of  $CO + HO_2 \rightarrow$  products: ab initio transition state theory study with master equation modeling," *The Journal of Physical Chemistry A*, vol. 111, no. 19, pp. 4031-4042, 2007.
- [247] R. R. Baldwin, P. N. Jones, and R. W. Walker, "Determination of the rate constant for  $HO_2 + CH_4 \rightarrow H_2O_2 + CH_3$  at 443 °C," *Journal of the Chemical Society, Faraday Transactions 2: Molecular and Chemical Physics*, vol. 84, no. 2, pp. 199-207, 1988.
- [248] D. L. Baulch *et al.*, "Evaluated kinetic data for combustion modeling: Supplement II," *Journal of Physical and Chemical Reference Data*, vol. 34, no. 3, pp. 757-1397, 2005, doi: 10.1063/1.1748524.
- [249] M. J. Rabinowitz, J. W. Sutherland, P. M. Patterson, and R. B. Klemm, "Direct rate constant measurements for  $H + CH_4$  yields  $CH_3 + H_2$ , 897-1729 K, using the flash photolysis-shock tube technique," *Journal of Physical Chemistry;(USA)*, vol. 95, no. 2, 1991.
- [250] C.-L. Yu, M. Frenklach, D. Masten, R. Hanson, and C. Bowman, "Reexamination of shock-tube measurements of the rate coefficient of  $H + O_2 \rightarrow OH + O$ ," *The Journal of Physical Chemistry*, vol. 98, no. 17, pp. 4770-4771, 1994.
- [251] J. V. Michael and J. W. Sutherland, "Rate constants for the reactions of hydrogen atom with water and hydroxyl with hydrogen by the flash photolysis-shock tube technique over the temperature range 1246-2297 K," *The Journal of Physical Chemistry*, vol. 92, no. 13, pp. 3853-3857, 1988/06/01 1988, doi: 10.1021/j100324a035.
- [252] J. Troe, "Detailed modeling of the temperature and pressure dependence of the reaction  $H + O_2 (+M) \rightarrow HO_2 (+M)$ ," *Proceedings of the Combustion Institute*, vol. 28, no. 2, pp. 1463-1469, 2000/01/01/ 2000, doi: [https://doi.org/10.1016/S0082-0784\(00\)80542-1](https://doi.org/10.1016/S0082-0784(00)80542-1).
- [253] J. V. Michael, J. W. Sutherland, L. B. Harding, and A. F. Wagner, "Initiation in  $H_2/O_2$ : Rate constants for  $H_2 + O_2 \rightarrow H + HO_2$  at high temperature," *Proceedings of the Combustion Institute*, vol. 28, no. 2, pp. 1471-1478, 2000/01/01/ 2000, doi: [https://doi.org/10.1016/S0082-0784\(00\)80543-3](https://doi.org/10.1016/S0082-0784(00)80543-3).
- [254] R. Zellner, F. Ewig, R. Paschke, and G. Wagner, "Pressure and temperature dependence of the gas-phase recombination of hydroxyl radicals," *The Journal of Physical Chemistry*, vol. 92, no. 14, pp. 4184-4190, 1988.
- [255] M. A. Mueller, T. J. Kim, R. A. Yetter, and F. L. Dryer, "Flow reactor studies and kinetic modeling of the  $H_2/O_2$  reaction," *International Journal of Chemical Kinetics*, vol. 31, no. 2, pp. 113-125, 1999/01/01 1999, doi: 10.1002/(SICI)1097-4601(1999)31:2<113::AID-KIN5>3.0.CO;2-0.
- [256] H. Hippler, H. Neunaber, and J. Troe, "Shock wave studies of the reactions  $HO + H_2O_2 \rightarrow H_2O + HO_2$  and  $HO + HO_2 \rightarrow H_2O + O_2$  between 930 and 1680 K," *The Journal of chemical physics*, vol. 103, no. 9, pp. 3510-3516, 1995.
- [257] A. V. Joshi and H. Wang, "Master equation modeling of wide range temperature and pressure dependence of  $CO + OH \rightarrow$  products," *International Journal of Chemical Kinetics*, vol. 38, no. 1, pp. 57-73, 2006/01/01 2006, doi: 10.1002/kin.20137.
- [258] G. Friedrichs, D. F. Davidson, and R. K. Hanson, "Direct measurements of the reaction  $H + CH_2O \rightarrow H_2 + HCO$  behind shock waves by means of Vis-UV detection of formaldehyde," *International Journal of Chemical Kinetics*, vol. 34, no. 6, pp. 374-386, Jun 2002, doi: 10.1002/kin.10059.

- [259] K. J. Hughes, A. Richard Pereira, and M. J. Pilling, "Direct measurement of the rate constant for  $\text{CH}_3 + \text{OH}$  recombination at 290 K," *Berichte der Bunsengesellschaft für physikalische Chemie*, vol. 96, no. 10, pp. 1352-1359, 1992.
- [260] W. Hack, H. G. Wagner, and A. Wilms, "A Study of the reaction of  $\text{CH}_2$  ( $\tilde{a}1A1$ ) with  $\text{H}_2\text{O}$  in the gas phase," *Berichte der Bunsengesellschaft für physikalische Chemie*, vol. 92, no. 5, pp. 620-627, 1988.
- [261] W. S. Staker, K. D. King, G. J. Gutsche, and W. D. Lawrance, "Direct measurement of methylene removal rates by species containing the OH functional group," *Journal of the Chemical Society, Faraday Transactions*, vol. 87, no. 15, pp. 2421-2425, 1991.
- [262] H. Oser, N. Stothard, R. Humpfer, and H. Grotheer, "Direct measurement of the reaction methyl+hydroxyl at ambient temperature in the pressure range 0.3-6.2 mbar," *The Journal of Physical Chemistry*, vol. 96, no. 13, pp. 5359-5363, 1992.
- [263] J. Bott and N. Cohen, "A shock tube study of the reaction of methyl radicals with hydroxyl radicals," *International journal of chemical kinetics*, vol. 23, no. 11, pp. 1017-1033, 1991.
- [264] C. Anastasi, S. Beverton, T. Ellermann, and P. Pagsberg, "Reaction of  $\text{CH}_3$  radicals with OH at room temperature and pressure," *Journal of the Chemical Society, Faraday Transactions*, vol. 87, no. 15, pp. 2325-2329, 1991.
- [265] M. Koch, F. Temps, R. Wagener, and H. G. Wagner, "Kinetics of the reactions of  $\text{CH}_2$  ( $\tilde{a}1A1$ ) with  $\text{CH}_3\text{C}_2\text{H}$ ,  $\text{HCN}$ ,  $\text{CO}_2$ ,  $\text{N}_2\text{O}$  and  $\text{COS}$ ," *Berichte der Bunsengesellschaft für physikalische Chemie*, vol. 94, no. 6, pp. 645-650, 1990.
- [266] P. H. Stewart, C. W. Larson, and D. M. Golden, "Pressure and temperature dependence of reactions proceeding via a bound complex. 2. Application to  $2\text{CH}_3 \rightarrow \text{C}_2\text{H}_5 + \text{H}$ ," *Combustion and Flame*, vol. 75, no. 1, pp. 25-31, 1989.
- [267] R. Baldwin and R. Walker, "Problems and progress in hydrocarbon oxidation," in *Symposium (International) on Combustion*, 1973, vol. 14, no. 1: Elsevier, pp. 241-257.
- [268] R. W. Bates, D. M. Golden, R. K. Hanson, and C. T. Bowman, "Experimental study and modeling of the reaction  $\text{H} + \text{O}_2 + \text{M} \rightarrow \text{HO}_2 + \text{M}$  ( $\text{M} = \text{Ar}, \text{N}_2, \text{H}_2\text{O}$ ) at elevated pressures and temperatures between 1050 and 1250 K," *Physical Chemistry Chemical Physics*, 10.1039/B010002L vol. 3, no. 12, pp. 2337-2342, 2001, doi: 10.1039/B010002L.
- [269] K.-Y. Lam, D. F. Davidson, and R. K. Hanson, "A shock tube study of  $\text{H}_2 + \text{OH} \rightarrow \text{H}_2\text{O} + \text{H}$  using OH laser absorption," *International Journal of Chemical Kinetics*, vol. 45, no. 6, pp. 363-373, 2013/06/01 2013, doi: 10.1002/kin.20771.
- [270] M. P. Burke, M. Chaos, Y. Ju, F. L. Dryer, and S. J. Klippenstein, "Comprehensive  $\text{H}_2/\text{O}_2$  kinetic model for high-pressure combustion," *International Journal of Chemical Kinetics*, vol. 44, no. 7, pp. 444-474, 2012/07/01 2012, doi: 10.1002/kin.20603.
- [271] L. F. Keyser, "Absolute rate constant and branching fractions for the atomic hydrogen+hydroperoxyl radical reaction from 245 to 300 K," *The Journal of Physical Chemistry*, vol. 90, no. 13, pp. 2994-3003, 1986.
- [272] U. Sridharan, L. Qiu, and F. Kaufman, "Kinetics and product channels of the reactions of perhydroxyl with oxygen and hydrogen atoms at 296 K," *The Journal of Physical Chemistry*, vol. 86, no. 23, pp. 4569-4574, 1982.
- [273] S. H. Mousavipour and V. Saheb, "Theoretical study on the kinetic and mechanism of  $\text{H} + \text{HO}_2$  reaction," *Bulletin of the Chemical Society of Japan*, vol. 80, no. 10, pp. 1901-1913, 2007/10/15 2007, doi: 10.1246/bcsj.80.1901.
- [274] A. Fernández-Ramos and A. J. C. Varandas, "A VTST study of the  $\text{H} + \text{O}_3$  and  $\text{O} + \text{HO}_2$  reactions using a six-dimensional DMBE potential energy surface for ground state  $\text{HO}_3$ ," *The Journal of Physical Chemistry A*, vol. 106, no. 16, pp. 4077-4083, 2002/04/01 2002, doi: 10.1021/jp014120k.
- [275] J. P. Senosiain, S. J. Klippenstein, and J. A. Miller, "A complete statistical analysis of the reaction between OH and CO," *Proceedings of the Combustion Institute*, vol. 30, no. 1, pp. 945-953, 2005.
- [276] M. P. Burke, S. J. Klippenstein, and L. B. Harding, "A quantitative explanation for the apparent anomalous temperature dependence of  $\text{OH} + \text{HO}_2 = \text{H}_2\text{O} + \text{O}_2$  through multi-scale modeling," *Proceedings of the Combustion Institute*, vol. 34, no. 1, pp. 547-555, 2013/01/01/ 2013, doi: <https://doi.org/10.1016/j.proci.2012.05.041>.

- [277] A. W. Jasper, S. J. Klippenstein, L. B. Harding, and B. Ruscic, "Kinetics of the reaction of methyl radical with hydroxyl radical and methanol decomposition," *The Journal of Physical Chemistry A*, vol. 111, no. 19, pp. 3932-3950, 2007/05/01 2007, doi: 10.1021/jp067585p.
- [278] P. Dagaut and M. J. Kurylo, "The gas phase UV absorption spectrum of CH<sub>3</sub>O<sub>2</sub> radicals: A reinvestigation," *Journal of Photochemistry and Photobiology A: Chemistry*, vol. 51, no. 2, pp. 133-140, 1990/03/01/ 1990, doi: [https://doi.org/10.1016/1010-6030\(90\)87047-F](https://doi.org/10.1016/1010-6030(90)87047-F).
- [279] M. J. Kurylo, T. J. Wallington, and P. A. Ouellette, "Measurements of the UV absorption cross-sections for HO<sub>2</sub> and CH<sub>3</sub>O<sub>2</sub> in the gas phase," *Journal of photochemistry*, vol. 39, no. 2, pp. 201-215, 1987.
- [280] J. Troe, "Theory of thermal unimolecular reactions at low pressures. I. Solutions of the master equation," *The Journal of Chemical Physics*, vol. 66, no. 11, pp. 4745-4757, 1977/06/01 1977, doi: 10.1063/1.433837.
- [281] T. K. Choudhury, Y. He, W. A. Sanders, and M. C. Lin, "Carbon monoxide formation in the thermal decomposition of methyl nitrite at high temperatures: kinetic modeling of the methoxy decomposition rate," *The Journal of Physical Chemistry*, vol. 94, no. 6, pp. 2394-2398, 1990/03/01 1990, doi: 10.1021/j100369a038.
- [282] H. Hippler, F. Striebel, and B. Viskolcz, "A detailed experimental and theoretical study on the decomposition of methoxy radicals," *Physical Chemistry Chemical Physics*, vol. 3, no. 12, pp. 2450-2458, 2001.
- [283] S. Wang, E. E. Dames, D. F. Davidson, and R. K. Hanson, "Reaction rate constant of CH<sub>2</sub>O + H = HCO + H<sub>2</sub> revisited: A combined study of direct shock tube measurement and transition state theory calculation," *The Journal of Physical Chemistry A*, vol. 118, no. 44, pp. 10201-10209, 2014/11/06 2014, doi: 10.1021/jp5085795.
- [284] A. S. AlRamadan *et al.*, "Mixed butanols addition to gasoline surrogates: Shock tube ignition delay time measurements and chemical kinetic modeling," *Combustion and Flame*, vol. 162, no. 10, pp. 3971-3979, 2015.
- [285] M. Alabbad *et al.*, "Ignition delay time measurements of diesel and gasoline blends," *Combustion and Flame*, vol. 222, pp. 460-475, 2020.
- [286] M. Lamnaouer, A. Kassab, E. Divo, N. Polley, R. Garza-Urquiza, and E. Petersen, "A conjugate axisymmetric model of a high-pressure shock-tube facility," *International Journal of Numerical Methods for Heat & Fluid Flow*, 2014.
- [287] J. Shao, "Shock tube studies of hydrocarbon fuels at elevated pressures," PhD, Mechanical Engineering, Stanford University, Stanford, 2019.
- [288] E. Hu, L. Pan, Z. Gao, X. Lu, X. Meng, and Z. Huang, "Shock tube study on ignition delay of hydrogen and evaluation of various kinetic models," *International Journal of Hydrogen Energy*, vol. 41, no. 30, pp. 13261-13280, 2016/08/10/ 2016, doi: <https://doi.org/10.1016/j.ijhydene.2016.05.118>.
- [289] R. X. Fernandes, K. Luther, J. Troe, and V. G. Ushakov, "Experimental and modelling study of the recombination reaction H + O<sub>2</sub> (+M) → HO<sub>2</sub> (+M) between 300 and 900 K, 1.5 and 950 bar, and in the bath gases M = He, Ar, and N<sub>2</sub>," *Physical Chemistry Chemical Physics*, 10.1039/B804553D vol. 10, no. 29, pp. 4313-4321, 2008, doi: 10.1039/B804553D.
- [290] F. Pignatelli *et al.*, "Pilot impact on turbulent premixed methane/air and hydrogen-enriched methane/air flames in a laboratory-scale gas turbine model combustor," *International Journal of Hydrogen Energy*, vol. 47, no. 60, pp. 25404-25417, 2022/07/15/ 2022, doi: <https://doi.org/10.1016/j.ijhydene.2022.05.282>.
- [291] Y. Jiang, G. d. Alamo, A. Gruber, M. R. Bothien, K. Seshadri, and F. A. Williams, "A skeletal mechanism for prediction of ignition delay times and laminar premixed flame velocities of hydrogen-methane mixtures under gas turbine conditions," *International Journal of Hydrogen Energy*, vol. 44, no. 33, pp. 18573-18585, 2019/07/05/ 2019, doi: <https://doi.org/10.1016/j.ijhydene.2019.05.068>.
- [292] A. Lifshitz, K. Scheller, A. Burcat, and G. B. Skinner, "Shock-tube investigation of ignition in methane-oxygen-argon mixtures," *Combustion and Flame*, vol. 16, no. 3, pp. 311-321, 1971.
- [293] R. K. Cheng and A. K. Oppenheim, "Autoignition in methane-hydrogen mixtures," *Combustion and Flame*, vol. 58, no. 2, pp. 125-139, 1984/11/01/ 1984, doi: [https://doi.org/10.1016/0010-2180\(84\)90088-9](https://doi.org/10.1016/0010-2180(84)90088-9).

- [294] J. Huang, W. K. Bushe, P. G. Hill, and S. R. Munshi, "Experimental and kinetic study of shock initiated ignition in homogeneous methane–hydrogen–air mixtures at engine-relevant conditions," *International Journal of Chemical Kinetics*, <https://doi.org/10.1002/kin.20157> vol. 38, no. 4, pp. 221-233, 2006/04/01 2006, doi: <https://doi.org/10.1002/kin.20157>.
- [295] E. L. Petersen, J. M. Hall, S. D. Smith, J. de Vries, A. R. Amadio, and M. W. Crofton, "Ignition of Lean Methane-Based Fuel Blends at Gas Turbine Pressures," *Journal of Engineering for Gas Turbines and Power*, vol. 129, no. 4, pp. 937-944, 2007, doi: 10.1115/1.2720543.
- [296] N. Chaumeix, S. Pichon, F. Lafosse, and C. E. Paillard, "Role of chemical kinetics on the detonation properties of hydrogen /natural gas/air mixtures," *International Journal of Hydrogen Energy*, vol. 32, no. 13, pp. 2216-2226, 2007/09/01/ 2007, doi: <https://doi.org/10.1016/j.ijhydene.2007.04.008>.
- [297] J. de Vries and E. L. Petersen, "Autoignition of methane-based fuel blends under gas turbine conditions," *Proceedings of the Combustion Institute*, vol. 31, no. 2, pp. 3163-3171, 2007/01/01/ 2007, doi: <https://doi.org/10.1016/j.proci.2006.07.206>.
- [298] S. Gersen, N. B. Anikin, A. V. Mokhov, and H. B. Levinsky, "Ignition properties of methane/hydrogen mixtures in a rapid compression machine," *International Journal of Hydrogen Energy*, vol. 33, no. 7, pp. 1957-1964, 2008/04/01/ 2008, doi: <https://doi.org/10.1016/j.ijhydene.2008.01.017>.
- [299] Y. Zhang, Z. Huang, L. Wei, and S. Niu, "Experimental and kinetic study on ignition delay times of methane/hydrogen/oxygen/nitrogen mixtures by shock tube," *Chinese Science Bulletin*, vol. 56, no. 26, p. 2853, 2011/08/24 2011, doi: 10.1007/s11434-011-4635-4.
- [300] Y. Zhang, Z. Huang, L. Wei, J. Zhang, and C. K. Law, "Experimental and modeling study on ignition delays of lean mixtures of methane, hydrogen, oxygen, and argon at elevated pressures," *Combustion and Flame*, vol. 159, no. 3, pp. 918-931, 2012/03/01/ 2012, doi: <https://doi.org/10.1016/j.combustflame.2011.09.010>.
- [301] Y. Zhang, X. Jiang, L. Wei, J. Zhang, C. Tang, and Z. Huang, "Experimental and modeling study on auto-ignition characteristics of methane/hydrogen blends under engine relevant pressure," *International Journal of Hydrogen Energy*, vol. 37, no. 24, pp. 19168-19176, 2012/12/01/ 2012, doi: <https://doi.org/10.1016/j.ijhydene.2012.09.056>.
- [302] O. Pryor *et al.*, "High pressure shock tube ignition delay time measurements during oxy-methane combustion with high levels of CO<sub>2</sub> dilution," *Journal of Energy Resources Technology-Transactions of the Asme*, vol. 139, no. 4, Jul 2017, Art no. 042208, doi: 10.1115/1.4036254.
- [303] Y. Wu *et al.*, "Understanding the antagonistic effect of methanol as a component in surrogate fuel models: A case study of methanol/n-heptane mixtures," *Combustion and Flame*, vol. 226, pp. 229-242, 2021.
- [304] M. Baigomohammadi *et al.*, "Comprehensive Experimental and Simulation Study of the Ignition Delay Time Characteristics of Binary Blended Methane, Ethane, and Ethylene over a Wide Range of Temperature, Pressure, Equivalence Ratio, and Dilution," *Energy & Fuels*, vol. 34, no. 7, pp. 8808-8823, 2020/07/16 2020, doi: 10.1021/acs.energyfuels.0c00960.
- [305] S. S. Nagaraja *et al.*, "A hierarchical single-pulse shock tube pyrolysis study of C<sub>2</sub>–C<sub>6</sub> 1-alkenes," *Combustion and Flame*, vol. 219, pp. 456-466, 2020/09/01/ 2020, doi: <https://doi.org/10.1016/j.combustflame.2020.06.021>.
- [306] A. A. El-Sabor Mohamed, S. Panigrahy, A. B. Sahu, G. Bourque, and H. J. Curran, "An experimental and kinetic modeling study of the auto-ignition of natural gas blends containing C<sub>1</sub>–C<sub>7</sub> alkanes," *Proceedings of the Combustion Institute*, vol. 38, no. 1, pp. 365-373, 2021/01/01/ 2021, doi: <https://doi.org/10.1016/j.proci.2020.06.015>.
- [307] B. Wang, H. Hou, L. M. Yoder, J. T. Muckerman, and C. Fockenberg, "Experimental and Theoretical Investigations on the Methyl–Methyl Recombination Reaction," *The Journal of Physical Chemistry A*, vol. 107, no. 51, pp. 11414-11426, 2003/12/01 2003, doi: 10.1021/jp030657h.
- [308] R. Patrick, M. J. Pilling, and G. J. Rogers, "A high pressure rate constant for CH<sub>3</sub> + H and an analysis of the kinetics of the CH<sub>3</sub> + H → CH<sub>4</sub> reaction," *Chemical Physics*, vol. 53, no. 3, pp. 279-291, 1980/12/01/ 1980, doi: [https://doi.org/10.1016/0301-0104\(80\)85118-4](https://doi.org/10.1016/0301-0104(80)85118-4).
- [309] N. Cohen, "Are reaction rate coefficients additive? Revised transition state theory calculations for OH+ alkane reactions," *International Journal of Chemical Kinetics*, vol. 23, no. 5, pp. 397-417, 1991.

- [310] J. M. Harman-Thomas, T. A. Kashif, K. J. Hughes, M. Pourkashanian, and A. Farooq, "Experimental and modelling study of syngas ignition in CO<sub>2</sub> bath gas," *[Manuscript submitted for publication]*, 2022.
- [311] C.-H. Wang *et al.*, "Molecular Dynamics of Combustion Reactions in Supercritical Carbon Dioxide. Part 5: Computational Study of Ethane Dissociation and Recombination Reactions C<sub>2</sub>H<sub>6</sub> ⇌ CH<sub>3</sub> + CH<sub>3</sub>," *The Journal of Physical Chemistry A*, vol. 123, no. 22, pp. 4776-4784, 2019/06/06 2019, doi: 10.1021/acs.jpca.9b02302.
- [312] C. R. Mulvihill and E. L. Petersen, "High-temperature argon broadening of CO<sub>2</sub> near 2190 cm<sup>-1</sup> in a shock tube," *Applied Physics B*, vol. 123, no. 10, p. 255, 2017/09/22 2017, doi: 10.1007/s00340-017-6830-8.
- [313] O. Mathieu, S. P. Cooper, S. Alturaifi, C. R. Mulvihill, T. M. Atherley, and E. L. Petersen, "Shock-tube laser absorption measurements of CO and H<sub>2</sub>O during iso-octane combustion," *Energy & Fuels*, vol. 34, no. 6, pp. 7533-7544, 2020/06/18 2020, doi: 10.1021/acs.energyfuels.0c00738.
- [314] A. E. Masunov, E. E. Wait, and S. S. Vasu, "Catalytic effect of carbon dioxide on reaction OH + CO → H + CO<sub>2</sub> in supercritical environment: Master equation study," *The Journal of Physical Chemistry A*, vol. 122, no. 31, pp. 6355-6359, 2018/08/09 2018, doi: 10.1021/acs.jpca.8b04501.
- [315] T. Varga *et al.*, "Development of a joint hydrogen and syngas combustion mechanism based on an optimization approach," *International Journal of Chemical Kinetics*, <https://doi.org/10.1002/kin.21006> vol. 48, no. 8, pp. 407-422, 2016/08/01 2016, doi: <https://doi.org/10.1002/kin.21006>.
- [316] W. Li, C. Zou, H. Yao, Q. Lin, R. Fu, and J. Luo, "An optimized kinetic model for H<sub>2</sub>/CO combustion in CO<sub>2</sub> diluent at elevated pressures," *Combustion and Flame*, vol. 241, p. 112093, 2022/07/01/ 2022, doi: <https://doi.org/10.1016/j.combustflame.2022.112093>.
- [317] T. Nagy, É. Valkó, I. Sedyó, I. G. Zsély, M. J. Pilling, and T. Turányi, "Uncertainty of the rate parameters of several important elementary reactions of the H<sub>2</sub> and syngas combustion systems," *Combustion and Flame*, vol. 162, no. 5, pp. 2059-2076, 2015/05/01/ 2015, doi: <https://doi.org/10.1016/j.combustflame.2015.01.005>.
- [318] N. A. Slavinskaya *et al.*, "Development of an Uncertainty Quantification Predictive Chemical Reaction Model for Syngas Combustion," *Energy & Fuels*, vol. 31, no. 3, pp. 2274-2297, 2017/03/16 2017, doi: 10.1021/acs.energyfuels.6b02319.
- [319] A. W. Jasper, "Predicting third-body collision efficiencies for water and other polyatomic baths," *Faraday Discussions*, vol. 238, pp. 68-86, 2022.
- [320] E. L. Petersen *et al.*, "Discrepancies between shock tube and rapid compression machine ignition at low temperatures and high pressures," in *Shock Waves*: Springer, 2009, pp. 739-744.
- [321] C. Zamfirescu and I. Dincer, "Using ammonia as a sustainable fuel," *Journal of Power Sources*, vol. 185, no. 1, pp. 459-465, 2008/10/15/ 2008, doi: <https://doi.org/10.1016/j.jpowsour.2008.02.097>.
- [322] Y. Bicer, I. Dincer, C. Zamfirescu, G. Vezina, and F. Raso, "Comparative life cycle assessment of various ammonia production methods," *Journal of Cleaner Production*, vol. 135, pp. 1379-1395, 2016/11/01/ 2016, doi: <https://doi.org/10.1016/j.jclepro.2016.07.023>.
- [323] R. H. Dolan, J. E. Anderson, and T. J. Wallington, "Outlook for ammonia as a sustainable transportation fuel," *Sustainable Energy & Fuels*, 10.1039/D1SE00979F vol. 5, no. 19, pp. 4830-4841, 2021, doi: 10.1039/D1SE00979F.
- [324] A. Valera-Medina *et al.*, "Ammonia–methane combustion in tangential swirl burners for gas turbine power generation," *Applied Energy*, vol. 185, pp. 1362-1371, 2017/01/01/ 2017, doi: <https://doi.org/10.1016/j.apenergy.2016.02.073>.
- [325] D. Pratt, "Performance of ammonia-fired gas-turbine combustors," California University of Berkeley Thermal Systems Division, 1967.
- [326] B. Shu, X. He, C. F. Ramos, R. X. Fernandes, and M. Costa, "Experimental and modeling study on the auto-ignition properties of ammonia/methane mixtures at elevated pressures," *Proceedings of the Combustion Institute*, vol. 38, no. 1, pp. 261-268, 2021/01/01/ 2021, doi: <https://doi.org/10.1016/j.proci.2020.06.291>.
- [327] Ammonia Energy News. "Ammonia-fueled gas turbine power generation." Ammonia Energy Association. <https://www.ammoniaenergy.org/articles/ammonia-fueled-gas-turbine-power-generation/> (accessed 18th May, 2020).

- [328] A. Valera-Medina *et al.*, "Premixed ammonia/hydrogen swirl combustion under rich fuel conditions for gas turbines operation," *International Journal of Hydrogen Energy*, vol. 44, no. 16, pp. 8615-8626, 2019/03/29/ 2019, doi: <https://doi.org/10.1016/j.ijhydene.2019.02.041>.
- [329] M. F. Ezzat and I. Dincer, "Energy and exergy analyses of a novel ammonia combined power plant operating with gas turbine and solid oxide fuel cell systems," *Energy*, vol. 194, p. 116750, 2020/03/01/ 2020, doi: <https://doi.org/10.1016/j.energy.2019.116750>.
- [330] S. Salimian, R. K. Hanson, and C. H. Kruger, "High temperature study of the reactions of O and OH with NH<sub>3</sub>," *International Journal of Chemical Kinetics*, vol. 16, no. 6, pp. 725-739, 1984, doi: <https://doi.org/10.1002/kin.550160609>.
- [331] S. Salimian, R. K. Hanson, and C. H. Kruger, "Ammonia oxidation in shock-heated NH<sub>3</sub>/N<sub>2</sub>O/Ar mixtures," *Combustion and Flame*, vol. 56, no. 1, pp. 83-95, 1984/04/01/ 1984, doi: [https://doi.org/10.1016/0010-2180\(84\)90007-5](https://doi.org/10.1016/0010-2180(84)90007-5).
- [332] L. J. Drummond, "High temperature oxidation of ammonia," *Combustion Science and Technology*, vol. 5, no. 1, pp. 175-182, 1972/03/01 1972, doi: 10.1080/00102207208952518.
- [333] N. Fujii, H. Miyama, M. Koshi, and T. Asaba, "Kinetics of ammonia oxidation in shock waves," *Symposium (International) on Combustion*, vol. 18, no. 1, pp. 873-883, 1981/01/01/ 1981, doi: [https://doi.org/10.1016/S0082-0784\(81\)80091-4](https://doi.org/10.1016/S0082-0784(81)80091-4).
- [334] H. Miyama and R. Endoh, "Ignition of ammonia-air mixtures by reflected shock waves," *Combustion and Flame*, vol. 11, no. 4, pp. 359-360, 1967/08/01/ 1967, doi: [https://doi.org/10.1016/0010-2180\(67\)90027-2](https://doi.org/10.1016/0010-2180(67)90027-2).
- [335] H. Miyama and R. Endoh, "Vibrational relaxation of nitrogen in shock-heated NH<sub>3</sub>-O<sub>2</sub>-N<sub>2</sub> mixtures," *The Journal of Chemical Physics*, vol. 46, no. 5, pp. 2011-2012, 1967/03/01 1967, doi: 10.1063/1.1840982.
- [336] T. Takeyama and H. Miyama, "A shock-tube study of the ammonia-oxygen reaction," *Symposium (International) on Combustion*, vol. 11, no. 1, pp. 845-852, 1967/01/01/ 1967, doi: [https://doi.org/10.1016/S0082-0784\(67\)80210-8](https://doi.org/10.1016/S0082-0784(67)80210-8).
- [337] T. Takeyama and H. Miyama, "Kinetic studies of ammonia oxidation in shock waves. I. The reaction mechanism for the induction period," *Bulletin of the Chemical Society of Japan*, vol. 38, no. 10, pp. 1670-1674, 1965/10/01 1965, doi: 10.1246/bcsj.38.1670.
- [338] X. He, B. Shu, D. Nascimento, K. Moshhammer, M. Costa, and R. X. Fernandes, "Auto-ignition kinetics of ammonia and ammonia/hydrogen mixtures at intermediate temperatures and high pressures," *Combustion and Flame*, vol. 206, pp. 189-200, 2019/08/01/ 2019, doi: <https://doi.org/10.1016/j.combustflame.2019.04.050>.
- [339] B. Shu *et al.*, "A shock tube and modeling study on the autoignition properties of ammonia at intermediate temperatures," *Proceedings of the Combustion Institute*, vol. 37, no. 1, pp. 205-211, 2019/01/01/ 2019, doi: <https://doi.org/10.1016/j.proci.2018.07.074>.
- [340] O. Mathieu and E. L. Petersen, "Experimental and modeling study on the high-temperature oxidation of Ammonia and related NO<sub>x</sub> chemistry," *Combustion and Flame*, vol. 162, no. 3, pp. 554-570, 2015/03/01/ 2015, doi: <https://doi.org/10.1016/j.combustflame.2014.08.022>.
- [341] P. Dagaut, P. Glarborg, and M. U. Alzueta, "The oxidation of hydrogen cyanide and related chemistry," *Progress in Energy and Combustion Science*, vol. 34, no. 1, pp. 1-46, 2008/02/01/ 2008, doi: <https://doi.org/10.1016/j.pecs.2007.02.004>.
- [342] O. Mathieu, A. Levacque, and E. L. Petersen, "Effects of N<sub>2</sub>O addition on the ignition of H<sub>2</sub>-O<sub>2</sub> mixtures: Experimental and detailed kinetic modeling study," *International Journal of Hydrogen Energy*, vol. 37, no. 20, pp. 15393-15405, 2012/10/01/ 2012, doi: <https://doi.org/10.1016/j.ijhydene.2012.07.071>.
- [343] G. Dayma and P. Dagaut, "Effects of air contamination on the combustion of hydrogen—effect of NO and NO<sub>2</sub> addition on hydrogen ignition and oxidation kinetics," *Combustion Science and Technology*, vol. 178, no. 10-11, pp. 1999-2024, 2006/12/01 2006, doi: 10.1080/00102200600793171.
- [344] R. Sivaramakrishnan, K. Brezinsky, G. Dayma, and P. Dagaut, "High pressure effects on the mutual sensitization of the oxidation of NO and CH<sub>4</sub>-C<sub>2</sub>H<sub>6</sub> blends," *Physical Chemistry Chemical Physics*, 10.1039/B703379F vol. 9, no. 31, pp. 4230-4244, 2007, doi: 10.1039/B703379F.

- [345] S. J. Klippenstein, L. B. Harding, P. Glarborg, and J. A. Miller, "The role of NNH in NO formation and control," *Combustion and Flame*, vol. 158, no. 4, pp. 774-789, 2011/04/01/ 2011, doi: <https://doi.org/10.1016/j.combustflame.2010.12.013>.
- [346] G. Issayev *et al.*, "Ignition delay time and laminar flame speed measurements of ammonia blended with dimethyl ether: A promising low carbon fuel blend," *Renewable Energy*, vol. 181, pp. 1353-1370, 2022/01/01/ 2022, doi: <https://doi.org/10.1016/j.renene.2021.09.117>.
- [347] G. Issayev *et al.*, "Combustion behavior of ammonia blended with diethyl ether," *Proceedings of the Combustion Institute*, vol. 38, no. 1, pp. 499-506, 2021/01/01/ 2021, doi: <https://doi.org/10.1016/j.proci.2020.06.337>.
- [348] T. Cai and D. Zhao, "Enhancing and assessing ammonia-air combustion performance by blending with dimethyl ether," *Renewable and Sustainable Energy Reviews*, vol. 156, p. 112003, 2022/03/01/ 2022, doi: <https://doi.org/10.1016/j.rser.2021.112003>.
- [349] S. S. Vasu, D. F. Davidson, and R. K. Hanson, "Jet fuel ignition delay times: Shock tube experiments over wide conditions and surrogate model predictions," *Combustion and Flame*, vol. 152, no. 1, pp. 125-143, 2008/01/01/ 2008, doi: <https://doi.org/10.1016/j.combustflame.2007.06.019>.
- [350] G. Flora *et al.*, "Chemical ignition delay of candidate drop-in replacement jet fuels under fuel-lean conditions: A shock tube study," *Fuel*, vol. 209, pp. 457-472, 2017/12/01/ 2017, doi: <https://doi.org/10.1016/j.fuel.2017.07.082>.
- [351] J. Merkisz, I. Pielecha, and A. Łęgowik, "The assessment of autoignition of modified jet fuels," *Energies*, vol. 14, no. 3, 2021, doi: 10.3390/en14030633.
- [352] T. Kathrotia, P. Oßwald, J. Zinsmeister, T. Methling, and M. Köhler, "Combustion kinetics of alternative jet fuels, Part-III: Fuel modeling and surrogate strategy," *Fuel*, vol. 302, p. 120737, 2021/10/15/ 2021, doi: <https://doi.org/10.1016/j.fuel.2021.120737>.
- [353] S. S. Vasu, D. F. Davidson, and R. K. Hanson, "Shock tube study of syngas ignition in rich CO<sub>2</sub> mixtures and determination of the rate of H+ O<sub>2</sub>+ CO<sub>2</sub>→ HO<sub>2</sub>+ CO<sub>2</sub>," *Energy & Fuels*, vol. 25, no. 3, pp. 990-997, 2011.
- [354] T. P. Mangan, J. M. Harman-Thomas, R. E. Lade, K. M. Douglas, and J. M. C. Plane, "Kinetic study of the reactions of AIO and OAIO relevant to planetary mesospheres," *ACS Earth and Space Chemistry*, vol. 4, no. 11, pp. 2007-2017, 2020/11/19 2020, doi: 10.1021/acsearthspacechem.0c00197.

## **A. Raw IDT Data**

This Appendix section details the raw ignition delay time data recorded as part of this EngD thesis.

### **A.1. Hydrogen IDT Data**

The details of this work are contained within Section 4 available for publication in Fuel [88]. Table A.1 to Table A.8 give the IDT and temperature and pressure of the respective data points for the eight different hydrogen mixtures studied. Table A.9 details the uncertainty range in the experimental data points as well as the average non-ideal pressure rise (dp/dt).

**Table A.1.** IDT data for hydrogen mixture 1 (\* denotes sidewall measurement).

<b>Solution No</b>	<b>T5 (K)</b>	<b>P5 (bar)</b>	<b>IDT (microsec)</b>
1	1103.4	21.7	1250*
2	1119.2	20.5	1030*
3	1140	21.2	670
4	1174.5	21.2	422
5	1182.7	21.5	341
6	1200	21.4	273
7	1215.7	20.9	220
8	1243.8	20.9	133

**Table A.2.** IDT data for hydrogen mixture 2.

<b>Solution No</b>	<b>T5 (K)</b>	<b>P5 (bar)</b>	<b>IDT (microsec)</b>
1	1142.3	19.4	680
2	1160	19.6	562
3	1164.8	19.2	528
4	1199.8	19.2	354

5	1221.4	18.5	237
6	1240.6	19.1	186
7	1261.4	19.1	145

**Table A.3.** IDT data for hydrogen mixture 3.

<b>Solution No</b>	<b>T5 (K)</b>	<b>P5 (bar)</b>	<b>IDT (microsec)</b>
1	1059.4	20.2	1812
2	1089.2	20.5	1130
3	1099.7	20.4	956
4	1122.4	20.2	609
5	1146.4	20	419
6	1169.2	19.6	241
7	1199.2	19.4	117
8	1214	19.2	77

**Table A.4.** IDT data for hydrogen mixture 4.

<b>Solution No</b>	<b>T5 (K)</b>	<b>P5 (bar)</b>	<b>IDT (microsec)</b>
1	1133.8	20.5	753
2	1163.2	20.7	456
3	1183.5	20.6	339
4	1212	20.2	220
5	1237.9	20.2	152
6	1123.3	21	900

**Table A.5.** IDT data for hydrogen mixture 5.

<b>Solution No</b>	<b>T5 (K)</b>	<b>P5 (bar)</b>	<b>IDT (microsec)</b>
1	1192	19.4	395
2	1225	19.5	231

<b>3</b>	1255	19.4	150
<b>4</b>	1162	19.9	544

**Table A.6.** IDT data for hydrogen mixture 6.

<b>Solution No</b>	<b>T5 (K)</b>	<b>P5 (bar)</b>	<b>IDT (microsec)</b>
<b>1</b>	1302	42	116
<b>2</b>	1288.8	42.6	144
<b>3</b>	1254.8	42	206
<b>4</b>	1218.2	42	303
<b>5</b>	1204.1	43	373

**Table A.7.** IDT data for hydrogen mixture 7.

<b>Solution No</b>	<b>T5 (K)</b>	<b>P5 (bar)</b>	<b>IDT (microsec)</b>
<b>1</b>	1299.8	41.7	106
<b>2</b>	1261.1	42.1	177
<b>3</b>	1235.2	42.1	224
<b>4</b>	1206.3	41.9	313
<b>5</b>	1182.8	41.7	460
<b>6</b>	1164	41.4	516

**Table A.8.** IDT data for hydrogen mixture 8.

<b>Solution No</b>	<b>T5 (K)</b>	<b>P5 (bar)</b>	<b>IDT (microsec)</b>
<b>1</b>	1225.4	41.5	205
<b>2</b>	1199.2	41.4	300
<b>3</b>	1167.5	41.2	418
<b>4</b>	1141.3	40.7	580
<b>5</b>	1265.6	41.6	137
<b>6</b>	1123.7	40.5	701

**Table A.9.** Mixture uncertainty and pressure rise for hydrogen IDT datasets.

Mixture No.	Uncertainty (%)	dp/dt (%/ms)
1	15-20	2.5
2	15-20	3.0
3	10-15	2.0
4	10-15	2.0
5	10-15	2.0
6	20	2.0
7	20	2.0
8	20	2.0

## A.2. Syngas IDT Data

This data was recorded using the KAUST HPST as part of a publication in Fuel [89]. The details of this work are contained in Section 4. Table A.10 to Table A.17 give the IDT and temperature and pressure of the respective data points for the eight different syngas mixtures studied. Table A.18 details the uncertainty range in the experimental data points as well as the average non-ideal pressure rise (dp/dt).

**Table A.10.** IDT data for syngas mixture 1.

Solution No	T5 (K)	P5 (bar)	IDT (microsec)
1	1134.9	22	764
2	1145.3	21.4	686
3	1172	21.1	445
4	1190	20.9	330
5	1212.1	20.6	228
6	1225.7	19.9	176
7	1231.1	20.1	157
8	1257.4	19.9	90

**Table A.11.** IDT data for syngas mixture 2.

<b>Solution No</b>	<b>T5 (K)</b>	<b>P5 (bar)</b>	<b>IDT (microsec)</b>
1	1102	21.3	1005
2	1123.2	21.4	736
3	1134.9	21.1	598
4	1160	21.3	369
5	1165.1	20.6	336
6	1182.7	20.4	270
7	1208.2	20.3	180
8	1231.1	20.2	121

**Table A.12.** IDT data for syngas mixture 3.

<b>Solution No</b>	<b>T5 (K)</b>	<b>P5 (bar)</b>	<b>IDT (microsec)</b>
1	1155.4	21.2	987
2	1173.9	21	726
3	1191.9	20.8	640
4	1209.7	20.5	447
5	1232.2	20.4	333
6	1258	20.3	202
7	1292.7	20.4	97

**Table A.13.** IDT data for syngas mixture 4.

<b>Solution No</b>	<b>T5 (K)</b>	<b>P5 (bar)</b>	<b>IDT (microsec)</b>
1	1187.1	20.7	523
2	1173	21.1	663
3	1155.5	21.2	799
4	1142.3	21.3	892

<b>5</b>	1211.5	20.3	329
<b>6</b>	1234.2	20.6	209
<b>7</b>	1262	20.1	135
<b>8</b>	1278.9	20	90

**Table A.14.** IDT data for syngas mixture 5.

<b>Solution No</b>	<b>T5 (K)</b>	<b>P5 (bar)</b>	<b>IDT (microsec)</b>
<b>1</b>	1126.5	20.4	878
<b>2</b>	1144.8	20.3	628
<b>3</b>	1161.1	20.1	462
<b>4</b>	1170.4	19.6	384
<b>5</b>	1189.3	19.5	266
<b>6</b>	1202	19.1	183

**Table A.15.** IDT data for syngas mixture 6.

<b>Solution No</b>	<b>T5 (K)</b>	<b>P5 (bar)</b>	<b>IDT (microsec)</b>
<b>1</b>	1135.2	20.4	1036
<b>2</b>	1154.2	20.2	883
<b>3</b>	1192.8	20.8	451
<b>4</b>	1179.2	20.7	612
<b>5</b>	1230.6	20.5	227
<b>6</b>	1241.6	20.41	174
<b>7</b>	1266.5	20.2	120

**Table A.16.** IDT data for syngas mixture 7.

<b>Solution No</b>	<b>T5 (K)</b>	<b>P5 (bar)</b>	<b>IDT (microsec)</b>
<b>1</b>	1139.2	20	499
<b>2</b>	1100.7	20.3	885

3	1124.3	20.4	612
4	1160.8	19.9	344
5	1183.9	19.8	228
6	1210.4	19.9	150
7	1225.7	19.8	105

**Table A.17.** IDT data for syngas mixture 8 (\* denotes sidewall measurement).

<b>Solution No</b>	<b>T5 (K)</b>	<b>P5 (bar)</b>	<b>IDT (microsec)</b>
1	1302	43.77	131
2	1211.3	40.5	371
3	1258	43.9	228
4	1193	42.6	443
5	1165.8	42.7	536
6	1145.1	42.3	622*

**Table A.18.** Mixture uncertainty and pressure rise for syngas IDT datasets.

<b>Mixture No.</b>	<b>Uncertainty (%)</b>	<b>dp/dt (%/ms)</b>
1	15-20	2.5
2	15-20	2.5
3	10-15	2.5
4	10-15	2.5
5	10-15	2.5
6	20	2.0
7	20	2.0
8	20	3.0

### **A.3. Methane and Methane/Hydrogen IDT Data**

The data listed in this section are discussed in Chapter 5 and are currently being worked on for subsequent publication. Table A.19 to Table A.28 give the sidewall and endwall IDTs determined for the ten different datasets recorded and Table A.29 the mixture uncertainty.

**Table A.19.** IDT data for mixture 1 at 20 bar.

<b>Mixture 1 – 20 bar</b>			<b>IDT (microsec)</b>	
<b>Solution No</b>	<b>T5 (K)</b>	<b>P5 (bar)</b>	<b>Sidewall</b>	<b>Endwall</b>
1	1387	20.7	149	231
2	1336	20.9	255	356
3	1305	21.2	354	404
4	1425	20.3	101	177
5	1286	21.9	415	456
6	1263	22.0	514	587

**Table A.20.** IDT data for mixture 1 at 40 bar.

<b>Mixture 1 – 40 bar</b>			<b>IDT (microsec)</b>	
<b>Solution No</b>	<b>T5 (K)</b>	<b>P5 (bar)</b>	<b>Sidewall</b>	<b>Endwall</b>
1	1315	40.4	245	269
2	1340	40.0	193	247
3	1269	39.4	402	435
4	1257	39.5	449	482
5	1313	39.0	261	313
6	1360	39.7	168	202

**Table A.21.** IDT data for mixture 2 for 20 bar.

<b>Mixture 2 – 20 bar</b>			<b>IDT (microsec)</b>	
<b>Solution No</b>	<b>T5 (K)</b>	<b>P5 (bar)</b>	<b>Sidewall</b>	<b>Endwall</b>
1	1148	19.1	1187	1160
2	1164	18.7	1027	1053
3	1207	19.5	556	562
4	1197	18.8	649	654

5	1221	18.9	503	506
6	1239	18.6	411	416
7	1285	18.8	231	237
8	1295	18.3	205	206

**Table A.22.** IDT data for mixture 2 for 40 bar.

Mixture 2 – 40 bar			IDT (microsec)	
Solution No	T5 (K)	P5 (bar)	Sidewall	Endwall
1	1141	35.6	838	827
2	1189	37.2	542	536
3	1223	37.3	376	366
4	1268	37.3	208	208

**Table A.23.** IDT data for mixture 3 for 20 bar.

Mixture 3 – 20 bar			IDT (microsec)	
Solution No	T5 (K)	P5 (bar)	Sidewall	Endwall
1	1502	19.9	146	248
2	1542	19.8	89	165
3	1458	20.0	220	320
4	1574	19.9	68	144
5	1430	20.0	299	444

**Table A.24.** IDT data for mixture 3 for 40 bar.

Mixture 3 – 40 bar			IDT (microsec)	
Solution No	T5 (K)	P5 (bar)	Sidewall	Endwall
1	1486	40.7	142	180
2	1512	39.8	114	127

<b>3</b>	1473	41.2	163	186
<b>4</b>	1409	39.8	343	378
<b>5</b>	1387	39.5	391	468

**Table A.25.** IDT data for mixture 4 for 20 bar.

<b>Mixture 4 – 20 bar</b>			<b>IDT (microsec)</b>	
<b>Solution No</b>	<b>T5 (K)</b>	<b>P5 (bar)</b>	<b>Sidewall</b>	<b>Endwall</b>
<b>1</b>	1504	20.1	238	313
<b>2</b>	1503	20.4	249	291
<b>3</b>	1509	21.0	254	307
<b>4</b>	1505	20.9	256	280
<b>5</b>	1481	20.7	326	389
<b>6</b>	1456	20.4	418	488
<b>7</b>	1446	20.5	433	494
<b>8</b>	1537	19.9	167	195
<b>9</b>	1554	19.9	136	182
<b>10</b>	1433	20.6	458	507

**Table A.26.** IDT data for mixture 4 for 40 bar.

<b>Mixture 4 – 40 bar</b>			<b>IDT (microsec)</b>	
<b>Solution No</b>	<b>T5 (K)</b>	<b>P5 (bar)</b>	<b>Sidewall</b>	<b>Endwall</b>
<b>1</b>	1442	39.2	295	312
<b>2</b>	1480	40.0	235	261
<b>3</b>	1479	39.3	231	244
<b>4</b>	1431	39.9	364	383

**Table A.27.** IDT data for mixture 5 for 20 bar.

Mixture 5 – 20 bar			IDT (microsec)	
Solution No	T5 (K)	P5 (bar)	Sidewall	Endwall
1	1548	20.2	196	230
2	1577	19.5	151	183
3	1519	20.3	309	351
4	1480	20.4	476	546
5	1614	19.1	108	113

**Table A.28.** IDT data for mixture 5 for 40 bar.

Mixture 5 – 40 bar			IDT (microsec)	
Solution No	T5 (K)	P5 (bar)	Sidewall	Endwall
1	1521	38.5	273	320
2	1507	35.6	284	314
3	1587	36.9	135	145
4	1470	38.1	392	431

**Table A.29.** Mixture uncertainty for the IDT datasets investigated.

Mixture No.	Pressure (bar)	Uncertainty (%)
1	20	20
	40	20
2	20	15
	40	15
3	20	15
	40	20
4	20	20
	40	20
5	20	20
	40	20

## B. UoS sCO<sub>2</sub> 1.0 Modelled IDT Data

The IDT data plots of the 52 datasets of methane, hydrogen and syngas combustion modelled by AramcoMech 2.0, DTU, GRI 3.0 and USC II and UoS sCO<sub>2</sub> 1.0 as modelled and discussed in Section 3.

### Hargis and Petersen (2015) [122]

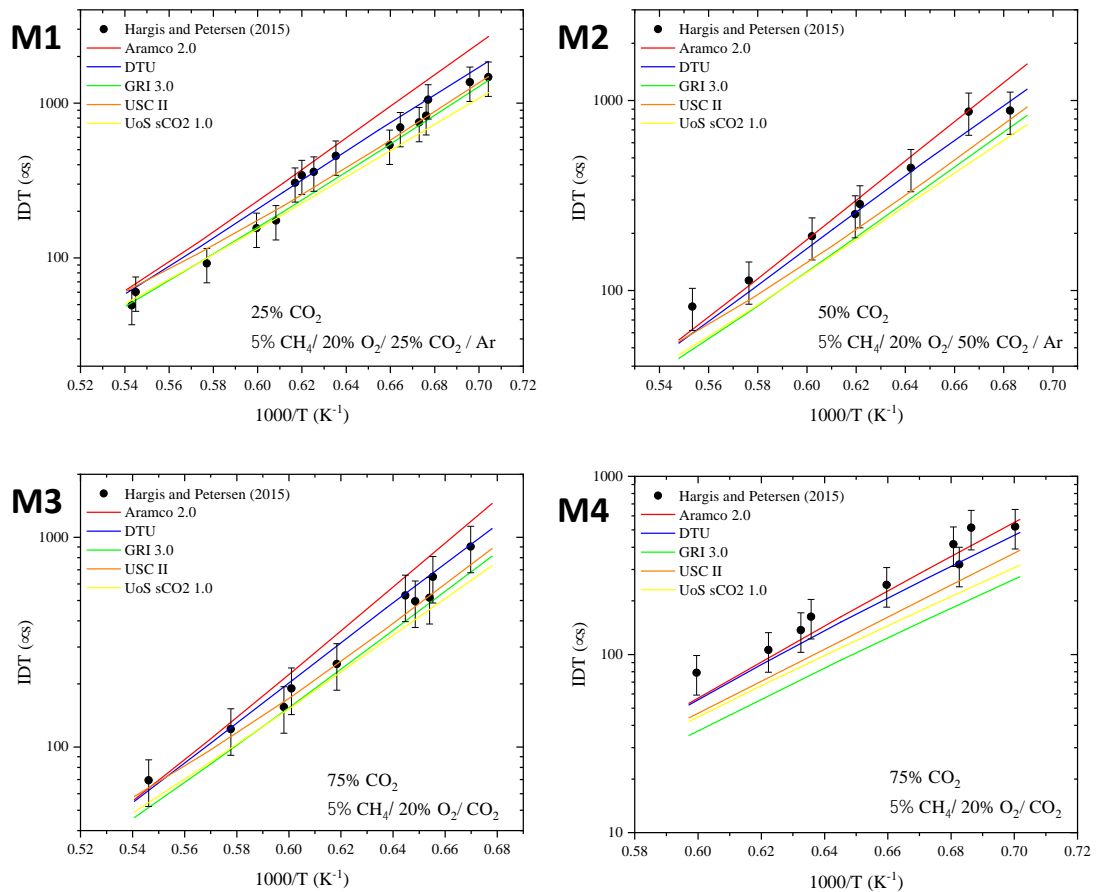


Figure B.1. Hargis and Petersen (2015) M1-M4 datasets [122].

Koroglu et al. (2016) [153]

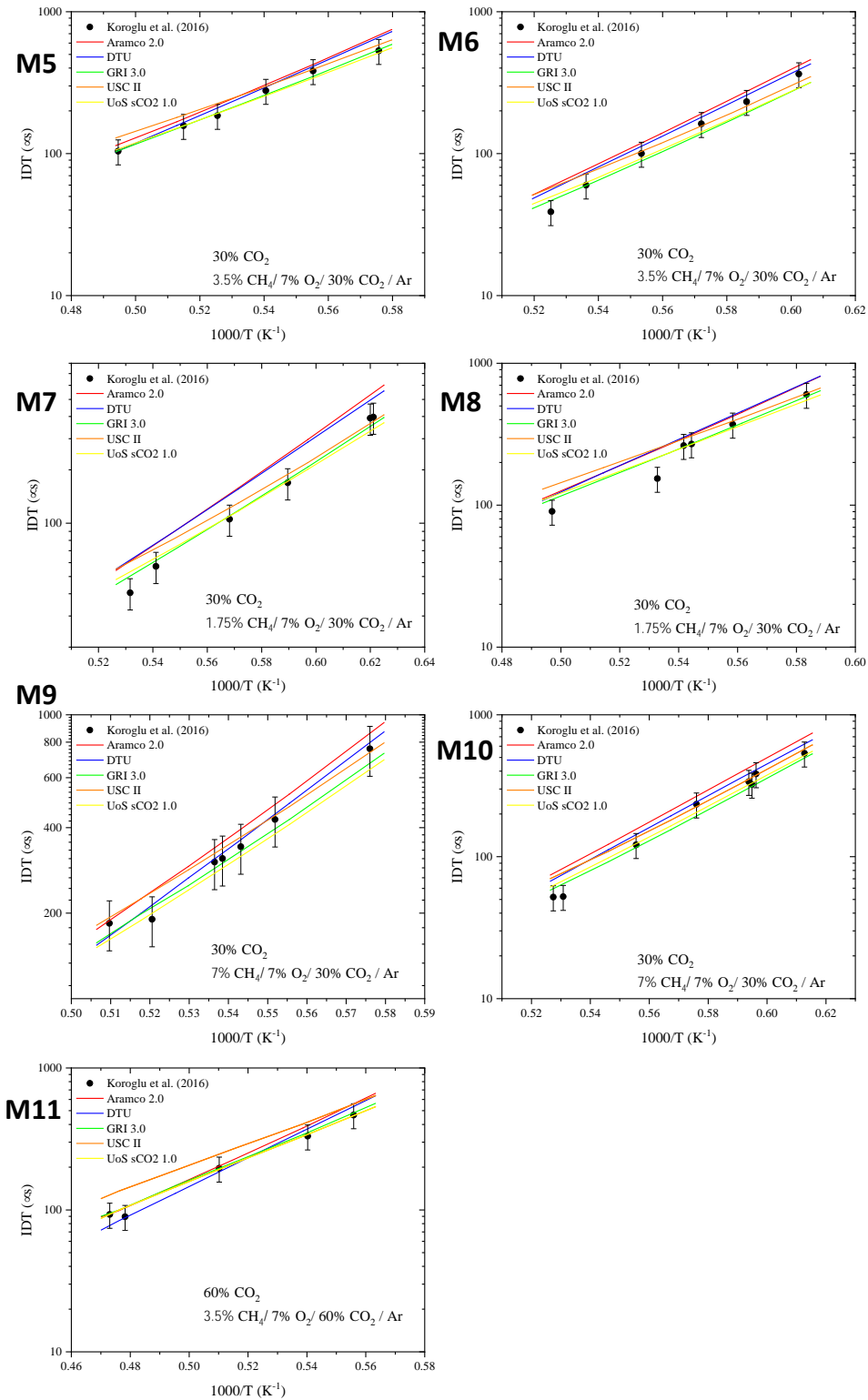


Figure B.2. Koroglu et al. (2016) M5-M11 datasets [122].

Pryor et al. (2017a) [194]

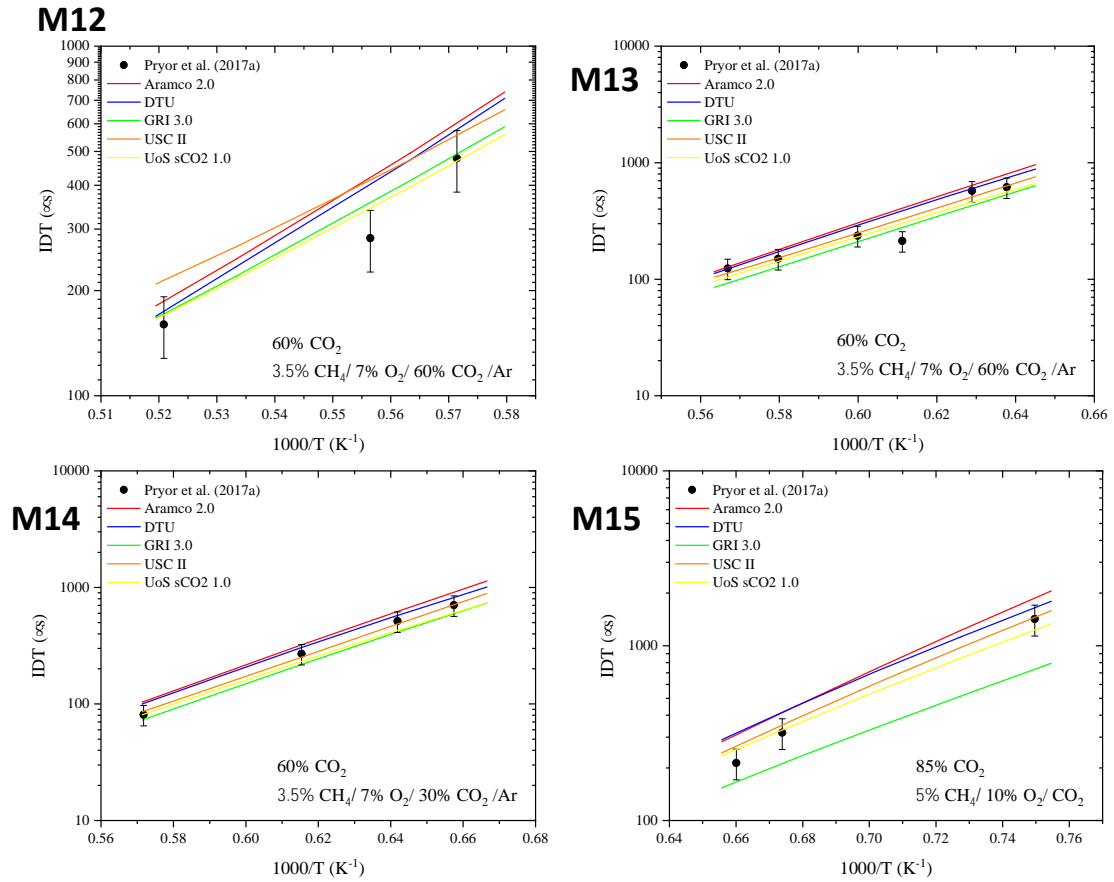


Figure B.3. Pryor et al. (2017a) M12-M15 datasets.

Pryor et al. (2017b) [195]

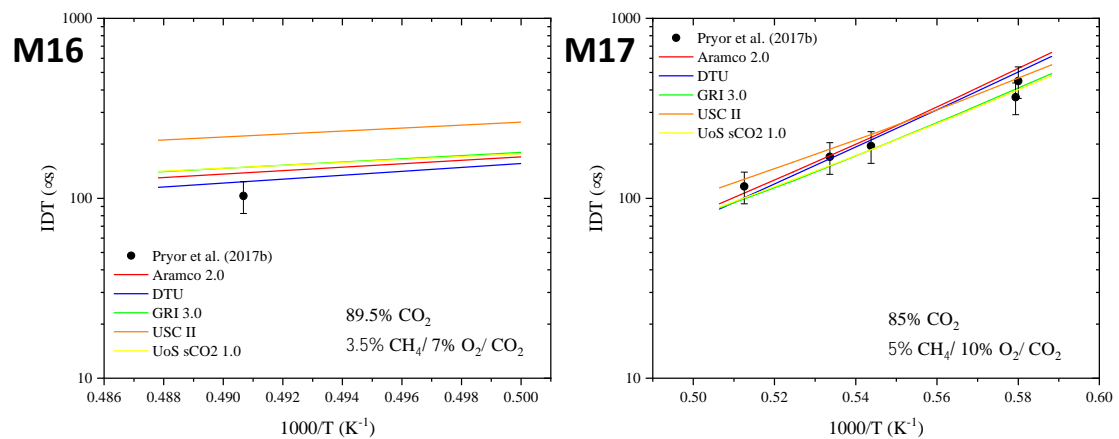


Figure B.4. Pryor et al. (2017b) M16-M17 datasets.

Liu et al. (2018) [151]

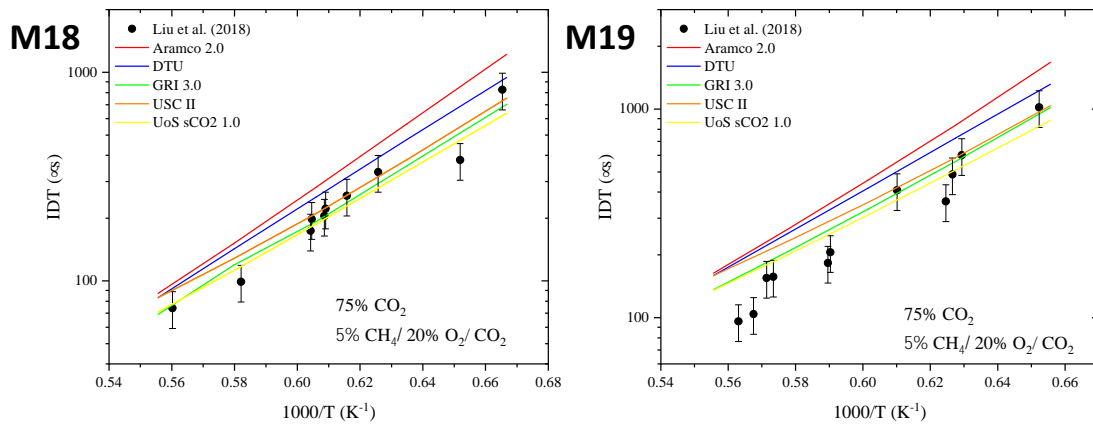


Figure B.5. Liu et al. (2018) M18-M19 datasets [151].

Shao et al. (2019) [85]

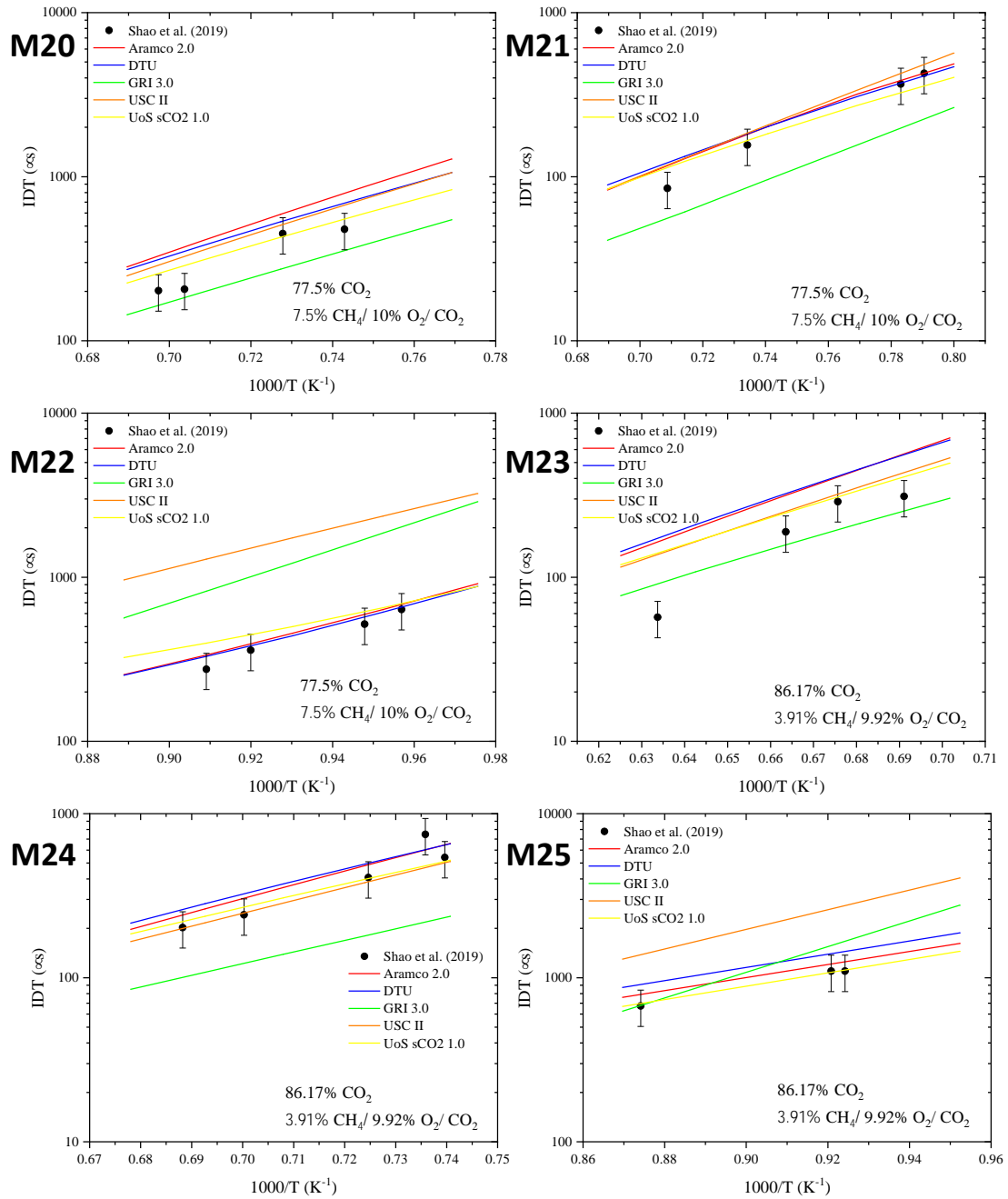
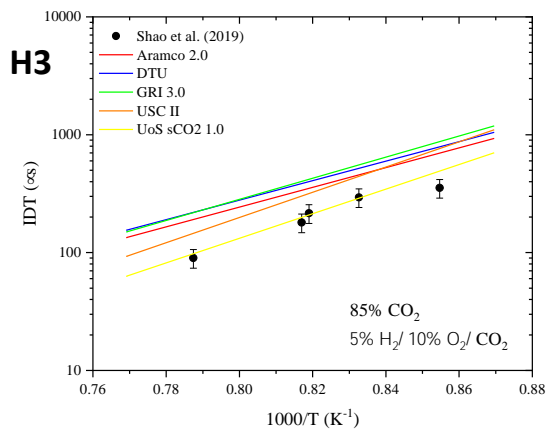
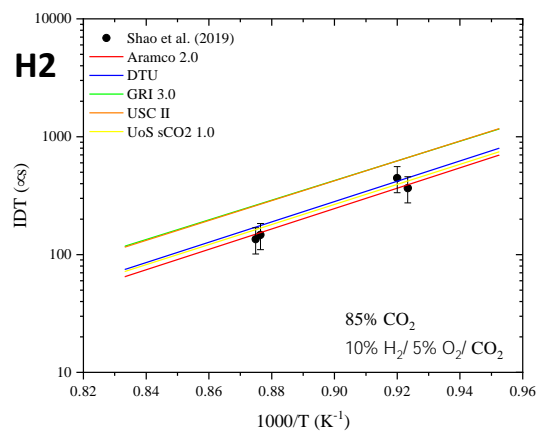
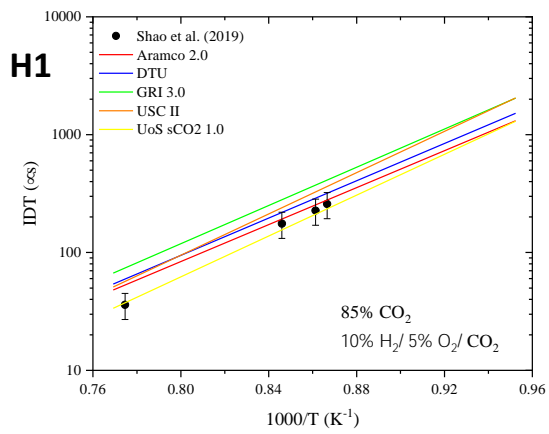


Figure B.6. Shao et al. (2019) M20-M25 dataset.



**Figure B.7.** Shao et al. (2019) M20-M25 dataset.

Karimi et al. (2019) [127]

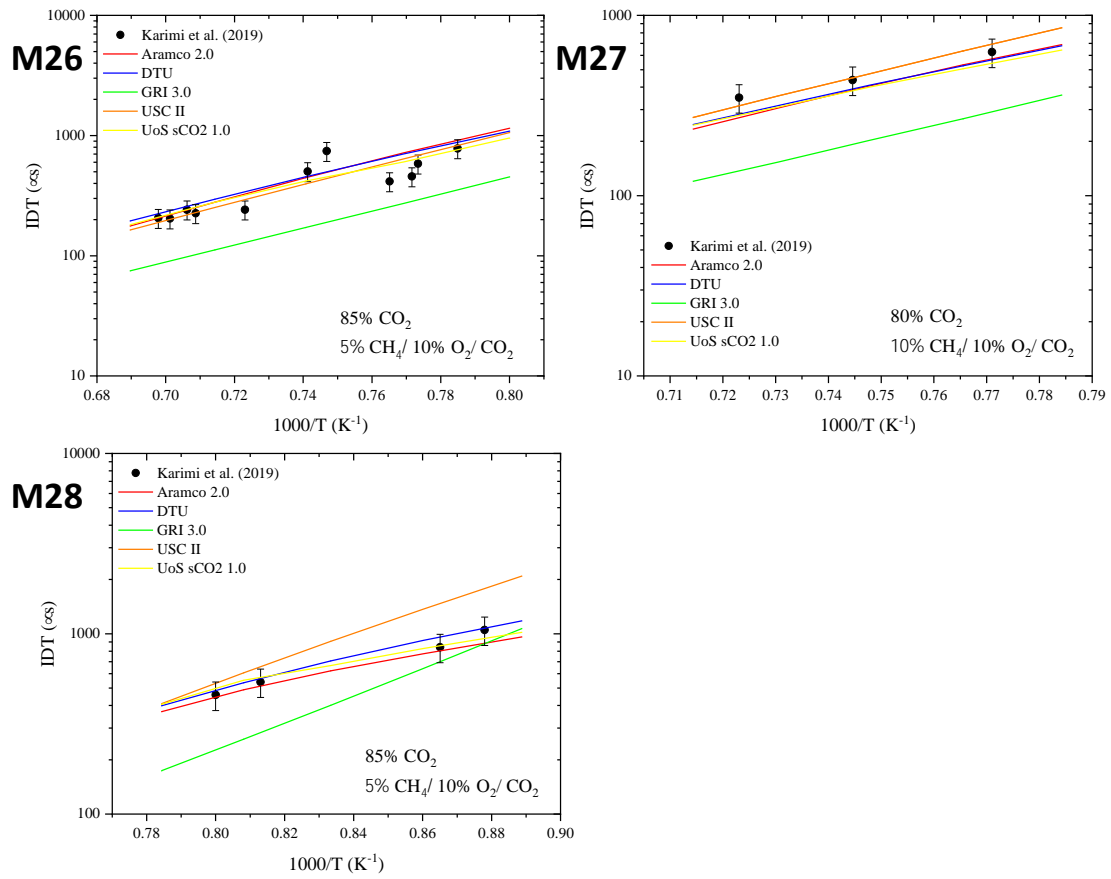


Figure B.8. Karimi et al. (2019) M26-M28 datasets [127].

Barak et al. (2020) [192]

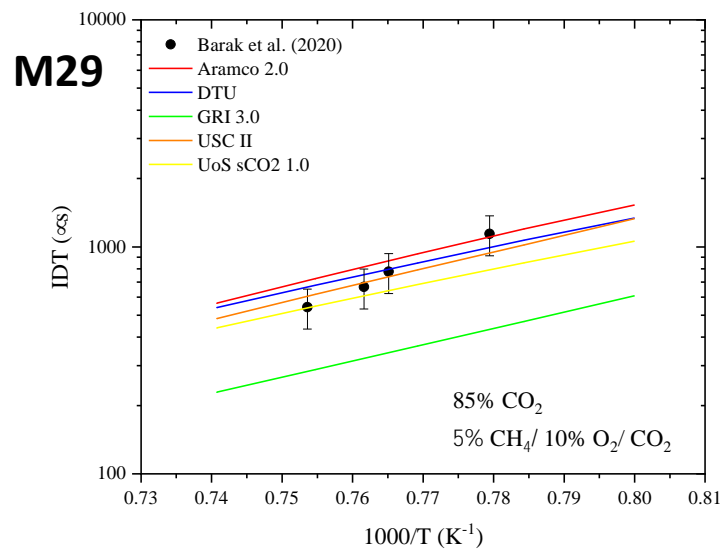


Figure B.9. Barak et al. (2020) M29 dataset [192].

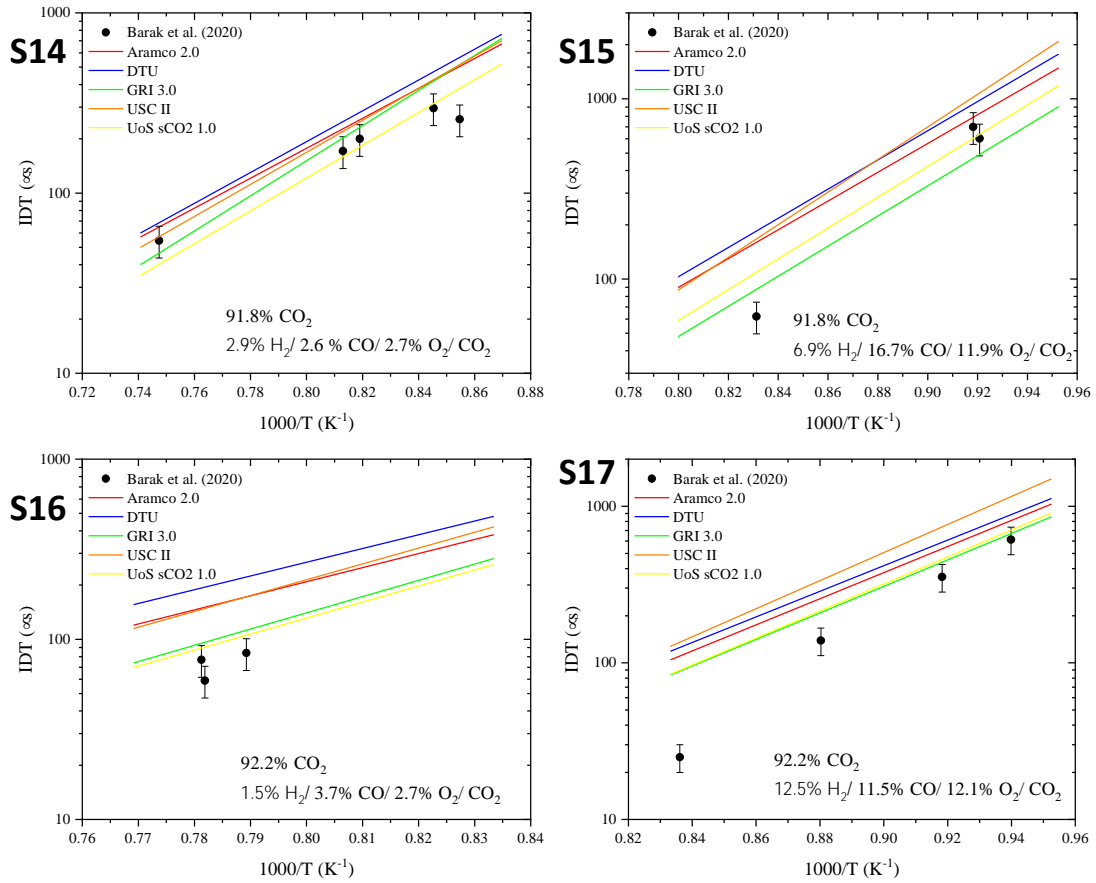


Figure B.10. Barak et al. (2020) S14-S17 dataset [192].

Vasu et al. (2011) [353]

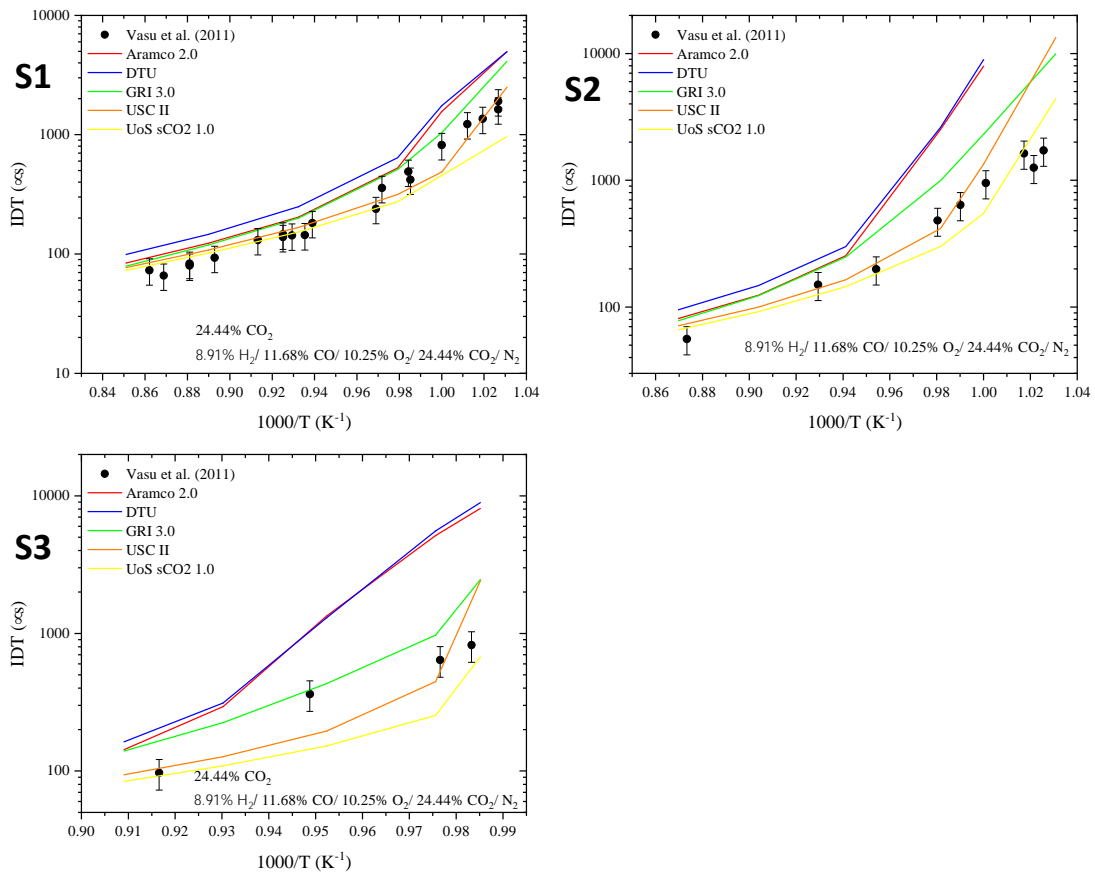


Figure B.11. Vasu et al. (2011) S1-S3 datasets [353].

Barak et al. (2017) [198]

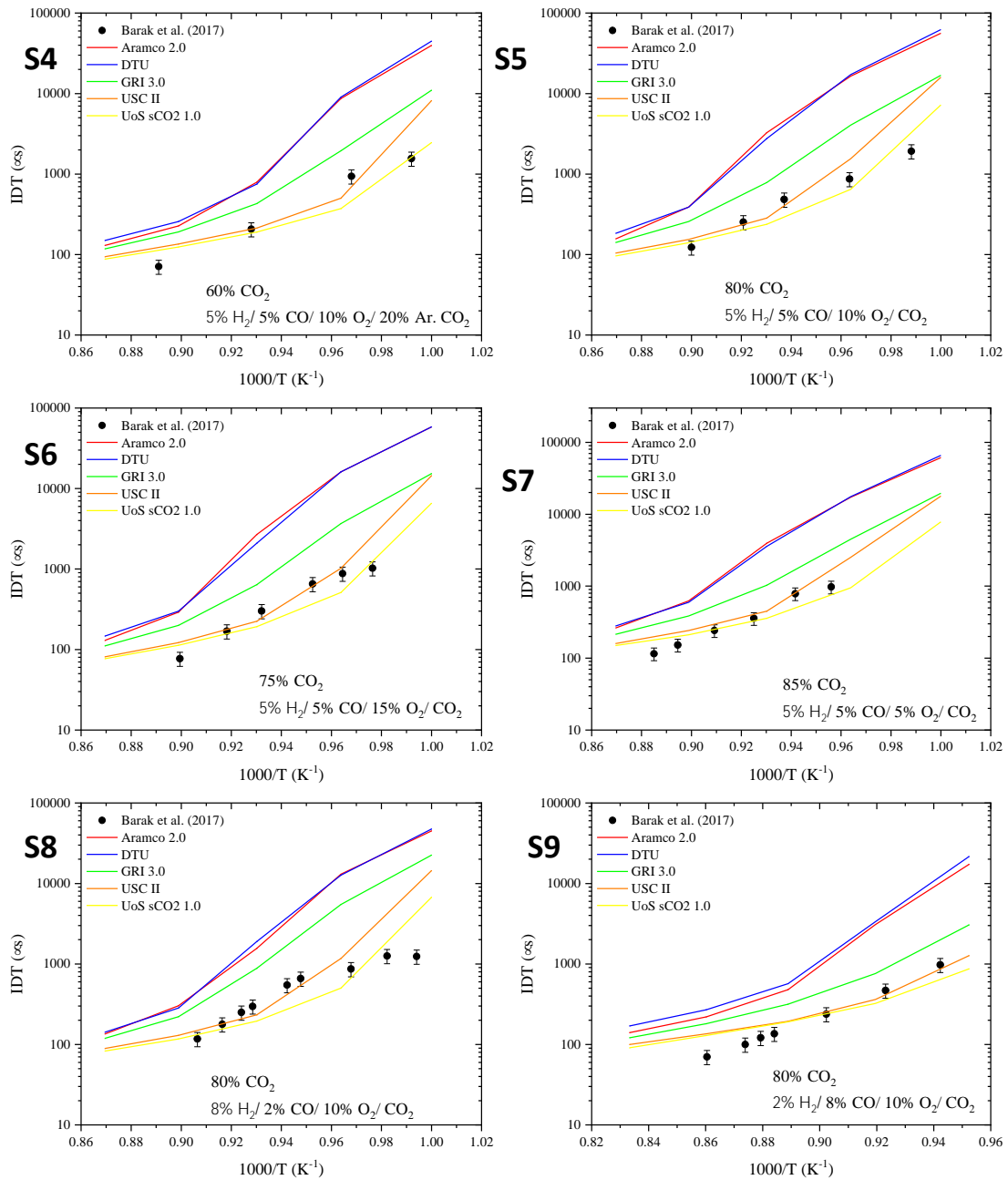


Figure B.12. Barak et al. (2017) S4-S9 datasets [198].

Barak et al. (2019) [199]

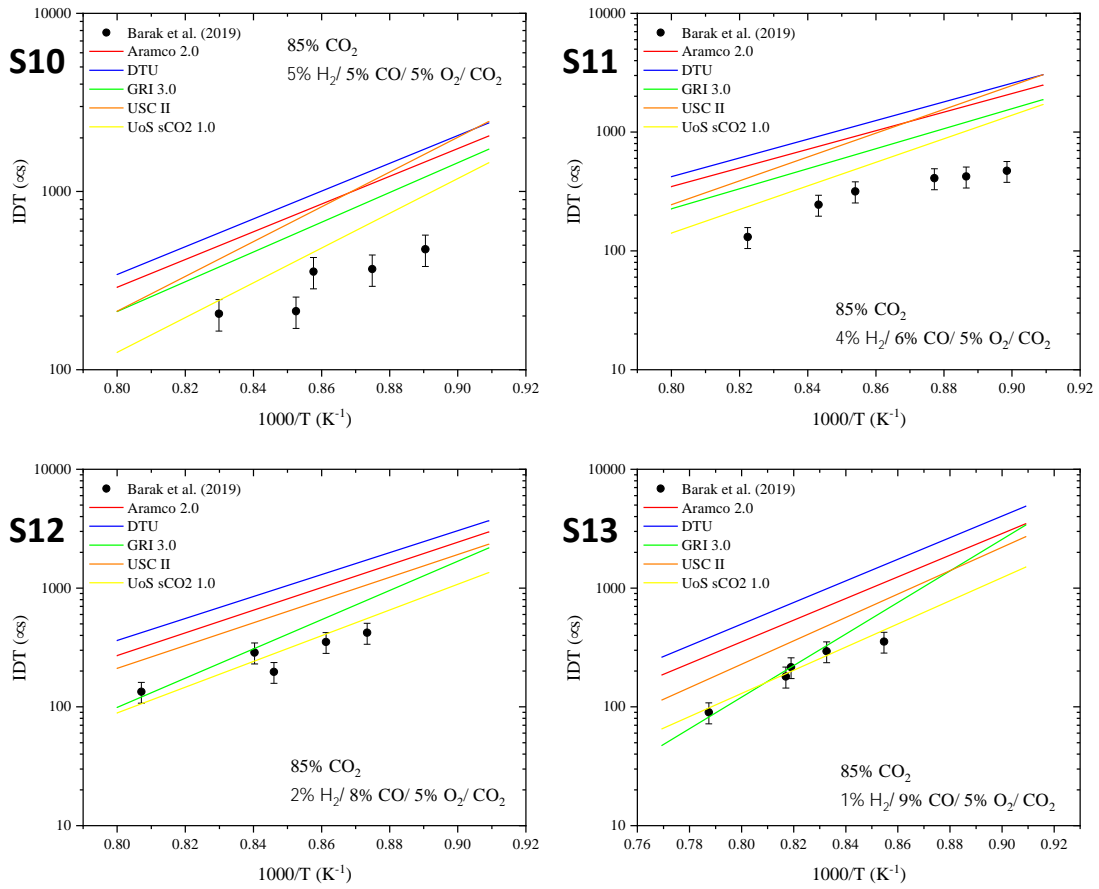


Figure B.13. Barak et al. (2019) S10-S13 datasets.

Karimi et al. (2020) [200]

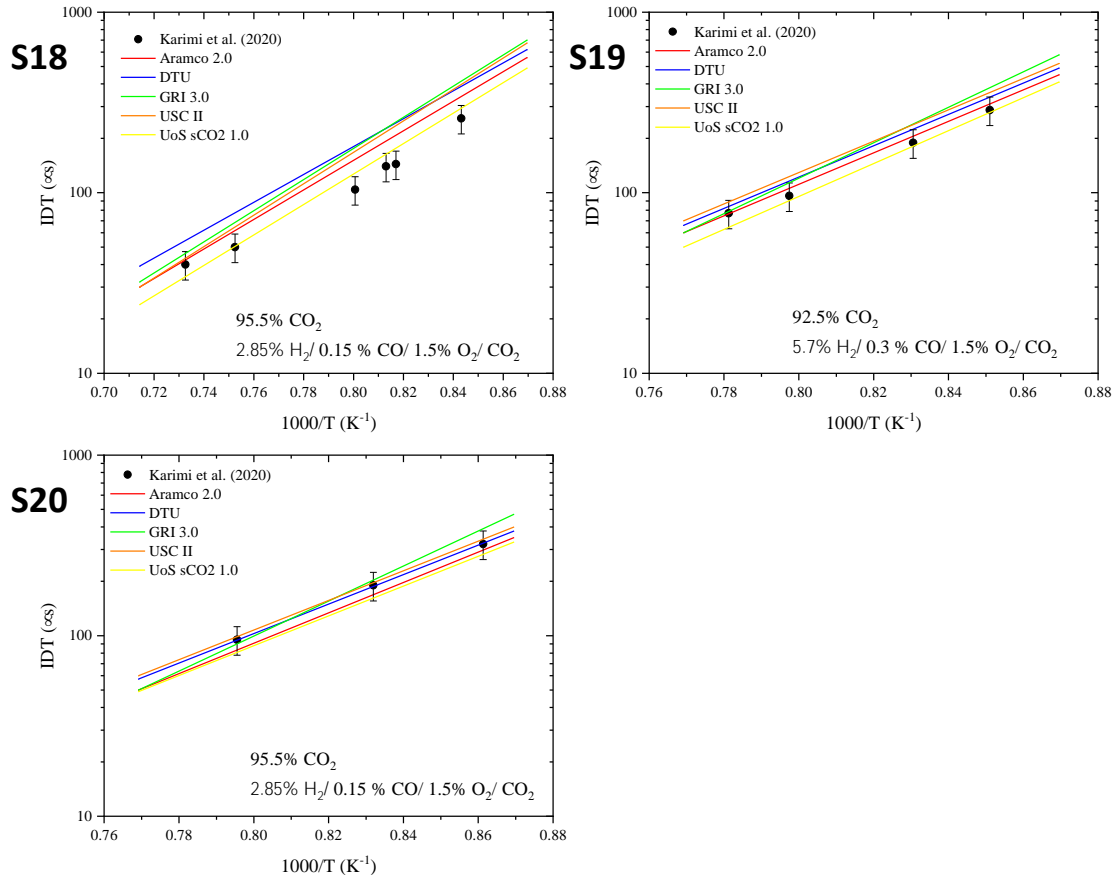


Figure B.14. Karimi et al. (2020) S18-S20 dataset [200].

## **C. Publication Output**

The work from this EngD project has been published and presented at as many opportunities as possible. Whilst the Covid-19 pandemic has significantly impacted the number of in-person meetings and presentations at work, every effort has been made to ensure a good level of in-person presentations.

### **C.1. Poster Presentations**

Royal Society of Chemistry (RSC) Faraday Joint Interest Group Conference, Online, 29<sup>th</sup>-31<sup>st</sup> March 2021.

Online poster presentation on the same work from the conference paper presented at the 4<sup>th</sup> European sCO<sub>2</sub> Conference for Energy Systems [Online].

1<sup>st</sup> FERIA Conference, Nottingham, UK, 6<sup>th</sup>-8<sup>th</sup> September 2021.

In-person conference presentation at the University of Nottingham presenting the work of the FUEL publication in the VSI of the work detailed in Section 3 from the 4<sup>th</sup> European sCO<sub>2</sub> Conference for Energy Systems.

CDT for Resilient Decarbonised Fuel Energy Systems, Spring School, Cardiff, UK, 25<sup>th</sup>-29<sup>th</sup> April 2022.

Annual CDT conference at the Mercure hotel in Cardiff. Presented a poster on the chemical kinetic modelling work which was previously presented at the 1<sup>st</sup> FERIA conference.

The University of Sheffield Mechanical Engineering 2<sup>nd</sup> Year Poster Presentation, Sheffield, UK, 14 June 2022.

Requirement for EngD completion at the University of Sheffield. Poster presentation on the development of a high-pressure shock tube.

IFRF TOTeM – Hydrogen for Decarbonisation, Paris, UK, 13<sup>th</sup> October 2022.

In-person meeting in Versailles, Paris at the Air Liquide campus on hydrogen as a future fuel hosted by the IFRF.

## **C.2. Conference Presentations**

The 4<sup>th</sup> European sCO<sub>2</sub> Conference for Energy Systems, Online, 23<sup>rd</sup>-24<sup>th</sup> March 2021.

Conference paper on the creation of a new chemical kinetic mechanism to model IDT data of methane, hydrogen and syngas combustion in a CO<sub>2</sub> bath gas and pressures more than 10 bar. This work is detailed in Section 4.4.4.

Available: <https://www.sco2.eu/conference-repository/4th-conference-online/>

1<sup>st</sup> FERIA Conference, Nottingham, UK, 6<sup>th</sup>-8<sup>th</sup> September 2021.

In-person conference presentation at the University of Nottingham presenting the work of the FUEL publication in the VSI of the work detailed in Section 3 from the 4<sup>th</sup> European sCO<sub>2</sub> Conference for Energy Systems.

CDT for Resilient Decarbonised Fuel Energy Systems Autumn School, Nottingham, UK, 8<sup>th</sup>-10<sup>th</sup> September 2021.

In-person presentation of an update of all my work undertaken so far on the PhD including modelling work and the fabrication of the shock tube at the Park Plaza Nottingham.

## **C.3. Conference Papers**

The 4<sup>th</sup> European sCO<sub>2</sub> Conference for Energy Systems, Online, 23<sup>rd</sup>-24<sup>th</sup> March 2021 [86].

*Chemical Kinetic Mechanism for Combustion in Supercritical Carbon Dioxide*

Conference paper on the creation of a new chemical kinetic mechanism to model IDT data of methane, hydrogen and syngas combustion in a CO<sub>2</sub> bath gas and pressures more than 10 bar. This work is detailed in Section 3.

Available: [https://duepublico2.uni-due.de/receive/duepublico\\_mods\\_00073944](https://duepublico2.uni-due.de/receive/duepublico_mods_00073944)

#### **C.4. Journal Papers**

Energy, Volume 255 (124490), Available online 16<sup>th</sup> June 2022 [87].

*The Development of a Chemical Kinetic Mechanism for Combustion in Supercritical Carbon Dioxide*

Expansion of the conference paper from the 4<sup>th</sup> European sCO<sub>2</sub> Conference for Energy Systems included in a virtual special edition of Energy.

Available:

<https://www.sciencedirect.com/science/article/pii/S0360544222013937?via%3Dihub>

Fuel, Volume 334 Part 1 (126664), Available online 13<sup>th</sup> November 2023 [88].

*Experimental and Modelling Study of Hydrogen Ignition in CO<sub>2</sub> Bath Gas.*

Discussion on the chemical kinetics of H<sub>2</sub> combustion in CO<sub>2</sub> using shock tube experiments at 20 and 40 bar as reported in Chapter 4.

Available:

<https://www.sciencedirect.com/science/article/pii/S0016236122034883?via%3Dihub>

Fuel, Volume 342 (127865), Available online 24<sup>th</sup> February 2023 [89].

*Experimental and Modelling Study of Syngas Combustion in CO<sub>2</sub> Bath Gas.*

Discussion of chemical kinetics of syngas mixtures at various pressures and equivalence ratios over large temperature ranges.

Available:

<https://www.sciencedirect.com/science/article/pii/S0016236123004787>

International Journal of Chemical Kinetics, 2023 1-13. Available online: 11<sup>th</sup> June 2023.

*Role of methyl peroxy radical chemistry in high-pressure methane combustion in CO<sub>2</sub>*

Investigation Into the role of the methyl peroxy radical at high pressures and CO<sub>2</sub> dilution relevant to direct fired supercritical CO<sub>2</sub> power cycles.

Available: <https://onlinelibrary.wiley.com/doi/full/10.1002/kin.21672>

## C.5. Online/Magazine Articles

### International Flame Research Federation

*IFRF supports another student at UK Centre for Doctoral Training*

Available: <https://ifrf.net/ifrf-blog/ifrf-supports-another-student-at-uk-centre-for-doctoral-training/>

Published: 2<sup>nd</sup> March 2020

Introduction to me and my project written by Philip Sharman with some project and personal details input by myself.

*IFRF-supervised student to investigate the 'Allam-Fetvedt' Cycle through Centre for Doctoral Training*

Available: <https://ifrf.net/ifrf-blog/ifrf-supervised-student-to-investigate-the-allam-fetvedt-cycle-through-centre-for-doctoral-training/>

Published: 25<sup>th</sup> May 2020

The foreword of the article written by Philip Sharman introduces the article I had written which introduces my research project and outlines the aims of my work.

### Resonance: Issue 12, Spring 2020

*Fossil Fuel Combustion with Zero-Emissions: Is it a Pipeline Dream?*

Available: [https://issuu.com/scienceatsheffield/docs/resonance\\_issue\\_12](https://issuu.com/scienceatsheffield/docs/resonance_issue_12)

Published: Spring 2020

Resonance is a student-led magazine within the Department of Chemistry at the University of Sheffield. My article on the Allam cycle was featured as a full-page piece within the research section of the issue.

### **Doctoral Times: Issue 20, Spring 2020**

*PhDad*

Available: <https://www.flipsnack.com/Tuostimes/doctoral-student-journey-part-1-experiences-challenges.html>

Published: Spring 2020

The Doctoral Times is a magazine published by the University of Sheffield for current and potential postgraduate students. My article was on balancing the postgraduate workload with parental responsibilities.

### **Good News Science Week, 2021**

*Zero-Emissions Electricity Generation from Fossil Fuels, coming to the UK?*

Available: <https://twitter.com/sheffielduni/status/1369964903713406977>

Published: 11<sup>th</sup> March 2021

A two-minute video covering the Allam cycle and the potential for a new Allam-cycle power plant to be constructed in Teesside, County Durham.

## **C.6. Previously Published Work**

*Kinetic Study of the Reactions of AIO and AIO Relevant to Planetary Mesospheres*

Thomas P. Mangan, James M. Harman-Thomas, Rachel E. Lade, Kevin M. Douglas, and John M. C. Plane\*. *ACS Earth Space Chem.* 2020, 4, 11, Publication Date: October 29, 2020 [354].

Available: <https://pubs.acs.org/doi/abs/10.1021/acsearthspacechem.0c00197>

## C.7. Published Mechanisms

This thesis discusses mechanisms that have been created to better model chemistry in CO<sub>2</sub>. There have been three iterations of the UoS sCO<sub>2</sub> mechanism that are available as supplementary material in the following publications.

UoS sCO<sub>2</sub> 1.0 - <https://doi.org/10.1016/j.energy.2022.124490>

UoS sCO<sub>2</sub> 2.0 - <https://doi.org/10.1016/j.fuel.2022.126664>

UoS sCO<sub>2</sub> 2.1 - <https://doi.org/10.1002/kin.21672>